Mass Spectrometry and Genetic Analysis of Biological Barrier Lipids

Clare Laura Louise Newell

University College London
and
The Francis Crick Institute
and
The National Physical Laboratory

Primary Supervisor: Dr Alex P. Gould (Crick)
Subsidiary Supervisors: Prof. Ian S. Gilmore (NPL),
Prof. Franck Pichaud (UCL)

A thesis submitted for the degree of
Doctor of Philosophy
University College London
March 2021

Declaration

I, Clare Laura Louise Newell, confirm that the work presented in this thesis is my own. Where information has been derived from other sources, I confirm that this has been indicated in the thesis.

Word count

Abstract 292/300

Impact statement 492/500

Total 60,979/100,000

Abstract

Malnutrition during embryonic development can have significant health ramifications for the adult organism. Such developmental programming effects have been studied in a variety of different organs but no research to date has looked at the largest organ in the body, the skin. One important and evolutionarily conserved role of the skin is to provide a lipid barrier against stresses in the external environment. Here, I utilise the short lifespan and powerful genetics of *Drosophila* melanogaster to investigate how cuticular barrier lipids are regulated by developmental diet and environmental stresses in the adult. The *Drosophila* cuticle is significantly different from the mammalian skin, yet both are coated with a waterproof lipid blend synthesised by specialised subepidermal cells - sebocytes in mammals and oenocytes in *Drosophila*. Research on the composition and regulation of lipid barriers has been hampered, at least in part, by the lack of methods for resolving surface lipids from intracellular lipids. I therefore optimise several techniques for analysing surface lipids, including a new cryogenic platform for mass spectrometry imaging. I demonstrate that developmental diet programmes the blend of adult cuticular lipids in both *Drosophila* and mice by increasing the adult skin wax esters. In *Drosophila*, I also show how adult environmental stresses impact upon the cuticle lipid blend. Combining mass spectrometry imaging with genetic analysis in *Drosophila*, I then identify a physiological feedback circuit that regulates the blend of adult cuticular hydrocarbons in response to increased housing density. This circuit involves the detection of housing density by an as yet unknown mechanism, information relay to oenocytes, and export of hydrocarbons to the cuticle surface via *Obp99b/Obp99d* odorant-binding proteins. Finally, I discuss the wider implications of this study and how mammals may regulate their skin lipids in line with a changing environment.

Impact statement

Animals develop from embryos into adults over a timescale that is generally much shorter than their lifespan. Nevertheless, the relatively short duration of development can exert a powerful influence on the future health of the organism throughout its life. Unfortunately, environmental conditions are rarely optimal in the real world. Factors with long-term negative effects during development include malnutrition, alcohol and drugs, all of which can increase the risk of non-communicable diseases of adulthood such as heart disease, hypertension and diabetes (the risk of which is 65% higher in those who experience severe malnutrition during development) (Portrait et al., 2011). These diseases put a significant strain on world health and current UK estimates show that 7.6 million live with a heart/vascular disease and 4 million with diabetes.

Studies on the effects of suboptimal developmental conditions on adult health and disease have largely neglected effects on the largest organ of the body – the skin. Skin diseases can have a large impact on quality of life, with 55% of the UK population thought to be affected (Rea et al., 1976). They result in a significant economic burden, both directly to the healthcare system and more indirectly via morbidity-related decreases in productivity (Basra and Shahrukh, 2009). A healthy skin needs to be covered by a blend of different lipids, which are an essential component of the protective barrier to a hostile external environment. Despite the relevance to health and also to the cosmetics industry, fundamental mechanistic research on skin lipids has been rather limited. In this thesis, I address this technical challenge by developing a cryogenic method of mass spectrometry imaging that enables lipids to be detected on the surface of the skin with high chemical and spatial precision. The potential applications of this new technique are extensive, ranging from the biomedical sciences to forensics and materials science.

In this thesis, I also apply the new cryogenic imaging method to study skin lipids in two model organisms, the fruit fly *Drosophila* and the mouse. In *Drosophila*, I have combined cryogenic imaging with state-of-the-art genetics to identify

molecular components of a novel feedback loop regulating the composition of skin lipids in response to environmental stress. Future work will determine if such a mechanism is also present in mammals, and if so would provide another avenue for investigating the cause of skin diseases where this homeostatic mechanism fails to operate correctly. For both *Drosophila* and mice, I show that malnutrition during development leads to long-lasting changes in the composition of skin lipids. This work demonstrates that, from insects to mammals, early life nutrition has a profound effect upon the lipid barrier of the skin. It also provides a foundation for future studies on how maternal/childhood nutrition influences the properties of human skin, with important implications for the societal and economic burden of skin disease. If successful, this could result in the implementation of preventative healthcare policies which could reduce the health, societal and economic burden of skin diseases.

Acknowledgements

I would first like to thank my supervisors Alex and Ian for all their guidance and support throughout my PhD. To Alex, for all your exciting hypotheses and countless hours spent discussing challenging results. To Ian, for introducing me to the world of SIMS in which I was a complete novice, and for providing constant encouragement throughout my PhD.

Many thanks to past and present members of the Gould Lab – Adrien, André, Andrew, Annick, Clara, Elisabeth, Eva, Fumiaki, Lena, Ola, Pata, Sebastian, Thari and Ying. Special thanks to Adrien and Pata who have always been there for discussion over a tea break, Lena, my hydrocarbon buddy and to Eva, my PhD twin, who has been there with words of encouragement from the start right up to the very end. To past and present members of the Gilmore Lab - Barry, Greg, Junting, Maria, Melissa, Rasmus and especially Jean-Luc who has always been there to help fix my mass spec problems and provide motivational discussion accompanied by coffee and cake.

To my undergraduate supervisor, Ivan Gout. You were willing to take the first chance on me. It is thanks to you that I made it to the Crick in the first place.

Thanks go to my thesis committee members Nic Tapon, Luis de Carvalho and Franck Pichaud for advising on my project throughout my PhD. To the fly community at the Crick who have always been supportive and willing to give advice, no matter how far the field of study is from their own. To our science operations administrators and quadrant managers who save us from excessive paperwork. To all the STPs at the Crick who have made this work possible: Advanced Sequencing, Media Preparation, Bioinformatics, Organic Chemistry, Experimental Histopathology, Biological Research Facility, Scientific Computing Structural Biology, Metabolomics. In particular, thanks go to Jim Ellis for his support with GC-MS work.

I would especially like to thank James MacRae, who taught me all I know about GC-MS and made the time to listen to my unusual theories throughout the years. Without your invaluable advice and support, I would not be where I am today.

To my parents, who have supported me right from the beginning to follow my dreams. And finally to Will, who by now knows more about *Drosophila* and mass spectrometry than anyone else in the field of accountancy. Thank you for all the encouragement and support you give me every day. Without you this journey would have been so much harder.

Table of Contents

List of figures

List of Figures located in Supplemetary material (separate file):

List of tables

List of Tables located in Supplemetary material (separate file):

Abbreviations

ØG	No glucose
ØY	No yeast
9ZT	(*Z*)-9-tricosene
Ac-CoA	Acetyl-CoA
ACTH	Adrenocorticotrophic hormone
AF	Ammonium formate
AMPs	Anti-microbial peptides
APCI	Atmospheric pressure chemical ionisation
APM	Arrector pili muscle
APPI	Atmospheric pressure photoionisation
ASTM	American Society of Testing Materials
BSTFA	N,O-Bis(trimethylsilyl)trifluoroacetamide
CL	Cardiolipin
CCD	Charge coupled device
CE	Cholesteryl ester
Cer	Ceramide
CHCA	Alpha-cyano-4-hydroxycinnamic acid
CI	Chemical ionisation
CID	Collision induced dissociation
CNS	Central nervous system
CRH	Corticotrophin releasing hormone
cVa	(*Z*)-11-Vaccenyl acetate
DC	Direct current
DCo	Dermal condensation
DDA	N-N,Dimethyldodecylamine
dd-MS	Data-dependent mass spectrometry
DESI	Desorption electrospray ionization
DG	Diacylglyceride
DMDS	Dimethyl disulphide
DOHaD	Developmental origins of health and disease

DP	Dermal papilla
DR	Dietary restriction
EA	Electron affinity
EI	Electron ionisation
ESI	Electrospray ionisation
ETC	Electron transport chain
FA	Fatty acid
FAME	Fatty acid methyl ester
FAS	Fatty acid synthase
FDR	False discovery rate
FFA	Free fatty acid
FoV	Field of view
FT-ICR	Fourier transform-ion cyclotron resonance
FWHM	Full width at half maximum
GC	Gas chromatography
GCIB	Gas cluster ion beam
GC-MS	Gas chromatography – mass spectrometry
GFP	Green fluorescent protein
GL	Glycerolipid
GO	Gene ontology
HC	Hydrocarbon
HCD	Higher energy collisional dissociation
HCOOH	Formic acid
HF	High fat
HPLC	High performance liquid chromatography
HRMS	High resolution mass spectrometry
hs	Hair shaft
HYHG	High yeast high glucose
IE	Ionisation energy
ICR	Ion cyclotron resonance
IM-MS	Ion mobility-mass spectrometry
IRS	Inner root sheath

ITO	Indium tin oxide
IUGR	Intra uterine growth restriction
LC	Liquid chromatography
LC-MS	Liquid chromatography – mass spectrometry
LDI	Laser desorption ionisation
LESA	Liquid extraction surface analysis
LiDHB	Lithium 2,5-dihydroxybenzoic acid
LMIG	Liquid metal ion gun
LN_2	Liquid nitrogen
LoD	Limit of detection
LP	Low protein
LY	Low yeast
MALDI	Matrix assisted laser desorption ionisation
MG	Monoacylglyceride
MIPC	Mannosylinositol phosphorylceramide
MRRF	Molar relative response factor
MS	Mass spectrometry
MS^1	Full mass spectrum
MS^2	Mass spectrum after mass selection and fragmentation
MSTFA	N-trimethylsilyl-N-methyl trifluoroacetamide
MSI	Mass spectrometry imaging
MVNTA	Metronidazole, vancomycin, neomycin, tetracycline, ampicillin
NCE	Normalised collision energy
NP-HPLC	Normal phase-high performance liquid chromatograph
NR	Nutrient restriction
Obp	Odorant binding protein
OR	Odorant receptor
OreR	Oregon R
ORS	Outer root sheath
PA	Proton affinity
PAH	Polycyclic aromatic hydrocarbon
PBS	Phosphate buffered saline

PC	Phosphatidylcholine
PCA	Principal component analysis
PE	Phosphatidylethanolamine
PE-Cer	Ceramide phosphoethanolamine
PFA	Paraformaldehyde
PFBHA	O-(2,3,4,5,6-pentafluorobenzyl)hydroxylamine hydrochloride
PG	Phosphatidylglycerol
PI	Phosphatidylinositol
PL	Phospholipid
PNS	Peripheral nervous system
ppm	Parts per million
PS	Phosphatidylserine
RF	Radio frequency
RH	Relative humidity
RNAi	RNA mediated interference
RT	Reverse transcription
RT-qPCR	Reverse transcription – quantitative polymerase chain reaction
SG	Sebaceous gland
Shh	Sonic hedgehog
SIMS	Secondary ion mass spectrometry
siRNA	Small interfering RNA
SM	Sphingomyelin
SNR	Signal-to-noise ratio
SPE	Solid phase extraction
STD	Standard
TG	Triacylglyceride
TLC	Thin layer chromatography
TMAH	Trimethylphenylammonium hydroxide
TMCS	Chlorotrimethylsilane
ToF	Time of flight
t_R	Retention time

qPCR	Quantitative polymerase chain reaction
QqQ	Triple quadrupole
WE	Wax ester

Chapter 1. Introduction

1.1 The skin as a biological barrier

The human skin is a complex organ composed of many different structures. This is split into three distinct regions, the epidermis, the dermis and the hypodermis (**Figure 1.1**). The epidermis is composed of four different cell types: keratinocytes, melanocytes, Langerhans' cells and Merkel cells. Langerhans' cells are specialised immune cells which are important for antigen presentation, and Merkel cells are sensory cells important for mechanoreception (Abraham and Mathew, 2019, Clayton et al., 2017). Melanocytes are responsible for producing melanin, which is transported in melanin granules from the melanocyte to the cytoplasm of the keratinocyte. Melanin in keratinocytes has a protective function against UV-induced cellular damage (Wicks et al., 2011). The dermis contains many important structures including the sebaceous glands, sweat glands, hair follicles, sensory neurons and blood vessels. The hypodermis is composed of sub-cutaneous fat, blood vessels and neurons.

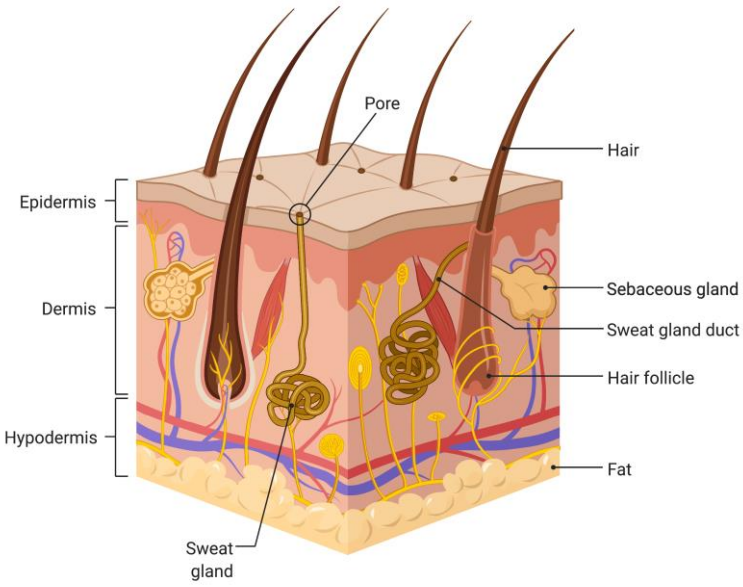

Figure 1.1 Anatomy of the human skin

Structures of the human skin, important in the maintenance of an effective barrier and in the production of skin lipids. Image produced by BioRender.

During early embryogenesis, the epidermis consists of a single layer of peridermal cells. These form a semi-permeable barrier and are involved in regulating exchange of sodium, water and glucose from the amniotic fluid to the embryo. In humans at approximately six months after conception, the peridermal cells differentiate and form the characteristic multi-layered epidermis. This epidermis acts primarily as a barrier rather than participating in active exchange. The multi-layered epidermis also includes several cell types which migrate to this location from different regions of the embryo. The melanocytes and the Merkel cells derive from the neural crest and migrate to the epidermis roughly midway through pregnancy, and the Langerhans' cell precursors migrate from the bone marrow at approximately 3 months gestation. To form the stratum corneum, the most proximal region of the epidermis, keratinocytes undergo differentiation and subsequently undergo a specialised form of apoptosis known as cornification. In this process, keratinocytes migrate towards the upper layers of the epithelium and begin to synthesise a new catalogue of structural proteins including keratin 1 and keratin 10. These proteins, alongside filaggrin, involucrin, loricrin and trichohyalin are cross-linked by transglutaminases to form the cornified envelope (Candi et al., 2016). The keratinocytes then undergo apoptosis and flatten, whereby the cornified envelopes interlock with keratin intermediate filaments to form the stratum corneum. The process of cornification is slow, taking approximately 20 days, in comparison with traditional apoptosis which occurs on a timescale of minutes. The Notch signalling pathway plays a key role in keratinocyte maturation, and defects in this pathway result in reduced skin barrier efficacy (Nowell and Radtke, 2013). Keratinocyte-derived keratin is responsible for anchoring together the keratinocytes and forms an important part of the skin barrier. This protein is key for the coupling of the epidermis to the dermis, and mutations in the keratin 14 protein in humans cause Epidermolysis Bullosa Simplex, a devastating skin disorder that results in skin blistering induced by mechanical trauma due to uncoupling of the epidermis from the dermis (Coulombe and Lee, 2012).

The developmental origin of the dermal cells that form the dermis depends on the skin region – the dorsal dermis of the trunk derives from the dermomyotome,

derived from the somites (**Figure 1.2B,C**), the ventral dermis of the trunk and the dermis of the limbs derives from the lateral plate mesoderm (**Figure 1.2,C**), and the facial dermis derives from the cranial neural crest endoderm (**Figure 1.2,C**). The differentiation of the ectoderm into epidermis and mesoderm into dermis rely on signalling between the two cell types - without the presence of one of these cell types, differentiation fails in the other.

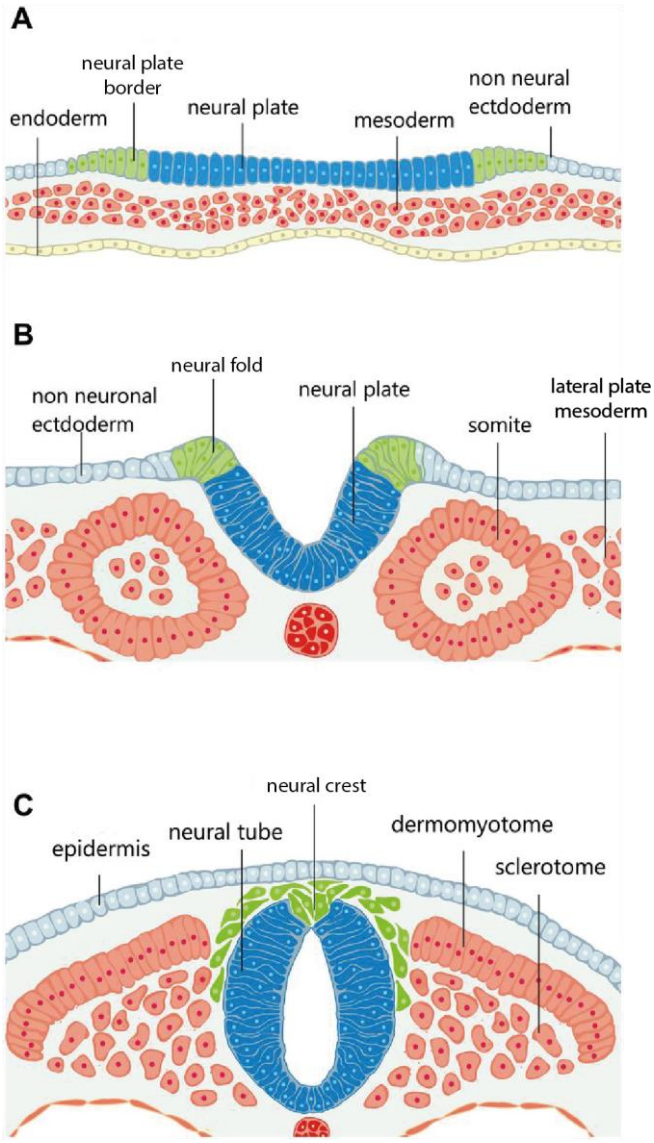

Figure 1.2 Features of early morphogenesis

Early morphogenesis showing the neural plate, which undergoes invagination to form the neural tube. Figure from Simões-Costa and Bronner (2013) with permission.

After the initial differentiation of the dermis and epidermis, the pilosebaceous units begin to form in certain regions of the body. The pilosebaceous units consist

of two sebaceous glands and one hair follicle. This initiates with the formation of the dermal papilla at approximately 12 weeks gestation (**Figure 1.3A**). The induction of aggregation of dermal cells to form the dermal papilla is dependent on the sonic hedgehog signalling pathway (*Shh*). Development continues over the course of 6 weeks when an early hair follicle is formed (**Figure 1.3C**). At this stage, the hair follicle does not yet protrude through the surface of the epidermis, and the sebaceous glands begin to form from stem cells expressing the *Lgr1* marker. At approximately 16 weeks gestation, the hairs begin to erupt through the epidermis. The sebaceous glands also begin to secrete lipids, which coat the developing fetus and form the vernix caseosa. This thick lipid layer is thought to act as a barrier protecting the epidermis whilst in the womb.

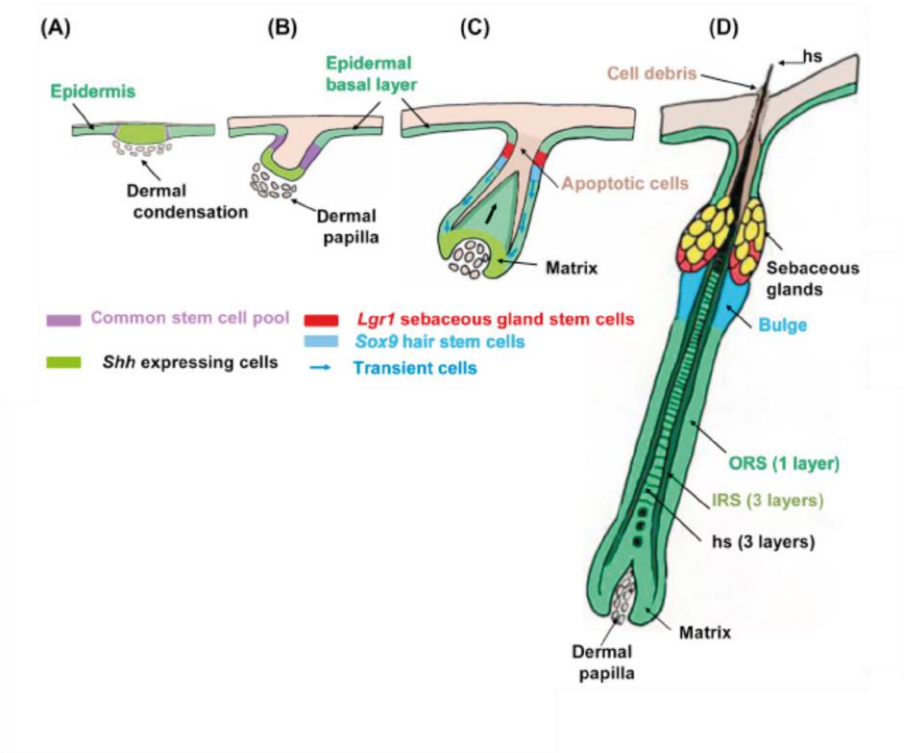

Figure 1.3 The developmental morphogenesis of the pilosebaceous unit

Morphogenesis of the hair follicle, from formation of the dermal papilla at approximately 12 weeks' gestation (A-B), formation of the early hair follicle (C) and eruption of the hair through the epidermis from 16 weeks gestation (D). hs=hair shaft, *Shh*=sonic hedgehog, ORS = outer root sheath, IRS = inner root sheath. Figure adapted from Dhouailly and Oftedal (2016) with permission.

After morphogenesis, the hair follicles begin a process of cycling. This cycle consists of three general phases – anagen (growth), catagen (regression) and

telogen (quiescence) (**Figure 1.4**). In humans, this process is asynchronous however, mice show a synchronous pattern that travels in waves along the length of the animal (Plikus et al., 2011). In mice, the telogen phase elongates with advanced age (Plikus et al., 2008).

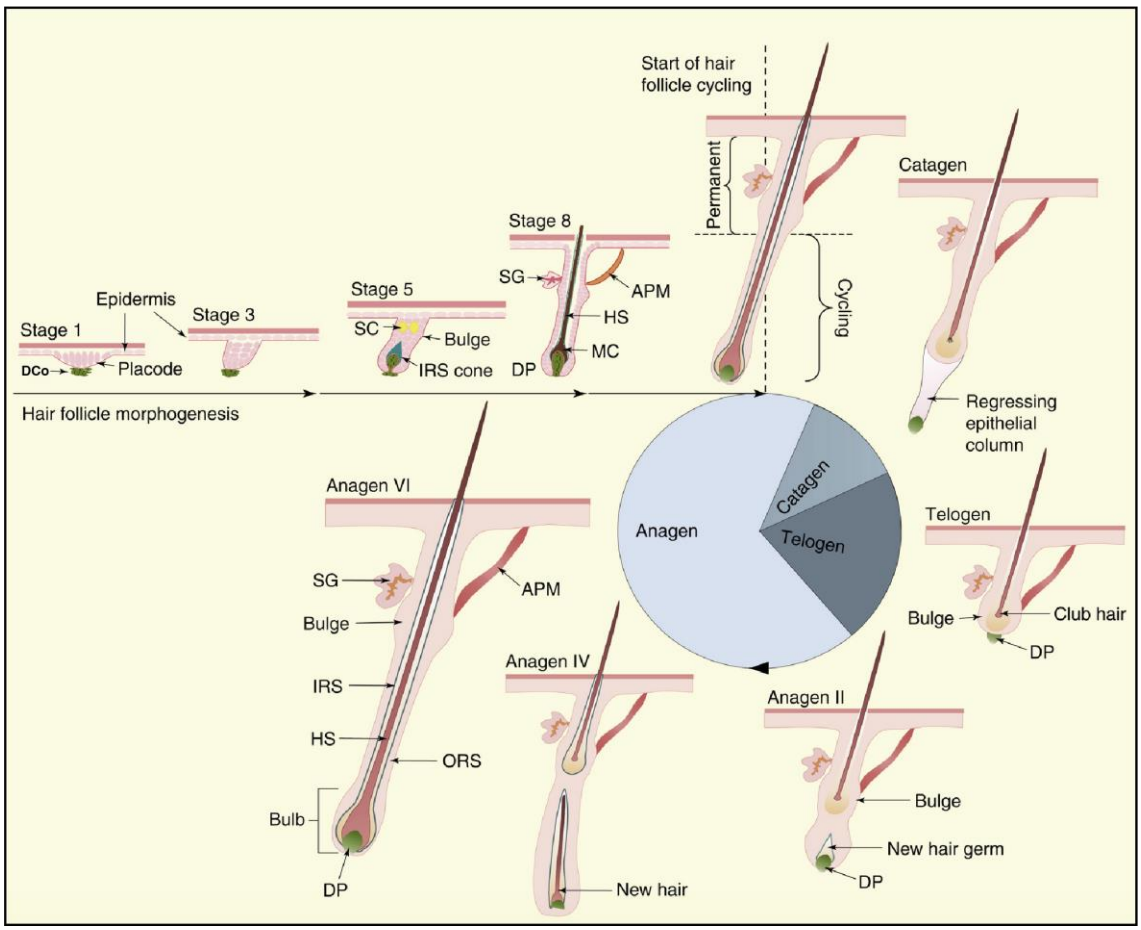

Figure 1.4 The hair follicle cycle

After morphogenesis (stages 1-8), the hair follicle undergoes cycling, where it passes through three main phases – catagen, telogen and anagen. Figure reproduced from Schneider et al. (2009) with permission. DCo= dermal condensation, SC = sebocyte, IRS = inner root sheath, DP = dermal papilla, HS = hair sheath, APM = arrector pili muscle, SG = sebaceous gland.

Skin lipids originate from the sebaceous glands, keratinocytes and sweat glands. The secretion of skin lipids from the sebaceous glands occurs via a complex process. Sebocytes, differentiated from Lrig1 positive stem cells, mature and accumulate lipid droplets within their cytoplasm containing sebaceous lipids (**Figure 1.5**). As the sebocytes migrate towards the junction of the sebaceous gland with the hair follicle, the sebocytes undergo controlled necrosis and release the sebaceous lipids via holocrine secretion. These lipids then transverse the hair follicle to the surface of the skin (Zouboulis, 2017). The sebaceous lipid blend includes wax esters, glycerolipids, fatty acids, cholesterol and squalene (Pappas, 2009).

Keratinocytes secrete free fatty acids, cholesterol and ceramides (Pappas, 2009). It is in these cells that Vitamin D is synthesised from cholesterol precursors, mediated via UV light (Deluca, 1997). Vitamin D has widespread effects on gene expression and metabolism throughout the body and a deficiency of this vitamin leads to the development of rickets which can result in stunted growth and skeletal deformities (Sahay and Sahay, 2012). The sweat glands are differentiated into two types: apocrine and eccrine. Eccrine glands occur over the majority of the skin and their pores empty directly to the surface of the skin. Apocrine sweat glands are located in specific areas of the body where hair is abundant, and their pores empty into the hair follicles. Alongside sweat, these glands also secrete a blend of lipids including fatty acids, cholesterols and phospholipids (Takemura et al., 1989). Interestingly, the apocrine and eccrine glands have been shown to accumulate lipid droplets with age, which may be caused by an age-related build-up of these lipids (Nasr, 1967).

Sebaceous glands express a number of enzymes involved in androgen metabolism, which act to convert low-level circulating androgens into more potent androgens. The amount of sebum produced is regulated by androgens (Strauss et al., 1962), and is therefore increased in states where androgen levels are increased such as during puberty, in patients with Parkinson's disease (Trivedi et al., 2019), and during pregnancy (Burton et al., 1970). The amount of sebum decreases in converse scenarios including patients with growth hormone

deficiency (Clayton et al., 2020), and after menopause in women (Zouboulis and Boschnakow, 2001). Interestingly, recent research implicates the central nervous system (CNS) and several pituitary gland hormones as key controllers of sebocyte secretion. Hypothalamic corticotrophin-releasing hormone (CRH), adrenocorticotrophic hormone (ACTH) form the anterior pituitary gland, and adrenal cortisol have all been implicated in sebum secretion (Clayton et al., 2020). In addition, the proximity of cutaneous nerve endings to sebocytes and keratinocytes raises the possibility that the peripheral nervous system (PNS) may locally secrete neuropeptides and neurotransmitters that influence the production of skin barrier lipids.

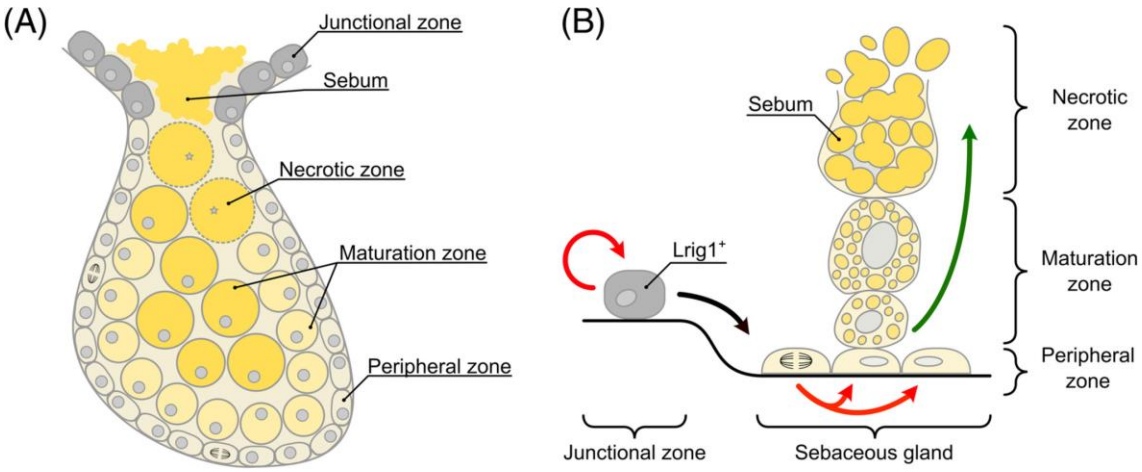

Figure 1.5 Sebocyte maturation within the sebaceous gland

Sebocytes undergo differentiation from *Lrig1* positive stem cells, mature and accumulate lipid droplets, and undergo controlled necrosis and holocrine secretion. Figure reproduced from Clayton et al. (2020) with permission.

One of the best understood functions of the skin is thermoregulation. This is a complex process which is influenced by the thickness of the sub-cutaneous fat, the action of the sweat glands, and the piloerector muscles which control the orientation of the hairs (Romanovsky, 2014). The epidermal lipid layer has also been shown to form an important barrier against microbial infection, with many classes of lipid such as free fatty acids, glycerolipids and fatty alcohols acting as strong antimicrobials (Drake et al., 2008). The skin lipid blend is also thought to be important in mediating a waterproofing barrier (Feingold, 2009). More generally, it seems that terrestrial life forms, whether animal or plant, coat

themselves in a layer of lipids as a common solution to the environmental threat of water loss (Hadley, 1989).

Dysregulation of the skin lipid blend can have significant consequences on the skin physiology and pathology. Atopic dermatitis is a pathology predominantly affecting the keratinocytes as a result of filaggrin deficiency which promotes inflammation and leads to decreased skin microbial diversity and impaired barrier function (Langan et al., 2020). One of the changes in lipid blend observed in atopic dermatitis patients is a decrease in ultra-long chain ceramides (Berdyshev et al., 2018). This was linked with a decrease in expression of two elongases, Elovl1 and Elovl4 which when genetically knocked out in mouse models resulted in severe trans-epithelial water loss and neonatal death (Li et al., 2007). Acne vulgaris is a pathology that predominantly affects the sebocytes, resulting in excess sebum production thought to be caused by increased androgen levels, which results in skin lesions (Heng and Chew, 2020). Recently, sebum production has been demonstrated to depend on de novo lipogenesis and chemical inhibition of this pathway has proved effective in reducing sebum levels in humans, highlighting a potential therapeutic target for treatment of this condition (Esler et al., 2019)

1.2 The developmental origins of health and disease

Environmental conditions have been shown to exert strong effects on skin pathophysiology alongside other organ systems. One example of this is an adult high fat diet, which induces inflammation in the skin and can also result in the development of coronary heart disease. In some cases, the environmental conditions can exert influence over health and physiology far beyond the period of exposure. The most sensitive period for this environmental exposure to influence future health is during development, a field known as the developmental origins of health and disease (DOHaD). DOHaD effects have been identified in a variety of organs including the heart and pancreas, but very little research has been carried out on the consequences to the skin which forms one of the questions addressed in this thesis.

The founding concept of the developmental origins of health and disease (DOHaD), sometimes known as the Barker Hypothesis, is that an organism can only develop to its full biological potential, as determined by its genetics, when environmental conditions are optimal (Barker and Osmond, 1986). Unfortunately, this is exceedingly rare in the real world outside controlled laboratory conditions. Suboptimal environments can result from a range of factors including maternal toxin exposure (Luebke et al., 2006), stress (Walsh et al., 2019), excessive alcohol intake (Lunde et al., 2016), smoking (Werhmeister et al., 2015), and malnutrition (Moore, 2017). The DOHaD field is therefore concerned with understanding the long-term effects of developmental exposure to these suboptimal environmental factors upon adult health, disease risk, and lifespan (Gluckman et al., 2016).

In mammals development occurs *in utero*, such that these suboptimal environmental conditions are experienced directly by the mother and then, in turn, they indirectly affect by the developing fetus. Kermack, McKendrick and McKinlay proposed that the driving factor in adult health was the environment experienced from birth until the age of 15 (Kermack et al., 2001). Much recent interest in the DOHaD field has been sparked by detailed longitudinal epidemiological studies

of fetal outcomes before, during and after the Dutch Famine of 1944-1945. Transport blockades during the Second World War combined with an especially harsh winter led to widespread severe malnutrition of approximately 4.5 million people over a period of six months. The adult food rations for pregnant women during this Dutch hunger winter provided only ~730 calories per day, considerably less than the recommended ~2000-2499 calories per day (Smith, 1947). This tragic event provided a unique insight on the effects of pre- and post-natal malnutrition on adult outcomes. One of the first studies from this cohort observed that malnutrition close to the time of conception led to increased rates of miscarriage and malformation (Smith, 1947). This led to the hypothesis of a "critical period" during which the fetus is particularly sensitive to damage. Large studies were carried out on the long-term effects of this famine, including a study of 300,000 19-year-old men which investigated the effect of maternal famine exposure during early versus late pregnancy. This revealed a surprising observation – famine during the first half of pregnancy resulted in a significantly higher rates of diabetes in the male offspring than with famine during the last trimester and first few pre-natal months, which had the opposite effect of an decrease in diabetes rates (Ravelli et al., 1976). This epidemiological study was one of the first to directly link developmental nutrition with an altered risk of adult morbidity.

Subsequent studies to Ravelli et al. have widened the conclusions, finding correlations between decreased birth weight and an increased risk of obesity (Dörner, 1973), arteriosclerosis (Dörner et al., 1973), type 2 diabetes (Dörner and Mohnike, 1973), hypertension (Gennser et al., 1988), and heart disease (Barker, 1998). Developmental diet was also reported to negatively affect height and weight, with a stronger effect observed in males than females (McCance and Widdowson, 1974). In females, varying effects of developmental malnutrition on fertility were observed including delayed menarche (Cooper et al., 1996), and reduced ovulation rate (Ibáñez and de Zegher, 2006). The discovery that metabolic phenotypes are involved led to the development of the "thrifty phenotype" hypothesis proposed by Hales and Barker (Hales and Barker, 1992). This hypothesis suggests that if the developing organism experiences nutrient

restrictive conditions, it permanently alters its metabolism in a way that is optimal under nutritional “times of need”. If the adult subsequently experiences nutritional “times of plenty”, the metabolism is not as well suited to these conditions which leads to higher risks of associated morbidities. This idea was further developed by Bateson and colleagues into the predictive adaptive response hypothesis, whereby conditions during development programme the organism to be better adapted for these same conditions during adulthood (Bateson et al., 2014).

The correlative evidence for DOHaD from human epidemiological studies led to the need for more controlled studies in model organisms to test for a causative link between developmental malnutrition and adult morbidities. There is now overwhelming evidence that such a causative link, known in the field as developmental programming, exists in mammals, and several of the human DOHaD phenotypes have now been reproduced in rat models. For example, low maternal protein diets are well documented to drive adult hypertension (Vickers et al., 2000, Langley and Jackson, 1994, Woodall et al., 1996). Prenatal undernutrition is also known to developmentally programme obesity in adult rats, associated with low levels of insulin and leptin. Interestingly, postnatal leptin treatment completely rescued the obesogenic phenotype, suggesting possible mechanistic links between prenatal nutrition, leptin production and an obesogenic phenotype (Vickers et al., 2005). Data from other experimental models including mice and sheep suggests that developmental programming effects may occur as a result of environmental influences exerted as early as conception itself (Todd et al., 2009, Watkins et al., 2008). Many of the metabolic DOHaD phenotypes in adults are age-related, such as the triglyceridaemia exhibited in rats exposed to a prenatal low protein diet (Erhuma et al., 2007).

The molecular mechanisms behind many permanent DOHaD phenotypes are not well understood but are thought to involve maternal stress-induced changes in tissue structure, cellular ageing and epigenetic modifications (Tarry-Adkins and Ozanne, 2017, Bianco-Miotto et al., 2017). Much current DOHaD research focuses on cataloguing genome-wide epigenetic modifications such as histone acetylation and DNA methylation, with relatively few mechanistic studies

elucidating how these changes alter the expression of the specific genes that mediate the DOHaD phenotype. One study in rats provides a link between maternal malnutrition and methylation levels of hepatic genes (Lillycrop et al., 2005). Indeed, a notable study by Godfrey et al. linked lower maternal carbohydrate intake with higher methylation levels of the retinoid X receptor-α and higher neonatal adiposity (Godfrey et al., 2011). Several recent studies have begun to link not only maternal, but also paternal stress to developmental programming phenotypes through epigenetic modifications induced in sperm (Guerrero-Bosagna et al., 2010, Ng et al., 2010).

Given that dietary developmental programming alters disease risk for several age-related diseases it is perhaps not surprising that it has also been shown to affect lifespan in mice and in *Drosophila* (Ozanne and Hales, 2004, Stefana et al., 2017). In a classic study in mice, a low protein (LP) prenatal diet was shown to significantly decrease lifespan by ~25% whereas a LP postnatal diet increased lifespan by ~6% (Ozanne and Hales, 2004). Furthermore, a postnatal LP developmental diet protected against the shortened lifespan induced by an adult obesogenic diet (Ozanne and Hales, 2004). This study suggests that the developmental stage of LP exposure is critical for determining whether or not the outcome is lifespan shortening. It also suggest that the precise combination of adult and developmental diets exerts a significant influence on longevity. A large body of literature now indicates that dietary restriction (DR) in adults is sufficient to increase lifespan in a wide range of organisms including yeast (Lin et al., 2000), *C. elegans* (Lakowski and Hekimi, 1998), *Drosophila* (Pletcher et al., 2002, Partridge et al., 2005), and mice (de Marte and Enesco, 1986, Miller et al., 2005). The molecular mechanisms underlying the DR effect are complex and not yet fully understood, however, there is strong evidence that it involves signalling mechanisms conserved from insects to mammals. Current research aims to target these signalling pathways with the overall aim not just to increase lifespan but rather to extend “healthspan” such that age-related morbidities are compressed towards the end of life (Partridge et al., 2018). In *C. elegans* and *Drosophila*, the interlinked insulin and TOR nutrient-sensing pathways are decreased via adult DR, and genetic manipulations directly decreasing the

activity of individual pathway components are sufficient to extend lifespan (Gems and Partridge, 2013). An interesting link to DOHaD here is that, in rats, a maternal LP diet decreases adult mTOR activity (Guzmán-Quevedo et al., 2013). So it is possible that mTOR signalling may contribute to the lifespan effects observed in rodent DOHaD models. In mammals, but not *Drosophila*, the time of onset of adult DR is crucial in determining its lifespan-extending effects (Hahn et al., 2019, Mair et al., 2003). A recent study in mice showed that application of dietary restriction in young adults elicited a stronger increase in lifespan than it did for older adults (Hahn et al., 2019). The effect was greatest when the dietary restriction was maintained throughout adult life, but was still present to a lesser extent when dietary restriction was removed in later-life.

Recent studies in *Drosophila* have shown that developmental undernutrition or developmental oxidant exposure can lead to substantial increases in lifespan (Stefana et al., 2017, Obata et al., 2018). Larval exposure to low-dose oxidants such as paraquat or tert-butyl hydroperoxide was found to induce a specific developmental switch in gut microbiota, eliminating *Acetobacter* and increasing *Lactobacilli* (Obata et al., 2018). Single-species bacterial transplants were then used to show that *Acetobacter* elimination from the microbiome is sufficient to ameliorate age-related gut dysfunction and, to extend lifespan (Obata et al., 2018). Developmental undernutrition in the form of decreased dietary yeast (LY) content was shown, under the majority of adult diets tested, to increase lifespan (Stefana et al., 2017). This was associated with a relative decrease in the ratio of unsaturated-to-saturated cuticular hydrocarbons. Synthetic alkenes but not alkanes were then shown to directly decrease adult survival. In this LY model hydrocarbon autotoxin production on the cuticle (“skin”) was ameliorated by early-life nutritional restriction (Stefana et al., 2017). Dietary developmental programming effects on the integument (skin or cuticle), the largest organ in the body, are underexplored in *Drosophila* and have not been reported in rodents, to my knowledge. This thesis therefore builds upon the Stefana et al. study in *Drosophila* and also extends some of its new findings to mice.

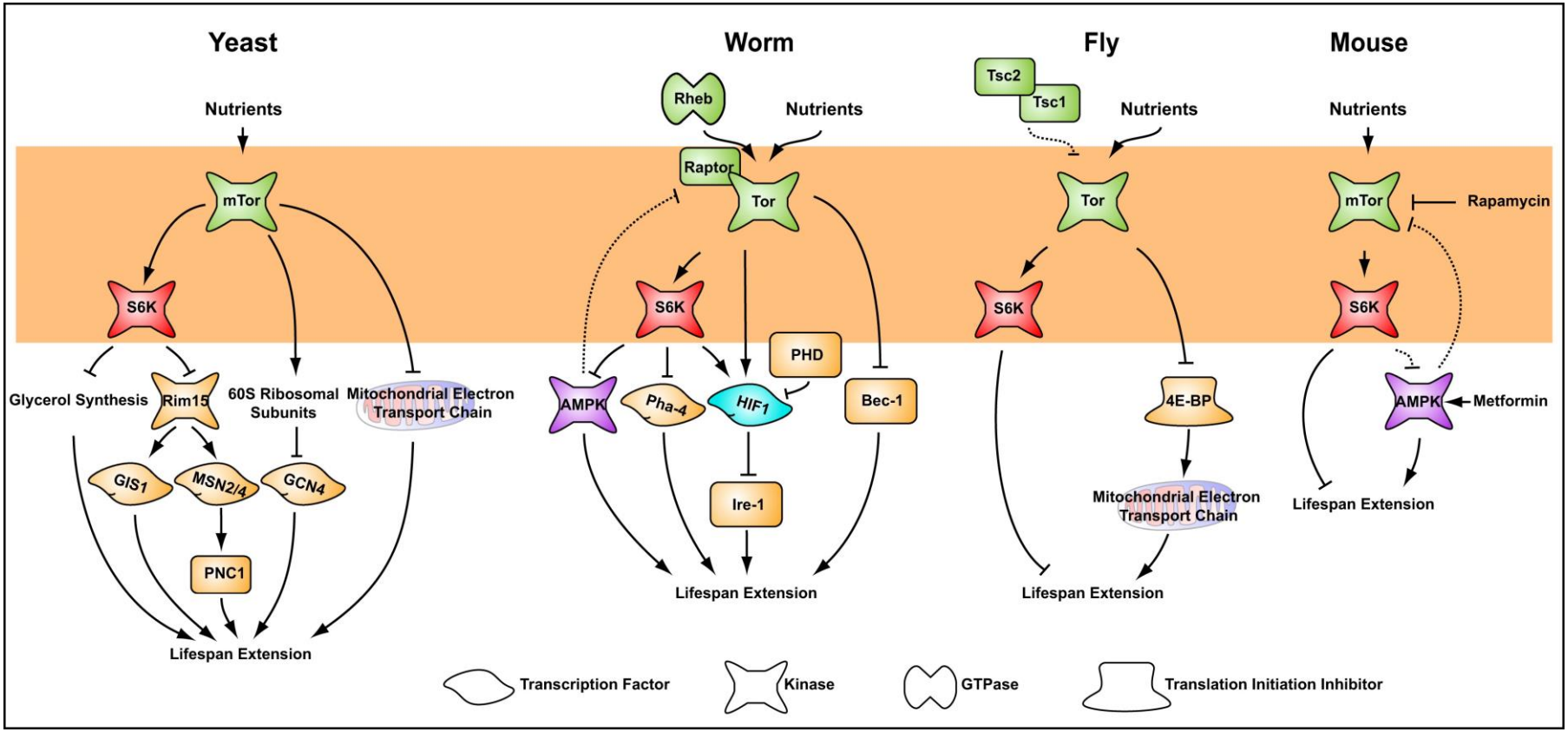

Figure 1.6 TOR pathway components important in mediating lifespan extension

Components of the nutrient-sensing TOR pathway that have been experimentally determined to contribute to DR-mediated lifespan extension in yeast, *C. elegans*, *Drosophila* and mouse. Figure reproduced from Kapahi et al. (2010) with permission.

1.3 *Drosophila melanogaster* as a model organism

In this thesis I primarily utilise the fruit fly *Drosophila melanogaster* as a model organism to investigate the functional consequences of alterations to the cuticular lipid blend and molecular mechanisms altering the composition of the lipid blend. When studying DOHaD in the context of lifespan, *Drosophila melanogaster* is a particularly useful experimental model due to its powerful genetics and short generation times (**Figure 1.7**). Most organ systems in humans have analogues in *Drosophila* which makes this model organism particularly tractable for research purposes (**Figure 1.8**). The degree of conservation of disease-causing genes is also particularly high – approximately 75% of disease-associated genes in humans are thought to be conserved in *Drosophila* (Reiter et al., 2001).

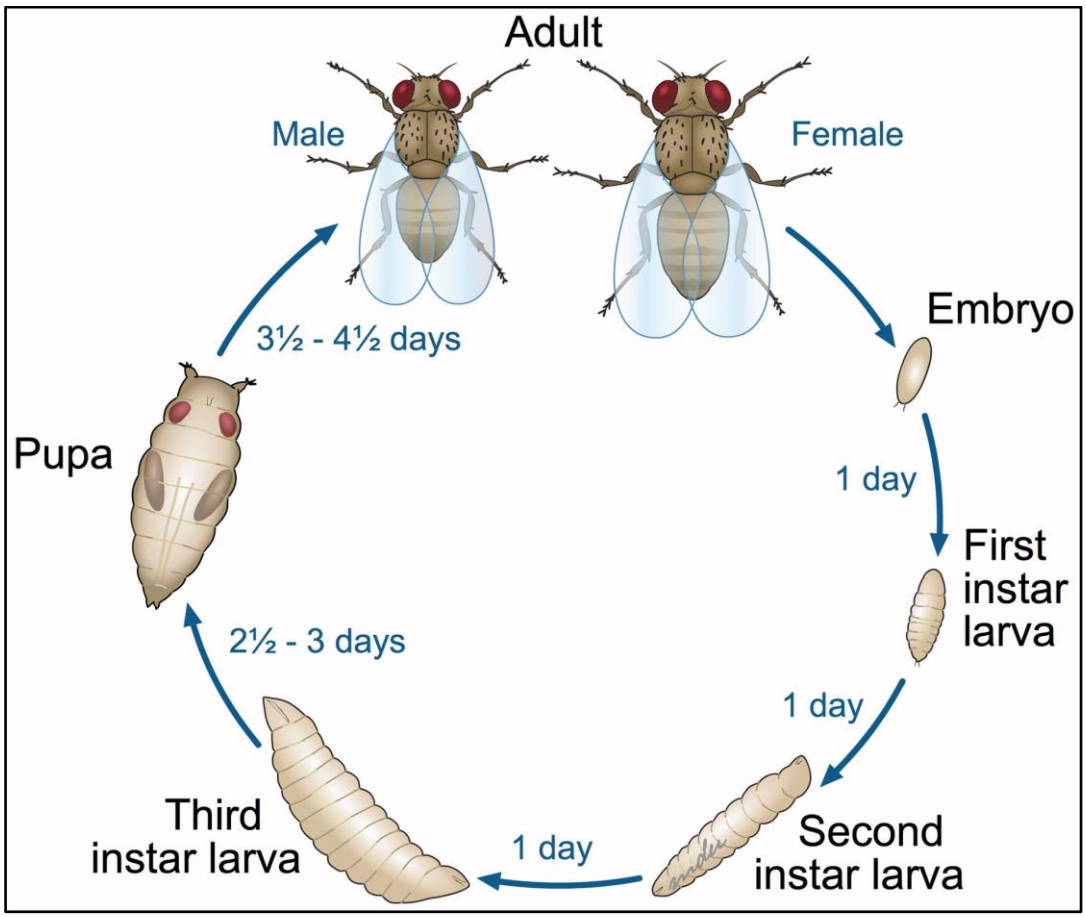

Figure 1.7 *Drosophila melanogaster* life cycle

The life cycle of *Drosophila melanogaster* when housed at 25℃. The total life cycle takes 9-10.5 days from embryo to adult. Reproduced with permission from Ong et al. (2015)

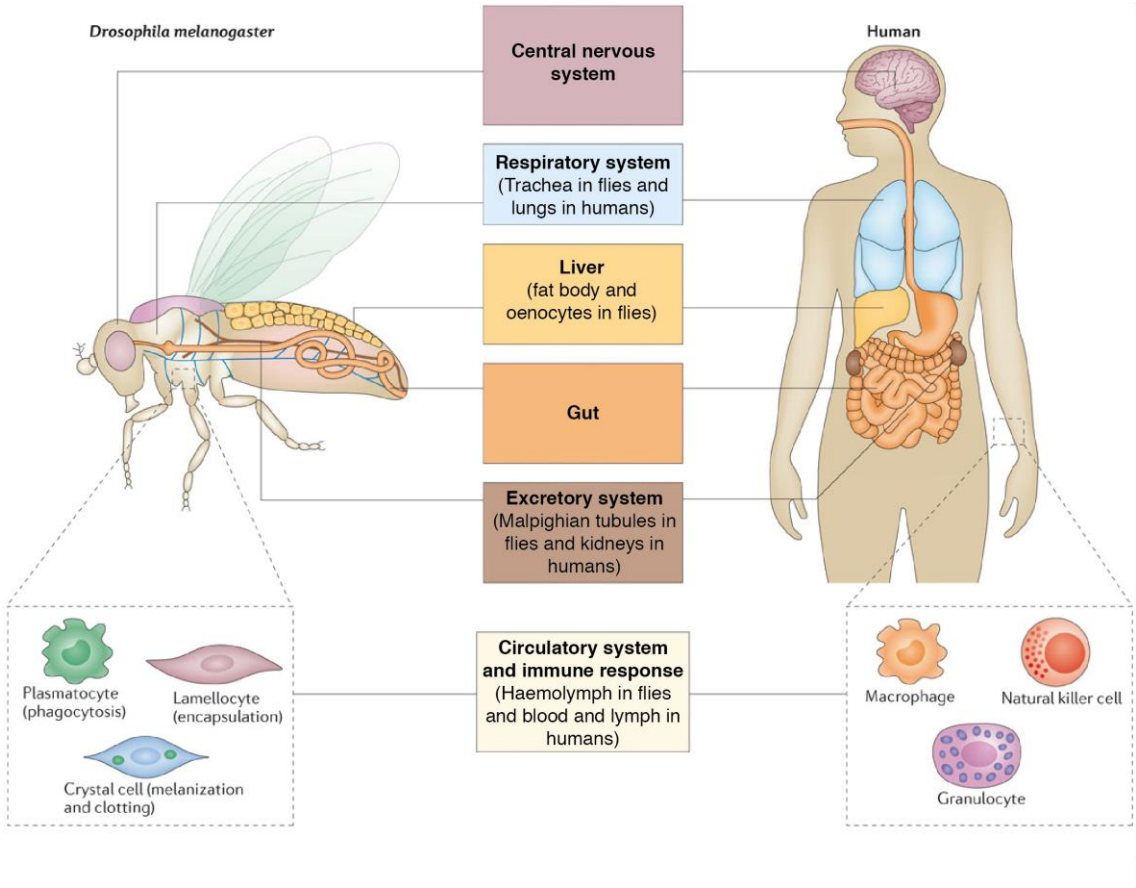

Figure 1.8 Organ analogies between humans and *Drosophila*

Summary of organ systems in humans and their analogous counterparts in *Drosophila*. Figure adapted from Buchon et al. (2014) with permission.

Development in flies and mammals proceeds via common themes such as the formation of three germ layers (ectoderm, mesoderm and endoderm) via the process of gastrulation but there are, however, major differences. For example, the *Drosophila* embryo and larva develop in the external environment whereas the mammalian embryo and fetus develop *in utero*. This makes it difficult, if not impossible, to directly equate developmental stages precisely between *Drosophila* and mammals. Nevertheless, the fetal (after embryonic implantation) and larval stages are similar in that they both correspond to the major period of body growth during development. Furthermore, in both species, these stages are when the cells of the future adult are “incubated” inside a carrier body that protects them from direct exposure to the external environment. This is because, in *Drosophila* and other holometabolous insects, the adult organs develop from small groups of cells called imaginal discs, which reside inside the larval body

(**Figure 1.9**). Imaginal discs grow throughout the larval stage and differentiate during the pupal stage to form the external tissues of the adult fly. Given this, the larva can be thought of as the mother of the fly, although these two *Drosophila* body forms are genetically identical – unlike the mammalian mother and fetus.

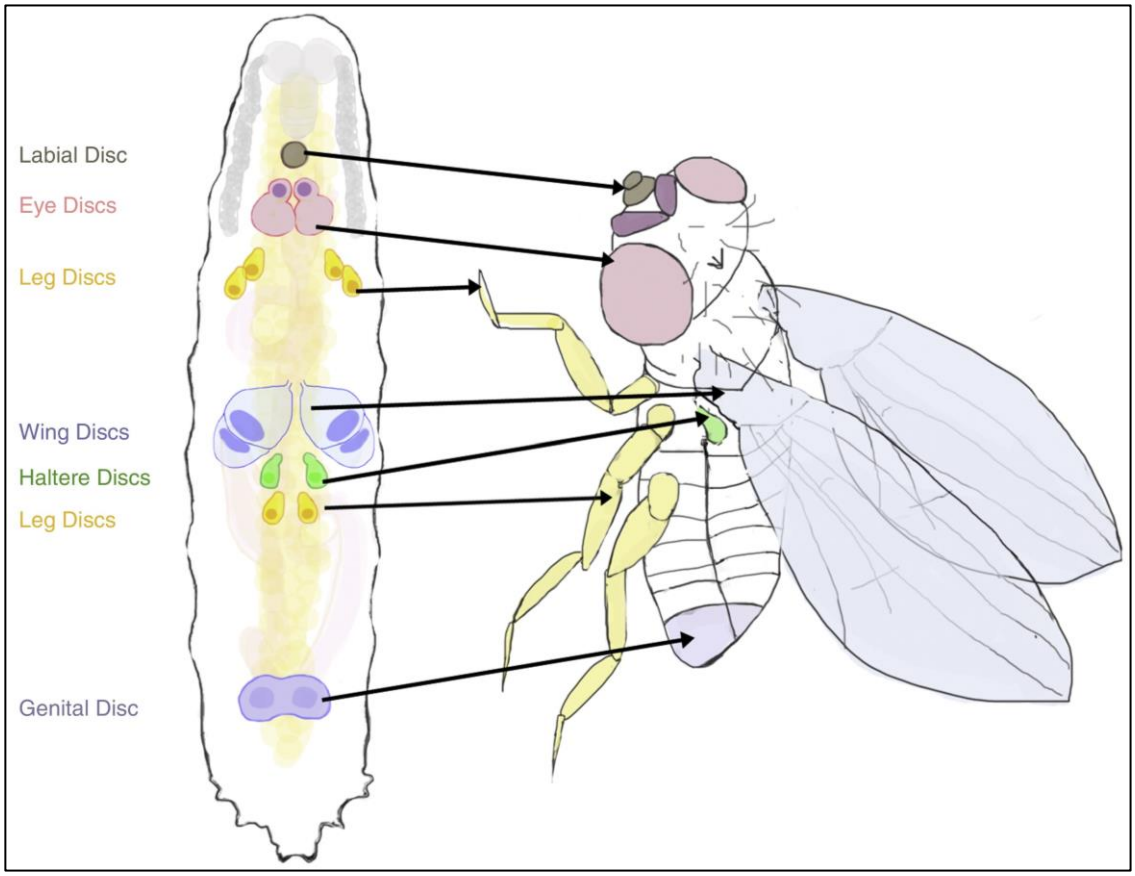

Figure 1.9 Larval imaginal discs

Larval imaginal discs and their corresponding adult tissues. Reproduced from Jaszczak and Halme (2016) with permission.

Drosophila melanogaster is a particularly tractable genetic model organism with only four sets of chromosomes, ~180 million base pairs of DNA and 13,969 predicted protein coding genes (Adams et al., 2000, Thurmond et al., 2018). In contrast, the human genome is composed of 23 chromosome pairs, ~3 billion base pairs of DNA and 19,000 predicted protein-coding genes (Ezkurdia et al., 2014, Mukherjee et al., 2020). Hence, there are numerous examples where a gene family is represented by one gene in *Drosophila* but multiple orthologues in mammals. This often makes genetic screens and loss-of-function genetic analysis more easily achievable in flies than in mice. Perhaps even more

importantly, there is a wide range of sophisticated genetic tools available in *Drosophila*. One of the most widely used of these tools is the binary GAL4-UAS expression system (**Figure 1.10**) (Brand and Perrimon, 1993). This valuable tool was generated using an expression system that naturally occurs in yeast but not in *Drosophila*. This enables the expression of a transgene of choice in a defined tissue within the organism. One common application of the GAL4-UAS system is to knockdown a gene of interest by expressing a UAS transgene containing an inverted repeat or hairpin of double-stranded RNA complementary to part of its mRNA sequence. This induces RNA-mediated interference (RNAi), a process whereby the double-stranded RNA hairpin is cleaved into small fragments by Dicer and these are then targeted by the RISC complex to the mRNA of the gene of interest, which is then cleaved and degraded (**Figure 1.11**) (Kennerdell and Carthew, 2000). Libraries of transgenic flies containing UAS-RNAi constructs for ~90% of all genes are available from stock centres such as the Vienna *Drosophila* Research Centre and the Bloomington *Drosophila* Stock Centre. The GAL4-UAS system can also be used to express any protein of choice, for example green fluorescent protein (GFP). The spatial specificity of the GAL4 system is imparted by the expression pattern of the GAL4 driver. Fortunately, a huge amount of work by a large number of laboratories has generated a vast collection of these GAL4 drivers, which are now available for most tissue and cell types in *Drosophila*. Some of these specific GAL4 drivers do however also have secondary sites of expression, which must be borne in mind when interpreting experimental outcomes. Temporal specificity can also be added to the GAL4-UAS system using GAL80^{ts}. A temperature-sensitive allele of GAL80 (GAL80^{ts}) can be used to repress GAL4 activity at lower temperatures (~18℃), and is itself inactivated at higher temperatures (~29℃) enabling GAL4 activity (McGuire et al., 2004). The recent development of CRISPR-Cas9 technology has expanded the *Drosophila* genetic toolkit even further, so that it is now possible to knockout any gene or to knock-in almost any transgene into a specific genomic location (Gratz et al., 2013). This thesis uses most of the genetic tools described above to investigate the regulation and function of barrier lipids.

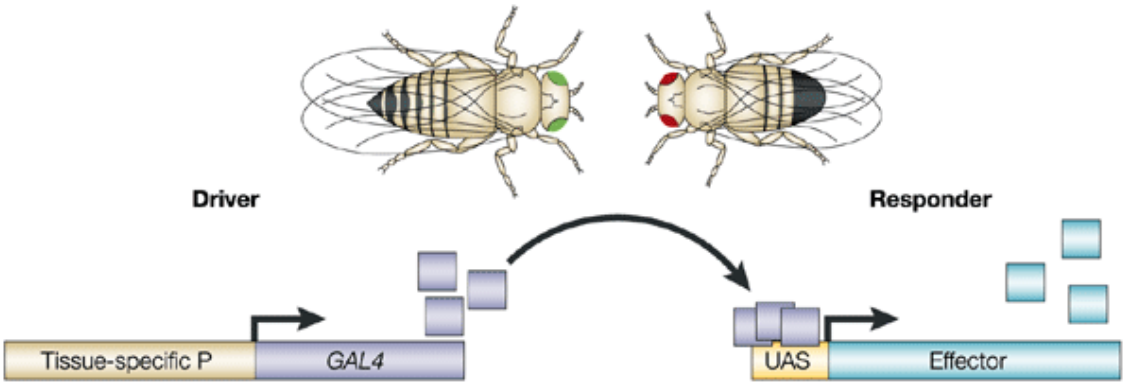

Figure 1.10 *Drosophila* GAL4-UAS system

Illustration of the GAL4-UAS system. A fly line containing GAL4 driven by a tissue-specific promoter is crossed to a fly line containing an effector transcript (e.g. RNAi) driven by the UAS promoter. When the two lines are combined, the GAL4 transcriptional activator induces the expression of the effector gene (Brand and Perrimon, 1993). Figure reproduced with modifications from Wimmer (2003) with permission.

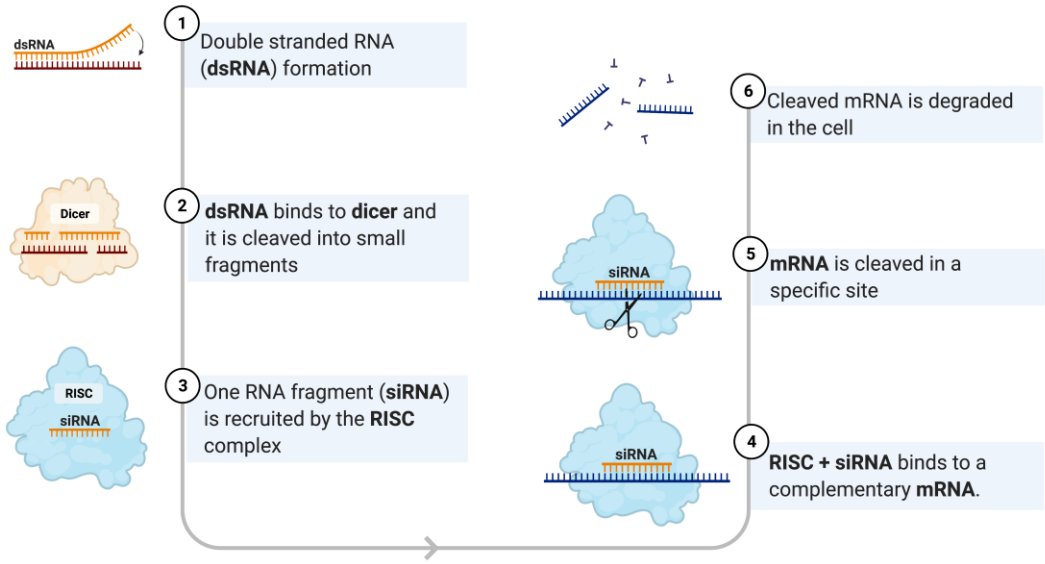

Figure 1.11 The RNA interference mechanism of action

The double stranded RNA (1) construct is expressed in a tissue-specific manner using the GAL4-UAS system in **Figure 1.10**. This double stranded RNA is cleaved to form a small interfering RNA (siRNA) (3), which promotes the cleavage and subsequent degradation of the mRNA encoding the target gene (4-6). Illustration produced by BioRender.

1.4 *Drosophila* barrier lipids and pheromones

The *Drosophila* cuticular barrier is primarily made up of a layer of chitinous exoskeleton (cuticle) coated with a blend of lipids. Below this is a layer of epidermal cells, and beneath these the oenocytes and fat body (**Figure 1.12**). The oenocytes are known to produce hydrocarbons, one of the barrier lipids that coat the external cuticle, and are thought to provide a waterproofing function (Makki et al., 2014). It has also been proposed recently that insect oenocytes fulfil functions in generating the integument lipid barrier that are analogous to those of sebocytes in mammals (Stefana et al., 2017). The fat body in *Drosophila* is broadly analogous to the mammalian adipose tissue, containing the main store of lipids in the body, much of which is in the form of lipid droplets (Kühnlein, 2012, Arrese and Soulages, 2010). Fat body cells and oenocytes also appear to share some functions that are associated with the liver in mammals, with the fat body storing large amounts of glycogen (Johnson and Butterworth, 1985), and the oenocytes working in tandem with the fat body to mobilise lipid stores during larval starvation (Gutierrez et al., 2007).

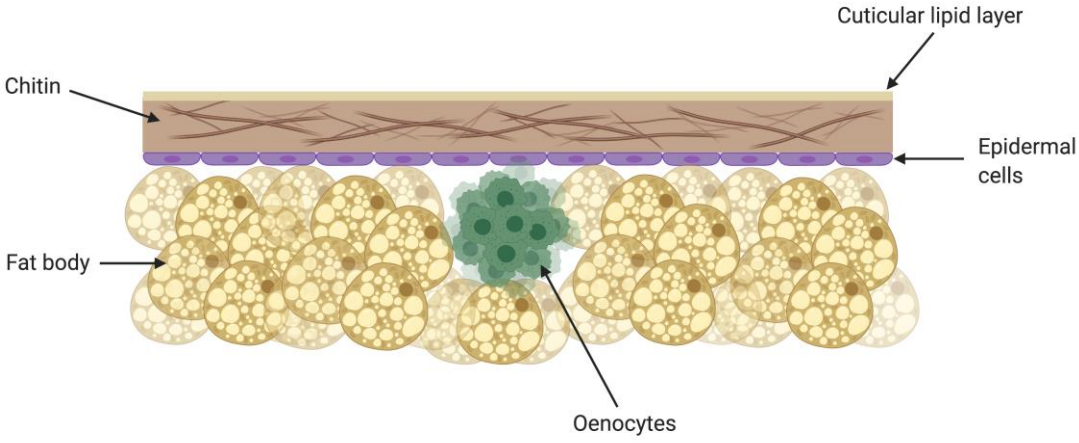

Figure 1.12 Anatomy of the *Drosophila* cuticle

The adult *Drosophila* cuticle is composed of a cuticular lipid layer, a chitin polymer exoskeleton, a layer of epidermal cells (purple), oenocytes (green) and fat body cells.

In the literature, the phrase “cuticular lipids” in *Drosophila* usually refers exclusively to hydrocarbons, which are very abundant components of this hydrophobic barrier (Blomquist and Ginzel, 2021). *Drosophila* cuticular hydrocarbons are composed of a blend of alkanes, methyl-branched alkanes, monoenes and female-specific dienes. Hydrocarbons are, however, not the only class of lipids on the cuticle and a small number of studies have also identified wax esters and triglycerides (Kaftan et al., 2014, Blomquist and Jackson, 1979). The paucity of reports on non-hydrocarbon cuticular lipids may be due to technical difficulties in specifically isolating these compounds from the cuticle and, if this could be overcome, it is likely that interesting new findings would be made. The presence of non-hydrocarbon lipids also provides the first hints that integument lipids may be more similar between *Drosophila* and mammals than previously thought.

The synthesis of hydrocarbons occurs via a metabolic pathway originating with *de novo* synthesis of free fatty acids and terminating with the cytochrome P450 reductase Cyp4g1 (Qiu et al., 2012) (**Figure 1.13**). For the production of alkenes, a double bond is introduced in the ω7 or ω5 position by Desat2 or Desat1 respectively (Bousquet et al., 2012, Dallerac et al., 2000). Dienes are exclusively produced by females, and the second double bond is introduced by the female-specific DesatF desaturase (Chertemps et al., 2006). The enzymes involved in the elongation and reduction steps of hydrocarbon biosynthesis remain to be characterised, with the exception of EloF, which is thought to be responsible for elongation of female long-chain hydrocarbons (Chertemps et al., 2006).

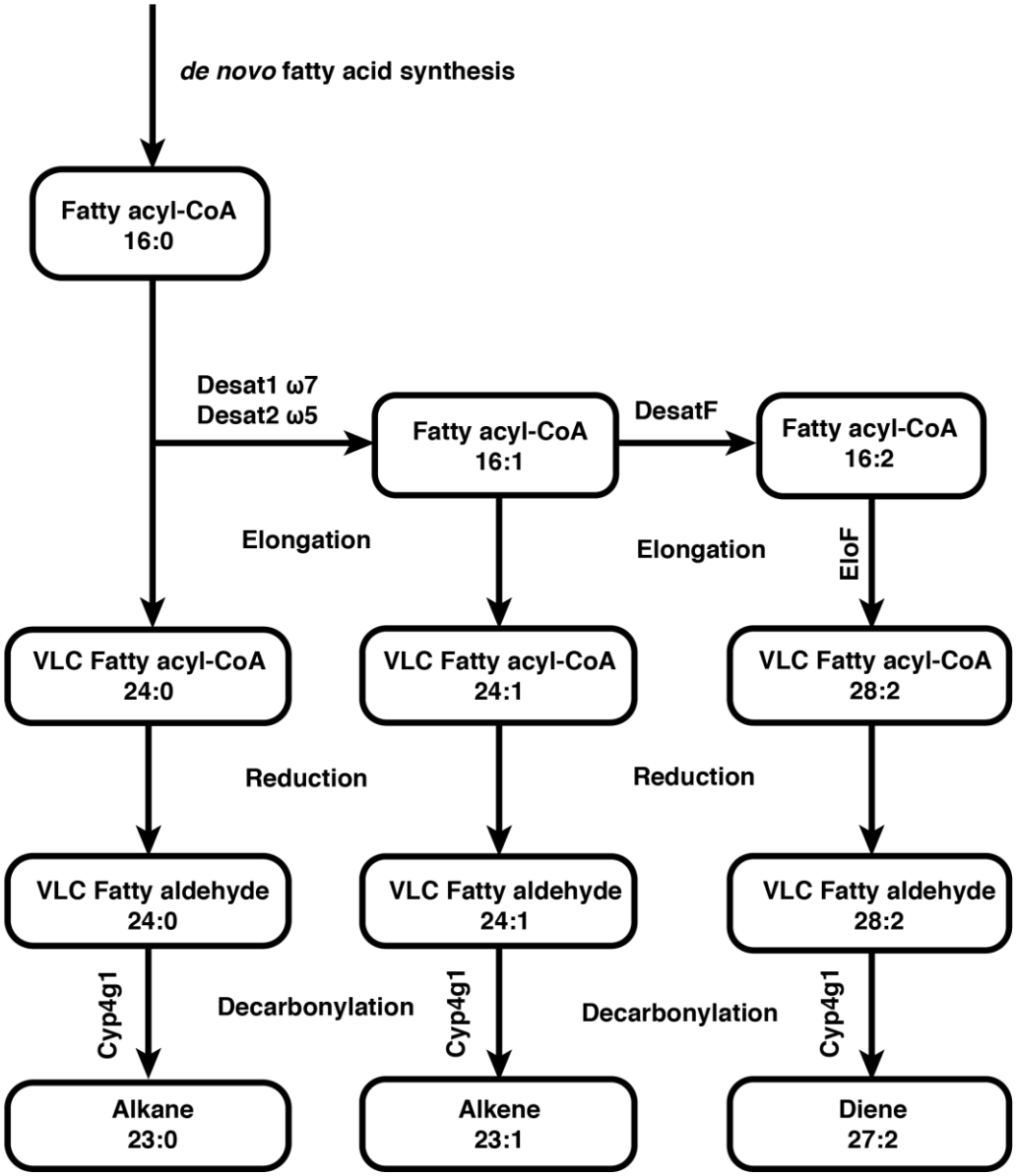

Figure 1.13 *Drosophila* hydrocarbon biosynthesis

Generic biosynthetic pathway for *Drosophila* hydrocarbons. The enzymes that have been definitively proven to perform certain steps are indicated (Wicker-Thomas and Chertemps, 2010, Qiu et al., 2012).

One key function of *Drosophila* hydrocarbons is thought to be as barrier lipids against water loss. The chain length of the hydrocarbon blend is not thought to influence the efficacy of the waterproofing barrier. Gibbs et al. have demonstrated in several *Drosophila* species that increasing the average length of hydrocarbons in the cuticular lipid blend does not result in a change in the total water loss from the flies (Gibbs et al., 1998, Gibbs et al., 2003). A recent study suggested that the proportion but not the overall amount of unsaturated cuticular hydrocarbons directly inferred the efficacy of the waterproofing barrier, but not the absolute amount of unsaturated hydrocarbons (Ferveur et al., 2018). The melting temperature of the lipid blend is considered to be a good predictor of the efficacy of the waterproofing barrier, and this is affected most strongly by lipid class as opposed to carbon chain length (Gibbs, 2002). As such, this suggests that an effective waterproofing barrier may be reliant on the ratio of different lipid classes as opposed to absolute abundance.

A second important function of cuticular hydrocarbons is as pheromones that regulate mating behaviour. In particular, the male pheromone (*Z*)-7-tricosene and the female pheromone (*Z,Z*)-7,11-heptacosadiene strongly regulate male-female interactions (Antony and Jallon, 1982, Scott, 1994). Experiments that genetically “feminise” the oenocytes result in the production of female pheromones by male flies, indicating that the sex-specific regulation of pheromonal production occurs in oenocytes (Savarit and Ferveur, 2002, Ferveur et al., 1997). This experiment did not result in a response by the males to their self-produced female pheromones, suggesting that the sexual dimorphism in the response to pheromones is oenocytes-independent. Feminisation of the antennal lobe did, however, result in an altered pheromonal response - inducing courtship with males alongside females (Ferveur et al., 1995). Male *Drosophila melanogaster* are also known produce a fatty acid methyl ester pheromone, (*Z*)-11-Vaccenyl acetate (cVa). This pheromone is not produced by the oenocytes, but instead by the male ejaculatory bulb (Guiraudie-Capraz et al., 2007). cVa has several identified pheromonal functions – at high concentration it stimulates male-male aggression and ant lower concentration it stimulates mating and acts as an aggregation pheromone (Ejima, 2015)

Hydrocarbon pheromones are detected by sensory neurons of both the olfactory and gustatory systems (Kohl et al., 2015). The way in which pheromonal information is subsequently processed by the CNS neural circuits is currently not well understood. Based on classic studies with cVa, hydrocarbons are thought to be transported through the aqueous sensillum lymph by odorant binding proteins (Obps) secreted from the supporting glia of the sensillum (Ha and Smith, 2006, Xu et al., 2005). Glial-derived Obps deliver hydrophobic pheromones and odorants to the sensory neuron where they induce a signalling response via a specific odorant receptor (OR) and its common co-receptor Or83b, otherwise known as Orco (**Figure 1.14**). In the case of cVa detection, the Obp involved is Lush and the specific OR is Or67d (Xu et al., 2005, Ha and Smith, 2006, Larsson et al., 2004). A similar detection mechanism but perhaps with different Obps and ORs may be responsible for the behavioural response to other pheromones including hydrocarbons. For many hydrocarbons, the details of which of the 62 ORs and 51 Obps encoded by the genome are involved are not yet clear (Saberi and Seyed-allaei, 2016, Vieira et al., 2007). In the case of the male-specific hydrocarbon (*Z*)-7-tricosene, its pheromonal activity in promoting female mating has been partially ascribed to the odorant receptor Or47b (Wang et al., 2011). However, (*Z*)-7-tricosene also induces male-male aggression and, in this case, pheromonal activity has been ascribed to the gustatory receptor Gr32a expressed in chemosensillar of the legs (Wang et al., 2011). More generally, the detection of molecules by gustatory receptors in chemosensillar on the legs and labellum is thought to occur in a broadly similar way to olfactory receptors in the antenna, except that it is contact-dependent (Amrein, 2016). Several contact chemoreceptors from the pickpocket family have also been implicated in the detection of hydrocarbon pheromones and their corresponding behavioural responses, including ppk23 (male pheromones such as (*Z*)-7-tricosene), ppk25 and ppk29 (female pheromones such as (*Z,Z*)-7,11-heptacosadiene) (Starostina et al., 2012, Thistle et al., 2012). Pickpocket ion channels are thought to form heterotrimers, so it is possible that pheromonal specificity could be mediated via different combinations of pickpocket subunits (Jasti et al., 2007, Liu et al., 2020).

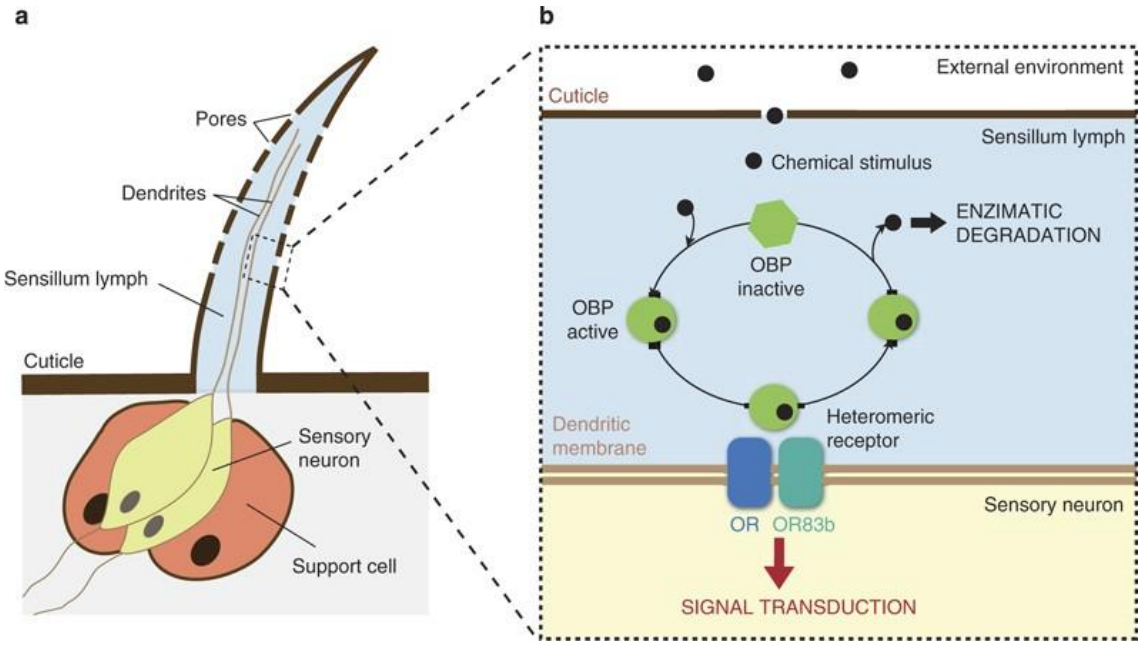

Figure 1.14 The *Drosophila* antennal sensory system

Volatile hydrophobic odorants are transported through the aqueous sensillum lymph by odorant binding proteins (Obps), where they induce signal transduction via a specific odorant receptor (OR) and its ubiquitous co-receptor OR83b (also known as Orco). Reproduced with permission from (Sánchez-Gracia et al., 2009)

A third function for cuticular hydrocarbons is as autotoxins that can decrease lifespan in a population density-dependent manner (Stefana et al., 2017). In this study, it was shown that the production of alkene pheromones such as (*Z*)-7-tricosene and (*Z,Z*)-7,11-heptacosadiene can account for why lifespan in both sexes decreases with increasing population density. The dual function of alkene hydrocarbons as pheromones and toxic molecules in *Drosophila* is similar to what has been shown for ascaroside lipids in *C. elegans* (Shi et al., 2017, Maures et al., 2014). The production of autotoxins in *Drosophila* was also linked with DOHaD, as it was shown that developmental restriction of dietary yeast decreases the production of cuticular alkenes and is associated with an increase in lifespan (Stefana et al., 2017). This link between DOHaD and cuticular lipid composition forms an important starting point for this thesis.

1.5 Past and current methods for lipidomics

To properly investigate the link between DOHaD and cuticular lipids, it is important to be able to accurately determine barrier lipid composition. The small physical size of *Drosophila* and the requirement for surface-specific analysis provides a unique analytical challenge that is addressed in this thesis. An optimal method needs to be able to detect a broad range of lipids including hydrocarbons, wax esters, glycerolipids, phospholipids, sphingolipids, fatty acids and steroids. For chromatography-based techniques, sample preparation necessitates extracting the lipids using an organic solvent, the polarity of which will determine the lipid classes extracted. In this study, the lipids of interest have a wide range of polarities from relatively hydrophilic lyso-phosphatidylcholines (lyso-PCs to extremely lipophilic hydrocarbons (**Figure 1.15**). As such, isolating these lipids using one common solvent is likely to result in inefficient extraction (Furse et al., 2015).

Lipidomics has its historical roots in separation science but it is a relatively young field (Lagarde et al., 2003, Wenk, 2005). The principle underlying chromatography separation science is the separation of a chemical mixture in a biphasic system composed of a stationary phase and a mobile phase. Typically, the stationary phase is housed on a solid support which is packed into a column for column-based chromatography, or coated onto a plate for thin layer chromatography (TLC). High separation efficiency relies on a fast rate of exchange between the two phases. The coupling of mass spectrometers to chromatography instruments opened a new field of analytical discovery. This enabled the discrimination of lipids with only minute differences in their chemical structure, as opposed to the broad “class-level” identification possible with chromatography techniques alone. This advancement in lipid identification has enabled putative characterisations of compounds of interest without possessing an authentic standard – leading to a rapid recent growth in untargeted metabolomics.

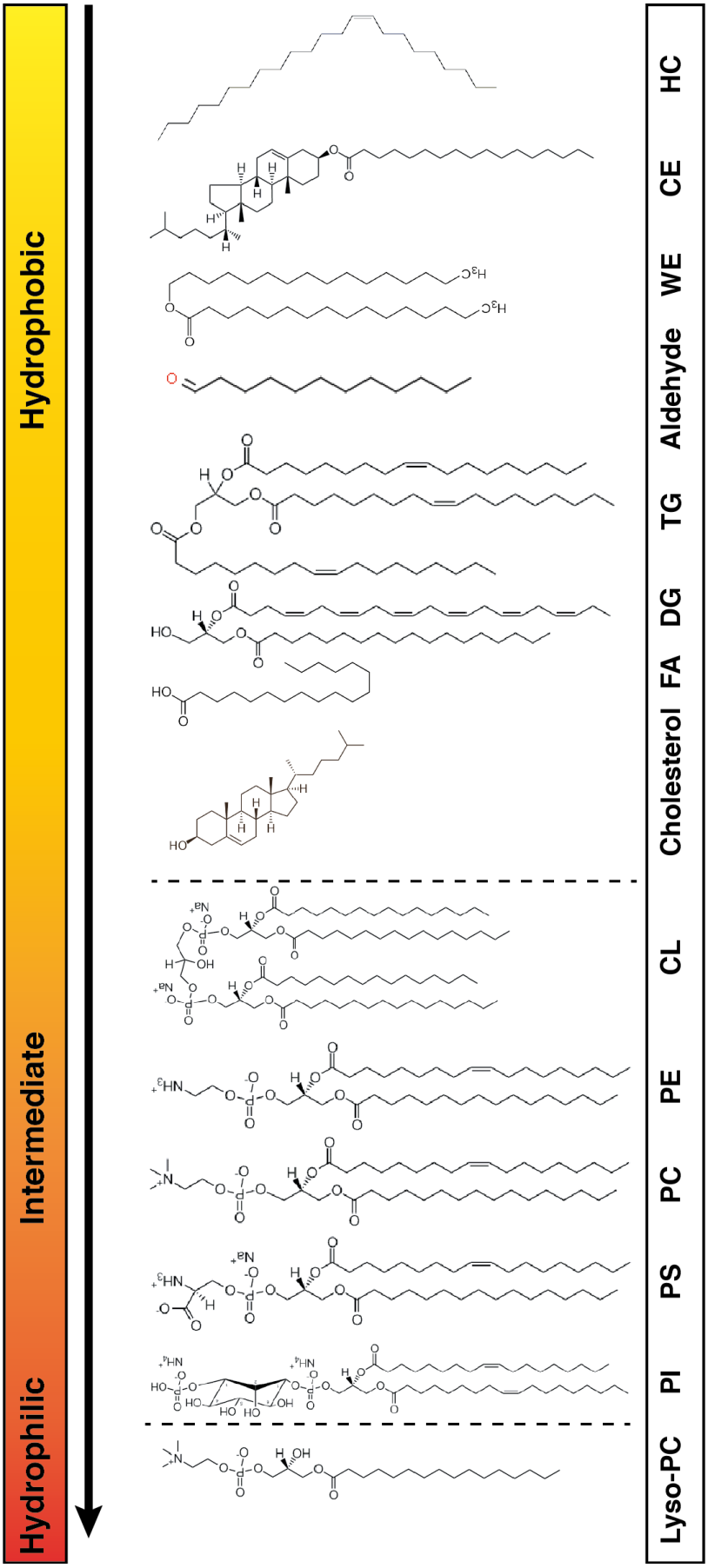

Figure 1.15 Structure and polarity of different lipid classes
Relative polarity of different lipid classes (Brown et al., 2012, Furse et al., 2015). PC = phosphatidylcholine, PI = phosphatidylinositol, PS = phosphatidylserine, PE = phosphatidylethanolamine, CL = cardiolipin, FA = fatty acids, DG = diacylglyceride, TG = triacylglyceride, WE = wax ester, CE = cholesteryl ester, HC = hydrocarbon.

1.5.1 Theory and methods for molecular ionisation in mass spectrometry

To detect a compound using mass spectrometry, it must first be ionised. Several thermochemical properties of a molecule predict it's ionisation efficiency using different ionisation methods. Ionisation energy (IE) is an important thermochemical property which defines the energy required to eject a single electron from a molecule at a temperature of 0 degrees Kelvin (0K) (1.1). A low IE value predicts efficient ionisation of the molecule, which may predict high degrees of compound fragmentation as a result of excess internal energy transferred by the ionisation source.

$$M \rightarrow M^{+} + e^{-} \qquad \Delta H = IE \qquad \textbf{1.1}$$

Conversely, electron affinity (EA) describes the opposite process, the gain of a single electron by a neutral molecule, and is defined as the negative of the energy required to attach a single electron at a temperature of 0K (1.2). This can only occur if the molecule of interest has acidic groups or electronegative elements.

$$M + e^{-} \rightarrow M^{-} \qquad \Delta H = EA \qquad \textbf{1.2}$$

Ionisation can be achieved in a wide variety of ways which can also involve more complex chemical reactions than those described above. In this sub-section, the most common methods will be discussed.

Electron ionisation

Electron ionisation (EI) refers to the ionisation of molecules through interactions with an electron beam perpendicular to the gaseous stream of molecules. Gaseous ions are exposed to an electron beam with a defined wavelength, and if the wavelength of the beam is close to that of the chemical bonds in the molecule and if the photon has sufficient energy, then this will result in a transfer of vibrational energy to the molecule and an electron will be expelled resulting in ionisation (de Hoffmann and Stroobant, 2007). This reaction follows the form of

1.1. The wavelength of the electron beam, λ, can be described using the de Broglie equation:

$$\lambda = \frac{h}{mv} \quad \textbf{1.3}$$

where h is Planck's constant of ~6.62×10^{-34} $Js^{-1,}$ m is the mass of the electron and v is the velocity. The frequency of the beam, v, can be derived using the following equation, where c is the speed of light:

$$c = \lambda v \quad \textbf{1.4}$$

The photon energy ,IE, required to ionise a molecule can then be defined as:

$$IE = \frac{hc}{\lambda} \quad \textbf{1.5}$$

The energy of the electron beam is critical for ionisation to occur effectively. If it is too low, not enough energy is transferred to ionise the molecule, whereas if it is too high, the electron beam becomes invisible to the molecules due to its de Broglie wavelength. An optimal value for a wide range of organic compounds is ~70 eV. As the transferred energy usually exceeds that of the ionisation energy, molecules ionised with EI typically display extensive fragmentation. Analysis of the resulting fragmentation pattern can produce useful structural information and improve reproducibility. Due to the mechanism of ionisation, EI most commonly produces positive ions. As the molecules of interest must be presented in a gaseous form, this method of ionisation is most commonly used with GC-MS.

Chemical ionisation

Chemical ionisation (CI) is a softer form of ionisation, typically used in GC-MS, that relies on molecule collisions with an ionised reagent gas such as methane or ammonia. Both the reagent gas and analyte gas are transferred to a high pressure chamber at ~60 Pa which induces collisions and results in the formation of an ionisation plasma. Within this plasma, a complex series of reactions can occur resulting in analyte ionisation with either a positive or negative charge (de Hoffmann and Stroobant, 2007).

The most common reaction to occur is proton transfer. This occurs when a proton is transferred from the ionised reagent gas to the analyte in a Brønsted acid-base reaction. In order for this to occur, the proton affinity of the analyte must be greater than that of the reagent gas (de Hoffmann and Stroobant, 2007). Proton affinity (PA) is defined as:

$$M + H^+ \rightarrow MH^+ = -PA$$

Experimentally determined values are available for a wide range of compounds and can be used to determine if a specific analyte will ionise with a particular reagent gas. If the reagent gas contains basic elements, then negative ions can also be formed if the proton affinity of the reagent gas is greater than that of the analyte (Benoit and Harrison, 1977). The enthalpy change of this reaction relative to the analyte defined as the gas phase acidity, $\Delta G_{acid,}$, can be described with the following equation:

$$MH \rightarrow M^- + H^+ = \Delta G_{acid}$$

Positive ions can also be induced via charge transfer, where the ionised radical cation reagent gas transfers charge directly to the analyte leading to the formation of a radical cation. This usually occurs when the reagent gas has a high ionisation potential. Negative ions can also be generated in a similar manner, through electron capture of thermal electrons in the ionisation plasma. It is also possible to generate ions through adduct formation with the reagent gas which are typically positively charged (de Hoffmann and Stroobant, 2007). Chemical

ionisation can also be performed under atmospheric pressure under certain circumstances (atmospheric pressure chemical ionisation, APCI). This can be beneficial due to the faster thermal stabilisation of the ions at atmospheric pressure with can result in an ionisation efficiency several orders of magnitude higher than in standard CI sources (Bruins, 1991, Huang et al., 1990).

Electrospray ionisation

The development of electrospray ionisation led to the joint award of the Nobel Prize for Chemistry to John Fenn (Fenn et al., 1989). ESI is one of the softest ionisation methods. Electrospray ionisation (ESI) operates by passing an electrical charge through an aqueous liquid passing through a capillary tube. This induces charge accumulation at the surface of the liquid, resulting in the formation of highly charged droplets. These droplets produce further generations of increasingly smaller, more highly charged droplets until the ions desorb from the surface of the droplets. This mechanism results in a specificity for lipophilic compounds which will localise to the surface of the droplets and can completely supress detection of hydrophilic compounds which would be located in the centre of the droplets. The formation of ions in ESI is an electrochemical process, and is therefore sensitive to concentration rather than absolute abundance (Ho et al., 2003).

A common ionisation mechanism in ESI is adduction of ions in solution, for example salts. In ESI coupled to liquid chromatography, the generation of charged particles often happens in solution before the sample reaches the electrospray source and the generation of these charged particles is influenced by the electrochemical properties of the compound of interest. The most common reaction is the addition or loss of a single proton to form an $[M-H]^-$ or $[M+H]^+$ adduct. This often occurs via traditional Brønsted acid-base reactions (de Hoffmann and Stroobant, 2007). Due to poor ionisation of extremely apolar molecules with ESI, this technique is not suitable for the more extremely lipophilic compounds such as hydrocarbons and wax esters. Instead, ionisation via APCI or atmospheric pressure photoionisation (APPI) is more appropriate and will achieve higher ionisation yields (Lung and Liu, 2015, Tada et al., 2005).

Atmospheric Pressure Photoionisation

Atmospheric pressure photoionisation (APPI) uses photons to ionise analytes at atmospheric pressure. The analyte in a solvent solution is nebulised and subsequently ionised by photons generated by a UV lamp. The energy of the photons is tuned so it is sufficient to ionise the analyte but not high enough to ionise the atmospheric gas or solvent (de Hoffmann and Stroobant, 2007). As the energy is much lower than that of EI, there is substantially less fragmentation of the molecules. In addition, dopants can be added to the solvent to induce ionisation via adduct formation. This technique is typically used in liquid chromatography-mass spectrometry (LC-MS).

Laser desorption ionisation

Laser desorption ionisation (LDI) is ionisation induced by a laser pulse. The laser pulse can directly ionise the analyte through energy transfer, and results in desorption of ions and atoms from the sample surface. Within the cloud of ions and atoms just above the surface of the sample, multiple reactions can occur which themselves induce ionisation such as adduction or charge transfer. Recent advancements in laser focussing now enable the generation of laser spot sizes < 2 µm in diameter (Kompauer et al., 2017). LDI is often used in the presence of a matrix coating the sample (matrix-assisted laser desorption ionisation, MALDI), which forms crystals on the surface of the sample and acts to transfer the laser energy to the co-crystallised analyte. Matrix compounds are chosen for their crystal structure and ability to efficiently absorb energy from the laser and transfer it to the analyte.

Ion beam bombardment

Ionisation can also be induced via bombardment of the sample with a primary ion beam. This can either be a monoatomic ion beam or a polyatomic ion beam. Monoatomic, or small cluster (<5 atoms), ion beams are typically generated using liquid metal ion sources. A thin film of liquid metal, such as gold or bismuth, flows over a microneedle and is ionised via application of an electric field and subsequent evaporation of surface ions, a process known as field evaporation. These ions are then accelerated to an energy of ~30 kV and focused to form the ion beam (Swanson, 1983). Monoatomic ion beams transfer a large amount of energy per atom, so cause a high degree of fragmentation and induce deep collision cascades through the sample, disrupting the lower layers (**Figure 1.16**). They can be focused to a relatively high degree, <200 nm, and cause a low degree of disturbance to the surrounding surface region.

Argon gas cluster ion beams (GCIBs) are generated through supersonic adiabatic expansion when the gas is forced from a high pressure environment into a vacuum, resulting in a near homogenous velocity distribution. Clusters form through Van der Waals interactions between the surrounding argon atoms. These clusters are then ionised by EI, typically gaining a single positive charge per cluster. These clusters are then accelerated to an energy of ~20 kV and focused to generate the primary ion beam (Yamada et al., 2001, Toyoda and Yamada, 2008). As the resulting ion beam has a low energy per atom ratio, the energy transferred per atom to the analyte is much lower than that of a monoatomic or polyatomic ion beam, resulting in reduced molecule fragmentation. This is particularly useful for the analysis of complex biological samples, but comes with a trade-off of image resolution due to the physical limits of the beam diameter. Bombardment with a GCIB also results in reduced collision cascades within the crater, which can preserve molecular structure throughout the depth of the sample (**Figure 1.16**).

Ionisation is thought to occur via a combination of mechanisms. The primary ion bombardment can directly induce formation of cation radicals as seen in EI. The formation of $[M+H]^+$ and $[M-H]^-$ adducts is thought to occur in a similar manner to

ESI, either pre-formed on the sample surface, or induced by the primary ion bombardment. It is also possible for adducts to be formed through association of neutral molecules with cations or anions which is thought to occur a few angstroms above the surface of the sample in the “cloud” of ions and neutral molecules formed from ion-beam induced desorption. This leads to the detection of analytes that are not directly ionised by the primary ion beam (Vickerman and Briggs, 2013).

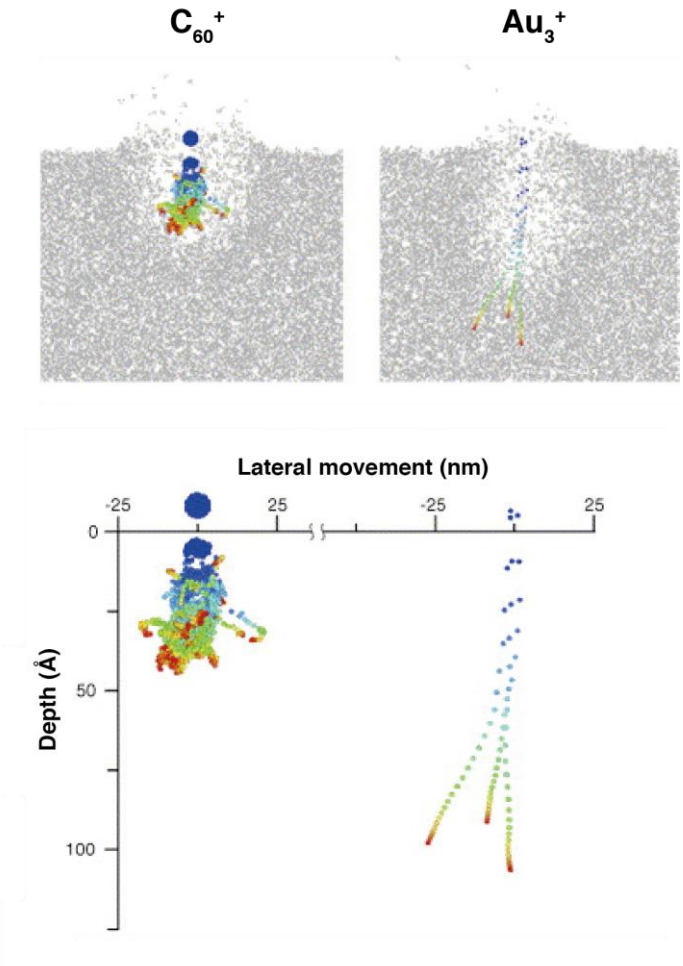

Figure 1.16 Collision cascades induced by a large cluster C_{60}^+ ion beam and a polyatomic Au_3^+ beam

Collision cascades induced on amorphous ice generated using molecular dynamics simulations for a large cluster ion beam (C_{60}^+) and a small cluster polyatomic ion beam (Au_3^+). Figure adapted from Russo et al. (2006) with permission.

1.5.2 Mass analysers

Mass analysers enable the determination of the mass to charge ratio, *m/z*, of an ion which can subsequently be used to identify the detected ion. The precision of the mass to charge ratio calculated by the mass spectrometer is measured using mass resolution. As it is not possible to determine the mass to charge ratio as an exact value due to error, it forms a normal distribution forming a “peak”. Mass resolution can be calculated for an individual peak using the following equation where *R* is resolving power, *m* is the *m/z* value at the peak maximum and *Δm* is the *m/z* value referring to the full width at half maximum (FWHM) of the peak:

$$R = \frac{m}{\Delta m} \quad \textbf{1.6}$$

Therefore it is possible to calculate the mass resolving power required to resolve two adjacent peaks using **Equation 1.6** where *m* is the *m/z* value for a peak maximum and *Δm* is the m/z value separating the two peaks at their half maximum (de Hoffmann and Stroobant, 2007).

Mass deviation in parts per million (ppm) is calculated using the following equation, where m_i is the experimentally measured mass, and m_a is the theoretical exact mass:

$$\Delta m_i = \frac{(m_i - m_a)}{m_a} \times 10^6 \quad \textbf{1.7}$$

The ability to identify an unknown mass of interest is enhanced with increasing mass resolution (**Figure 1.17**). This can be further analysed by taking into account the isotope distribution of the ion. The development of mass spectrometers with ultra-high mass resolution has resulted in the ability to accurately determine the chemical formula of the compound of interest from the mass value alone without the requirement for an identical chemical standard. This

is extremely valuable for untargeted lipidomics analysis, ensuring that novel results are not overlooked due to a lack of commercial chemical standards.

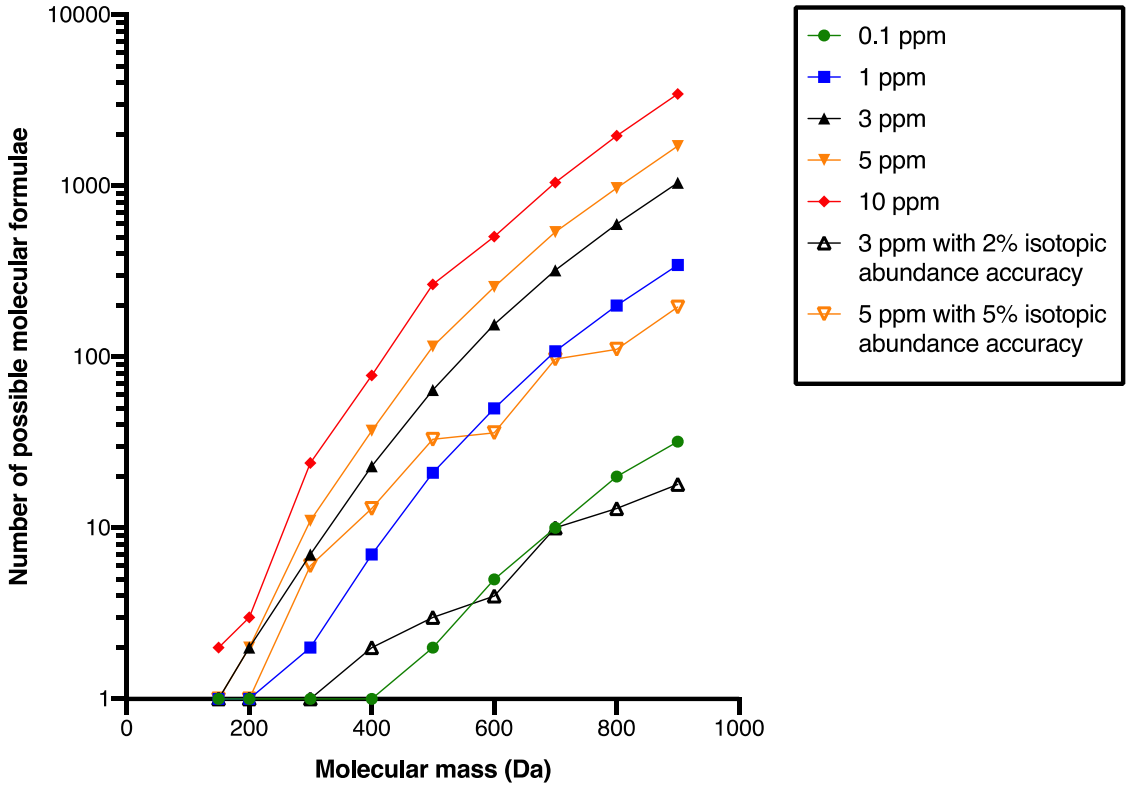

Figure 1.17 Number of possible molecular assignments with differing mass

The number of possible molecular formulas at different molecular masses calculated when the mass value is calculated with varying degrees of certainty (mass deviation in parts per million, ppm). The open triangles indicate how this changes when isotopic abundance is factored into the calculation, with an accuracy of 2% or 5%. Data derived from Kind and Fiehn (2006) with permission.

The chemical separation step provided by chromatographic or ion-mobility methods is very beneficial, as it reduces the mass resolving power required for compound identification when combined with commercial standards. It is often common to see gas chromatography-mass spectrometry (GC-MS) and LC-MS instruments with lower resolution quadrupole analysers utilised for the analysis of biological samples. These analysers are beneficial due to their good sensitivity, fast analysis rate and low cost. For these reasons, they can be particularly powerful for targeted analyses. More recently, time-of-flight (ToF) analysers have gained popularity due to their higher sensitivity (Allen and McWhinney, 2019).

ToF analysers can also be operated with relatively high mass resolving power when coupled with a buncher, however this increases the analysis time.

In the absence of ion mobility or chromatography, it becomes more important to utilise mass analysers with a high resolving power and tandem MS to enable compound identification in complex biological samples. In this case, Orbitrap analysers have a number of advantages due to their high mass resolving power, enabling accurate determination of chemical composition. Recently, Fourier transform-ion cyclotron resonance (FT-ICR) instruments have begun to be introduced for the analysis of biological samples which provides even higher mass resolving power, a greater degree of mass accuracy and higher sensitivity than Orbitrap analysers (Stopka et al., 2019). However, these instruments require powerful magnets; the most recent example of this being the 21 Tesla ion cyclotron resonance (ICR) magnet at the National High Magnetic Field Laboratory in Florida. These instruments are incredibly expensive – the magnet alone costs $12.5 million (Stopka et al., 2019); therefore are a long way from being commercially viable for large numbers of samples or routine biological research. For the near future, the most popular mass analysers for biological research appear to be quadrupoles, ToFs and Orbitraps.

Quadrupole

Quadrupoles are formed of four parallel rods with either a positive or negative direct current (DC) and radio frequency (RF) potential. The stability of ions for a given mass depends sensitively of the relative DC and RF potentials and this can be tuned so that ions of a particular mass will travel through the electric field in an oscillating manner without colliding with the rods. They are typically low mass resolution mass analysers and are operated at a mass unit resolution. The electric field of the quadrupole quickly cycles through a range of potentials corresponding to the stable transmission of ions of a different mass to charge ratios, and these ions are subsequently detected (Campana, 1980). Quadrupoles can also be used with an oscillating potential as an ion guide to transfer ion beams, or for mass selection before a collision cell for MS^2 analysis. Due to their

relatively low cost and fast scan times, these mass analysers are used in a variety of industrial settings.

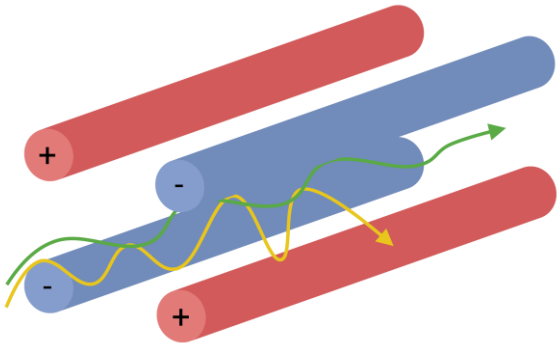

Figure 1.18 Quadrupole mass analyser

Illustration of a quadrupole mass analyser with a stable transmitted ion (green) and an unstable ion which is not transmitted (yellow).

Time-of-Flight

Time-of-Flight (ToF) analysers determine the mass of the ion based on the time it takes to reach the detector. The ions are accelerated before reaching the ToF, and their mass to charge ratio determines the velocity at which the ion travels. When properly calibrated, the time interval before the ion reaches the detector, a proxy of the velocity, can be used to determine the mass to charge ratio. The precision of the time intervals therefore determines the mass resolving power of the analyser. As a result, the time interval is very short. In a ToF analyser, the resolving power can be increased by increasing the length of the ion path, which can either be linear or reflected to increase the ion path without substantially increasing the size of the instrument and providing first order correction of the initial energy spread of the ions. Using this method, ToF analysers can now reach a resolving power of ~100,000 $m/\Delta m$ (Siek et al., 2013), although this comes at the cost of increased acquisition time. The resolving power is maintained across the entire mass range, which is not the case for other types of mass analyser.

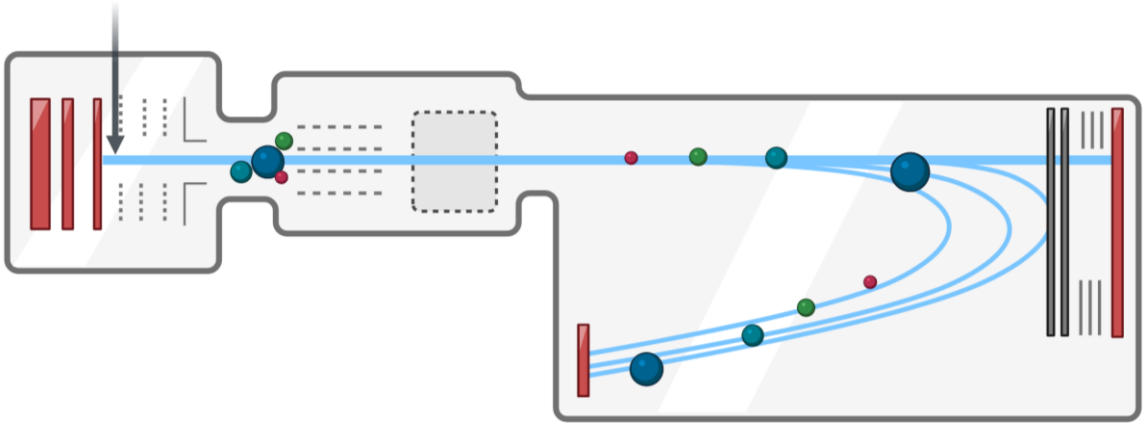

Figure 1.19 Time-of-Flight mass analyser

Schematic of a Time-of-Flight analyser showing the ions travelling at different velocities dependent on their mass to charge ratios and determining the time at which they hit the detector.

Orbitrap

Orbitraps, or orbital traps, are one of the most recent designs of mass analysers (Hu et al., 2005, Makarov, 2000). They operate by injection of a packet of ions into a "trap" composed of an inner and outer electrode (**Figure 1.20**). Ions are first collected into a curved trap, or c-trap, allowing simultaneous injection of all ions in a tightly focussed ion packets with low energy spread. This enables efficient grouping of ions with the same mass within the orbitrap, improving sensitivity. The ions then oscillate around the inner electrode in complex patterns. The frequency of the harmonic axial oscillations can then be used to determine the mass to charge ratio via detection of the generated image current measured by the outer electrodes (Zubarev and Makarov, 2013). The frequency of the oscillations can be calculated using a series of equations (de Hoffmann and Stroobant, 2007). The electric force, F_z, induced by an ion with a specific mass to charge ratio when it is accelerated in the z direction (axial) can be described as:

$$F_z = \frac{d^2z}{dt^2} = -\frac{q}{m}kz \qquad \textbf{1.8}$$

where d^2z/dt^2 is the acceleration of the ion, q is the charge of the ion, m is the mass of the ion and *kz* is the voltage gradient in the *z* direction along the trap. The energy of the ion, qE_z, can be taken into account as:

$$qE_z = \frac{m}{2} \cdot \left(\frac{dz_0}{dt}\right)^2 \qquad \textbf{1.9}$$

then solving **Equation 1.8** gives:

$$z(t) = z_0 cos\omega t + \sqrt{\frac{2E_z}{k}} \cdot sin\omega t \qquad \textbf{1.10}$$

where ω represents the angular frequency of the ion which can be described as:

$$\omega = \sqrt{\left(\frac{q}{m}\right)k} \qquad \textbf{1.11}$$

This clearly shows that the angular frequency of the ion depends on the charge to mass ratio and not on the kinetic energy of the ion. These frequencies can then be converted into mass to charge ratios using Fourier transform.

The dynamic range of Orbitraps can be somewhat limited, if too many ions are injected, they induce space-charge effect which influence the accuracy of *m/z* determination. In addition, they have a relatively slow scan rate of ~1 second per cycle. This makes them less suitable for instruments that require higher scan rates such as GC-MS. Orbitraps are now able to achieve extremely high mass resolving power, in excess of 1 million *Δm/m* (Denisov et al., 2012).

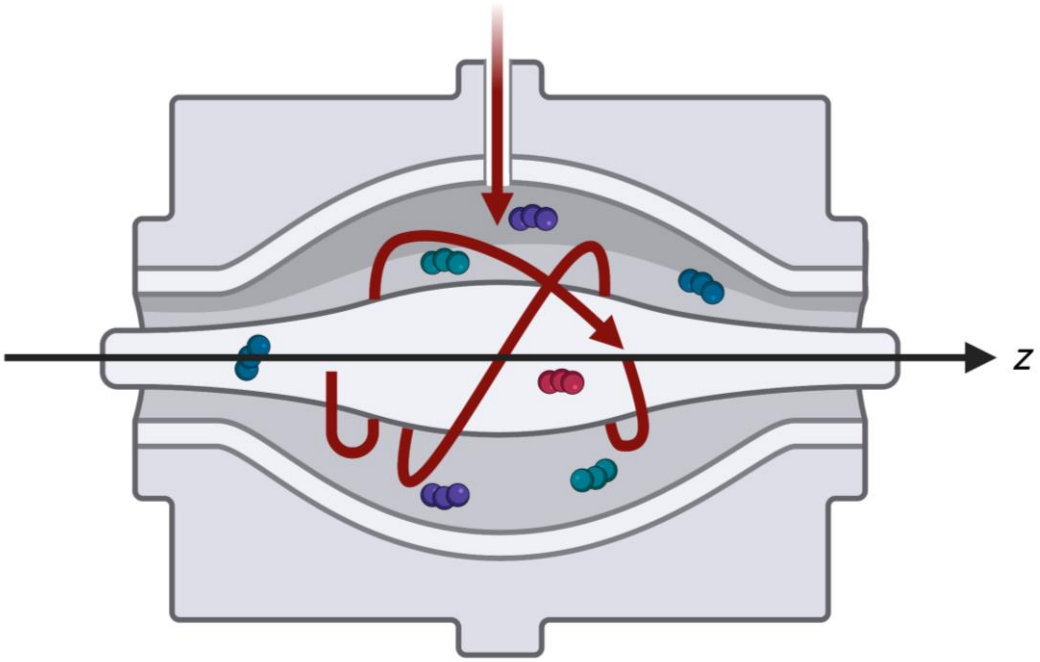

Figure 1.20 Orbitrap mass analyser

Schematic of an Orbitrap mass analyser with the ions oscillating around the central electrode.

Magnetic sector

Magnetic sector instruments utilise a magnetic field to separate ions of different mass to charge ratios in space. Through the application of a magnetic field perpendicular to the direction of the ion beam, an arc is induced in the flight path which is unique to each mass to charge ratio (de Hoffmann and Stroobant, 2007). The resolution of the instrument is then determined primarily by the diameter of the ion beam and the diameter of the detector. This can result in a very high mass resolving power with the trade-off limited mass range. In instruments with cycling magnetic fields, this typically occurs very slowly leading to long acquisition times. Magnetic sectors are commonly used on NanoSIMS instruments, with detectors placed to detect up to seven different mass to charge ratios.

Fourier transform-Ion Cyclotron Resonance

Like Orbitraps, Fourier transform-ion cyclotron resonance (FT-ICR) also operates through trapping ions. Instead of trapping ions in an electrical field, ICR instruments trap the ions in circular trajectory in a strong magnetic field produced

by a superconducting magnet. A series of radio frequencies are then applied which result in the excitation of ions of a certain mass through absorption of this energy. As these ion packets increase their orbit, they approach the detector plates and interact with the electrons contained within them. This produces a current that is detected, and the signal is then transformed into a mass spectrum with a Fourier transform (Tsybin et al., 2019).

These instruments have the highest mass resolving power currently achievable with mass spectrometry techniques. As such, it comes with the trade-off of long acquisition times and high costs, but is very useful for determining fine isotopic distributions.

MS/MS

To supplement the information provided by the mass analysers described above, it is also possible to perform MS^2 analysis with most mass analysers. In this setup, a parent ion is selected, then fragmented in a collision cell. The resulting fragments are then detected, and this information can be used to determine the chemical structure of the molecule (de Hoffmann and Stroobant, 2007). There are increasing numbers of chemical libraries which store fragmentation data, and this is often different when modifying experimental parameters.

1.5.3 Chemical separation

Thin layer chromatography

The most historical method of determining the composition of lipid blends is thin layer chromatography (TLC). This method is an adaptation of the original chromatography method developed at the start of the 20th century (Tswett, 1905). It involves separating lipids based on their polarity on a silica gel coated aluminium plate and detecting them using a fluorescent dye. It has a broad specificity which places this technique ideally for identifying broad changes in the lipid composition of a sample. It is also possible in certain circumstances to separate molecules by their saturation index to view any changes in lipid saturation (Dołowy and Pyka, 2015). This technique also provides a relatively fast

method to screen large numbers of samples for strong alterations in lipid composition as the samples can be run concurrently. This method forms the basis of the chromatography-coupled mass spectrometry analytical methods used more commonly in recent times. Although TLC is a more basic technique, it still contributes information that is not easily gained using more complex techniques.

Gas chromatography

Gas chromatography was developed in the 1950s by Anthony James and Archer Martin (James and Martin, 1954), enabling the rapid and efficient separation of mixtures of analytes requiring relatively small sample sizes. The subsequent coupling of gas chromatography (GC) to mass spectrometry has resulted in a robust and reliable analytical technique which is now the mainstay of analytical science laboratories.

In GC, the mixture of analytes is volatilised at high temperature, then transferred to the carrier gas mobile phase (an inert gas, most commonly helium). The mobile phase is then passed through a column containing the stationary phase. In GC, this can be either a solid adsorbent such as silica, or a liquid bonded to a solid support such as silica-bonded polysiloxane. The composition of the stationary phase determines the sensitivity of the technique for different classes of molecule, and a wide range of stationary phases are commercially available to meet these different requirements.

The retention time (t_R) of a compound on the column depends on a number of different factors which can be represented in the following equation (Guiochon and Guillemin, 1990):

$$t_R = (1 + k') \cdot (L/\bar{u}) \qquad \textbf{1.12}$$

where t_R is the retention time, k' is the retention factor, L is the column length and $\bar{u}$ is the mobile phase velocity. k' can be described as:

$$k' = \frac{RT\rho}{\gamma P^0 M} \cdot \frac{V_L}{V_G} \qquad \textbf{1.13}$$

where R is the universal gas constant of ~8.314 $JK^{-1}mol^{-1}$, T is the column temperature, ρ is the density of the stationary phase, M is the γ is the activity coefficient (a thermodynamics factor used to account for deviations from ideal behaviour, a theoretical state in which a gas is not subject to inter-molecule interactions) of the compound of interest in solution in the stationary phase at infinite dilution, P^0 is the vapour pressure of the compound of interest at the column temperature, M is the molecular weight of the stationary phase, V_L is the volume of column liquid phase and V_G is the volume of the column liquid phase that is accessible by the gas phase. **Equation 1.13** can be split into two parts: the thermodynamic constant of phase equilibrium of the compound of interest between the stationary and mobile phase ($RT\rho/\gamma P^0 M$) and the phase ratio (V_L/V_G) which is defined by the design of the column. In reality, this means that the factors that affect the retention time of a compound the most in an experiment with a standard set-up are the temperature of the column, the activity coefficient of the compound of interest and the vapour pressure of the compound of interest. These three factors are intricately linked. Therefore the selection of the stationary phase combined with the oven temperature gradient will determine the quality of the chemical separation (Guiochon and Guillemin, 1990). The thermodynamic constant of phase equilibrium is also influenced by compound polarity, due to adsorption at the liquid-gas interphase (Dorman et al., 2010). Closely matching the polarity of the compound of interest and the stationary phases leads to stronger interactions and increased retention times. This must be matched well enough to achieve high quality separation, but still allow elution of the compound of interest off the stationary phase. This will enable separation between compounds that are very chemically similar, such as aliphatic alkanes which differ only in carbon chain length. By introducing chiral stationary phases, it is even possible to separate compounds which differ only by chirality (Schurig, 2002).

GC-MS is most suitable for extremely lipophilic, low molecular weight compounds such as hydrocarbons due to their relatively low vapour pressures. As a result, its' most common use in the field of lipidomics is for the detection of fatty acids (Quehenberger et al., 2011). To increase the range of measurement to more polar compounds, derivatisation reactions can be applied to decrease the vapour pressure (Dettmer et al., 2007).

Liquid chromatography

High performance liquid chromatography (HPLC), more commonly referred to simply as liquid chromatography (LC) when in combination with mass spectrometry, relies on similar principles to GC in that the retention time relies on the phase equilibrium of the compound of interest between the stationary and mobile phases. However, instead of relying on temperature, LC relies strongly on compound polarity. The two most common types of liquid chromatography are reverse phase (RP-HPLC) and normal phase (NP-HPLC).

The quality of chemical separation obtained by LC is reliant on the relative affinity of the analyte between the mobile and stationary phases. This is very strongly influenced by compound polarity, and to some degree analyte structure depending on the pore size of the stationary phase (Dorsey et al., 1996).

Ion mobility

Another more recently utilised non-chromatographic method of chemical separation is ion mobility mass spectrometry (IM-MS). Although many different forms of this technology exist, they all rely on similar principles. Ions are separated (post-ionisation) through a drift gas and the time spend travelling through this gas determines the degree of separation. This is determined by the collisional cross section of the molecule; the number of collisions it will undergo with the drift gas. Therefore, this method of chemical separation is dependent on structure rather than polarity; more compact molecules will travel through the drift gas faster than those that are less compact (Giles et al., 2010, Hamid et al.,

2015). This technique of separation is suitable for a wide range of instruments, and enables chemical separation in various non-chromatographic techniques.

Mass spectrometry imaging

Chromatography-based techniques are robust methods for measuring the lipidome of a sample and can be coupled to a wide range of mass analysers as discussed in this chapter to fit a wide range of analytical needs. However, due to the requirement of solvent extraction prior to analysis, the spatial dimension of the data is destroyed. The use of mass spectrometry imaging (MSI) techniques retains this important dimension of data, revealing biologically interesting patterning of metabolites within the sample.

MSI is a relatively new field which encompasses a range of techniques, each with their own benefits. Instead of analysing a “bulk” sample isolated from a tissue homogenate, MSI utilises a whole sample, or tissue section, to identify the spatial localisation of metabolites within the sample. The analysis region is split into pixels, with a mass spectrum collected for each pixel, and this information is then mapped back into an image form by generation of an intensity heatmap for each mass detected. This preserves a dimension of information that is typically lost using chromatographic-based techniques, which comes with its own advantages and trade-offs.

Imaging techniques often do not utilise a chemical separation step, which can make the data harder to interpret. In particular, it is often not possible to differentiate between isobaric compounds. To address this challenge, many instruments have begun to incorporate ion mobility technology to provide chemical separation and this is particularly well incorporated into a variety of commercial MALDI instruments. Other instruments have adopted different solutions to address this issue. The OrbiSIMS addresses this challenge with spectral MS^2 capacity, enabling the differentiation of isobaric compounds by fragmentation patterns (Passarelli et al., 2017). Another approach to this experimental challenge has been the development of ToF-ToF-SIMS instruments such as the Ionoptika J105 which have imaging MS^2 capacity. This development

is particularly powerful and has been show to illustrate differential localisation of isobaric species (Phan et al., 2017).

Desorption electrospray ionisation

Desorption electrospray ionisation (DESI) is currently one of the most common MSI methods used when analysing biological tissues and the initial ionisation step is performed at ambient pressure. The ionisation mechanism works in a similar way to that of ESI; a charged spray of solvent is used to ionise the analytes within each pixel of the analysis field. Due to the difficulty of focusing the solvent beam at ambient pressure, the resolution of this technique is quite low with a typical resolution of ~40-60 µm (Tillner et al., 2017). As the DESI desorption process relies on a charged spray solvent, it also is sensitive to polarity in a similar way to standard solvent extraction (Green et al., 2010).

Matrix-associated laser desorption ionisation

Matrix-associated laser desorption ionisation (MALDI) instruments utilise a UV laser for ionisation of the sample analytes. The sample is coated with a matrix which acts to efficiently transfer the laser energy to the analytes. The chemical composition of the matrix acts as a selective process to promote ionisation of certain species. For example, CHCA (alpha-cyano-4-hydroxycinnamic acid) matrices are commonly used for the analysis of proteins and peptides (Jaskolla et al., 2008), whereas LiDHB (lithium 2,5-dihydroxybenzoic acid) matrices have been shown to be especially efficient at mediating ionisation of hydrocarbons (Cvacka and Svatos, 2003).

MALDI samples can be very challenging to prepare due to the complex nature of matrix application. Ideal matrix application results in the formation of a homogenous layer of crystals with a small size. These are applied in solution with an organic solvent, typically via a heated sprayer that aids with solvent evaporation. The solvent acts to liberate the analytes from the sample and enable them to co-crystalise with the matrix. To reduce any diffusive effects caused by the matrix application, it is important that the organic solvent evaporation and

crystal formation happen as quickly as possible. Even with optimal preparation, it is not possible to avoid segregation of analytes within the crystals (Bouschen and Spengler, 2007). Therefore the spatial resolution of MALDI is limited not only by the laser spot size, but also by the limits of matrix application.

Due to recent developments in MALDI matrices, this technique does not have the same dependence on polarity (Wang et al., 2017, Zhang et al., 2011, Macha et al., 2000), however it is also less suitable for analysing the samples of interest as it is not as surface-sensitive; depending on the matrix, the laser can consume ~1-3 µm within a single measurement (Vickerman, 2011, Jaskolla et al., 2009). MALDI also requires application of a matrix that co-crystallises with the analyte of interest which infers a degree of bias depending on the matrix selected (Perry et al., 2020).

Secondary ion mass spectrometry

Secondary ion mass spectrometry (SIMS) refers to an MSI technique where the sample ionised by a primary ion beam, typically either a gas cluster ion beam (GCIB) or a liquid metal ion gun (LMIG), and mass spectral information is acquired for each pixel within a field of interest. This data is then mapped to the image location and used to generate heatmaps that correspond to the intensity of each *m/z* on a pixel-by-pixel basis. The ion beams used do not penetrate deeply in the sample which results in surface sensitivity of the technique. Higher energy ion beams can also be employed to generate 3D maps of the sample by milling away the sample surface after the acquisition of an image from a single plane. The resolution of the images is limited at the focus achievable by the primary ion beams. Currently, this is approaching 50 nm for an LMIG and is ~2 µm for a GCIB (Senoner and Unger, 2007). As the acquisition of an image at high resolution requires collection of an extremely large number of mass spectra (an image of a 400 µm x 400 µm square at a resolution of 200 nm contains 4 million pixels), the speed of the mass analyser is key to achieving reasonable acquisition times. The mass analyser of choice is often a ToF analyser, although the resolution is limited to ~ 10,000 $\Delta m/m$ usually depending on the surface topography.

SIMS analysis requires the samples to be relatively flat therefore a minimal degree of dissection of samples is required to achieve this (Lee et al., 2011). As the SIMS process involves a substantial degree of charge deposition, it is critical that the sample is mounted on a conductive surface for charge dissipation (Lee et al., 2012). In practice, this is straightforward as a large number of silicon and indium-tin oxide coated supports are commercially available.

OrbiSIMS

To improve the application of SIMS to imaging of complex biological samples, the OrbiSIMS instrument was designed by Ian Gilmore at the National Physical Laboratory (Passarelli et al., 2017). This instrument differs from standard SIMS instruments in the addition of an Orbitrap mass analyser to complement the ToF analyser (**Figure 1.21**). The Orbitrap mass analyser enables acquisition of high resolution mass spectra, with the additional capacity of tandem mass spectrometry (MS) to separate isobaric compounds. When carrying out imaging experiments, it is important to consider the acquisition time which may be quite substantial. The ToF analysers traditionally used in SIMS instruments operate with a relatively low mass resolving power, but this comes with the benefit of short cycle times which enables image acquisition at high resolution with acceptable acquisition times. Increasing the mass resolving power of the mass analyser is beneficial for the analysis of chemically complex samples but is detrimental to the analysis time which can result in lengthy for image acquisitions (**Figure 1.22**). The acquisition time is linearly related to the number of pixels in an image and consequently the square of the number of pixels along one side. Therefore the acquisition time is long for Orbitrap images. For example, a 500 x 500 µm image acquired with a ~1.5 µm pixel size will take >14 hours with an Orbitrap analyser at full mass resolving power (500 ms transient time) but will only take ~20 seconds with the ToF analyser (although in practice, 20 minutes or longer is typical to achieve sufficient signal to noise). Therefore, the strength of the Orbitrap analyser is primarily in acquiring high resolution spectra rather than imaging. The OrbiSIMS combines the benefits of each of these analysers, as images can be acquired with the ToF analyser at a fast speed with relatively poor

mass resolution and directly compared with Orbitrap spectra of the same region at high mass resolution. In this set-up, the relative benefits of the ToF and Orbitrap analysers are fully utilised.

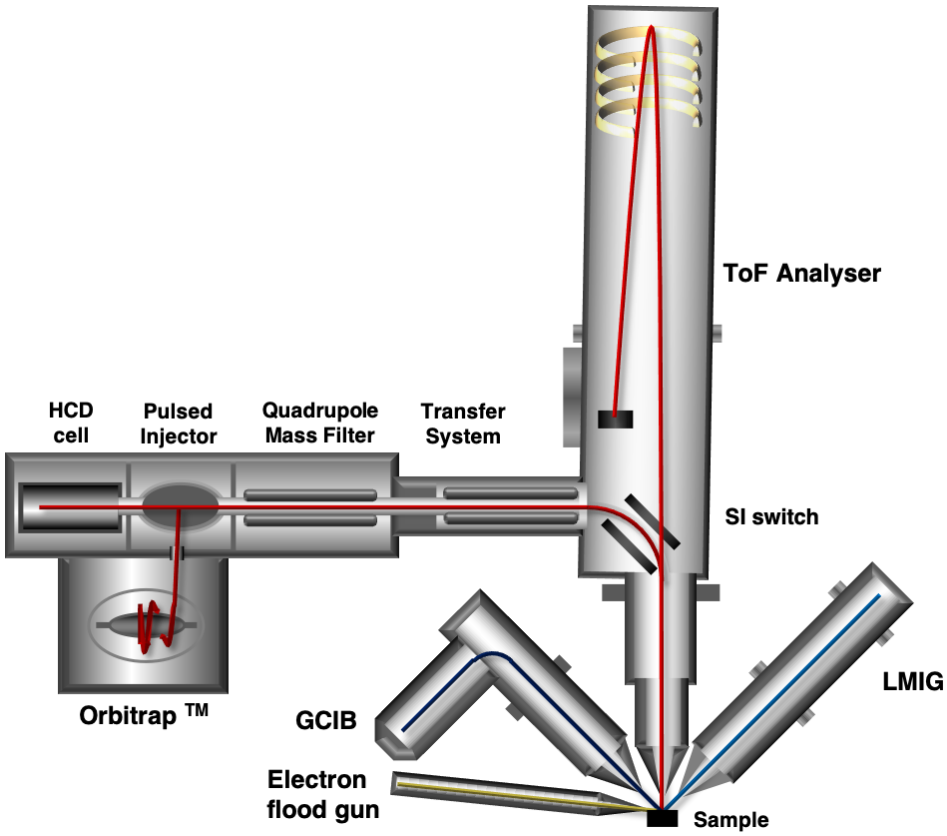

Figure 1.21 Schematic of the OrbiSIMS secondary ion mass spectrometer
Illustration of the OrbiSIMS instrument highlighting the dual detector design incorporating a ToF analyser and an Orbitrap analyser. The instrument has two primary ion beams, a liquid metal ion gun (LMIG) utilising bismuth, and a gas cluster ion beam (GCIB) utilising argon. The instrument utilises an electron flood gun for charge compensation. Schematic modified from Passarelli et al. (2017) with permission.

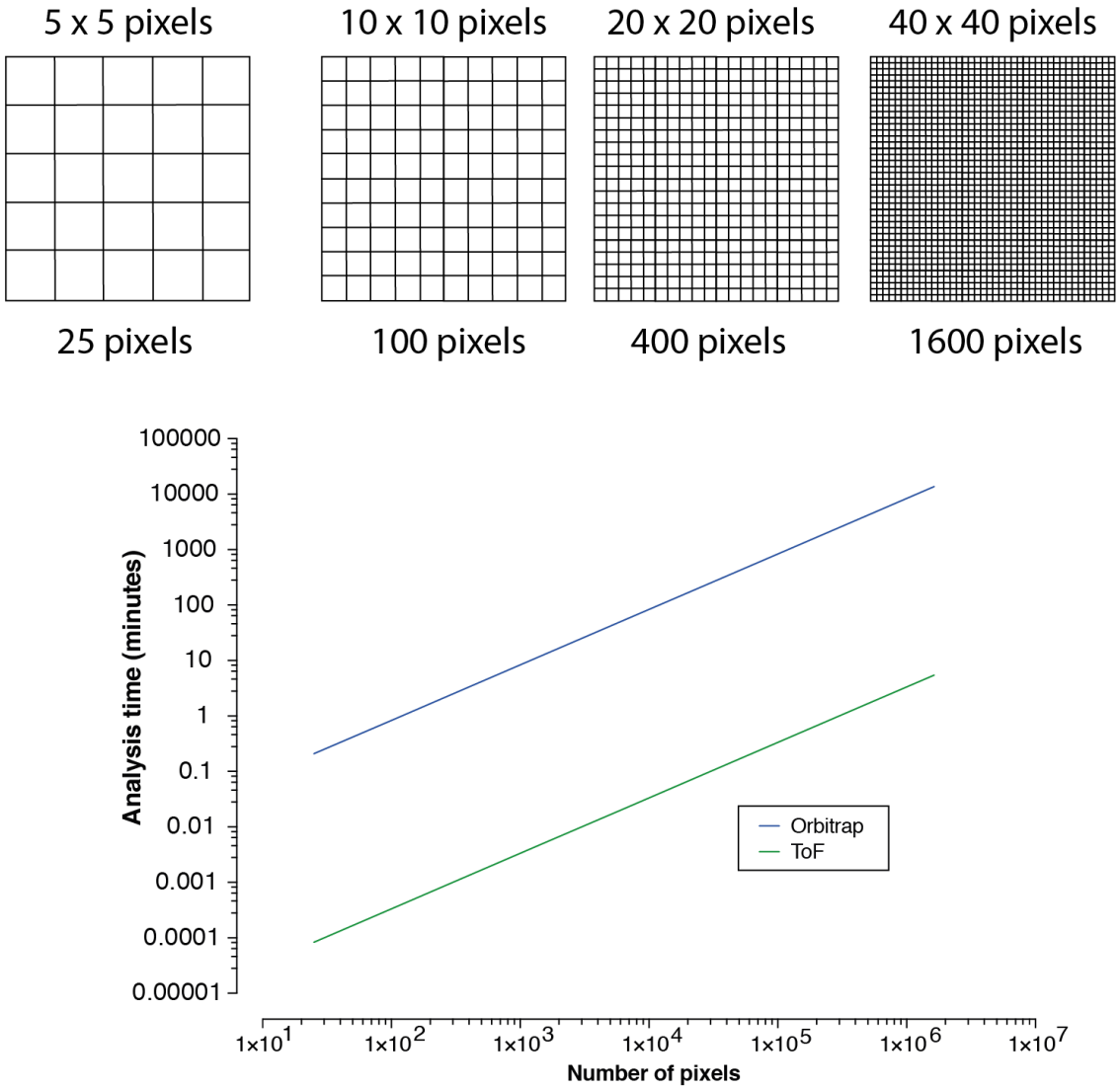

Figure 1.22 The relationship between image resolution and acquisition time
Illustration of how doubling image resolution results in quadrupling pixel number and therefore acquisition time for a 500 x 500 µm analysis area. The graph illustrates the acquisition time in minutes for a ToF or Orbitrap image for an increasing number of pixels (both axes plotted on a logarithmic scale).

1.6 Aims of this thesis

The aims of this thesis are:

- To develop imaging and non-imaging analytical methods for barrier lipids
- To identify the *in vivo* mechanisms that regulate barrier lipids
- To understand how barrier lipids function

In this thesis, I demonstrate how imaging and non-imaging mass spectrometry techniques can be adapted for the analysis of barrier lipids. Using these techniques, I then investigate the effects of developmental nutrition upon the composition of the adult lipid barrier in mice and *Drosophila*. Finally, I investigate the homeostatic mechanisms that regulate the composition of this lipid blend and the functional consequences of disrupting it.

Chapter 2. Materials & Methods

2.1 OrbiSIMS

2.1.1 Sample preparation

Supplementary Table 9.1 located in the Supplementary Material indicates the details of the commercial standards used in this study. Authentic standards were drop deposited on the suitable substrate immediately before introduction into the instrument loadlock. The substrate used was either 10 x 10 x 0.5 mm silicon wafers (Agar Scientific #AGG3390-10), indium tin oxide (ITO) coated glass slides with a surface resistivity of 70 – 100 Ω (Sigma-Aldrich #703176) or 18 x 18 mm ITO coated glass coverslips with a resistivity of 70 – 100 Ω (SPI Supplies #06462-AB). Substrates were thoroughly cleaned by sonication in 70:30 acetone:water, followed by 2:1 chloroform:methanol, followed by hexane.

Plants were grown without the use of pesticides and kindly provided by Diana Topham. A list of plant samples used in this study can be found in **Supplementary Table 9.2** located in the Supplementary Material. Plant samples were collected and stored at 4℃ for a maximum of 24 hours before mounting. Fruit skin samples were harvested and mounted directly onto gold-coated silicon wafers. Plant leaf samples were attached to gold-coated silicon wafers using silver conductive paint (Electrolube, #1LABLSCP/1).

Latent fingerprint samples were collected in accordance with local ethical guidelines from consenting volunteers. Volunteers were asked to perform a fingerprint conditioning protocol (Pleik et al., 2016) before depositing fingerprint samples onto gold-coated silicon wafers. Samples were anonymised and stored at 4℃ for 24 hours before analysis.

For *Drosophila* carcass samples, Pyrex 9-well plates and dissecting implements were thoroughly cleaned before dissection with 70:30 acetone:water, followed by 2:1 chloroform:methanol, followed by hexane before each dissection. *Drosophila* were anesthetised using CO_2, then carcass samples were dissected away from

other tissues in phosphate buffered saline (PBS), then washed several times in ddH_2O, then several times in 150 mM ammonium formate (AF) prepared in ddH_2O. Samples were then mounted on ITO coated glass slides or coverslips as mentioned above for ambient analysis. For cryogenic analysis, samples were mounted on gold-coated silicon wafers. *Drosophila* wing samples were detached from CO_2 anesthetised flies using clean forceps, and attached to the substrate using silver conductive paint (Electrolube, #1LABLSCP/1).

Mouse skin samples were collected immediately post-mortem and dissected to remove the tail bone. A small section of skin was mounted on a cleaned ITO coated glass slide, and fur removed manually with clean forceps from half the sample. In the case of improper sample adherence, the sample was mounted on the ITO coated glass slide using electrically conductive carbon tape.

2.1.2 Instrumentation

A detailed description of the OrbiSIMS instrumentation is published by Passarelli et al. (2017). The OrbiSIMS instrument is equipped with dual ionisation sources – a 20 kV argon gas cluster ion beam (GCIB) and a 30 kV bismuth liquid metal ion gun (LMIG), and dual mass analysers – a ToF (IONTOF GmbH) and an Orbitrap (QExactive HF, ThermoFisher Scientific). The GCIB is capable of operating in quasi-DC mode in conjunction with the Orbitrap mass analyser. The argon cluster size and beam focus are tuneable parameters, and within this study are used at a cluster size of between Ar_{1000}- Ar_{5000}, and a beam focus of between 3 µm – 20 µm. The LMIG is capable of operating either in pulsed mode suitable for use in conjunction with the ToF mass analyser, or quasi-DC mode suitable for use in conjunction with the Orbitrap mass analyser. The bismuth cluster size and beam focus are tuneable parameters, and within this study are used at a cluster size of between Bi_1^+ – Bi_3^{2+}, and a beam focus of between 200 nm – 1 µm. The main analysis chamber has neutral gas flooding capability and is equipped with argon gas used at pressures between 1x 10^{-9} mbar – 1 x 10^{-6} mbar. The main chamber is equipped with an electron flood gun that produces electrons at an energy of 21 eV and a current of ~ -10 µA for charge compensation purposes.

The ion extraction potential is operable between values of 500 V and 2 kV, with the option of delayed extraction for ToF analysis. The secondary ions can either be detected with the ToF analyser, or deflected with a 90 degree electrostatic deflector to the Orbitrap analyser. Ions deflected toward the Orbitrap mass analyser pass through a collisional cooling cell using helium at pressures between 1.2 x 10^{-1} mbar and 4.2 x 10^{-2} mbar. The Orbitrap can be operated at a mass resolving power up to 240,000 at 200 *m/z*, with a tuneable injection time. The mass window is tuneable between defined ranges. The Orbitrap is calibrated within a 24h window of analysis based on silver clusters generated from a silver standard. The ToF is calibrated individually for each measurement based on known ions within the mass spectrum.

2.1.3 Spectral acquisition

The most common parameters for data acquisition are shown in Table 2.1 OrbiSIMS standard analysis parameters. For the majority of samples, Orbitrap spectra acquisition was performed with an Ar_{3500}^+ GCIB with a current of ~12.6 pA, a duty cycle of 15% and a cycle length of 200 µs (**Figure 2.3**). The beam lateral resolution was calculated using an electroformed grid placed over a Faraday cup and the lateral resolution was determined from line scans across the image. This was calculated for both x axis and y axis resolution (**Figure 2.1**). A Gaussian curve was fitted to determine the 15%-85% width for each scan. The resulting values were plotted in a frequency distribution graph, and the lateral resolution value was determined by fitting a normal distribution then using the lateral resolution at the peak apex as described by Passarelli et al. (2017). The beam resolution was calculated as 19.2 µm (*x* axis) and 19.4 µm (*y* axis). For mouse skin samples, the GCIB was operated with a beam resolution of ~20 µm, a current of ~0.3 nA and a duty cycle of 5% to compensate for reduced secondary ion formation due to increased thickness of the sample and subsequent increase in ion suppression due to charge build-up. The Orbitrap was operated at a mass resolution of 240,000 at 200 *m/z*, with an injection time of 500 ms and the mass window was set at 100 – 1500 *m/z*. Spectra represent the sum of 50 scans from 400 x 400 µm field of view (FoV) at a resolution of 40 x 40 pixels per scan. Using

these settings, approximately 125000 shots at 200 µs per cycle were accumulated in the C-trap per acquisition.

2.1.4 Orbitrap image acquisition

Orbitrap images were acquired with the Ar_{3500}^+ GCIB at, a current of ~12.6 pA and a duty cycle of 15% and a cycle length of 200 µs. The beam lateral resolution was calculated using an electroformed grid placed over a Faraday cup and the lateral resolution was determined from line scans across the image. This was calculated for both *x* axis and *y* axis resolution (**Figure 2.1**). A Gaussian curve was fitted to determine the 15%-85% width for each scan. The resulting values were plotted in a frequency distribution graph, and the lateral resolution value was determined by fitting a normal distribution then using the lateral resolution at the peak apex as described by Passarelli et al. (2017). The beam resolution was calculated as 3.9 µm (*x* axis) and 4.0 µm (*y* axis) (**Figure 2.2**). Images were taken of a 400 x 400 µm FoV at a resolution of 80 x 80 pixels per scan, showing the sum of two consecutive scans. Using these settings, approximately 72250 shots at 200 µs per cycle were accumulated in the C-trap per acquisition.

Table 2.1 OrbiSIMS standard analysis parameters

	Orbitrap					ToF
	***Drosophila* spectra**	**Mouse skin spectra**	**MS^2**	**Imaging**	**Depth profiling**	**Imaging**
Ion beam	Ar_{3500}^+ GCIB	Ar_{3500}^+ GCIB	Ar_{3500}^+ GCIB	Ar_{3500}^+ GCIB	Ar_{3500}^+ GCIB	Bi_3^+ LMIG
Beam energy	20 keV	20 keV	20 keV	20 keV	20 keV	30 keV
Beam focus	~ 5 µm	~20 µm	~20 µm	~5 µm	~20 µm	~200 nm
Beam current	~ 12.6 pA	~0.3 nA	~0.3 nA	~ 12.6 pA	~0.3 nA	~0.2 pA
Beam duty cycle	15%	5%	5%	5%	5%	n/a

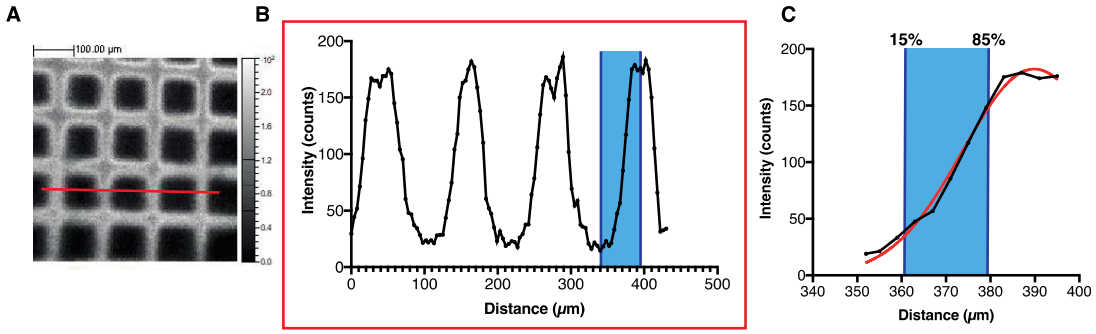

Figure 2.1 Method for determining ion beam lateral resolution
To determine beam lateral resolution, a line scan (red line) was taken from a secondary ion image of an electroformed grid (**A**). From this line scan, the resolution was determined by selecting each half peak, describing the intensity at the grid edge (**B**). Lateral resolution was determined from the 15% - 85% width after fitting the data to a gaussian distribution (red line) (**C**).

.

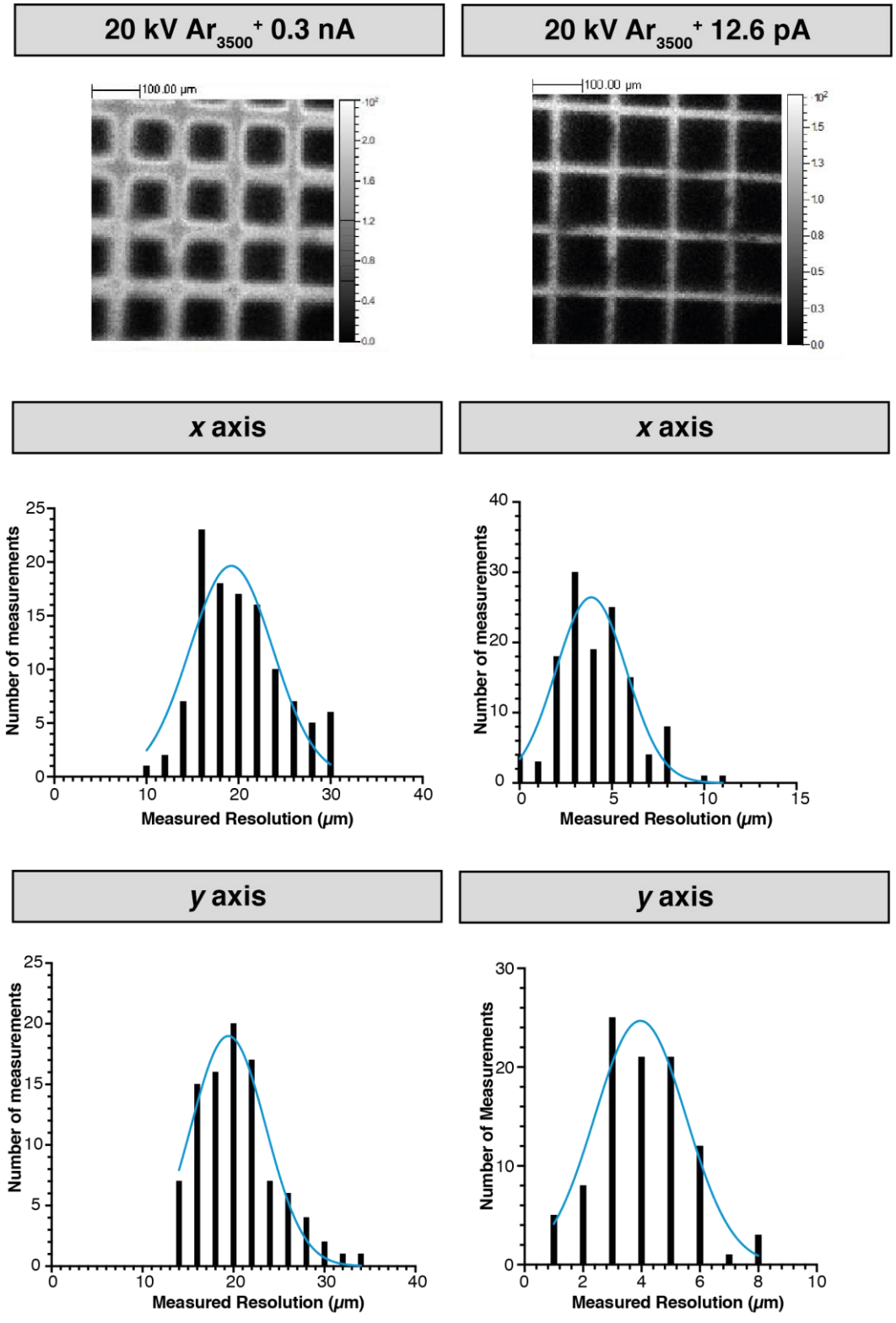

Figure 2.2 OrbiSIMS GCIB lateral resolution

Experimentally determined *x* and *y* axis lateral resolution of the 20 kV Ar_{3500}^+ GCIB. The resolution values are determined using the method illustrated in **Figure 2.1**, and these values are plotted on a histogram as shown in this figure. The value for lateral resolution is determined by the apex of a gaussian fit on this data (blue line).

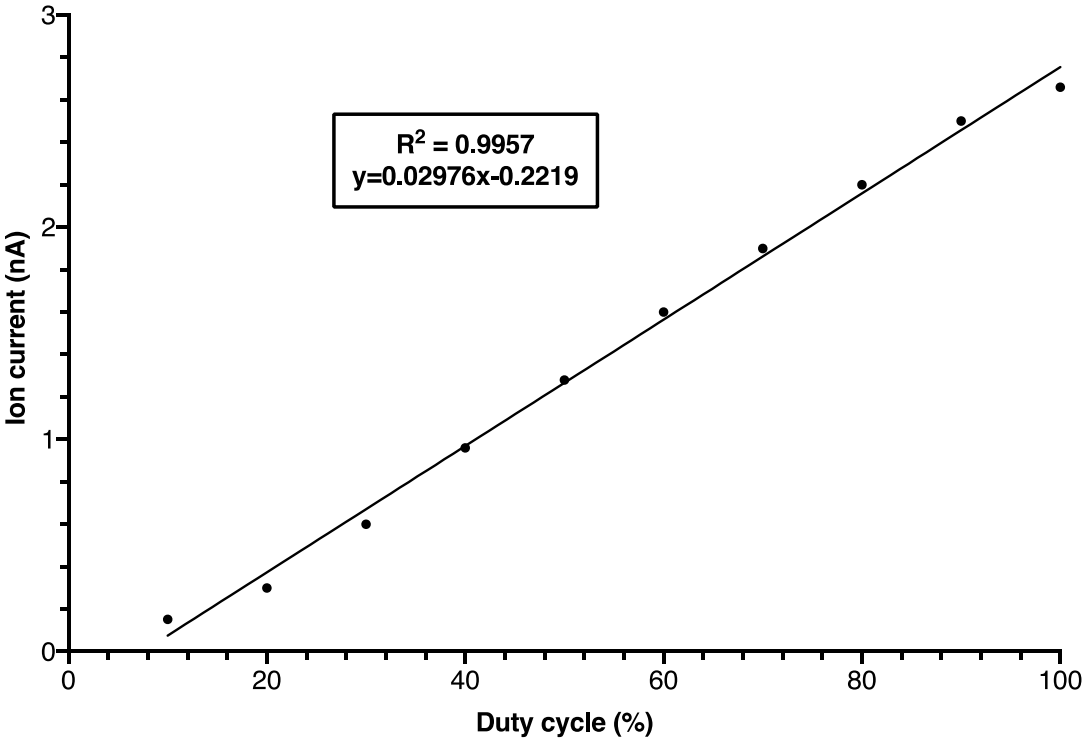

Figure 2.3 Relationship between GCIB duty cycle and ion current
Experimentally determined ion current values for different GCIB duty cycle lengths for a 20 kV Ar_{3500}^{+} GCIB. Linear regression was used to determine the r-squared value and equation of the best-fit line.

2.1.5 Depth profile acquisition

Depth profiles were acquired using the DC Ar_{3500}^+ GCIB with a focus of ~20 µm, a current of ~0.3 nA and a duty cycle of 5%. Acquisition was continued until complete removal of the sample and appearance of the substrate were apparent using the charge-coupled device (CCD) optical camera view. Measurements were taken over a FoV of 40 x 40 µm.

2.1.6 ToF image acquisition

OrbiSIMS ToF image acquisition was performed as follows, as presented in Newell et al. (2020). The LMIG was operated using 30 kV Bi_3^+ cluster beam with a current of 0.06 pA in short pulses mode. Spectral calibration was performed using reference ions of C^+, CH^+, CH_2^+ and CH_3^+. The pine needle ToF image represents a 500 x 500 µm analysis area and 1024 x 1024 pixels per scan in sawtooth raster mode, with the image showing the sum of 35 scans with 1 shot per pixel and a cycle time of 200 µs. The total ion dose was 2.75 x 10^9 ions cm^{-2}. This image was acquired between the temperatures of -112ºC and -106ºC. The fingerprint ToF image was acquired using a stage scan of a 2.5 x 2.5 cm area and 1250 x 1250 pixels per scan made up of 500 x 500 µm tiles automatically stitched during acquisition, with the image showing the sum of 2 scans with 1 shot per pixel and a cycle time of 400 µs. The total ion dose was 2.02 x 10^9 ions cm^{-2}. The image was acquired between the temperatures of -125ºC and -111ºC. The *Drosophila* ToF images represent a 500 x 500 µm analysis area and 1024 x 1024 pixels per scan in sawtooth raster mode, with the image showing the sum of 10 scans with 1 shot per pixel, with an LMIG current of 0.2 pA and a cycle time of 200 µs. The total ion dose for this image was 7.85 x 10^9 ions cm^{-2}.

2.1.7 Cryogenic analysis

The cryogenic OrbiSIMS methodology is described in detail in Newell et al. (2020). An overview of the process for loading cryogenically cooled samples into the OrbiSIMS is illustrated in **Figure 2.4**. To analyse samples cryogenically, samples were mounted initially at room temperature on gold-coated silicon

wafers as mentioned in **Section 2.1.1**. These samples were then snap-frozen in liquid nitrogen in the Leica EM-VCM system and attached to the modified Leica sample holder (**Figure 2.5**) designed and produced in collaboration with Alan Ling of the Crick Mechanical Engineering Facility. The modified sample holder was then transferred to the Leica EM-VCT 500 cryogenic transfer shuttle, which is engineered to dock with the OrbiSIMS loadlock. The OrbiSIMS cryogenic sample stage was previously loaded into the instrument loadlock and cooled using a copper cooling finger. The modified sample holder was then transferred under vacuum onto the pre-cooled OrbiSIMS sample stage once the stage had reached a temperature of < -130℃. The Leica EM-VCT 500 cryogenic transfer shuttle was then disconnected from the loadlock and the sample stage transferred into the instrument main chamber where it docked with a mechanically articulated copper cooling finger for the duration of the analysis.

Several modifications were made to the standard analysis conditions to enable optimal data collection under these conditions. To reduce the build-up of charge on the sample, neutral argon gas flooding was enabled in the analysis chamber to a pressure of 1×10^{-6} mBar. The cycle time for Orbitrap imaging was increased to 400 µs and the GCIB duty cycle decreased to 15% with a current of 12.6 pA and a cycle length of 400 µs. The Orbitrap injection time was increased to 2901 ms. Analysis was only carried out at temperatures < -100 ℃, if the sample temperature increased above this value the stage was moved back into the instrument loadlock for further cooling until the temperature reached a value of < -130℃.

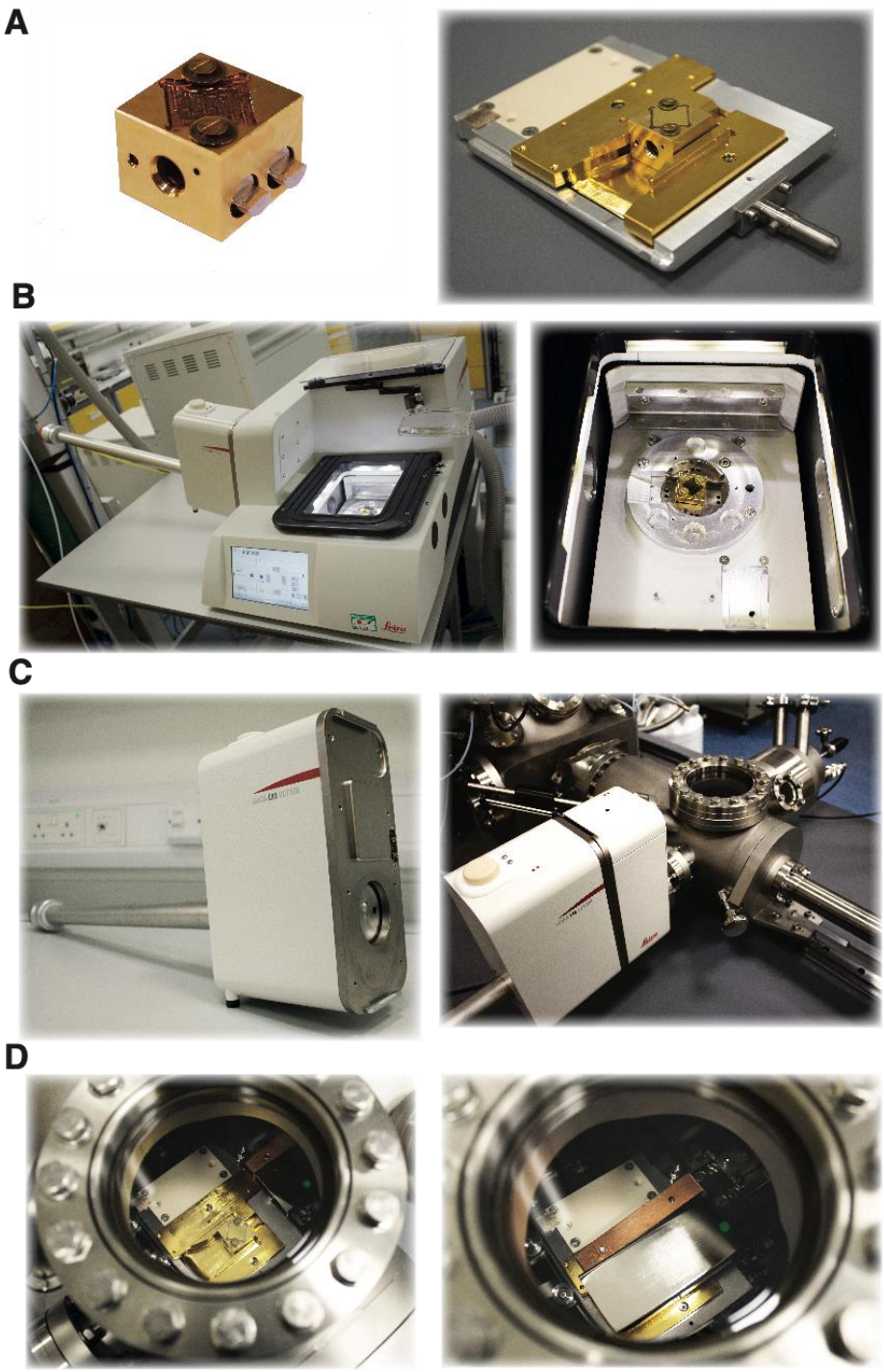

Figure 2.4 Cryogenic OrbiSIMS sample workflow
Visual depiction of cryogenic workflow for sample loading into the OrbiSIMS.
A. Modified Leica sample block and its mounting onto the OrbiSIMS cryo sample stage when holding a gold-coated silicon wafer sample substrate.
B. The sample is loaded inside the Leica EM VCM in a liquid nitrogen bath.
C. The sample holder is retracted into the cryogenically cooled Leica EM VCT500 sample shuttle, which then docks onto the loadlock of the OrbiSIMS.
D. The sample is transferred to the pre-cooled OrbiSIMS cryo sample stage under vacuum. The stage temperature is then stabilised with the copper cooling finger illustrated before transfer to the instrument main chamber.

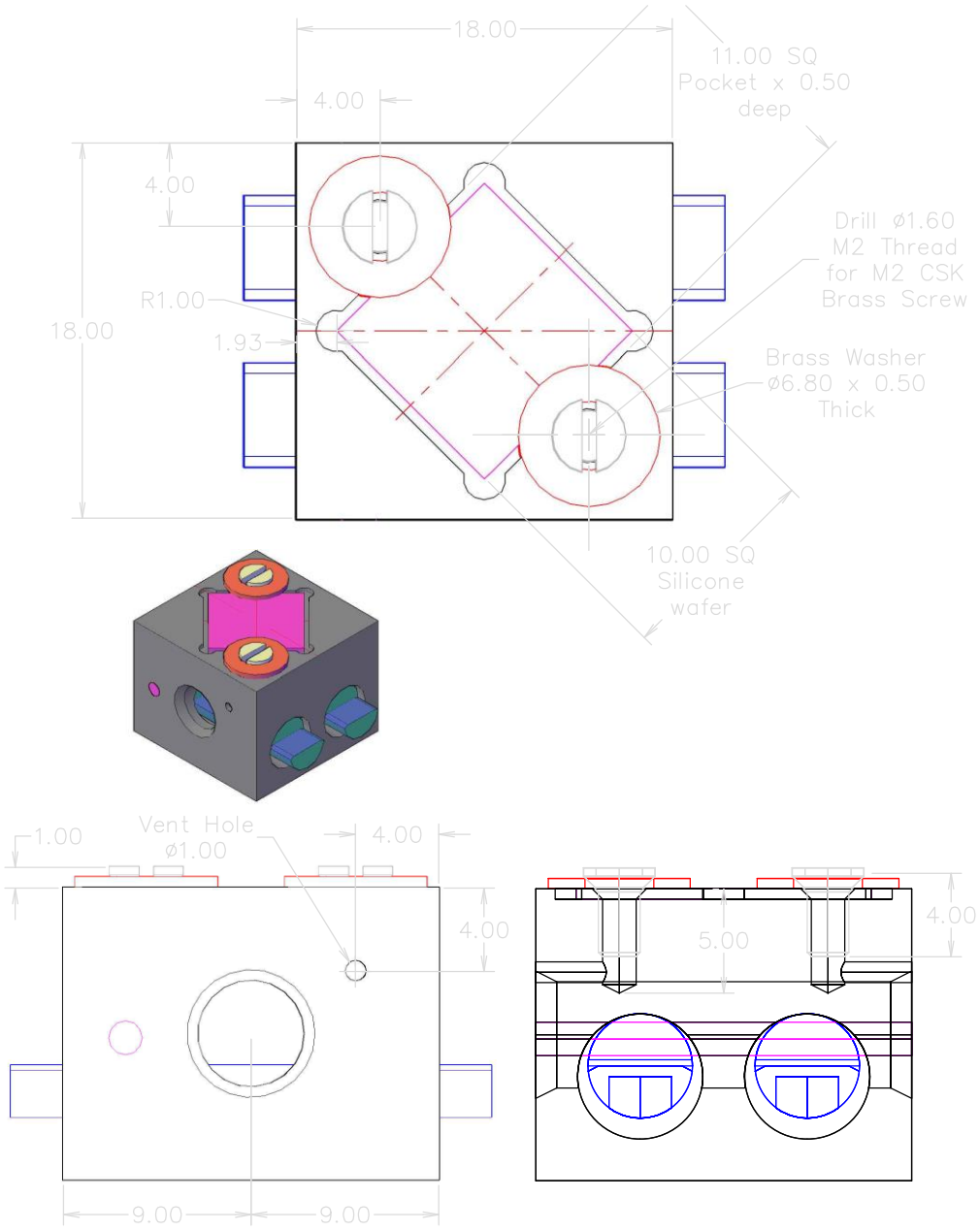

Figure 2.5 Technical drawing of a modified Leica sample holder for Cryo-OrbiSIMS
Modifications to the standard Leica sample holder include machining of a recessed region to house the silicon wafer on which the sample is mounted, and creation of vented screw threads to secure the silicon wafer with brass screws and brass washers. Figure reproduced from Newell et al. (2020) with permission.

2.1.8 Orbitrap collision-induced dissociation

Secondary ions for Orbitrap MS^2 were generated using the Ar_{3500}^+ GCIB with a beam resolution of ~20 µm, a current of ~0.3 nA and a duty cycle of 5%. The mass isolation window was generated based around a centre mass generated from a high resolution mass spectrometry (HRMS) spectrum (mass resolving power of 240,000 at 200 *m/z*). The mass window was set at 0.4 *m/z* around this centre mass. A background spectrum containing Orbitrap-generated electronic noise signal was collected by reducing the GCIB duty cycle to 0%, and this was subtracted from the subsequent spectra. After mass selection, the secondary ions were transferred to the higher energy collisional dissociation (HCD) cell where they underwent collision induced dissociation (CID) with nitrogen as a collisional gas, at normalised collision energies (NCE) between 0 and 40.

2.1.9 Data analysis

For the majority of samples, peaks were picked using the automatic peak picking tool in SurfaceLab 7.0 with a minimum counts and signal-to-noise ratio (SNR) set at 1,000 counts. The minimum SNR was set at the same value as the minimum counts to avoid the selection of peaks representing Orbitrap electronic noise as opposed to true biological signal.

For mouse skin lipid data, peaks were picked using the automatic peak picking tool in SurfaceLab 7.0. A visualisation of the data analysis pipeline used for these samples is illustrated in **Figure 2.6**. The minimum counts for peak selection was adjusted per sample so that the picked peaks summed a total intensity between 90 and 95% of the total spectrum intensity with a minimum counts value and minimum SNR set at 300. Four independent measurements were taken for each sample and the average of these four values was taken forward for further analysis. Peaks that were not detectable in samples after the averaging of technical replicates were set at a value calculated as half the minimum detected value for that sample.

For OrbiSIMS Orbitrap relative quantification, the peak area was used as calculated by SurfaceLab. These peak area values were normalised to the summed total intensity across all scans to correct for any intensity differences due to charge accumulation on the sample and subsequent suppression effects. The peak centroid *m/z* value was then rounded to three decimal places and data from replicates collated using a piece of Visual Basic code in Microsoft Excel kindly provided by Henrik Takacs. This code is available in the Supplementary Material. The data was then formatted and analysed for statistical significance using MetaboAnalyst (Chong et al., 2019) which included several pre-processing steps. First, the data was filtered to remove features which were missing in more than 75% of the samples, and the remaining missing values were replaced with a value that was 1/5 of the minimum detected value. The data was then Pareto-scaled to remove effects caused by large differences in peak area between different lipid classes. Statistical significance was calculated using either a Student's T-test correcting for false discovery at a rate of 5%, or ANOVA as appropriate.

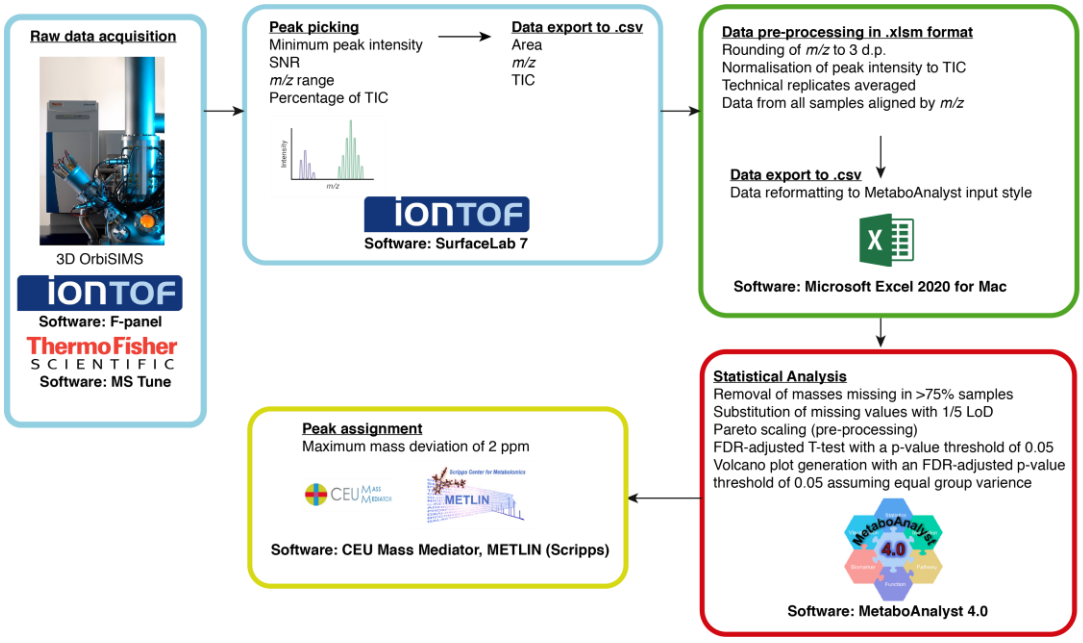

Figure 2.6 OrbiSIMS spectral data analysis pipeline

Peak assignments were made using exact mass with a mass deviation < 2 ppm (increased to < 2.5 ppm for peaks above *m/z* 1,000). Exact mass was cross-

referenced with several lipidomics databases using the CEU mass tool (Gil-de-la-Fuente et al., 2019) which compares data against the HMDB, LipidMaps, Metlin, Kegg and in-house CEU mass libraries. In positive polarity, the following adducts were allowed: $[M+H]^+$, $[M+Na]^+$, $[M+K]^+$, $[M+NH_4]^+$, $[M+H-H_2O]^+$, $[M+2Na-H]^+$, $[M+2K-H]^+$, $[M+H-2H_2O]^+$, and $[M+NH_4-H_2O]^+$. In negative polarity, the following adducts were allowed: $[M-H]^-$, $[M+Cl]^-$, $[M+HCOOH-H]^-$ (*Drosophila* samples only), $[M-H-H_2O]^-$, $[M-H+HCOONa]^-$ (*Drosophila* samples only), $[M+Na-2H]^-$, and $[M+K-2H]^-$. Adducts were assessed for chemical plausibility before putative assignments were made. For a selection of peaks, isotopologue analysis was performed for increased confidence in peak assignment. If available, Orbitrap MS/MS data was used to improve further the confidence in peak assignments.

For Orbitrap and ToF image acquisition, images of the fly cuticle were normalised to total ion intensity to correct for artifacts caused by differing topology. For the images shown in **Figure 4.24**, Orbitrap spectral peaks were picked using a minimum mass of *m/z* 100, a maximum mass of *m/z* 1500 and a minimum intensity (counts) of 10,000. The peak intensities were then subjected to the Keenan scaling method (Keenan and Kotula, 2004) and resulting data subjected to principal component analysis (PCA) analysis. This analysis was performed by Dr Junting Zhang and Prof Ian Gilmore at NPL using a custom MATLAB code.

Stable isotope labelling experiments were performed in collaboration with Dr Lena Lampe in the Gould Lab.

2.2 ToF-SIMS

The ToF-SIMS method was as follows, as presented in Newell et al. (2020): A homogenous layer of a triolein standard (Sigma-Aldrich #T7140) was drop cast on to a 10 x 10 mm^2 silicon wafer that was then mounted on a cooling stage compatible with the TOF-SIMS 5 instrument. The loadlock was flooded with nitrogen gas prior to cooling during pump-down. For analysis, the sample was cooled with a copper cooling finger to temperatures between -140ºC and -80 ºC. A 20 kV Ar_n^+ gas cluster ion beam was operated in pulsed analysis mode with a

cycle time of 200 µs. Secondary ions were extracted with a voltage of 2 kV and spectra collected from a field of view of 100 x 100 µm with a resolution of 8 x 8 pixels acquired in sawtooth raster mode. Measurements shown are a sum of 2,000 scans. To compensate for sample charging, an electron flood gun was applied during analysis with an energy of 21 eV and a current of -10 µA.

2.3 GC-MS

The details of all commercial standards used in this work are available in **Supplementary Table 9.1** located in the Supplementary Material. Commercial standards were prepared as a concentrated solution in hexane.

2.3.1 Native hydrocarbon detection

Hydrocarbons were extracted from plant tissues and fingerprints using 500 µl hexane and dried down before resuspending in 50 µl hexane and then run immediately. For *Drosophila* samples, five flies were anesthetised on a CO_2 pad, then immediately extracted with 50 µl hexane containing 0.1 mM octadecane internal standard in clean GC vials. For vial extracts, one vial was extracted using 200 µl hexane containing 0.1 mM octadecane internal standard. The hexane was pipetted over the sides of the vial three times and the vial shaken so the hexane covered the food. Extracts were transferred to 200 µl GC vial inserts in clean vials, capped, then immediately analysed.

The gas chromatography method used for hydrocarbon analysis was as previously reported by Stefana et al. (2017) with minor modifications. GC-MS was using an Agilent 7890B-5977A GC–MS system in EI mode. Data was acquired and analysed using MassHunter (Version B.06.00, Agilent Technologies, Inc). Splitless injection of 1µl (injection temperature 310°C, or 270°C where indicated) onto a 30 m + 10 m × 0.25 mm DB-5MS + DG column (J&W, Agilent Technologies) was used, with helium as the carrier gas. The initial oven temperature was 50°C (1 min), followed by temperature gradients to 150°C at 10°C/min, from 150 to 249°C at 3°C/min, from 249 to 300°C at 10°C/min with a hold time of 5 min, and from 300 to 325°C at 10 °C/min and a hold time of 12 min.

Sample running order was randomised using the MassHunter sample sequence randomiser. The detector gain was set at 10.

For several experiments, a modified shortened GC method was used. Splitless injection of 1µl was used with an injection temperature of 310°C. The initial oven temperature was 100°C (1 min), followed by temperature gradients to 160°C at 30°C/min, from 160 to 270°C at 4°C/min, and from 270 to 325°C at 10°C/min with a hold time of 2 min. The detector gain was set at 10.

The GC method used for MS^2 data differed from the above. GC-MS was using an Agilent 7890B-5977A GC-QqQ system in EI mode with helium as the carrier gas, and nitrogen as the collision gas. The injection temperature was 270°C. The initial oven temperature was 80°C (2 min), followed by temperature gradients to 140°C at 30°C/min, from 140 to 250°C at 5°C/min, and from 250 to 320°C at 15°C/min with a hold time of 6 min. Mass selection was performed at unit mass around the precursor of interest, with a normalised collision energy of 0.5 and the detector gain set at 10, with retention time windows determined from a previous MS^1 run on the same sample.

Stable isotope labelling experiments and hydrocarbon response to desiccation stress experiments were performed in collaboration with Dr Lena Lampe in the Gould Lab.

2.3.2 Hydrocarbon dimethyl disulphide derivatisation

For dimethyl disulphide (DMDS) derivatisation, a method was adapted from published protocols by Dunkelblum et al. (1985) and Buser et al. (1983).50 µl 0.1 mM standard hydrocarbon standard mixture was used, or the hydrocarbon extract from ten adult flies. The hydrocarbon extracts were diluted to a total volume of 200 µl in hexane containing an internal standard of 10 µM N,N-dimethyldodecylamine (DDA) (Tokyo Chemical Industry #D3338) in clean GC-MS vials. To this, 200 µl neat DMDS (Sigma Aldrich #471569) and 100 µl 60 mg/mL iodine solution (Sigma Aldrich #207772) in diethyl ether were added and the GC-MS vials were covered loosely with foil. The vials were heated in an oven

in a fume hood at 40℃ for 4 hours. After the vials had cooled, the samples were diluted with 200 µl hexane. Iodine was then removed with 400 µl 5% aqueous sodium thiosulphate and the organic phase transferred to a clean vial. The aqueous phase was then re-extracted with 100 µl hexane and added to the first organic extract. Any remaining water was removed with the addition of anhydrous sodium sulphate powder, and the sample transferred to a clean GC-MS vial ensuring no transfer of particulates. The sample was then dried in a speedvac at 300 rpm, then resuspended in 50 µl hexane containing an internal standard of 0.1 mM octadecane and transferred to a clean GC-MS vial insert, capped then run immediately on the GC-MS.

The GC method used was as used for hydrocarbons in Section 2.3.1, with an inlet temperature of 270℃ and an altered oven method as follows: The initial oven temperature was 50°C (1 min), followed by temperature gradients to 150°C at 10°C/min, from 150 to 249°C at 6°C/min, from 249 to 300°C at 5°C/min with a hold time of 5 min, and from 300 to 325°C at 5 °C/min and a hold time of 12 min.

2.3.3 Aldehyde derivatisation

The method was adapted from a previously published protocol by Bao et al. (2014). Standards were prepared in hexane at a concentration of 100 mM, then diluted to a concentration of 10 mM in 500 µl water in a clean GC-MS vial, vortexing to ensure even distribution. To this solution, 50 µl of 20 mg/mL aqueous pentafluorobenzylhydroxylamine solution (PFBHA) (Sigma Aldrich #194484) was added and the vial was capped and placed in the dark at room temperature for two hours. Then, two drops of neat sulphuric acid were added to stop the reaction. The derivatised compounds were extracted using 200 µl hexane and vortexing. The organic phase was transferred to a GC-MS vial insert, then centrifuged at top speed for 2 minutes, before transfer to a clean GC-MS vial insert. The samples were then run on the GC-MS immediately.

The GC method used was similar to that used in Section 2.3.1 with an inlet temperature of 270℃ and modifications to the oven protocol as follows: the initial oven temperature was 50°C (1 min), followed by temperature gradients to 190°C

at 5°C/min with a hold time of 3 min, from 190 to 242°C at 5°C/min with a hold time of 2 min, from 242 to 292°C at 5°C/min with a hold time of 6 min, and from 292 to 312°C at 10 °C/min and a hold time of 2 min.

2.3.4 Native wax ester detection

The gas chromatography method used was similar to that used in Section 2.3.1 with modifications to the oven protocol as follows: the initial oven temperature was 50°C (1 min), followed by temperature gradients to 150°C at 10°C/min, from 150 to 249°C at 3°C/min, from 249 to 300°C at 3°C/min with a hold time of 5 min, and from 300 to 325 °C at 3°C/min with a hold time of 12 min.

2.3.5 Wax ester methanolysis

Glass capillaries were sealed at one end with a butane torch, and sample added to the glass capillary. The capillaries were placed inside eppendorf tubes and samples dried in a speedvac at 300 rpm for 30 minutes. 50 µl methanol was added to each capillary and the samples dried in a speedvac at 300 rpm for 30 minutes. This process was repeated twice. 50 µl methanolic hydrochloric acid was added to each capillary with a gel loading tip, then the capillary placed under slight vacuum using plastic tubing attached to a syringe to remove air from the capillary tube, then the capillary tube sealed with a butane torch. The capillary tubes were heated in a heating block overnight at 95℃. The capillary tubes were then scored and snapped open and 10 µl pyridine added to each capillary using a glass positive displacement pipette. The contents of each capillary were then transferred into glass GC vial inserts and placed inside eppendorf tubes, then dried in a speedvac for 30 minutes at 1500 rpm. The glass GC vial inserts were transferred into GC vials and 25 µl N,O-Bis(trimethylsilyl)trifluoroacetamide (BSTFA) added to each sample with a glass positive displacement pipette. The samples were then capped and run immediately on the GC.

Wax ester methanolysis was performed with assistance from Dr James MacRae in the Crick Metabolomics Science Technology Platform.

2.3.6 Fatty acid derivatisation

The derivatisation protocol was adapted from a published protocol (Bravo-Santano et al., 2019). For exclusive derivatisation of fatty acids but not triacylglycerides, 2mM fatty acid standards were diluted in a total volume of 40 µl acetonitrile. 40 µl N-trimethylsilyl-N-methyltrifluoroacetamide (MSTFA) + 1% chlorotrimethylsilane (TMCS) was added to the samples (ThermoFisher Scientific #TS48915) and the samples were vortexed. The samples were then heated in an oven at 37 ℃ for 30 min, with vortexing at 10 min intervals. The samples were then diluted 1 in 5 in acetonitrile, then run immediately.

For extraction of fatty acids from fly food, approximately 300 mg food was transferred into clean GC vials and the lipids extracted using 600 µl 2:1 chloroform: methanol, containing an internal standard of 2 mM $^{13}C_1$ palmitic acid, by vortexing. After centrifugation in an eppendorf tube at 13 x g for 5 minutes, the organic phase (lower phase) was transferred to a clean GC vial and water removed with sodium sulphate crystals. The extract was dried and resuspended in 40 µl acetonitrile. Derivatisation was performed as indicated above, and the samples diluted 1 in 4 (standard food), 1 in 20 (high fat food) and 1 in 2 (standard mixture of 2 mM linoleic acid and 2 mM $^{13}C_1$ palmitic acid) then run immediately.

The GC-MS method used was the same as for aldehydes in Section 2.3.3 for fatty acids and hydrocarbons combined. For fatty acids alone the GC method was similar to that used in Section 2.3.1 with an inlet temperature of 270℃ and modifications to the oven protocol as follows: the initial oven temperature was 70℃ (1 min) followed by temperature gradients to 230°C at 15°C/min with a hold time of 2 min, and from 230 to 325°C at 25°C/min with a hold time of 3 min.

Fatty acid extraction from fly food was performed in collaboration with Elisabeth Kamper and Eva Islimye in the Gould Lab.

2.3.7 Transesterification derivatization of total lipids

Fatty acid methyl esters (FAMEs) were identified in relation to a standard mixture of 37 FAMEs (Supelco 37 Component FAME Mix, Sigma Aldrich #CRM47885)

which was run at a dilution of 1 in 20 prepared in 20 µl 2:1 chloroform:methanol and derivatised with 5 µl m-trifluoromethylphenyl trimethylammonium hydroxide (TMAH) (0.5 M methanolic trimethylphenylammonium hydroxide solution, Sigma Aldrich #79266). Derivatisation efficiency was determined using free fatty acid standard mixtures run at a concentration of 1 mM in 20 µl and derivatised with 5 µl TMAH.

The GC method used was similar to that used in Section 2.3.1 with an inlet temperature of 250℃ and modifications to the oven protocol as follows: the initial oven temperature was 70℃ (1 min), followed by temperature gradients to 230℃ at 15℃/min with a hold time of 2 min, and from 230 to 325℃ at 25℃/min with a hold time of 3 min.

This derivatization protocol was adapted from one kindly shared by Jim Ellis in the Crick Metabolomics Science Technology Platform. The FAME standard, saturated fatty acid standard mixture, and unsaturated fatty acid standard mixture were shared by Jim Ellis in the Crick Metabolomics Science Technology Platform.

2.3.8 Data analysis

Data analysis was performed using MassHunter Qualitative Analysis and MassHunter Quantitative Analysis (Agilent, version B.06.00 or version 10.0, Agilent Technologies). Peaks were first normalised to an internal standard spiked within the sample at the time of metabolite extraction. Absolute quantification was calculated in relation to the extraction volume and number of flies per sample.

For individual samples where it was not possible to detect the compound of interest, the peak area value was set at a low value defined as the limit of detection (LoD). This value was set at half the minimum measured value within each run. All measurements of alkene/alkane ratio were performed using calculated absolute abundance in nanograms per fly.

For stable isotope labelling experiments, data analysis was performed using the in-house software MANIC developed by Dr James MacRae and Dr Jim Ellis in the Crick Metabolomics Science Technology Platform. Natural isotopic

abundance was accounted for using the average of the observed natural abundance in experimental unlabelled samples for each metabolite of interest.

Chromatograms displayed have been background subtracted with a minimum value of zero using the blank sample run alongside the experimental sample. Chemical structures were drawn using ACD Chem/Sketch 2018.1.1.

2.4 LC-MS

The details of all commercial standards used in this work are available in **Supplementary Table 9.1** located in the Supplementary Material.

One week old male *Drosophila* samples for LC-MS were prepared by extracting surface lipids from 20 flies/sample using 100 µl 2:1 chloroform:methanol for 30 seconds in a clean GC-MS vial. For measurements in positive polarity, extracts from 20 flies per sample were used and for measurements in negative polarity, extracts from 40 flies per sample were used.

The LC-MS method is as follows, as presented in Newell et al. (2020): LC-MS measurements were performed with assistance from Dr Mariana Silva Dos Santos and Dr Nathalie Legrave of the Crick Metabolomics Science Technology Platform. The LC-MS method was adapted from a published protocol (Amiar et al., 2016). The extracts were dried and resuspended in 50 µL of a mix of 1-butanol/10 mM ammonium formate in methanol (1:1, v/v). 5 µL aliquots were analysed using the following LC-MS method. Metabolite analysis was performed by LC-MS using a Q-EXACTIVE (Orbitrap) mass spectrometer from ThermoFisher Scientific (Bremen, Germany) coupled with a Dionex UltiMate LC system from ThermoFisher Scientific (Bremen, Germany) equipped with a C18 Zorbax Elipse plus column (2.1 × 100 mm, 1.8 µm, Agilent). A 20-min elution gradient of 45–55% solvent B was used, followed by a 5 min wash of 100% solvent B and 3-min re-equilibration, where solvent B was water:acetonitrile:isopropanol, 5:20:75 (v/v/v) with 10 mM ammonium formate (Optima HPLC grade, Sigma-Aldrich) and solvent A was 10 mM ammonium formate in water (Optima HPLC grade, Sigma-Aldrich). Other parameters were

as follows: flow rate 600 µl/min; column temperature 60°C; and autosampler temperature 4°C. MS was performed with positive/negative polarity switching using a Q Exactive Orbitrap (ThermoFisher Scientific) with a HESI II probe. MS parameters were as follows: spray voltage 3.5 and 2.5 kV for positive and negative modes, respectively; probe temperature 275°C; sheath and auxiliary gases were 55 and 15 arbitrary units, respectively; and full scan range: 150–2,000 *m/z* with settings of AGC target and resolution as balanced and high ($3e^6$ and 70,000), respectively. Data were recorded using Xcalibur 3.0.63 software (ThermoFisher Scientific). Mass calibration was performed for both ESI polarities before analysis using the standard Thermo Scientific Calmix solution. To enhance calibration stability, lock-mass correction was also applied to each analytical run using ubiquitous low-mass contaminants. Data-dependant MS (dd-MS) were acquired in positive and negative polarities with the following parameters: AGC target and resolution set as balanced and high ($2e^5$ and 17,500), respectively; collision energy set as stepped from 10 to 20 to 30 NCE in HCD (high-energy collisional dissociation) mode; TopN was 5; the isolation window was set at 0.4 *m/z*.

Peak assignments were made using exact mass with a mass deviation < 3 ppm. Exact mass was cross-referenced with several lipidomics databases using the CEU mass tool (Gil-de-la-Fuente et al., 2019) which compares data against the HMDB, LipidMaps, Metlin, Kegg and in-house CEU mass libraries. In positive polarity, the following adducts were allowed: $[M+H]^+$, $[M+Na]^+$, $[M+K]^+$, $[M+NH_4]^+$, $[M+H-H_2O]^+$, $[M+2Na-H]^+$, $[M+2K-H]^+$, $[M+H-2H_2O]^+$, $[M+NH_4-H_2O]^+$, $[2M+H]^+$, $[2M+Na]^+$, $[M+H+HCOONa]^+$, $[2M+H-H_2O]^+$, $[2M+K]+$, $[2M+NH_4]^+$, $[2M+ACN+H]^+$, $[M+ACN+H]^+$, $[M+CH_3OH+H]^+$, and $[M+C_3H_8O+H]^+$. In negative polarity, the following adducts were allowed: $[M-H]^-$, $[M+Cl]^-$, $[M+HCOOH-H]^-$, $[M-H-H_2O]^-$, $[M-H+HCOONa]^-$, $[M+Na-2H]^-$, $[M+K-2H]^-$, $[2M-H]^-$, $[M+C_2H_4O_2-H]^-$, $[2M+HCOOH-H]^-$, $[2M+C_3H_8O-H]^-$, $[3M-H]^-$, and $[M+F]^-$. Adducts were assessed for chemical plausibility on a case-by-case basis before putative assignments were made. For a selection of peaks, isotopologue analysis was performed for increased confidence in peak assignment. Chromatograms were plotted using peak centroid information. If available, Orbitrap MS/MS data was used to improve

further the confidence in peak assignments. Peak area was calculated using XCalibur Quan using peak centroid filtering using base peak trace. Peak integration was calculated using the ICIS method with smoothing points of 5, baseline window of 40, area noise factor of 5 and peak noise factor of 10.

2.5 Orbitrap direct infusion

Analytical standards were prepared at a concentration of 10 mg/ml. The Orbitrap method was as stated by Newell et al. (2020). The syringe flow rate was 200 µl/min with a nitrogen sheath gas flow rate of 15.54, mass resolving power of 140,000 at *m/z* 200 and a mass range of 200 – 1500 *m/z*. The capillary voltage was set at -0.4 V and the capillary temperature at 350 ºC. The spray voltage was set at 4.5 keV. Orbitrap direct infusion was performed with assistance from Dr Mariana Silva Dos Santos in the Crick Metabolomics Science Technology Platform.

2.6 *Drosophila* strains, husbandry and dietary manipulations

A full list of *Drosophila* strains used in this study can be found in **Table 2.2** and a full list of food compositions per litre of food in **Table 2.3**. *Drosophila* diets were kindly produced by the Crick Media Facility. Fly lines were maintained in bottles containing ~50 mL STD fly food at 25℃ and 80% relative humidity (RH) with a 12 h light/dark cycle for general use. Stocks were maintained long-term in vials containing ~15 mL STD fly food at 18℃ and 80% RH with a 12 h light/dark cycle. For large scale synchronisation within 1 day for use in lifespan assays, flies were housed in large population cages with grape-juice agar plates and live yeast. Embryos were collected from the grape-juice agar plates after 22 h laying. Embryos were gently removed with a paintbrush into surrounding PBS, and allowed to sink in an eppendorf tube. The excess PBS was aspirated, and embryos pipetted at an approximate volume of 10 µl per bottle. For L1 larvae collection used for U-^{13}C glucose experiments and high fat diet experiments, the live yeast was removed from the grape-juice agar plate at 22 h and replaced with a very small amount of live yeast paste. Larvae were collected over the course

of 4 h with blunt forceps and transferred to vials at a concentration of 30 larvae/vial. For pupal transfer used for U-^{13}C glucose and $^{13}C_2$ acetate experiments, pupae were transferred between vials using a wet paintbrush and vials were kept horizontally for 30 mins before returning to the upright position. In experiments assaying housing density, flies were transferred to the stated density within 24 hours of eclosion and held at the stated densities for 2 weeks before assaying. For crosses, virgin females were collected over the course of 4 h after complete clearance of live flies from bottles. Crosses were set up in fly vials, with seven virgin females and five males per vial. Crosses utilising adult-specific GAL4 expression via the temperature sensitive GAL80^{TS} system were set up in an incubator at 18℃, 80% RH with a 12 h light/dark cycle. Within 24 h of eclosion, adult flies were transferred to a 29℃, 80% RH incubator with a 12 h light/dark cycle for 5 days before proceeding with the experiment (**Figure 2.7**).

For ^{13}C labelling experiments using U-^{13}C glucose, glucose-free fly food was heated until liquid and allowed to cool slightly. Labelled glucose powder was added to reach the standard glucose concentration in fly food (58.5g/L) and mixed thoroughly. Liquid food was then transferred into fly vials and allowed to cool. For experiments using less than 100% labelled glucose, the glucose-free fly food was used and a mixture of labelled and unlabelled glucose added. For $^{13}C_2$ acetate labelling experiments, 100 mM $^{13}C_2$ acetate was added to standard fly food in the manner described above. In experiments utilising an adult high yeast high glucose (HYHG) diet, flies were separated by sex and transferred to vials containing HYHG food within 24 hours of eclosion. In experiments utilising a developmental LY or no yeast (ØY) diet, embryos were pipetted into bottles containing the desired food in 50 ml aliquots of food per bottle. The flies were then separated by sex and transferred to vials containing standard food at a density of 15 flies per vial within 24 hours of eclosion.

For Reactive Yellow 86 treatment, flies were anesthetised on a CO_2 pad then transferred into a 96-well plate pre-cooled on ice containing Reactive Yellow 86 powder dye. The plate was then sealed and shaken until the flies were fully coated with yellow powder. The flies were then transferred to a petri-dish pre-

cooled on ice and shaken to remove excess powder. Flies were transferred to fresh vials carefully using forceps touching the wing only. A “sham” treatment was performed using the same procedure, excluding the powder dye.

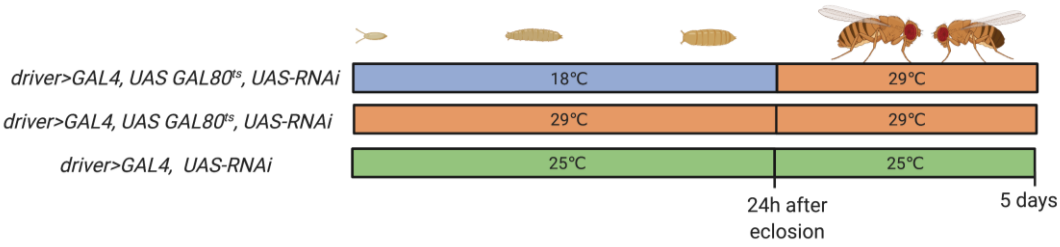

Figure 2.7 Schematic of *Drosophila* genetic manipulations

Schematic illustrating the general timescales and housing temperatures used for *Drosophila* genetic manipulations.

Table 2.2 List of *Drosophila* lines used in this study

Genetic construct	Source	Description
w^{1118} iso31 Wolbachia-	Gould Lab	Isogenic wild type fly line
Oregon R	Gould Lab	Non-isogenic fly line
PromE-GAL4, tub-GAL80^{TS}, UAS-CD8::GFP	Gould Lab	Oenocyte driver line, with temperature controlled expression, marking oenocytes with GFP
UAS-Obp99d RNAi	VDRC GD16139	Obp99d RNA interference line
UAS-Obp99b RNAi	VDRC GD1298	Obp99b RNA interference line
UAS-Cyp4g1 RNAi	Gould Lab	Cyp4g1 RNA interference line
UAS-Desat1 RNAi	VDRC GD2950	Desat1 RNA interference line
UAS-SREBP^{DN}	Gould Lab	Line enabling overexpression of a dominant negative form of SREBP
UAS-Hnf4 RNAi	Gould lab	Hnf4 RNA interference line
UAS-TSC1/2	Gould lab	Line enabling overexpression of TSC1/2

Table 2.3 Composition of *Drosophila* diets (per litre)

Standard (STD)	High yeast high glucose (HYHG)	Low yeast (LY)	No yeast (ØY)
7.5 g agar	7.5 g agar	7.5 g agar	7.5 g agar
58.5 g glucose	400 g glucose	58.5 g glucose	58.5 g glucose
66.3 g cornmeal	66.3 g cornmeal	66.3 g cornmeal	66.3 g cornmeal
23.4 g yeast	93.6 g yeast	1 g yeast	0 g yeast
19.5 mL antimycotic solution	19.5 mL antimycotic solution	19.5 mL antimycotic solution	19.5 mL antimycotic solution

MVNTA (antibiotic)	STD + acetate	NR (starvation)
7.5 g agar	7.5 g agar	1 g agar
58.5 g glucose	58.5 g glucose	100 mL PBS
66.3 g cornmeal	66.3 g cornmeal	
23.4 g yeast	23.4 g yeast	
19.5 mL antimycotic solution	19.5 mL antimycotic solution	
100 mg metronidazole	5.9 g sodium acetate	
50 mg vancomycin		
100 mg neomycin		
50 mg tetracycline		
100 mg ampicillin		

4% NaCl	No glucose (ØG)
7.5 g agar	7.5 g agar
58.5 g glucose	0 g glucose
66.3 g cornmeal	66.3 g cornmeal
23.4 g yeast	23.4 g yeast
19.5 mL antimycotic solution	19.5 mL antimycotic solution
40 g NaCl	

2.7 Fecundity measurements

Fecundity was measured by analysing female egg laying at 25℃ within a defined period of 20 h. per day. Once mated female flies at 7 days of age were used for this experiment, with a density of 15 flies/vial. The vials were treated either with hexane alone, or 250 µg (*Z*)-7-tricosene dissolved in 250 µl hexane. Per experiment, an average was calculated over six biological replicates and the experiment was performed three independent times. Statistical significance was calculated using 2-way ANOVA with multiple comparisons.

The final replicate of this experiment was performed in collaboration with Dr Fumiaki Obata in the Gould Lab.

2.8 Lifespan

Lifespan assays were performed using male flies with the lifespan assay commencing 6 days after eclosion. Flies were separated by sex at 24 hours after eclosion and kept in vials at a density of 15 flies/vial until the lifespan assay commenced. Mortality was recorded every 3 – 4 days, and the vials replaced with fresh vials.

Two replicates of lifespan experiment to determine the dose-dependency effect of alkene exposure and one replicate of lifespan experiments to determine toxicity dynamics of alkene exposure on the HYHG diet were performed in collaboration with Dr Lena Lampe in the Gould Lab.

2.9 Desiccation resistance

Desiccation resistance was performed with 6-day old adult *Drosophila*, with the sex of interest indicated for each individual experiment. The flies were held inside a desiccation chamber with silica gel (Sigma-Aldrich #10087). To further decrease the humidity, vials were sliced in half and placed with a intervening layer of silica gel as illustrated in **Figure 2.8**. To control for death due to starvation, a nutrient restriction (NR) control was used. These vials contained 1% agarose

prepared in PBS. Survival was measured at one hour intervals until 100% mortality was reached. For experiments assaying tricosene exposure, a pre-treatment was used of 24h 500 µg (*Z*)-9-tricosene per vial, and upon commencement of the starvation assay the tricosene was removed.

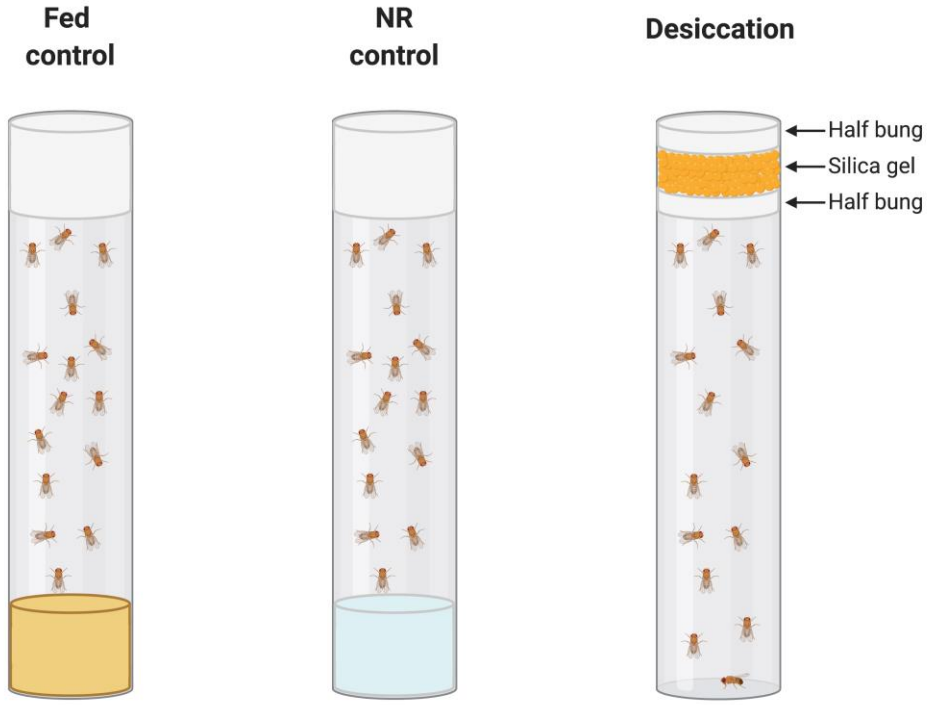

Figure 2.8 Schematic of desiccation assay set-up
Fed control shows 15 flies in a vial containing standard fly food. NR control shows 15 flies in a vial containing 1% agarose/PBS. Desiccation shows 15 flies in a vial with no medium, closed with half a bung, filled with silica gel, and closed with the second half bung.

2.10 Salt stress resistance

Salt stress assays were performed with 6-day old adult *Drosophila*. The standard fly food recipe was supplemented with 4% NaCl and survival recorded several times a day until 100% mortality was reached. For experiments assaying tricosene exposure, a pre-treatment was used of 24h 500 µg (*Z*)-9-tricosene per vial, and upon commencement of the starvation assay the tricosene was removed.

2.11 Starvation resistance

Starvation assays were performed with 6-day old adult *Drosophila*. A nutrient restriction (NR) media was used containing 1% agarose prepared in PBS. Survival was measured at two hour intervals until 100% mortality was reached. For experiments assaying tricosene exposure, a pre-treatment was used of 24h 500 µg (*Z*)-9-tricosene per vial, and upon commencement of the starvation assay the tricosene was removed.

2.12 Fly weight

Male flies were housed at a density of 15 flies per vial. The weight of all individual flies was measured on day 0 using a Sartorius microbalance. The flies were then transferred to vials containing 500 µg (*Z*)-9-tricosene or control vials. The weight of the flies was measured on 0, 1, 2, 3, 4 or 5 days after treatment. After measuring the wet weight of the flies, the flies were transferred to eppendorf tubes and stored at -20℃. To measure dry weight, flies were desiccated in an oven at 60℃ for 6 hours before weighing. Fly wet weights were represented relative to the weight of the same flies at day 0, and fly dry weights were represented relative to the dry weight of a control group of flies at day 0.

2.13 Reverse transcription quantitative polymerase chain reaction (RT-qPCR)

Adult *Drosophila* were sedated on CO_2 pads, then snap frozen in liquid nitrogen (LN_2) (whole fly samples), or dissected in PBS (tissue samples). Dissected samples were transferred individually to RNALater solution (ThermoFisher Scientific, #AM7023M) immediately upon completion of dissection, and transferred to Eppendorf tubes and snap frozen in liquid nitrogen (LN_2) upon completion of dissection of experimental conditions. Per sample of whole adult *Drosophila*, 7 flies were used, and 10 flies were used for dissected tissues (abdominal carcass and digestive tract). After snap freezing, 100 µl Qiazol was added to the samples, and they were homogenised on ice for 30 seconds using

a pestle homogeniser. 400 µl Qiazol was added to each sample before incubation at room temperature for 30 minutes. The samples were snap frozen in LN_2 and then defrosted. 100 µl chloroform was added and the samples were vortexed before centrifugation at 12,000 x g for 15 minutes at 4℃. 200 µl aqueous phase was collected and added to 200 µl 100% ethanol and then transferred onto a column from the RNeasy Micro Kit (Qiagen, #74004). The kit protocol was followed and after completion, RNA was eluted from the columns with a volume of 13 µl RNAse-free water (Invitrogen #10977035). The RNA concentration was measured using a Nanodrop, and 200 µg RNA used per reverse transcriptase (RT) reaction using the Superscript IV cDNA kit (ThermoFisher Scientific #18091050). Synthesised cDNA was diluted to a 1 in 5 concentration with RNAse-free water and 1 µl used per qPCR reaction. qPCR was performed in 96 well multiwell plates (Roche #04729692001) with 2 µl 5 µM primers, 3 µl RNAse-free water, and 10 µl 2x SybrGreen Mastermix (Roche #04887352001) per well on a Roche Lightcycler 480 instrument. Each sample was run alongside a serial dilution standard for the cDNA of interest, generated from a previous qPCR run from material that originated from the same source (whole fly, abdominal carcass or digestive tract). The serial dilution standards ranged from 10^{-2} to 10^{-13} dilution from the end product of the qPCR reaction. Statistical calculations were performed using an efficiency-corrected method of the $-\Delta\Delta C_q$ calculation as performed by the Roche LightCycler software (Rao et al., 2013). When multiple reference genes were analysed, the geometric mean of these was used for statistical analysis. Statistical significance was determined in GraphPad Prism using a Student's T-test or 1-way ANOVA with a p value <0.05 determined as significant. qPCR primers were designed using the Roche PrimerDesign tool. The sequence of qPCR primers is listed in **Supplementary Table 9.3** located in the Supplementary Material.

2.14 RNASeq

RNA was extracted from samples as described in Section 2.11. RNA quality control was performed using a Bioanalyzer by Deb Jackson of the Crick Advanced Sequencing Facility. Samples were diluted to the same concentration

and library preparation performed by Meena Anissi of the Crick Advanced Sequencing Facility using the KAPA mRNA HyperPrep kit (Roche, #KK8581) according to manufacturer's instructions. Sequencing was performed by Ben Phillimore of the Crick Advanced Sequencing Facility using the Illumina HiSeq 2500 with a read length of 75 bp in single-end mode with a coverage of 25 million. Data was analysed by Dr Nourdine Bah in the Crick Bioinformatics Science Technology Platform. Raw reads were quality and adapter trimmed using cutadapt v1.9.1(Martin, 2011) prior to alignment. Reads were then aligned and quantified using RSEM v1.3.0 and STAR v2.5.2 (Li and Dewey, 2011) against the fly genome BDGP6 and annotation release 86, both from Ensembl. FPKM (Fragments Per Kilobase Million) and TPM (Transcripts Per Kilobase Million) values were also generated using RSEM/STAR. Differential gene expression analysis was performed in R v3.4.0 (R Core Team, 2018) using the DESeq2 v1.16.1 package (Love et al., 2014). Differential genes were selected using a 0.05 false-discovery rate (FDR) threshold. Normalisation and variance-stabilizing transformation (VST) was applied on raw counts before performing principal component analysis and Euclidean distance-based clustering. GO (Gene Ontology) enrichment analysis was performed in R v3.4.0 using the clusterProfiler v3.4.4 package (Yu et al., 2012) and the org.Dm.eg.db v3.4.1 annotation (Carlson, 2019), with a p- and q-value cut-off of 0.01 and 0.05 respectively.

2.15 Neutral lipid staining and confocal microscopy

Male fly carcasses were dissected in PBS, then pinned flat using insect pins on a silicone plate. Carcasses were fixed with 4% paraformaldehyde (PFA) prepared from a 16% stock solution (Agar Scientific #AGR1026) by dilution with PBS at room temperature for 2 hours in a humid box. Samples were washed thoroughly with PBS, unpinned and transferred to a Pyrex multiwell plate. Samples were incubated in HCS LipidTOX^{TM} Red Neutral Lipid Stain (ThermoFisher Scientific #H34476) at a concentration of 1 in 1,000 prepared in PBS at 4℃. The LipidTOX^{TM} solution was removed and the samples transferred to VECTASHIELD Antifade Mounting Medium (Vector Labs #H-1000-10) and

mounted on a slide. Two strips of Scotch tape were used as spacers and the slide was covered with a 0.17 mm thickness coverslip and sealed with clear nail polish.

Samples were imaged using a Leica SP5 confocal microscope. Images were taken using an oil immersion 40x objective at a pixel resolution of 2048 x 2048 of an area of 387.5 µm x 387.5 µm using a 65.4 µm pinhole and a line average of 2. For excitation, an argon laser was used with a power of 20%. For GFP, an excitation wavelength of 488 nm with an intensity of 50% was used with the PMT detector set to collect between 500nm – 540 nm with a gain of 626. For LipidTOX^{TM} an excitation wavelength of 633 nm with an intensity of 10% was used with the PMT detector set to collect between 645 nm and 685 nm with a gain of 16.

2.16 Mouse husbandry and dietary regimes

All mouse experiments were performed in collaboration with Patricia Serpente in the Gould Lab. C57BL/6J mice were used in this study. Female mice were mated to begin experiments once they had reached a weight of >20 g and above an age of 10 weeks old.

For the low protein prenatal diet, mothers were transferred to STD diet at E18.5 to avoid mothers eating the young. Where this became impossible to prevent, a fostering scheme was introduced and the pups were transferred at birth to a foster CD-1 strain mother. The foster mother cared for a maximum of 8 pups including her own litter. Low protein diets were specially developed and provided by Envigo. Basic calorific information is provided in **Table 2.4**, and more in-depth information including vitamin and mineral content is provided in **Supplementary Table 9.4** located in the Supplementary Material.

Table 2.4 Calorific information on different mouse diets

	STD	LP (4%)
Energy density (kcal/g)	3.1	3.5
Calories from protein (%)	24	4.6
Calories from fat (%)	18	11.1
Calories from carbohydrate (%)	58	84.3

Chapter 3. Optimisation of analytical techniques for biological barrier lipids

3.1 Introduction

Barrier lipids on the body surface are challenging to analyse, due to potential problems of contamination with internal lipids. These two pools of lipids can be challenging to separate chemically - many well-established techniques rely on solvents that can extract lipids not only from the surface but also from internal lipid pools in the epidermal and subcutaneous fat cells. In Chapter 1.1, the composition and conservation of barrier lipids is discussed in depth. In general, the lipid classes that appear to be prominent amongst a large variety of species of interest are hydrocarbons, aldehydes, free fatty acids, glycerolipids, phospholipids, sphingolipids, wax esters and steroids. When modifying analytical techniques for the detection of these lipid classes, there are a variety of different steps to consider to ensure optimal detection. These analytical considerations include sample preparation, instrumental transmission, ionisation efficiency and mass resolving power, as discussed in Chapter 1.5. In this Chapter, I describe the development of a new platform, cryo-OrbiSIMS, that overcomes this challenge and enables imaging of semi-volatile surface lipids with high spatial and chemical resolution. I also describe how several well-established techniques, such as GC-MS and LC-MS, can be optimised for analysing surface lipids and used to support the OrbiSIMS findings.

3.2 Optimisation of GC-MS methods for lipid detection

3.2.1 Hydrocarbons

For analysis that does not require spatial information, GC-MS is a very valuable tool to analyse hydrocarbons at relatively high throughput with minimal sample preparation required. It is also able to differentiate between isobaric compounds due to the gas chromatographic separation, providing an additional dimension to the data. Analysis of a mixture of 15 hydrocarbon standards using a GC method previously developed in the lab (Stefana et al., 2017) shows good separation of different alkene isomers (**Figure 3.1**). Importantly, it also highlights the substantial difference in calculated molar-relative response factors (MRRF) between compounds of different chain length and saturation index (**Figure 3.2**). Given this, it is important to take into account the MRRF of each species in order to accurately calculate its absolute concentration. In addition, this method must be used in order to generate correct ratiometric measurements of saturation index are only valid when using calculated absolute concentrations, as has been done throughout this study. Using GC-MS analysis of underivatised hydrocarbons, it is only possible to determine the double bond position through comparison with a commercial standard. It is not possible to determine double bond position using MS/MS on an instrument with an electron ionisation source (such as the instruments used in this study) due to migration of the double bond (**Figure 3.3**) (Gohlke and McLafferty, 1993). For many of the alkenes of interest, no commercial standard is available. Therefore, a previously published derivatisation technique was applied using dimethyl disulphide (DMDS) to derivatise the alkene at the site of the double bond and introduce methyl sulphide group either side of the double bond (**Figure 3.4**) (Dunkelblum et al., 1985, Buser et al., 1983). As illustrated for (Z)-9-tricosene, optimisations to the chromatographic technique combined with DMDS derivatisation enable accurate resolution of both unmodified alkanes and derivatised alkenes (**Figure 3.4, Figure 3.5**). This suggests the technique is suitable for the analysis of complex samples, however, when analysing hydrocarbons from complex chemical sample such as ASTM reference gas oil (**Figure 3.6**), it is clear that although reasonable

chemical separation is achievable using GC-MS, there is a large proportion of the sample that is not resolvable using this technique as indicated by the high chromatographic baseline and relatively poor peak resolution. The use of this technique alongside an additional suitable technique would provide the highest degree of analytical certainty.

A

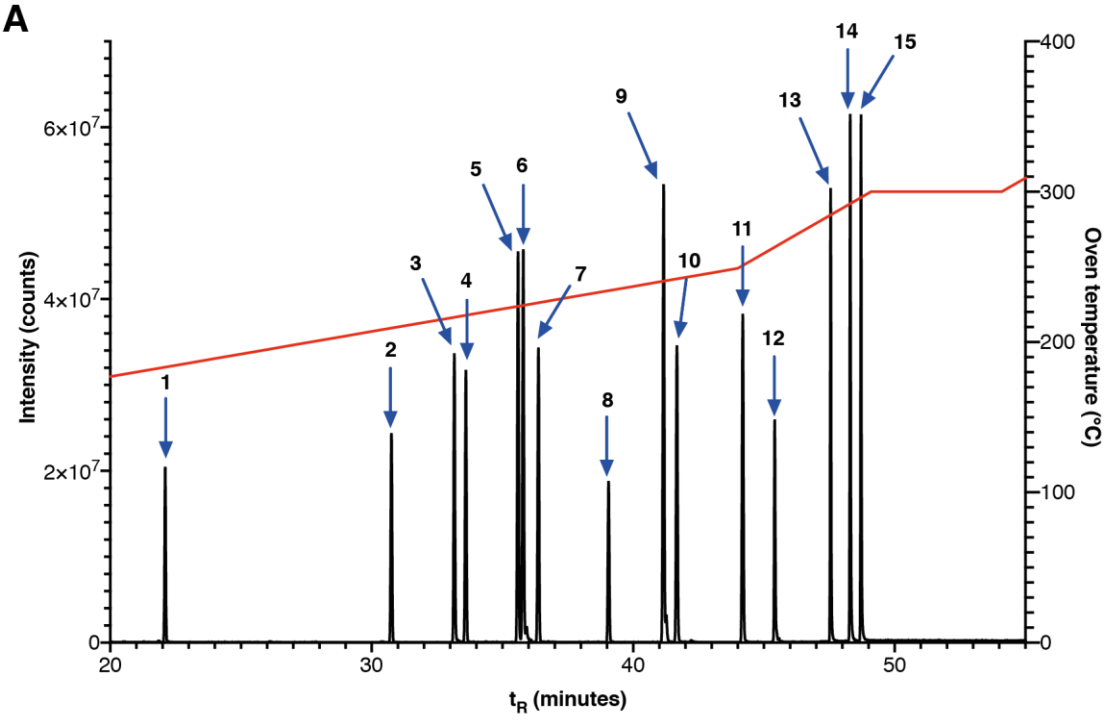

B

Peak no.	Standard	Formula (molecular)	Monoisotopic mass (M_{mi})	t_R (minutes)
1	Octadecane	$C_{18}H_{38}$	254.2974	22.089
2	Heneicosane	$C_{21}H_{44}$	296.3443	30.743
3	(*Z*)-11-Vaccenyl acetate	$C_{20}H_{38}O_2$	310.2872	33.157
4	Docosane	$C_{22}H_{46}$	310.3600	33.582
5	(*Z*)-9-tricosene	$C_{23}H_{46}$	322.3600	35.584
6	(*Z*)-7-tricosene	$C_{23}H_{46}$	322.3600	35.779
7	Tricosane	$C_{23}H_{48}$	324.3756	36.358
8	Tetracosane	$C_{24}H_{50}$	338.3913	39.051
9	(*Z*)-7-pentacosene	$C_{25}H_{50}$	350.3913	41.145
10	Pentacosane	$C_{25}H_{52}$	352.4069	41.661
11	Hexacosane	$C_{26}H_{54}$	366.4226	44.175
12	(*Z,Z*)-7,11-heptacosadiene	$C_{27}H_{52}$	376.4069	45.407
13	Octacosane	$C_{28}H_{58}$	394.4539	47.542
14	(*Z,Z*)-7,11-nonacosadiene	$C_{29}H_{56}$	404.4382	48.296
15	Nonacosane	$C_{29}H_{60}$	408.4695	48.700

Figure 3.1 GC-MS of hydrocarbon standards
Detection of a mixture of 15 commercial hydrocarbon standards by GC-MS on a DB-5MS column. **A**. Gas chromatogram. The black line indicates total intensity (counts) as measured by the quadrupole detector. The red line indicates the oven temperature gradient (℃), illustrating the elution temperature for each hydrocarbon standard.
B. Retention times and masses of hydrocarbon standards labelled in **A**.

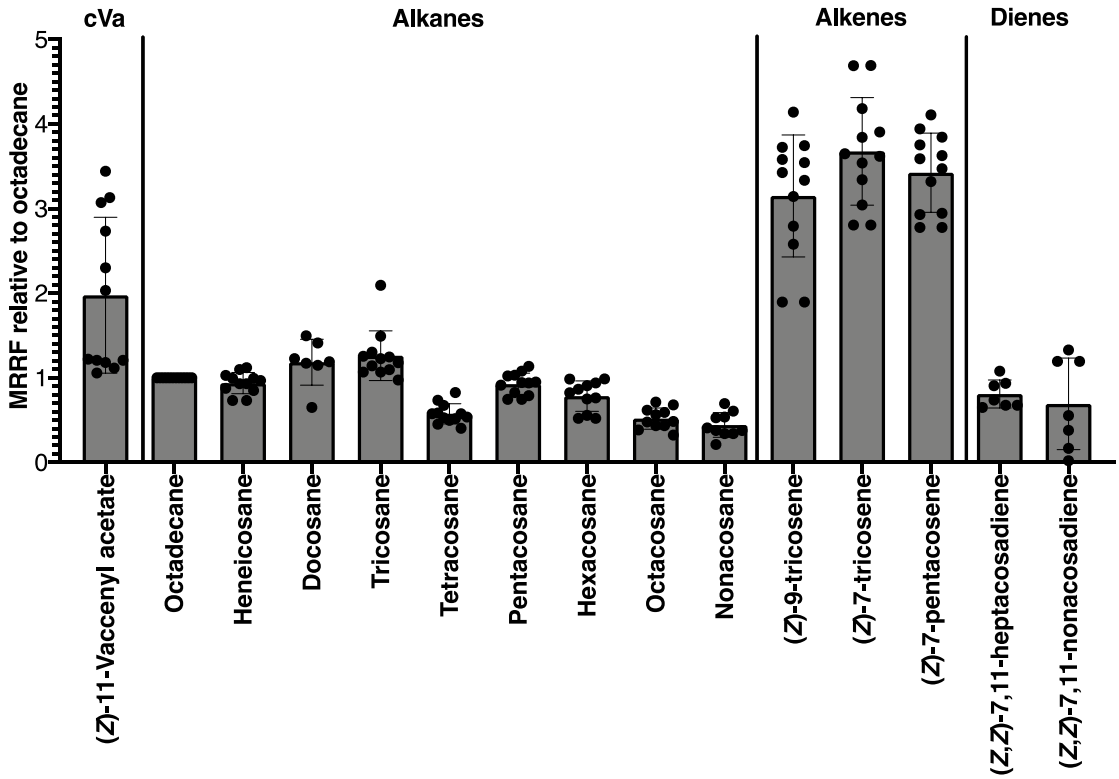

Figure 3.2 Molar relative response factors of hydrocarbon standards
Molar relative response factors (MRRFs) of hydrocarbon standards illustrated relative to an octadecane internal standard. Data points are from 12 independent runs using the same GC-MS method.

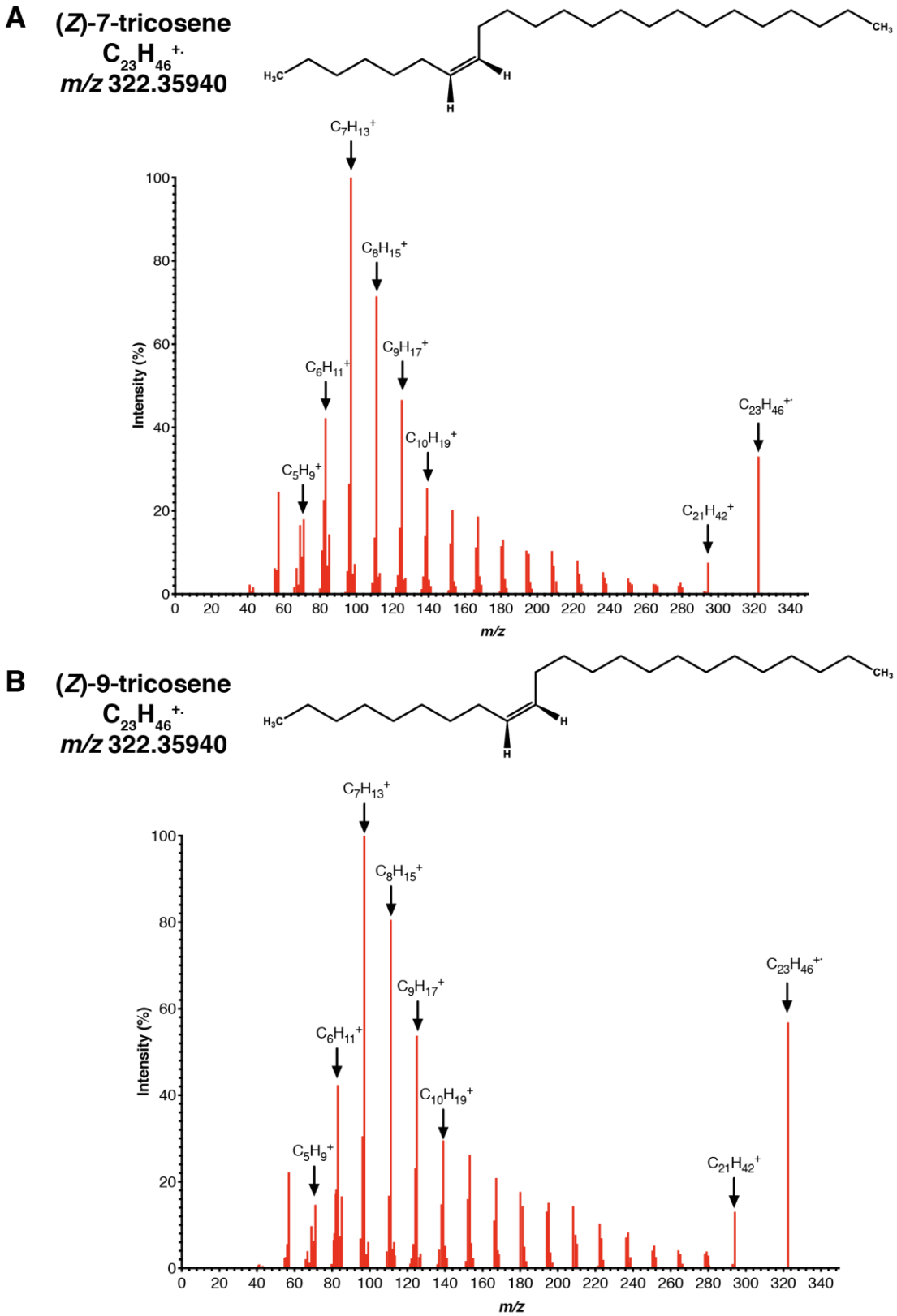

Figure 3.3 GC-MS/MS fragmentation of (*Z*)-7-tricosene and (*Z*)-9-tricosene
MS^2 spectrum indicating the fragmentation patterns of **A**. (*Z*)-7-tricosene and **B**. (*Z*)-9-triosene commercial standards at a normalised collisional energy (NCE) of 0.5. Major fragment ions are labelled with their chemical formulae. The *m/z* value indicated refers to the theoretical experimental mass/charge ratio of the detected ion.

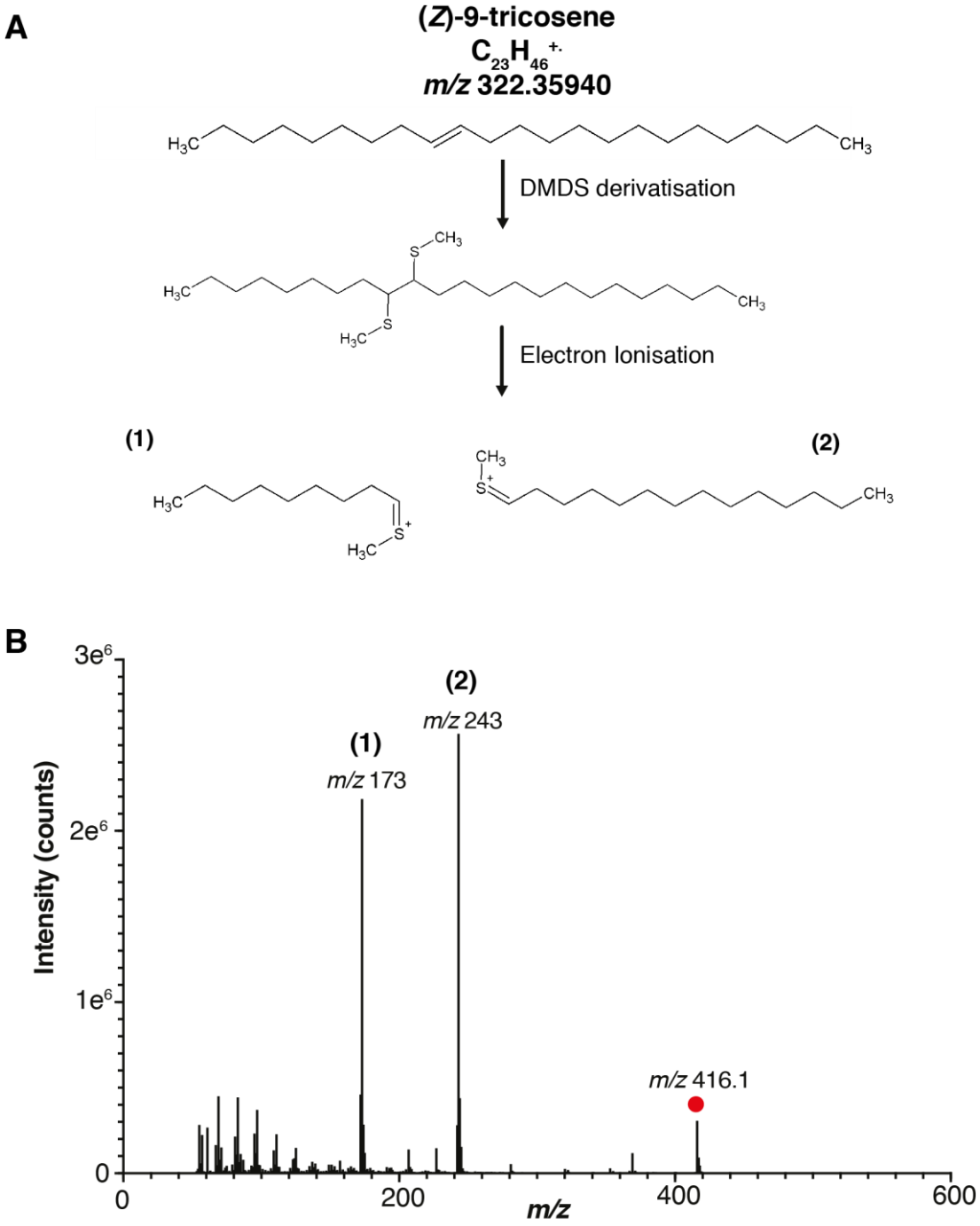

Figure 3.4 GC-MS detection of DMDS derivatised (*Z*)-7-tricosene
A. Derivatisation mechanism dimethylsulphide (DMDS) derivatisation of (*Z*)-9-tricosene and the fragmentation pattern induced by electron ionisation (EI) in GC-MS.
B. The mass spectrum of DMDS derivatised (*Z*)-9-tricosene indicating the intact derivatisation product with the red dot, and the two main fragmentation products labelled (1) and (2) respectively

.

A

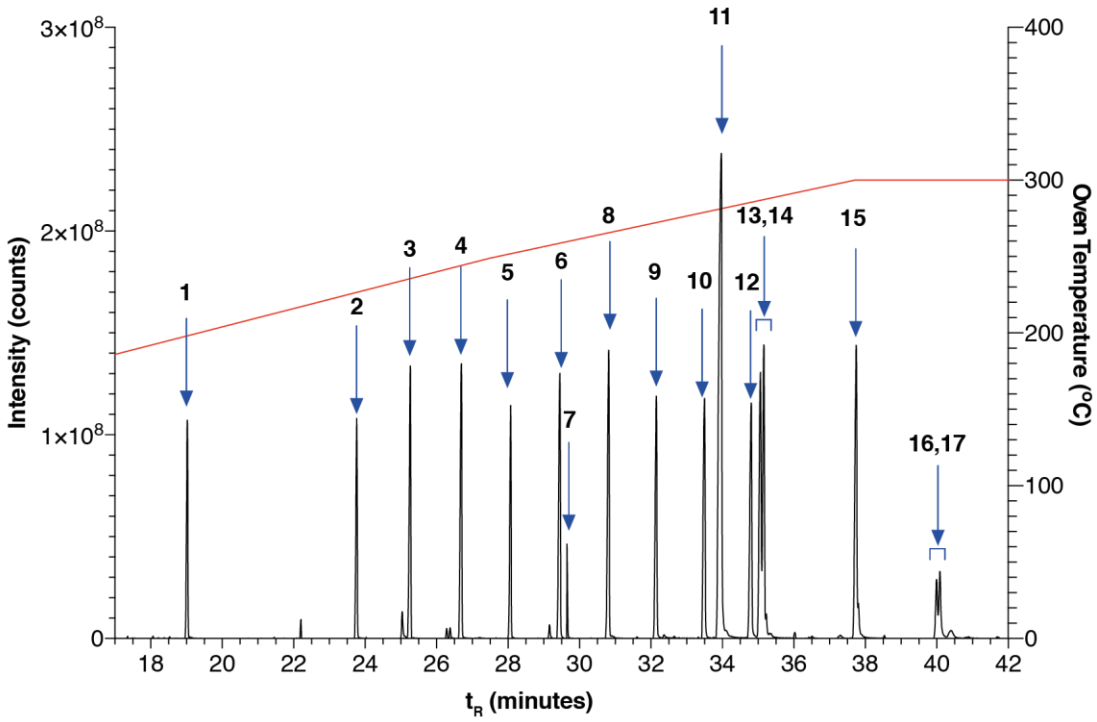

B

Peak no.	Standard	Formula (molecular)	Derivatised?	Key ions (*m/z*)	t_R (minutes)
1	Octadecane	$C_{18}H_{38}$	x	254.2	19
2	Heneicosane	$C_{21}H_{44}$	x	296.3	23.760
3	Docosane	$C_{22}H_{46}$	x	310.3	25.251
4	Tricosane	$C_{23}H_{48}$	x	324.3	26.683
5	Tetracosane	$C_{24}H_{50}$	x	338.3	28.061
6	Pentacosane	$C_{25}H_{52}$	x	352.4	29.435
7	N-N,Dimethyldodecylamine	$C_{14}H_{31}N$	x	212.1	29.663
8	Hexacosane	$C_{26}H_{54}$	x	366.4	30.809
9	Heptacosane	$C_{27}H_{56}$	x	380.4	32.129
10	Octacosane	$C_{28}H_{58}$	x	394.4	33.503
11	(*Z*)-11-Vaccenyl acetate	$C_{20}H_{38}O_2$	✓	404.1, 259.0, 145.0	33.964
12	Nonacosane	$C_{29}H_{60}$	x	408.4	34.823
13	(*Z*)-9-tricosene	$C_{23}H_{46}$	✓	416.1, 243.0, 173.0	35.048
14	(*Z*)-7-tricosene	$C_{23}H_{46}$	✓	416.1, 271.0, 145.0	35.164
15	(*Z*)-7-pentacosene	$C_{25}H_{50}$	✓	444.1, 299.0, 145.0	37.760
16	(*Z*,*Z*)-**7**,11-heptacosadiene	$C_{27}H_{52}$	✓	470.0, 423.0, 375.0, **271.0**	39.993
17	(*Z*,*Z*)-7,**11**-heptacosadiene	$C_{27}H_{52}$	✓	470.0, 423.0, 375.0, **299.0**	40.088

Figure 3.5 GC-MS of DMDS derivatised hydrocarbon standards
GC-MS detection of a mixture of 16 commercial standards after DMDS derivatisation.
A. The black line indicates a GC-MS chromatogram of a mixture of hydrocarbon standards, labelled and described in the above table. The red line indicates the oven temperature gradient in degrees Celsius, illustrating the elution temperature for each hydrocarbon.
B. The key ions listed in the table for DMDS derivatised hydrocarbons represent the intact ion and the two main fragment ions. The diene (*Z*,*Z*)-7,11-heptacosadiene produces two peaks, with the double bond derivatised for each peak indicated in bold.

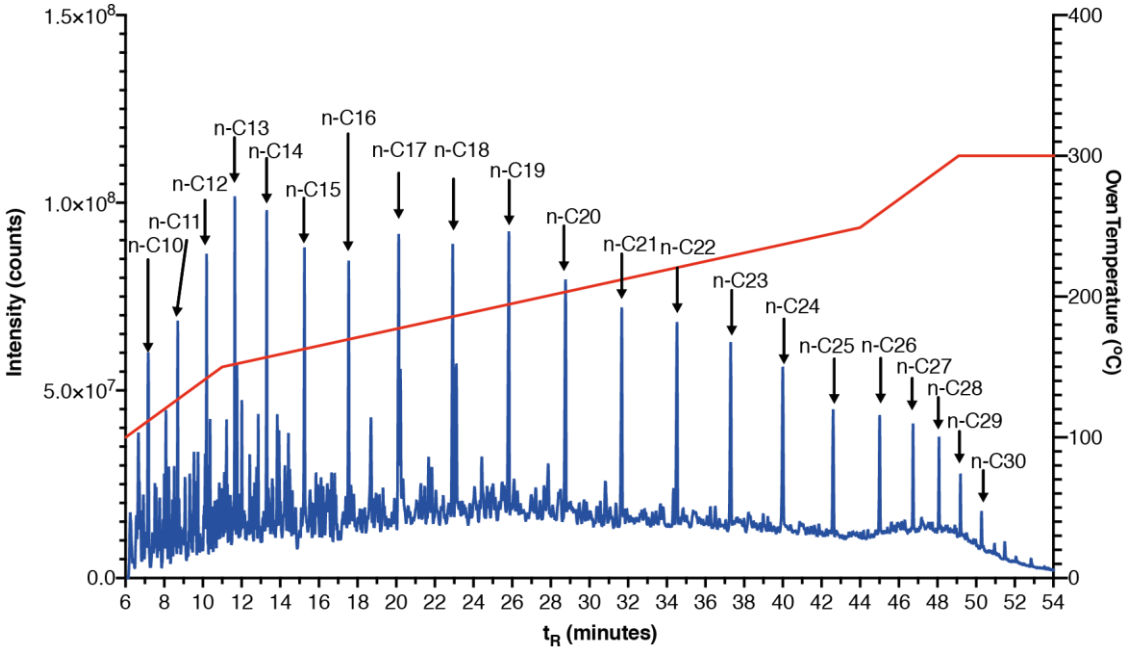

Figure 3.6 GC-MS analysis of hydrocarbons from ASTM reference gas oil
GC-MS analysis of an American Society of Testing Materials (ASTM) reference gas oil at a dilution of 1 in 200. The red line indicates the oven temperature gradient (℃), illustrating the elution temperature for each hydrocarbon. Peaks identified as linear alkanes have been annotated on the chromatogram.

3.2.2 Wax esters

Wax esters (WEs) are another class of lipids on the cuticle of *Drosophila* and on the skin of mammals. These compounds have been reported in a variety of organisms to contribute to the surface barrier protecting organisms, from plants to animals, from excess water loss (Pappas, 2009). Due to their low polarity, it is often possible to detect WEs using GC-MS without a derivatisation step (**Figure 3.7A)**. These lipids can be chromatographically separated, although isobaric compounds are not well resolved. Fortunately, the structural differences between isobaric WEs lead to different in-source fragmentation patterns (**Figure 3.7B**) It is therefore it is possible to perform deconvolution to separate these peaks. However, WEs require a very high elution temperature, with the largest commercially available wax ester standard (C32:0) eluting at a temperature of ~300℃ (**Figure 3.7**). The maximum column temperature using our GC-MS platform with a DB-5MS column is ~320℃, therefore it is not possible to detect intact waxes at much longer carbon chain lengths than C32. Nevertheless, waxes with much longer chain lengths have been detected in other organisms, for example, there is a polyunsaturated C60 wax ester in the lipid coating of the nematode *P. pacificus* (Penkov et al., 2014). Therefore, the GC-MS platform that I have used is unlikely to detect waxes composed of very long-chain fatty acids and alcohols. Even for smaller detectable WEs, their MRRF is ten times lower than for hydrocarbons, which coexist with WEs in *in vivo* hexane extracts of *Drosophila* cuticle. Therefore, if the contribution of wax esters to the cuticular lipid pool is substantially lower than the contribution from hydrocarbons then these compounds may fall below the limit of detection. In order to improve the MRRF of these compounds a derivatisation protocol was applied which utilised methanolysis followed by trimethylsilylation as illustrated in **Figure 3.8**. This method had the benefit of dramatically increasing the MRRF of wax esters but it hydrolyses WEs into fatty acids and alcohols. The fatty acid is then derivatised into a fatty acid methyl ester (FAME) which is indistinguishable from a free fatty acid. Additionally, it is not possible to determine the full length of the original WE due to the hydrolysis step. Despite these drawbacks, methanolysis and trimethylsilylation are still be useful tools in determining any overall changes in

the total abundance of cuticular waxes – a quantitation that is not possible to answer using OrbiSIMS analysis alone.

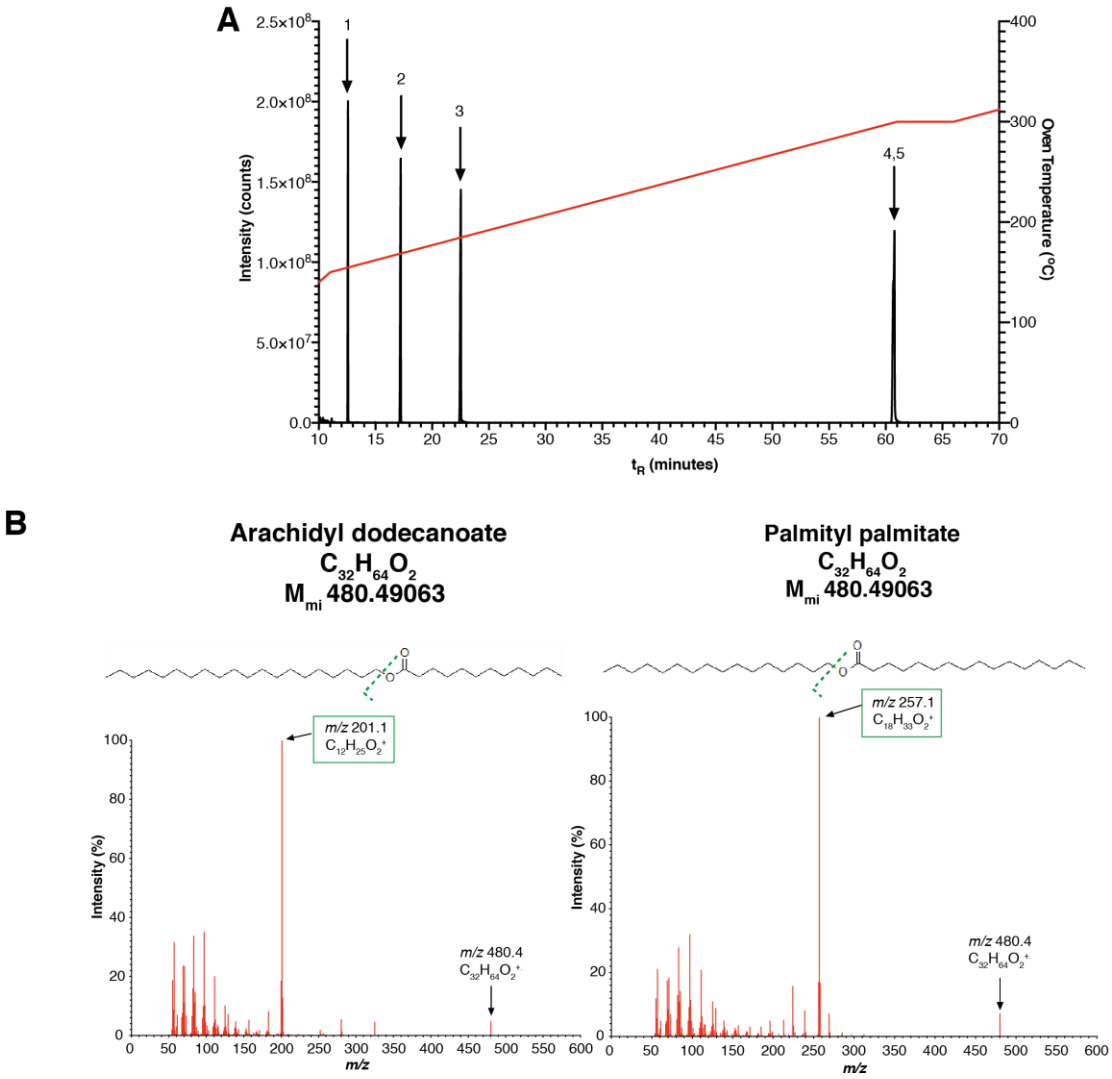

C

Peak no.	Standard	Formula (molecular)	Key ions (*m/z*)	t_R (minutes)
1	Ethyl decanoate	$C_{12}H_{24}O_2$	200.1, 157.0	12.570
2	Ethyl dodecanoate	$C_{14}H_{28}O_2$	228.1, 185.0	17.223
3	Ethyl tetradecanoate	$C_{16}H_{32}O_2$	256.1, 213.0	22.514
4	Palmityl palmitate	$C_{32}H_{64}O_2$	480.4, 257.1	60.649
5	Arachidyl dodecanoate	$C_{32}H_{64}O_2$	480.4, 201.1	60.765

Figure 3.7 GC-MS detection of native wax ester standards
A. Chromatogram showing separation of commercial underivatised wax ester standards. The black line indicates a GC-MS chromatogram of a mixture of hydrocarbon standards, labelled and described in the above table. The red line indicates the oven temperature gradient in degrees Celsius, illustrating the elution temperature for each wax.
B. Mass spectra of two isobaric waxes showing the structure-specific EI-induced fragmentation patterns. Major fragments are indicated in green, following the dotted green cleavage line illustrated on the structure..

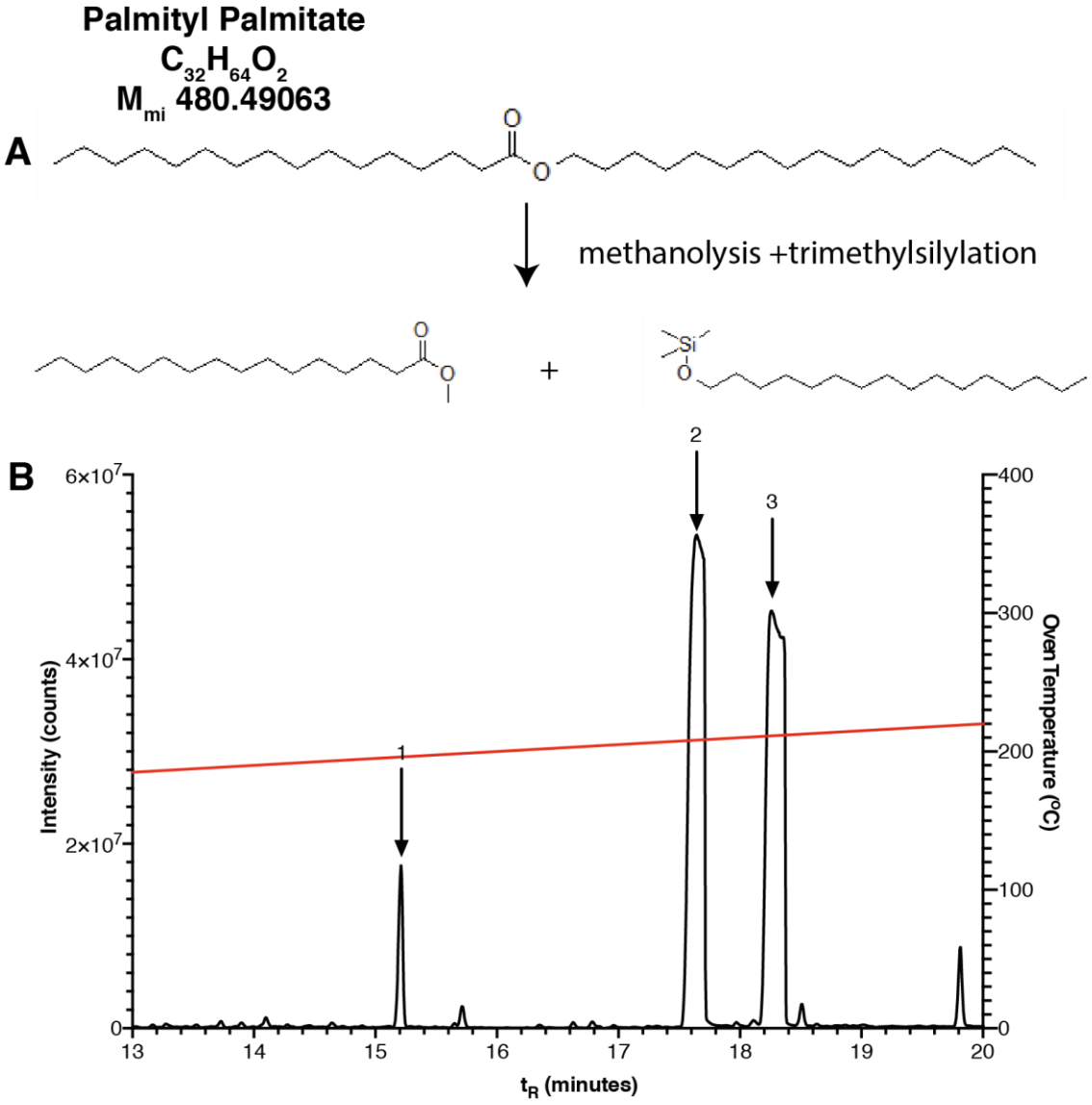

C

Peak no.	Standard	Formula (observed)	Derivatised?	Key ions (*m/z*)	t_R (minutes)
1	Octadecane	$C_{18}H_{38}^+$	x	281.3	15.21
2	Palmityl palmitate	$C_{18}H_{39}SiO^+$	✓	270.3	17.639
3	Palmityl palmitate	$C_{17}H_{34}O_2^+$	✓	299.3	18.304

Figure 3.8 GC-MS of fatty acid and fatty alcohol chains from a derivatised wax ester standard

A. Derivatisation products from methanolysis followed by trimethylsilylation of a palmityl palmitate wax ester standard.

B. Gas chromatogram of a derivatised wax ester (black). The red line indicates the oven temperature gradient in degrees Celsius, illustrating the elution temperature for each wax derivative.

C. Products of palmityl palmitate derivatisation as detected by quadrupole mass spectrometry after gas chromatography.

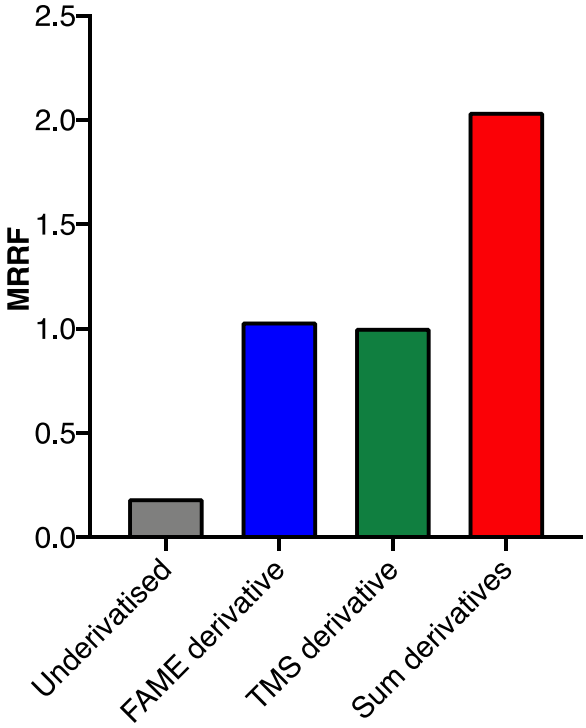

Figure 3.9 GC-MS Molar relative response factor for a native and derivatised wax ester
Molar-relative response factor (MRRF) calculated for 50 nmol palmityl palmitate relative to 50 nmol octadecane. The FAME derivative represents the derivatised fatty acid chain after hydrolysis, and TMS derivative represents the derivatised fatty alcohol chain after hydrolysis.

3.2.3 Fatty acids and glycerolipids

For several questions posed in this study, it is desirable to measure other lipid species such as TGs and free fatty acids. To detect these compounds with GC-MS it is first necessary to derivatise them to decrease the compound polarity. Several methods were tested for this application. Initially, the commercial lipid standard was run using TMAH derivatisation which involves transesterification of all lipid species to produce FAMEs (**Figure 3.10**). This derivatises all free fatty acids, phospholipids and glycerolipids, however the downside of this analysis is the inability to differentiate between the source of the fatty acid chains detected and is therefore more suitable for detection of bulk changes in total lipid (fatty acid chain) abundance. Additionally, a method was optimised to exclusively detect free fatty acids and hydrocarbons in a complex mixture of lipids through selective derivatisation using trimethylsilylation with MSTFA (N-methyl-N-(trimethylsilyl)trifluoroacetamide) with a TMCS (trimethylchlorosilane) catalyst (**Figure 3.12, Table 3.2**). Given that fatty acids from TG species were not derivatised, this method is indeed selective for free fatty acids and gives sufficient chromatographic separation to be useful for the analysis of complex lipid extracts from *Drosophila*.

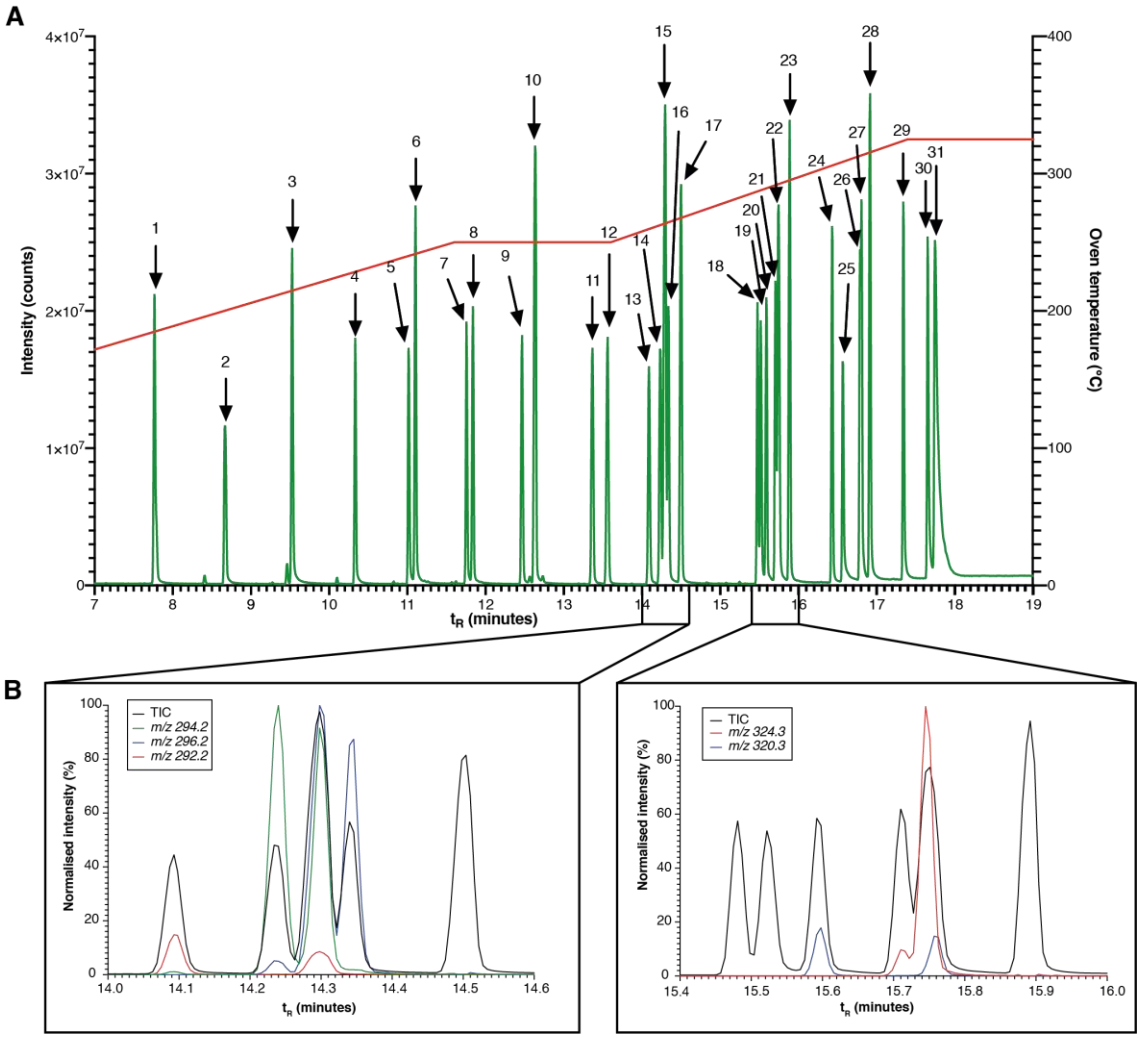

Figure 3.10 Detection of FAMEs with GC-MS

A. Chromatographic separation of FAMEs in a commercial 37 FAME mix. Peaks are numbered and relevant information displayed in **Table 3.1**.
B. Extracted ion chromatograms (EICs) for compounds that co-elute between t_R 14.40 and 14.6 mins, and t_R 15.4 and 16.0 mins.

Table 3.1 Detection of FAMEs with GC-MS

Peak number	t_R (minutes)	Compound	Concentration	Molar concentration (µM)	Formula	*m/z*
-	-	Methyl butyrate	400 µg/mL	3.92	$C_5H_{10}O_2$	102.1
-	-	Methyl hexanoate	400 µg/mL	3.07	$C_7H_{14}O_2$	130.1
-	-	Methyl octanoate	400 µg/mL	2.53	$C_9H_{18}O_2$	158.1
1	7.764	Methyl decanoate	400 µg/mL	2.15	$C_{11}H_{22}O_2$	186.2
2	8.669	Methyl undecanoate	200 µg/mL	1.00	$C_{12}H_{24}O_2$	200.2
3	9.522	Methyl dodecanoate	400 µg/mL	1.87	$C_{13}H_{26}O_2$	214.2
4	10.334	Methyl tridecanoate	200 µg/mL	0.88	$C_{14}H_{28}O_2$	228.2
5	11.022	Methyl (*Z*)-myristoleate tetradec-9-enoate	200 µg/mL	0.83	$C_{15}H_{28}O_2$	240.2
6	11.105	Methyl tetradecanoate	400 µg/mL	1.65	$C_{15}H_{30}O_2$	242.2
7	11.757	Methyl (*Z*)-pentadec-10-enoate	200 µg/mL	0.79	$C_{16}H_{30}O_2$	254.2
8	11.834	Methyl pentadecanoate	200 µg/mL	0.78	$C_{16}H_{32}O_2$	256.2
9	12.475	Methyl (*Z*)-hexadec-9-enoate	200 µg/mL	0.75	$C_{17}H_{32}O_2$	268.2
10	12.634	Methyl hexadecanoate	600 µg/mL	2.22	$C_{17}H_{34}O_2$	270.3
11	13.363	Methyl (*Z*)-heptadec-10-enoate	200 µg/mL	0.71	$C_{18}H_{34}O_2$	282.3
12	13.557	Methyl heptadecanoate	200 µg/mL	0.70	$C_{18}H_{36}O_2$	284.3
13	14.093	Methyl (*Z,Z,Z*)-octadeca-6,9,12-trienoate	200 µg/mL	0.68	$C_{19}H_{32}O_2$	292.2
15	14.298	Methyl (*Z,Z,Z*)-octadeca-9,12,15-trienoate	200 µg/mL	0.68	$C_{19}H_{32}O_2$	292.2
14	14.24	Methyl (*Z,Z*)-octadeca-9,12-dienoate	200 µg/mL	0.68	$C_{19}H_{34}O_2$	294.3
15	14.298	Methyl (*E,E*)-octadeca-9,12-dienoate	200 µg/mL	0.68	$C_{19}H_{34}O_2$	294.3
15	14.298	Methyl (*Z*)-octadec-9-enoate	200 µg/mL	0.67	$C_{19}H_{36}O_2$	296.3
16	14.346	Methyl (*E*)-octadece-9-enoate	400 µg/mL	1.35	$C_{19}H_{36}O_2$	296.3
17	14.504	Methyl octadecanoate	400 µg/mL	1.34	$C_{19}H_{38}O_2$	298.3
18	15.481	Methyl (*Z,Z,Z,Z,Z*)-icosa-5,8,11,14,17-pentaenoate	200 µg/mL	0.63	$C_{21}H_{32}O_2$	316.2
19	15.552	Methyl (*Z,Z,Z,Z*)-icosa-5,8,11,14-tetraenate	200 µg/mL	0.63	$C_{21}H_{34}O_2$	318.3
20	15.592	Methyl (*Z,Z,Z*)-icosa-8,11,14-trienoate	200 µg/mL	0.62	$C_{21}H_{36}O_2$	320.3
22	15.751	Methyl (*Z,Z,Z*)-icosa-11,14,17-trienoate	200 µg/mL	0.62	$C_{21}H_{36}O_2$	320.3
21	15.71	Methyl (*Z,Z*)-icosa-1,14-dienoate	200 µg/mL	0.62	$C_{21}H_{38}O_2$	322.3
22	15.751	Methyl (*Z*)-icos-11-enoate	200 µg/mL	0.62	$C_{21}H_{40}O_2$	324.3
23	15.892	Methyl icosanoate	400 µg/mL	1.23	$C_{21}H_{42}O_2$	326.3
24	16.434	Methyl heneicosanoate	200 µg/mL	0.59	$C_{22}H_{44}O_2$	340.3
25	16.575	Methyl (*Z,Z,Z,Z,Z,Z*)-docosa-4,7,10,13,16,19-hexaenoate	200 µg/mL	0.58	$C_{23}H_{34}O_2$	342.3
26	16.792	Methyl (*Z,Z*)-docosa-13,16-dienoate	200 µg/mL	0.57	$C_{23}H_{42}O_2$	350.3
27	16.81	Methyl (*Z*)-docos-13-enoate	200 µg/mL	0.57	$C_{23}H_{44}O_2$	352.3
28	16.992	Methyl docosanoate	400 µg/mL	1.13	$C_{23}H_{46}O_2$	354.3
29	17.345	Methyl tricosanoate	200 µg/mL	0.54	$C_{24}H_{48}O_2$	368.4
30	17.657	Methyl (*Z*)-tetracos-15-enoate	200 µg/mL	0.53	$C_{25}H_{48}O_2$	380.4
31	17.757	Methyl tetracosanoate	400 µg/mL	1.05	$C_{25}H_{50}O_2$	382.4

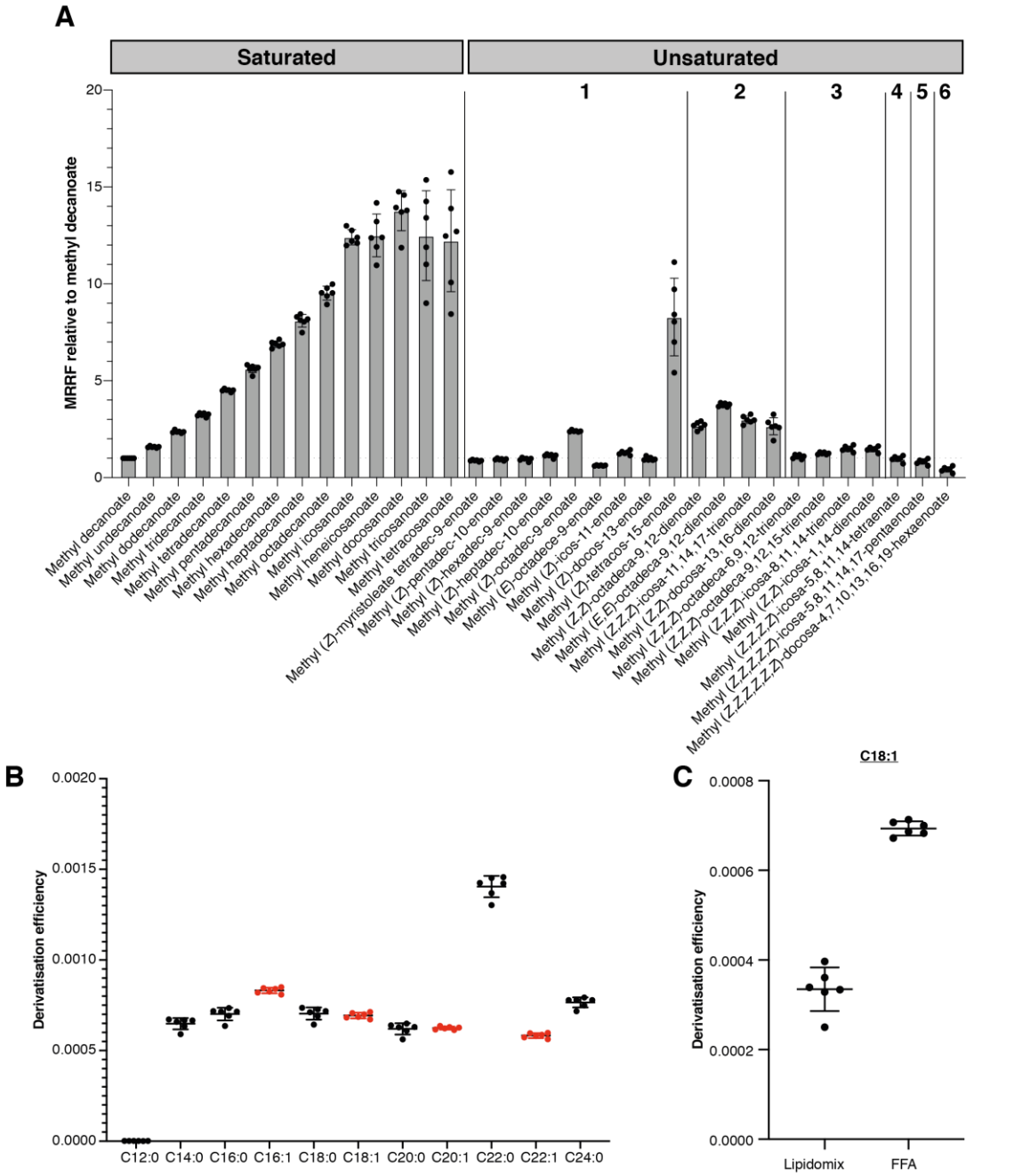

Figure 3.11 Derivatisation and detection efficiency of FAMEs

A. Molar relative response factors calculated for FAME standards with varying degrees of saturation, presented relative to methyl decanoate.
B. Derivatisation efficiency of a range of free fatty acids when compared with detected FAME standards (representing a value of 1). Red indicates unsaturated fatty acids.
C. Derivatisation efficiency of C18:1 free fatty acid (FFA) compared with C18:1 fatty acid chains contained within lipids (triglyceride, sphingomyelin, ceramide and lyso-phosphatidylcholine).

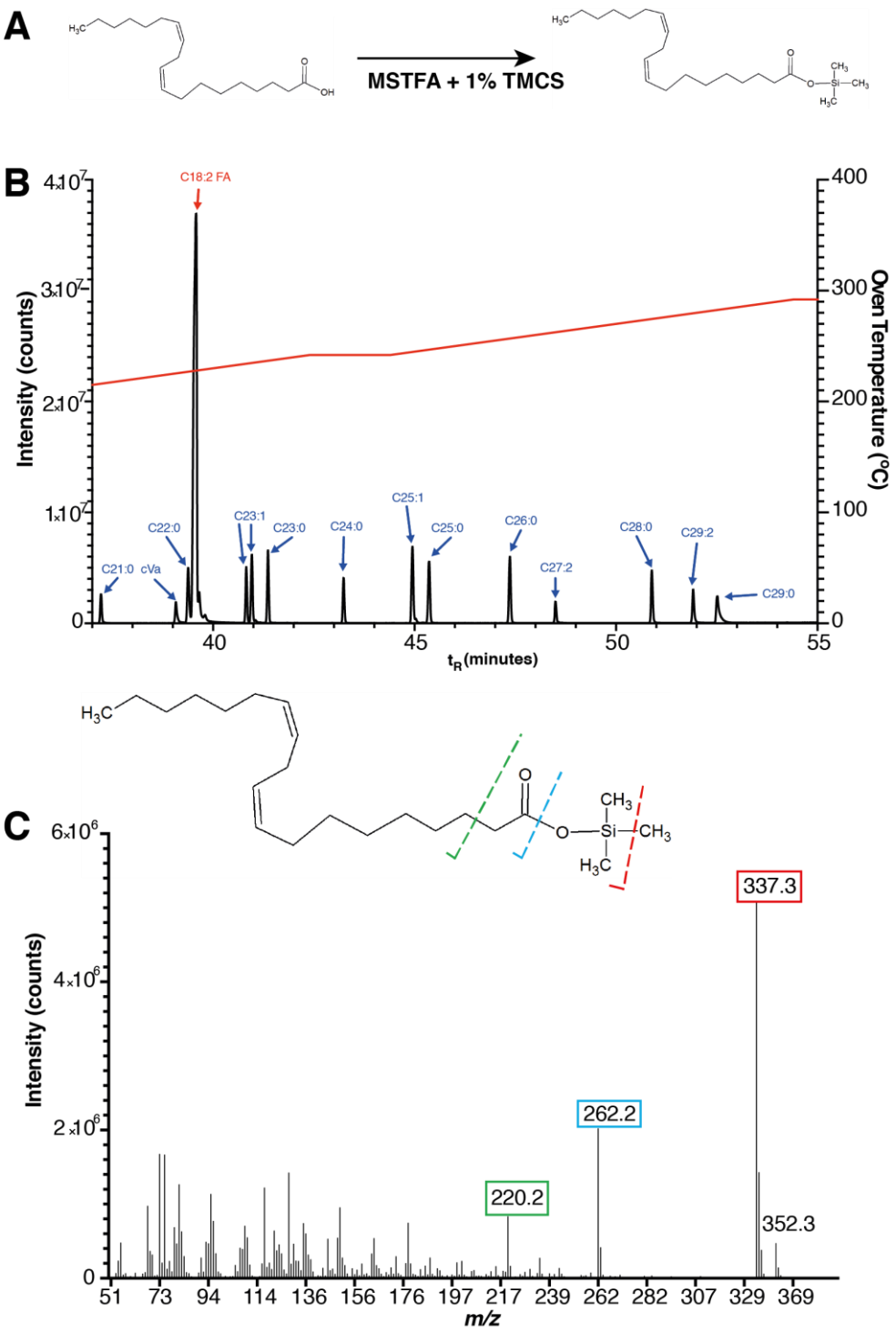

Figure 3.12 Dual detection of hydrocarbons and free fatty acids with MSTFA derivatisation

A. Derivatisation reaction of linoleic acid with MSTFA to form a FAME.

B. Chromatogram showing chromatographical separation of a MSTFA derivatised C18:2 fatty acid standard and a hydrocarbon standard mixture. The black line indicates the GC-MS chromatogram, labelled and described in the above table. The red line indicates the oven temperature gradient in degrees Celsius, illustrating the elution temperature for each standard.

B. Mass spectrum of the derivatised linoleic acid standard *m/z* 352.3 indicates the intact derivatised fatty acid, and subsequent fragmentations are colour coded. The EI-induced fragmentation pattern shows fragmentation in proximity to the TMS group.

Table 3.2 Dual detection of hydrocarbons and a free fatty acid with MSTFA derivatisation
Key ions and retention times of fatty acid and hydrocarbon standards under this gas chromatography method.

Standard	Formula	Derivatised?	Key ions (*m/z*)	t_R (minutes)
Heneicosane	$C_{21}H_{44}$	x	296.3	37.215
(*Z*)-11-Vaccenyl acetate	$C_{20}H_{38}O_2$	x	250.3, 310.3	39.085
Docosane	$C_{22}H_{46}$	x	310.3	39.379
Linoleic acid	$C_{18}H_{32}O_2$	✓	352.3, 337.3, 262.3	39.573
(*Z*)-7-tricosene	$C_{23}H_{46}$	x	322.3	40.82
(*Z*)-9-tricosene	$C_{23}H_{46}$	x	322.3	40.967
Tricosane	$C_{23}H_{48}$	x	324.3	41.367
Tetracosane	$C_{24}H_{50}$	x	338.3	43.232
(*Z*)-7-pentacosene	$C_{25}H_{50}$	x	350.4	44.955
Pentacosane	$C_{25}H_{52}$	x	352.4	45.361
Hexacosane	$C_{26}H_{54}$	x	366.4	47.361
(*Z,Z*)-7,11-heptacosadiene	$C_{27}H_{52}$	x	376.4	48.496
Octacosane	$C_{28}H_{58}$	x	394.4	50.89
(*Z,Z*)-7,11-nonacosadiene	$C_{29}H_{56}$	x	404.4	51.902
Nonacosane	$C_{29}H_{60}$	x	408.4	52.514

3.2.4 Aldehydes

Fatty aldehydes are known to be the metabolic precursors of hydrocarbons in *Drosophila (Wicker-Thomas et al., 2015)*, and have been detected as surface lipids in a variety of other organisms (Yeats and Rose, 2013, Nordby and Nagy, 1977, Machin, 1980). As these reactive lipids can be detected on the surface of the biological organisms used as the focus of this study, it was important to develop a GC-MS based analytical method. Using PFBHA (O-(2,3,4,5,6-pentafluorobenzyl)hydroxylamine hydrochloride) derivatisation to form PFBHA oximes from aldehyde standards, it was possible to detect both species within the same GC-MS sample (**Figure 3.13**). The in-source fragmentation pattern enables determination of compound structure (**Figure 3.14)**. In the case of lauric aldehyde, due to the limited mass resolving power of the quadrupole, the fatty acyl chain fragment is not resolvable from the ^{13}C isotope of the PFBHA group, Therefore its presence has to be determined through correction of peak intensity for natural abundance of ^{13}C. This optimised method is important for the validation of aldehydes detected using cryo-OrbiSIMS.

A

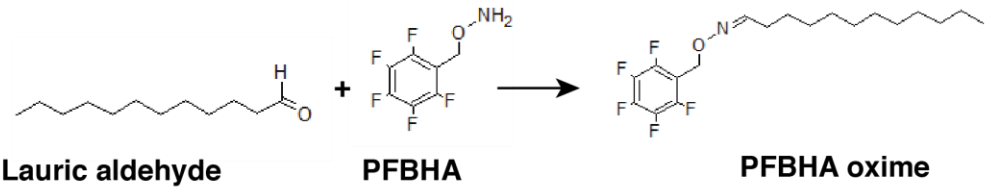

B

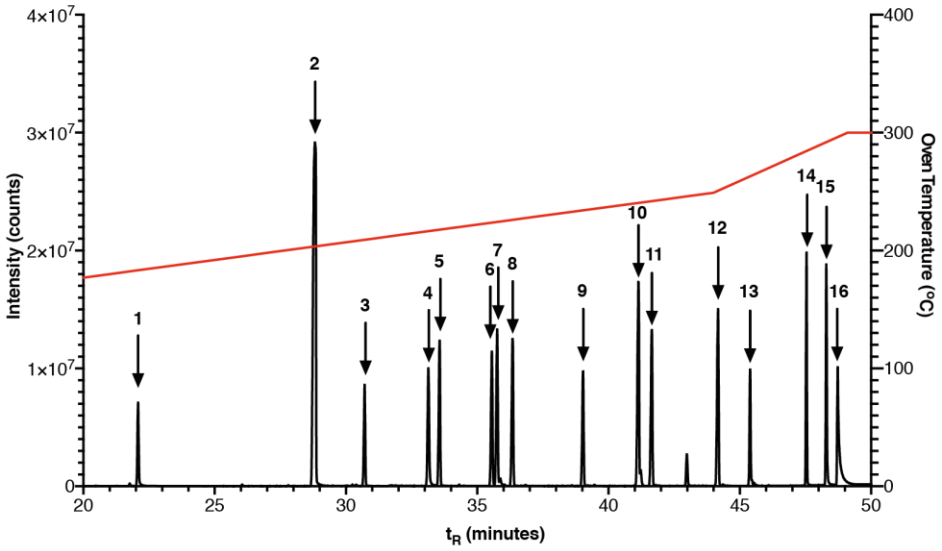

C

Peak no.	Standard	Formula	Derivatised?	Key ions (*m/z*)	t_R (minutes)
1	Octadecane	$C_{18}H_{38}$	x	281.3	22.098
2	Lauric aldehyde	$C_{12}H_{24}O$	✓	181.1, 198.1	28.809
3	Heneicosane	$C_{21}H_{44}$	x	296.3	30.733
4	(*Z*)-11-vaccenyl acetate	$C_{20}H_{38}O_2$	x	250.3, 310.3	33.127
5	Docosane	$C_{22}H_{46}$	x	310.3	33.568
6	(*Z*)-9-tricosene	$C_{18}H_{32}O_2$	x	322.3	35.521
7	(*Z*)-7-tricosene	$C_{23}H_{46}$	x	322.3	35.727
8	Tricosane	$C_{23}H_{46}$	x	324.3	36.332
9	Tetracosane	$C_{23}H_{48}$	x	338.3	39.032
10	(*Z*)-7-pentacosene	$C_{24}H_{50}$	x	350.4	41.156
11	Pentacosane	$C_{25}H_{50}$	x	352.4	41.626
12	Hexacosane	$C_{25}H_{52}$	x	366.4	44.156
13	(*Z*,*Z*)-7,11-heptacosadiene	$C_{26}H_{54}$	x	376.4	45.408
14	Octacosane	$C_{27}H_{52}$	x	394.4	47.532
15	(*Z*,*Z*)-7,11-nonacosadiene	$C_{28}H_{58}$	x	404.4	48.308
16	Nonacosane	$C_{29}H_{56}$	x	408.4	48.744

Figure 3.13 Dual detection of hydrocarbons aldehydes with PFBHA derivatisation
A. Derivatisation of a lauric aldehyde standard with PFBHA to form a PFBHA oxime.
B. Chromatogram showing separation of a PFBHA derivatised aldehyde standard and a mixture of 15 hydrocarbon standards. The black line indicates a GC-MS chromatogram. The red line indicates the oven temperature gradient (℃), illustrating the elution temperature for each standard.
C. Retention time and ions detected for each peak labelled in **B**.

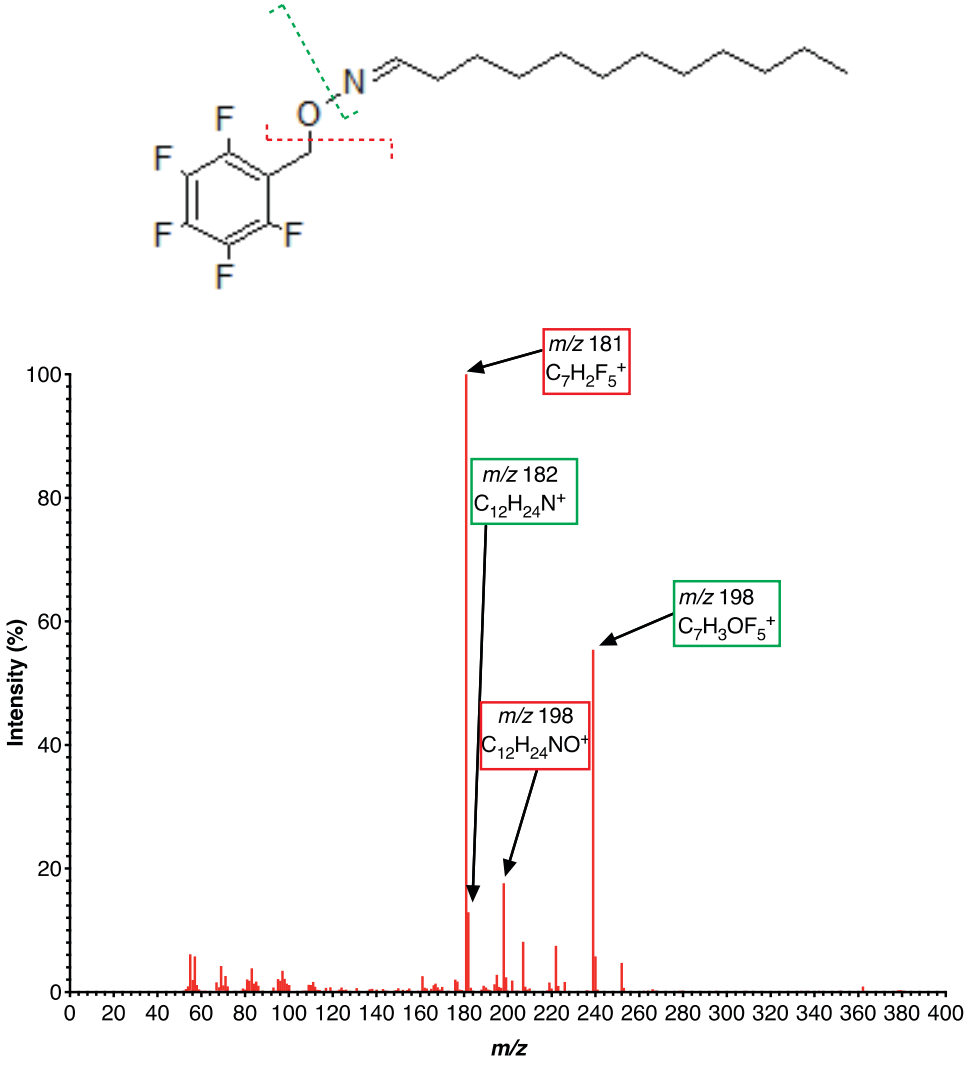

Figure 3.14 In-source fragmentation of lauric aldehyde PFBHA oxime
EI-induced fragmentation pattern of the PFBHA oxime produced from PFBHA derivatisation of a lauric acid commercial standard.

3.3 LC-MS

GC-MS is well-suited for the quantitative analysis of hydrocarbons, wax esters, and other lipids but, as I have illustrated, derivatisation methods preclude analysis of several types of intact native lipids. In particular, it is not possible to identify the exact source of the fatty acid chains detected in derivatised mixtures of phospholipids and glycerolipids. Therefore, to analyse these complex lipid classes, I used LC-MS. To determine the range of lipids readily detectible with LC-MS and to provide standards against the retention time and MS2 fragmentation pattern of different lipid classes, a commercially available lipid mix of phospholipids, glycerolipids and sterols was run using a previously published protocol (Amiar et al., 2016). This protocol shows clear separation between different classes of phospholipid and glycerolipid classes, providing a useful platform for analysis of complex biological samples (**Figure 3.15**, **Figure 3.16**). In positive polarity mode, it is possible to detect all major lipid classes in the commercial lipid mixture (**Figure 3.15**). In negative polarity mode, however, there are several classes that do not ionise well such as TG, cholesterol and CE (**Figure 3.16A**). Given that species with a lower detection efficiency are often non-polar, this suggests the polarity of the liquid chromatography mobile phase may be problematic for very non-polar lipids such as hydrocarbons, wax esters and sterols.

In general, there is a substantially decreased diversity in adduct formation in negative polarity (**Figure 3.16B**) but this comes with the cost of decreased ionisation efficiency, providing a poorer degree of sensitivity than positive polarity measurements. Using this information, it is possible to calculate a the relative detection efficiency of the different lipid classes which encompasses ionisation efficiency and instrumental transfer efficiency (**Figure 3.17**). This indicates that ionisation efficiency across the lipid classes appears to be higher in positive polarity than negative polarity. This is likely caused by the ionisation chemistry inherent to ESI. This increased detection efficiency in positive polarity is accompanied by a broader range of adduct formation which can often complicate quantification. As the sample matrix may influence proportional adduct formation,

it is important to consider this when attempting absolute quantification. This highlights a key point when analysing mass spectrometry data – it is important to avoid drawing conclusions on absolute abundance of lipid classes without side-by-side analysis of appropriate standards in a comparable matrix.

The MS^2 compound fragmentation patterns in both positive and negative polarity are useful for interpreting OrbiSIMS MS^2 fragmentation patterns. From the fragmentation patterns displayed for these lipid standards (**Supplementary Figures 9.1-9.14** located in the Supplementary Material), previously reported key markers of fragmentation were identified (Fahy et al., 2007). Although the use of LC-MS for lipidomics is far more established than SIMS, there are still uncommon and unreported adducts produced using the chemical standard preparation and method described in this chapter (**Figure 3.16**). Notably, the cardiolipin standard is detected most commonly as an adduct that appears as $[M+H]^-$, but is more likely this is produced from the loss of two sodium ions and subsequent addition of a proton. The loss of two positively charged sodium ions and addition of a negatively charged hydrogen ion result in a net charge of -1 which is reflected in the isotopic distribution pattern.

A

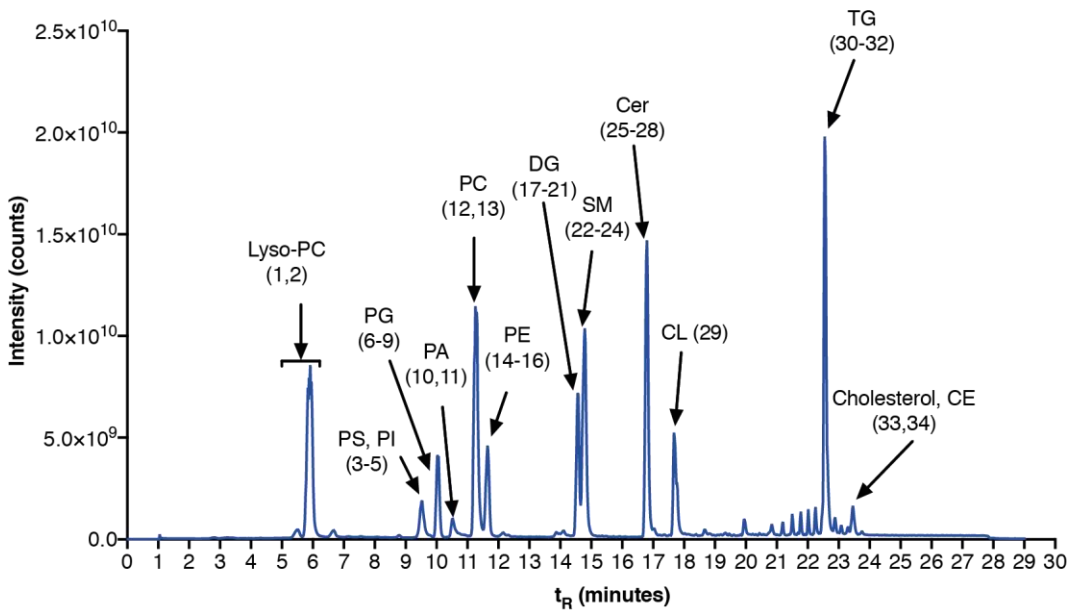

B

Peak no.	t_R (minutes)	*m/z*	I.D.	Formula (observed)	Adduct	Mass deviation (ppm)	MS^2?
1	5.91	522.3568	Lyso-PC(18:1/0:0)	$C_{26}H_{53}NO_7P^+$	$[M+H]^+$	2.64	✓
2	5.91	1043.7020	Lyso-PC(18:1/0:0)	$C_{52}H_{105}N_2O_{14}P_2^+$	$[2M+H]^+$	-1.51	✓
3	9.52	676.4163	PS(14:1/14:1)	$C_{34}H_{63}NO_{10}P^+$	$[M+H]^+$	-3.12	✓
4	9.52	1351.8290	PS(14:1/14:1)	$C_{68}H_{125}N_2O_{20}P_2^+$	$[2M+H]^+$	-0.40	✓
5	9.52	768.4630	PI(14:1/14:1)	$C_{37}H_{71}NO_{13}P^+$	$[M+NH_4]^+$	-3.58	✓
6	10.03	663.4218	PG(14:1/14:1)	$C_{34}H_{64}O_{10}P^+$	$[M+H]^+$	-2.05	✓
7	10.03	680.4472	PG(14:1/14:1)	$C_{34}H_{67}NO_{10}P^+$	$[M+NH_4]^+$	-3.69	✓
8	10.03	1325.8415	PG(14:1/14:1)	$C_{68}H_{127}O_{20}P_2^+$	$[2M+H]^+$	1.85	✓
9	10.03	1342.8681	PG(14:1/14:1)	$C_{68}H_{130}NO_{20}P_2^+$	$[2M+NH_4]^+$	1.86	✓
10	10.53	606.4129	PA(14:1/14:1)	$C_{31}H_{61}NO_8P^+$	$[M+NH_4]^+$	-0.05	✓
11	10.53	1194.7932	PA(14:1/14:1)	$C_{62}H_{118}NO_{16}P_2^+$	$[2M+NH_4]^+$	0.94	✓
12	11.29	674.4724	PC(14:1/14:1)	$C_{36}H_{69}NO_8P^+$	$[M+H]^+$	-4.64	✓
13	11.29	1347.9438	PC(14:1/14:1)	$C_{72}H_{137}N_2O_{16}P_2^+$	$[2M+H]^+$	0.01	✓
14	11.66	632.4270	PE(14:1/14:1)	$C_{33}H_{63}NO_8P^+$	$[M+H]^+$	-2.50	✓
15	11.66	1263.8482	PE(14:1/14:1)	$C_{66}H_{125}N_2O_{16}P_2^+$	$[2M+H]^+$	-1.34	✓
16	11.66	1285.8302	PE(14:1/14:1)	$C_{66}H_{124}N_2NaO_{16}P_2^+$	$[2M+Na]^+$	-1.27	✓
17	14.53	491.4080	DG(14:1/14:1/0:0)	$C_{31}H_{55}O_4^+$	$[M+H-H_2O]^+$	-3.03	✓
18	14.53	526.4457	DG (14:1/14:1/0:0)	$C_{31}H_{60}NO_5^+$	$[M+NH_4]^+$	-1.71	✓
19	14.53	531.3999	DG(14:1/14:1/0:0)	$C_{31}H_{56}NaO_5^+$	$[M+Na]^+$	-3.95	✓
20	14.53	1039.8110	DG(14:1/14:1/0:0)	$C_{62}H_{112}NaO_{10}^+$	$[2M+Na]^+$	-3.63	✓
21	14.53	283.2256	DG(14:1/14:1/0:0)	$C_{17}H_{31}O_3^+$	$[M+H-H_2O-FA]^+$	-3.99	✓
22	14.78	729.5879	SM(18:1/18:1)	$C_{41}H_{82}N_2O_6P^+$	$[M+H]^+$	-3.56	✓
23	14.78	751.5669	SM(18:1/18:1)	$C_{41}H_{81}N_2NaO_6P^+$	$[M+Na]^+$	-7.40	✓
24	14.78	1458.1667	SM(18:1/18:1)	$C_{82}H_{163}N_4O_{12}P_2^+$	$[2M+H]^+$	-4.82	✓
25	16.79	546.5238	Cer(18:1/18:1)	$C_{36}H_{68}NO_2^+$	$[M+H-H_2O]^+$	-1.21	✓
26	16.79	564.5330	Cer(18:1/18:1)	$C_{36}H_{70}NO_3^+$	$[M+H]^+$	-3.54	✓
27	16.79	1128.0593	Cer(18:1/18:1)	$C_{72}H_{139}N_2O_6^+$	$[2M+H]^+$	-3.08	✓
28	16.79	1150.0412	Cer(18:1/18:1)	$C_{72}H_{138}N_2NaO_6^+$	$[2M+Na]^+$	-3.05	x
29	17.68	1250.8172	CL(14:1/14:1/14:1/14:1)	$C_{65}H_{122}NO_{17}P_2^+$	$[M-2Na+2H+NH_4]^+$	-0.84	✓
30	22.56	902.8157	TG(18:1/18:1/18:1)	$C_{57}H_{108}NO_6^+$	$[M+NH_4]^+$	-1.57	✓
31	22.56	603.5341	TG(18:1/18:1/18:1)	$C_{39}H_{71}O_4^+$	$[M+H-H_2O-FA]^+$	-1.01	✓
32	22.56	1787.6114	TG(18:1/18:1/18:1)	$C_{114}H_{212}NO_{12}^+$	$[2M+NH_4]^+$	6.13	x
33	23.47	369.3507	Cholesterol	$C_{27}H_{45}^+$	$[M+H-H_2O]^+$	-2.38	✓
34	23.47	684.6624	CE(19:0)	$C_{46}H_{86}NO_2^+$	$[M+NH_4]^+$	-4.32	✓

Figure 3.15 Positive polarity LC-MS analysis of a commercial lipid mixture
A. Chromatographic separation of lipid classes using liquid chromatography, and **B**. the associated masses of the adducts formed by these lipid classes.

A

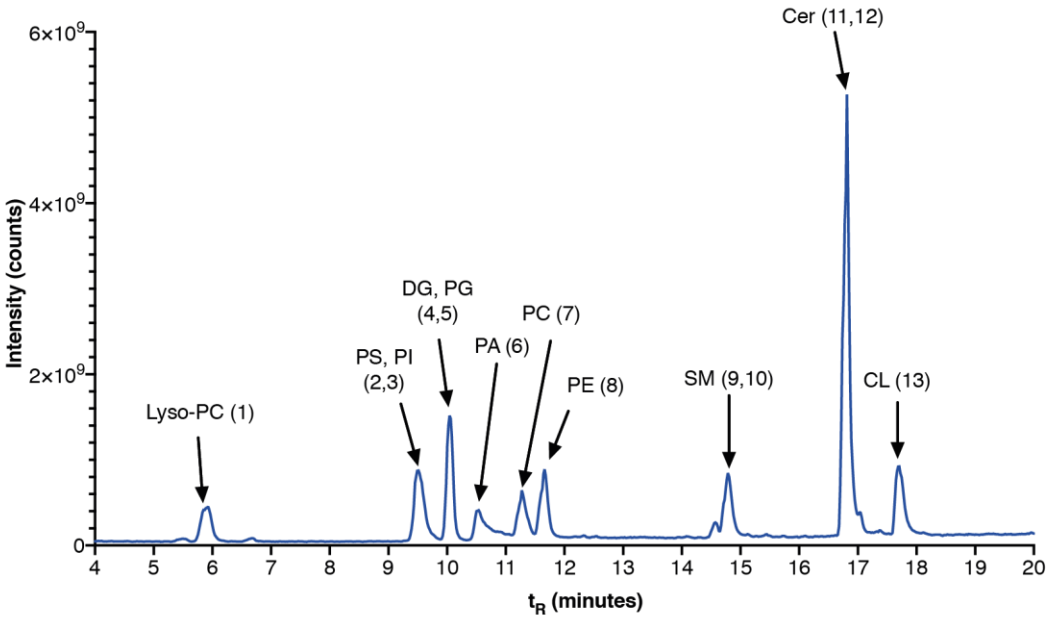

B

Peak no.	t_R (minutes)	*m/z*	I.D.	Formula (observed)	Adduct	Mass deviation (ppm)	MS^2?
1	5.93	566.3463	Lyso-PC(18:1/0:0)	$C_{27}H_{53}NO_9P^-$	$[M+CH_2O_2-H]^-$	-0.07	✓
2	9.52	674.4039	PS (14:1/14:1)	$C_{34}H_{61}NO_{10}P^-$	$[M-H]^-$	0.06	✓
3	9.52	749.4198	PI(14:1/14:1)	$C_{37}H_{66}O_{13}P^-$	$[M-H]^-$	-6.54	✓
4	10.05	491.4084	DG(14:1/14:1/0:0)	$C_{31}H_{55}O_4^-$	$[M-H-H_2O]^-$	-4.44	x
5	10.05	661.4085	PG (14:1/14:1)	$C_{34}H_{62}O_{10}P^-$	$[M-H]^-$	-0.17	✓
6	10.53	587.3721	PA (14:1/14:1)	$C_{31}H_{56}O_8P^-$	$[M-H]^-$	0.46	✓
7	11.31	708.4386	PC (14:1/14:1)	$C_{36}H_{68}ClNO_8P^-$	$[M+Cl]^-$	1.33	✓
8	11.67	630.4144	PE (14:1/14:1)	$C_{33}H_{61}NO_8P^-$	$[M-H]^-$	0.59	✓
9	14.78	763.5534	SM (18:1/18:1)	$C_{41}H_{81}ClN_2O_6P^-$	$[M+Cl]^-$	1.01	✓
10	14.78	773.5817	SM (18:1/18:1)	$C_{42}H_{82}N_2O_8P^-$	$[M+CH_2O_2-H]^-$	0.35	✓
11	16.85	598.4973	Cer (18:1/18:1)	$C_{36}H_{69}ClNO_3^-$	$[M+Cl]^-$	0.25	x
12	16.85	608.5254	Cer (18:1/18:1)	$C_{37}H_{70}NO_5^-$	$[M+CH_2O_2-H]^-$	-0.90	✓
13	17.71	1231.7783	CL(14:1/14:1/14:1/14:1)	$C_{65}H_{117}O_{17}P_2^-$	$[M-2Na+H]^-$	0.93	✓

Figure 3.16 Negative polarity LC-MS analysis of a commercial lipid mixture
A. Chromatographic separation of lipid classes using liquid chromatography, and **B**. the associated masses of the adducts formed by these lipid classes

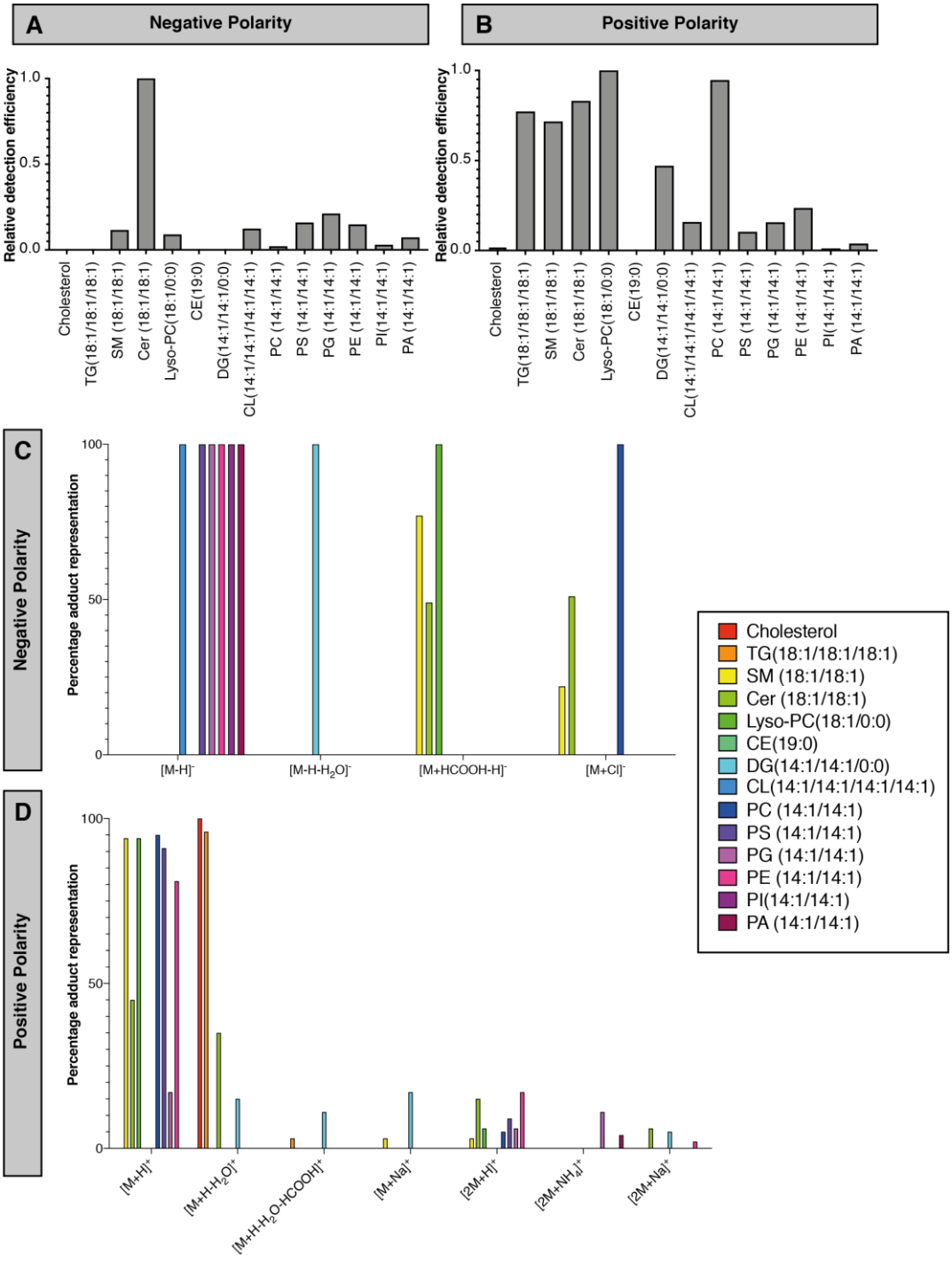

Figure 3.17 LC-MS ionisation efficiency and adduct formation of a commercial lipid standard

A,**B**. Relative ionisation and detection efficiency of lipid species within a commercial standard mixture measured via LC-MS with ESI ionisation and an Orbitrap mass analyser in negative (**A**) and positive (**B**) polarity. Data is presented relative to the lipid with highest detection efficiency in each polarity (assigned a value of 1.0). In negative polarity, cholesterol, TG ad CE have values of zero.

C,**D**. Relative representation of adduct formation observed for different lipid classes in negative (**C**) and positive (**D**) polarity. Values are calculated as a percentage relative to the sum of all adducts for a particular lipid class.

3.4 OrbiSIMS

OrbiSIMS is a mass spectrometry imaging method that offers the promise of retaining the spatial localisation information of lipids that is lost during the sample preparation for LC-MS, GC-MS, and related methods. This new instrument, designed by Ian Gilmore and developed at the National Physical Laboratory, combines ToF-SIMS imaging with an Orbitrap detector (**Figure 1.21**) (Passarelli et al., 2017). The addition of a high mass resolution Orbitrap detector to a SIMS instrument is a vital advance in reducing the need for a trade-off between high mass resolving power. ToF-SIMS has traditionally been used for the analysis of inorganic samples such as semiconductors (Vickerman, 2009). Therefore the technique has required substantial optimisation to make it suitable for the analysis of lipids in biological specimens such as the *Drosophila* cuticle and the mouse skin – the focus of this thesis.

The main challenges for using OrbiSIMS for analysing barrier lipids on these complex biological samples are ion suppression induced by charge build-up on these electrically insulating samples, and compound identification and relative quantification within a complex mixture. To address the challenge of charge build-up, two different analytical settings were used – a high current beam with a larger spot size used for spectral acquisition and MS^2 analysis, and a low current beam with a smaller spot size used for imaging (**Figure 2.2**).

Once these analytical parameters had been modified for the different sample types, the next step of method optimisation required characterisation of the ionisation properties of different lipid species of interest, both individually and within a mixture. As compounds are known to form complex adducts during SIMS ionisation, it was important to characterise the most common adducts formed for each lipid class. The data helped to improve the accuracy of lipid assignments within a complex mixture by determining the most probable adducts for each lipid class (**Table 9.5** and **Table 9.6**). Interestingly, it is apparent from this data that the majority of lipids ionise in negative polarity preferentially as $[M-H]^-$ which is also common to other ionisation techniques such as ESI (**Figure 3.18**). However,

in positive polarity there is a high level of sodium adduct formation suggesting the addition of sodium to the commercial preparation. From this data, it was also possible to calculate a relative ionisation efficiency for each lipid class within a mixture, assigning the lipid with highest ionisation efficiency as 1 (**Figure 3.18**). Unfortunately, due to the complex nature of biological matrices present on the samples, it is not possible to use these values to calculate correction factors as each sample will have a slightly different matrix which will influence ionisation to different extents. However, it is possible to use this as a general guideline for the relative ionisation efficiency of different lipid classes, to indicate which polarity the lipids would be visible in, and to identify any lipid classes which appear to ionise particularly poorly in SIMS analysis. This data is particularly useful for the assignment of phosphatidylcholine (PC) and phosphatidylethanolamine (PE) lipid groups which are often isobaric. Measurements taken in negative polarity would fail to detect PC lipids as they only ionise positively (**Figure 3.18**). Therefore, all peak identities in negative polarity would refer to PE lipids despite their apparent low relative ionisation efficiency compared with other classes of lipid. It is also apparent that cholesteryl esters (CE) and cholesterol ionise particularly poorly in this mixture of lipids. To detect these lipids efficiently, it may be necessary to remove competing lipid classes. This has been reported successfully by Tian et al. (2017) for detection of cardiolipin (CL), by removing phospholipids from the sample enzymatically. Diacylglycerides (DG) and triacylglycerides (TG) show an apparent low level of detection (**Figure 3.18**). However, it is possible that this is due to fragmentation as these species require a relatively lower degree of energy to fragment than other lipid species (Fahy et al., 2007). The absolute intensities measured for these samples, and subsequent samples, show higher values for negative polarity measurements compared with positive polarity. This is surprising, as charge compensation is more effective when extracting positively charged secondary ions. Therefore, this suggests that either the ionisation efficiency or transfer efficiency is improved when collecting data in negative polarity. This data, compared against data of the same standard generated using LC-MS, indicates the large divergence in efficiency between the techniques

(**Figure 3.17**, **Figure 3.18**). This indicates that several techniques may be beneficial or even necessary to get broad coverage of the analytes of interest.

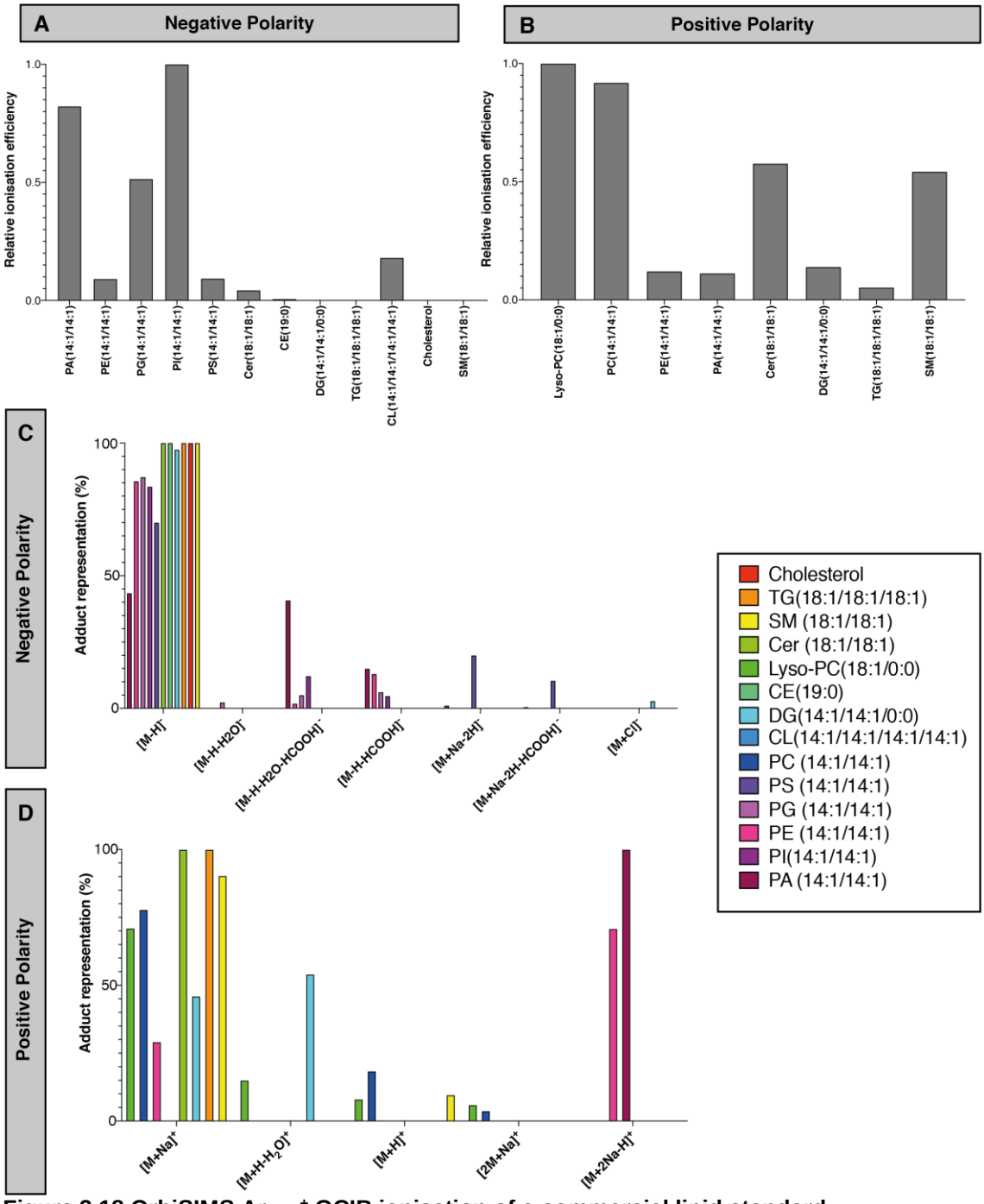

Figure 3.18 OrbiSIMS Ar_{3500}^+ GCIB ionisation of a commercial lipid standard

A,**B**. Relative ionisation and detection efficiency of lipid species within a commercial standard mixture measured via OrbiSIMS using the 20 kV Ar_{3500}^+ GCIB and Orbitrap detector in negative (**A**) and positive (**B**) polarity. Data is presented relative to the lipid with highest detection efficiency in each polarity (assigned a value of 1.0).

C,**D**. Relative representation of adduct formation observed for different lipid classes in negative (**C**) and positive (**D**) polarity. Values are calculated as a percentage relative to the sum of all adducts for a particular lipid class.

Information for all ions detected from this commercial lipid mix are available in **Supplementary Table 9.5-9.6 located** in the Supplementary Material.

Alongside this data, MS^2 data was collected using collision-induced dissociation (CID) (**Supplementary Figures 9.15-9.22** located in the Supplementary Material). Tandem MS is an important tool for the characterisation of chemical structures from mass spectrometry data and can be used to distinguish between isobaric compounds which are not separable. This type of information is especially important when collecting MSI data, as there is no chemical separation as would be available in standard chromatography set-ups. It is important to consider the influence of different chemical adducts on the fragmentation patterns of the compounds, as chemical adduction can be quite different in the context of SIMS analysis. This can make it difficult to directly compare reference MS^2 datasets which are often collected using GC-MS or LC-MS with OrbiSIMS data as the adduct formation is often different. Therefore, this analysis produced an important reference dataset of OrbiSIMS MS^2 data for lipids of different classes, which can be used in future to compare with MS^2 spectra collected from complex biological samples.

It is also interesting to note the substantially higher degree of sodium adduct formation seen in the commercial lipid standard in OrbiSIMS compared with LC-MS (**Figure 3.16 and Figure 3.18**). This can perhaps be explained due to an increased concentration of sodium on the surface of the sample in SIMS, due to the evaporation of the chloroform organic solvent under ultra-high vacuum.

3.5 Cryo-OrbiSIMS

In the initial work I performed to optimise the OrbiSIMS analytical conditions for my sample types, it became clear that a key class of compounds were missing from the analysis. Hydrocarbons form a distinct proportion of the cuticular lipids in *Drosophila* therefore they are of significant interest in this project, however, it was clear that these compounds were not visible under standard operating conditions. It was also clear through observations made during analysis that several classes of lipid were transitioning to a liquid phase upon probing with the primary ion beam. This presented many theoretical challenges for the future analysis of biological samples; there may be many key classes of compound that

are not visible in the analysis, and imaging under these conditions may lead to migration of more labile lipids. Upon further investigation, it became clear that this was directly linked to the chemical properties of the lipids, in particular the vapour pressure. Under standard operating conditions inside the analysis chamber, many compounds were becoming volatile rendering them invisible to analysis. In order to preserve these compounds, it would be necessary to reduce the temperature of the sample from first introduction into the vacuum to reduce the vapour pressure and prevent unwanted volatility. **Figure 3.19** indicates the vapour pressures of a variety of compounds in different chemical classes at a range of temperatures and pressures. These theoretical vapour pressure values can be calculated in one of two ways – firstly, using the Clausius-Clapeyron Equation as indicated in **Equation** 3.1, where P_1 and P_2 are the vapour pressures (atm) at two different temperatures T_1 and T_2 (K), R is the gas constant (8.3145 $Jmol^{-1}K^{-1}$), and ΔH_{vap} is the Enthalpy of Vaporisation (Alibakhshi, 2017):

$$\ln\left(\frac{P_1}{P_2}\right) = -\frac{\Delta H_{vap}}{R}\left(\frac{1}{T_2} - \frac{1}{T_1}\right) \quad \textbf{3.1}$$

Using this equation, alongside an experimentally de determined T_1, P_1 and ΔH_{vap} for a specific compound reported in the literature, it is possible to determine a theoretical T_2 and P_2 for a variety of different temperatures. This equation can be rearranged to the following:

$$P_2 = P_1 \cdot e^{\left[-\left(\frac{\Delta H_{vap}}{R}\right)\left(\frac{1}{T_1} - \frac{1}{T_2}\right)\right]} \quad \textbf{3.2}$$

However, for this analysis to be performed, it is necessary to have a value for the enthalpy of vaporisation for each compound of interest. In many cases, this value does not exist in the literature, therefore this analysis is not possible without experimentally determining this value. An alternative formula to calculate the theoretical vapour pressure of compounds is the Antoine Equation, indicated in **Equation 3.3** where P is pressure in bar, T is temperature in Kelvin, and A, B and C represent constants calculated experimentally for each compound:

$$\log_{10}(P) = A - \left(\frac{B}{T + C}\right) \quad \textbf{3.3}$$

Rearranged to give vapour pressure at a defined temperature:

$$P = 10^{\left[A - \left(\frac{B}{T+C}\right)\right]} \quad \textbf{3.4}$$

For this analysis, it is also crucial to possess the Antoine Constant values for each compound of interest, however, these are more freely available through the NIST online database. By calculating the theoretical vapour pressures at ten degree intervals within the scope of analysis (-150℃ to +30℃) (**Figure 3.19**), it is clear that under standard operating conditions, theoretically these compounds, in a pure preparation, should be volatile and would not be visible to analysis. Therefore, it is reasonable to assume that these compounds would be volatile, if not extremely labile under ambient temperature analysis in a complex biological sample. To address this challenge, we optimised a workflow for the loading and analysis of samples under cryogenic temperatures (**Figure 2.4**). The workflow was designed to prevent sublimation of water onto the sample surface throughout cryogenic transfer, removing the potential of surface contamination through condensation of airborne substances onto the sample that could occur before transfer into the vacuum. To enable compatible mounting of the samples in the cryogenic system it was necessary to design and modify a sample holder (**Figure 2.5**).

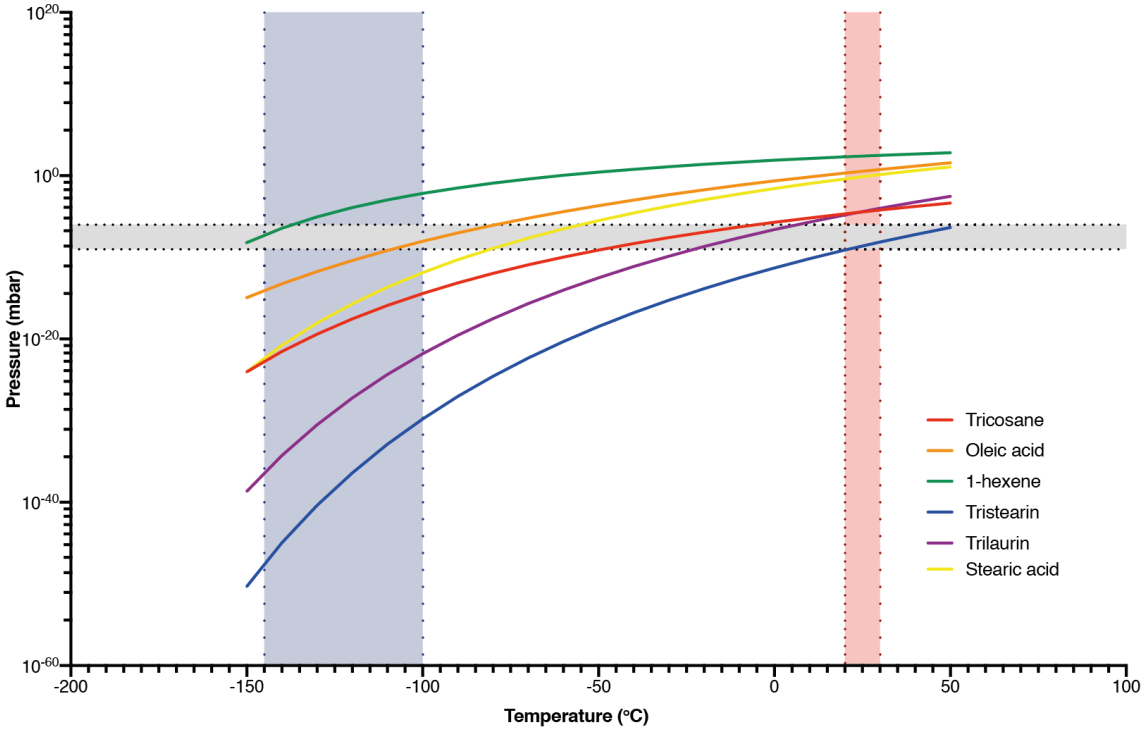

Figure 3.19 Predicted vapour pressure of pure hydrocarbons and lipids
Predicted vapour pressures for different pure lipid species of interest. The red highlighted zone represents the ambient temperature operating zone of the OrbiSIMS, the blue highlighted zone the cryogenic operating zone of the OrbiSIMS and the grey highlighted zone the standard operating pressure inside the analysis chamber. A line that is within or below the grey zone at the desired temperature would theoretically not be volatile under the standard operating pressure when present as a pure compound. Tricosane (C23:0 hydrocarbon), 1-hexene (C10:1 hydrocarbon), oleic acid (C18:1 fatty acid) and stearic acid (C18:0 fatty acid) vapour pressure values were calculated using the Antoine Equation as stated in **Equation 3.4** using Antoine constants available from the NIST database (Tricosane A=6.55706, B=4200.069, C=1.864; oleic acid A=12.947, B=5380.57, C=51.111; 1-hexene A=3.99063, B=1152.971, C=-47.301; stearic acid A=11.91, B=4289.055, C=-13.022). Vapour pressure values for tristearin (TG(18:0/18:0/18:0)) and trilaurin (TG(12:0/12:0/12:0)) were calculated based on the Clausius-Claperyon Equation stated in **Equation 3.2** using ΔH_{vap} values calculated by Zong et al. (2010) (tristearin ΔH_{vap} =1.68x10^{8}; trilaurin ΔH_{vap}=1.38x10^{8}). Figure modified from Newell et al. (2020)and reproduced with permission.

Having established a cryogenic workflow had been set up, I characterised the ionisation of the compounds of interest using the optimised ion beam setups. Ionisation of the C_{23} saturated hydrocarbon, tricosene, produces different ions when ionised with either a Bi_3^+ LMIG or an Ar_{3000}^+ GCIB in pulsed or DC modes with the ToF and Orbitrap detectors (**Figure 3.20**). Interestingly, tricosane appears to form nitrogen-containing adducts; a type of adduct which has not been previously described in the literature. These features are also recapitulated when analysing the corresponding unsaturated alkene, (*Z*)-9-tricosene (**Figure 3.21A**). It is possible that these adducts could either originate from ammonia in the sample or residual nitrogen gas present in the instrument. However, it is unlikely that ammonia would be present in these samples as there was no source present in the sample preparation process and the samples are pure standards tested for purity commercially. In support of the hypothesis that nitrogen gas is contributing to the formation of these novel adducts, this unique adduct formation does not occur in another instrument, the IONTOF TOF.SIMS 5 (**Figure 3.20B**) which is identical to the OrbiSIMS ToF setup with the exception of the presence of nitrogen gas in the instrument. In the OrbiSIMS, nitrogen gas is utilised in the bent flatapole, in the ion optics transmitting ions to the Orbitrap. Fragmentation of the nitrogen adduct by collision-induced dissociation (CID) with helium as the collision gas in cryo-OrbiSIMS formed from (*Z*)-9-tricosene (**Figure 3.21B**) forms many of the same fragments seen with GC-MS/MS CID with nitrogen as the collision gas (**Figure 3.3**). This information strengthens the evidence that nitrogen-adducted compounds are formed by nitrogen gas in the instrument reacting with hydrocarbon standards. In conclusion, this characterisation indicates that nitrogen adducts are a useful diagnostic ion for the analysis of hydrocarbons from biological samples.

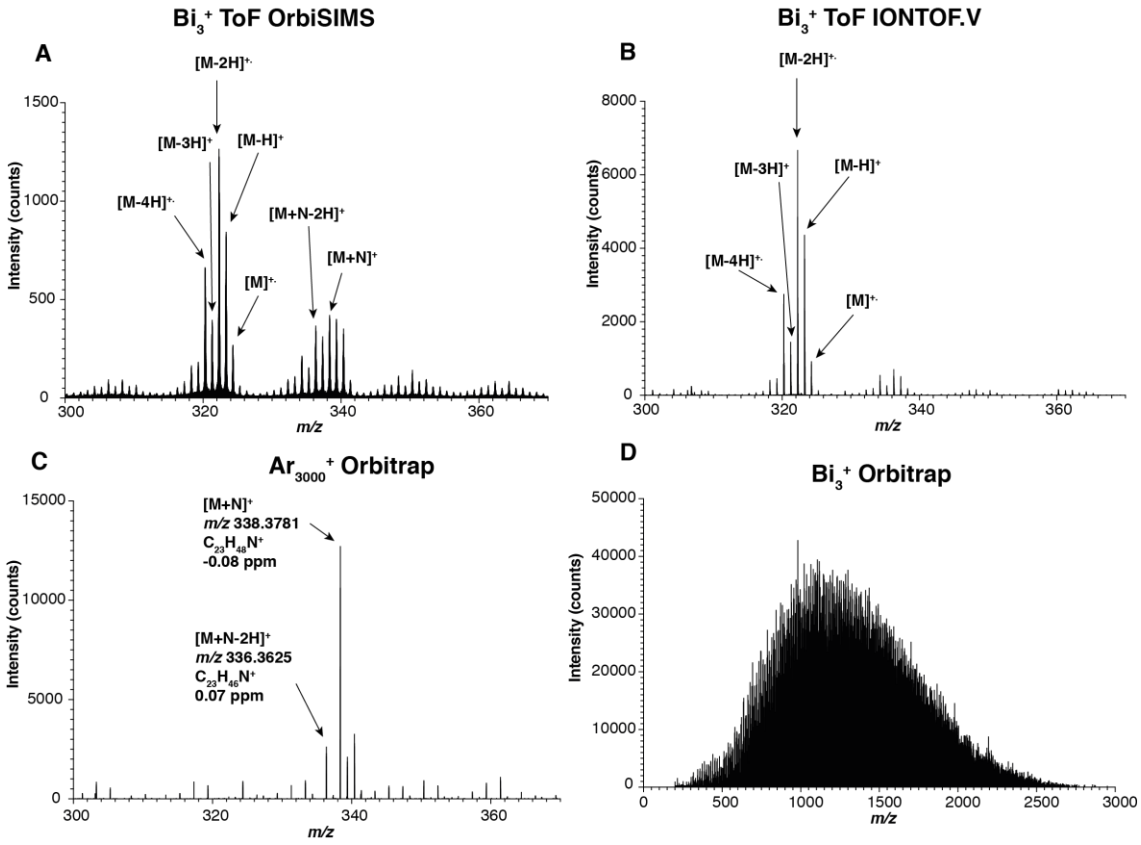

Figure 3.20 Ionisation of tricosane under different analysis conditions

A. Bi_3^+ ToF analysis in the OrbiSIMS indicating the presence of $[M\text{-}2H]^+$ and $[M+N]^+$ ions.
B. Bi_3^+ ToF analysis in the IONTOF.V indicating the presence of $[M\text{-}2H]^+$ ions and the absence of nitrogen adducts.
C. Ar_{3000}^+ Orbitrap analysis in the OrbiSIMS indicating the presence of $[M+N]^+$ ions and the absence of non-adducted ions.
D. DC Bi_3^+ Orbitrap analysis indicating massive reaction cascades causing the formation of large hydrocarbons.

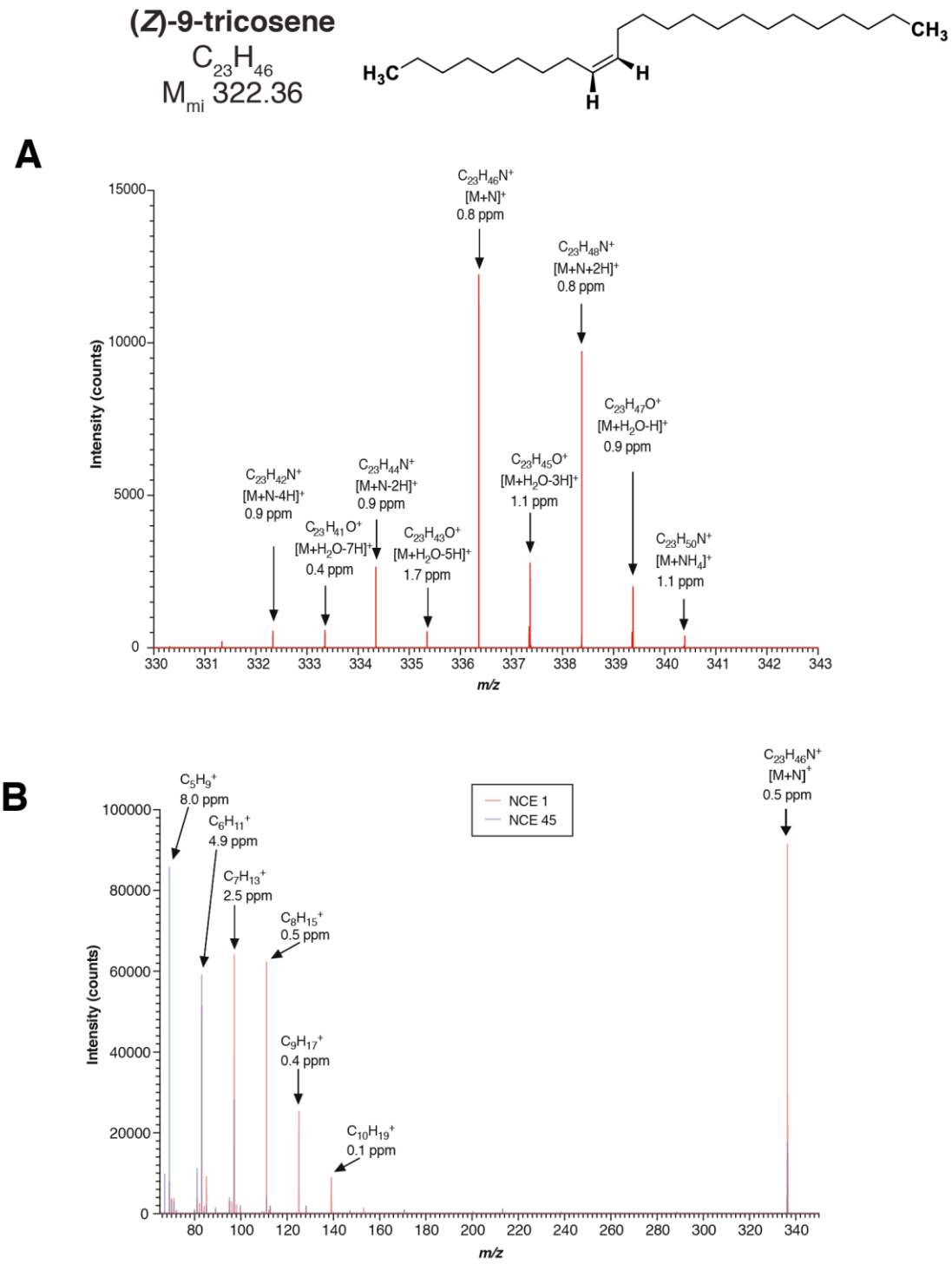

Figure 3.21 Cryogenic OrbiSIMS MS^1 and MS^2 analysis of (*Z*)-9-tricosene
A. MS^1 analysis of a commercial standard of (*Z*)-9-tricosene.
B. MS^2 analysis at normalised collision energies (NCE) of 1 and 45.
Figure adapted from Newell et al. (2020) and reproduced with permission.

Subsequently, it was then important to verify the application of the technique when analysing a complex mixture of hydrocarbons. To this end, I analysed an ASTM reference gas oil sample in parallel with cryo-OrbiSIMS and GC-MS (**Figure 3.22, Figure 3.6**). This data verifies the detection of the same alkanes in both GC-MS analysis and cryo-OrbiSIMS analysis confirming the suitability of this technique for the analysis of complex mixtures. Alongside the use of this dataset to validate the cryo-OrbiSIMS methodology, it also highlights an important benefit of this new technique. From the chromatography, it is clear that it is hard to achieve good separation of these compounds, even with a long chromatography programme such as that used for this analysis (**Figure 3.6**). Due to the high mass resolution and relatively soft ionisation process of cryo-OrbiSIMS, it is possible to putatively assign chemical formulae to a much wider variety of peaks than is possible with GC-MS alone.

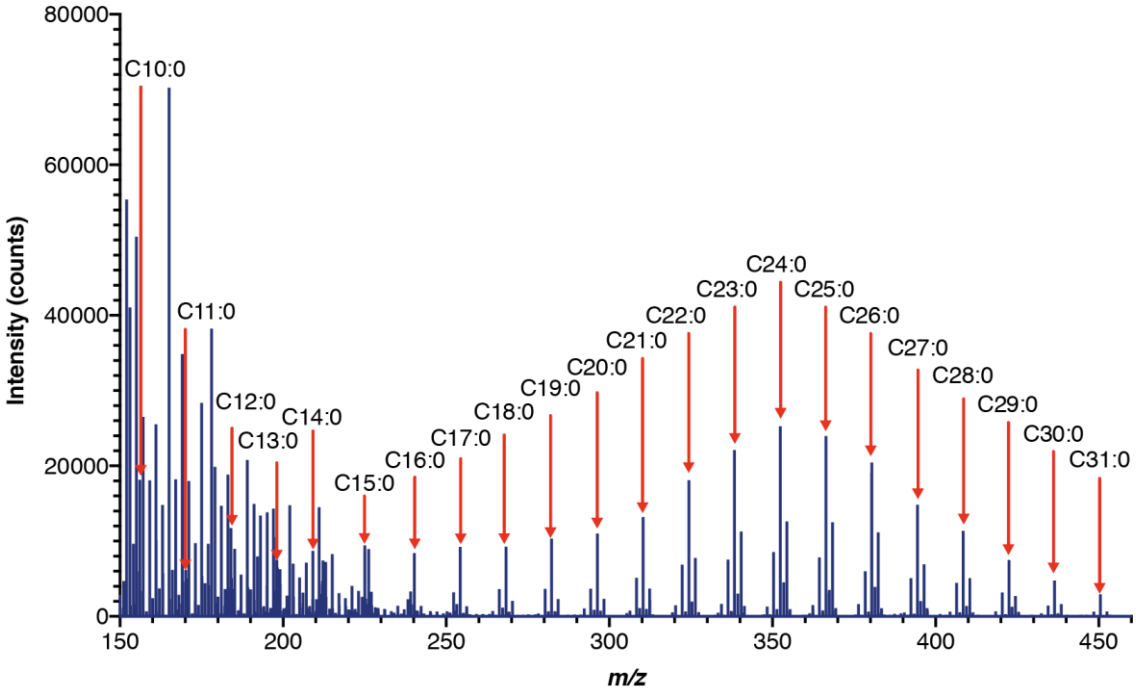

Figure 3.22 Cryogenic OrbiSIMS analysis of ASTM reference gas oil
Annotated Cryogenic OrbiSIMS Orbitrap spectrum of ASTM reference gas oil. Measurement was acquired at -121℃. Figure adapted from Newell et al. (2020) with permission.

According to vapour pressure data for a variety of different pure TG compounds (**Figure 3.19**), TGs would likely also benefit from cryogenic analysis. However, we know from previous studies that these compounds are detectable in biological systems in ambient SIMS which supports the knowledge that the surrounding chemical environment has a strong influence on the experimental volatility of a compounds. Although it is possible to detect these compounds at ambient temperature, they suffer from a substantial degree of fragmentation, reducing the sensitivity. To investigate how cryogenic temperatures influenced not only detection of normally volatile species, but also species that undergo a substantial degree of fragmentation, I performed an experiment to analyse the proportional fragmentation of a commercial TG standard under cryogenic and ambient temperatures for a variety of different GCIB cluster sizes. Altering the cluster size of the GCIB alters the energy per atom transferred to the sample – a lower energy per atom value for the primary ion beam due to an increased cluster size should induce lower levels of compound fragmentation. This experiment shows not only that compound fragmentation is reduced under cryogenic temperatures, but also that the effect of altering the primary ion beam cluster size is greater under cryogenic conditions than ambient conditions (**Figure 3.23**). However, it is important to note that although increasing the argon cluster size decreases fragmentation, it comes with a significantly lower ionisation yield resulting in an absolute decrease in signal intensity compared with smaller cluster sizes (**Figure 3.23**). The decrease in fragmentation seen under cryogenic temperatures does not come with a subsequent decrease in absolute signal intensity, on the contrary it increases the absolute signal intensity. This makes it a more useful way of increasing the absolute abundance of the quasi-molecular ion than increasing the argon cluster size.

The cryo-OrbiSIMS spectra collected from different standards suggest two factors in play that increase the abundance of scientifically “useful” signal. Primarily, there is the advantage of detection of species that are volatile at ambient temperature, but also a substantial decrease in fragmentation accompanied by retention of molecular signal. These two factors combined result

in a significant increase in useful information collected and broader application to complex biological samples.

To work towards absolute quantification in SIMS, it is critical to understand the ionisation chemistry behind the formation of different (quasi-)molecular ions, and the factors which influence the ionisation probability for different compounds. If this were fully characterised for all compounds within a sample, it may be possible to perform absolute quantifications using spiked reference standards. The first step towards enabling this type of analysis remains in understanding the ionisation chemistry, as several adducts seen in this study are novel or specific to SIMS analysis such as the nitrogen adduct observed for hydrocarbons.

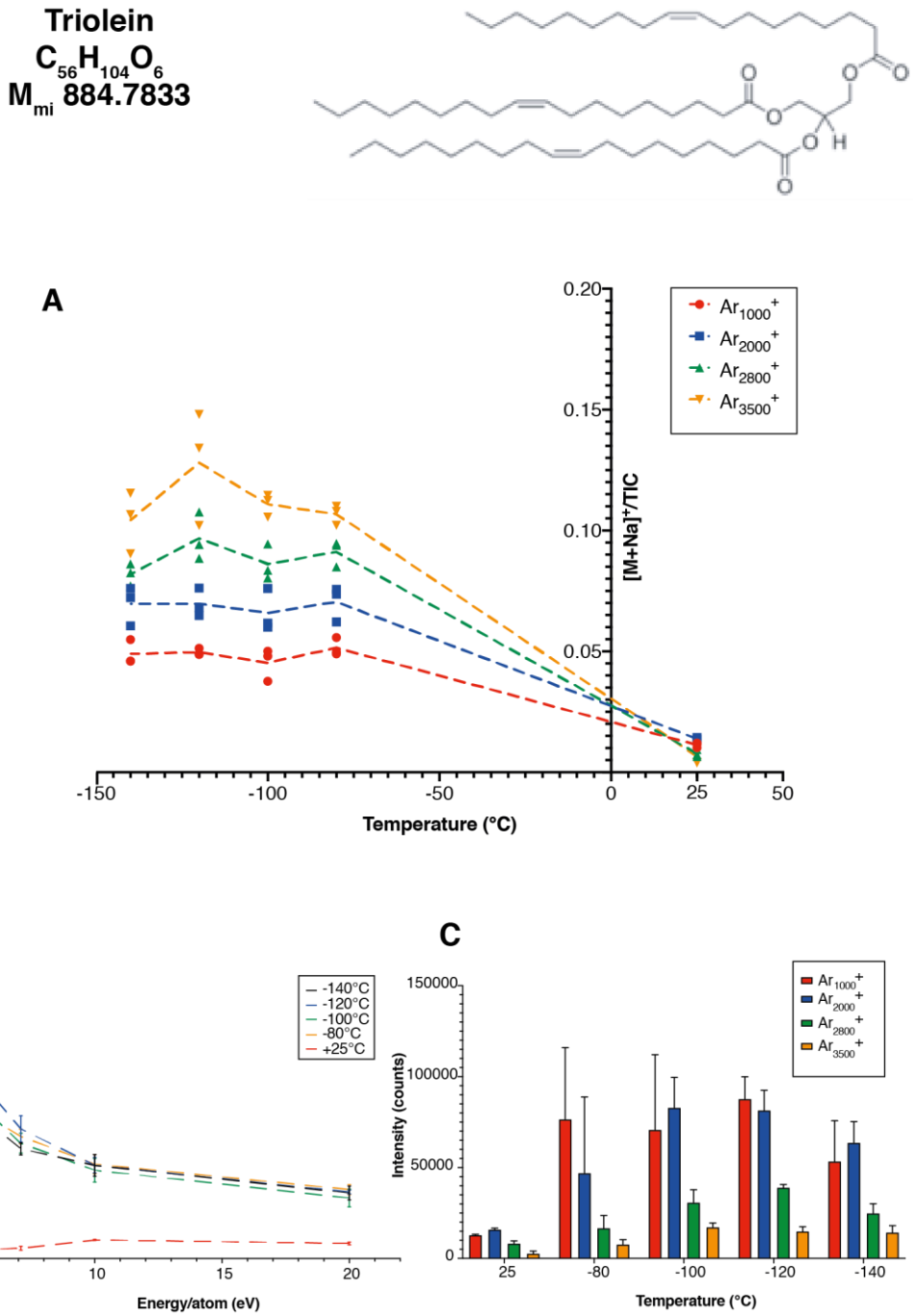

Figure 3.23 Triolein fragmentation dependence on primary projectile energy under cryogenic conditions

Fragmentation of a triolein commercial standard drop casted on a silicon wafer under ambient and cryogenic analysis conditions using different primary ion cluster sizes conferring different energy per atom values for the primary projectile. Fragmentation is determined by plotting the intensity of the quasi-molecular ion $[M+Na]^+$ against the total ion count (TIC). Figure adapted from Newell et al. (2020) with permission.

A. Temperature reduces compound fragmentation in a degree dependent on the argon cluster size. Each point represents an individual measurement, with three replicates shown per condition.

B. Fragmentation is dependent on the energy per atom of the primary projectile under a range of analysis temperatures. Error bars indicate standard deviation.

C. Argon cluster size decreases absolute intensity of quasi-molecular ion $[M+Na]^+$. Bars represent mean values with error bars representing standard deviation.

3.6 Hydrocarbon ionisation in direct-infusion ESI-Orbitrap

To further investigate the mechanism of hydrocarbon ionisation observed in the cryo-OrbiSIMS and the source of the nitrogen adduct, the same compound was analysed using ESI-Orbitrap direct infusion (**Figure 3.24**). Curiously, this compound appears to ionise within an ESI system, even though theoretically it should not ionise well due to the extremely low polarity of the compound. Interestingly, tricosane appears to form adducts with oxygen which would either originate from condensation of water in the atmosphere, or oxygen gas. Tricosane also forms adducts with nitrogen in this context, as seen in the cryo-OrbiSIMS (**Figure 3.20**). This data provides important insights on the hypothetical ionisation mechanism of hydrocarbons, as mentioned in the chapter discussion.

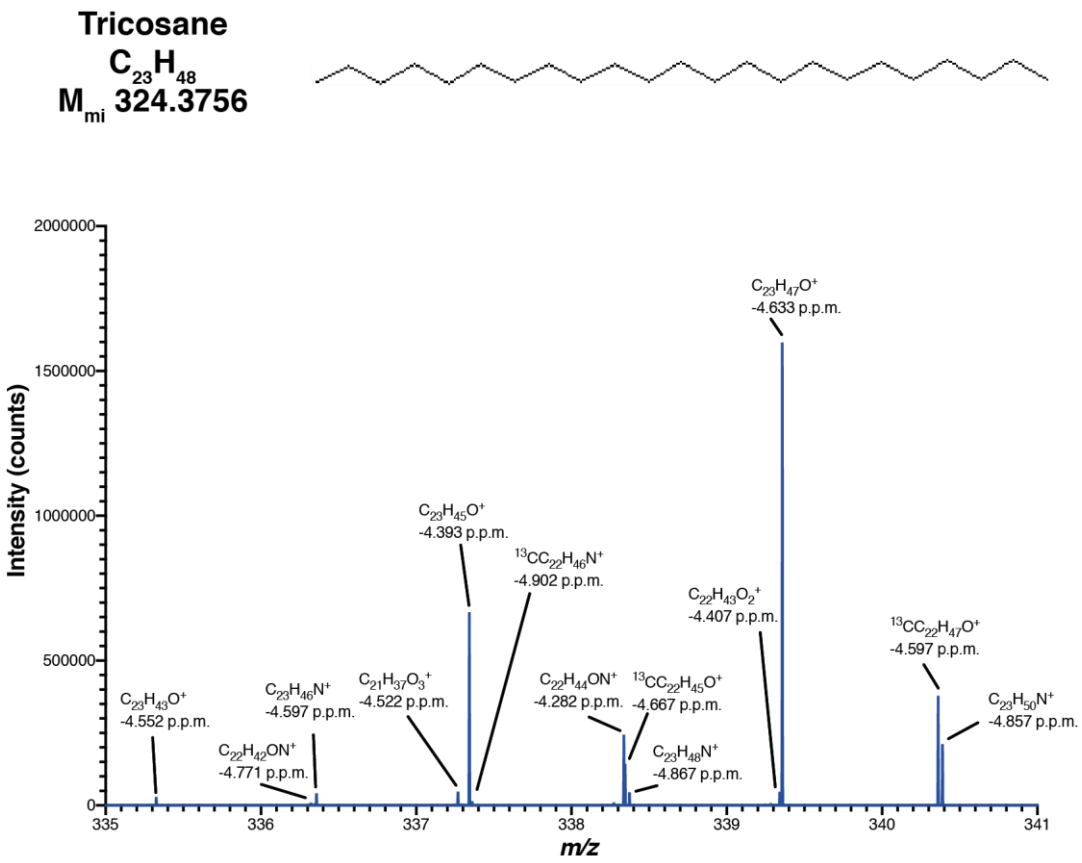

Figure 3.24 ESI-Orbitrap direct infusion of tricosane standard
ESI-Orbitrap direct infusion of a commercial tricosane standard shows complex adduct formation with both nitrogen and oxygen.

3.7 Discussion

Despite the clear benefits offered by imaging mass spectrometry techniques, they have yet to achieve as commonplace application in biological research as non-imaging techniques such as GC-MS and LC-MS. This is perhaps unsurprising, due to the relative age of these respective techniques – ToF-SIMS has been commonplace in the analysis of semiconductors since its' development in the 1960s. This is in line with the development of GC-MS technology which was also developed in the 1960s (Gohlke and McLafferty, 1993, Hites, 2016, Gohlke, 1959), but has achieved routine status in the analysis of biological samples. One reason for this may be due to the chemical separation offered by GC-MS which quickly decoupled the need for an analyser with high mass resolving power to extract useful information from the samples. In a ToF-SIMS system, there is no degree of chemical separation, therefore historically the technique has lent itself far better to the analysis of clearly defined and less chemically complex samples. The introduction of the OrbiSIMS has dramatically improved the ability to extract chemically and biologically useful data from SIMS analysis due to the introduction of the Orbitrap detector with its high mass resolving power. However, the SIMS ionisation process is not understood in as much depth as EI commonly used in GC-MS or ESI commonly used in LC-MS, therefore it can often be difficult to interpret the mass spectra. This is compounded by advances in ion beam technology to improve sensitivity, particularly of biomolecules. Whilst these improvements are welcome, they can radically change the mass spectrum complicating interpretation. Therefore, as I have indicated in this chapter, it is still important to verify data from imaging mass spectrometry modalities with corresponding data from another modality if possible.

A comparative illustration of the overlap between the methods described in this chapter for OrbiSIMS, cryo-OrbiSIMS, GC-MS and LC-MS is illustrated in **Figure 3.25**. As is clear in this comparison, there is not one single method suitable for the analysis of all lipids of interest. Although cryo-OrbiSIMS appears to cover all lipid classes of interest, it has an extremely low throughput making it unsuitable for large-scale experimental work. The main compound class of interest that is

excluded when performing OrbiSIMS analysis at ambient temperature is hydrocarbons, and GC-MS has been clearly indicated in Section 3.2 to excel at this type of analysis. The decision was made to primarily utilise GC-MS for hydrocarbon analysis and ambient temperature OrbiSIMS analysis for other lipid classes.

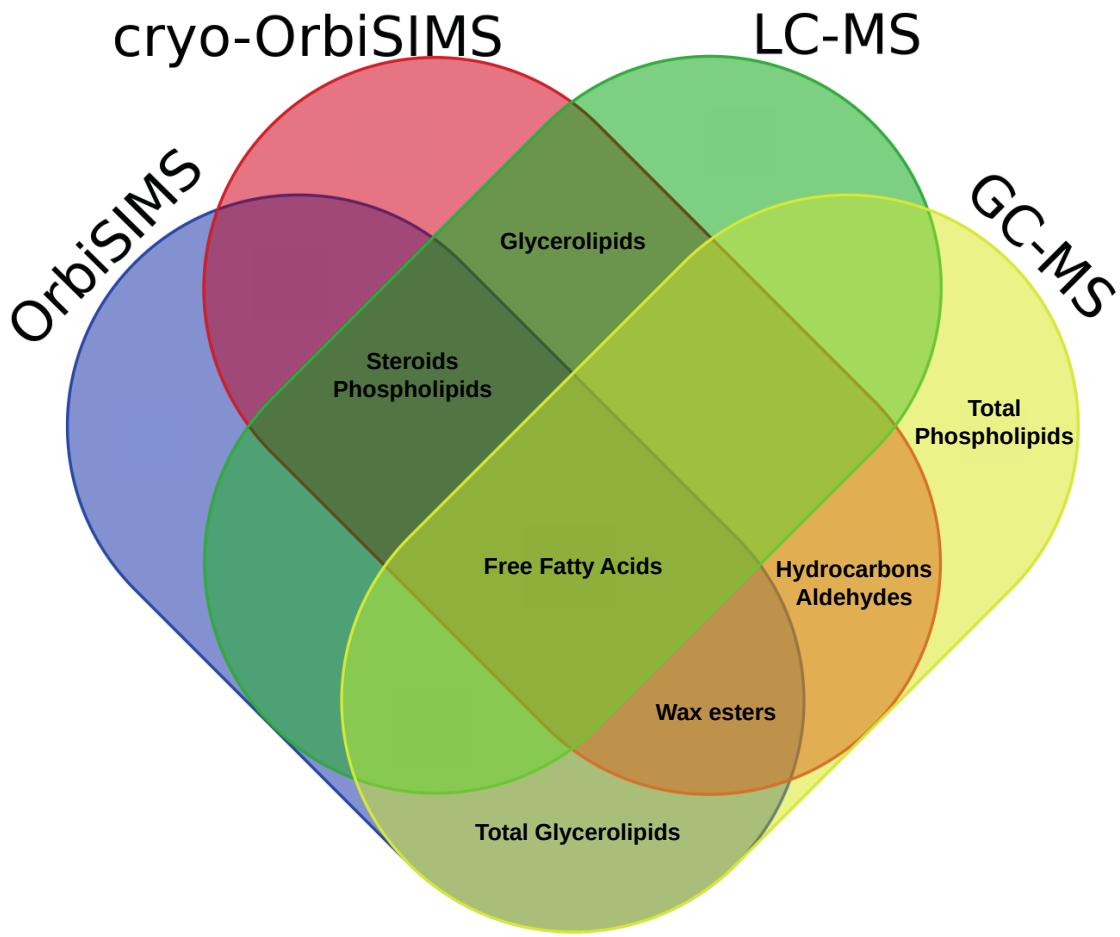

Figure 3.25 Comparison of analysis scope of different analytical techniques
This figure indicates the chemical scope demonstrated in this chapter of the available analysis techniques using available commercial standards. The terms “total phospholipids” and “total glycerolipids” highlight the inability of these techniques to discriminate individual intact lipid species.

Although it may be possible to utilise several different techniques to strengthen analytical confidence, it may not be necessary or efficient to do so in all cases. It is important in the first instance to validate OrbiSIMS lipid annotations due to the lack of chemical separation and relative novelty of the technique. To this end, LC-MS provides a strong platform for analysing a wide range of more polar lipids,

therefore it is not necessary or efficient to also perform this analysis with GC-MS which involves time-consuming derivatisation protocols.

Chromatography-based techniques are beneficial as a reference technique as it is possible to calculate absolute abundance in the presence of a commercial standard, and this is not possible with OrbiSIMS.

The data shown highlighting the application of cryo-OrbiSIMS clearly indicates the benefits of cryogenic work through reducing compound volatility and fragmentation. Although theoretical vapour pressures have been used to indicate the possible volatility of compounds within the ultra-high vacuum operating conditions under ambient temperature, it is important to recognise that these values are only theoretical indicators. In many cases, the experimentally valid temperature ranges for the Antoine constants used have been surpassed, reducing the confidence in these predicted values. The vapour pressure values are also representative of a compound in its pure form – in a complex sample, these values would no longer be valid as the vapour pressure of the compound is influenced by its surrounding chemical environment. However, these values still retain use as guidelines for predicting the need for cryogenic analysis in a cautionary capacity.

The data in this chapter clearly illustrates the capability of the OrbiSIMS technique for use in the detection of lipid species likely to form part of the cuticular barrier in a variety of organisms. It illustrates particularly broad concurrent detection in regards to lipid species when compared with current standard techniques. This, combined with the small sample size required, is particularly advantageous. When considering application of the technique within this study, it is important to note the surface analysis nature of the technique which enables spatially segregated detection of lipid species to the surface of the sample enabling detection of surface lipids without complex extraction procedures. Although this technique forgoes the chemical separation possible using chromatography-based techniques, this comes with the benefit of decreased analysis times. A typical Orbitrap spectrum taken using the OrbiSIMS takes ~36 seconds, whereas a typical GC-MS measurement takes ~70 minutes – nearly

120 times longer. Therefore a substantial amount of time can be saved in initial data acquisition.

It is currently not possible to calculate absolute abundances from SIMS data from intact biological samples. This is due to complex matrix effects and the current lack of published techniques on the application of internal standards evenly within a three dimensional sample. To overcome these current limitations, it is crucial to understand the factors that influence ionisation so the effects can be accurately modelled and accounted for in a complex system. As this is a very challenging aim and may take years to achieve, alternatively, the application of multiple internal standards would allow for a corrective factor to be applied to the analysis which may be more achievable in the short term. This is quite straightforward in a homogenised sample, but relatively complicated when dealing with an intact biological sample. The addition of an internal standard within a solvent would likely lead to migration of the analytes of interest rendering images useless and potentially misleading. It is likely that the internal standards would have to be applied to the living organism and would have to be non-toxic. The addition of internal standards to living organisms also introduces a vast array of complications including uneven distribution due to varying levels of abundance of transport proteins and channels, and risk of the internal standard being metabolised. One possible approach when trying to detect more polar compounds such as amino acids and glucose may be to administer stable isotope labelled optical isomers which the organism would be unable to metabolise and would be analytically differentiable by mass. The absolute abundance of these compounds within a specified volume could be calculated by chromatographic methods, then the values applied to SIMS calculations. To address the problem of even compound distribution, a genetic approach may be better suited. For polar compounds, variants could be designed with molecular “tags” which could then be transported via genetically overexpressed membrane transport proteins designed to exclusively recognise these compounds. As long as these proteins worked unidirectionally, and were overexpressed to a large enough degree, this should ensure homogenous distribution of the designed internal standards. For lipids, homogenous distribution should be easier to achieve due to cell membrane

permeability, but it may be necessary to modify the structures to avoid accumulation within lipid droplets which could be quite challenging. Although these hypothetical methods are possible to achieve, they are complex and would require many years of optimisation before they become mainstream.

The cryogenic analysis developed initially for the detection of hydrocarbons and other semi-volatile species has revealed further unexpected analytical advantages. Cryogenic analysis clearly highlights an increase in the ionisation yield of certain molecular species, indicated in this chapter for TGs. This may be due to an increased aqueous environment due to sublimation of water onto the surface of the sample which would volatilise under ambient temperature analysis. As this particular lipid appears to preferentially form adducts with sodium ions, it is possible the aqueous environment aids this process. Importantly, cryogenic analysis is illustrated to both minimise the degree of compound fragmentation and at the same time increase the ionisation yield. This is in contrast to current practice where the energy per atom of the primary projectile is decreased which comes with a trade off in reduced ionisation yield and therefore worse sensitivity. Although cryogenic analysis appears to provide substantial benefits when compared with ambient temperature analysis, this does not come cost-free. Due to the geometry of the instrument, it is currently only possible to load a single sample which must fit within a 1 cm^2 area, and exchanging samples can take ~45 minutes substantially decreasing the throughput. The liquid nitrogen consumption can also be quite high, with the OrbiSIMS and Leica instruments consuming a combined volume of ~50 litres in 24 hours which can make experiments relatively costly. Future improvements in instrumental cooling efficiency should decrease this consumption and therefore decrease the associated cost, and design of larger sample holders will assist this with the ability to mount multiple samples reducing the consumption associated with sample exchange.

Due to the relative lack of understanding of the complex ionisation chemistry occurring in SIMS, as illustrated in this chapter, it remains critical to validate results obtained with another mass spectrometry technique if at all possible. Here, I have shown the successful application of GC-MS for the detection of

hydrocarbons, aldehydes, free fatty acids, wax esters and fatty acid chains from phospholipids and triacylglycerides. This broad range of detected compounds covers the vast majority of analytes of interest when investigating skin lipid biology. The data, supplemented with LC-MS/MS data providing intact and structural information about phospholipids, triacylglycerides and free fatty acids, provide a strong base for validating and further characterising results from OrbiSIMS analysis.

With suitable mass spectrometry-based methods in place to analyse skin lipids, the following chapter will discuss their application to the analysis of barrier lipids in both *Drosophila* and mice initially in a healthy state, then investigating the effect of developmental malnutrition on the composition of these lipid barriers.

Chapter 4. OrbiSIMS analysis of barrier lipids in animals and plants

4.1 Introduction

Chapter **3** described the development of cryogenic OrbiSIMS for the analysis of a wide range of lipids, with compound identities cross-validated via GC-MS and LC-MS. The development of this new OrbiSIMS technique addresses one of the key analytical challenges facing research on barrier lipids – surface specificity. In this chapter, I apply OrbiSIMS to the analysis of the barrier lipids coating animals and plants of several different species.

The lipid barrier or envelope coating an organism is a physiological feature that is ubiquitous in all land-based species from plants to mammals. One key function of the barrier is to protect terrestrial species from dehydration, thus making an important contribution to overall water homeostasis (Pappas, 2009). Compromising the lipid barrier results in severe consequences that are illustrated by deletion of fatty acid desaturases in mice. Deletion of either the SCD1 or SCD2 desaturases leads to significant changes in the skin lipid blend, including a reduction of WE, CE and TG and an increase in free cholesterol, and a failure of thermoregulation (Miyazaki et al., 2005, Sampath and Ntambi, 2014). Despite the importance of the skin lipid barrier, it is not yet clear which lipid classes are required for each specific barrier function such as waterproofing, UV protection, and anti-microbial defence. All organisms require to a lesser or greater degree these three barrier functions and so it is not unreasonable to hypothesise that evolutionary comparisons of barrier lipids may help to pinpoint functionally important molecular classes. Most previous studies of barrier lipids have tended to focus on single species and direct comparisons between studies (and thus species) has been challenging due to the different chemical coverages of the analytical methods used. In this chapter, I use a OrbiSIMS, supported by GC-MS and LC-MS, to investigate the composition and distribution of barrier lipids in humans, mice, flies and several plants. I then use this information to determine

the relative correlation in lipid blend between the species and to speculate about the possible importance of different barrier lipids.

4.2 Plant cuticular lipids

Using the newly developed cryo-OrbiSIMS platform, the cuticles of the leaves and fruits from seven different plant species of the dicotyledon clade of *Spermatophyta* were analysed to determine their lipid blend (**Figure 4.1**). This analysis revealed a broad spectrum of lipid classes, with a strong signals detected for hydrocarbons, fatty acids, waxes and aldehydes (**Figure 4.2**, **Table 4.1**, and **Supplementary Table 9.8-9.13** located in the Supplementary Material). Cuticular waxes ranging from 10 to 38 carbons and 0 to 4 carbon-carbon double bonds were detected in seven species, and these have been shown to play an important role in waterproofing leaves with longer chain cuticular waxes correlating with decreased transpiration through the cuticle (Pappas, 2009, Bueno et al., 2019). In addition, hydrocarbons, free fatty acids and wax esters were also present across all seven different plant species tested, correlating well with published literature suggesting these classes of lipids are abundant on the cuticle of plants (Eglinton et al., 1962). The presence of hydrocarbons in all species tested suggests that they may be functionally important, although this remains to be demonstrated directly. GC-MS analysis identified the plant hydrocarbon species as mainly corresponding to linear alkanes and methyl-branched alkanes (**Table 4.1**). These hydrocarbons are not volatile and so they are unlikely to function as olfactory pheromones. Instead, they may play a role in waterproofing.

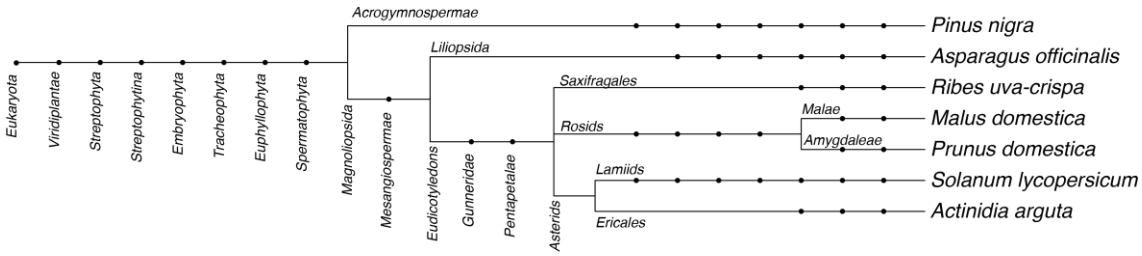

Figure 4.1 Phylogenetic tree of plant species analysed with cryo-OrbiSIMS

Phylogenetic tree illustrating the points of evolutionary divergence between all plant species analysed using cryo-OrbiSIMS. Data generated using the iTOL tool (Letunic and Bork, 2007).

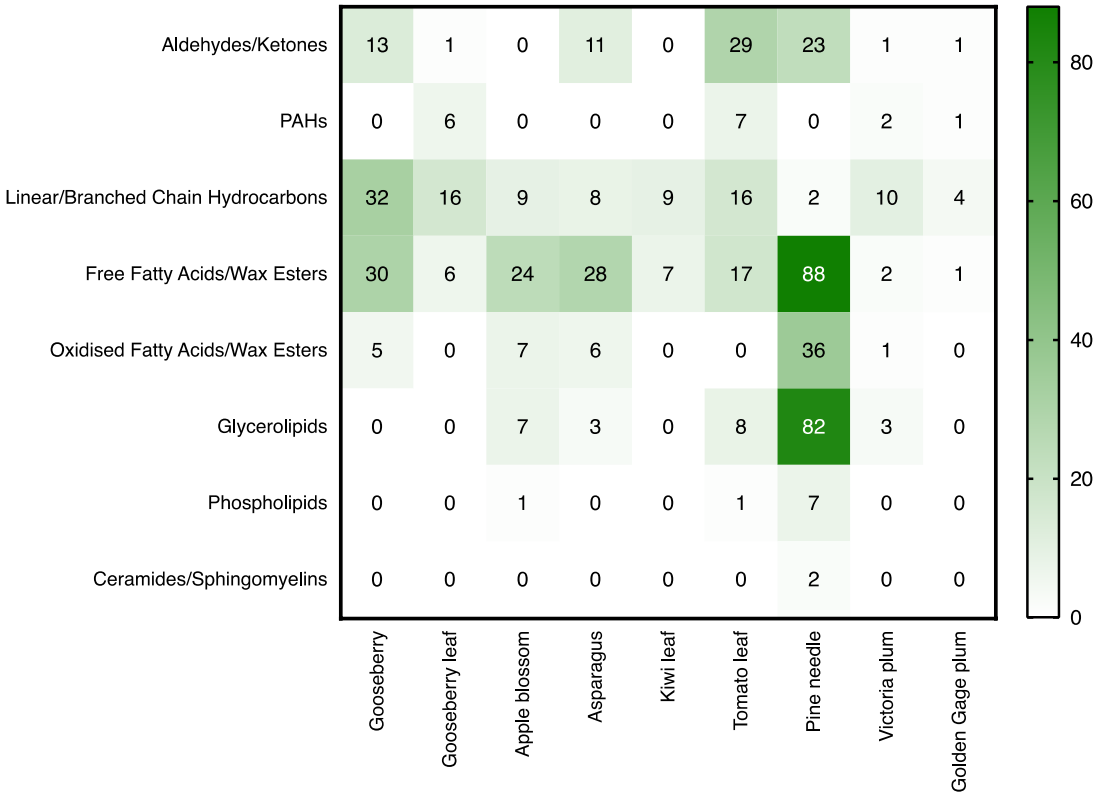

Figure 4.2 Cryo-OrbiSIMS analysis of plant cuticular lipids
Summary of lipid species identified on different plant samples using cryo-OrbiSIMS. A detailed breakdown of lipid species can be found in **Supplementary Table 9.8-9.13** located in the Supplementary Material.

Table 4.1 GC-MS analysis of plant cuticular hydrocarbons

					Linear/branched chain hydrocarbons						
t_R (minutes)	Parent ion (*m/z*)	Diagnostic ions (*m/z*)	Formula (observed)	Putative I.D.	Pine needle	Gooseberry leaf	Tomato leaf	Victoria plum	Golden gage plum	Gooseberry fruit	Standard?
8.353	114.2	-	$C_8H_{18}^+$	Octane				✓	✓		
24.771	268.4	-	$C_{19}H_{40}^+$	Nonadecane				✓			
30.553	296.2	-	$C_{21}H_{44}^+$	Heneicosane				✓	✓	✓	✓
33.324	310.3	-	$C_{22}H_{46}^+$	Docosane	✓						
36.176	324.3	-	$C_{23}H_{48}^+$	Tricosane	✓	✓		✓	✓	✓	✓
38.704	336.3	-	$C_{24}H_{48}^+$	x-tetracosene			✓				
41.471	352.4	-	$C_{25}H_{52}^+$	Pentacosane	✓	✓	✓	✓	✓	✓	✓
43.85	364.3	-	$C_{26}H_{52}^+$	x-hexacosene			✓				
45.992	380.4	-	$C_{27}H_{56}^+$	Heptacosane	✓	✓	✓	✓	✓	✓	
48.207	408.3	393.3, 365.3	$C_{29}H_{60}^+$	x-methyl octacosane		✓	✓			✓	
48.623	408.3	-	$C_{29}H_{60}^+$	Nonacosane	✓	✓	✓	✓	✓	✓	✓
49.244	422.4	407.3, 393.3	$C_{30}H_{62}^+$	x,x-methyl nonacosane		✓	✓				
49.373	422.3	393.3	$C_{30}H_{62}^+$	x-methyl nonacosane		✓	✓			✓	
49.631	422.4	-	$C_{30}H_{62}^+$	Triacontane		✓	✓	✓	✓	✓	
50.314	436.3	421.4, 393.3	$C_{31}H_{64}^+$	x-methyl triacontane		✓	✓			✓	
50.767	436.5	-	$C_{31}H_{64}^+$	Hentriacontane		✓	✓	✓	✓	✓	
51.479	450.4	435.3, 407.2	$C_{32}H_{66}^+$	x,x-methyl triacontane		✓	✓		✓		
51.621	450.4	435.3, 421.3	$C_{32}H_{66}^+$	x-methyl hentriacontane		✓	✓				
51.962	450.4	-	$C_{32}H_{66}^+$	Dotriacontane		✓	✓				
52.824	464.4	449.3, 421.3	$C_{33}H_{68}^+$	x-methyl dotriacontane		✓	✓				
53.419	464.5	-	$C_{33}H_{68}^+$	Tritriacontane		✓	✓				

Other lipid classes were observed to be less species ubiquitous, such as aldehydes/ketones, oxidised fatty acids/wax esters and glycerolipids. This is highlighted even between different regions of the same plant – for example, the gooseberry (*Ribes uva-crispa*) fruit which displays a variety of aldehydes/ketones that are not present on the leaf (**Figure 4.2, Table 4.1,** and **Supplementary Table 9.8** located in the Supplementary Material). This is consistent with but does not prove the hypothesis that fruits are rich in volatile aldehydes/ketones because they function as pheromones in order to repel damaging insects such as aphids. To ensure the detected lipids were originating from the surface of the sample, cryo-OrbiSIMS depth profiling was carried out on the skin from the gooseberry fruit. This clearly identified a surface enrichment of several lipids including hydrocarbons and wax esters (**Figure 4.4**). In contrast, free fatty acids were present below the surface of the fruit skin, indicating they may for part of a lower barrier layer, or have an alternative function from barrier maintenance.

To investigate the potential link between barrier lipid composition and evolutionary conservation, hierarchical clustering was performed on the cryo-OrbiSIMS spectral data. This revealed a clustering pattern that was more closely correlated with the type of sample (e.g. leaf vs fruit) than the points of evolutionary divergence (**Figure 4.3**). This suggests that the chemical features observed in cryo-OrbiSIMS analyses may have arisen independently of each other in an evolutionary context.

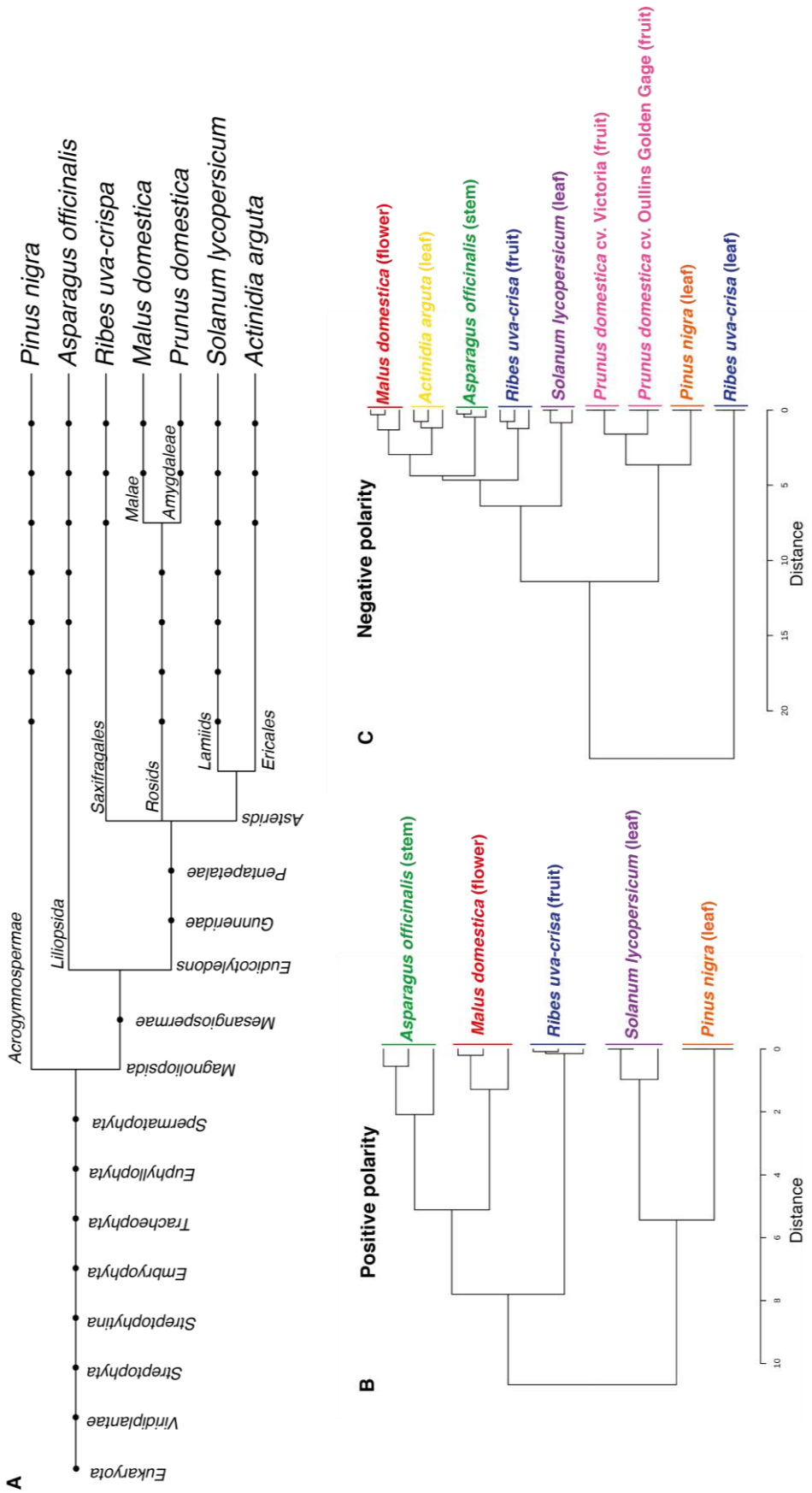

Figure 4.3 Hierarchical clustering of plant cryo-OrbiSIMS data

A. Phylogenetic tree showing the points of evolutionary divergence of the plant species analysed.
B,**C**. Hierarchical clustering of cryo-OrbiSIMS positive (**B**) and negative (**C**) polarity mass spectral data.

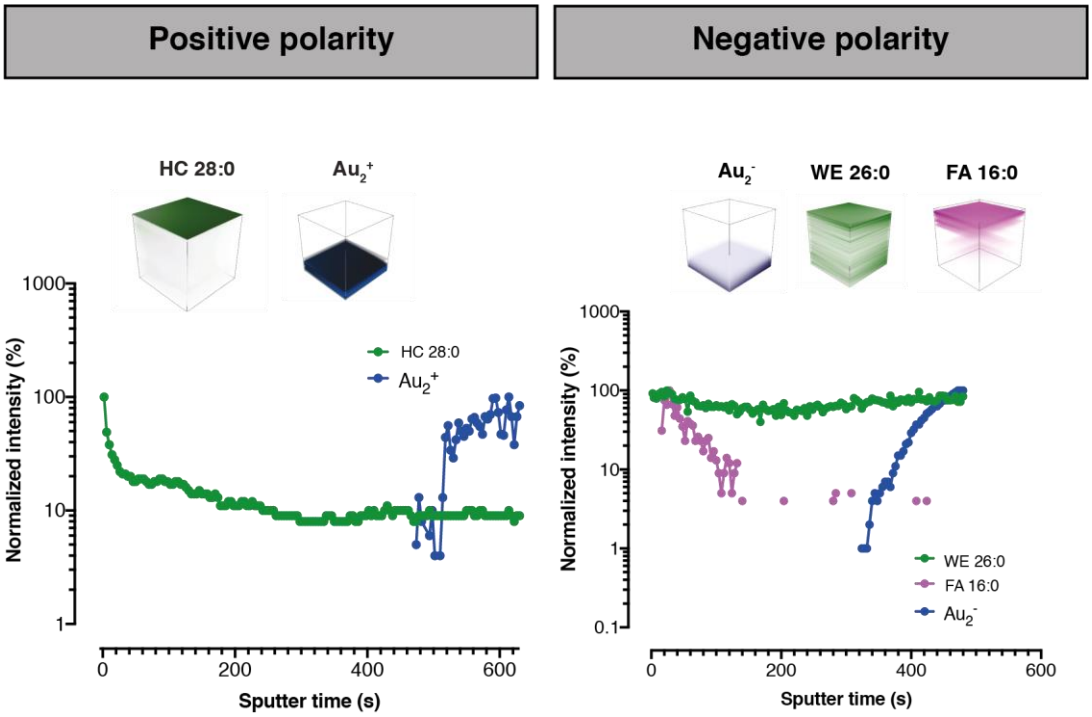

Figure 4.4 Cryo-OrbiSIMS depth profiling of gooseberry fruit skin
Dynamic continuous depth profiling of a gooseberry fruit skin sample in positive and negative polarities using a 0.3 nA Ar_{3500}^{+} GCIB with a spot size of 20 µm, of a 40 x 40 µm field of view. Gold peaks refer to the sample substrate, a gold-coated silicon wafer. HC 28:0, $C_{28}H_{58}^{+}$, $[M]^{+\cdot}$, -0.1 ppm; Au_2^{+}, 0.2 ppm; Au_2^{-}, 0.1 ppm; WE 26:0, $C_{26}H_{51}O_2^{-}$, $[M-H]^{-}$, 0.0 ppm; FA 16:0, $C_{16}H_{31}O_2^{-}$, $[M-H]^{-}$, 0.0 ppm. Figure adapted from Newell et al. (2020) with permission.

I next used cryogenic OrbiSIMS in imaging rather than spectrometric mode to map the spatial distribution of lipids in a pine needle (*Pinus nigra*). The distribution of many lipid species such as a C29:0 hydrocarbon and a C16:1 fatty acid were largely homogenous across the surface of the pine needle (**Figure 4.5)**. Interestingly, however, several ions including *m/z* 366.90 shown in **Figure 4.5** appear to be concentrated around the stomatal pores. Unfortunately, these ions were not visible in Orbitrap spectra so further investigation would be required to putatively identify these compounds. Another interesting feature of these samples was the presence of puncta correlating to water and ammonia which were only visible at cryogenic temperatures. Ammonia in plant leaves has been previously suggested to be indicative of the presence of amino acids, which is also a possibility in this sample (Kafkafi and Ganmore - Neumann, 1997). These do not co-localise with the stomatal pores, or any other features on the sample which are visible to the naked eye. It is possible they may correlate with the resin ducts, and this could be confirmed through the analysis of pine needle cross sections (Pongrac et al., 2019).

Polycyclic aromatic hydrocarbons (PAHs) were also detected in about half the plant samples (**Figure 4.2** and **Supplementary Table 9.9** located in the Supplementary Material). This class of molecules are not synthesised by plants, but provide a specific example of a man-made environmental pollutant. PAHs have been shown to accumulate in soil, can cause phototoxicity in plants and are known carcinogens in humans (Jajoo et al., 2014, Abdel-Shafy and Mansour, 2016). The detection of PAHs by cryo-OrbiSIMS illustrates that this method could be used to aid research into where and how these and other toxic pollutants accumulate in specific regions of plants.

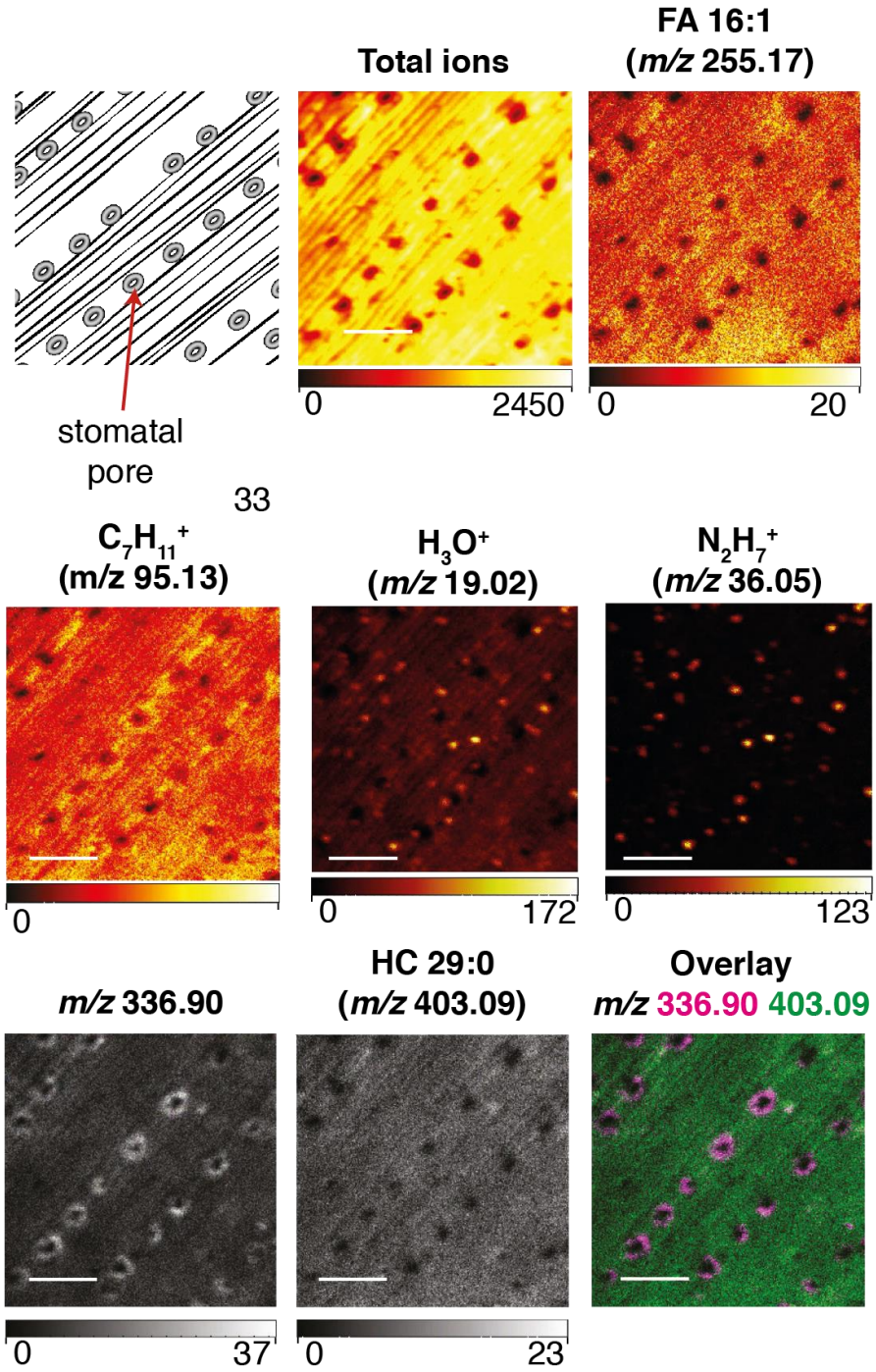

Figure 4.5 Cryo-OrbiSIMS ToF imaging of a pine needle
Positive polarity Cryo-OrbiSIMS ToF imaging of a pine needle sample. Analysis performed using a 30 kV Bi_3^+ LMIG with a spot size of ~0.5 µm and a field of view of 500 x 500 µm. Complimentary GCIB-Orbitrap spectra were acquired of the same area before LMIG-ToF analysis for the purpose of putative chemical assignments. The illustration in the top left panel shows the structural features of the sample, including the large stomatal pores indicated. Total ions refers to the total ion counts measured for each pixel. Scale bar ranges are in ion counts. Figure adapted from Newell et al. (2020) with permission.

4.3 Composition of mouse skin lipid blend

To characterise the skin lipid blend in mice, skin from the tail of 6 week old C57Bl/6J adults was mounted and analysed using OrbiSIMS at ambient temperature. This revealed a very chemically complex blend of lipids, with putative identifications assigned to over 200 different molecules. Fur from the tail of the same mice showed a very similar lipid blend to the tail skin (**Figure 4.6**), consistent with the idea that these lipids are synthesised in the skin and transferred to the fur via grooming. This is not surprising but it is an important observation as, for LC-MS validation purposes, it enables the use of fur as a pure source of surface lipids that are not contaminated with subcutaneous fat. In particular, there were strong signals from glycerolipids (79 species), ceramides (44 species) and fatty acids/wax esters (30 species) (**Supplementary Tables 9.14-9.16** located in the Supplementary Material). Sterols such as cholesterol sulphate were also detected in mice and these appear to be mammal-specific as they were not observed in *Drosophila* or plant samples. The mouse skin blend also showed strong sexual dimorphism, with enrichments of glycerolipids such as DG in females and longer chain wax esters in males (**Figure 4.7**).

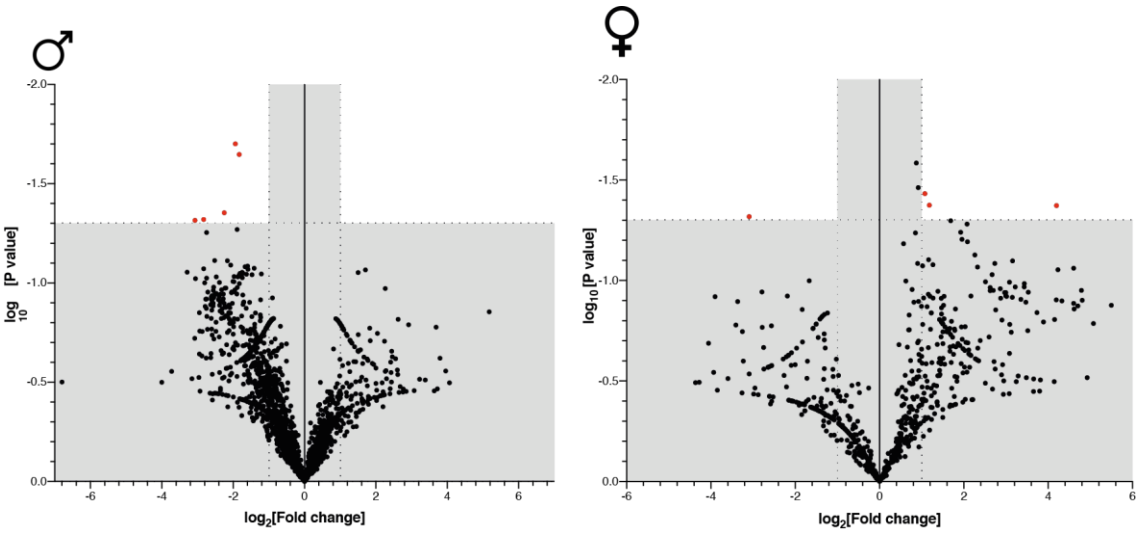

Figure 4.6 The fur lipidome shows no significant differences to the skin lipidome in male and female mice

Volcano plots illustrating the fold change in relative abundance of lipid species on the tail fur when compared with the tail skin at the base of the tail in male and female mice at an postnatal age of 42 days. Each point indicates a unique mass as determined by OrbiSIMS Orbitrap analysis with the Ar_{3500}^{+} GCIB in negative polarity.

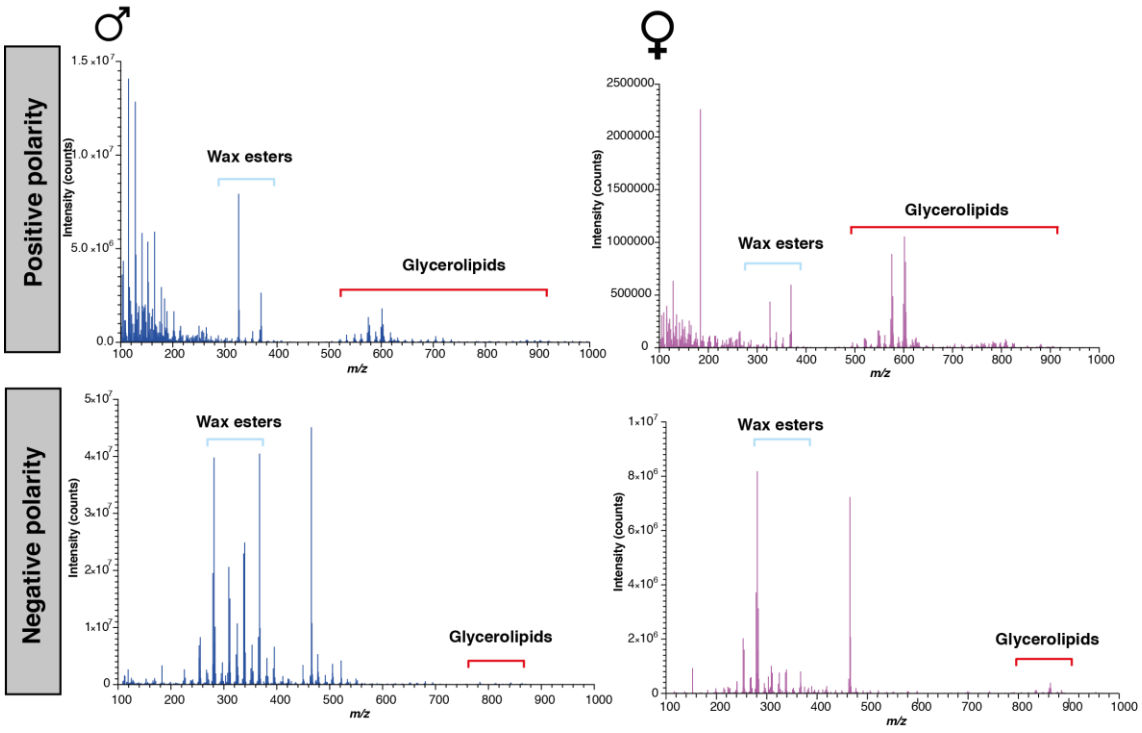

Figure 4.7 OrbiSIMS detection of mouse skin lipids

Example mass spectra of male and female mouse skin acquired using the Ar_{3500}^{+} GCIB and Orbitrap mass analyser. Indicated in light blue is the region of the mass spectrum dominated by wax esters, and in red the region of the mass spectrum dominated by glycerolipids.

4.4 The human fingerprint lipidome

The majority of work applying mass spectrometry imaging to the analysis of latent fingerprints has focussed on applications in forensic sciences. As a result, several analyses have focused on detecting drugs and chemicals which may pertain to criminal cases. One particularly interesting example of this work illustrates the detection of trace amounts of cocaine on a human fingerprint using DESI, MALDI and SIMS (Bailey et al., 2015). Despite the array of studies that image fingerprints for forensic application, very few show the detection of lipid species in these samples. Instead, the lipid composition of fingerprints has largely been determined through non-imaging techniques such as LC-MS. This results in the loss of spatial information regarding the localisation of lipid species. When analysing latent human fingerprint samples collected from two adult female and one male volunteer using OrbiSIMS, analysis at ambient temperature produced only sparse spectra. Therefore, I switched to cryogenic analysis temperatures and analysed fingerprints from the same volunteers, which revealed far more diverse and complex mass spectra (**Figure 4.8**). Cryogenic OrbiSIMS was able to detect signals from ~40 lipids covering a range of classes including some free fatty acids, a large number of DGs and TGs, and some PI-Ceramides (**Table 4.2**). Imaging data acquired for these samples indicated that the signals from the free fatty acids that were concentrated in small discrete regions corresponding to eccrine (sweat) pores (**Figure 4.9**). It is possible that these free fatty acids may be eccrine gland derived, as the presence of fatty acids within sweat has been previously determined (Takemura et al., 1989). This is, however, unlikely to be the sole origin of fatty acids, which are also abundant in the sebum secreted by sebaceous glands (Pappas, 2009). Although sebaceous glands are lacking from fingerprint skin, sebum is known to be transferred there from other sources via “grooming” behaviours such as hair touching (Gao et al., 2019).Interestingly, PI-Ceramides were also detected in human fingerprints but as these lipids are not thought to be synthesised by mammals, they may have been acquired from the diet, skin microbiota, or the environment (Gronnier et al., 2016).

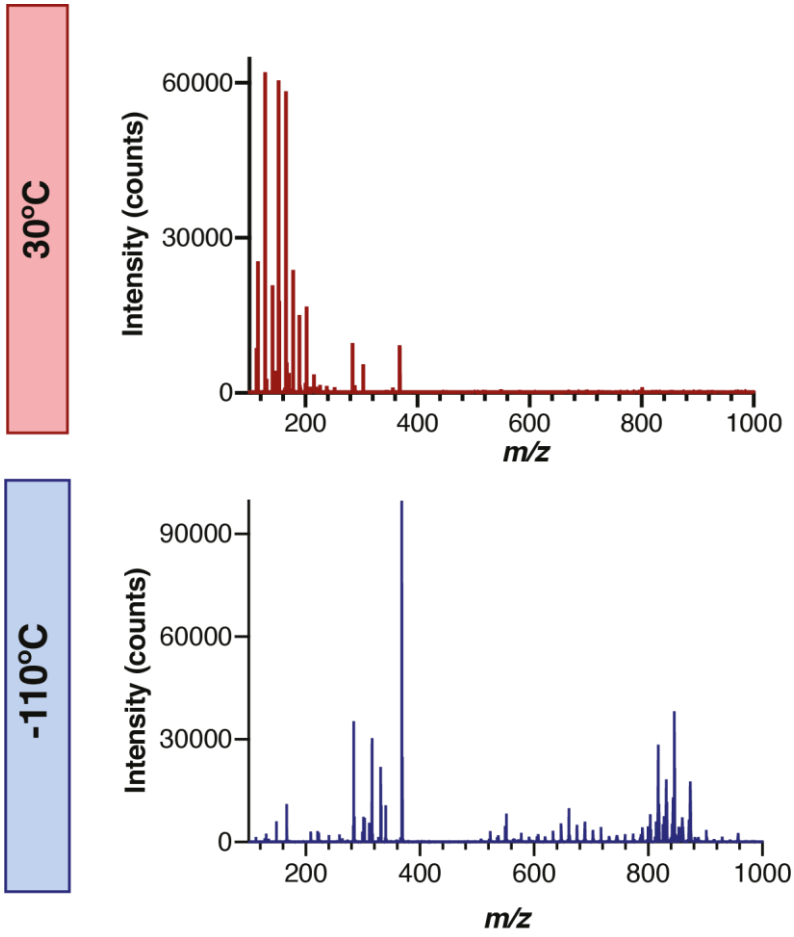

Figure 4.8 Cryo-OrbiSIMS detects more human fingerprint lipids than room temperature OrbiSIMS

OrbiSIMS analysis of a latent fingerprint sample using the Ar_{3500}^{+} analysis beam and Orbitrap mass analyser. Analysis was performed under ambient temperature analysis conditions (30℃) or cryogenic analysis conditions (-110℃). Figure modified and reproduced from Newell et al. (2020) with permission.

Table 4.2 Lipids detected from latent fingerprints with OrbiSIMS

Observed *m/z*	Putative I.D.	Formula (observed)	Polarity	OrbiSIMS Adduct	Mass deviation (p.p.m)	Female 1		Female 2		Male 1	
						Ambient	Cryogenic	Ambient	Cryogenic	Ambient	Cryogenic
264.268	C18:2 hydrocarbon	$C_{18}H_{34}N^+$	Positive	$[M+N]^+$	-2.19	-	✓	-	✓	-	-
283.263	C18:1 fatty acid	$C_{18}H_{35}O_2^+$	Positive	$[M+H]^+$	-0.56	-	✓	✓	✓	✓	✓
299.196	C16:1 fatty acid	$C_{16}H_{29}Na_2O_2^+$	Positive	$[M+2Na-H]^+$	0.84	-	✓	-	✓	-	-
301.211	C16:0 fatty acid	$C_{16}H_{31}Na_2O_2^+$	Positive	$[M+2Na-H]^+$	-1.33	-	✓	-	✓	✓	-
311.294	C20:1 fatty acid	$C_{20}H_{39}O_2^+$	Positive	$[M+H]^+$	-1.48	-	✓	✓	✓	✓	✓
316.186	peptide fragment	$C_{14}H_{26}N_3O_5^+$	Positive	$[M+H]^+$	-2.21	-	✓	-	-	-	-
327.227	C18:1 fatty acid	$C_{18}H_{33}O_2Na_2^+$	Positive	$[M+2Na-H]^+$	-0.15	-	✓	-	✓	-	-
332.160	peptide fragment	$C_{17}H_{22}N_3O_4^+$	Positive	$[M+H-H_2O]^+$	-1.44	-	✓	-	-	-	-
521.457	DG(30:1)	$C_{33}H_{61}O_4^+$	Positive	$[M+H-H_2O]^+$	1.07	-	✓	-	✓	-	✓
523.472	DG(30:0)	$C_{33}H_{63}O_4^+$	Positive	$[M+H-H_2O]^+$	-0.17	-	✓	-	✓	✓	✓
535.472	DG(31:1)	$C_{34}H_{63}O_4^+$	Positive	$[M+H-H_2O]^+$	-0.17	-	✓	-	✓	✓	✓
537.488	DG(31:0)	$C_{34}H_{65}O_4^+$	Positive	$[M+H-H_2O]^+$	0.44	-	✓	-	✓	✓	✓
549.488	DG(32:1)	$C_{35}H_{65}O_4^+$	Positive	$[M+H-H_2O]^+$	0.47	-	✓	-	✓	✓	✓
551.504	DG(32:0)	$C_{35}H_{67}O_4^+$	Positive	$[M+H-H_2O]^+$	1.10	-	✓	-	-	✓	-
563.504	DG(33:1)	$C_{36}H_{67}O_4^+$	Positive	$[M+H-H_2O]^+$	1.08	-	✓	-	-	✓	-
565.519	DG(33:0)	$C_{36}H_{69}O_4^+$	Positive	$[M+H-H_2O]^+$	-0.07	-	✓	-	✓	✓	✓
577.519	DG(34:1)	$C_{37}H_{69}O_4^+$	Positive	$[M+H-H_2O]^+$	-0.07	-	✓	-	✓	✓	✓
785.663	TG(45:1)	$C_{48}H_{90}NaO_6^+$	Positive	$[M+Na]^+$	0.05	-	✓	-	✓	-	-
787.678	TG(45:0)	$C_{48}H_{92}NaO_6^+$	Positive	$[M+Na]^+$	-0.77	-	✓	-	-	-	-
799.679	TG(46:1)	$C_{49}H_{92}NaO_6^+$	Positive	$[M+Na]^+$	0.49	-	✓	-	✓	-	-
801.694	TG(46:0)	$C_{49}H_{94}NaO_6^+$	Positive	$[M+Na]^+$	-0.32	-	✓	-	✓	✓	-
811.679	TG(47:2)	$C_{50}H_{92}NaO_6^+$	Positive	$[M+Na]^+$	0.48	-	✓	-	✓	-	-
813.694	TG(47:1)	$C_{50}H_{94}NaO_6^+$	Positive	$[M+Na]^+$	-0.32	-	✓	-	✓	-	-
815.575	PI-Cer(34:0)	$C_{40}H_{84}N_2O_{12}P^+$	Positive	$[M+NH_4]^+$	-0.78	-	✓	-	-	-	-
815.710	TG(47:0)	$C_{50}H_{96}NaO_6^+$	Positive	$[M+Na]^+$	0.11	-	✓	-	✓	✓	-
825.694	TG(48:2)	$C_{51}H_{94}NaO_6^+$	Positive	$[M+Na]^+$	-0.31	-	✓	-	✓	-	-
827.575	PG(38:1)	$C_{44}H_{85}NaO_{10}P^+$	Positive	$[M+Na]^+$	-2.73	-	✓	-	-	-	-
827.710	TG(48:1)	$C_{51}H_{96}NaO_6^+$	Positive	$[M+Na]^+$	0.11	-	✓	-	✓	✓	-
829.726	TG(48:0)	$C_{51}H_{98}NaO_6^+$	Positive	$[M+Na]^+$	0.53	-	✓	-	✓	✓	-
839.710	TG(49:2)	$C_{52}H_{96}NaO_6^+$	Positive	$[M+Na]^+$	0.11	-	✓	-	✓	-	-
841.591	PI-Cer(36:0(2OH))	$C_{42}H_{86}N_2O_{12}P^+$	Positive	$[M+NH_4-H_2O]^+$	-0.34	-	✓	-	-	-	-
841.726	TG(49:1)	$C_{52}H_{98}NaO_6^+$	Positive	$[M+Na]^+$	0.52	-	✓	-	✓	✓	-
843.606	PI-Cer(36:0)	$C_{42}H_{88}N_2O_{12}P^+$	Positive	$[M+NH_4]^+$	-1.11	-	✓	-	✓	-	-
851.710	TG(50:3)	$C_{53}H_{96}NaO_6^+$	Positive	$[M+Na]^+$	0.11	-	✓	-	✓	-	-
853.726	TG(50:2)	$C_{53}H_{98}NaO_6^+$	Positive	$[M+Na]^+$	0.52	-	✓	-	✓	-	-
855.741	TG(50:1)	$C_{53}H_{100}NaO_6^+$	Positive	$[M+Na]^+$	-0.25	-	✓	-	✓	-	-
869.621	PI-Cer(38:0(2OH))	$C_{44}H_{90}N_2O_{12}P^+$	Positive	$[M+NH_4-H_2O]^+$	-1.83	-	✓	-	-	-	-
871.637	PI-Cer(38:0)	$C_{44}H_{92}N_2O_{12}P^+$	Positive	$[M+NH_4]^+$	-1.42	-	✓	-	✓	-	-
881.757	TG(52:2)	$C_{55}H_{102}NaO_6^+$	Positive	$[M+Na]^+$	0.16	-	✓	-	✓	-	-

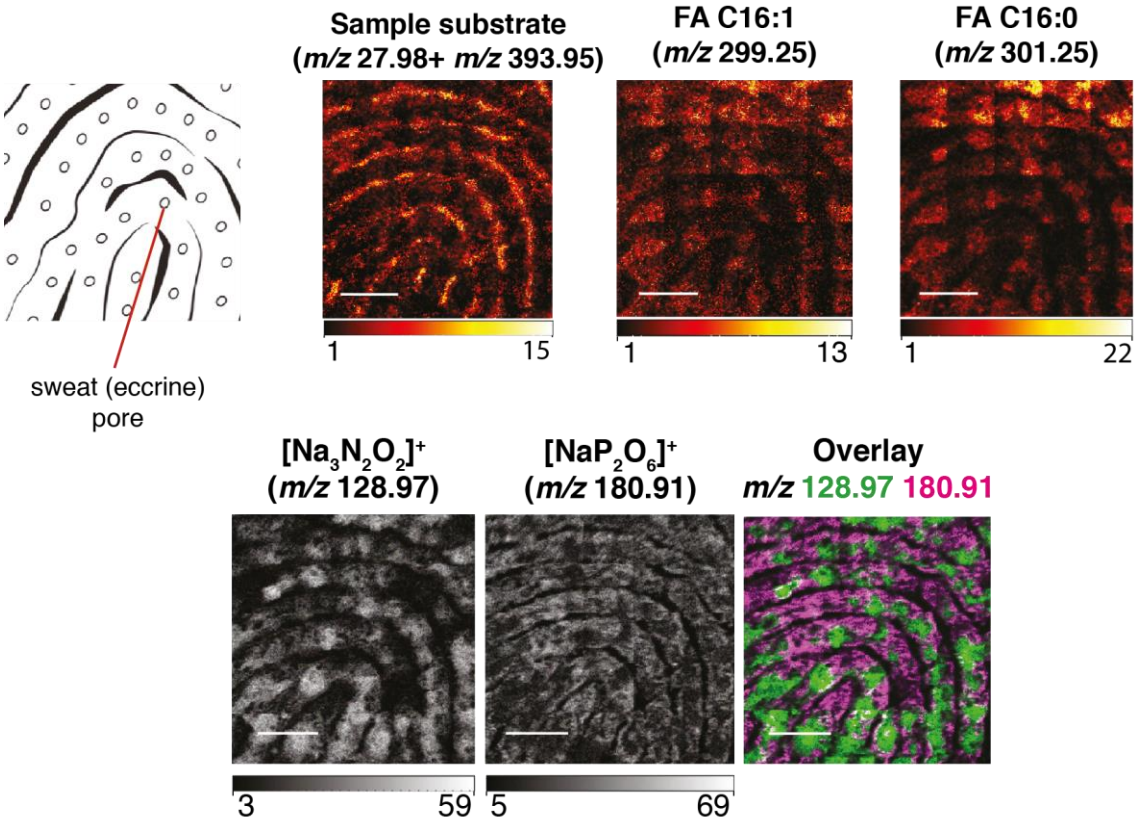

Figure 4.9 Cryo-OrbiSIMS imaging of a latent fingerprint

Cryo-OrbiSIMS ion images of a latent fingerprint sample alongside an illustration of fingerprint morphology indicating the corresponding location of the eccrine pores on the finger. Data was acquired using the Bi_3^+ analysis beam at a lateral resolution of 0.5 µm and ToF mass analyser. Scale bars on the images indicate 625 µm and intensity scales below the images are represented in counts. Images were acquired at a resolution of 5120 x 5120 pixels and binned to 1280 x 1280 pixels. Figure modified and reproduced from Newell et al. (2020) with permission.

Squalene, a known sebaceous-gland derived hydrocarbon (Pappas, 2009) was unexpectedly not detected with cryo-OrbiSIMS analysis of human fingerprints. However, a pure standard of squalene was detectable using cryo-OrbiSIMS, albeit ionising primarily as an $[M+H]^+$ adduct and associated dimer (**Figure 4.10**) as opposed to the $[M+N]^+$ adduct observed for linear hydrocarbons (**Figure 3.21**). It is therefore possible that the failure to detect squalene in human fingerprints is due to a matrix effect, perhaps caused by the high ionisation yield of glycerolipids that then inhibits hydrocarbon ionisation. It is not possible to exclude a second possibility, namely that the chemical environment of the fingerprint drives formation of different adducts than that detected in the pure standard. Together, the fingerprint data illustrate that OrbiSIMS analysis at cryogenic temperatures is a powerful method for analysing fingerprint lipids and that it is superior to analysis at ambient temperature. Nevertheless, as cryo-OrbiSIMS is not optimal for hydrocarbon analysis in all sample types, other methods such as GC-MS may be more appropriate.

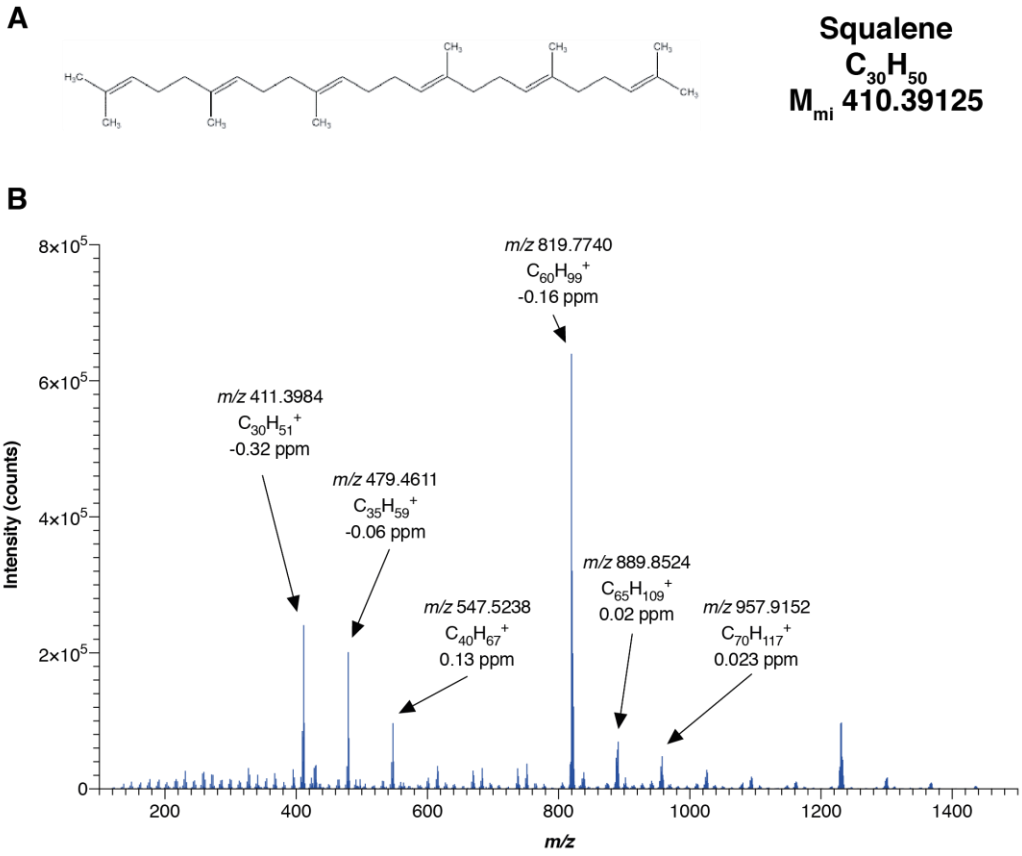

Figure 4.10 Cryo-OrbiSIMS detection of a squalene standard

A. Chemical structure of squalene.
B. Cryo-OrbiSIMS mass spectrum of a pure squalene standard using the Ar_{3500}^+ analysis beam and Orbitrap detector at an analysis temperature of -122℃.

Using GC-MS as a complementary technique to cryo-OrbiSIMS, it was possible to identify a wide range of hydrocarbons, including squalene (**Figure 4.11**). The majority of these hydrocarbons showed structural similarities to squalene, as many of them were methyl-branched and had 6 double bonds. Surprisingly, the main hydrocarbon detected on the latent fingerprint samples was not squalene, it was a methyl-branched saturated C30 hydrocarbon, likely squalane. Squalane has also been reported as a component of human sebum, however its presence is often underestimated as it is an inert lipid (Kim and Karadeniz, 2012). In summary, human fingerprints have complex lipid profiles, composed predominantly of methyl-branched hydrocarbons, fatty acids and glycerolipids. In the hydrocarbon profile, methyl-branched hydrocarbons dominate, with many containing up to six double bonds.

A

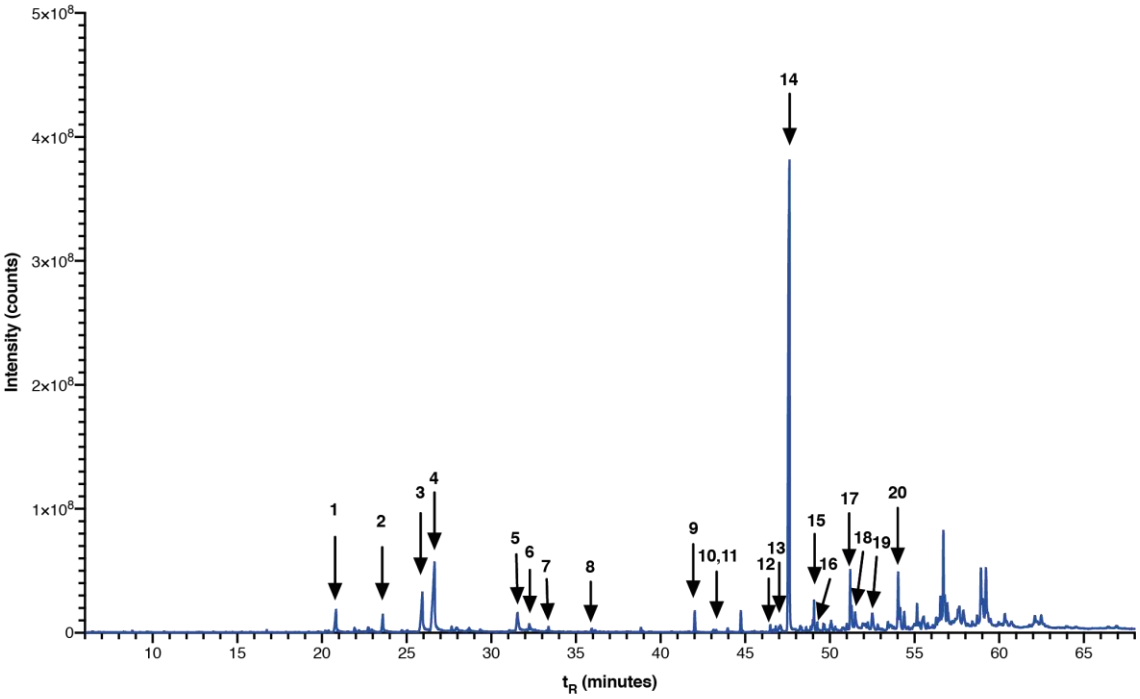

B

Peak number	t_R (minutes)	*m/z*	Formula	I.D.	Double bonds	Methyl-branched/linear?	Standard
1	20.95	228	$C_{17}H_{24}$	-	6	Methyl-branched	x
2	23.589	242	$C_{18}H_{26}$	-	6	Methyl-branched	x
3	26.07	254	$C_{18}H_{38}$	-	0	Methyl-branched	x
4	26.84	256	$C_{19}H_{26}$	-	6	Methyl-branched	x
5	31.649	282	$C_{20}H_{42}$	-	0	Methyl-branched	x
6	32.252	284	$C_{21}H_{32}$	-	6	Methyl-branched	x
7	33.372	310	$C_{22}H_{46}$	docosane	0	Linear	✓
8	35.933	316	$C_{23}H_{40}$	-	4	Methyl-branched	x
9	42.027	279	$C_{26}H_{54}$	-	0	Methyl-branched	x
10	43.118	366	$C_{27}H_{44}$	-	6	Methyl-branched	x
11	43.26	368	$C_{26}H_{54}$	hexacosane	0	Linear	✓
12	46.494	279	$C_{28}H_{48}$	-	5	Linear	x
13	46.807	384	$C_{30}H_{50}$	squalene	6	Methyl-branched	✓
14	47.656	410	$C_{30}H_{62}$	-	0	Methyl-branched	x
15	49.067	422	$C_{31}H_{52}$	-	6	Methyl-branched	x
16	49.254	424	$C_{32}H_{66}$	-	0	Methyl-branched	x
17	51.207	450	$C_{33}H_{56}$	-	6	Methyl-branched	x
18	51.486	452	$C_{34}H_{58}$	-	6	Methyl-branched	x
19	52.493	466	$C_{34}H_{70}$	-	0	Methyl-branched	x
20	54.038	478	$C_{34}H_{70}$	-	0	Methyl-branched	x

Figure 4.11 GC-MS analysis of latent fingerprint hydrocarbons

A. Gas chromatogram of a hexane extract from a female latent human fingerprint.
B. Mass spectrometry analysis of chromatography peaks indicated in (**A**). Compound identifications (I.D.) made using comparisons to a commercial standard run in parallel are indicated in the "Standard" column. The determination of linear or methyl-branched structure is made based on the EI fragmentation pattern.

4.5 Composition and localisation of *Drosophila* cuticular lipids

The *Drosophila* abdominal cuticle is composed of three main regions, the tergites located on the dorsal side of the abdomen, and the sternites and the pleura located on the ventral side of the abdomen. The sternites are hard inflexible plates of cuticle, whereas the pleura is stretchy and flexible (Yoder, 2012). The oenocytes are located below the sternites and tergites of the abdominal cuticle. The thickness of the sternite and pleural cuticle has been estimated using confocal microscopy (**Figure 4.12**). This shows that the sternites are composed of a thicker layer of cuticle (~5.9 µm), whereas the pleura is a much thinner layer of cuticle (~2.8 µm). This abdominal cuticle is coated with a layer of lipids which acts as a protective barrier, the composition of which will be discussed in this chapter.

The hydrocarbon profile of the *Drosophila* melanogaster cuticle has been well characterised in the literature (Blomquist, 2010). For these non-polar lipids , GC-MS analysis of solvent-dipped whole flies provides an efficient way of quantifying cuticular hydrocarbons as it produces higher throughput measurements than cryo-OrbiSIMS, albeit without information about spatial localisation. GC-MS analysis of hydrocarbons extracted from an isogenic strain of flies ($w^{1118\ iso31}$) provides a reproducible baseline for future analyses, with hydrocarbons ranging in length from 18 to 29 carbons (**Figure 4.13**, **Figure 4.14**). C20 – C30 methyl-branched alkanes including 2-methylhexacosane were also detected, all with branching points at carbon-2 indicated by the fragmentation pattern induced by electron ionisation (EI), which is in agreement with previous studies (**Figure 4.15**) (Wicker-Thomas et al., 2015). The cuticular hydrocarbon blend is strongly sexually dimorphic, not only in the levels of mono and diene alkenes, known to act as pheromones (Antony and Jallon, 1982), but also for methyl-branched hydrocarbons (**Figure 4.16A**). When looking at the absolute abundance of different hydrocarbons, it can be seen that the relative lack of monoenes in females is compensated for by an abundance of dienes (**Figure 4.16B**). To identify the position of double-bonds in monoenes and dienes where no commercial standards were available, DMDS (dimethyl disulphide) derivatisation

was utilised (**Figure 4.17**). This information can be used to unpin the underlying biochemistry of alkene production, due to the specificity of oenocyte desaturases for creating double bonds at defined positions on the carbon chain (Dallerac et al., 2000, Chertemps et al., 2006, Bousquet et al., 2012). DMDS derivatisation revealed that the most common double bond positions in monoenes were at C5, C7 and C9, which likely reflects the specificity of the desaturases involved in hydrocarbon biosynthesis (**Figure 4.17**).

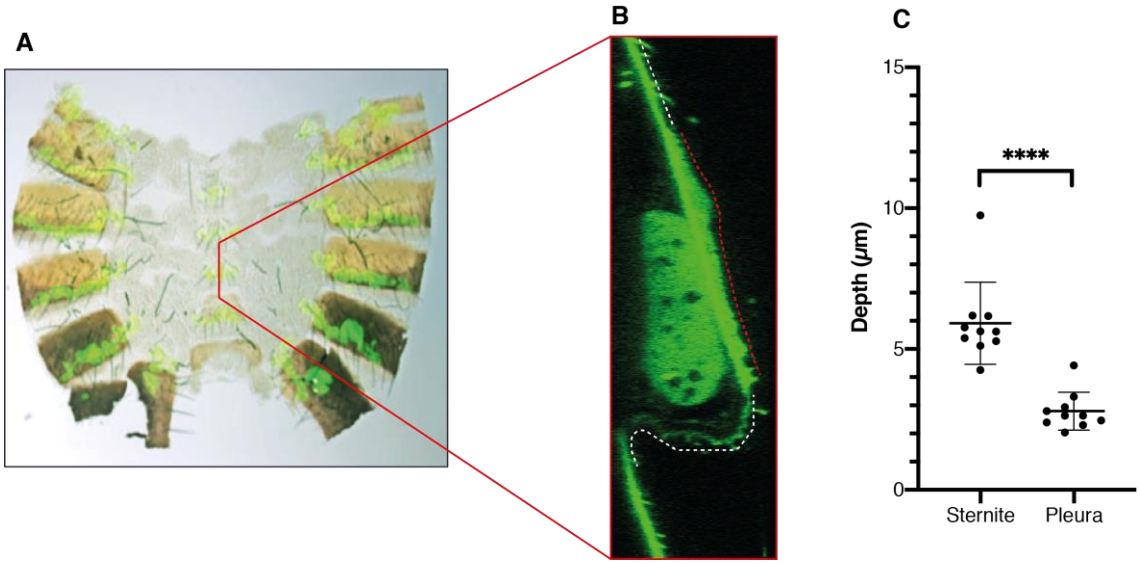

Figure 4.12 The sternites, pleura and oenocytes of the abdominal cuticle

A. Image of the dissected adult male carcass, with the oenocytes labelled in green. Image reproduced with permission from (Makki et al., 2014)
B. *YZ* slice of a confocal stack using 1 µm z stacks showing autofluorescence in green. The white dotted line indicates the region defined as pleura and the red dotted line indicates the region defined as sternite.
C. Cuticle thickness measured at ten different points across the defined regions in **B**, calculated using Fiji.

A

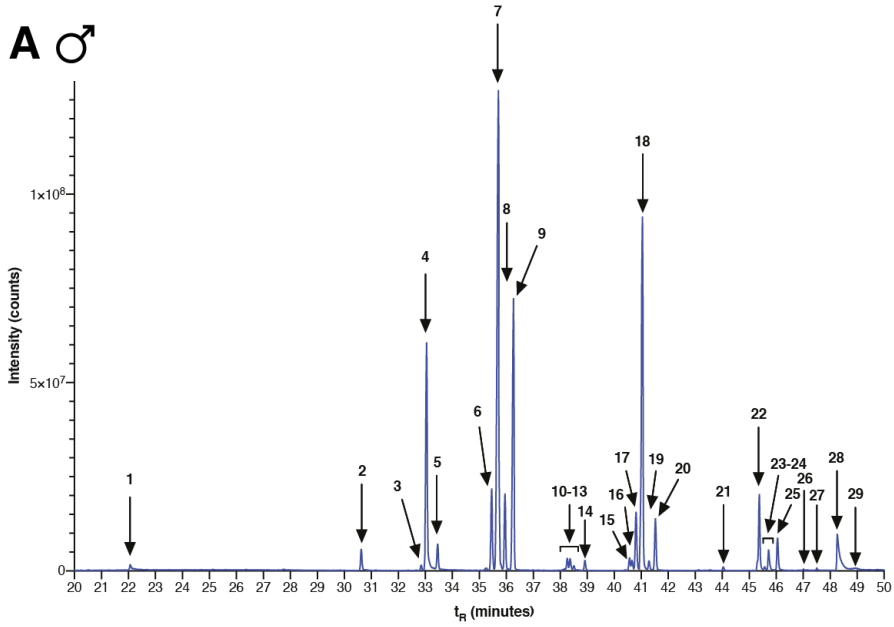

B

Peak number	t_R (minutes)	Parent ion (*m/z*)	Diagnostic ions (*m/z*)	Formula	Putative I.D.	Standard?
1	22.064	254.3	-	$C_{18}H_{38}$	Octadecane	✓
2	30.626	296.3	-	$C_{21}H_{44}$	Heneicosane	✓
3	32.867	308.2	-	$C_{22}H_{44}$	7-docosene	
4	33.049	310.2	250.1	$C_{20}H_{38}O_2$	(*Z*)-11-Vaccenyl acetate	✓
5	33.474	310.3	-	$C_{22}H_{46}$	Docosane	✓
6	35.455	322.3	-	$C_{23}H_{46}$	(*Z*)-9-tricosene	✓
7	35.705	322.3	-	$C_{23}H_{46}$	(*Z*)-7-tricosene	✓
8	35.946	322.3	-	$C_{23}H_{46}$	5-tricosene	
9	36.271	324.3	-	$C_{23}H_{48}$	Tricosane	✓
10	38.165	336.3	-	$C_{24}H_{48}$	9-tetracosene	
11	38.265	336.3	-	$C_{24}H_{48}$	8-tetracosene	
12	38.365	336.3	-	$C_{24}H_{48}$	7-tetracosene	
13	38.506	336.3	-	$C_{24}H_{48}$	6-tetracosene	
14	38.918	338.3	-	$C_{24}H_{50}$	Tetracosane	✓
15	50.554	352.3	337.3, 309.2	$C_{25}H_{52}$	2-methyltetracosane	
16	40.663	348.3	-	$C_{25}H_{48}$	x,x-pentacosadiene	
17	40.804	350.2	-	$C_{25}H_{50}$	9-pentacosene	
18	41.041	350.2	-	$C_{25}H_{50}$	(*Z*)-7-pentacosene	✓
19	41.291	350.2	-	$C_{25}H_{50}$	5-pentacosene	
20	41.524	352.3	-	$C_{25}H_{52}$	Pentacosane	✓
21	44.043	366.2	-	$C_{26}H_{54}$	Hexacosane	✓
22	45.375	380.3	365.3, 337.3	$C_{26}H_{54}$	2-methylhexacosane	
24	45.570	378.3	-	$C_{27}H_{54}$	9-heptacosene	
25	45.724	378.3	-	$C_{27}H_{54}$	7-heptacosene	
27	46.049	380.3	-	$C_{27}H_{56}$	Heptacosane	
28	47.011	394.3	351.1	$C_{28}H_{58}$	2-methylheptacosane	
29	47.502	394.4	-	$C_{28}H_{58}$	Octacosane	✓
31	48.268	408.3	393.3, 365.3	$C_{29}H_{60}$	2-methyloctacosane	
34	48.955	408.3	-	$C_{29}H_{60}$	Nonacosane	✓

Figure 4.13 Male *Drosophila* cuticular hydrocarbons

A. GC chromatogram illustrating the male *Drosophila* cuticular hydrocarbons. Flies were co-housed for 24 hours followed by a two-week period housing in vials with 10 male flies per vial.
B. Mass spectral information on the hydrocarbons detected from male flies. Octadecane is the internal standard, and is not detected on flies.

A

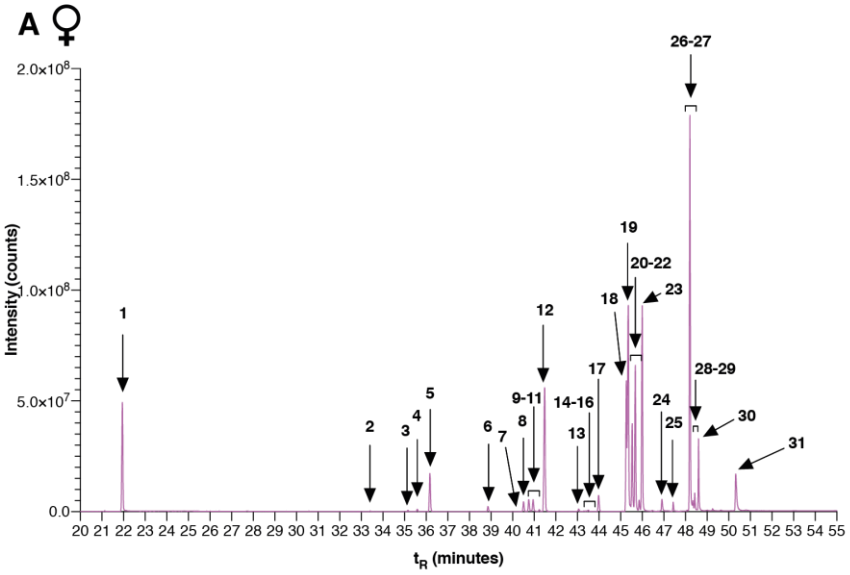

B

Peak number	t_R (minutes)	Parent ion (m/z)	Diagnostic ions (m/z)	Formula	Putative I.D.	Standard?
1	21.944	254.1	-	$C_{18}H_{38}$	Octadecane	✓
2	33.403	310.3	-	$C_{22}H_{46}$	Docosane	✓
3	35.147	324.2	309.3, 281.2	$C_{23}H_{48}$	2-methyldocosane	
4	35.605	322.3	-	$C_{23}H_{46}$	(*Z*)-7-tricosene	✓
5	36.188	324.3	-	$C_{23}H_{48}$	Tricosane	✓
6	38.864	338.3	-	$C_{24}H_{50}$	Tetracosane	✓
7	40.35	348.1	-	$C_{25}H_{48}$	x,x-pentacosadiene	
8	40.504	352.3	337.3, 309.2	$C_{25}H_{52}$	2-methyltetracosane	
9	40.746	350.2	-	$C_{25}H_{50}$	9-pentacosene	
10	40.962	350.2	-	$C_{25}H_{50}$	(*Z*)-7-pentacosene	✓
11	41.237	350.2	-	$C_{25}H_{50}$	5-pentacosene	
12	41.499	352.3	-	$C_{25}H_{52}$	Pentacosane	✓
13	43.056	366.3	351.3, 323.2	$C_{26}H_{54}$	2-methylpentacosane	
14	43.31	364.3	-	$C_{26}H_{52}$	A-hexacosene	
15	43.397	364.3	-	$C_{26}H_{52}$	B-hexacosene	
16	43.501	364.3	-	$C_{26}H_{52}$	C-hexacosene	
17	43.988	366.2	-	$C_{26}H_{54}$	Hexacosane	✓
18	45.262	376.2	291.1, 152.0	$C_{26}H_{50}$	(*Z,Z*)-7,11-heptacosadiene	✓
19	45.349	380.3	365.3, 337.3	$C_{26}H_{54}$	2-methylhexacosane	
20	45.533	378.3	-	$C_{27}H_{54}$	9-heptacosene	
21	45.683	378.3	-	$C_{27}H_{54}$	7-heptacosene	
22	45.853	378.3	-	$C_{27}H_{54}$	5-heptacosene	
23	45.991	380.3	-	$C_{27}H_{56}$	Heptacosane	
24	46.915	394.3	351.1	$C_{28}H_{58}$	2-methylheptacosane	
25	47.435	394.4	-	$C_{28}H_{58}$	Octacosane	✓
26	48.213	404.3	-	$C_{29}H_{56}$	(*Z,Z*)-7,11-nonacosadiene	✓
27	48.234	408.3	393.3, 365.3	$C_{29}H_{60}$	2-methyloctacosane	
28	48.313	406.3	-	$C_{29}H_{58}$	A-nonacosene	
29	48.426	406.3	-	$C_{29}H_{58}$	B-nonacosene	
30	48.605	408.3	-	$C_{29}H_{60}$	Nonacosane	✓
31	50.324	421.3	393.3	$C_{30}H_{62}$	2-methylnonacosane	

Figure 4.14 Female *Drosophila* cuticular hydrocarbons

A. GC chromatogram illustrating the female *Drosophila* cuticular hydrocarbons. Flies were co-housed for 24 hours followed by a two-week period housing in vials with 10 female flies per vial. **B**. Mass spectral information on the hydrocarbons detected from female flies. Octadecane is the internal standard, and is not detected on flies.

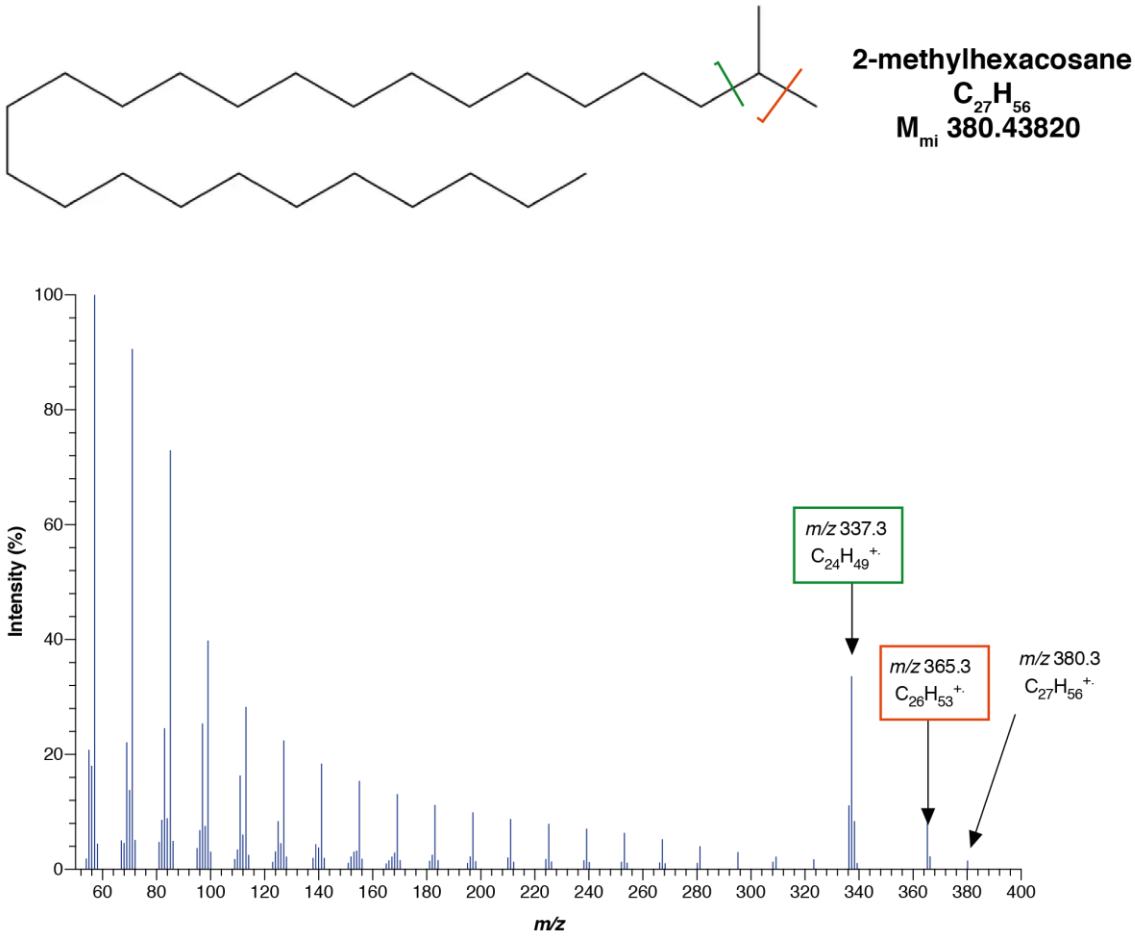

Figure 4.15 EI fragmentation pattern of *Drosophila* 2-methylhexacosane

Resulting EI fragmentation spectrum from GC-MS analysis of the *Drosophila* cuticular hydrocarbon 2-methylhexacosane. The fragmentation points are indicated on the chemical structure.

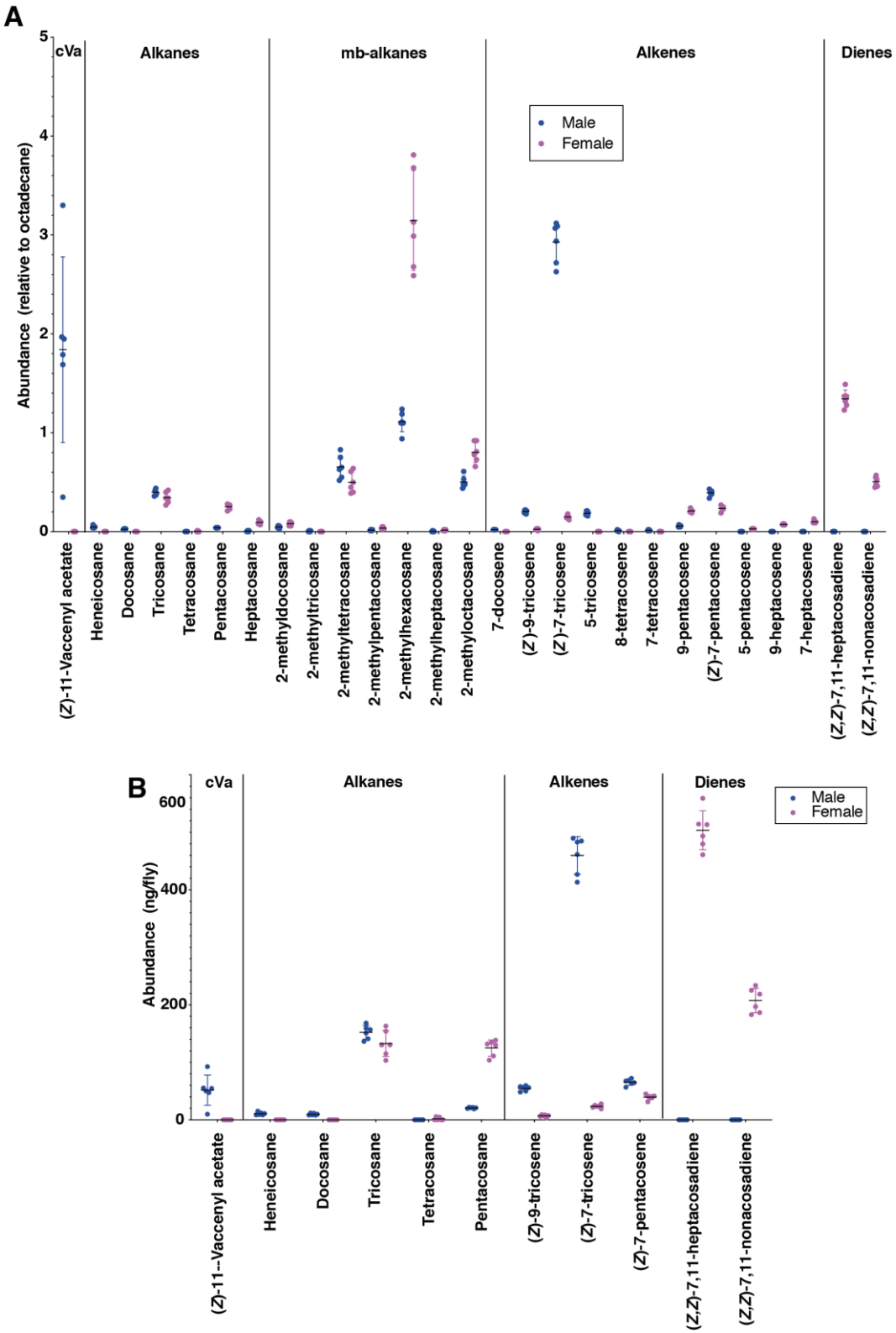

Figure 4.16 Relative and absolute abundance of *Drosophila* cuticular hydrocarbons

A. Relative hydrocarbon abundance calculated as a ratio compared to an octadecane internal standard.
B. Absolute hydrocarbon abundance (ng per fly), calculated for those hydrocarbons with a commercial standards available.

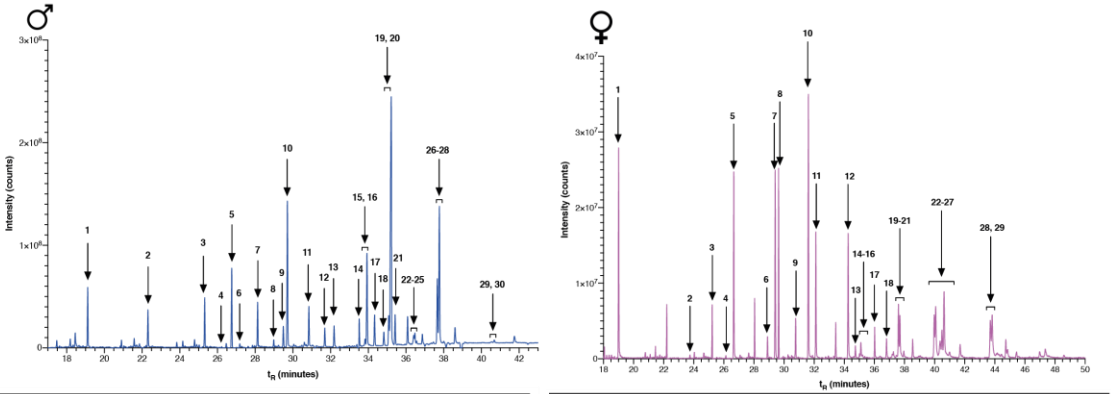

Peak number	t_R (minutes)	m/z	I.D.	Standard?	Derivatised?
1	19.139	254.2	Octacosane	✓	x
2	22.838	296.3	Heneicosane	✓	x
3	25.316	310.3	Docosane	✓	x
4	26.288	281.2, 309.2	2-methyl docosane	x	x
5	26.757	342.3	Tricosane	✓	x
6	27.181	295.2, 323.2	2-methyltricosane	x	x
7	28.126	338.3	Tetracosane	✓	x
8	29	309.2, 337.2	2-methyl tetracosane	x	x
9	29.504	352.4	Pentacosane	✓	x
10	29.737	212.2	N,N-Dimethyldodecylamine	✓	x
11	30.845	366.3	Hexacosane	✓	x
12	31.698	337.2, 365.2	2-methyl hexacosane	x	x
13	32.193	380.3	Heptacosane	✓	x
14	33.517	394.3	Octacosane	✓	x
15	33.838	145, 257, 402.1	7-docosene	x	✓
16	33.929	145, 259, 404.1	(Z)-11-Vaccenyl acetate	✓	✓
17	34.342	365.3, 393.3	2-methyl octacosane	x	x
18	34.821	408.4	Nonacosane	✓	x
19	35.091	173, 243, 416.1	(Z)-9-tricosene	✓	✓
20	35.191	145, 271, 416.1	(Z)-7-tricosene	✓	✓
21	35.424	117, 299, 416.1	5-tricosene	x	✓
22	36.373	173, 257, 430	9-tetracosene	x	✓
23	36.415	159, 271, 430	8-tetracosene	x	✓
24	36.473	145, 285, 430.1	7-tetracosene	x	✓
25	36.561	131, 299, 430.1	6-tetracosene	x	✓
26	37.66	173, 271, 444.1	9-pentacosene	x	✓
27	37.764	145, 299, 444.1	(Z)-7-pentacosene	✓	✓
28	38.014	117, 327, 444	5-pentacosene	x	✓
29	40.549	173, 299, 471.9	9-heptacosene	x	✓
30	40.687	145, 327, 472.1	7-heptacosene	x	✓

Peak number	t_R (minutes)	m/z	I.D.	Standard?	Derivatised?
1	19.021	254.3	Octacosane	✓	x
2	23.76	296.3	Heneicosane	✓	x
3	25.231	310.3	Docosane	✓	x
4	26.136	281.1, 309.5	2-methyldocosane	x	x
5	26.659	324.3	Tricosane	✓	x
6	28.9	309.3, 337.3	2-methyl tetracosane	x	x
7	29.415	352.3	Pentacosane	✓	x
8	29.631	212.1	N,N-Dimethyldodecylamine	✓	x
9	30.764	366.4	Hexacosane	✓	x
10	31.611	337.3, 365.4	2-methylhexacosane	x	x
11	32.129	380.4	Heptacosane	✓	x
12	34.26	365.3, 393.3	2-methyloctacosane	x	x
13	34.79	408.4	Nonacosane	✓	x
14	35.015	173, 243, 416.1	(Z)-9-tricosene	✓	✓
15	35.107	145, 271, 416.1	(Z)-7-tricosene	✓	✓
16	35.202	117, 299, 416.1	5-tricosene	✓	✓
17	36.02	408.4	Nonacosane	✓	x
18	36.813	393.2, 421.3	2-methylnonacosane	x	x
19	37.602	173, 271, 444.2	9-pentacosene	x	✓
20	37.694	145, 299, 444.1	(Z)-7-pentacosene	✓	✓
21	37.959	206.8, 326.9, 444.9	5-pentacosene	x	✓
22	39.989	145, 375.2, 423, 470	7,x-heptacosadiene	✓	✓
23	40.088	271, 375.2, 423, 470.1	x,11-heptacosadiene	✓	✓
24	40.372	299, 375.1, 423, 470	9,x-heptacosadiene	x	✓
25	40.492	173, 299, 472.3	9-heptacosene	x	✓
26	40.629	145, 327, 472.2	7-heptacosene	x	✓
27	40.638	229, 423, 470	x,13-heptacosadiene	x	✓
28	43.706	145, 435, 451, 483.1	7,x-nonacosadiene	x	✓
29	43.827	299,435, 451, 483.1	x,11-nonacosadiene	x	✓

Figure 4.17 DMDS derivatisation to determine hydrocarbon double bond positions

GC chromatogram illustrating the detection of male and female *Drosophila* hydrocarbons after derivatisation with DMDS. The corresponding mass spectral information is displayed in the tables below each corresponding chromatogram. The column entitled “Standard” indicates if a commercial standard was available, and the column entitled “Derivatised” indicates if the GC-MS data shows a derivatised or native molecule.

Although the hydrocarbons are relatively well characterised, other lipid components in the cuticular lipid blend are relatively poorly characterised. This may in part be due to the fact that several cuticular lipid classes are also abundant in internal fly tissues. Therefore, with chromatography-based detection methods requiring the extraction the sample with harsh organic solvents, it is often difficult to extract the surface fraction without contamination. To circumvent this limitation, the *Drosophila* cuticle was instead analysed using the OrbiSIMS, a surface-specific method of analysis. Impressively, OrbiSIMS was able to detect over 200 different lipid species (**Supplementary Tables 9.17-9.18** located in the Supplementary Material). This number is much higher than those previously described for the Drosophila cuticular lipid blend (Kaftan et al., 2014, Chin et al., 2014), and includes putative lipid species that have not been previously reported on the fly cuticle such as ceramides. Interestingly, ceramides are also a significant component of mammalian skin (Pappas, 2009). The identity of 47 of the 200 putative lipids from OrbiSIMS analysis could be validated with LC-MS (**Figure 4.18**). This comparison highlights the relative biases of the two techniques, and good overlap was only observed for fatty acids and ceramide phosphoethanolamine (PE-Cer) classes. The LC-MS sample extraction protocol involves using a harsh solvent (chloroform), which is also likely to extract internal lipids (e.g. from the fat body), which could account for the relative enrichment in phospholipids and glycerolipids observed using this method. When comparing male and female cuticular lipids, cryo-OrbiSIMS analysis highlights a clear sexual dimorphism, with females substantially enriched in glycerolipids compared with males (**Figure 4.19**). Flies were housed in single sex environments for two weeks prior to analysis to avoid cross-contamination of male and female lipids, therefore it is unlikely that the glycerolipids observed on the female cuticles in my analysis originated from males. It is surprising to observe glycerolipids on female and not male cuticles, as previous data has indicated that glycerolipids such as TAGs are synthesised by males, secreted via the ejaculatory bulb and only transferred to the female cuticle via mating as an anti-aphrodisiac (Chin et al., 2014).

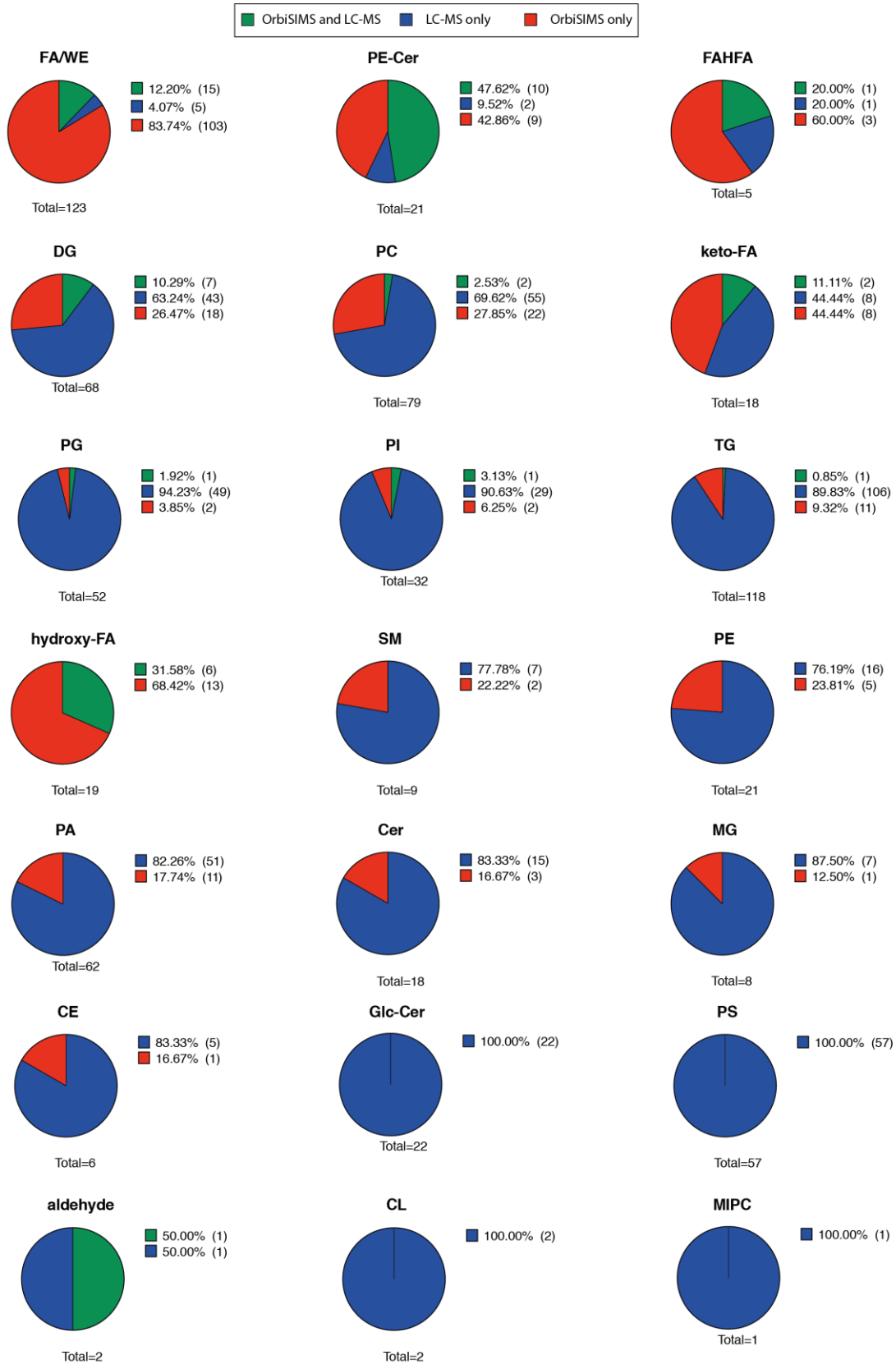

Figure 4.18 Cross-validation of OrbiSIMS lipid identities with LC-MS

Illustration of the overlap between OrbiSIMS and LC-MS detection of *Drosophila* cuticular lipids, separated by lipid class.

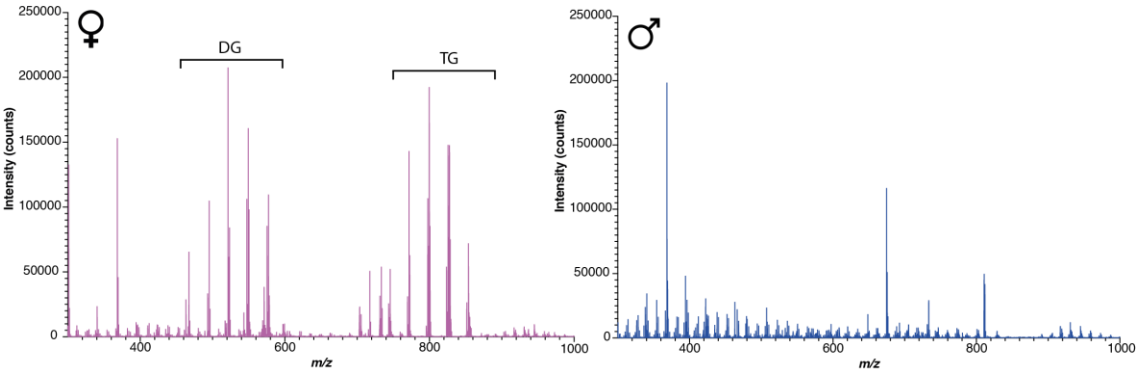

Figure 4.19 Sexual dimorphism of *Drosophila* cuticular lipids

Cryo-OrbiSIMS analysis of a male and female *Drosophila* abdominal cuticle using the Ar_{3500}^{+} analysis beam and Orbitrap detector in positive ion polarity. The female mass spectrum indicates the mass regions where DG and TG are abundant.

OrbiSIMS also enables the collection of spatial information about the localisation of cuticular lipids. Using depth profiling, the male pheromone tricosene is localised to the surface of the abdominal cuticle, and the same surface localisation is also observed for the alkene pentacosene on the wing cuticle (**Figure 4.20**). OrbiSIMS also revealed clear differences in lipid composition between different regions of the cuticle such as the wing and abdomen. 36 lipid species showed specificity for the wing alone and 17 lipid species showed specificity for the abdomen alone (**Figure 4.21**). In particular, the wing appeared to be enriched in PE-Cer, compared with the abdominal cuticle. This enrichment was unexpected as wing epidermal cells die before adulthood and it is the abdomen and not the with that is thought to contain the cuticule lipid-secreting cells – the oenocytes.

Using cryogenic OrbiSIMS imaging, I observed that the signals from hydrocarbons such as tricosane are evenly distributed across the surface of the *Drosophila* wing cuticle (**Figure 4.22A**). Hydrocarbons are known to be produced by the oenocytes of the abdomen, so presumably these are transferred to the wing and other body parts via grooming behaviour (Mueller et al., 2020, Zhang et al., 2020). In striking contrast, wax esters show specific patterns of enrichment on the wing blade surface. For example, strong signals from WE(50:0) are observed surrounding the veins whereas signals for WE(28:0) predominate in intervein regions (**Figure 4.22B**). Overall, there is a tendency for longer chain waxes to concentrate around the wing veins whereas shorter chain waxes localise in the complementary pattern. For the cuticle of the abdomen, hydrocarbons are homogenously distributed, as they are in the wing (**Figure 4.23B**). Again, like the wing, wax esters show specific patterns of localisation. For example, the signal for WE(50:0) localises to the flexible cuticle of the pleura whereas that from WE(58:1) is enriched in the hard cuticle plates of the sternites (**Figure 4.23C**).

Keenan-scaled principal component analysis of an OrbiSIMS image of the male *Drosophila* cuticle was used to identify the different chemical sub-domains of the abdominal cuticle. This method of data scaling accounts for the Poisson

distribution of noise in the acquired data (Keenan and Kotula, 2004). This method is able to discriminate three sub-domains of cuticle with unique chemical signatures (**Figure 4.24**). Clear chemical separation is identified between the sternite and pleura regions of the cuticle, and interestingly an unexpected third region of ~40 μm diameter is identified as a chemically distinct boundary region between the sternite and pleura. This illustrates how multivariate analysis on mass spectrometry imaging data can be used to reveal a previously “invisible” sub-domain of the fly cuticle. This region is not distinguishable by the naked eye, but chemical specificity of the lipid composition in this region would make sense biologically, as it forms the border between two visible domains of cuticle. The principal component analysis identifies several interesting chemical features pertaining to the three identified cuticle sub-domains. The PCA loadings identify the sternite region to be rich in shorter chain wax esters (C22-C36) and phospholipids. The pleura region is rich in longer chain wax esters (C48-C52) and some fatty acids (C14-C18). Meanwhile, PC1 and PC5 identify the border region between the sternites and pleura as having a chemical signature with some but not all features of the two independent regions. The border region displays a large abundance of free fatty acids (C14-C18) enriched above that seen in the pleura region, and an abundance of short chain wax esters (C28-C34), similar to what is seen in the sternites. The different chemical composition of sternite and pleura cuticular lipids correlates with a ~2 fold increase in cuticle thickness for the sternites compared with the pleura (**Figure 4.12**). The different chemical composition of the lipid blend may act functionally to provide an effective barrier for these two different thicknesses of abdominal cuticle.

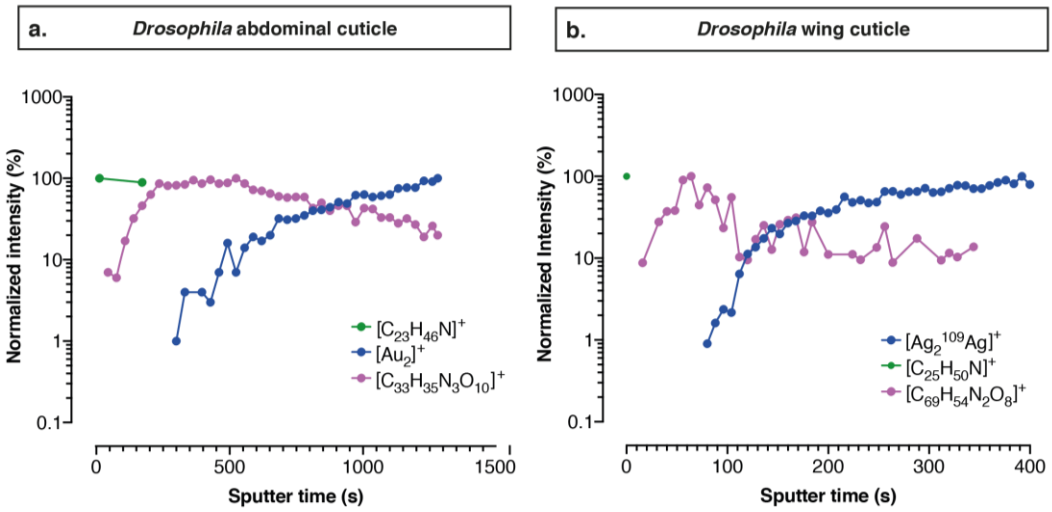

Figure 4.20 Hydrocarbons are specific to the surface of the wing and abdominal cuticle

Cryo-OrbiSIMS depth profile analysis through a male *Drosophila* abdominal cuticle (**a**) and male *Drosophila* wing cuticle (**b**) with the Ar_{3500}^+ beam and Orbitrap detector. Sputter time correlates with the depth through the sample. Green represents hydrocarbon, pink represents part of the chitin polymer and blue represents the gold and silver of the sample substrate. Data modified and reproduced from Newell et al. (2020) with permission.

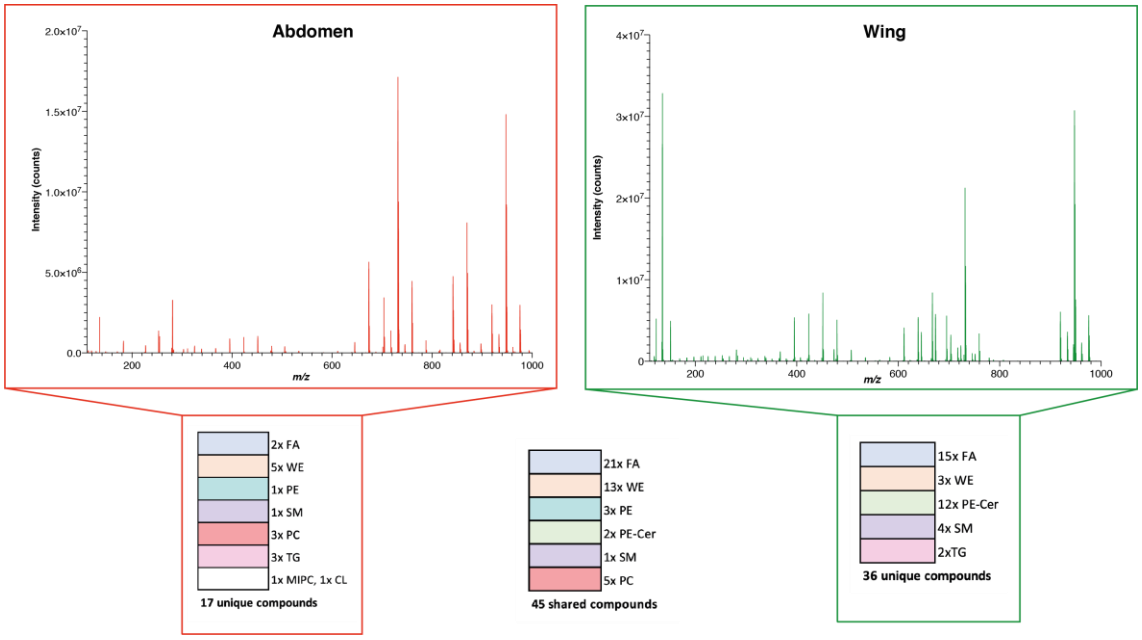

Figure 4.21 Differences in the *Drosophila* wing and abdominal cuticular lipid blend

OrbiSIMS analysis in negative polarity analysis of the male *Drosophila* wing and abdominal cuticle. Orbitrap mass spectra acquired using the Ar_{3500}^+ GCIB detects 98 distinct lipids, with spatial localisation on either the wing (right) or abdominal cuticle (left). Lipids that are found in both tissues are shown in the central table. A full list of identified compounds is shown in **Supplementary Table 9.19** located in the Supplementary Material.

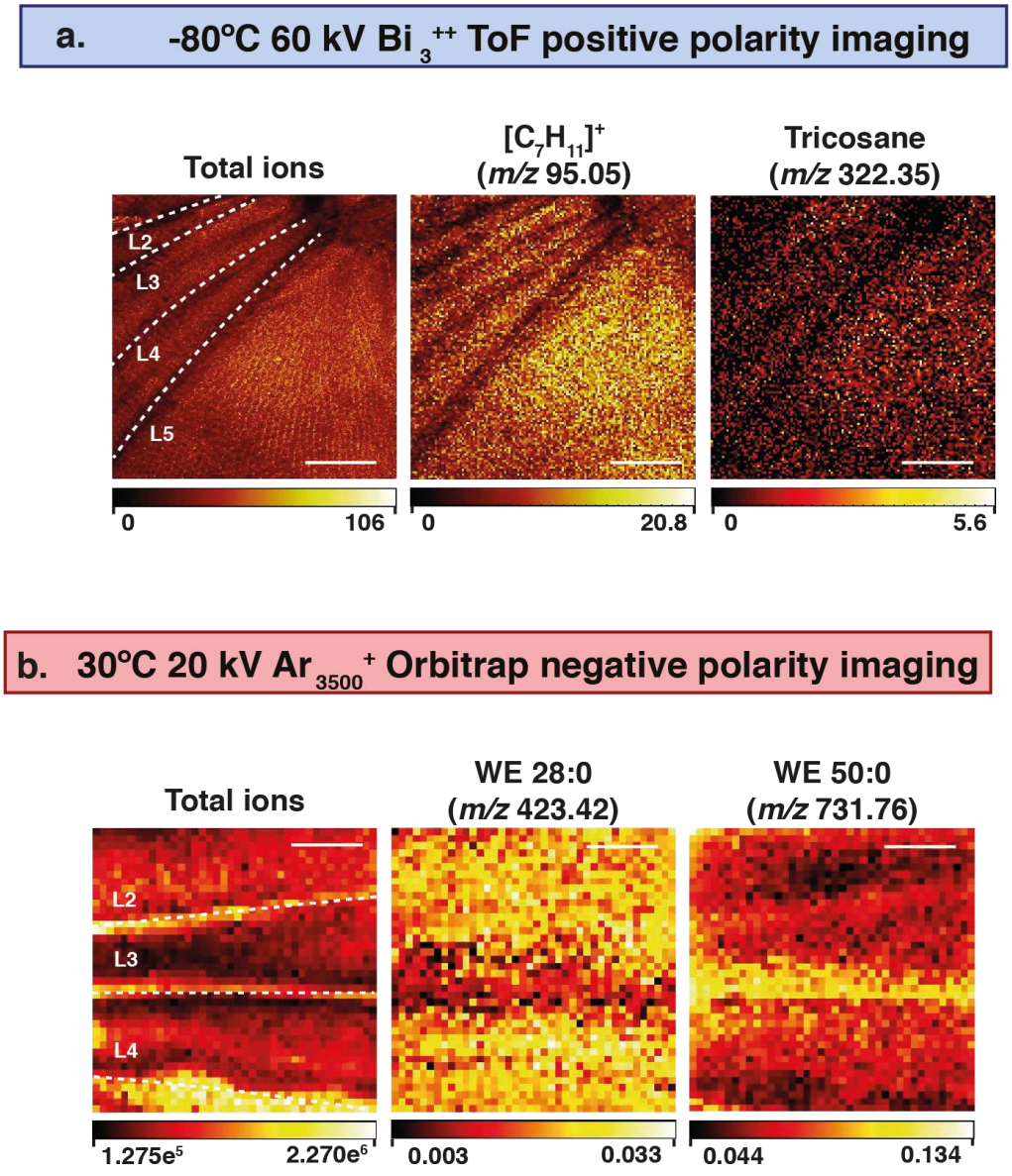

Figure 4.22 Spatial localisation of lipids on the *Drosophila* wing

a. Cryo-SIMS imaging of a male *Drosophila* wing. The locations of the wing veins are indicated on the image. Scale bars represent 125 µm. The image was acquired over an area of 500 x 500 µm with a beam resolution of 0.5 µm and an image resolution of 1024 x 1024 pixels, binned to 256 x 256 pixels.
b. OrbiSIMS imaging of a male *Drosophila* wing. The locations of the wing veins are indicated on the image. Scale bars represent 100 µm. The image was acquired over an area of 400 x 400 µm with a beam resolution of 5 µm and an image resolution of 40 x 40 pixels.
Ion images are normalised to total ion intensity to correct for intensity differences caused by topography. Data reproduced from (Newell et al., 2020) with permission.

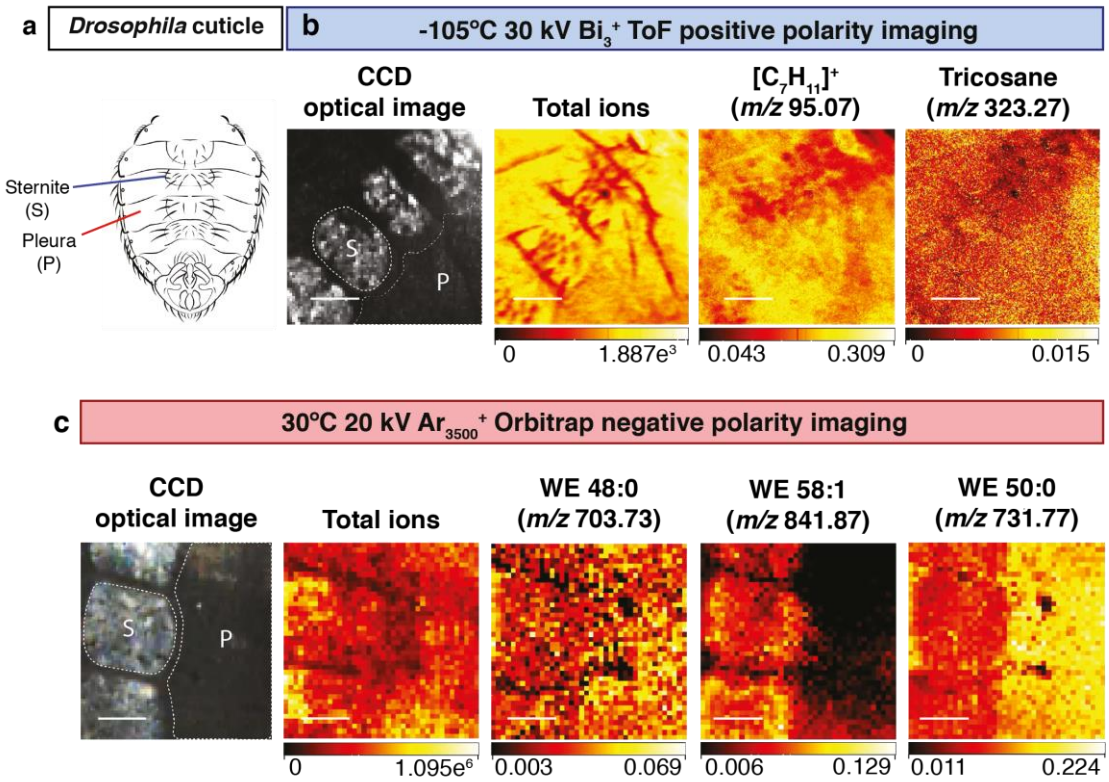

Figure 4.23 Spatial distribution of lipids on the *Drosophila* abdominal cuticle

a. Illustration of the structure of the male *Drosophila* abdominal cuticle, indicating the sternite (S) and pleura (P) sub-domains.
b. Cryo-OrbiSIMS imaging of the *Drosophila* abdominal cuticle. Scale bars represent 125 µm. The image was acquired over an area of 500 x 500 µm with a beam resolution of 0.5 µm and an image resolution of 1024 x 1024 pixels and binned to 256 x 256 pixels.
c. OrbiSIMS imaging of the D*rosophila* abdominal cuticle. Scale bars represent 100 µm. The image was acquired over an area of 400 x 400 µm with a beam resolution of 5 µm and an image resolution of 40 x 40 pixels. WE = wax ester.
Ion images are normalised to total ion intensity to correct for intensity differences caused by topography. Data reproduced from Newell et al. (2020) with permission.

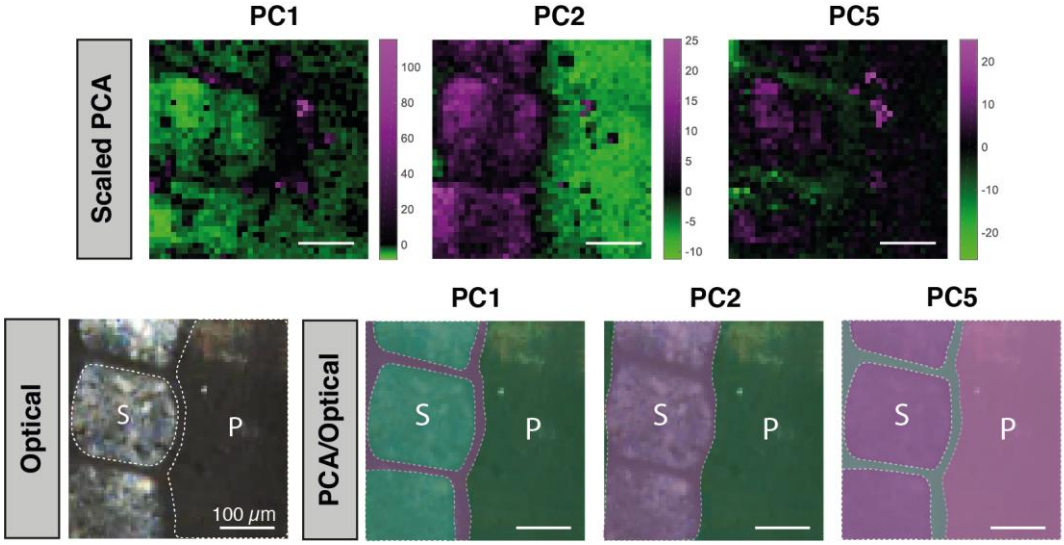

Figure 4.24 The *Drosophila* abdominal cuticle has three chemically distinct sub-domains
Keenan-scaled PCA analysis of an Orbitrap image of the fly cuticle taken with the OrbiSIMS at 10 µm lateral resolution. The PCA analysis was performed on the top 314 picked peaks. The images show the scores plots for PC1, PC2 and PC5, with graphical illustrations of the domains they isolate shown in the second row, overlaid on the optical image. S=sternite, P=pleura.

4.6 Discussion

My survey of barrier lipids on the surfaces of plants, flies, mice and humans provides some interesting evolutionary comparisons. Using the data in this chapter, it is possible to generate a schematic "pseudo-phylogenetic tree" illustrating which major classes of barrier lipids are present in the species analysed (**Figure 4.25**).

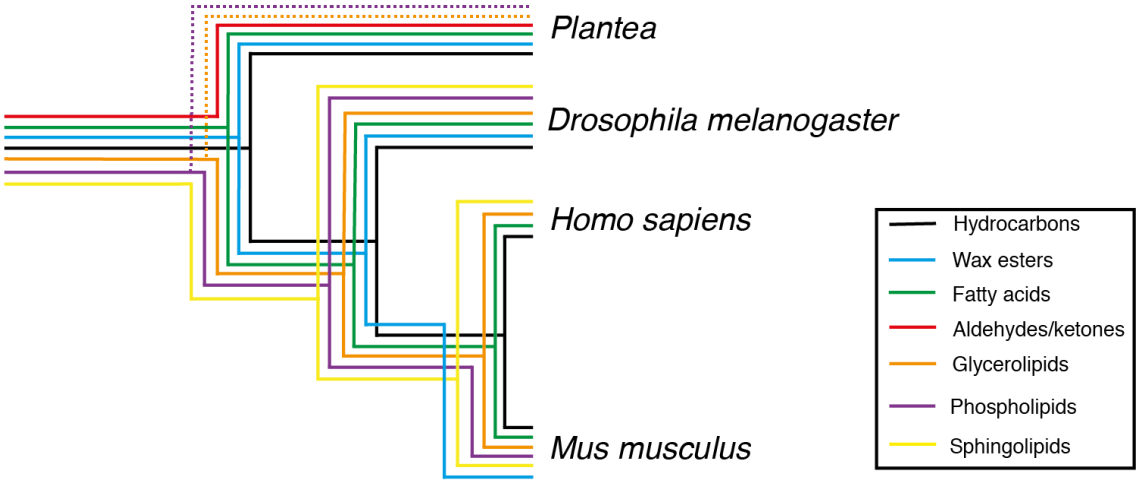

Figure 4.25 *Pseudo*-phylogenetic tree of barrier lipid composition in terrestrial organisms
Diagram illustrating the presence of different barrier lipid classes within different species. Diagram represents a schematic version of a simple phylogenetic tree, distinguishing the relative points at which the species diverge. A dotted line refers to lipids that are present in some but not all plant species analysed.

From this diagram, it can be seen that several classes of barrier lipids such as hydrocarbons, fatty acids and glycerolipids are present in plants, insects and mammals. From an evolutionary perspective, it is important to make the distinction between whether similar molecular classes of barrier lipids observed in two species result from evolutionary conservation or convergent evolution. Conservation occurs when genetic features shared between species are derived from a common ancestor, whereas convergence occurs when different genetic features arise independently of each other (Galperin and Koonin, 2012). Evolutionary convergence occurs via the emergence of a common "solution" to selective pressure such as a dry external environment. In both situations, the species of interest would display the same phenotype e.g. barrier lipid composition. To determine whether this shared barrier phenotype arose as a

consequence of a common evolutionary origin or convergence, it would likely be necessary to survey in detail many more terrestrial species and, importantly, also aquatic organisms. It will also be important to perform a genetic and phylogenetic analysis of the relevant lipid biosynthetic enzymes – many of which are not yet identified. Nevertheless, from my analysis thus far, it does appear that aldehydes and ketones are largely plant specific whereas sphingolipids are animal-specific. Wax esters are interesting as they are found in all species except humans.

Importantly, hydrocarbons, free fatty acids and glycerolipids are common components of the lipid barrier shared between plants, insects and mammals. This suggests that they may be functionally important for common terrestrial barrier functions, such as waterproofing, microbial/fungal defence and UV protection (Pappas, 2009). It is also possible they could have inter/intra-species pheromonal properties, as although classes of lipid are conserved, there is often variation in the exact lipids present in each species. This is observed between different sub-species of *Drosophila*, where alkene double bond positions are modified, and even the same lipid can induce an opposing behavioural response in different sub-species. For example, the female pheromone (*Z*,*Z*)-7,11-heptacosadiene is attractive to *Drosophila melanogaster* males and repulsive to *Drosophila simulans* males (Sato and Yamamoto, 2020). It is possible that glycerolipids could also act as pheromones in a wider range of species, as they have been previously identified as pheromones in some insect species (Chin et al., 2014). It is interesting that glycerolipids are enriched in males relative to females, both in mice and *Drosophila*. The sexual dimorphism of this lipid class may indicate a possible pheromonal role, as has been suggested for *Drosophila* (Chin et al., 2014).

Within the hydrocarbon class of molecules, it is interesting to note that linear alkanes and methyl-branched alkanes appear to have been preserved within all species analysed. However, alkenes, dienes and branched chain alkenes appear to have arisen later as they show a far greater degree of species specificity. As monoenes and dienes in *Drosophila* are well-established as sex-specific pheromones (Antony and Jallon, 1982), it is very possible that these molecules

have pheromonal or signalling functions in other organisms. As the proportion of methyl-branched alkane species appears dramatically lower in *Drosophila* when compared with most other species analysed including plants and human sebum, it is possible that alkanes and methyl-branched alkanes fulfil similar roles. Experimental data indicates the melting point of methyl-branched alkanes is not substantially different from alkanes of the same carbon backbone length which may result in a functional redundancy between the two (**Figure 4.26**). This is perhaps supported by the dominance of methyl-branched hydrocarbons and relative loss of straight chain alkanes in the human skin lipid blend (**Figure 4.11**).

The biosynthetic pathway involved in the synthesis of highly branched mammalian hydrocarbons such as squalene is distinct from that involved in the synthesis of singly branched hydrocarbons. In *Drosophila*, the synthesis of methyl-branched hydrocarbons utilises branched chain amino acids as a substrate for fatty acid synthase, followed by Cyp4g1 decarbonylation (Holze et al., 2021). In mammals, however, highly branched hydrocarbons such as squalene are instead synthesised via the mevalonate pathway through condensation of isoprene pyrophosphates with no elongation step involved. Moreover, between insect species, the enzymes involved in the synthesis of isoprenes do not show genetic similarities, indicating their independent evolution (Darragh et al., 2021). Thus, the hydrocarbons provide a clear example of convergent evolution, with different biosynthetic pathways utilised in different species to make very similar components of the lipid barrier.

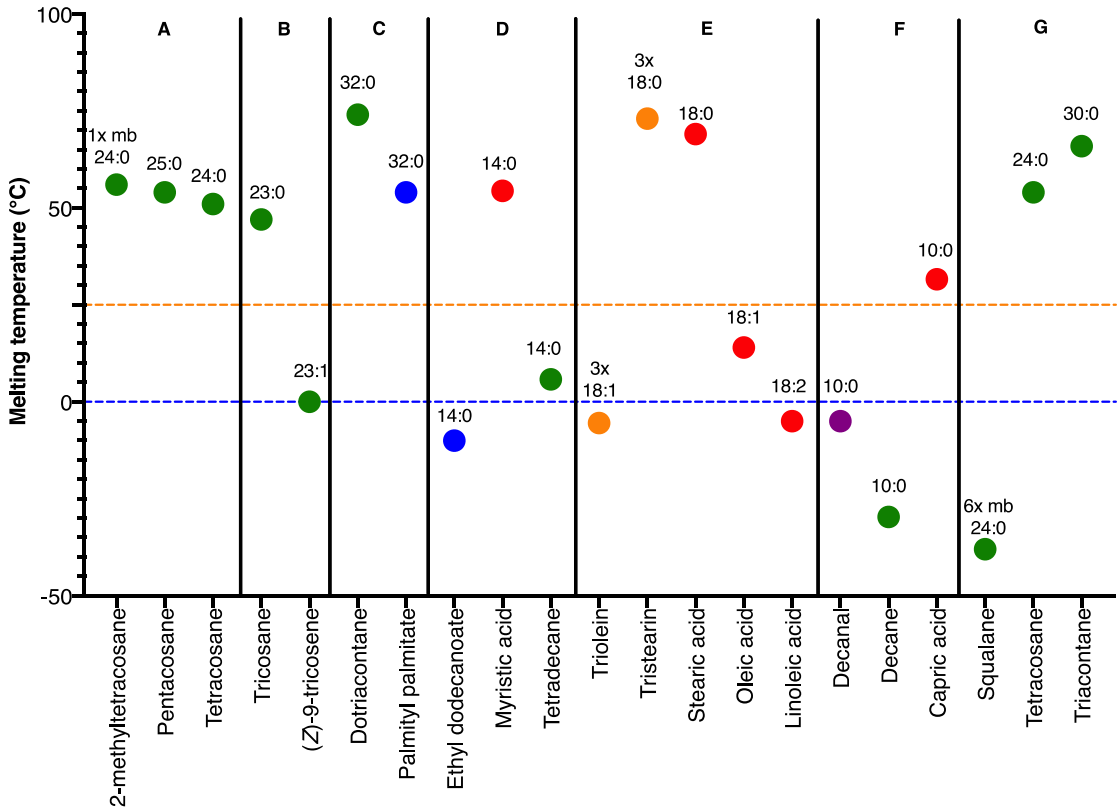

Figure 4.26 Melting points of different lipid classes

Experimentally reported melting points of different compounds. The number of carbons and double bonds is indicated above each point. Green=hydrocarbon, blue=wax ester , red=free fatty acid, orange=triglyceride, purple=fatty aldehyde. The blue line indicates 0℃ and the orange line 25℃ (room temperature). Data from Ayers (2012).

A. Effect of single methyl branching and increasing carbon chain length on melting point of hydrocarbons.

B. Effect of saturation on melting point of hydrocarbons of the same carbon chain length.

C. Difference in melting point of a alkane and wax ester with the same length of carbon backbone.

D. Difference in melting point of a wax ester, free fatty acid and hydrocarbon with the same length of carbon backbone

E. Effect of saturation and esterification of fatty acids on melting point.

F. Difference in melting point of an aldehyde, alkane and free fatty acid.

G. Effect of multiple branching points on melting point of hydrocarbons.

It is interesting to consider the reason for differential distribution of lipids on the surface of an organism. This could be to cater to the different requirements of underlying structures in relation to waterproofing. For example, the differential localisation of lipids on the *Drosophila* abdominal cuticule correlates with different types of cuticle with differing thicknesses. A plausible hypothesis for the differential localisation of cuticular lipids would be that they provide different barrier properties to the sternites and pleura. Although the mechanism that leads to these lipids becoming spatially localised is unclear, it is possible that this involves selective adsorbance of wax esters to the sternites versus pleura. Interestingly, these two cuticle subdomains are composed of different types of the polysaccharide polymer chitin (Madhavan and Madhavan, 1980), and this could affect surface adsorption. From a functional perspective, some lipids may have good barrier functions on a stiff substrate like the sternites but perform poorly on a constantly flexing and expanding substrate like the pleura. An important first step towards unravelling the mechanism by which cuticular WEs localise is to determine which tissues are responsible for the synthesis of non-hydrocarbon cuticular lipids and at which stage they are produced in the fly lifecycle, a question which has not been addressed in the literature but that I address in Chapter 6.

In plants, recently published data supports the hypothesis that different types of cuticle utilise different lipids to maintain their barrier. In the tomato plant, the epicuticular lipid blend has been shown to directly influence trans-cuticular water loss in the fruit, but not in the leaf which relies on the intra-cuticular lipid blend (Zeisler-Diehl et al., 2018). In this chapter, a striking difference is shown in the composition of the surface lipid blend in the leaf and fruit of a gooseberry plant, which may well exhibit a similar phenomenon to the tomato plant in this published study. There is also published evidence for the role of linear alkanes as a molecular sieve, controlling the entry of molecules and micro-organisms into the leaf (Luque et al., 1995). This is a role which, if accurate, could explain the presence of hydrocarbons in all species analysed. Another proposed role for hydrocarbons in plants is as chemotactic agents (Nordby and Nagy, 1977), which

is a role that could also be considered to be conserved in *Drosophila* where hydrocarbons act as pheromones.

Differential localisation of lipids on the human skin has also been reported, suggesting that this function may also be conserved in mammals (Bouslimani et al., 2015). In humans, the differential localisation of several lipid species has been correlated with the presence of different species of bacteria. This suggests a symbiotic relationship in the different skin niches which could contribute to effective barrier maintenance. As none of the organisms used in this chapter were grown in germ-free environments, it is important to consider bacteria as the origin of some of these lipid species, as is proposed in humans. Therefore, it cannot be excluded that the evolutionary conservation of barrier lipids proposed in this chapter may also occur instead from a conserved symbiotic relationship with bacteria. To exclude this, experiments would have to be performed in a germ-free environment.

The concurrent detection of many key lipid classes in the cuticular lipid blend of a diverse range of species highlights the importance of this blend. It is therefore critical that the organism regulates the composition of the cuticular lipid blend to maintain an effective barrier. However, there are situations where the composition of this blend is dysregulated. In the next chapter, I investigate the developmental origins of the cuticular lipid blend in flies and mice, and the consequences of any observed dysregulation.

Chapter 5. Dietary programming of barrier lipid composition

5.1 Introduction

DOHaD is now a well-established phenomenon supported by extensive data from both human epidemiological studies and animal models. Amongst all these data, however, there is virtually nothing reported in any species for the effects of developmental diet upon the largest organ in the adult body, the skin. In flies, a DOHaD effect upon “skin” has recently been demonstrated, whereby developmental dietary yeast levels programme the saturation index of cuticular hydrocarbons (Stefana et al., 2017). As shown in the previous chapter, hydrocarbons are by no means the only lipid present on the surface of the *Drosophila* cuticle. This therefore raises the question of whether non-hydrocarbon cuticular lipids are also programmed by developmental nutrition. Using the new OrbiSIMS analytical methods developed in Chapter 3, I now determine the effect of developmental diet on both hydrocarbon and non-hydrocarbon components of the *Drosophila* cuticular lipid blend. I then investigate the generality of my findings by asking whether developmental diet can also influence skin lipids in mammals.

5.2 Developmental dietary regulation of *Drosophila* cuticular lipids

I use two different paradigms for dietary programming of adult cuticular lipids: a high fat diet and a low protein diet. On a high fat (HF) diet, elevated fatty acids could feed directly into boosting the synthesis of cuticular lipids (Wicker-Thomas et al., 2015), and could therefore contribute to hydrocarbon biosynthesis. Linoleic acid was used, as this is one of the most abundant lipids in the *Drosophila* diet, and it cannot be synthesised by flies (Ziegler et al., 2015). However, I observed that a standard diet supplemented ~2.5 fold with linoleic acid (**Figure 5.1**) from development through to adulthood had minimal effects on the majority of cuticular hydrocarbon species (**Figure 5.2B, C**). Intriguingly, however, the HF linoleate diet

decreases rather than increases the desaturation index of cuticular hydrocarbons (**Figure 5.2D**). One exception to this rule is the significant increase of cuticular dienes in males fed a high linoleate diet. In addition, a diene species with different double bond positions than normal is observed in females on a high linoleate diet. Chemical derivatisation of this novel C27 diene revealed that the double bond positions correspond to ω6 and ω9 in contrast to ω7 and ω11 in (*Z,Z*)-7,11-heptacosadiene (**Figure 5.3**). This correlates directly with the double bond positions in linoleic acid (ω6 and ω9), suggesting that diet-derived fatty acids can contribute to and also modify the biosynthesis of hydrocarbons. It will be interesting in future to investigate if novel diene production in females and "ectopic" dienes in males have significant effects on mating behaviour and/or fecundity.

In contrast to the very selective effect on particular cuticular hydrocarbons, a high fat diet throughout development and adulthood has a more widespread effect on cuticular wax esters (**Figure 5.4**). Interestingly, although a broad range of lipids are detected on the fly cuticle including phospholipids, glycerolipids and sphingolipids, the only class of lipids substantially affected by a high fat diet are wax esters (**Figure 5.4B, D**). The HF diet induced changes in wax ester signals corresponding to increased desaturation of their fatty acid/alcohol chains. An increase in the signal corresponding to free cuticular linoleic acid but not oleic or stearic acid is also apparent (**Figure 5.4C**). The increase in linoleic acid signal on the surface of the fly, as estimated by OrbiSIMS analysis, is approximately 3.5 fold, reasonably close to the 2.5 fold increase of linoleic acid in the HF diet (**Figure 5.1**). It is therefore not possible to exclude the possibility that the source of linoleic acid on the fly cuticle comes directly from dietary linoleic acid stuck to the body surface. The increased desaturation observed in wax esters, however, must originate via ingestion and fly biosynthesis and likely reflects a strong dietary contribution of linoleate to the fatty acid pool used for wax ester biosynthesis. To quantify dietary linoleic acid incorporation into wax ester biosynthesis, stable isotope labelling approaches could be used, similar to those used later in this chapter. Additionally, high oleate and stearate diets could be used to determine if these lipids can act as precursors for monoenes and alkanes.

To investigate whether HF diet induced changes in the desaturation indexes of hydrocarbons and wax esters affect barrier function, a desiccation assay was performed. This showed no substantial effect on desiccation survival, making it unlikely that hydrocarbon dienes or the desaturation status of wax esters significantly impact cuticular barrier function (**Figure 5.5**). It is still possible that wax esters may be important as barrier lipids regardless of their desaturation status. In addition, there may be functional redundancy between different lipid species present on the fly cuticle.

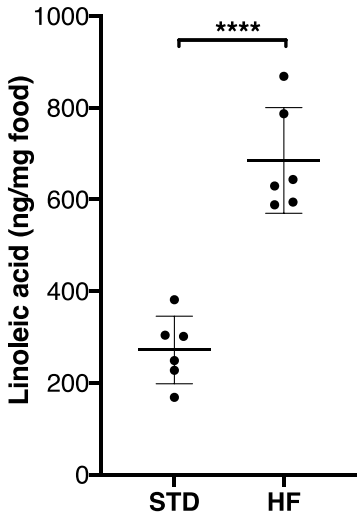

Figure 5.1 Linoleic acid quantification in Standard (STD) and High Fat (HF) fly diets

Free linoleic acid amount calculated in STD and HF fly diets measured from TMS derivatives. The amount of linoleic acid in HF food is approximately 2.5 fold higher than in STD food.

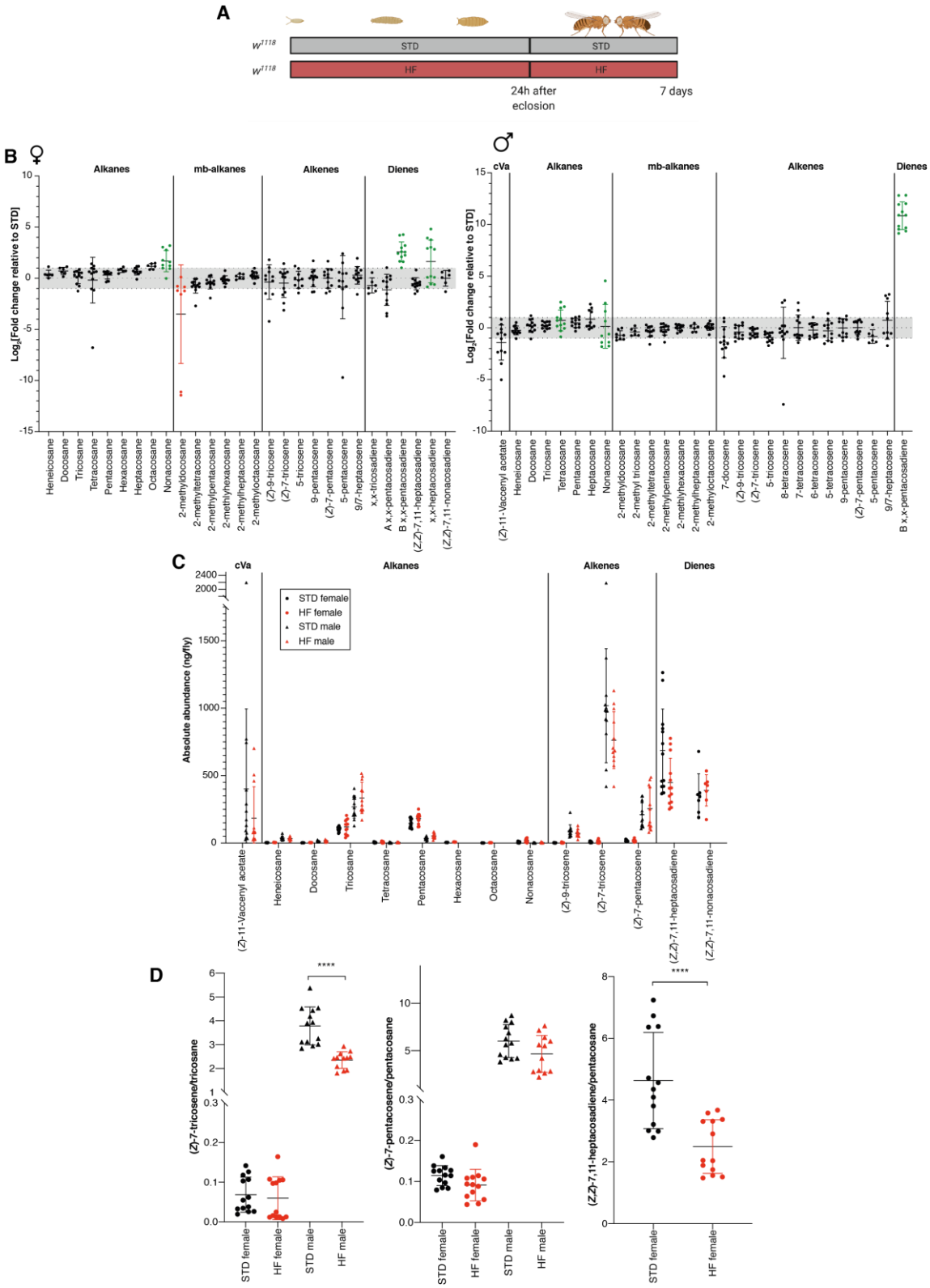
A
w1118
STD
STD
w1118
HF
HF
24h after eclosion
7 days
B ♀
Alkanes
mb-alkanes
Alkenes
Dienes
Log2[Fold change relative to STD]
Heneicosane
Docosane
Tricosane
Tetracosane
Pentacosane
Hexacosane
Heptacosane
Octacosane
Nonacosane
2-methyldocosane
2-methyltetracosane
2-methylpentacosane
2-methylhexacosane
2-methylheptacosane
2-methyloctacosane
(Z)-9-tricosene
(Z)-7-tricosene
5-tricosene
9-pentacosene
(Z)-7-pentacosene
5-pentacosene
9/7-heptacosene
x,x-tricosadiene
A x,x-pentacosadiene
B x,x-pentacosadiene
(Z,Z)-7,11-heptacosadiene
x,x-heptacosadiene
(Z,Z)-7,11-nonacosadiene
♂
cVa
(Z)-11-Vaccenyl acetate
7-docosene
8-tetracosene
7-tetracosene
6-tetracosene
5-tetracosene
9-pentacosene
B x,x-pentacosadiene
C
Absolute abundance (ng/fly)
STD female
HF female
STD male
HF male
D
(Z)-7-tricosene/tricosane
(Z)-7-pentacosene/pentacosane
(Z,Z)-7,11-heptacosadiene/pentacosane
****

Figure 5.2 A diet high in linoleic acid does not substantially alter most cuticular hydrocarbons
GC-MS analysis of flies exposed to a diet high in linoleic acid (20 mM) show very few alterations to the cuticular hydrocarbon blend. Results show replicates from three independent experiments with n=12-14 over the three experiments.
A. Schematic of dietary manipulation. Isogenic flies were fed a diet high in linoleic acid throughout development and into adulthood at 25℃. Flies were separated by sex 24 hours after eclosion. Samples were collected seven days after eclosion.
B. Relative hydrocarbon abundance shown for male and female flies, normalised to the mean of the control for each gender. Green indicates a statistically significant increase and red indicates a statistically significant decrease. Statistical significance is as follows- Female: nonacosane (***), 2-methyldocosane (**), B x,x-pentacosadiene (****), x,x-heptacosadiene (*); Male: tricosane (*), nonacosane (*), B x,x-pentacosadiene (****).
C. Absolute abundance of hydrocarbons as determined using commercial standards.
D. Ratiometric analysis of desaturation index using two different alkenes, and in females using a diene.

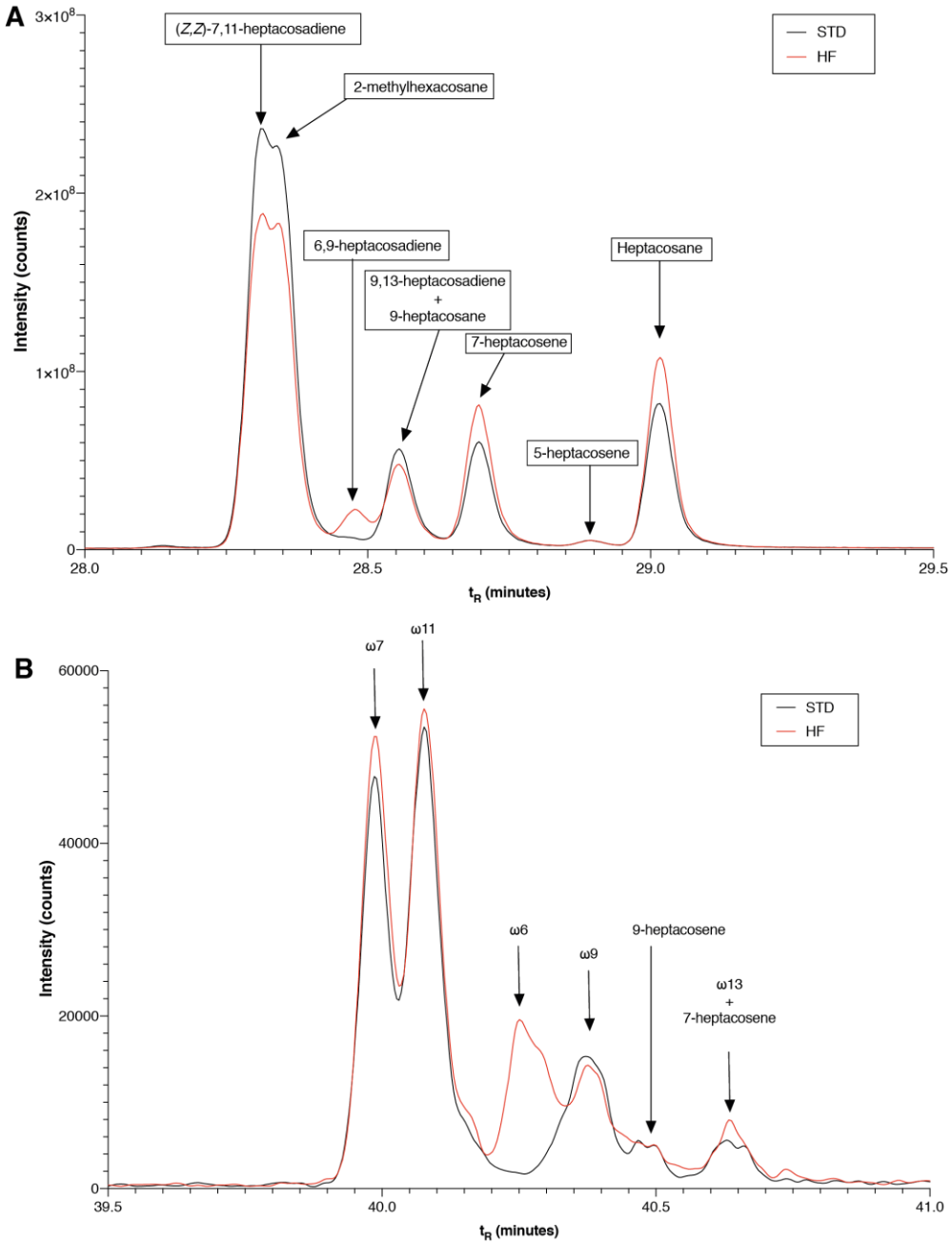

Figure 5.3 Biosynthesis of a novel diene in females fed a HF diet

A. Underivatised chromatogram of a STD and HF female fly extract illustrating the presence of 6,9-heptacosadiene in HF flies but not in STD flies.
B. DMDS derivatised hydrocarbons from STD and HF female flies, showing the identified double bond positions in heptacosadiene. The chromatogram shows the trace of the *m/z* 421 ion, a main fragment of all isomers of heptacosadiene.

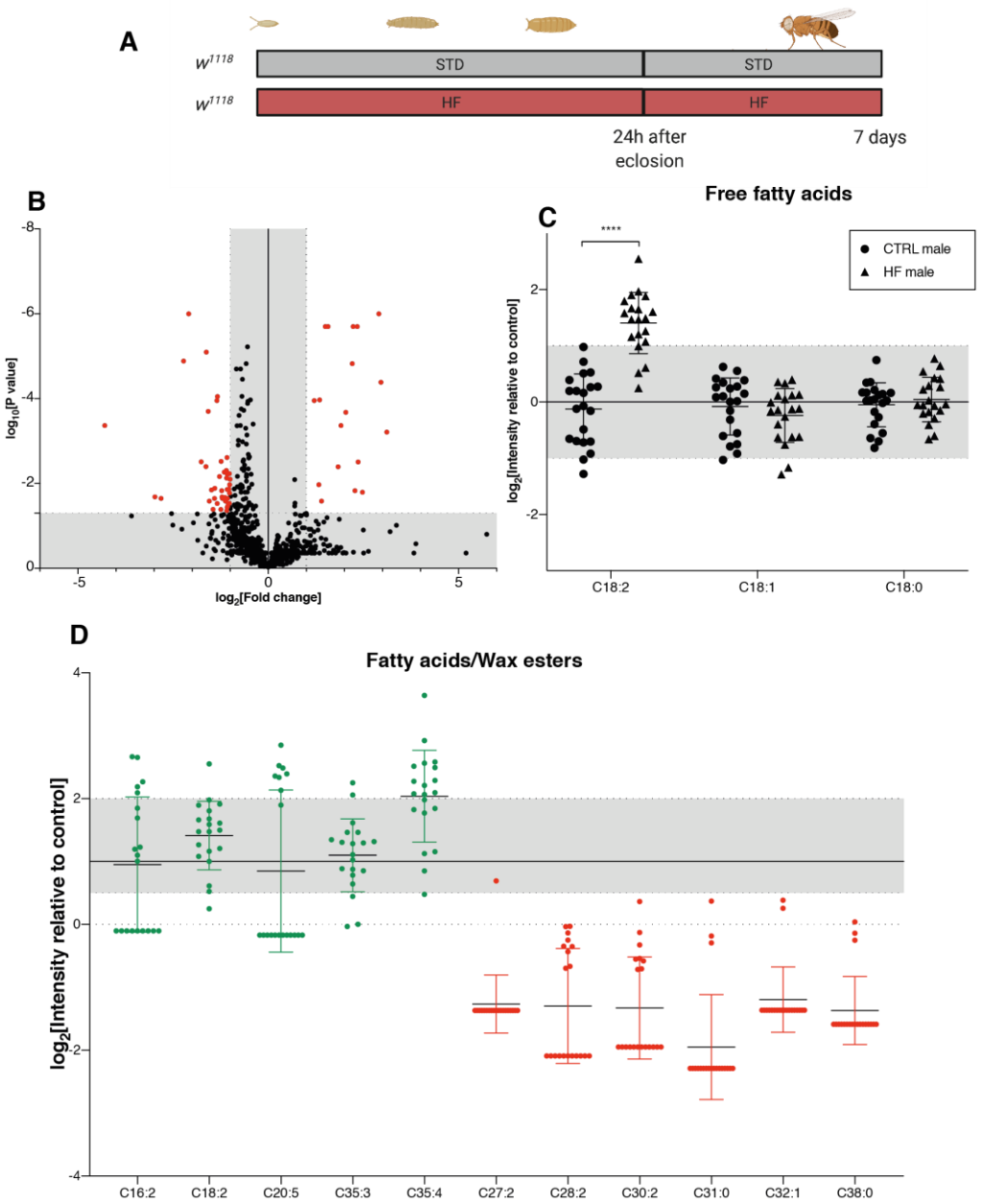

Figure 5.4 A diet high in linoleic acid increases the desaturation of wax esters
OrbiSIMS analysis of flies exposed to a diet high in linoleic acid (20 mM) throughout development show an alteration in wax ester saturation levels.
(**A**) Schematic of dietary manipulation. Isogenic flies were raised at 25 ℃ on a diet high in linoleic acid (20 mM) throughout development and adulthood. Samples were collected at seven days post-eclosion.
(**B**) Volcano plot illustrating statistically significant peaks using multiple Students' T tests with correction for multiple comparisons using a FDR of 5%. Data points highlighted in red represent those that are both statistically significant, and greater than two-fold change from the control. The y axis P value represents the value after correction for multiple comparisons. P value and fold change are plotted on a $\log_2$ scale.
(**C**) Abundance of C18 free fatty acids of varying saturation indexes normalised to the mean of the control, and plotted on a $\log_2$ scale.
(**D**) Putatively annotated, statistically significant results from untargeted OrbiSIMS analysis. Data is plotted on a $\log_2$ scale, relative to the mean of the control and representative of two independent replicates.

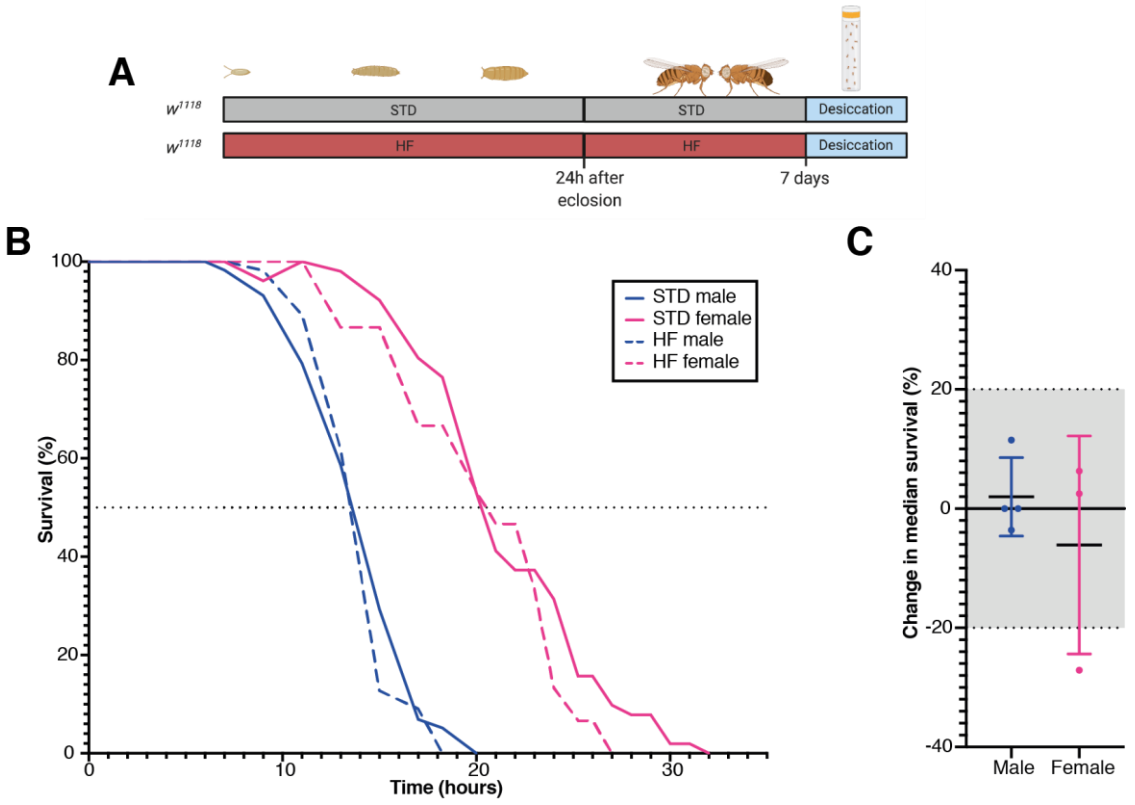

Figure 5.5 A high linoleate diet does not substantially alter desiccation resistance
A. Experimental paradigm. Flies were raised on a diet high in linoleic acid throughout development and adulthood. Within 24 hours after eclosion, flies were separated by sex, and housed at a density of 15 flies/vial on HF food for a further week before the desiccation assay was performed.
B. One example desiccation curve of three independent replicates (four in males). The dotted line on the Y axis indicates 50% survival. In this experiment Male STD=159, Male HF=110, Female STD=91, Female HF=55. Median survivals are as follows: Male STD=13.5 hours, Male HF=13.5 hours (0% change compared with STD), Female STD=20 hours, Female HF=20.5 hours (+2.5% change compared with STD). Additional independent experimental replicates are shown in **Supplementary Figure 9.23** located in the Supplementary Material.
C. Comparison of three (female) or four (male) independent experiments showing the percentage change in median survival for HF flies compared with STD flies. Each point represents an independent experimental replicate plotted relative to the STD control in that experiment, and the error bars indicate standard deviation. Neither males nor females appear to exhibit altered desiccation resistance in response to a high fat diet.

Another nutritional paradigm used to study developmental programming in *Drosophila* is to lower the yeast content of the diet ~20 fold, from ~2% to 0.1%. Using GC-MS, Stefana et al. (2017) showed that this developmental low yeast (LY) diet gives rise to slower developing and small flies with a longer median lifespan than STD controls when raised from adult eclosion on several, although not all, adult diets tested. The developmental LY diet also leads to a decrease in the alkene-to-alkane desaturation index of adult cuticular hydrocarbons. To follow this up, I began using a cornmeal-agar diet with -/1% yeast (LY), identical to that used by Stefana et al. (2017). However, since moving Institutes and changing batches of fly food ingredients, a cornmeal-agar diet with 0% yeast (ØY) has been shown by others in the Gould lab to more closely replicate the fly weights reported by Stefana et al. (2017). Importantly, this is not a zero protein diet as some dietary protein still comes from the cornmeal (Bruce et al., 2013).

Using the OrbiSIMS techniques developed in Chapter 3, I set out to determine whether LY developmental diet changes non-hydrocarbon cuticular lipids. OrbiSIMS analysis of male flies at one week after eclosion indicated that a LY developmental diet induces a large increase in the proportion of total signal represented by fatty acid and wax ester signals (**Figure 5.6**). This result indicates that developmental diet can programme non-hydrocarbon as well as hydrocarbon cuticular lipids.

After determining that developmental diet does indeed have a significant impact on cuticular lipids, it was important to determine if this has a functional consequence to the organism. As shown by Stefana et al. (2017), a LY diet not only has a functional consequence on lifespan, but also affects responses to several physiological stresses, increasing ethanol resistance and decreasing paraquat resistance. Given the increased alkene-alkane ratio, I therefore tested the resistance of LY flies to desiccation stress. In this experiment, LY flies of both sexes showed a decrease in survival of 2.5 hours compared to their STD counterparts – a decrease of ~25% for males and a decrease of ~10% for females (**Figure 5.7**). Size might be expected to have a significant impact on desiccation survival as a smaller fly would have a larger surface:volume ratio over which to

lose water. However, it is clear that this cannot be the only factor that is influencing desiccation resistance as the ØY females are smaller than STD males, yet have a longer median survival.

qPCR of a small panel of genes thought to be involved in hydrocarbon and/or wax ester biosynthesis revealed an increase of ~2 fold in the expression of *Far* (*CG17562*) (**Figure 5.8**). Adult oenocyte-specific knockdown of this gene has been shown to decrease alkene levels in females but not in males (Chiang et al., 2016) However, conflicting data shows expression of this gene in embryos but not in adult flies (Finet et al., 2019). My qPCR data and detection in an RNASeq dataset (showing ~40 fold in oenocytes compared with whole body, using RiboTag technology) (Huang et al., 2019), combined with the RNAi phenotype shown by Chiang et al. (2016) suggest that it is likely that this gene is indeed expressed in adults. As the expression is increased, it is unlikely it is responsible for the change in cuticular hydrocarbon saturation index observed by Stefana et al. (2017). However, given that Far is predicted to encode a fatty acyl reductase involved in the synthesis of fatty alcohols, it may well contribute to the biosynthesis of wax esters. This would provide a potential mechanism for the observed increase in cuticular wax esters that I observe.

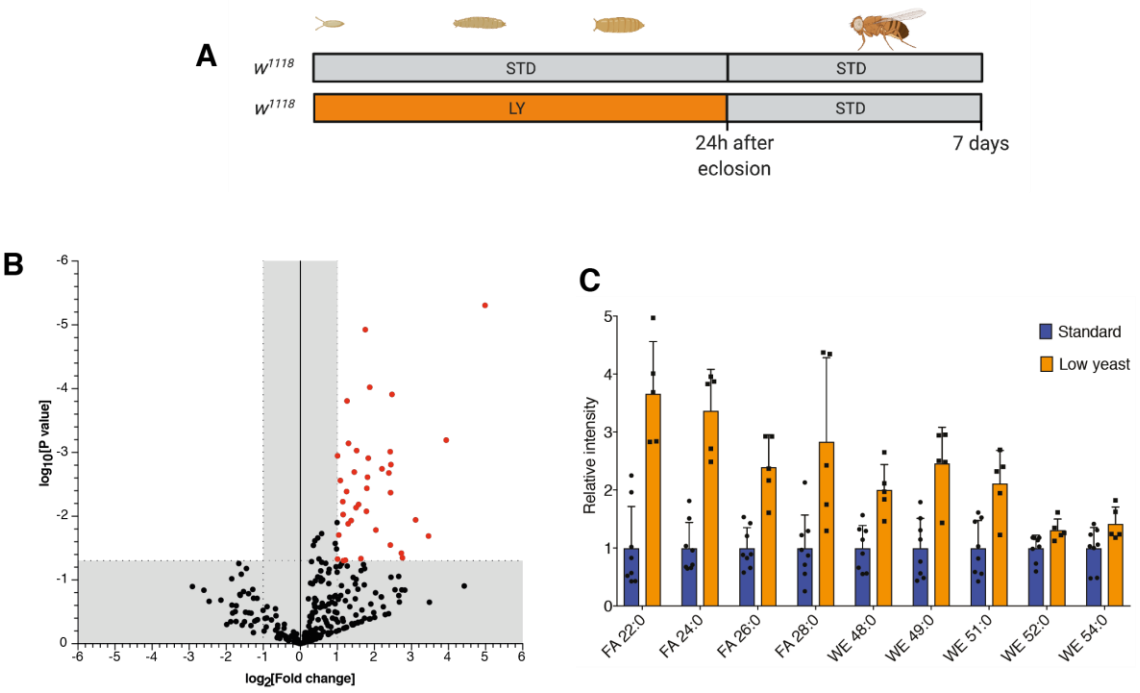

Figure 5.6 A low yeast developmental diet increases adult cuticular wax esters

A. Male flies were raised on either a standard diet, or a diet containing 0.1% yeast (LY) during development. Within 24 hours of eclosion, flies were transferred to a standard diet for seven days before analysis,
B. Volcano plot showing the fold change between STD and LY male flies for all mass spectral peaks detected with ambient temperature OrbiSIMS analysis.
C. Relative intensity of lipids significantly altered in LY male flies compared with STD flies, normalised to the mean of the value for the STD sample group.

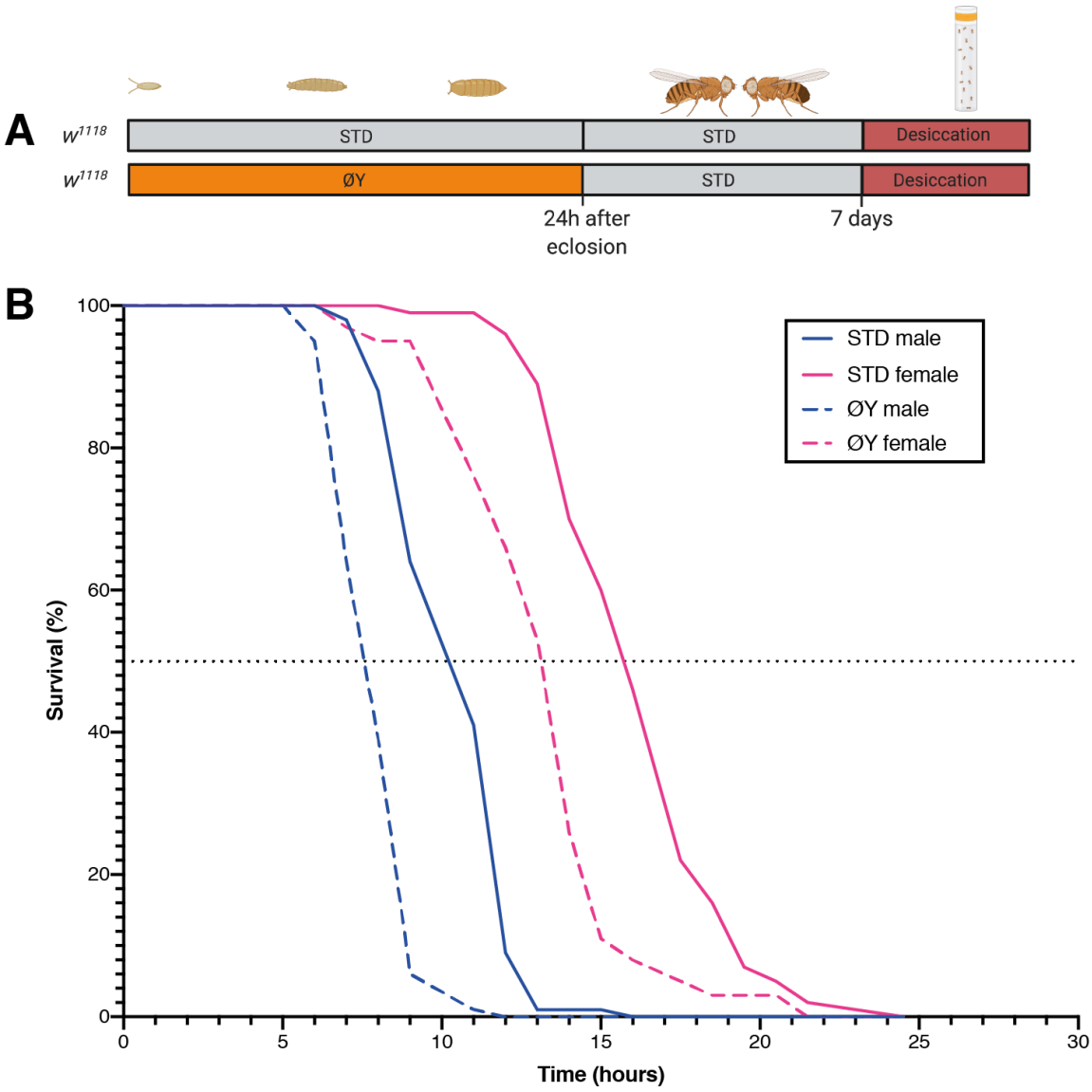

Figure 5.7 ØY flies show increased sensitivity to desiccation stress
Survival of STD and ØY flies when exposed to a low-humidity desiccating environment. STD males show a median survival of ~10h, ØY males show a median survival of ~7.5h, STD females show a median survival of ~15.5h and ØY females show a median survival of ~13h. This represents a ~25% decrease in median survival for males and a ~10% decrease in median survival for females. Data shown is one representative experiment from two independent experiments (one for females). The second male replicate is shown in **Supplementary Figure 9.24** located in the Supplementary Material.

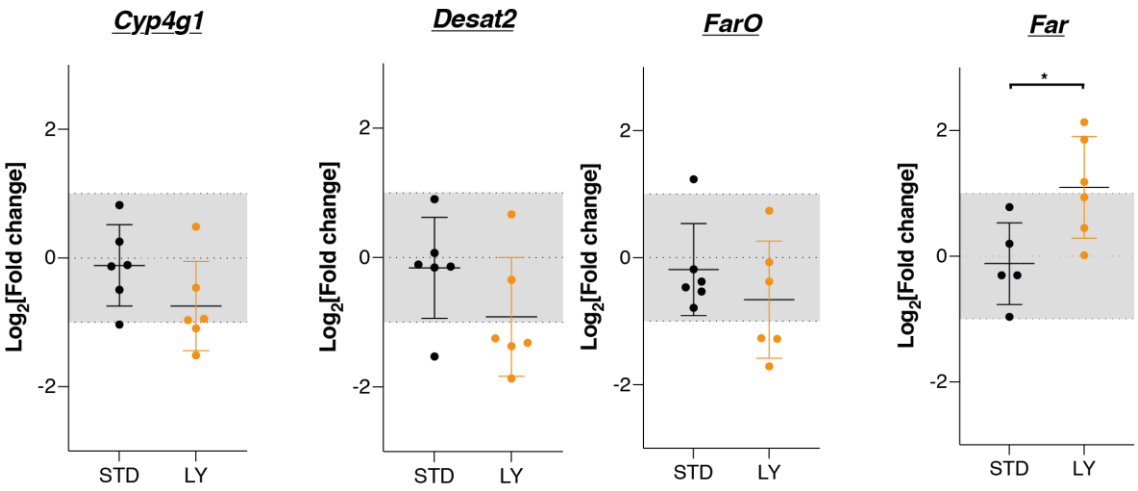

Figure 5.8 Differential expression of fatty acyl-CoA reductase in LY flies

mRNA expression of hydrocarbon and wax ester biosynthetic enzymes in whole male flies as determined with qPCR. Expression is shown relative to the mean of the control using *RP49* as a reference gene. Each datapoint represents one sample which is composed of seven flies (STD) or ten flies (LY) to compensate for the decreased size.

5.3 Developmental diet contributes carbons to adult cuticular lipids

The yeast content of the developmental diet is known to influence the adult cuticular hydrocarbon blend (**Figure 5.6**) (Stefana et al., 2017). Building upon this observation, I set out to understand at which point during development the hydrocarbon and non-hydrocarbon components of the cuticular lipid barrier are produced. In principle, these lipids could be synthesised in a one-off "burst" during pupariation, continuously throughout adulthood, or a via combination of both. To address this question, three different stable isotope tracer regimes using ^{13}C labelled nutrients were developed (**Figure 5.9**). As hydrocarbons are reported to be synthesised via *de novo* fatty acid synthesis (Dembeck et al., 2015), it is reasonable to assume that glucose is a suitable dietary substrate for this pathway. An alternative carbon source of acetate, which is a more direct precursor of *de novo* fatty acid synthesis, was also used during adulthood. Using these three developmental versus adult labelling regimes, hydrocarbons were measured via GC-MS and other lipid classes via OrbiSIMS.

Figure 5.9 U-^{13}C glucose and $^{13}C_2$ acetate labelling regimes

Three different stable isotope labelling regimes used in this study. Green indicates addition of stable isotope label and red indicates no stable isotope label (standard food).

The male sex pheromone (*Z*)-11-Vaccenyl acetate (cVa) provides an interesting control for hydrocarbon biosynthesis. This compound is produced by the male accessory gland and not by the oenocytes (Ejima et al., 2007), and is synthesised through elongation of palmitic acid (**Figure 5.10**). The pattern of ^{13}C incorporation from both developmental U-^{13}C glucose and adult U-^{13}C glucose show a sharp peak at two ^{13}C atoms per molecule, and a second broader peak at between 7-9 ^{13}C atoms per cVa molecule (**Figure 5.11B,C**). This label incorporation pattern is consistent with dietary glucose carbons from either the developmental or adult diets contributing to both the palmitate (C16:0) synthesis and subsequent elongation steps of cVa production. The developmental labelling regime results could be explained by ^{13}C incorporation into de novo synthesised fatty acids and storage as triglycerides in the larval fat body. The developmental fatty acids could then be liberated by histolysis of the larval fat body in the late pupa and early adult (Nelliot et al., 2006, Aguila et al., 2007), and used as precursors for cVa biosynthesis. For the adult U-^{13}C labelling regime, although the proportion of labelled molecules increases with time, the peaks at M+2 and M+8 labelled carbons per molecule are retained (**Figure 5.11C**). The $^{13}C_2$ acetate adult diet regime indicates a fractional labelling pattern with a single peak at 2 carbons per cVa molecule, supporting a contribution mainly to the elongation rather than the de novo synthesis of palmitic acid (**Figure 5.11D**). Together, these results suggest that glucose from the developmental and adult diets is the major carbon source for cVa biosynthesis.

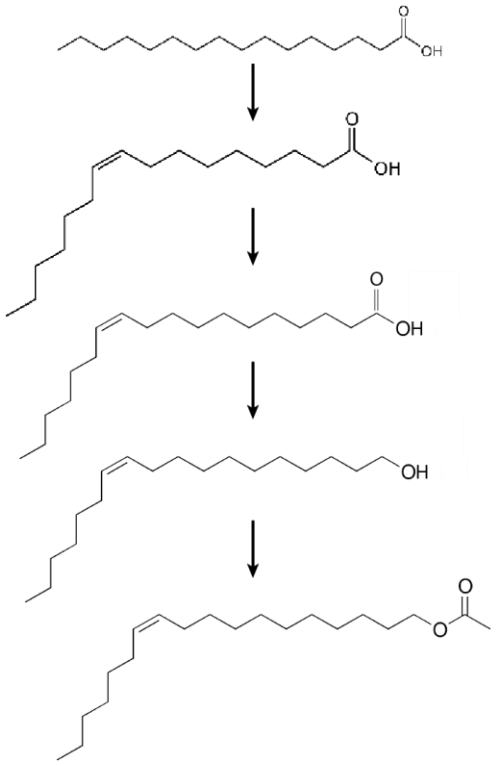

Figure 5.10 Biosynthetic pathway for (*Z*)-11-Vaccenyl acetate

Biosynthesis of (*Z*)-11-Vaccenyl acetate (cVa) from dietary palmitic acid. Information from Guiraudie-Capraz et al. (2007)

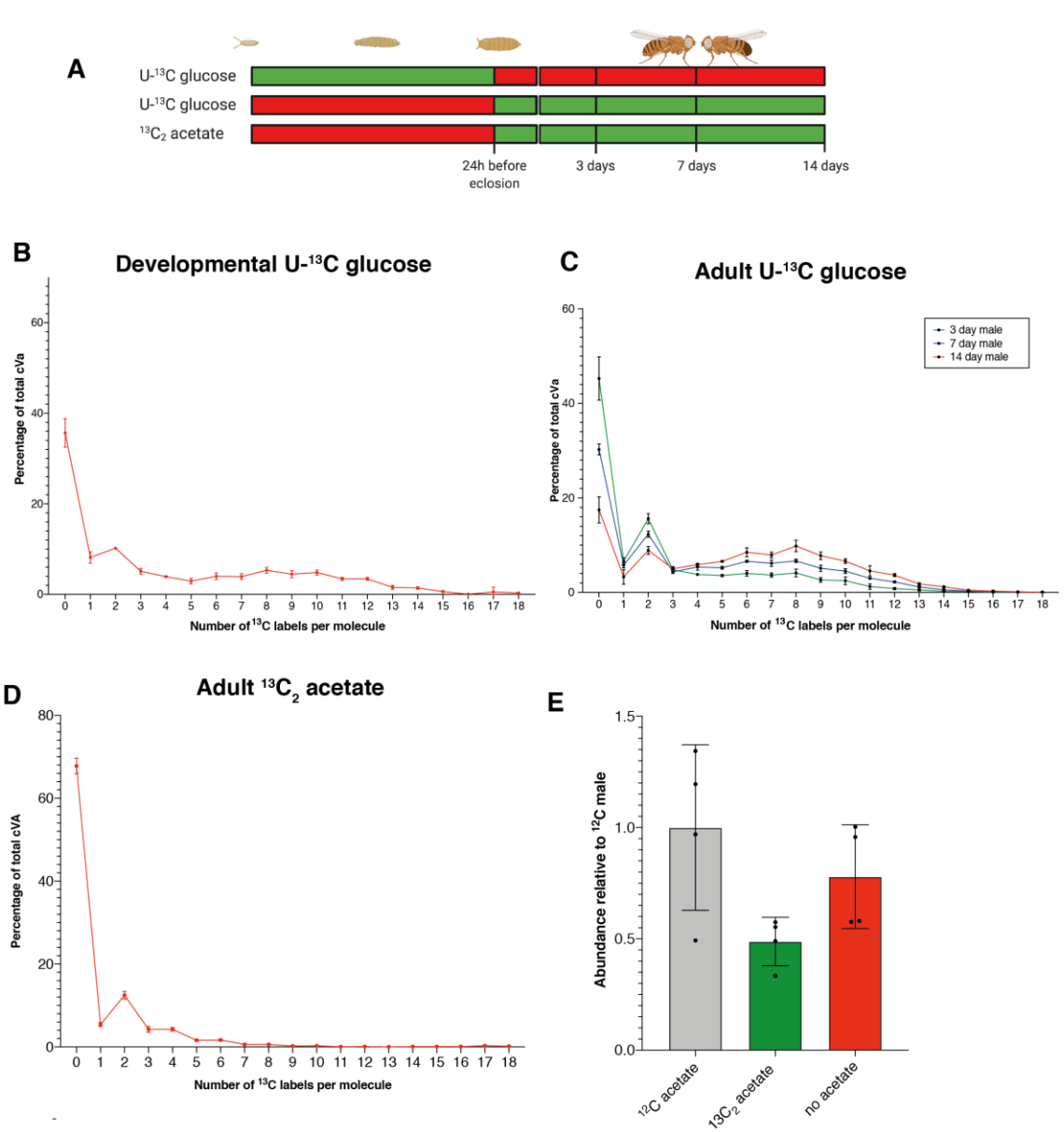

Figure 5.11 ^{13}C incorporation into cVa for the three different labelling regimes

A. Experimental schematic. Green indicates label feeding and red indicates no label feeding.
B-D. Fractional incorporation of ^{13}C into (*Z*)-11-Vaccenyl acetate (cVa) calculated from GC-MS data. **B** and **D** show label incorporation after seven days.
E. Total abundance of cVa in $^{13}C_2$ acetate, ^{12}C acetate and no acetate conditions. There is no significant difference between these conditions as determined with one-way ANOVA.
Datapoints show the mean of four replicates and error bars are standard deviation. Each replicate is composed of hexane extract from five flies.

Adult diet labelled with U-^{13}C glucose resulted in rapid ^{13}C incorporation into adult cuticular hydrocarbons. Following three days of post-eclosion exposure to a U-^{13}C glucose diet, nearly 100% of all tricosane molecules from both males and females contained at least one ^{13}C label (**Figure 5.12**). The pattern of adult dietary U-^{13}C glucose incorporation occurred in a pattern whereby the numbers of ^{13}C labels per molecule increased with time and all hydrocarbon classes appeared to behave in a similar way (**Figure 5.13**). These results indicate rapid adult biosynthesis and turnover of hydrocarbons, perhaps reflecting requirements for abundant hydrocarbons as sex pheromones as well as part of the desiccation barrier. As the proportion of labelled carbons within a single hydrocarbon molecule increases from 3 to 14 days post-eclosion, it is likely that unlabelled carbons from developmental stores are gradually replaced over time with the labelled ones derived from the adult diet.

Developmental diet labelled with U-^{13}C glucose yielded a much more restricted pattern of fractional labelling than for adult diet containing U-^{13}C glucose (**Figure 5.14**). Furthermore, the patterning of ^{13}C incorporation shows a peak at two ^{13}C atoms (M+2) per hydrocarbon molecule (**Figure 5.14B, C, G, H**). This is compatible with the hypothesis that acetyl-CoA and malonyl-CoA from developmental stores contribute, with this experimental tracer-to-tracee ratio, an average of 2-3 carbons per hydrocarbon precursor. After Cyp4g1 decarbonylation, this will correspond to an average of 1-2 carbons in the final hydrocarbon molecule. Given that using an identical tracer-to-tracee ratio of U-^{13}C glucose in the adult diet gives an average of 6-7 labelled carbons per hydrocarbon molecule, it is clear that carbons from the developmental diet contribute less to hydrocarbon molecules than those from the adult diet. As expected, increasing the percentage of labelled glucose (the tracer-to-tracee ratio) in the developmental diet led to a corresponding increase in proportion of hydrocarbons containing at least one ^{13}C (**Figure 5.14C-D**). Interestingly, however, the pattern of fractional label incorporation of 1-2 carbons per hydrocarbon molecule did not change substantially, suggesting that there is a block to the incorporation of 3 or more ^{13}C atoms (**Figure 5.14C**). This unexpected observation indicates that U-^{13}C glucose from the developmental diet

is stored in pupae in a form that contributes, via acetyl-CoA and malonyl-CoA, very specifically to only one or two elongation steps of the fatty acid precursors of hydrocarbons. Adult diet labelled with $^{13}C_2$ acetate was also used to probe hydrocarbon biosynthesis. This dietary regime required a carful control for osmotic stress as the labelled sodium acetate contributes 20 mM sodium to the diet. However, lethality is only reached when the salt concentration is ~400 mM and some lines can tolerate a salt concentration of up to 1 M (Riedl et al., 2016). Compared to no acetate, unlabelled ^{12}C acetate notably decreases cuticular hydrocarbons in males but not in females (**Figure 5.15C, F**). This may explain why females show a higher proportion of label incorporation (**Figure 5.15D, G**). However, the pattern of label incorporation remained the same in both males and females (**Figure 5.15B, E**). One might expect the ^{13}C labelling pattern in this scenario to look much like that seen with adult U-^{13}C glucose, but it more closely reflected that of the developmental U-^{13}C glucose regime (**Figure 5.15)**. This suggests that dietary acetate, like developmental dietary glucose, only contributes to one or two steps of elongation in the precursors of hydrocarbons. Together the labelled acetate and glucose tracing experiments suggest the surprising conclusion that something other than glucose in the developmental diet contributes the majority of carbons to the early phase of hydrocarbon synthesis during the peri-eclosion period. To clarify the source of developmental carbon contribution, adult hydrocarbons could be analysed peri-eclosion in flies that hatch onto PBS/agar and therefore would not have any carbon contribution from the adult diet. This experiment could be performed using $^{13}C_2$ acetate, or ^{13}C glutamine in the case that the carbon source originates from the breakdown of larval protein.

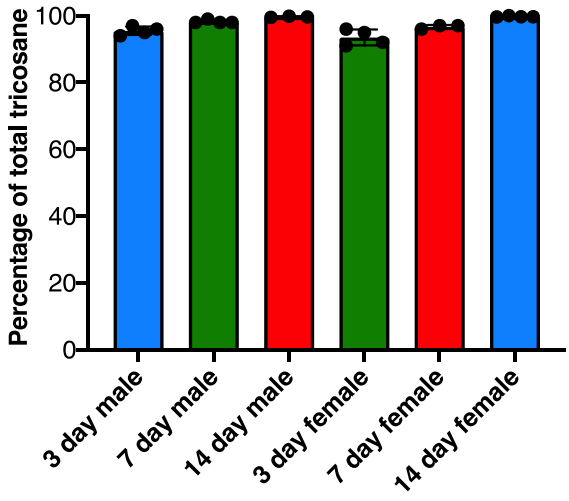

Figure 5.12 Percentage of ^{13}C labelled tricosane molecules after 3-14 days on an adult U^{13}C glucose diet

Percentage of tricosane molecules containing at least one ^{13}C label as calculated by GC-MS. Each datapoint represents one sample composed of hexane extract from five flies. Error bars represent standard deviation.

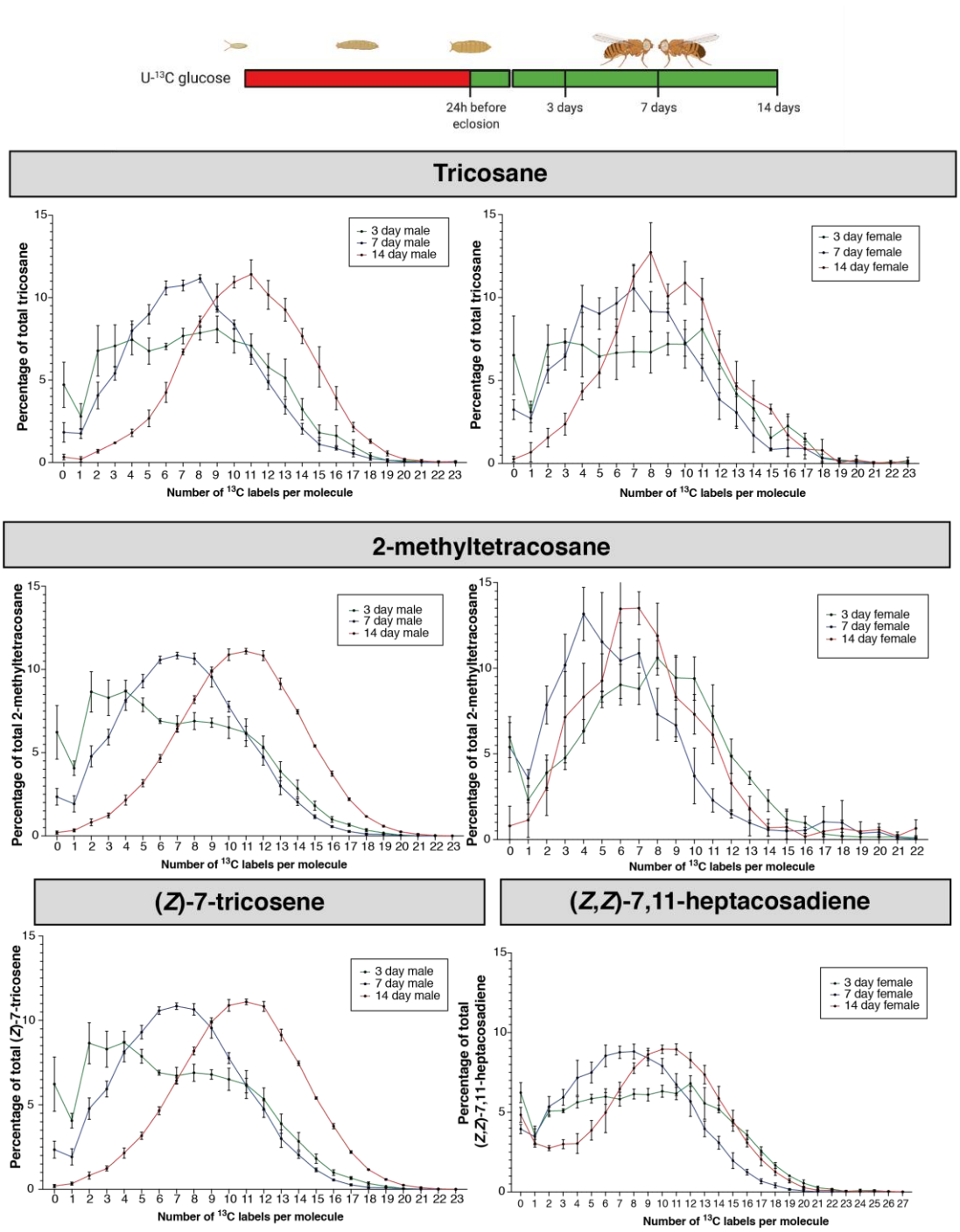

Figure 5.13 Adult dietary U-^{13}C glucose incorporation into hydrocarbons

Fractional incorporation of ^{13}C from U-^{13}C glucose into hydrocarbons calculated from GC-MS data. Flies were fed a diet with 100% of added glucose replaced with U-^{13}C glucose throughout adulthood. Datapoints show the mean of four biological replicates and error bars are standard deviation.

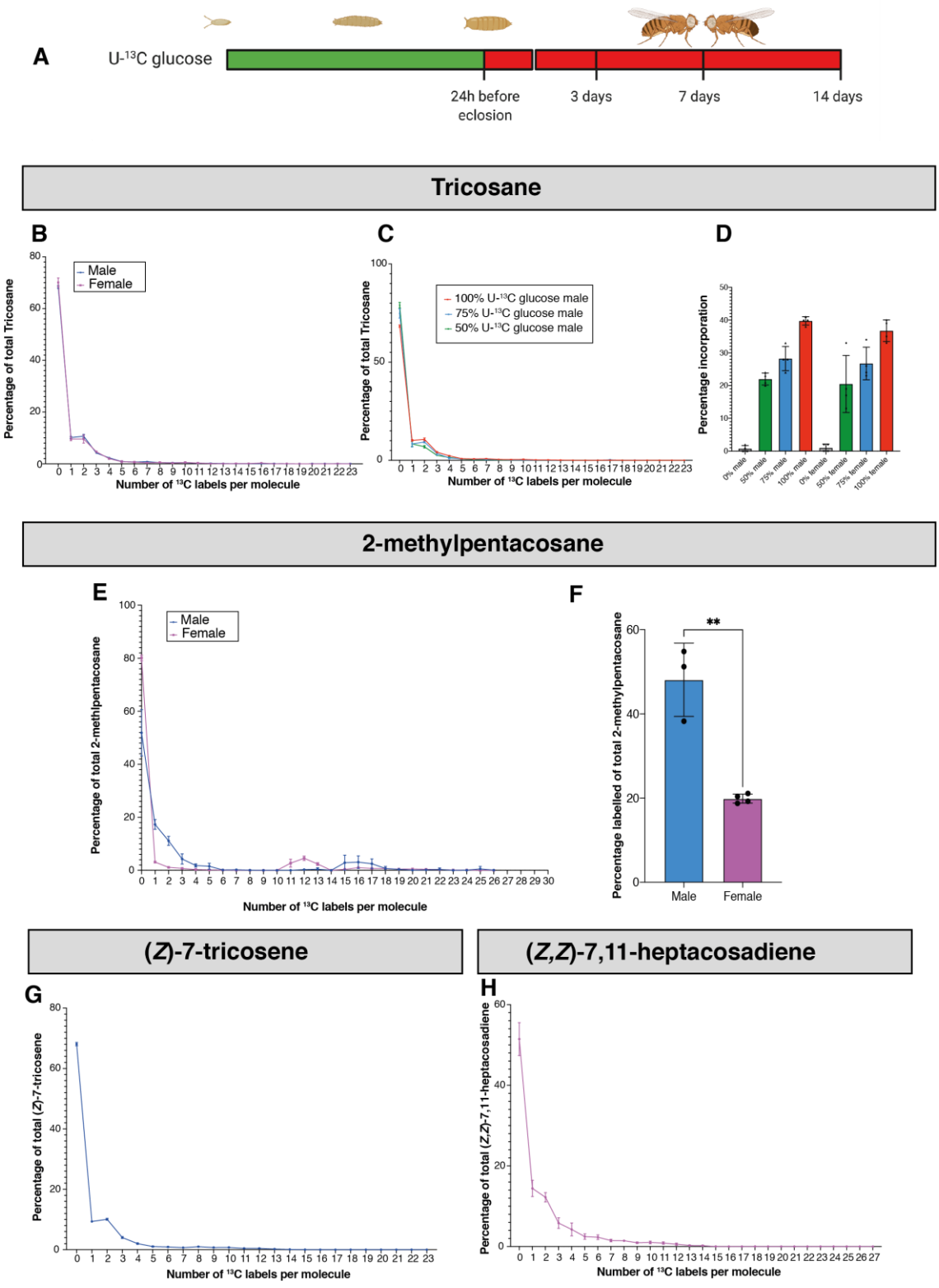
A
U-13C glucose
24h before eclosion
3 days
7 days
14 days
Tricosane
B
Male
Female
Percentage of total Tricosane
Number of 13C labels per molecule
C
100% U-13C glucose male
75% U-13C glucose male
50% U-13C glucose male
Percentage of total Tricosane
Number of 13C labels per molecule
D
Percentage incorporation
0% male
50% male
75% male
100% male
0% female
50% female
75% female
100% female
2-methylpentacosane
E
Male
Female
Percentage of total 2-methlpentacosane
Number of 13C labels per molecule
F
**
Percentage labelled of total 2-methylpentacosane
Male
Female
(Z)-7-tricosene
G
Percentage of total (Z)-7-tricosene
Number of 13C labels per molecule
(Z,Z)-7,11-heptacosadiene
H
Percentage of total (Z,Z)-7,11-heptacosadiene
Number of 13C labels per molecule

Figure 5.14 Developmental dietary U-^{13}C glucose incorporation into hydrocarbons

A. Experimental schematic with green indicating periods of label feeding and red indicating no label feeding. Larvae were transferred onto food containing U-^{13}C glucose (0%, 50%, 75% or 100% of added glucose as U^{13}C glucose) within two hours of hatching. Pupae were transferred to unlabelled food 24h before eclosion. Hydrocarbons were extracted 7 days after eclosion and analysed by GC-MS.
B. Fractional label incorporation into tricosane showing both male and female flies with 100% U-^{13}C glucose at a timepoint of seven days post-eclosure. Data represents the mean of four replicates and error bars represent standard deviation.
C. Fractional label incorporation into tricosane in male flies showing the difference between 50%, 75% and 100% U^{13}C glucose in the developmental diet. Data represents the mean of four replicates and error bars represent standard deviation.
D. Percentage of molecules of tricosene containing one or more ^{13}C labels with the different labelling regimes of 50%, 75% or 100% U^{13}C glucose during development. Each datapoint represents one sample composed of hexane extract from five flies. Error bars represent standard deviation.
E. Fractional label incorporation into 2-methylpentacosane showing both male and female flies with 100% U-^{13}C glucose at a timepoint of seven days post-eclosure. Data represents the mean of four replicates and error bars represent standard deviation.
F. Percentage of 2-methylpentacosane molecules containing one or more ^{13}C labels in males and females on a 100% U-^{13}C glucose developmental diet. Each datapoint represents one sample composed of hexane extract from five flies. Error bars represent standard deviation.
G. Fractional label incorporation into (*Z*)-7-tricosene in male flies on a 100% U-^{13}C glucose developmental diet. Data represents the mean of four replicates and error bars represent standard deviation.
H. Fractional label incorporation into (*Z*,*Z*)-7,11-heptacosadiene in female flies on a 100% U-^{13}C glucose developmental diet. Data represents the mean of four replicates and error bars represent standard deviation.

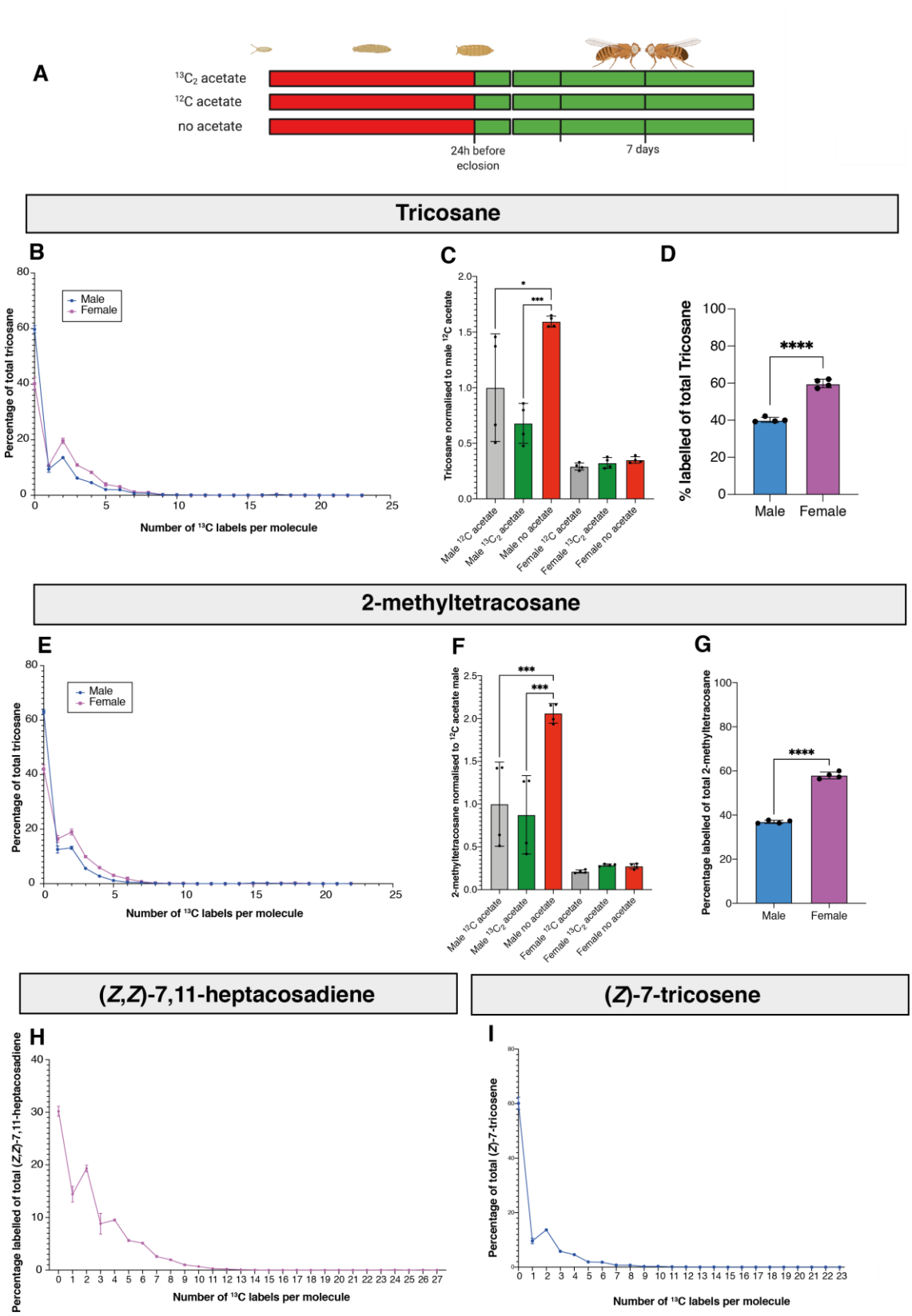
A
$^{13}C_2$ acetate
^{12}C acetate
no acetate
24h before eclosion
7 days
Tricosane
B
Male
Female
Percentage of total tricosane
Number of ^{13}C labels per molecule
C
Tricosane normalised to male ^{12}C acetate
Male ^{12}C acetate
Male $^{13}C_2$ acetate
Male no acetate
Female ^{12}C acetate
Female $^{13}C_2$ acetate
Female no acetate
D
% labelled of total Tricosane
Male
Female
2-methyltetracosane
E
Male
Female
Percentage of total tricosane
Number of ^{13}C labels per molecule
F
2-methyltetracosane normalised to ^{12}C acetate male
Male ^{12}C acetate
Male $^{13}C_2$ acetate
Male no acetate
Female ^{12}C acetate
Female $^{13}C_2$ acetate
Female no acetate
G
Percentage labelled of total 2-methyltetracosane
Male
Female
(Z,Z)-7,11-heptacosadiene
(Z)-7-tricosene
H
Percentage labelled of total (Z,Z)-7,11-heptacosadiene
Number of ^{13}C labels per molecule
I
Percentage of total (Z)-7-tricosene
Number of ^{13}C labels per molecule

Figure 5.15 Adult dietary $^{13}C_2$ acetate incorporation into hydrocarbons

A. Experimental schematic with green indicating periods of label feeding and red indicating no label feeding. Pupae were transferred to food containing 20 mM $^{13}C_2$ acetate, 20 mM ^{12}C acetate or no acetate 24 hours before eclosion. Hydrocarbons were extracted seven days after eclosion and analysed by GC-MS.
B. Fractional label incorporation into tricosane in both males and females. Data represents the mean of four replicates and error bars represent standard deviation.
C. Relative abundance of tricosane in all three experimental conditions in male and female flies. Data is shown relative to the abundance of tricosane in male flies fed with ^{12}C acetate. Each datapoint represents one sample composed of hexane extract from five flies. Error bars represent standard deviation.
D. Percentage of all tricosane molecules containing at least one ^{13}C label in males and females. Each datapoint represents one sample composed of hexane extract from five flies. Error bars represent standard deviation.
E. Fractional label incorporation into 2-methyltetracosane in both males and females. Data represents the mean of four replicates and error bars represent standard deviation.
F. Relative abundance of 2-methyltetracosane in all three experimental conditions in male and female flies. Data is shown relative to the abundance of 2-methyltetracosane in male flies fed with $^{12}C_2$ acetate. Each datapoint represents one sample composed of hexane extract from five flies. Error bars represent standard deviation.
G. Percentage of all 2-methyltetracosane molecules containing at least one ^{13}C label in males and females. Each datapoint represents one sample composed of hexane extract from five flies. Error bars represent standard deviation.
H. Fractional label incorporation into (*Z*,*Z*)-7,11-heptacosadiene in female flies on an adult diet containing 20 mM $^{13}C_2$ acetate.
I. Fractional label incorporation into (*Z*)-7-tricosene in male flies on an adult diet containing 20 mM $^{13}C_2$ acetate.

OrbiSIMS imaging provides a unique platform to investigate the biosynthesis of non-hydrocarbon cuticular lipids, which are inaccessible using solvent extractions LC-MS as they fail to accurately discriminate between external (cuticular) and internal lipids. By combining OrbiSIMS with the three dietary labelling regimes (**Figure 5.9**), valuable information was obtained on the biosynthetic origin of two non-hydrocarbon cuticular lipids – a free fatty acid (C18:1) and a ceramide phosphoethanolamine (PE-Cer C36:1).

For a free fatty acid (C18:1), adult dietary U-^{13}C glucose labelling gave a pattern of incorporation that increases with time and that has a single broad peak centred at ~9 ^{13}C atoms per molecule (**Figure 5.17A-C**). This pattern is characteristic of *de novo* fatty acid biosynthesis. However, $^{13}C_2$ acetate labelling gives low incorporation but with a small M+2 peak, which may indicate that one elongation step from C16 to C18 is required for a subset of C18:1 molecules (**Figure 5.18**). The proportion of labelled molecules at 1 or 2 weeks is rather low at ~40% (**Figure 5.17B,C**). However, the same adult U-^{13}C glucose regime labelled 100% of all hydrocarbon molecules with at least one ^{13}C atom (**Figure 5.12**). These comparisons suggest the possibility that non-glucose nutrients in the adult diet, such as preformed fatty acids, make a significant contribution to cuticular fatty acids but not to hydrocarbons.

For PE-Cer(36:1), the pattern of adult dietary U-^{13}C glucose incorporation is different than for C18:1 as it shows a distinct peak at M+2 as well as the much broader peak stretching up to 21 labelled carbons per molecule (**Figure 5.17D**). This pattern therefore shows characteristics of both *de novo* fatty acid synthesis and elongation. Consistent with an elongation step, adult $^{13}C_2$ acetate labelling gives low incorporation but with a small M+2 peak into PE-Cer(36:1) (**Figure 5.18**). This can perhaps be explained by the asymmetry of the two fatty acid chains in the PE-Cer molecule (**Figure 5.16**). PE-Cer molecules in mammals typically have one carbon chain of C16:1, however in *Drosophila* this can also be C14:1 or C18:1 1 (Panevska et al., 2019). For PE-Cer(36:1), this would mean that the second fatty acid chain is likely to range from C18:0 to C22:0. If the chain

length is greater than C18:0, then at least one further elongation step of a *de novo* synthesised or diet-derived C18:0 would be required.

The most striking of the three labelling regimes was with developmental dietary U-^{13}C glucose, where much more extensive incorporation into free fatty acid (C18:1) and PE-Cer(36:1) was observed than with hydrocarbons (**Figure 5.19**). For PE-Cer(36:1), a remarkable ~90% of molecules retained at least one ^{13}C atom at one week post-eclosion, and by two weeks the value still remained high at ~60% (**Figure 5.19G**). The pattern of fractional label incorporation, with a small M+2 peak and a much broader peak stretching to ~M+24 is suggestive of *de novo* FA synthesis and elongation, and the position of these peaks does not change substantially from 1 to 2 weeks post-eclosion on a label-free diet (**Figure 5.19E, F**). In summary, the three labelling regimes provide evidence that nutrients from the developmental diet make a much greater “carry over” contribution to the non-hydrocarbons than to the hydrocarbons of the adult cuticular lipid blend during the first few weeks after eclosion. At least part of this difference may be explained by the much higher biosynthesis and more rapid turnover of hydrocarbons during the peri-eclosion period.

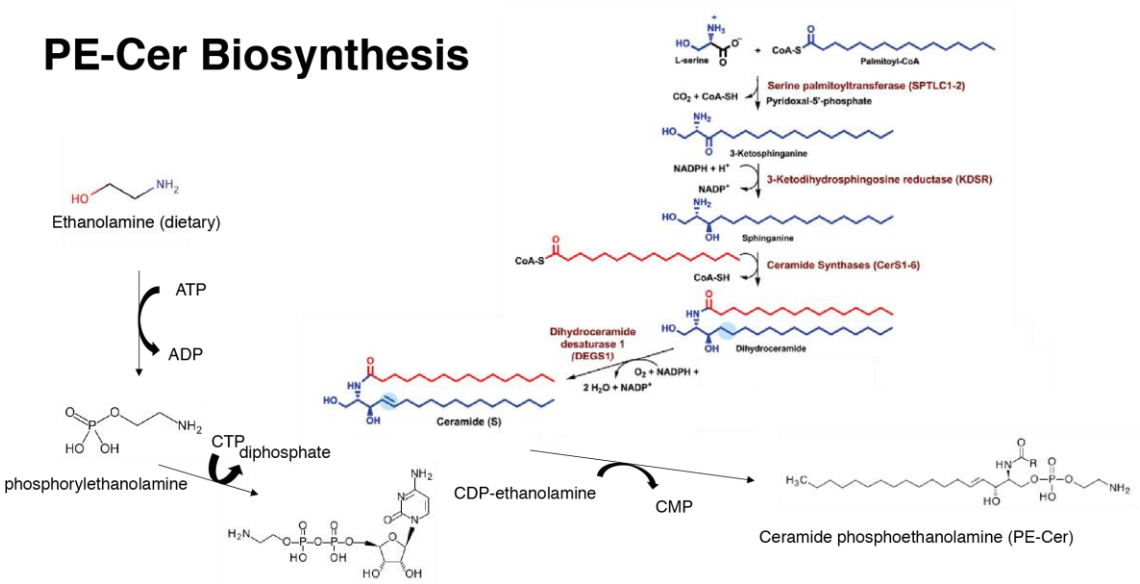

Figure 5.16 PE-Cer biosynthetic pathway

Biosynthetic pathway of ceramide phosphoethanolamines (PE-Cer). Information from Rabionet et al. (2014) and Patel and Witt (2017).

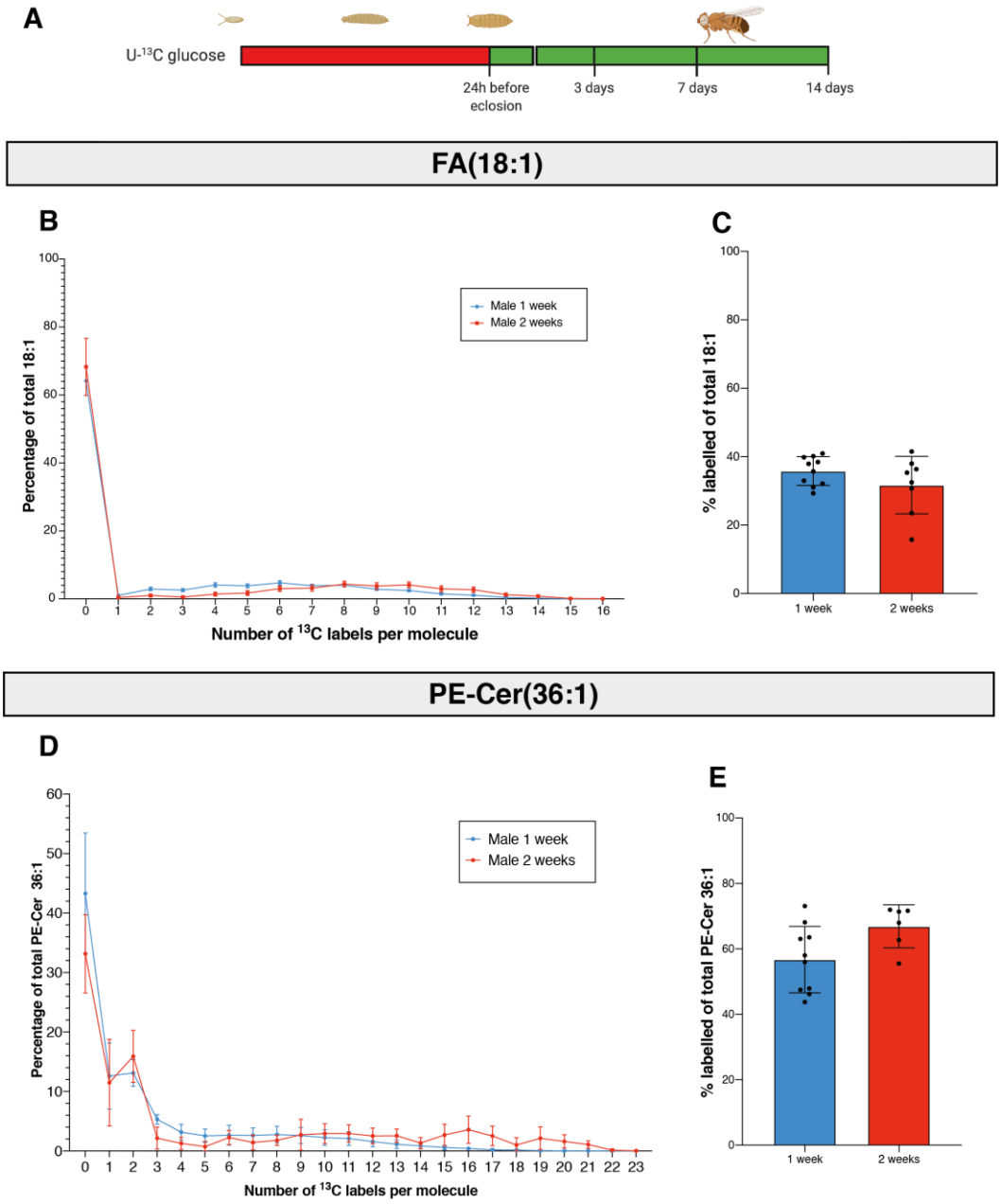

Figure 5.17 Labelling of adult cuticular lipids from U-^{13}C glucose in the adult diet

A. Experimental schematic. Pupae were transferred to food containing 100% U^{13}C glucose 24 hours before eclosion. Samples for OrbiSIMS analysis were taken at 7 and 14 days post-eclosion (1 week and 2 weeks).
B. Fractional label incorporation into FA(18:1) at one and two weeks post-eclosion in male flies. Data shown is the average of ten samples with error bars showing standard deviation.
C. Percentage of molecules containing at least one ^{13}C label at one and two weeks post-eclosion. Each datapoint represents an individual fly abdominal cuticle with error bars representing standard deviation.
D. Fractional label incorporation into PE-Cer(36:1) at one and two weeks post-eclosion in male flies. Data shown is the average of ten samples with error bars showing standard deviation.
E. Percentage of PE-Cer(36:1) molecules containing at least one ^{13}C label at one and two weeks post-eclosion. Each datapoint represents an individual fly abdominal cuticle with error bars representing standard deviation.

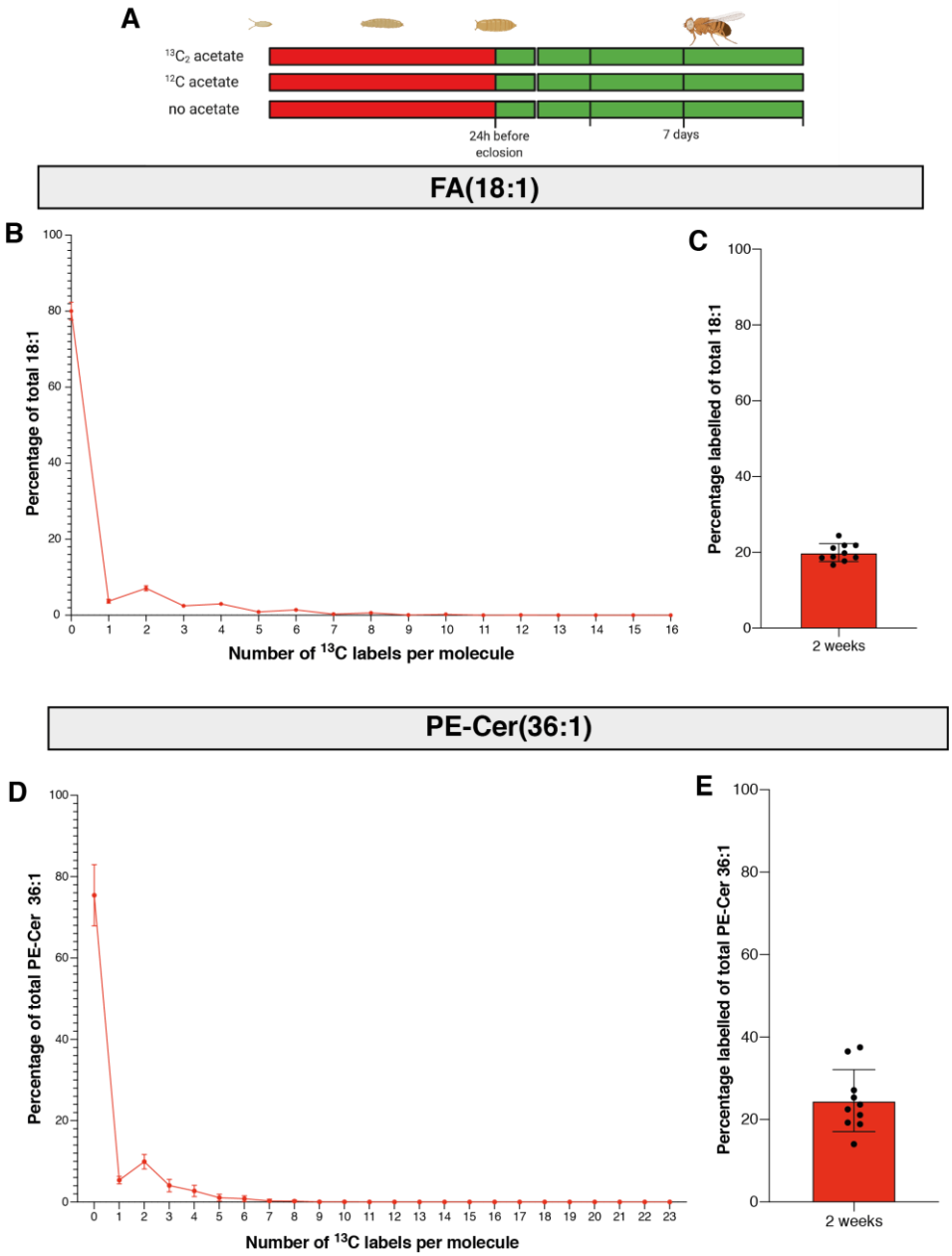

Figure 5.18 ^{13}C incorporation into adult cuticular lipids from $^{13}C_2$ acetate in the adult diet

A. Experimental schematic with green indicating periods of label feeding and red indicating no label feeding. Pupae were transferred to food containing 20 mM $^{13}C_2$ acetate, 20 mM ^{12}C acetate or no acetate 24 hours before eclosion. Abdominal cuticule samples were collected 14 days after eclosion and analysed by OrbiSIMS.
B. Fractional incorporation of 13C label into FA(18:1) at two weeks post-eclosion. Data shows the average of ten samples with error bars representing standard deviation.
C. Percentage of molecules containing at least one ^{13}C label at two weeks post-eclosion. Each datapoint represents an individual abdominal carcass with error bars representing standard deviation.
D. Fractional incorporation of 13C label into PE-Cer(36:1) at two weeks post-eclosion. Data shows the average of ten samples with error bars representing standard deviation.
E. Percentage of molecules containing at least one ^{13}C label at two weeks post-eclosion. Each datapoint represents an individual abdominal carcass with error bars representing standard deviation.

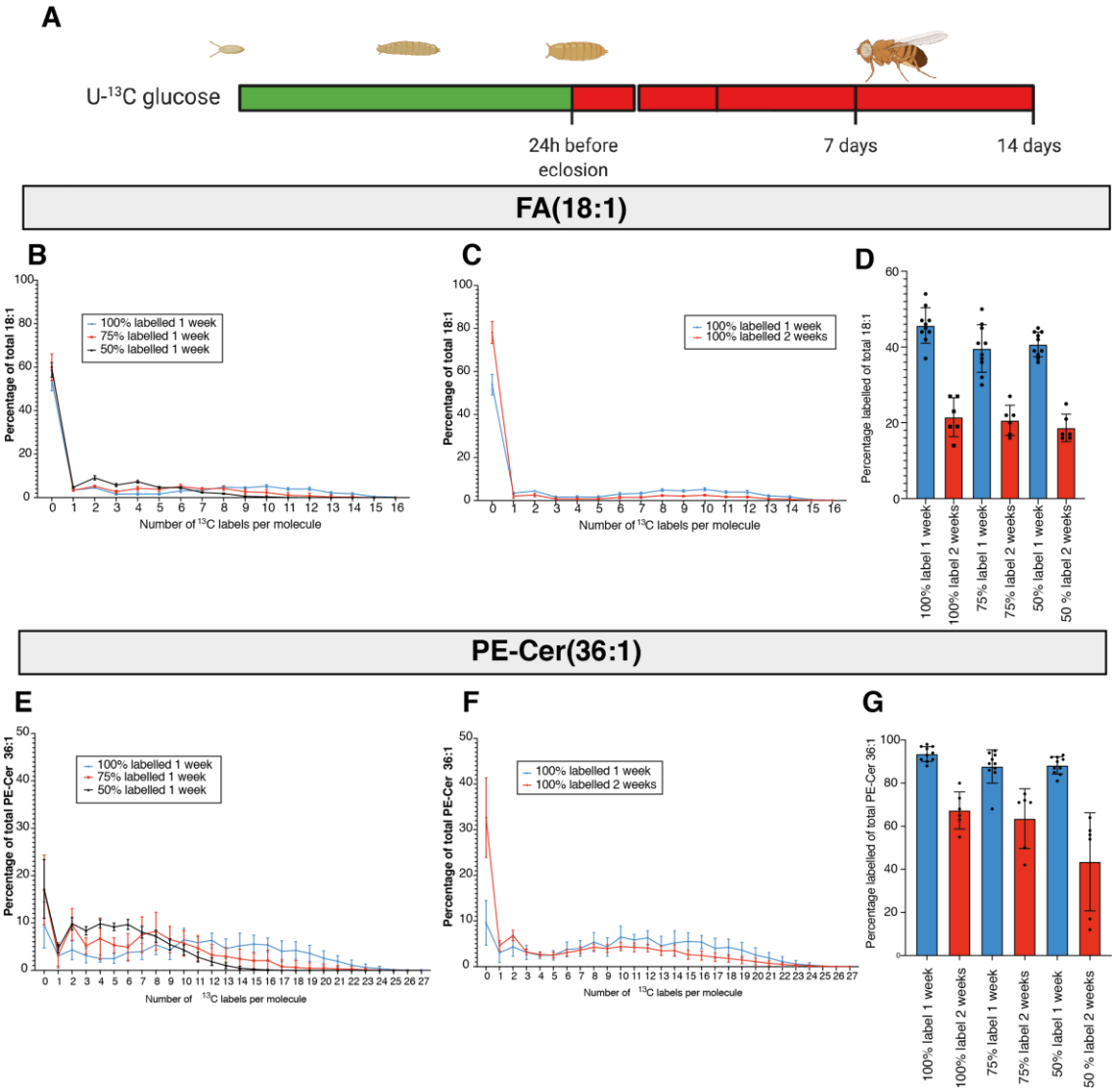

Figure 5.19 Incorporation of ^{13}C into adult cuticular lipids from developmental U-^{13}C glucose

A. Experimental schematic with green indicating periods of label feeding and red indicating no label feeding. Larvae were transferred onto food containing U-^{13}C glucose (0%, 50%, 75% or 100% of added glucose as U^{13}C glucose) within two hours of hatching. Pupae were transferred to unlabelled food 24h before eclosion. Abdominal cuticle samples were collected 7 days and 14 days post-eclosion (1 week and 2 weeks) and analysed by OrbiSIMS.
B. Fractional incorporation of ^{13}C label into FA(18:1) at one week post-eclosion with 100%, 75% or 50% of added glucose present as U-^{13}C.
C. Fractional incorporation of ^{13}C label into FA(18:1) at one week compared with two weeks post-eclosion in flies fed 100% U-^{13}C glucose during development.
D. Percentage of all FA(18:1) molecules containing at least one ^{13}C label.
E. Fractional incorporation of ^{13}C label into PE-Cer(26:1) at one week post-eclosion with 100%, 75% or 50% of added glucose present as U-^{13}C.
F. Fractional incorporation of ^{13}C label into PE-Cer(36:1) at one week compared with two weeks post-eclosion in flies fed 100% U-^{13}C glucose during development.
G. Percentage of all PE-Cer(36:1) molecules containing at least one ^{13}C label on the different dietary regimes at both timepoints.
Each datapoint represents an individual abdominal carcass with error bars representing standard deviation.

5.4 Developmental programming of skin lipids in mice

A maternal low-protein diet applied during prenatal fetal stages has been shown to result in a wide range of long-term impacts on physiology and health in rodent models (Nicholas and Ozanne, 2019). The effects of prenatal nutrient deficiency have not, however, been investigated on the skin. To do this, I used a C57Bl/6J mouse model where mothers were provided with a diet containing 4.6% protein (LP) as opposed to the 24% protein in the standard diet (STD). After transferring the mothers and pups back to a standard diet upon birth, the skin lipids of the male and female progeny were analysed via OrbiSIMS at post-natal day 42 (P42). At P0, LP pups weight ~30% less than their STD counterparts but they subsequently undergo catch up growth such that by P42, LP and STD weights are indistinguishable. Due to the current technical limitations of OrbiSIMS, it is not possible to perform quantitative analysis, therefore these data measure changes in the composition of the lipid blend relative to the total skin signal intensity. The OrbiSIMS analysis yielded surprising results, as a highly sex-specific effect was observed. Females exhibited very little change in the majority of skin lipids under these dietary conditions (**Figure 5.20**). In contrast, a substantial effect of a prenatal LP diet was observed in males (**Figure 5.21**). To further validate the OrbiSIMS results and to understand if LP males have altered absolute abundances of individual lipids, LC-MS analysis could be performed using fur from these same individuals which I have shown represents the lipid blend of the skin in Chapter 4. Nevertheless, the OrbiSIMS analysis clearly demonstrates that the LP prenatal diet programmes adult mouse skin lipids in a sex-specific manner.

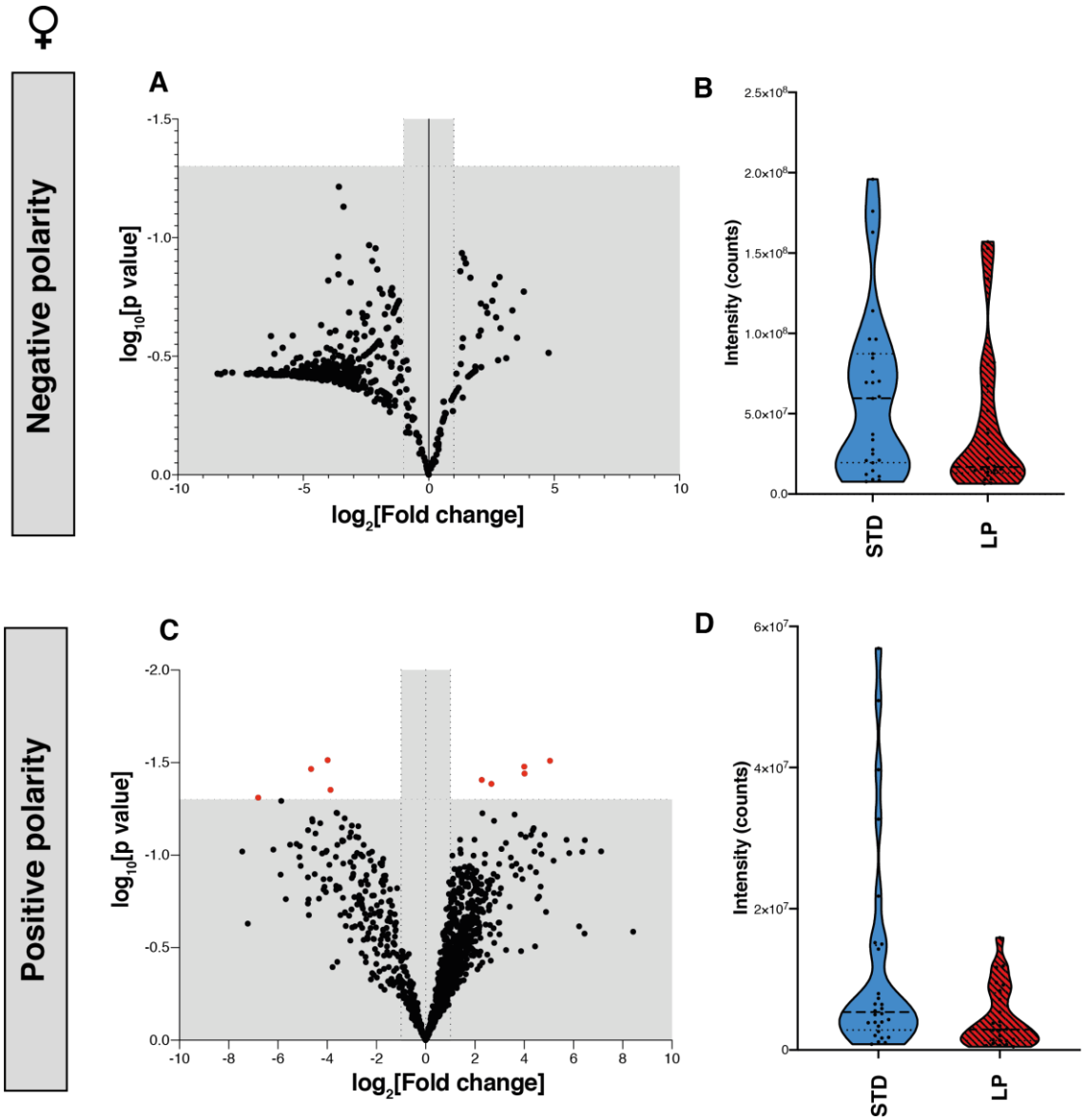

Figure 5.20 LP diet only affects a small minority of adult skin lipids in females

A,C. Volcano plots showing log_2 fold change for all OrbiSIMS detected masses in LP females at P42 compared with STD females at P42. Data points labelled in red are statistically significant.
B,D. Total ion intensity for all measurements used in this analysis for STD and LP females.

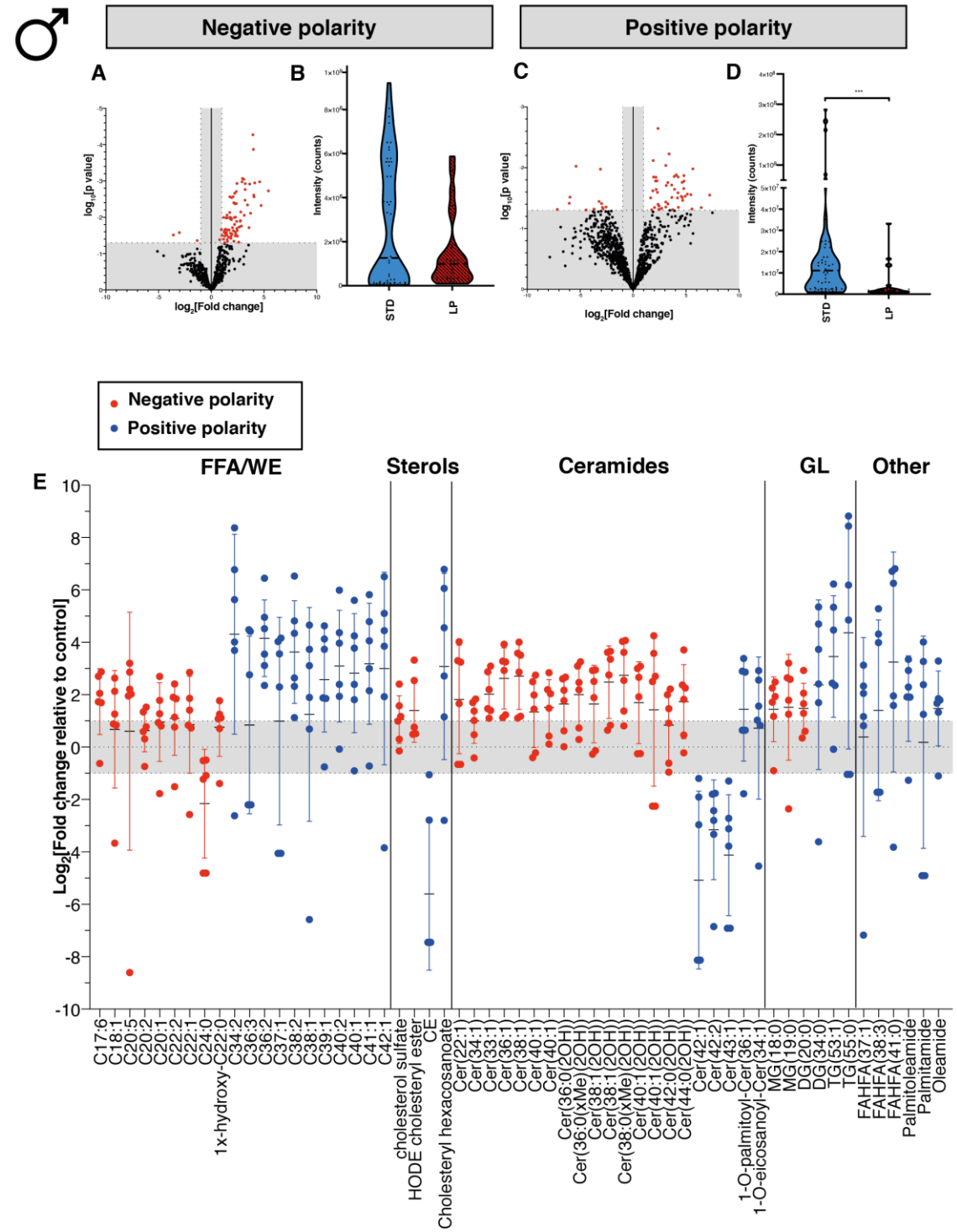

Figure 5.21 Male mouse skin lipids are programmed by a LP prenatal diet

A,C. Volcano plots showing log_2 fold change for all OrbiSIMS detected masses in LP males at P42 compared with STD males at P42. Data points labelled in red are statistically significant.
B,D. Total ion intensity for all measurements used in this analysis for STD and LP males.
E. Statistically significant peaks that are putatively assigned to lipids, showing the log_2 fold change in LP males compared with STD males. Each datapoint represents the average of four technical repeats taken from an individual animal. n=6 animals. FFA=free fatty acid, WE=wax ester, GL=glycerolipid.

5.5 Discussion

In this chapter, I have illustrated the impact that both developmental and adult nutrition have on the composition of the adult skin lipid blend. Interestingly, I observed DOHaD effects of developmental nutrition on the adult integument in both flies and mice. More work would be required to address whether this similarity is due to an underlying evolutionarily conserved mechanism or whether it reflects evolutionary convergence. Although very few studies have been carried out in humans, there are indications in the literature that diet plays a very important role in skin health. For example, Lee et al. (2006) report observations of xerosis (skin dryness) in prisoners held in concentration camps subjected to extreme dietary protein deficiency. In this case, it is also important to note that the subjects would also have had extreme deficiency of additional micronutrients and minerals that could also contribute to the observed pathology. It does, however, identify the key link between diet and skin health, and the skin conditions resolved once the diet was no longer restricted.

Using flies, I found that a LY developmental diet increased the relative proportion of wax esters in the adult *Drosophila* cuticular lipid blend. I also found that larvae raised on a LY diet developed into flies with increased expression of *Far*, a predicted fatty acyl CoA reductase that may be involved in wax ester biosynthesis. To test whether *Far* mediates the observed increase in cuticular wax esters, OrbiSIMS analysis could be performed on *PromE-GAL4>Far RNAi* flies. Flies raised during development on a ØY diet show decreased desiccation resistance. However, given that LY and ØY flies are smaller than their STD counterparts, it could be that an increased surface area:volume ratio also contributes to greater water loss. It is also conceivable that changes in behavioural aspects such as spiracle opening/closing rates may also have a substantial impact on desiccation survival. Nevertheless, one interesting possibility is that small LY/ØY flies are able to at least partially improve their barrier function by upregulating cuticular wax esters. Manipulations of genes such as *Far* may help to address the contribution of wax esters to the desiccation barrier.

I have subsequently shown direct contribution of larval dietary carbon to the synthesis of adult cuticular lipids. The combination of several different metabolic labelling approaches highlight the contribution of both adult and larval carbon sources to the synthesis of cuticular lipids. This provides the basis for a direct metabolic link between developmental stress and an adult phenotype in a mechanism that is perhaps driven by energy stores and metabolism in comparison to many classical DOHaD effects which are thought to be driven ultimately by epigenetic changes. That is not to say that epigenetic changes play no role in the LY phenotype observed in this chapter. To determine this with confidence, various sequencing approaches would have to be carried out which could include bisulphate conversion to identify methylation events.

It is very possible that many of the non-hydrocarbon lipids could be produced by the larval oenocytes, as these are one of the last larval cell types to undergo programmed cell death, fragmenting during mid-to-late pupal stages (Gutierrez et al., 2007). Therefore, one possibility to explain the developmental carry-over of non-hydrocarbon cuticular lipids is that they are released from larval oenocytes in the pupa, via a burst of holocrine secretion upon death. It is important to realise that adult oenocytes are not derived from larval oenocytes, instead they are formed from abdominal precursors called histoblasts, which also make the adult epidermis (Makki et al., 2014). To test the hypothesis that non-hydrocarbons originate from dying larval oenocytes, cell death could be blocked using *PromE>p35* and adult cuticular lipids measured using OrbiSIMS.

The isotope labelling experiments in this chapter also raise interesting questions about the metabolic origins of non-hydrocarbon cuticular lipids. For example, the pattern of ^{13}C incorporation from labelled acetate into hydrocarbons and other lipids was unexpectedly indicative of one or two steps of fatty acid elongation rather than *de novo* fatty acid synthesis. This might be explained by the existence of multiple (at least three) distinct cellular pools of acetyl-CoA: mitochondria, nucleo-cytosolic and endoplasmic reticulum (**Figure 5.22**) (Pietrocola et al., 2015). These pools of acetyl-CoA are not in equilibrium with each other and acetate has been shown to penetrate the mitochondria very slowly, leading to a

failure of equilibrium between endogenous acetyl-CoA and exogenous labelled acetate (Dietschy and Brown, 1974). The mitochondrial pool of acetyl-CoA is primarily used for *de novo* synthesis of fatty acids. Therefore, poor enrichment of labelled acetate in the mitochondria would lead to a failure to label *de novo* synthesised fatty acids. The nucleo-cytosolic pool of acetyl-CoA, so called due to the ready permeability of the nuclear envelope to acetyl-CoA and subsequent "mixing" of the pools, is primarily utilised for elongation of *de novo* synthesised fatty acids (Jump, 2009). This may explain why I observed with OrbiSIMS that labelled glucose but not acetate is incorporated into *de novo* synthesised cuticular fatty acids. To test this idea, label incorporation into free fatty acids could also be measured using GC-MS to provide a more quantitative picture of the relative contributions of de novo biosynthesis versus elongation. To label both *de novo* lipogenesis and elongation efficiently, U-^{13}C octanoate could be used, which has been shown to be rapidly oxidised into acetyl-CoA in all intracellular acetyl-CoA pools (Dietschy and Brown, 1974). This would enable a more accurate determination of lipid synthesis and turnover rates. The involvement of a mitochondrial rather than cytosolic fatty acid synthase (FAS) for the *de novo* synthesis of the fatty acid precursors of hydrocarbons could also be part of the explanation for the observed patterns of label incorporation. It has been shown in yeast that mitochondrial FAS can act as a nutrient sensing mechanism, via mitochondrial acetyl-CoA levels, and that it has a direct effect on electron transport chain (ETC) complex assembly (Kursu et al., 2013).

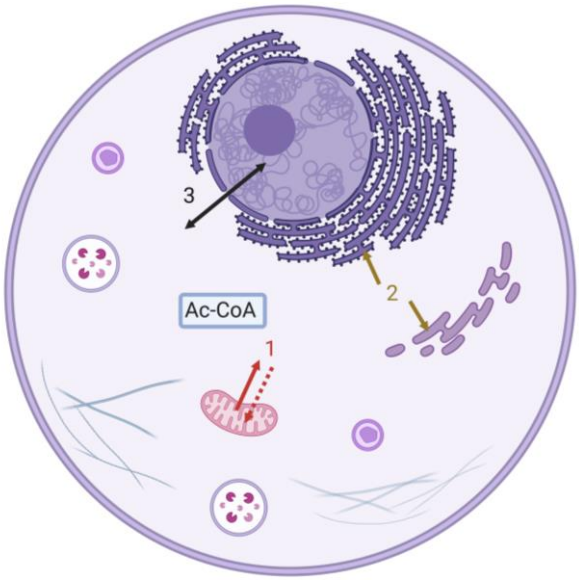

Figure 5.22 Intracellular pools of Acetyl-CoA

Eukaryotic cell illustrating the intracellular pools of Acetyl-CoA (Ac-CoA). 1. Mitochondrial: acetyl-CoA biosynthesis occurs here, and this pool is the substrate for *de novo* lipogenesis. 2. ER: No acetyl-CoA biosynthesis occurs here, only import. Uses of acetyl-CoA include elongation of dietary lipids and acetylation of proteins. 3. Nucleo-cytosolic: Acetyl-CoA can pass freely through the nuclear envelope so these pools are considered one due to their equilibrium. Acetyl-CoA in this pool is used for elongation of *de novo* synthesised fatty acids.

In mice, I was surprised to find a very sex-specific DOHaD effect. The nutritional programming effect of a prenatal low protein diet on skin lipids was observed only in male mice. This may reflect inputs from sex hormones in the DOHaD programming mechanism. In addition, for the fly LY paradigm, it would also be interesting to measure cuticular non-hydrocarbon lipids in females as well as in males. In mice, I found a LP developmental diet induced changes in wax esters, free fatty acids and triglycerides, which are produced by the sebocytes, and also changes in free fatty acids, ceramides and sterols, produced by keratinocytes (Smith and Thiboutot, 2008, Pappas, 2009). Given that I observed that both classes are altered by the LP developmental diet, this suggests that the DOHaD skin phenotype involves both keratinocytes and sebocytes. The proportional increase in ceramides in the male LP skin lipid blend is particularly interesting, as this class of lipids has been demonstrated to directly contribute to the waterproofing barrier. Ceramides are highly abundant in the stratum corneum of the skin, and are thought to form crystalline sheets (Coderch et al., 2003). Skin

ceramide levels have also been shown in humans to decrease with increasing age (Rogers et al., 1996). This decrease in skin ceramides is thought to contribute to the decreased barrier efficacy observed in aged skin. Therefore, it is possible that a proportional increase in skin ceramides in the LP mice may result in improved skin barrier efficacy. This could be tested by measuring trans-epithelial water loss (TEWL), an effective measure of waterproofing barrier efficacy.

To understand the mechanisms that underlie the developmental programming of the cuticular lipid blend, it is important to have a strong understanding of the biochemical processes involved in cuticular lipid biosynthesis. Although this process is understood well in mice and humans, this area is less well understood in *Drosophila*. As longitudinal studies of the developmental origins of health and disease are more accessible using *Drosophila* due to their short generation times and genetic plasticity, it is worth investing time in understanding the cuticular lipid biosynthetic process as fully as possible to access the underlying molecular mechanisms underpinning the developmental programming of the cuticular lipid blend.

Chapter 6. Synthesis and regulation of cuticular lipid barrier composition in *Drosophila*

6.1 Introduction

In Chapter 3, OrbiSIMS was used to reveal a diverse range of >100 different lipid species in the *Drosophila* cuticular barrier. Many of these are non-hydrocarbon lipids such as ceramide phosphoethanolamines which have not previously been reported as components of the *Drosophila* epicuticle and their cellular and biosynthetic origins are therefore unclear. Interestingly, I also found that the cuticular lipid blend is chemically different from one body part to another and also from one zone to another within the same body part. Chapter 5 reported that the composition of the hydrocarbon and non-hydrocarbon lipid blend is modulated by both the developmental and adult diets, and that the developmental diet directly contributes carbons to cuticular lipid biosynthesis. In this chapter, I investigate the environmental and genetic regulation of adult cuticular lipids in *Drosophila*.

6.2 Oenocytes regulate non-hydrocarbon cuticular lipids

Oenocytes are known to be the site of synthesis of cuticular hydrocarbons in *Drosophila* (Ferveur et al., 1997, Billeter et al., 2009). Furthermore, the last step of hydrocarbon synthesis requires oenocyte-specific activity of the cytochrome P450 decarbonylase enzyme Cyp4g1 (Qiu et al., 2012). The cellular site of synthesis of non-hydrocarbon cuticular lipids is, however, not yet known. A series of oenocyte genetic manipulations were therefore performed to begin to address this issue and also to investigate whether separate or common genetic mechanisms regulate hydrocarbon and non-hydrocarbon cuticular lipids. First, I targeted various known upstream regulators of lipogenesis and lipolysis enzymes, including TSC1/2 and SREBP (lipogenesis) and Hnf4 (lipolysis) (Laplante and Sabatini, 2013, Palanker et al., 2009).

SREBP is thought to be a key regulator of de novo fatty acid synthesis, although much of this information is from mammalian studies or studies in different *Drosophila* tissues (Seegmiller et al., 2002, Laplante and Sabatini, 2013). Therefore, to investigate the role of fatty acid synthesis, the transcription factor SREBP was manipulated in oenocytes, specifically during the adult stage, using *PromE-GAL4* in combination with *tubulin-GAL80^{ts}* (*PromE^{ts}*). A dominant negative form of the protein (*SREBP^{DN}*) was expressed in adult *Drosophila* oenocytes (*PromE^{ts}>SREBP^{DN}*) (**Figure 6.1A**). In this experiment, seven days of SREBP inhibition led to dramatic decreases in many but not all cuticular hydrocarbons in adult females (**Figure 6.1B**). Relatively little change was seen in straight-chain alkanes, with a slight decrease in shorter chain methyl-branched alkanes and a more pronounced decrease in alkenes. This selective effect is surprising as SREBP is thought to regulate the synthesis of the FA precursors used to make both alkanes and alkenes. Nevertheless, methyl-branched alkanes are thought to originate from fatty acids, synthesised not in the oenocytes but in the fat body using an amino acid precursor (Holze et al., 2021). The strong decrease in alkenes on the female cuticle is not equally distributed amongst all carbon chain lengths, with the shorter carbon chains largely exempt from this effect and, in the case of tricosene, even increased. The result of these selective

changes is to lower the alkene-to-alkane ratio of the hydrocarbon blend, largely as a result of a substantial decrease in the most abundant female dienes, (*Z,Z*)-7,11-heptacosadiene and (*Z,Z*)-7,11-nonacosadiene (**Figure 6.1C**). Together these results are consistent with previous studies showing that oenocytes are the hydrocarbon source and they go further – demonstrating that oenocyte SREBP stimulates the production of female hydrocarbons, and is more strongly required for alkenes than alkanes.

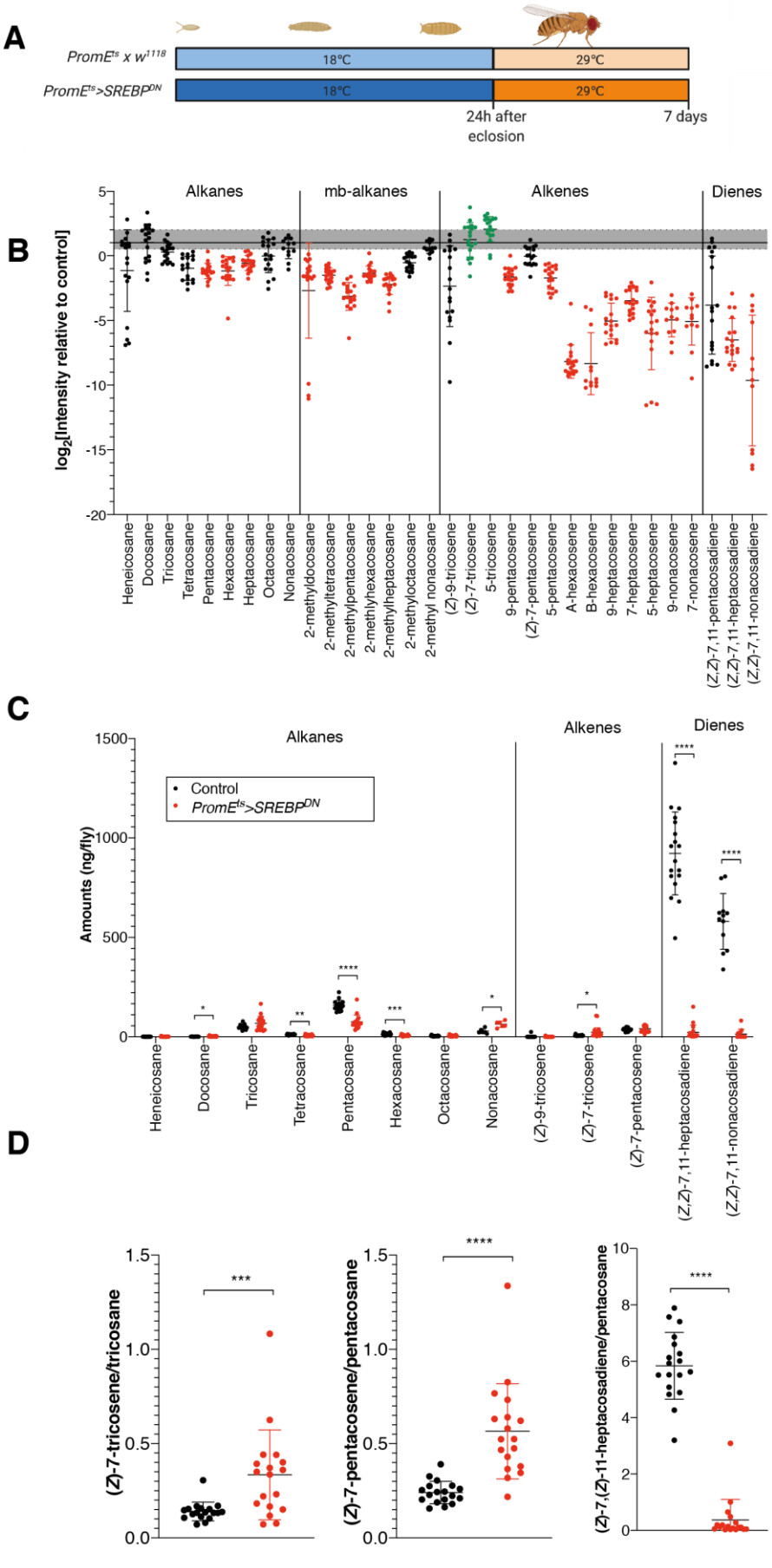
A
PromE^ts x w^1118
PromE^ts>SREBP^DN
18°C
29°C
18°C
29°C
24h after eclosion
7 days
B
Alkanes
mb-alkanes
Alkenes
Dienes
log2[Intensity relative to control]
5
0
-5
-10
-15
-20
Heneicosane
Docosane
Tricosane
Tetracosane
Pentacosane
Hexacosane
Heptacosane
Octacosane
Nonacosane
2-methyldocosane
2-methyltetracosane
2-methylpentacosane
2-methylhexacosane
2-methylheptacosane
2-methyloctacosane
2-methyl nonacosane
(Z)-9-tricosene
(Z)-7-tricosene
5-tricosene
9-pentacosene
(Z)-7-pentacosene
5-pentacosene
A-hexacosene
B-hexacosene
9-heptacosene
7-heptacosene
5-heptacosene
9-nonacosene
7-nonacosene
(Z,Z)-7,11-pentacosadiene
(Z,Z)-7,11-heptacosadiene
(Z,Z)-7,11-nonacosadiene
C
Alkanes
Alkenes
Dienes
Control
PromE^ts>SREBP^DN
Amounts (ng/fly)
1500
1000
500
0
Heneicosane
Docosane
Tricosane
Tetracosane
Pentacosane
Hexacosane
Octacosane
Nonacosane
(Z)-9-tricosene
(Z)-7-tricosene
(Z)-7-pentacosene
(Z,Z)-7,11-heptacosadiene
(Z,Z)-7,11-nonacosadiene
D
(Z)-7-tricosene/tricosane
(Z)-7-pentacosene/pentacosane
(Z),(Z)-11-heptacosadiene/pentacosane

Figure 6.1 SREBP^{DN} expression in adult oenocytes alters female cuticular hydrocarbons
Adult oenocyte-specific inhibition of SREBP by overexpression of a dominant negative form (SREBP^{DN}) results in substantial changes in cuticular hydrocarbon blend. The results shown above illustrate the sum of three independent experiments, each with six replicates.
A. Schematic of genetic manipulation showing temperature sensitive overexpression of SREBP^{DN} in adult oenocytes 24 hours after eclosion. Measurements were taken at seven days of age.
B. Relative intensity of hydrocarbon species when compared with the average of the control (*PromE^{ts} x w^{1118}*). Results are shown on a $\log_2$ scale. The grey region illustrates results which fall within a two-fold increase or decrease. Red or green colouring indicates significantly decreased or increased contribution respectively. Statistical significance is as follows: pentacosane (****), hexacosane (***), heptacosane (*), 2-methyldocosane (***), 2-methyltetracosane (****), 2-methylpentacosane (****), 2-methylheptacosane (****), (*Z*)-7-tricosene (**), 5-tricosene (***), 9-pentacosene (****), 5-pentacosene (****), A-hexacosene (****), B-hexacosene (****), 9-heptacosene (****), 7-heptacosene (****), 5-heptacosene (****), 9-nonacosene (****), 7-nonacosene (****), (*Z,Z*)-7,11-heptacosadiene (****), (*Z,Z*)-7,11-nonacosadiene (****).
C. Saturation index as measured by alkene/alkane ratio or diene/alkane ratio as labelled. Black dots represent control measurements and red dots represent experimental (*PromE^{ts}>SREBP^{DN}*) measurements.

To investigate whether oenocytes SREBP contributes to synthesis of non-hydrocarbon cuticular lipids, *PromE^{ts}>SREBP^{DN}* flies were analysed using OrbiSIMS at ambient temperature (**Figure 6.2A**). In this experiment, SREBP was inhibited in oenocytes throughout development and adulthood, and this resulted in significant changes in the majority of non-hydrocarbon species analysed, whereas the signal from some species increased, for others it decreased (**Figure 6.2B**). Inhibition of SREBP resulted in a decrease in the signals from wax esters and phospholipids, a result that would be consistent with fatty acid precursors being de novo synthesised by the oenocytes. Surprisingly, however, increases in the signals for free fatty acids and glycerolipids were observed (**Figure 6.2C**). One possible explanation here is that blocking FA synthesis in oenocytes stimulates the import of more FAs from outside the oenocyte (Parvy et al., 2012), which might favour those cuticular lipids produced in oenocytes from fatty acids synthesised in the fat body or obtained preformed from the diet. Interestingly, SREBP^{DN} also gives a significant increase in two C18 hydroperoxy fatty acids (C18:3 and C18:2) (**Figure 6.2D**). As hydroperoxy-fatty acids are the result of damaging lipid peroxidation chain reactions, this result hints that SREBP is required to maintain an optimal cuticular lipid blend that protects against oxidation. Together, the SREBP^{DN} data provide clear evidence for a new role for oenocytes in the biosynthesis and/or regulation of non-hydrocarbon cuticular lipids – adding to their previously known role in hydrocarbon synthesis.

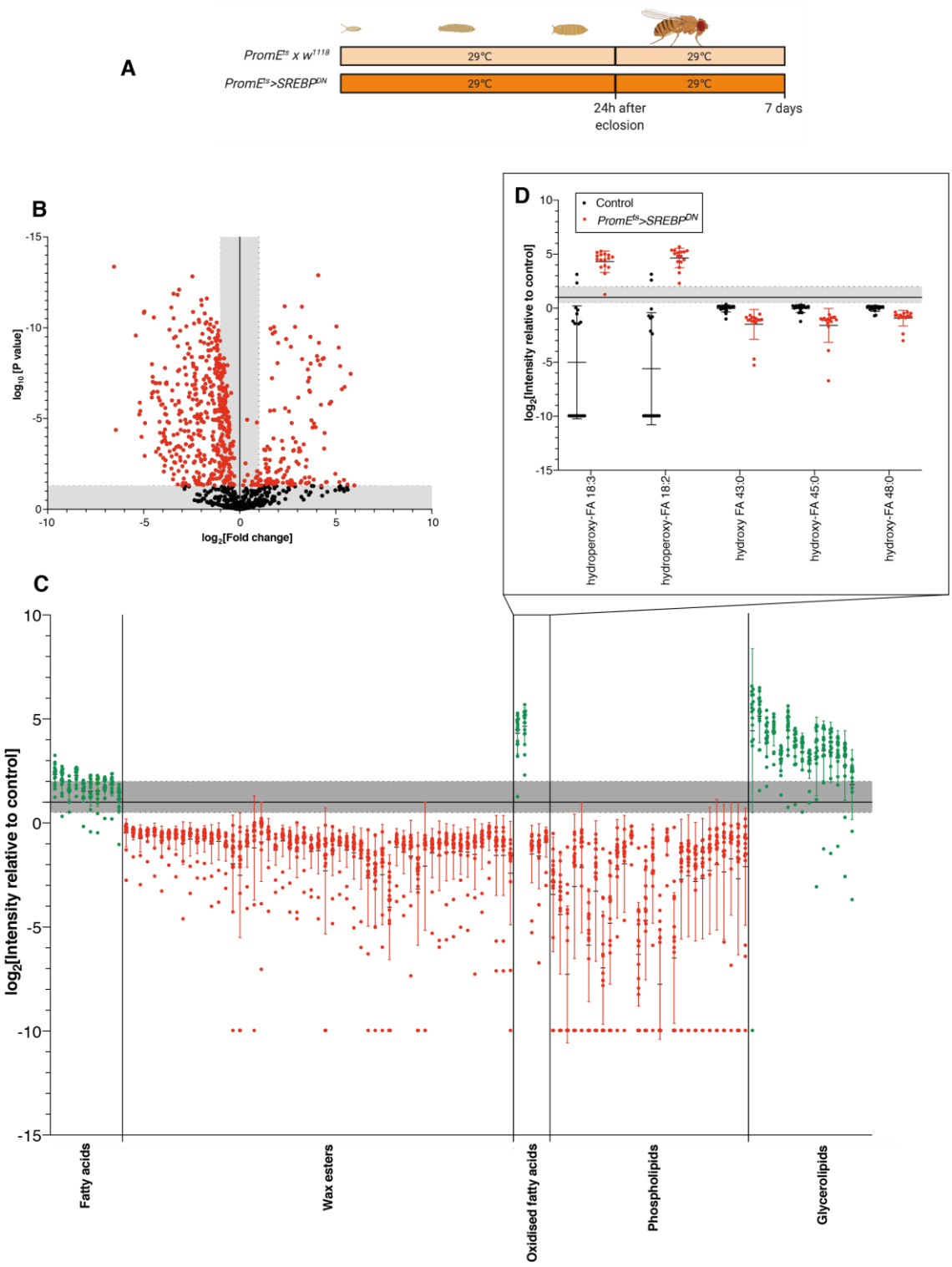
A
PromE^ts x w^1118
PromE^ts>SREBP^DN
29°C
29°C
29°C
29°C
24h after eclosion
7 days
B
log10 [P value]
log2[Fold change]
C
log2[Intensity relative to control]
Fatty acids
Wax esters
Oxidised fatty acids
Phospholipids
Glycerolipids
D
Control
PromE^ts>SREBP^DN
log2[Intensity relative to control]
hydroperoxy-FA 18:3
hydroperoxy-FA 18:2
hydroxy FA 43:0
hydroxy-FA 45:0
hydroxy-FA 48:0

Figure 6.2 SREBP^{DN} expression in oenocytes alters female cuticular non-hydrocarbons
Oenocyte-specific inhibition of SREBP by overexpression of a dominant negative form of the protein (SREBP^{DN}) throughout development results in significant alterations to the cuticular lipid blend. The results shown illustrate one independent experiment with n=18 for the control (*Prome^{ts} x w^{1118})* and n=16 for the experimental group (*PromE^{ts}>SREBP^{DN}*)
(**A**) Schematic of the genetic manipulation showing continuous SREBP^{DN} expression throughout development and into adulthood.
(**B**) Volcano plot showing peaks that are statistically significant using a Student's T test corrected for multiple comparisons with a FDR of 20% labelled in red.
(**C**) Relative intensity statistically significant, positively identified lipid species when compared with the average of the control (*PromE^{ts} x w^{1118}*). Results are shown on a $\log_2$ scale. Lipids are arranged in order of ascending carbon chain length and are labelled by lipid class. The grey region illustrates results which fall within a two-fold increase or decrease. Red or green colouring indicates significantly decreased or increased contribution respectively.
(**D**) Analysis of oxidised free fatty acids indicates an increase in hydroperoxy-fatty acids and a decrease in hydroxy-fatty acids. Black dots represent the control group and red dots represent the experimental group.

In several tissues, SREBP has been shown to be indirectly negatively regulated by TSC1/2 via inhibition of mTORC1 (Laplante and Sabatini, 2013). If this is also the case in oenocytes, then overexpression of TSC1/2 will produce similar effects on cuticular lipids as does SREBP^{DN}. Moreover, it was previously shown that TSC1/2 overexpression in adult oenocytes (*PromE^{ts}>TSC1/2*) dramatically decreases the production of alkane and alkene hydrocarbons (Stefana et al., 2017). TSC1/2 was therefore overexpressed in oenocytes (*PromE^{ts}>TSC1/2*), specifically during adulthood but this resulted in only minor changes in the signals from most of the non-hydrocarbon cuticular lipids in male flies (**Figure 6.3**). Importantly, the oenocyte TSC1/2 overexpression was confined exclusively to adult stages, in contrast to the previous SREBP^{DN} manipulation throughout development. It is therefore possible that either TSC1/2 regulates hydrocarbons but not most other cuticular lipids, or that it regulates both lipid classes but for non-hydrocarbons this requires gene function during development. To discriminate between these possibilities, it will be interesting to use OrbiSIMS analysis with a temperature shift regime for *PromE^{ts}>TSC1/2 t*hat overexpresses TSC1/2 during development rather than adulthood.

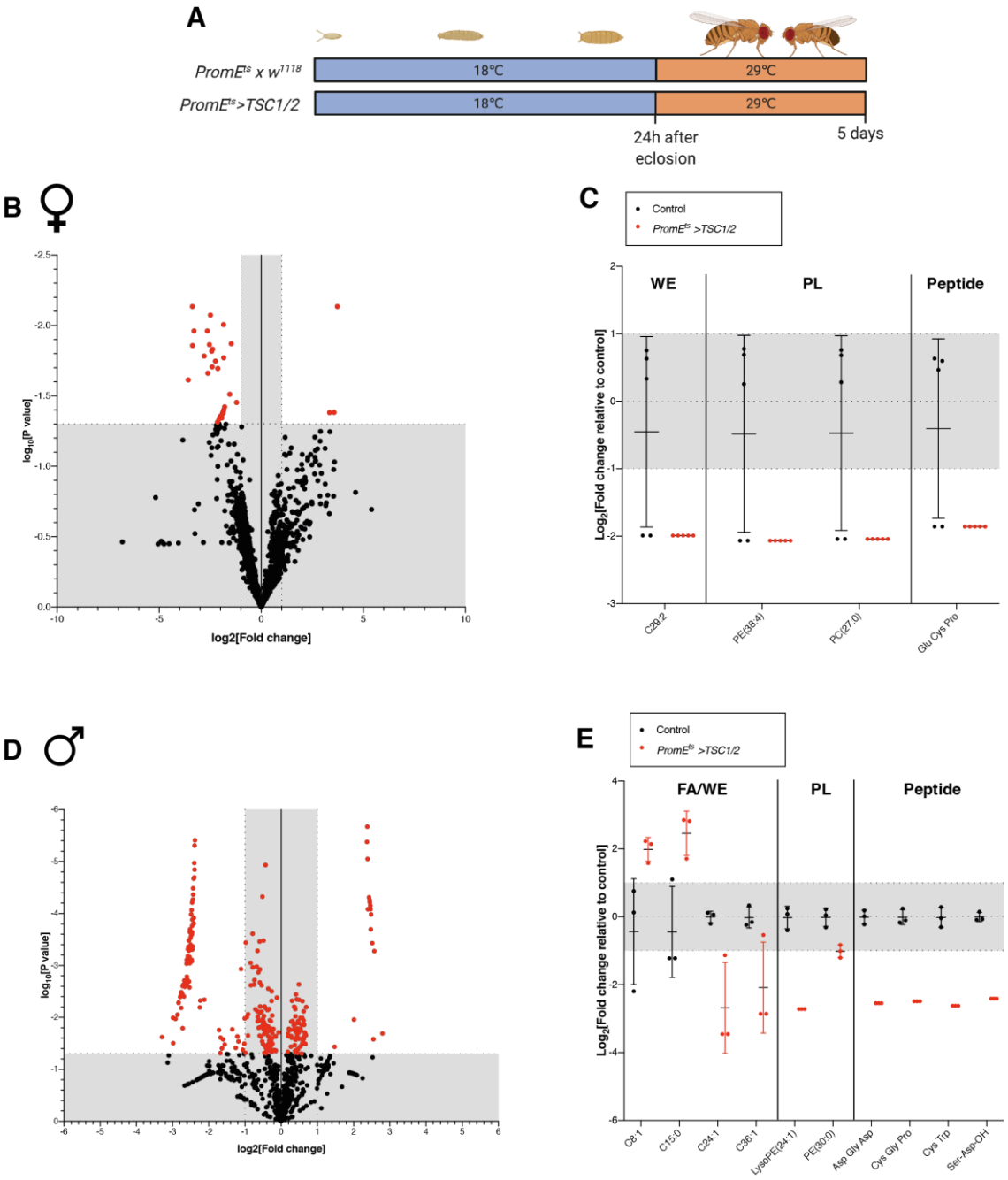

Figure 6.3 Oenocyte TSC overexpression in adults does not significantly alter most cuticular non-hydrocarbons

A. Flies were housed at 18℃ and transferred to 29℃ within 24 hours of eclosion in vials separated by sex containing a maximum of 10 flies per vial. After 5 days housing at 29℃, flies were dissected and cuticular lipids analysed with ambient temperature OrbiSIMS.
B,D. Volcano plot showing the fold change in cuticular ions in female (**B**) and male (**D**) *PromE^{ts}>UAS-TSC1/2* flies compared with the control.
C,E. Significantly up or down regulated lipids on the fly cuticle. Each datapoint represents a single fly.

Not all classes of cuticular lipids were decreased in *PromE^{ts}>UAS-SREBP^{DN}* flies, such as free fatty acids and glycerolipids, and one explanation for this could be that they are synthesised from preformed fatty acid substrates. For example, the transcription factor Hnf4 is known to be required in oenocytes for converting fat stores into very-long-chain fatty acids and hydrocarbons (Storelli et al., 2019). In several other contexts, it is known that Hnf4 is negatively regulated by the nutrient sensitive AMPK signalling pathway (Error! Reference source not found.). Adult-restricted oenocyte-specific knockdown of Hnf4 (*PromE^{ts}>Hnf4 RNAi*) was therefore performed and showed moderate changes to the cuticular lipid blend, including a relative decrease in free FAs and PLs (**Figure 6.4A-C**). There was also a surprising increase in amino acids and peptides in the epicuticule. It is possible that this could correspond to secreted proteins such as antimicrobial peptides (AMPs), although there is currently no published evidence to link Hnf4 to the expression of AMPs. In future, LC-MS based proteomics could be used to identify these proteins, or potentially cryo-OrbiSIMS after recent developments that enable the use of OrbiSIMS for protein imaging (Kotowska et al., 2020).

To investigate the interplay between hydrocarbon and non-hydrocarbon biosynthesis, OrbiSIMS was used to analyse the cuticles of flies with adult-specific oenocyte-driven *Cyp4g1 RNAi*. Knockdown of this enzyme in oenocytes has been previously shown to ablate nearly all hydrocarbons from the fly cuticle (Qiu et al., 2012), and this was confirmed using cryo-OrbiSIMS (**Figure 6.5 D,E**). Consistent with Qiu et al. (2012), ambient temperature OrbiSIMS also showed that Cyp4g1 knockdown leads to a build-up of very-long chain fatty acids, the precursors for hydrocarbons. Interestingly, however, knockdown of Cyp4g1 also resulted in a substantial decrease in saturated free fatty acids (FFAs) and GLs (**Figure 6.5 B, C**). This suggests that saturated FFAs and glycerolipids (GLs) could depend upon the same oenocyte biosynthetic pathway as hydrocarbons, and that Cyp4g1 may positively regulate this.

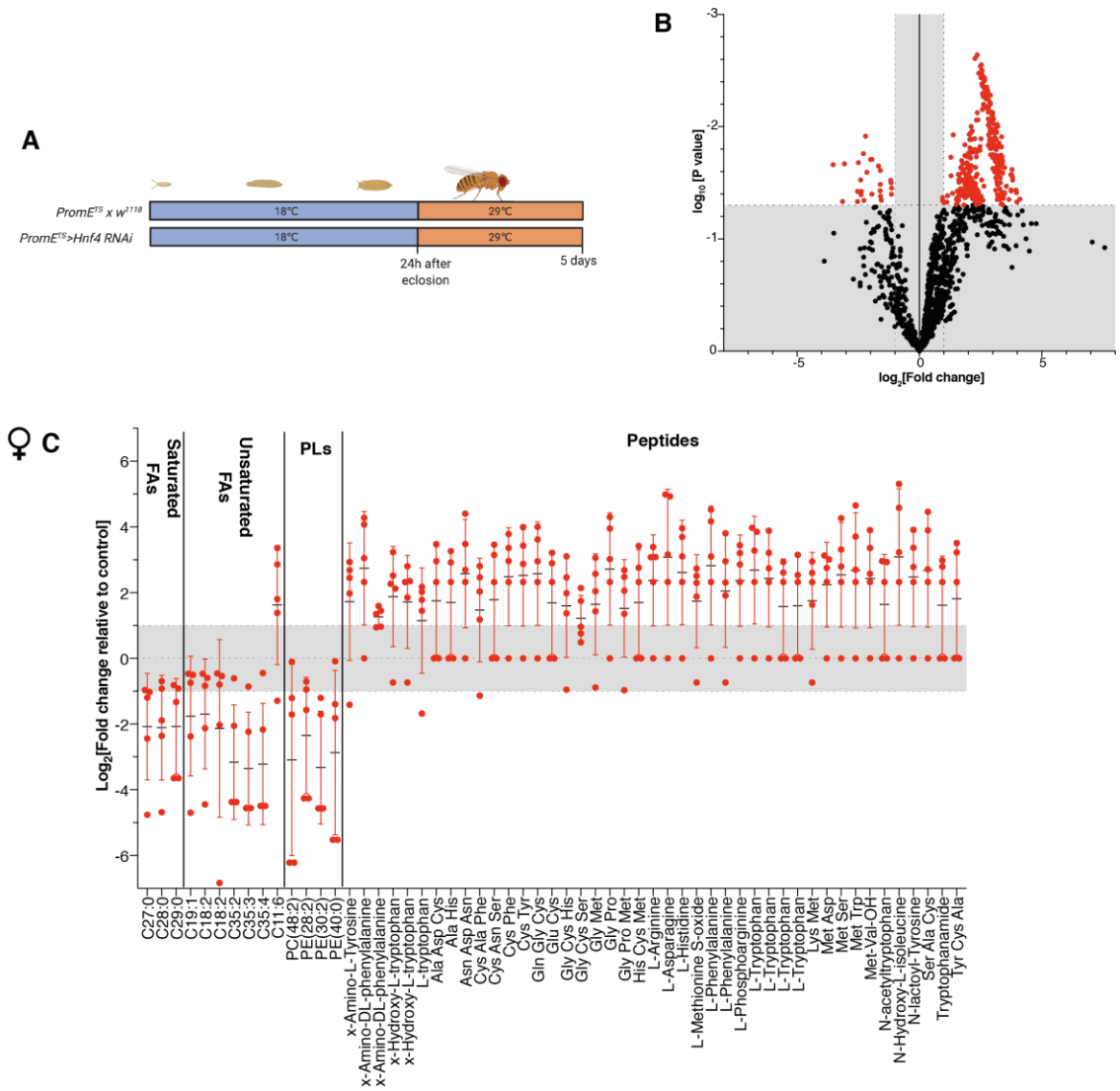

Figure 6.4 Oenocyte Hnf4 knockdown has minor effects on the cuticular lipid blend

A. Flies were housed at 18℃ during development and transferred to single sex vials at 29℃ containing a maximum of 10 flies within 24 hours of eclosion. After 5 days, flies were dissected and analysed with ambient temperature OrbiSIMS.
B. Volcano plot showing the fold change in cuticular ions in female *Hnf4 RNAi* flies compared with the control. Statistically significant ions are indicated in red.
C. Fold change in statistically significant lipids from (**B**) in female *Hnf4 RNAi* flies compared with the control. Each datapoint represents a single fly.

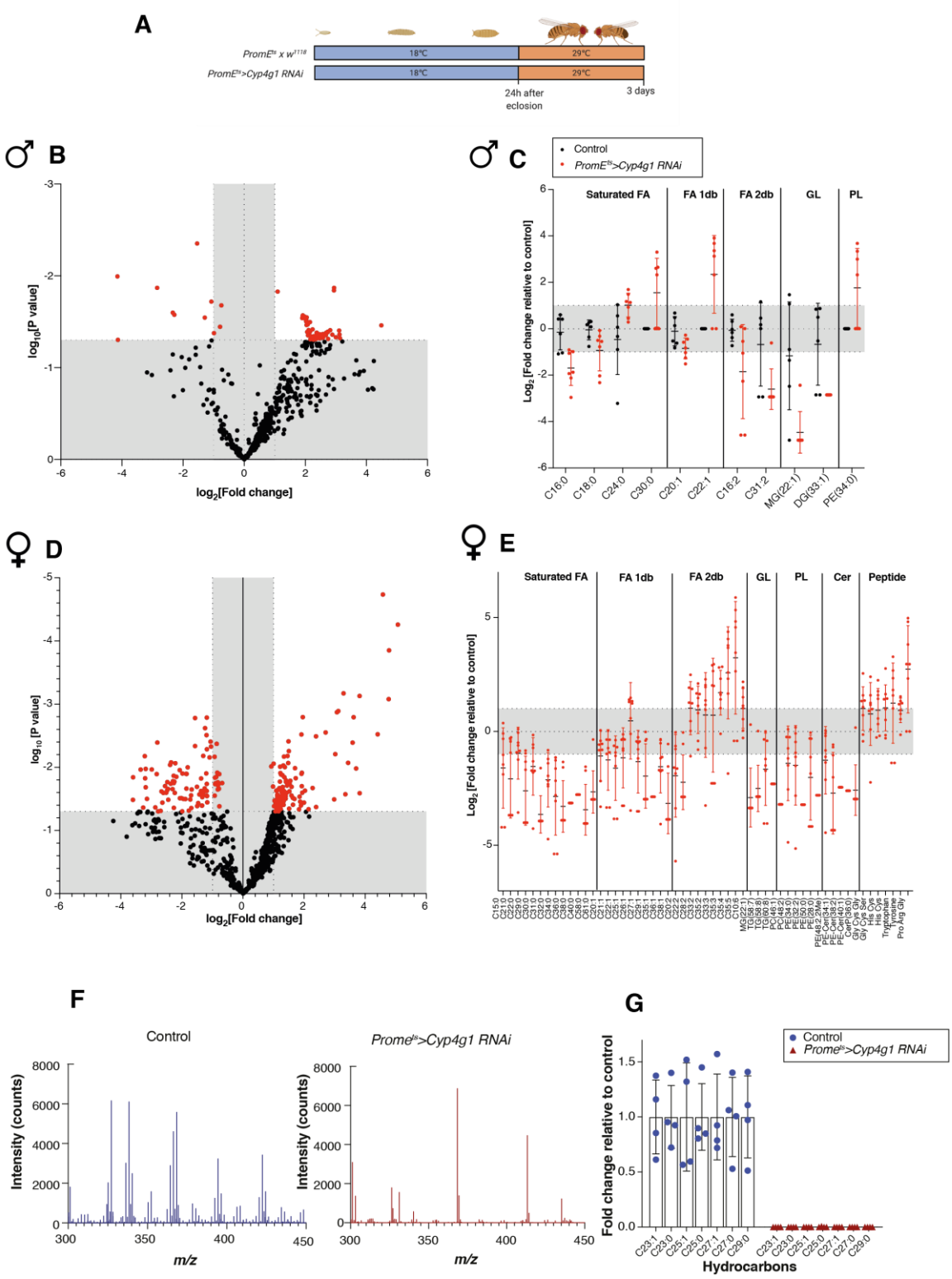
A
PromE^ts x w^1118
PromE^ts>Cyp4g1 RNAi
18°C
29°C
24h after eclosion
3 days
♂ B
log10[P value]
log2[Fold change]
♂ C
Control
PromE^ts>Cyp4g1 RNAi
Saturated FA
FA 1db
FA 2db
GL
PL
Log2 [Fold change relative to control]
C16:0
C18:0
C24:0
C30:0
C20:1
C22:1
C16:2
C31:2
MG(22:1)
DG(33:1)
PE(34:0)
♀ D
log10 [P value]
log2[Fold change]
♀ E
Saturated FA
FA 1db
FA 2db
GL
PL
Cer
Peptide
Log2 [Fold change relative to control]
F
Control
Promets>Cyp4g1 RNAi
Intensity (counts)
m/z
G
Control
Promets>Cyp4g1 RNAi
Fold change relative to control
C23:1
C23:0
C25:1
C25:0
C27:1
C27:0
C29:0
Hydrocarbons

Figure 6.5 Oenocyte Cyp4g1 oppositely regulates very-long chain fatty acids and hydrocarbons

A. Flies were housed at 18℃ during development and transferred to 29℃ within 24 hours of eclosion in vials housing 10 male flies. Abdominal cuticles were dissected for OrbiSIMS analysis after 3 days housing at 29℃.
B. Volcano plot of peak intensities in *PromE^{ts}>Cyp4g1 RNAi* flies as compared with the control. The grey region on the y axis indicates features with a p value>0.05, and the grey region on the x axis indicates features with a < 2 fold change when compared with the control. Features in red are statistically significant. Features shown are peak intensities measured using negative polarity ambient temperature OrbiSIMS with an Ar_{3500}^+ analysis beam.
C. Relative intensity of fatty acids in *PromE^{ts}>Cyp4g1 RNAi* flies plotted as $\log_2$[Fold change] when compared with the control. Each datapoint represents a single fly, with 6 replicates (control) or 7 replicates (*PromE^{ts}>Cyp4g1 RNAi*) acquired from two independent experiments.
D. Cryo-OrbiSIMS mass spectra of an example control and *PromE^{ts}>Cyp4g1 RNAi* fly acquired in positive polarity with an Ar_{3500}^+ analysis beam.
E. Relative intensity of hydrocarbons in *PromE^{ts}>Cyp4g1 RNAi* plotted as a fold change when compared with the control. Hydrocarbon peaks were undetectable in *PromE^{ts}>Cyp4g1 RNAi* flies. Each datapoint represents a single fly, with 4 replicates acquired from one experiment.
D. and **E**. adapted from Newell et al. (2020) with permission.

6.3 Environmental regulation of cuticular hydrocarbon blend

The barrier lipid blend in *Drosophila* is known to protect against stresses such as desiccation and temperature and also, via pheromones, to be involved in social and sexual interactions. All of these factors are environmental, so it is therefore reasonable to ask whether the environment regulates the cuticular lipid blend in a “plastic” manner, allowing the organism to adapt during its lifetime to sudden changes in environment. In this section, I investigate the effects of different environmental stresses on the cuticular hydrocarbon blend. Several stresses are investigated including housing density, temperature and humidity.

To address whether acute desiccation stress alters the cuticular hydrocarbon blend in the isogenic fly strain (*w^{1118} iso31*) used in the majority of work in this thesis, two different paradigms were used - a 6 hour exposure (before any death occurred), and a 12 hour exposure (at approximately median survival). However, in both these paradigms change in cuticular hydrocarbons was observed (**Figure 6.6, Figure 6.7**). This indicates that flies do not accurately respond to desiccation by altering their cuticular hydrocarbon blend. This is in contrast to published data showing a small change in cuticular hydrocarbon composition under acute (4h) desiccation stress (Stinziano et al., 2015). The difference can perhaps be explained by the differing genetic backgrounds or desiccation paradigms used. Nevertheless, both studies are consistent in reporting that acute desiccation stress does not lead to major changes in the cuticular hydrocarbon blend.

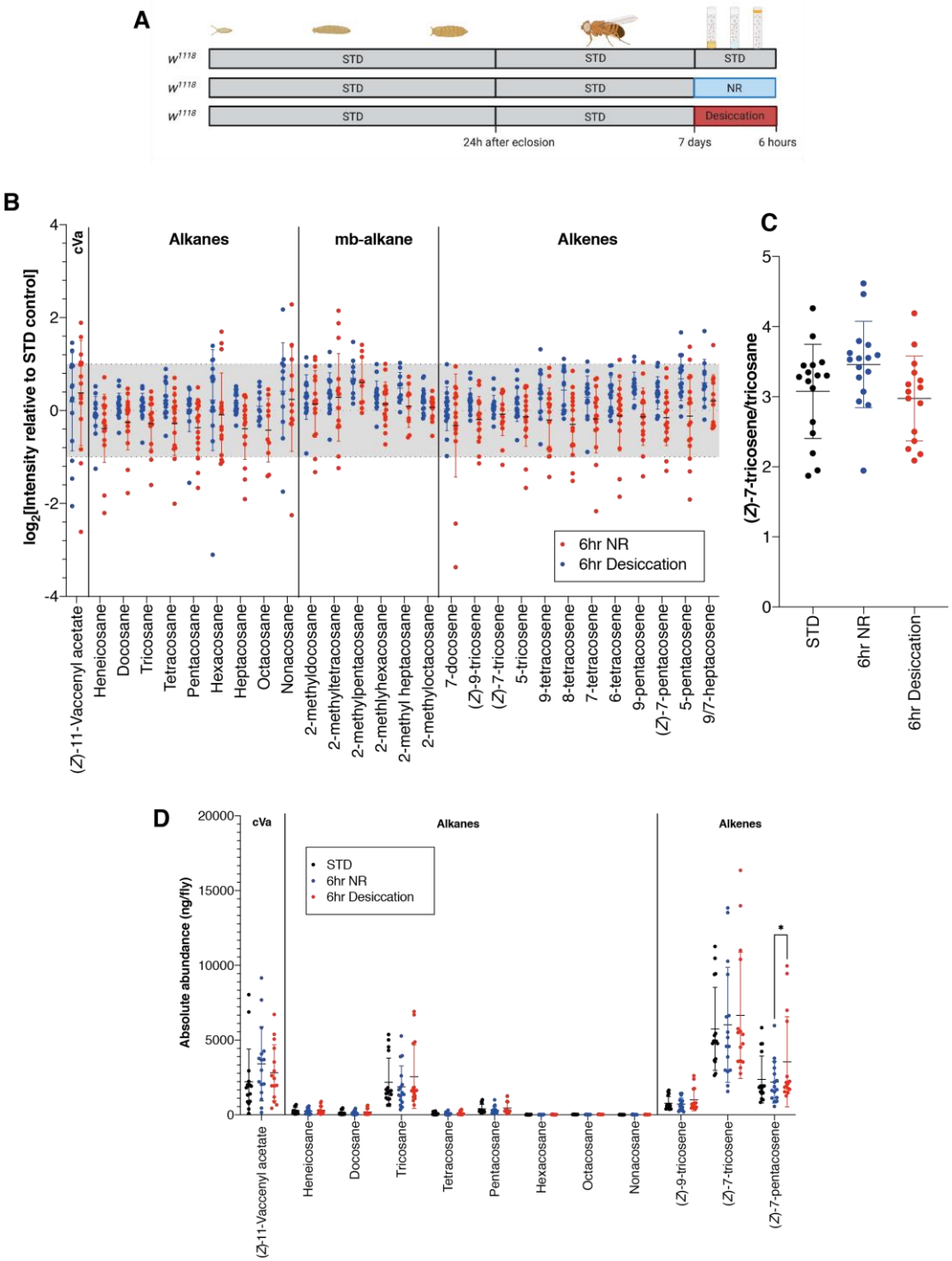

Figure 6.6 6 hours of desiccation stress does not substantially change cuticular hydrocarbons

A. Flies were housed at 25℃ throughout development and separated into vials of 10 male flies within 24 hours of eclosion. At seven days of age, the flies were exposed to no stress (STD), nutrient restriction (NR) or desiccation for 6 hours and hydrocarbons were then extracted.
B. Relative abundance of cuticular hydrocarbons shown relative to the fed control.
C. Desaturation index of cuticular hydrocarbons illustrated with the (*Z*)-7-tricosene to tricosane ratio.
D. Absolute abundance of cuticular hydrocarbons as determined using commercial standards of known concentration.

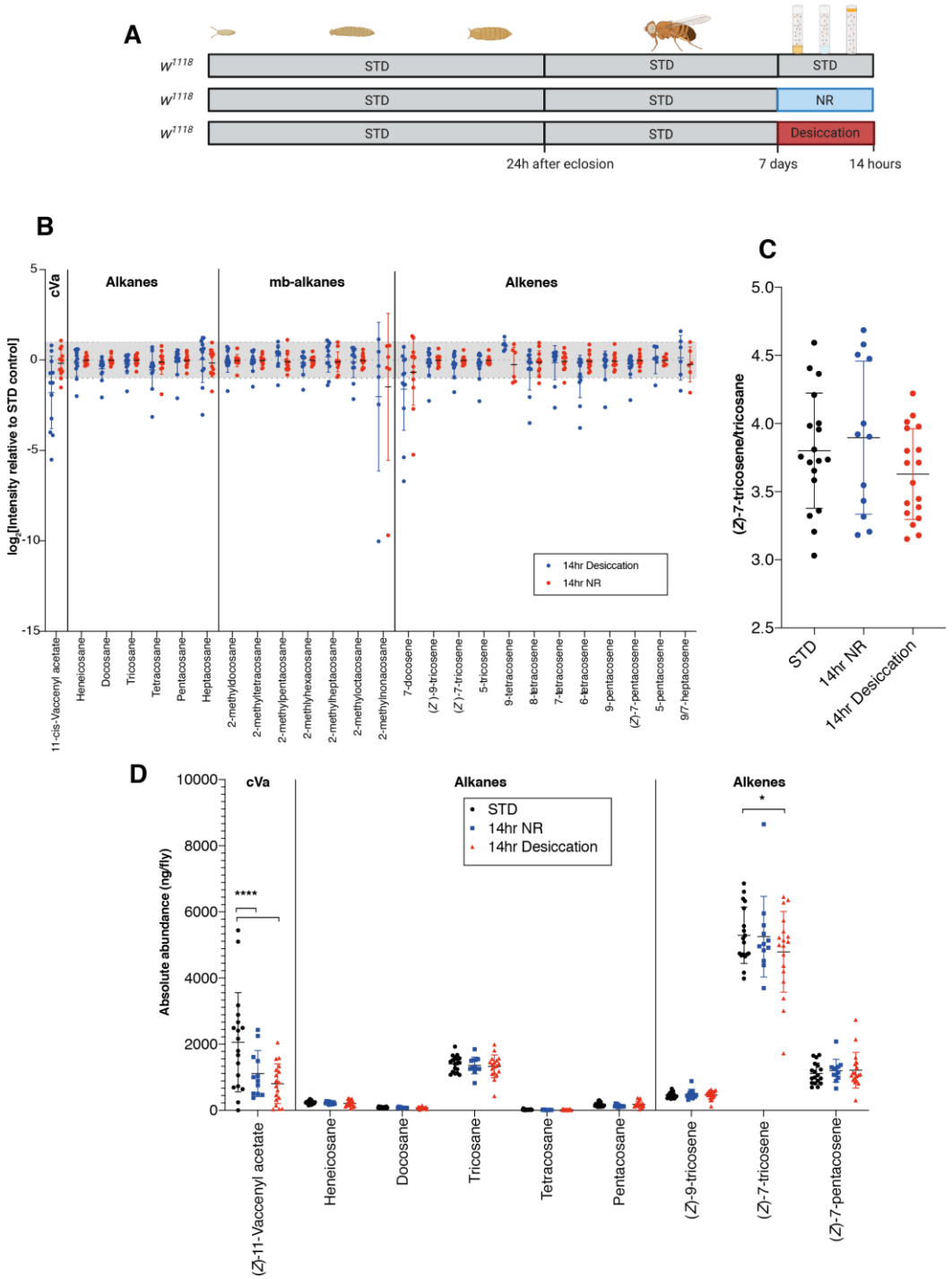

Figure 6.7 12 hours of desiccation stress does not substantially alter cuticular hydrocarbons

A. Flies were housed at 25℃ throughout development and separated into vials of 10 male flies within 24 hours of eclosion. At seven days of age, the flies were exposed to no stress (STD), nutrient restriction (NR) or desiccation for 12 hours and hydrocarbons were then extracted.
B. Relative abundance of cuticular hydrocarbons shown relative to the fed control.
C. Desaturation index of cuticular hydrocarbons illustrated with the (*Z*)-7-tricosene to tricosane ratio.
D. Absolute abundance of cuticular hydrocarbons as determined using commercial standards of known concentration.

I next investigated the effect of chronic temperature changes during adulthood on the cuticular hydrocarbon blend. Previous studies have found that flies housed throughout development and adulthood at higher temperatures (30℃) are enriched in longer chain cuticular hydrocarbons whereas flies housed at lower temperatures (18℃) are enriched in shorter chain cuticular hydrocarbons. This effect was also recapitulated in wild geographically distinct *Drosophila melanogaster* populations in the US (Rajpurohit et al., 2017). An acute response to temperature has been demonstrated in *Drosophila mojavensis*, a desert resident species, which show an increase in cuticular hydrocarbon chain length from approximately 5 days after the temperature shift (17℃ versus 33℃) (Gibbs et al., 1998). I utilised a temperature-shift protocol that occurred post-eclosion to investigate if adult *Drosophila melanogaster* were able to adapt the hydrocarbons they produce in response to this change in environment. Flies were housed at three separate temperatures (18℃, 25℃ and 29℃) for two weeks post-eclosion (**Figure 6.9A**). This revealed striking changes in the cuticular lipid blend, indicating a preference for shorter chain hydrocarbons at colder temperatures and longer chain hydrocarbons at higher temperatures, an effect which was observed for all hydrocarbon species (**Figure 6.8. Figure 6.9D**). This was also accompanied by an apparent decrease in the proportion of alkenes at higher temperatures (**Figure 6.9B, C**). This trend for cuticular hydrocarbons was also replicated in the “shed” hydrocarbons extracted from the fly vials(**Figure 6.9B-D**). To ensure the observed changes were not experimentally induced artefacts, a control hydrocarbon blend was extracted from vials after 24 hours at the three different temperatures. This important control indicated a decreased recovery of shorter chain alkanes and alkenes from vials at 29℃ compared to 18℃ (**Figure 6.10**). For a C18 chain length alkane, the decreased recovery at 29℃ compared to 18℃ was more than three-fold but for chain lengths of C23 ((*Z*)-9-tricosene and tricosane) and longer, there was less than a two-fold drop. This is likely due to the greater volatility 0f shorter chain alkanes and alkenes at higher temperatures. Therefore it is not possible to determine if the observed decrease in the proportion of alkenes on the fly surface at higher housing temperatures reflects lower biosynthesis or just increased volatility at higher temperatures. In

support of the latter argument, the C23 desaturation ratio ((*Z*)-7-tricosene/tricosane) decreases at higher temperatures but the C25 desaturation ratio ((*Z*)-7-pentacosene/pentacosane) does not (**Figure 6.9B,C**). Either way, the increase in longer chain hydrocarbons on the cuticule at higher temperature cannot be accounted for by volatility, and so likely equates to increased production. The changes in hydrocarbon blend are also accompanied by an increase in overall amount of "shed" hydrocarbons at 25℃ and 29℃ compared to 18℃ (**Figure 6.9E**). This could be due to increased grooming and perhaps overall fly activity at higher temperatures.

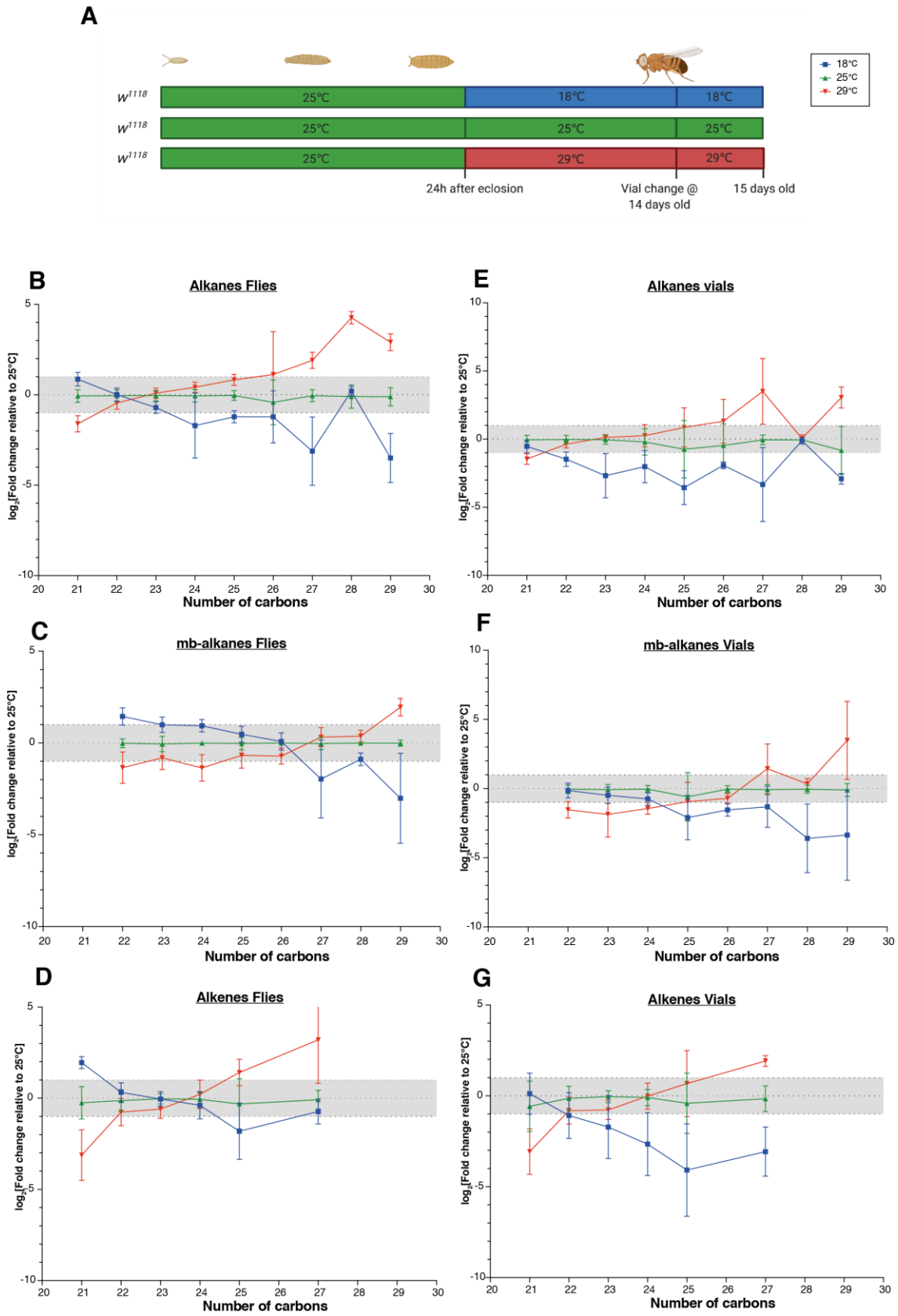
A
w1118
25°C
18°C
18°C
w1118
25°C
25°C
25°C
w1118
25°C
29°C
29°C
18°C
25°C
29°C
24h after eclosion
Vial change @ 14 days old
15 days old
B
Alkanes Flies
E
Alkanes vials
C
mb-alkanes Flies
F
mb-alkanes Vials
D
Alkenes Flies
G
Alkenes Vials
log2[Fold change relative to 25°C]
Number of carbons

Figure 6.8 Adult housing temperature influences the chain length of cuticular hydrocarbons

A. Flies were housed at a temperature of 25℃ and switched to a temperature of 18℃, 25℃ or 29℃ within 24h of eclosion. Male flies were housed at a density of 10 flies per vial for a period of 14 days. The vials were then exchanged and the flies housed in fresh vials for 24 hours at which time hydrocarbons were extracted from both flies and vials.
B-G. Log_2 fold change in hydrocarbon abundance at the three temperatures calculated relative to 25℃. The grey region indicates a +/- 2 fold change. Hydrocarbons are displayed by number of carbons in the molecule. **B-D** show relative abundance on the surface of the fly, **E-G** show relative abundance of "shed" hydrocarbons in the vials. **B,E** show alkanes, **C,F** show methyl-branched alkanes, **D,G** show alkenes. When there is more than one alkene for an indicated carbon chain length, the log_2 fold change values for each alkene all contribute to the mean and standard deviation shown.
Graphs show the mean of three independent experiments, each containing six replicates. Error bars represent standard deviation. Data showing the log_2 fold change for all individual hydrocarbons is shown in **Supplementary Figure 9.25** and **Supplementary Tables 9.20-9.21** located in the Supplementary Material.

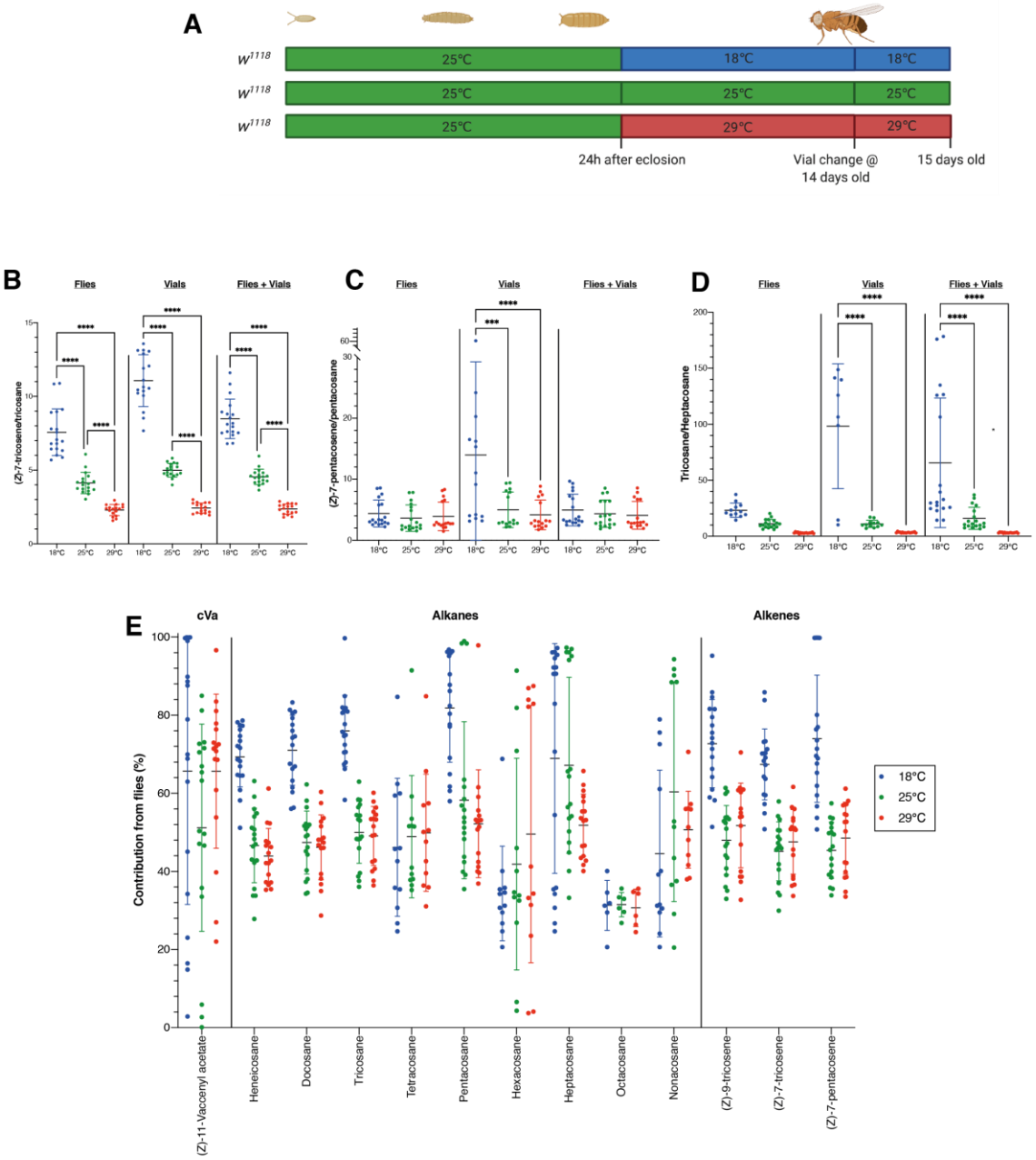

Figure 6.9 Adult housing temperature alters the cuticular hydrocarbon saturation index

A. Flies were housed at a temperature of 25℃ and switched to a temperature of 18℃, 25℃ or 29℃ within 24h of eclosion. Male flies were housed at a density of 10 flies per vial for a period of 14 days. The vials were then exchanged and the flies housed in fresh vials for 24 hours at which time hydrocarbons were extracted from both flies and vials.
B. Hydrocarbon saturation as measured using the ratio of (*Z*)-7-tricosene to tricosane.
C. Hydrocarbon saturation as measured using the ratio of (*Z*)-7-pentacosene to pentacosane.
D. Hydrocarbon elongation as measured using the ratio of tricosane to heptacosane.
E. Relative proportion of hydrocarbons on the surface of the fly compared with the total hydrocarbons on both the fly and the vial. Statistical significance for the comparisons shown is illustrated in **Supplementary Table 9.28** located in the Supplementary Material.

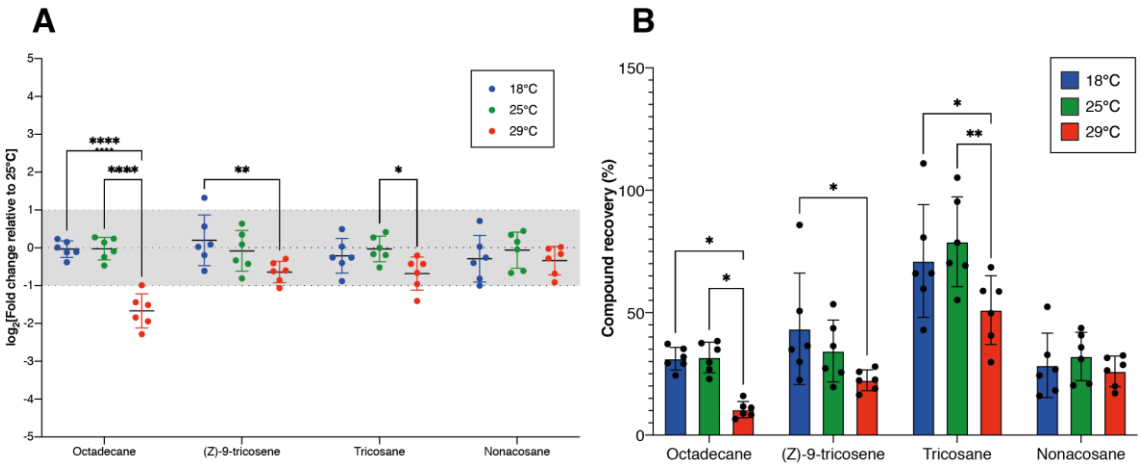

Figure 6.10 Shorter chain hydrocarbons have a lower recovery at high temperatures

Experimental control showing the recovery rate of different synthetic hydrocarbons when added to fly vials and stored at 18℃, 25℃ or 29℃ for 24 hours.
A. Log_2 fold change of hydrocarbon abundance relative to hydrocarbons stored at 25℃.
B. Percentage recovery of each hydrocarbon at each temperature when compared with a freshly prepared mixture of the same standards at the same concentrations.

As discussed in the Introduction, an increase in housing density (crowding) tends to decrease fly lifespan (Stefana et al., 2017). Remarkably, this decrease in longevity can be rescued by oenocyte expression of *Desat1 RNAi* (Stefana et al., 2017). Together with the finding that vial supplementation with cuticular alkenes but not alkanes is sufficient to decrease lifespan, this suggests that high housing densities raise alkene levels to the point where they become toxic (Stefana et al., 2017). Therefore, I wanted to test the hypothesis that increasing housing density influences the levels of cuticular hydrocarbons. To address this, *w^{1118} iso31* flies were housed at densities from 1 to 80 flies per vial for two weeks and then cuticular and vial ("shed") hydrocarbons analysed. Interestingly, this revealed that higher housing densities tend not to increase total (flies plus vial) hydrocarbons but they do lead to an increase in cuticular hydrocarbons at the expense of vial hydrocarbons (**Figure 6.11B, C, Figure 6.12B**). The proportion of total (flies plus vial) hydrocarbons recovered from the surface of the fly increased with increasing density, from ~10% at 1 fly per vial to more than 50% at >20 flies per vial (**Figure 6.12D**). This indicates that even for the increase from 1 to 20 flies per vial, there is either decreased shedding or a decrease in subsequent hydrocarbon "loss" from the vials. To generalise this finding, a further experiment was carried out using a different strain of flies (*Oregon R*), which gave very similar results (**Figure 6.13**). For both *w^{1118} iso31* and *Oregon R*, I also observed a second and very intriguing effect of increasing housing density, namely that desaturation index (e.g. (*Z*)-7-tricosene/tricosane) does not change overall (flies plus vial), yet it significantly increases on the fly cuticle when decreasing in the vial (**Figure 6.12C, Figure 6.14C**). Taken together, these results indicate that higher housing densities increase the absolute amounts of oenocyte-derived hydrocarbons on the cuticle and that this increase is particularly large for "autotoxic" alkenes. Hence, an increase in cuticular alkenes could contribute to the density-dependent decrease in lifespan.

As a result, the absolute amount of "autotoxic" alkenes on the surface of the fly increases with density, which may in part explain the density-dependent decrease in lifespan.

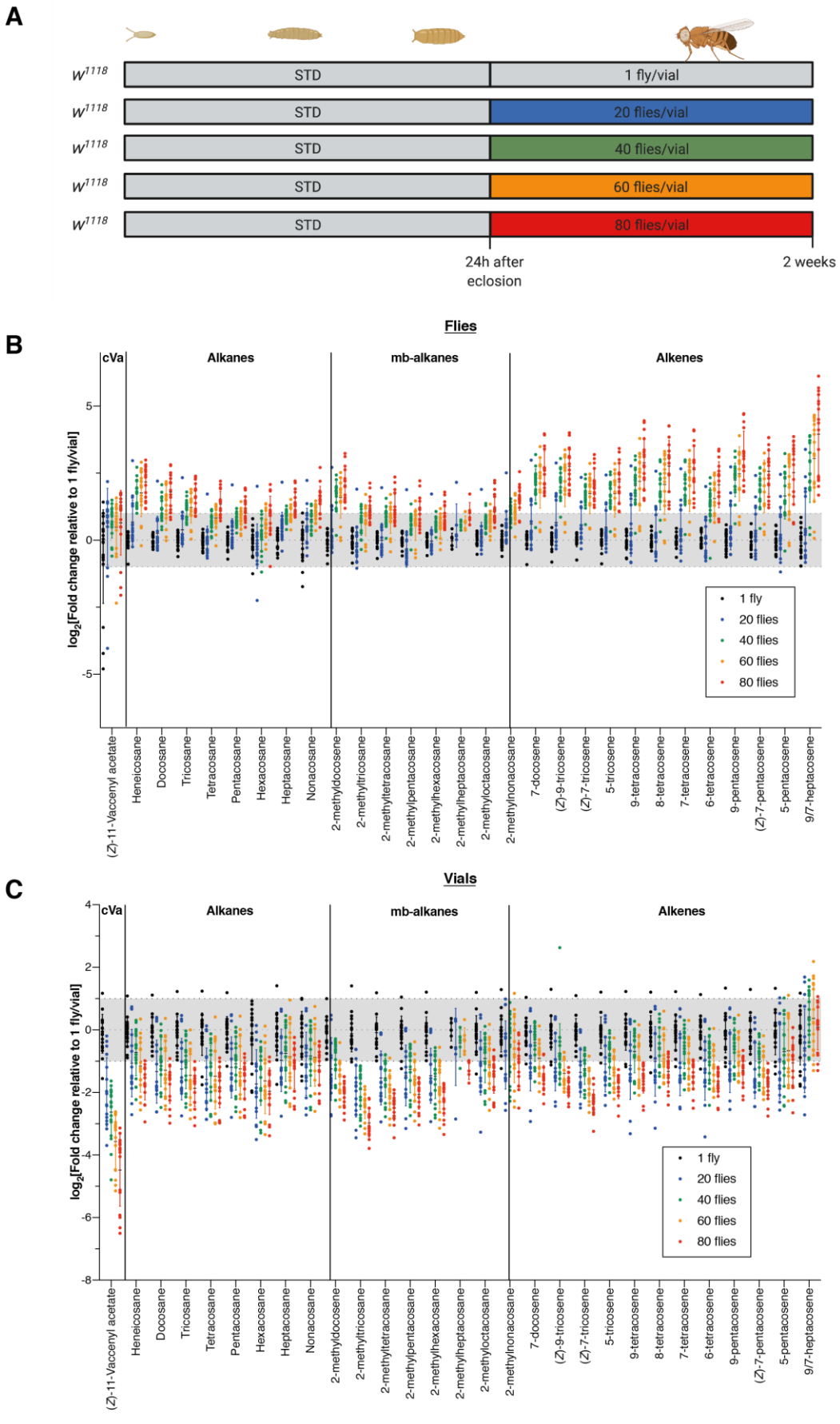
A
w1118
STD
1 fly/vial
20 flies/vial
40 flies/vial
60 flies/vial
80 flies/vial
24h after eclosion
2 weeks
B
Flies
cVa
Alkanes
mb-alkanes
Alkenes
log2[Fold change relative to 1 fly/vial]
1 fly
20 flies
40 flies
60 flies
80 flies
(Z)-11-Vaccenyl acetate
Heneicosane
Docosane
Tricosane
Tetracosane
Pentacosane
Hexacosane
Heptacosane
Nonacosane
2-methyldocosene
2-methyltricosane
2-methyltetracosane
2-methylpentacosane
2-methylhexacosane
2-methylheptacosane
2-methyloctacosane
2-methylnonacosane
7-docosene
(Z)-9-tricosene
(Z)-7-tricosene
5-tricosene
9-tetracosene
8-tetracosene
7-tetracosene
6-tetracosene
9-pentacosene
(Z)-7-pentacosene
5-pentacosene
9/7-heptacosene
C
Vials

Figure 6.11 Housing density alters the amounts of cuticular and vial hydrocarbons

A. Schematic of the housing density conditions used. Male flies were transferred to the densities indicated within 24 hours of eclosion for a period of two weeks.
B. Relative abundance of hydrocarbons extracted from the fly surface at different densities. Information on statistical significance values for comparisons in this graph are shown in **Supplementary Table 9.23** located in the Supplementary Material.
C. Relative abundance of hydrocarbons extracted from the fly vial at different densities. Information on statistical significance values for comparisons in this graph are shown in **Supplementary Table 9.24** located in the Supplementary Material.
Data in this figure represents three independent experiments, each experiment with six replicates per condition. Each datapoint represents one sample obtained from five flies.

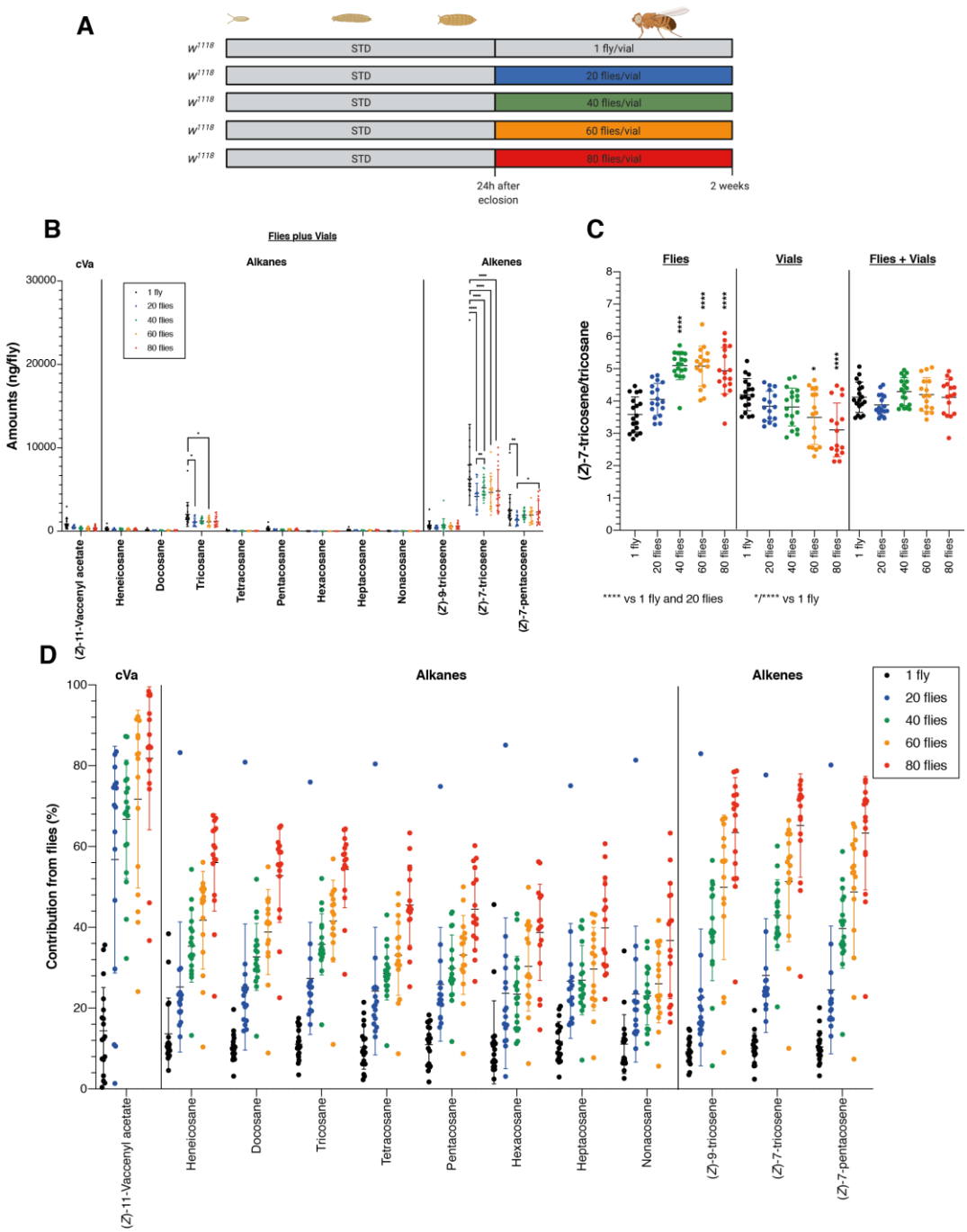

Figure 6.12 Housing density alters the fly versus vial hydrocarbon balance - the saturation index but not the total amount of hydrocarbons

A. Schematic of housing density conditions used.
B. Total amounts of hydrocarbon species present on the fly surface and vial combined presented for each vial density.
C. Saturation index calculated as a ratio of (*Z*)-7-tricosene/tricosane.
D. Relative proportion of hydrocarbons present on the surface of the fly compared to the total amounts on the fly surface and vial combined. Information on the statistical significance of individual comparisons for this graph is available in **Supplementary Table 9.25** located in the Supplementary Material.
Data in this figure represents three independent experiments, each experiment with six replicates per condition. Each datapoint represents one sample obtained from five flies.

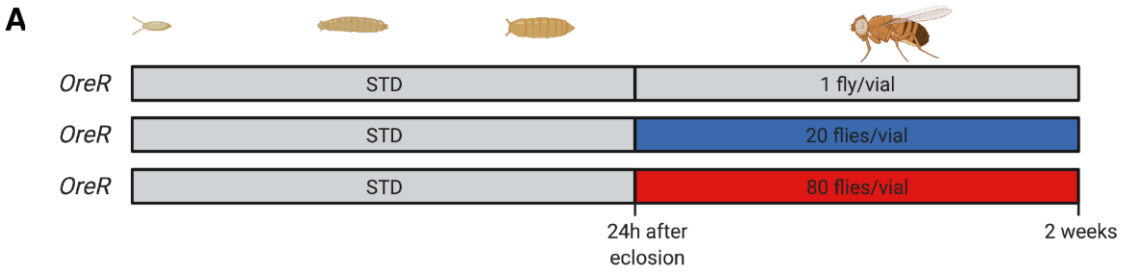
A
OreR
STD
1 fly/vial
OreR
STD
20 flies/vial
OreR
STD
80 flies/vial
24h after eclosion
2 weeks

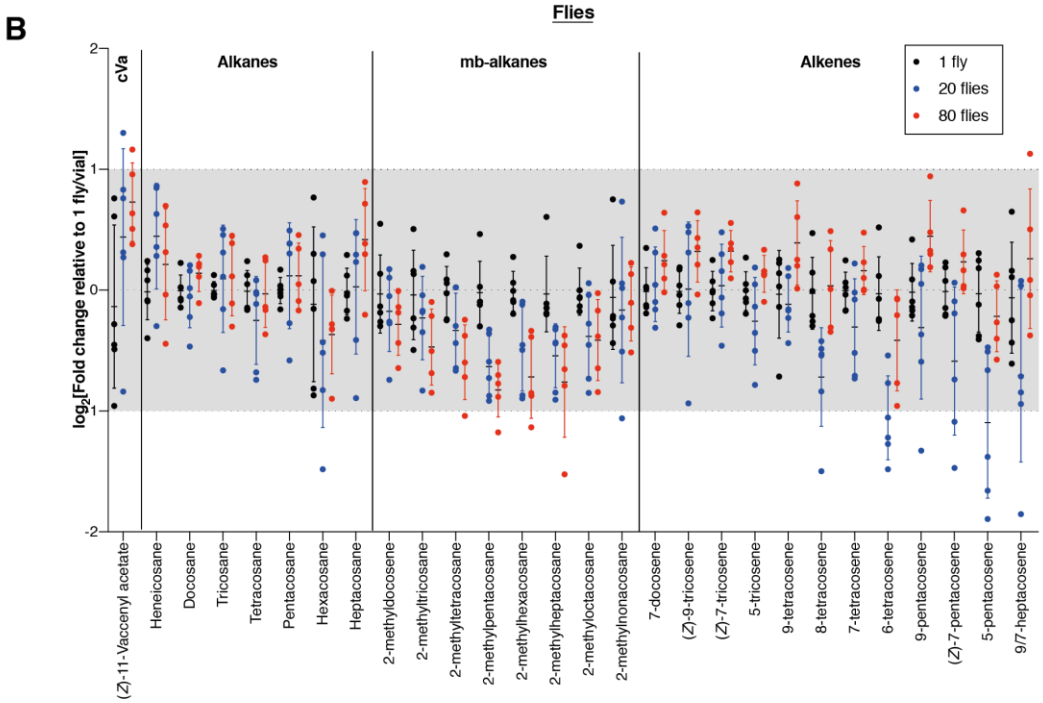
B
Flies
cVa
Alkanes
mb-alkanes
Alkenes
1 fly
20 flies
80 flies
log2[Fold change relative to 1 fly/vial]
(Z)-11-Vaccenyl acetate
Heneicosane
Docosane
Tricosane
Tetracosane
Pentacosane
Hexacosane
Heptacosane
2-methyldocosene
2-methyltricosane
2-methyltetracosane
2-methylpentacosane
2-methylhexacosane
2-methylheptacosane
2-methyloctacosane
2-methylnonacosane
7-docosene
(Z)-9-tricosene
(Z)-7-tricosene
5-tricosene
9-tetracosene
8-tetracosene
7-tetracosene
6-tetracosene
9-pentacosene
(Z)-7-pentacosene
5-pentacosene
9/7-heptacosene

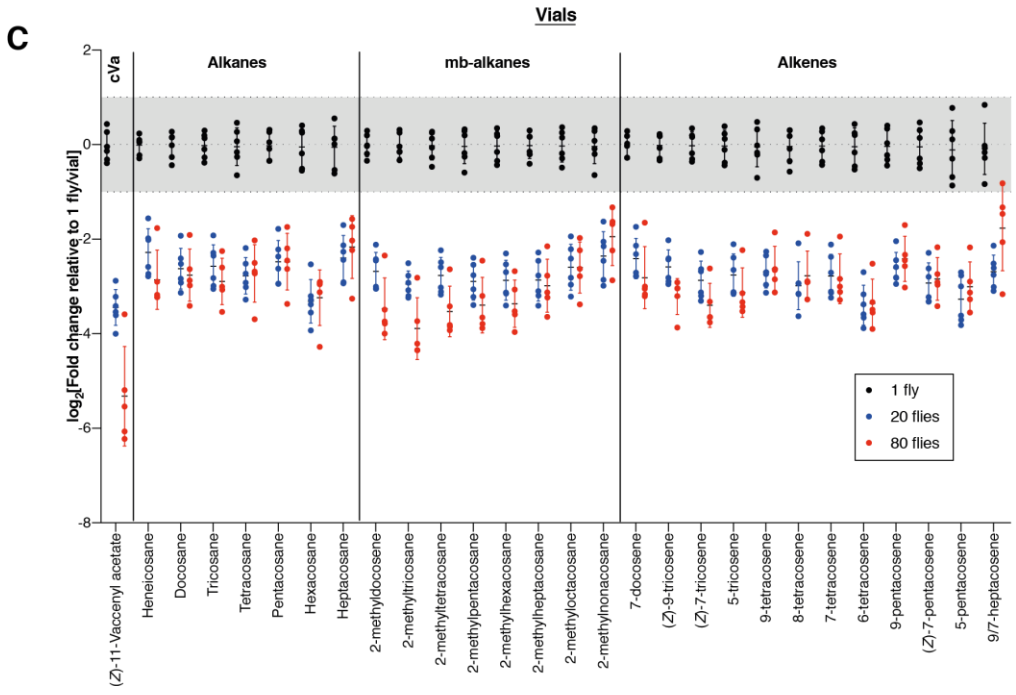
C
Vials
cVa
Alkanes
mb-alkanes
Alkenes
1 fly
20 flies
80 flies
log2[Fold change relative to 1 fly/vial]
(Z)-11-Vaccenyl acetate
Heneicosane
Docosane
Tricosane
Tetracosane
Pentacosane
Hexacosane
Heptacosane
2-methyldocosene
2-methyltricosane
2-methyltetracosane
2-methylpentacosane
2-methylhexacosane
2-methylheptacosane
2-methyloctacosane
2-methylnonacosane
7-docosene
(Z)-9-tricosene
(Z)-7-tricosene
5-tricosene
9-tetracosene
8-tetracosene
7-tetracosene
6-tetracosene
9-pentacosene
(Z)-7-pentacosene
5-pentacosene
9/7-heptacosene

Figure 6.13 Housing density effects on the hydrocarbons of *OreR* flies

A. Schematic of housing density conditions used. Male flies were transferred to fresh vials at the indicated densities within 24 hours of eclosion and housed for two weeks before hydrocarbon extraction.
B. Relative hydrocarbon abundance on the surface of the fly expressed relative to a density of one fly per vial. Statistical information for comparisons shown in this graph is displayed in **Supplementary Table 9.26** located in the Supplementary Material.
C. Relative hydrocarbon abundance on the fly vial expressed relative to a density of one fly per vial. Statistical information for comparisons shown in this graph is displayed in **Supplementary Table 9.27** located in the Supplementary Material.
Data in this figure represents one independent experiment with six replicates per condition. Each datapoint represents one sample obtained from five flies.

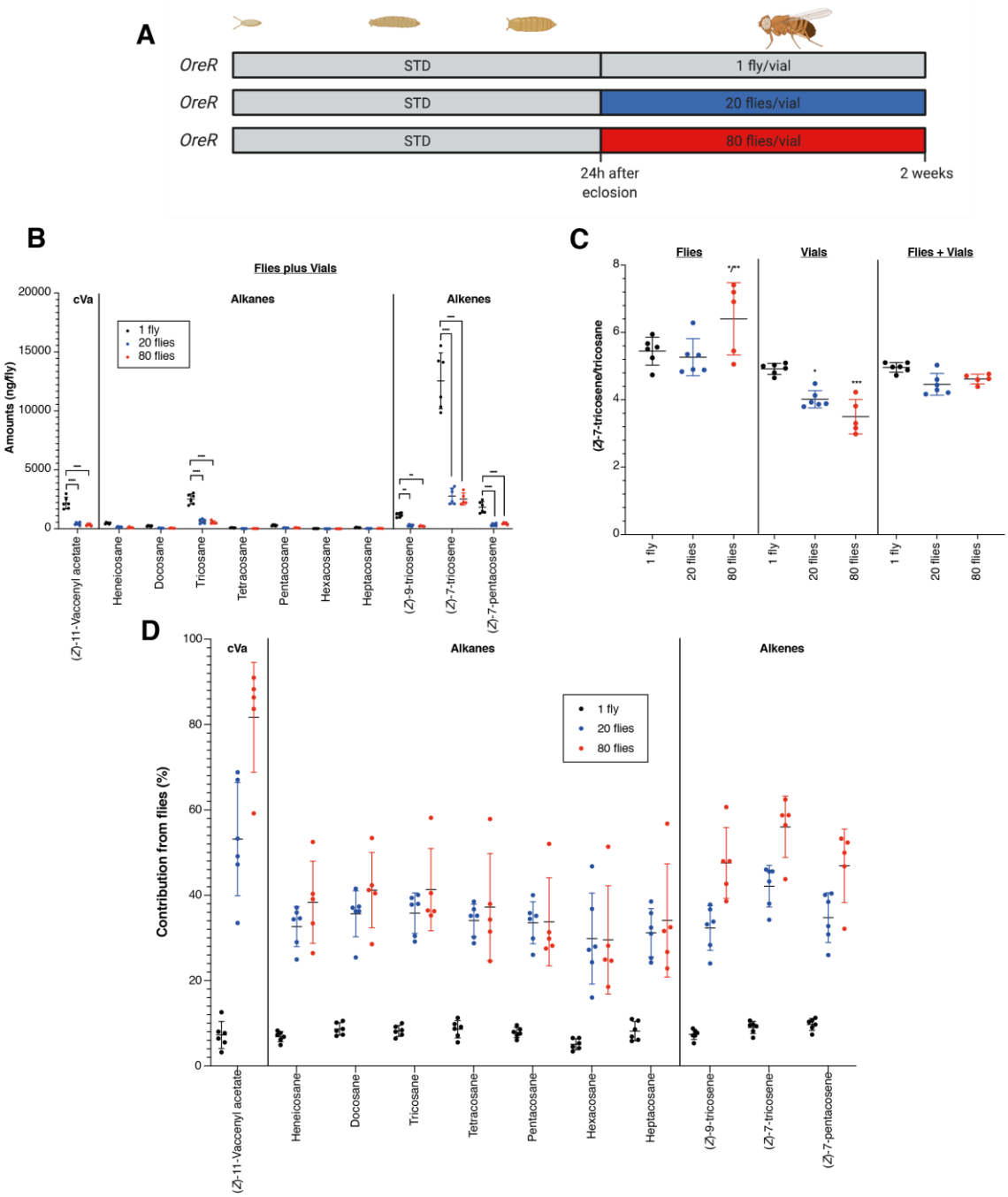

Figure 6.14 Housing density alters the fly versus vial balance of hydrocarbons in *OreR* flies

A. Schematic of the housing density conditions used.
B. Absolute abundance of hydrocarbons on the surface of the fly and the vial combined in nanograms per fly.
C. Saturation index shown by the ratio of (*Z*)-7-tricosene/tricosane.
D. Percentage of total hydrocarbons present on the surface of the fly compared with the fly surface and the vial combined. Statistical information for the comparisons made in this graph is displayed in **Supplementary Table 9.28** located in the Supplementary Material.
Data in this figure represents one independent experiment with six replicates per condition. Each datapoint represents one sample obtained from five flies.

I next addressed why the proportion of total hydrocarbons ending up in the vial decreases with increasing housing density. One possibility is that there is an increase in bacteria that metabolise vial hydrocarbons at higher densities. Therefore, a similar housing density experiment was performed in the presence of a broad-spectrum antibiotic cocktail known to abolish fly microbiota (Obata et al., 2018). This showed a similar response to the antibiotic-free experiment with an increase in cuticular hydrocarbons and a decrease in vial hydrocarbons at higher housing densities (**Figure 6.15, Figure 6.16**). Interestingly, however, the abundance of all hydrocarbons on both the fly and in the vial increased in the presence of antibiotics, suggesting either that bacteria do indeed metabolise hydrocarbons or that antibiotics induce some kind of cuticular stress response in flies. Either way, the antibiotic experiments reveal that bacteria cannot account for the effects of housing density on shed hydrocarbons. A second possibility that could explain why flies at higher densities shed less hydrocarbons could be decreased grooming behaviour. To test this, flies were coated with Reactive Yellow 86, a dye powder that is known to increase grooming (Zhang et al., 2020), and hydrocarbons measured at a density of one fly per vial. I observed that Reactive Yellow 86 did not change total hydrocarbon levels or hydrocarbon desaturation index, but it did significantly decrease the proportion of hydrocarbons on the fly cuticular surface versus vial by about 10% in 24 hours (**Figure 6.17B-D**). This percentage decrease is less than that observed with dense housing but still remains compatible with the initial hypothesis that decreased grooming increases the proportion of hydrocarbons that are retained on the surface of the fly rather than being shed into the vial. Although a decrease in grooming behaviour may explain why densities above 1 fly per vial tend to increase the amounts of cuticular hydrocarbons, it does not account for the observed changes in desaturation index on the fly surface. In combination, the housing density results strongly suggest that flies can sense and respond to an increase in their surrounding conspecifics via two separate regulatory mechanisms. First, they decrease grooming and retain more cuticular hydrocarbons in general. And second, they are able to increase specifically the alkene-to-alkane ratio of the lipid blend on the cuticle. Together, both effects will

tend to increase the absolute amounts of alkenes on the cuticle per fly when they are housed in groups rather than alone. In turn, this is likely to have significant effects on fly lifespan in both the pheromonal and autotoxic actions of alkenes.

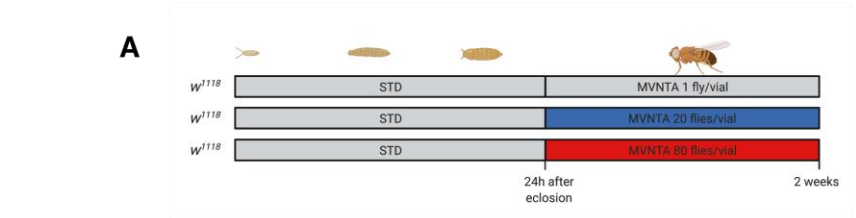
A
w1118
STD
MVNTA 1 fly/vial
w1118
STD
MVNTA 20 flies/vial
w1118
STD
MVNTA 80 flies/vial
24h after eclosion
2 weeks

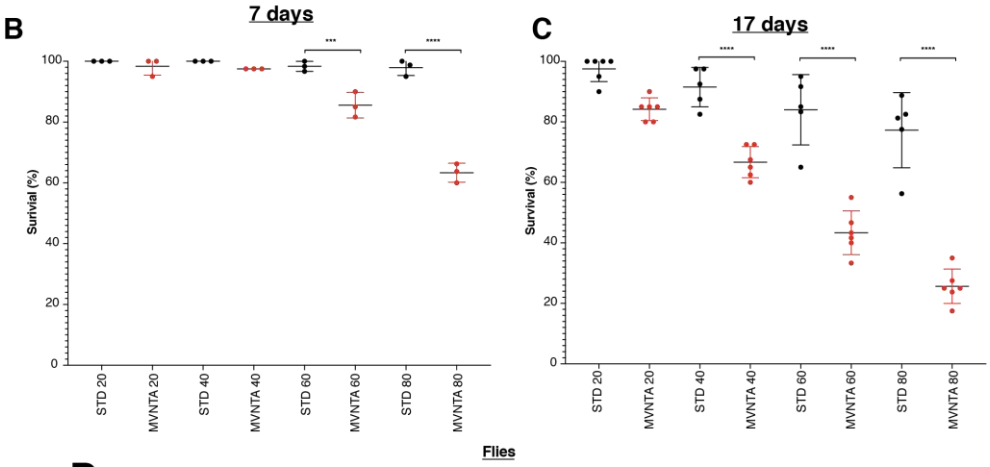
B
7 days
Survival (%)
STD 20
MVNTA 20
STD 40
MVNTA 40
STD 60
MVNTA 60
STD 80
MVNTA 80
C
17 days
Survival (%)
STD 20
MVNTA 20
STD 40
MVNTA 40
STD 60
MVNTA 60
STD 80
MVNTA 80

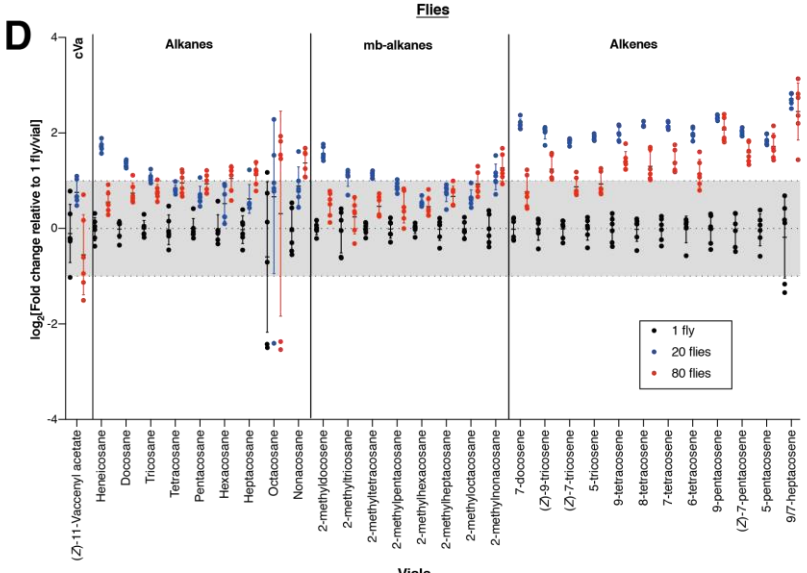
Flies
D
cVa
Alkanes
mb-alkanes
Alkenes
log2[Fold change relative to 1 fly/vial]
1 fly
20 flies
80 flies
(Z)-11-Vaccenyl acetate
Heneicosane
Docosane
Tricosane
Tetracosane
Pentacosane
Hexacosane
Heptacosane
Octacosane
Nonacosane
2-methyldocosene
2-methyltricosane
2-methyltetracosane
2-methylpentacosane
2-methylhexacosane
2-methylheptacosane
2-methyloctacosane
2-methylnonacosane
7-docosene
(Z)-9-tricosene
(Z)-7-tricosene
5-tricosene
9-tetracosene
8-tetracosene
7-tetracosene
6-tetracosene
9-pentacosene
(Z)-7-pentacosene
5-pentacosene
9/7-heptacosene

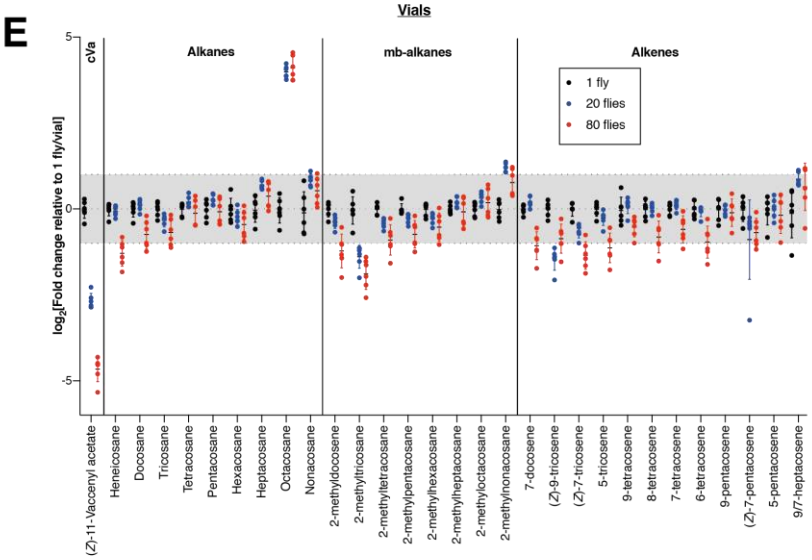
Vials
E
cVa
Alkanes
mb-alkanes
Alkenes
log2[Fold change relative to 1 fly/vial]
1 fly
20 flies
80 flies
(Z)-11-Vaccenyl acetate
Heneicosane
Docosane
Tricosane
Tetracosane
Pentacosane
Hexacosane
Heptacosane
Octacosane
Nonacosane
2-methyldocosene
2-methyltricosane
2-methyltetracosane
2-methylpentacosane
2-methylhexacosane
2-methylheptacosane
2-methyloctacosane
2-methylnonacosane
7-docosene
(Z)-9-tricosene
(Z)-7-tricosene
5-tricosene
9-tetracosene
8-tetracosene
7-tetracosene
6-tetracosene
9-pentacosene
(Z)-7-pentacosene
5-pentacosene
9/7-heptacosene

Figure 6.15 Antibiotics do not block the effect of housing density on cuticular hydrocarbons

A. Flies were raised on standard food throughout development and male flies were transferred to antibiotic-containing food at the densities indicated within 24 hours of eclosion. Hydrocarbons were measured two weeks after this date and the vials were not changed within this period.
B. Fly survival at different densities on standard and antibiotic-containing food after 7 days.
C. Fly survival at different densities on standard and antibiotic-containing food after 17 days.
D. Relative abundance of hydrocarbons extracted from the fly surface after two weeks at the indicated density. Results are shown relative to a density of one fly per vial. Results shown are from one experiment containing six replicates. Each datapoint represents one sample collected from five flies. Statistical significance information is shown in **Supplementary Table 9.29** located in the Supplementary Material.
E. Relative abundance of hydrocarbons extracted from the fly vials after two weeks at the indicated density. Results are shown relative to a density of one fly per vial. Results shown are from one experiment with six replicates. Each datapoint represents one sample obtained from five flies. Statistical significance information is shown in **Supplementary Table 9.30** located in the Supplementary Material.

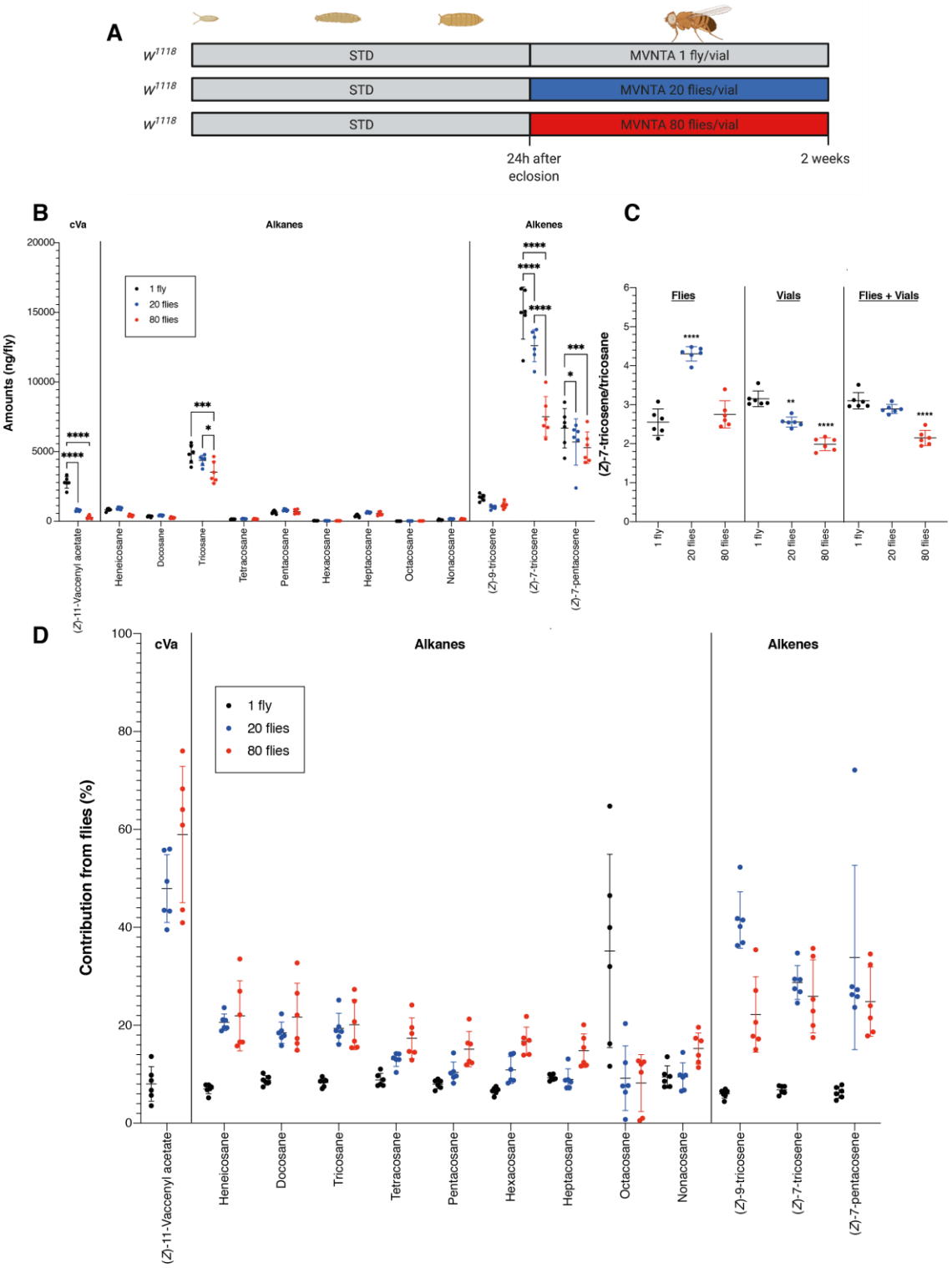
A
w1118
STD
MVNTA 1 fly/vial
MVNTA 20 flies/vial
MVNTA 80 flies/vial
24h after eclosion
2 weeks
B
cVa
Alkanes
Alkenes
1 fly
20 flies
80 flies
Amounts (ng/fly)
(Z)-11-Vaccenyl acetate
Heneicosane
Docosane
Tricosane
Tetracosane
Pentacosane
Hexacosane
Heptacosane
Octacosane
Nonacosane
(Z)-9-tricosene
(Z)-7-tricosene
(Z)-7-pentacosene
C
Flies
Vials
Flies + Vials
(Z)-7-tricosene/tricosane
D
Contribution from flies (%)

Figure 6.16 Housing density alters the proportion of hydrocarbons on the fly cuticle in the presence of antibiotics

A. Schematic of the housing density conditions used.
B. Absolute abundance of hydrocarbons on the surface of the fly and the vial combined in nanograms per fly.
C. Saturation index shown by the ratio of (*Z*)-7-tricosene/tricosane.
D. Percentage of total hydrocarbons present on the surface of the fly compared with the fly surface and the vial combined. Statistical information for the comparisons made in this graph is displayed in **Supplementary Table 9.31** located in the Supplementary Material.
Data in this figure represents one independent experiment with six replicates per condition. Each datapoint represents one sample obtained from five flies.

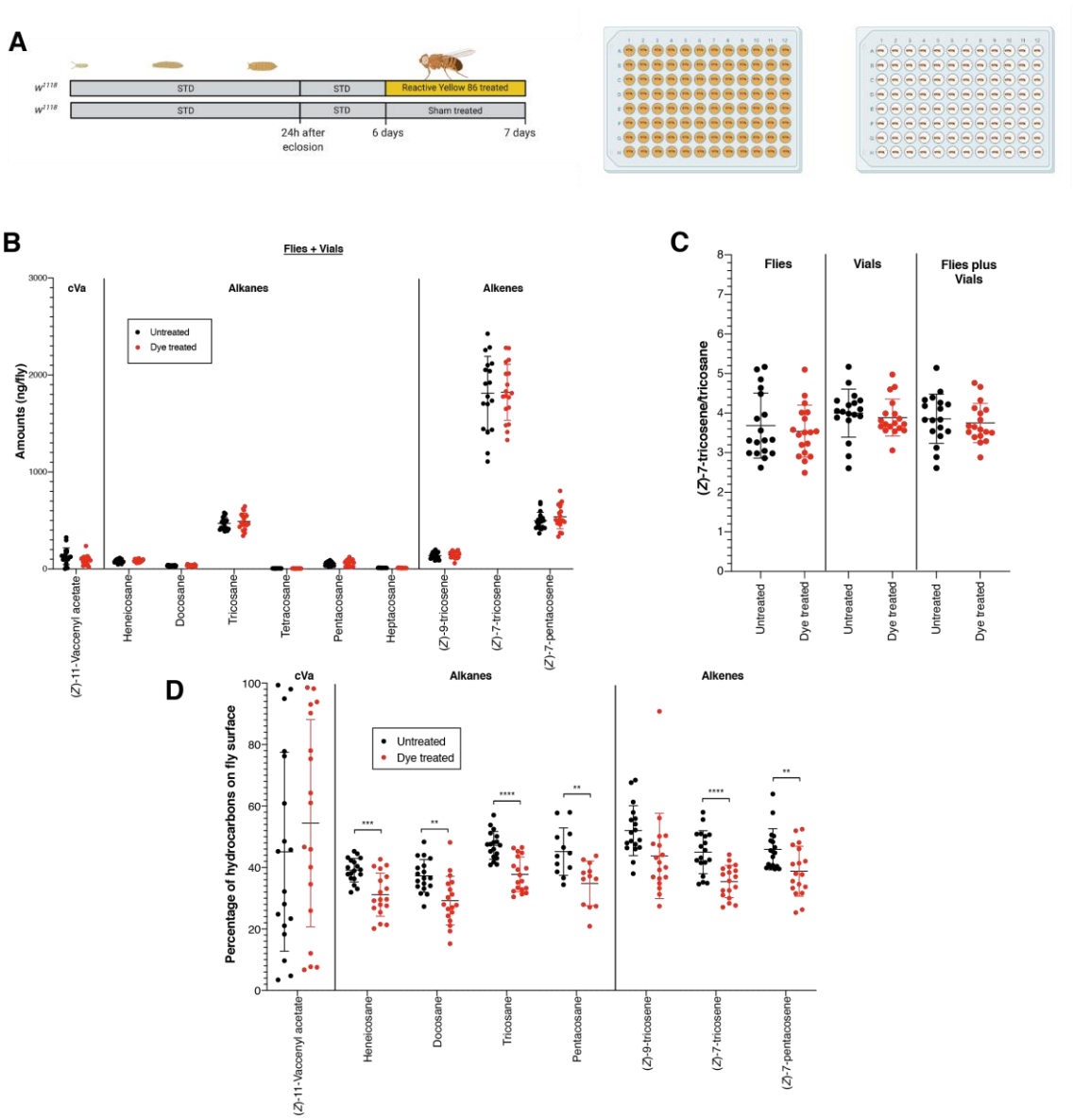

Figure 6.17 Grooming decreases the amount but not the blend of cuticular hydrocarbons

A. Experimental schematic. Flies were coated in Reactive Yellow 86 dye powder while anesthetised in multiwell plates, and the untreated flies were exposed to a similar "sham" treatment without the dye powder. After treatment with dye powder, flies were transferred to fresh vials at a density of 1 fly per vial. Hydrocarbons were then extracted 24 hours after treatment.
B. Absolute abundance of hydrocarbons per fly extracted from the surface of the fly and the fly vial combined, as calculated using GC-MS. There are no statistically significant differences between the treatment group and control group in total abundance of hydrocarbons.
C. Saturation index of hydrocarbons as measured using (*Z*)-7-tricosene/tricosane ratio. There are no statistically significant differences between the control group and treatment group in either three groups (flies, vials, and flies plus vials).
D. Percentage of total hydrocarbons extracted from the surface of the fly (when compared with the sum of surface and vial hydrocarbons). Statistical significance is indicated on the graph.
Additional data showing the relative and absolute hydrocarbon levels on the fly surface and vial separately is available in **Supplementary Figure 9.26** located in the Supplementary Material.
Data in this figure represents three independent experiments, each experiment with six replicates per condition. Each datapoint represents one sample obtained from five flies.

6.4 Discussion

In Chapter 5, I identified that carbons from both the developmental and adult diet contribute to the biosynthesis of cuticular lipids. I also proposed the contribution of free fatty acids from two different intracellular pools (mitochondrial and cytoplasmic) to the synthesis of cuticular lipids. In this chapter, I investigated the molecular regulation of lipid production in adult oenocytes using a variety of different genetic manipulations. This revealed oenocytes as a key part of the cellular machinery required to synthesise/regulate non-hydrocarbon cuticular lipids and that this process requires SREBP. It would be interesting to use a different temperature-shift regime with *PromE>SREBPDN* to test directly whether a larval or pupal phase of SREBP activity is required for non-hydrocarbon cuticular lipids in early adults. Together, the genetic manipulations shown in this chapter indicate that the oenocyte activity of SREBP, HNF4 and Cyp4g1 (but not TSC1/2 during adulthood) influences non-hydrocarbon cuticular lipids (**Table 6.1**). An unexpected finding here was that Cyp4g1 knockdown not only decreased hydrocarbons but also saturated FFAs and GLs. Therefore, the biosynthesis of these, but not other non-hydrocarbon lipid species, is positively regulated in some way by a Cyp4g1 dependent mechanism, perhaps reflecting a positive regulation of oenocyte mitochondrial FAS by hydrocarbons. The combination of these data has contributed further understanding to the regulation of cuticular lipid synthesis (**Figure 6.18**).

Table 6.1 Outcomes of oenocyte-specific genetic manipulations on cuticular lipid composition

	Alkenes	Dienes	Alkanes	Methyl-branched alkanes	Saturated FFA	Unsaturated FFA	Saturated WE	Unsaturated WE	PL	GL	Cer	Peptides
Cyp4g1 RNAi	↓↓	↓↓	↓↓	↓↓	↓	-	↓	↑	↓	↓	-	↑
SREBP^{DN} (throughout development)	↓	↓	-	-	↑↑	↑	↓↓	↓↓	↓↓	↑↑	-	-
Hnf4 RNAi					-	↓	-	↓	↓	-	-	↑
TSC1/2					-	-	-	-	-	-	-	-

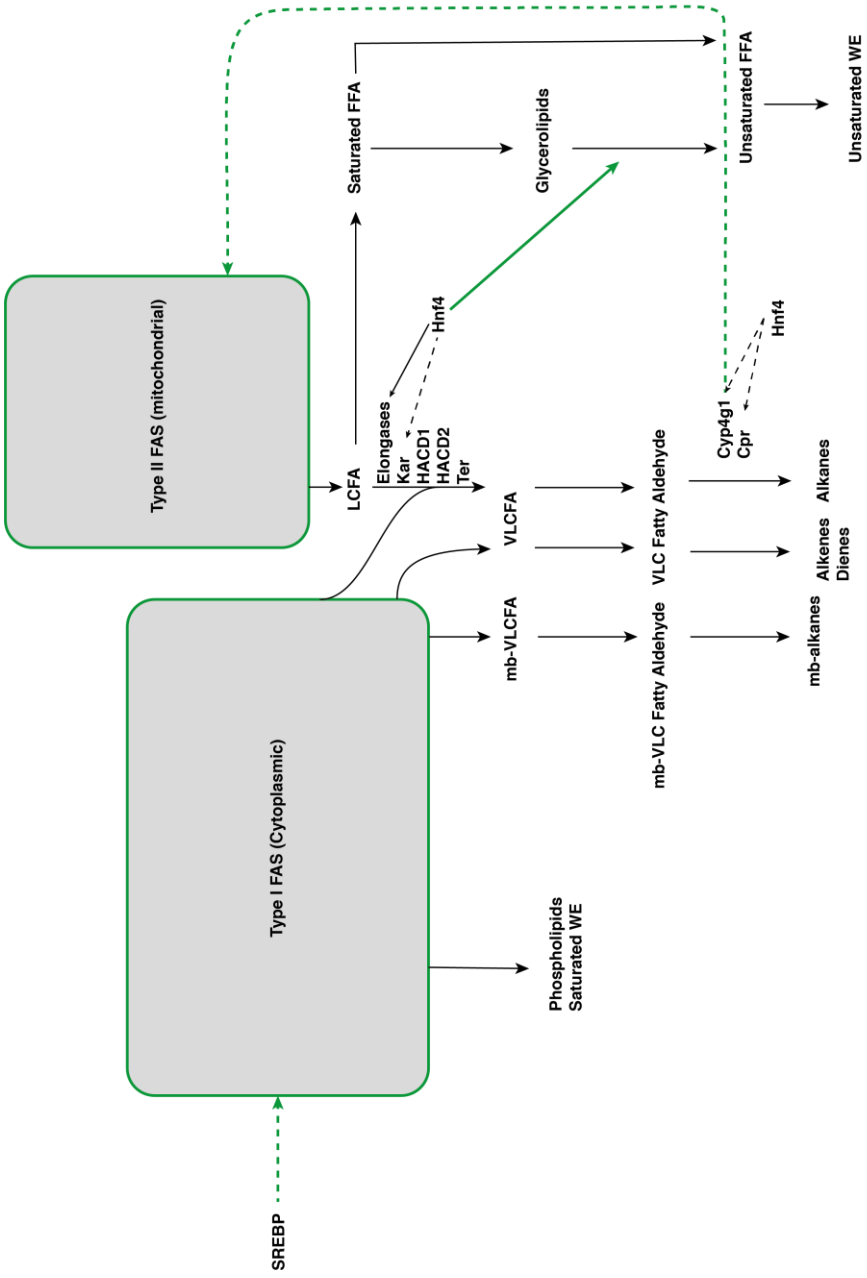

Figure 6.18 Proposed model for the molecular regulation and biochemical synthesis pathways underlying cuticular lipid synthesis
Proposed biosynthetic model for cuticular lipids. Steps highlighted in green represent contributions from Chapter 5 and Chapter 6 of this thesis.

This chapter also identified temperature and housing density (bu
as two adult environmental factors that strongly affect tl

composition of cuticular hydrocarbons. Some temperature effects on hydrocarbon chain length had been previously reported (Gibbs et al., 1998, Rajpurohit et al., 2021), but my result add to this by showing that the apparent decrease in shorter chain hydrocarbons at higher temperatures is enhanced by increased volatility. The increased hydrocarbon chain length observed at higher temperatures does not appear to decrease water loss (Gibbs et al., 1998). It is unclear what, if any, functional benefit this may provide. One possibility is that increasing chain length with temperature is important for maintaining an optimal degree of volatility, which may be important for pheromonal communication via odorant receptor pathways. As increased temperature also results in increased levels of volatile alkene pheromones, it is possible this could have a knock-on effect on behaviour. Indeed, this could in part explain the increase in fecundity seen when housing *Drosophila* at higher temperatures (Lazzaro et al., 2008). Either way, a potentially simple underlying mechanism for increased chain length would be a temperature effect on the rate of the FA elongase reaction.

A very exciting finding from this chapter is that housing density alters both the amount and composition of cuticular hydrocarbons in a way that may account for why it decreases lifespan. In particular, I found that increased densities above one fly per vial increased the amount of hydrocarbons on the fly cuticle, and correspondingly decreased the amount of hydrocarbons “shed” in the fly vials. I found that decreased shedding into the vial, likely accounted for by decreased grooming, may explain why the absolute amounts of cuticular hydrocarbons increase with housing density. I also observed that the housing-density dependent increase in the alkene:alkane ratio of the cuticle inversely correlated with that of the vial. This effect was not recapitulated with experimentally-induced grooming, suggesting that increased grooming alone cannot account for the cuticular increase in the alkene:alkane ratio. The housing density experiments together provide evidence that flies can sense and respond to an increase in their surrounding conspecifics via two separate regulatory mechanisms. First, they decrease grooming and retain more hydrocarbons in general. Second, they are able to increase specifically the alkene-to-alkane ratio of the lipid blend on the cuticle. Together, both effects will tend to increase the absolute amounts of

alkenes on the cuticule per fly when they are housed in groups rather than alone. In turn, this is likely to have significant effects on fly lifespan via both the pheromonal and autotoxic actions of alkenes. To understand the molecular mechanisms underlying the observed environmental regulation of cuticular hydrocarbons via housing density and also temperature, it will be essential to learn more about how hydrocarbons are delivered to the cuticle and how they may shorten lifespan (Chapter 7).

Chapter 7. Transcriptional and phenotypic responses to autotoxins

7.1 Introduction

In Chapter 5, I have showed that the cuticular lipid blend of adults is programmed by the developmental diet of larvae. In Chapter 6, I then identified a candidate mechanism mediating at least part of this DOHaD effect – the larval/pupal nutrient stores that contribute to cuticular lipid biosynthesis in the first weeks of adulthood. Given these findings, it is then important to understand the functional consequences of developmental diet induced changes in the adult cuticular lipid blend. My starting point here is that Stefana et al. (2017) showed that developmental diet altered specific components of the cuticular lipid blend, alkene hydrocarbons, that are autotoxic i.e. they decrease the lifespan of conspecifics, In this chapter, I therefore investigate the mechanism of alkene toxicity by characterising the transcriptional and physiological response to exogenous alkene exposure. This approach focuses on the direct effects of altering the cuticular lipid blend, rather than the more widespread effects of dietary manipulations. Exogenous alkene exposure is predicted to have the inverse effect of a low yeast (LY) developmental diet, which decreased the proportion of cuticular alkenes. It is also designed to mimic the increased concentration of shed alkenes predicted to occur when flies are housed at high density.

7.2 Cuticular autotoxins decrease lifespan in a dose-dependent manner

To determine the nature of alkene toxicity, I determined whether it was acting in a dose-dependent manner. It was suggested that this may be the case by Stefana et al. (2017), however, this was only performed for two independent concentrations. Dosing experiments are also useful for determining the appropriate concentration of alkene to use for future experiments. This lifespan assay shows the dose-response relationship between 250 µg and 1000 µg (*Z*)-7-tricosene and (*Z*)-9-tricosene, using tricosane and hexane as controls (**Figure 7.1**). These data clearly show a dose-dependent survival decreases (toxicity) for alkenes but not alkanes, which is statistically significant for (*Z*)-9-tricosene, and confirm the results published by Stefana et al. (2017) (*Z*)-7-tricosene gave less pronounced dose-dependency toxicity than (*Z*)-9-tricosene and was substantially more variable from experiment to experiment. Therefore, the decision was made to perform the majority of future assays using 500 µg (*Z*)-9-tricosene, as this concentration of toxin gives a robust and reproducible increase in toxicity. This amount represents the approximately amount of tricosene that 50 flies would shed into vials over the course of 10 days, so is within physiological range.

There is often a trade-off between fecundity and lifespan, such that it is thought that a decrease in survival correlates with an increase in fecundity (Djawdan et al., 1996). To assess the possibility that autotoxins might increase fecundity, I measured egg-laying in female *Drosophila* during a week-long exposure to (*Z*)-7-tricosene on both standard food (STD), and the more toxic high yeast-high glucose diet (HYHG) (Stefana et al., 2017). In this assay, (*Z*)-7-tricosene not (*Z*)-9-tricosene was used because of its demonstrated role in mating behaviour. For both STD and HYHG diets, the (*Z*)-7-tricosene treated flies showed no significant difference in egg laying behaviour (**Figure 7.2**). This clearly shows that alkene autotoxicity is not mediated via increased fecundity.

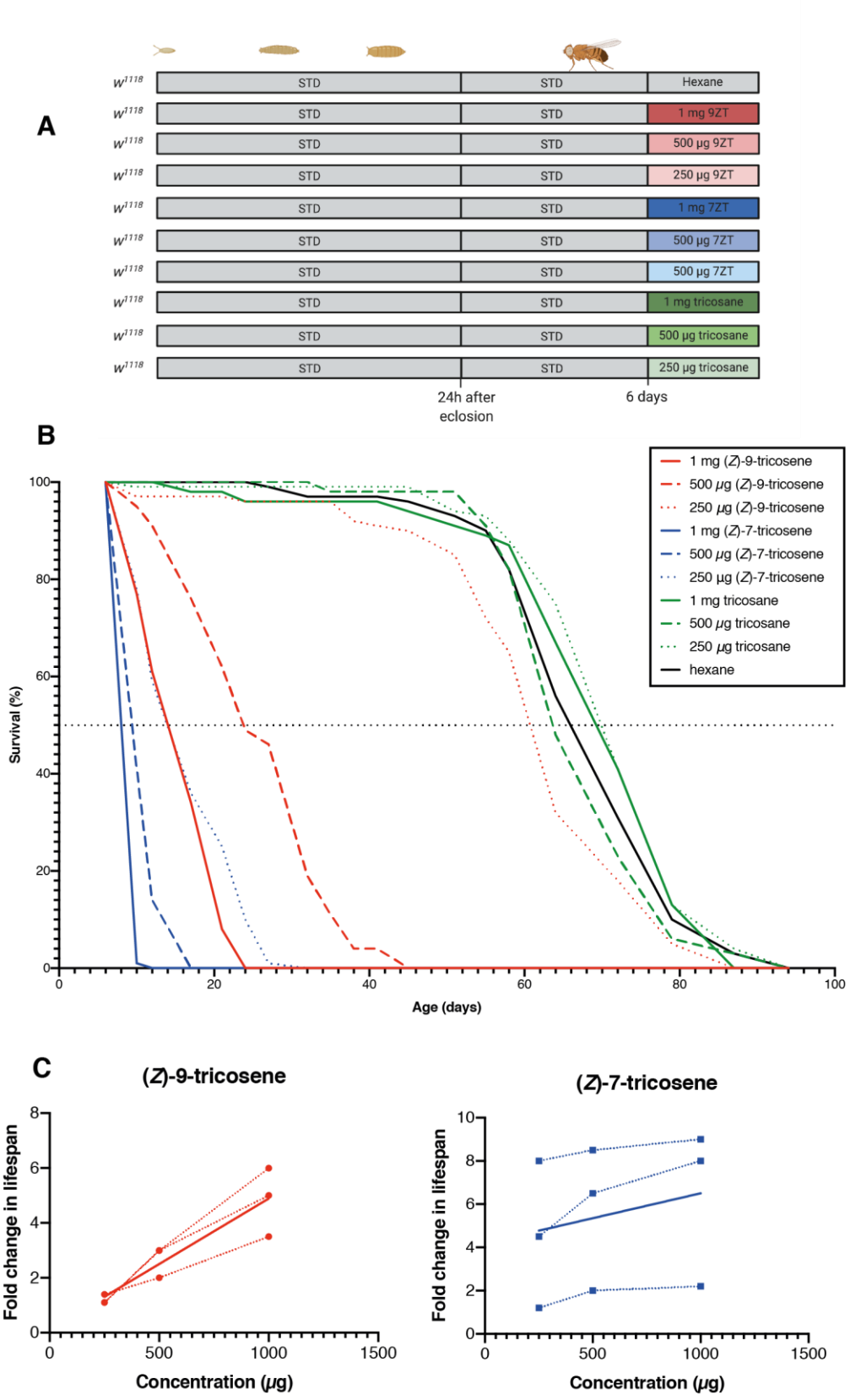
A
w1118
STD
STD
Hexane
1 mg 9ZT
500 µg 9ZT
250 µg 9ZT
1 mg 7ZT
500 µg 7ZT
500 µg 7ZT
1 mg tricosane
500 µg tricosane
250 µg tricosane
24h after eclosion
6 days
B
1 mg (Z)-9-tricosene
500 µg (Z)-9-tricosene
250 µg (Z)-9-tricosene
1 mg (Z)-7-tricosene
500 µg (Z)-7-tricosene
250 µg (Z)-7-tricosene
1 mg tricosane
500 µg tricosane
250 µg tricosane
hexane
Survival (%)
Age (days)
C
(Z)-9-tricosene
(Z)-7-tricosene
Fold change in lifespan
Concentration (µg)

Figure 7.1 Dose-dependency of alkene toxicity
A. Lifespan of w^{1118} $iso31$ male flies on a standard (STD) diet housed at a density of 15 flies per vial, exposed to varying concentrations of toxic alkenes (*Z*)-9-tricosene and (*Z*)-7-tricosene with varying concentrations of non-toxic alkane tricosane and hexane solvent as controls.
B. Lifespan plots with different concentrations of (*Z*)-9-tricosene and (*Z*)-7-tricosene. 1 mg (*Z*)-9-tricosene n=87, median survival ~14 days; 500 µg (*Z*)-9-tricosene n=79, median survival ~24 days, 250 µg (*Z*)-9-tricosene n=79, median survival ~61 days; 1 mg (*Z*)-7-tricosene n=87, median survival ~8 days; 500 µg (*Z*)-7-tricosene n=71, median survival ~10 days, n=73, median survival ~14 days; 1 mg tricosane n=54, median survival ~70 days; 500 µg tricosane n=66, median survival ~64 days; 250 µg tricosane n=69, median survival ~69 days; hexane n=68, median survival ~66 days. Median survival of control conditions ~67 days. 1 mg (*Z*)-9-tricosene shows a ~5 fold decrease in survival, 500 µg (*Z*)-9-tricosene shows a ~3 fold decrease in survival and 250 µg (*Z*)-9-tricosene shows a ~1.1 fold decrease in survival. 1 mg (*Z*)-7-tricosene shows a ~8 fold decrease in survival, 500 µg (*Z*)-7-tricosene shows a ~6.5 fold decrease in survival and 250 µg (*Z*)-7-tricosene shows a ~4.5 fold decrease in survival. Data shown represents one of three independent replicates, with additional replicates show in **Supplementary Figure 9.27** located in the Supplementary Material.
C. Linear regression analysis on three independent experiments shows (*Z*)-9-tricosene follows a linear response with respect to dose with an R squared value of 0.8321, and (*Z*)-7-tricosene does not follow a linear response with respect to dose with an R squared value of 0.06008. Individual experiments are marked with dotted lines and linear regression analysis with a solid line.

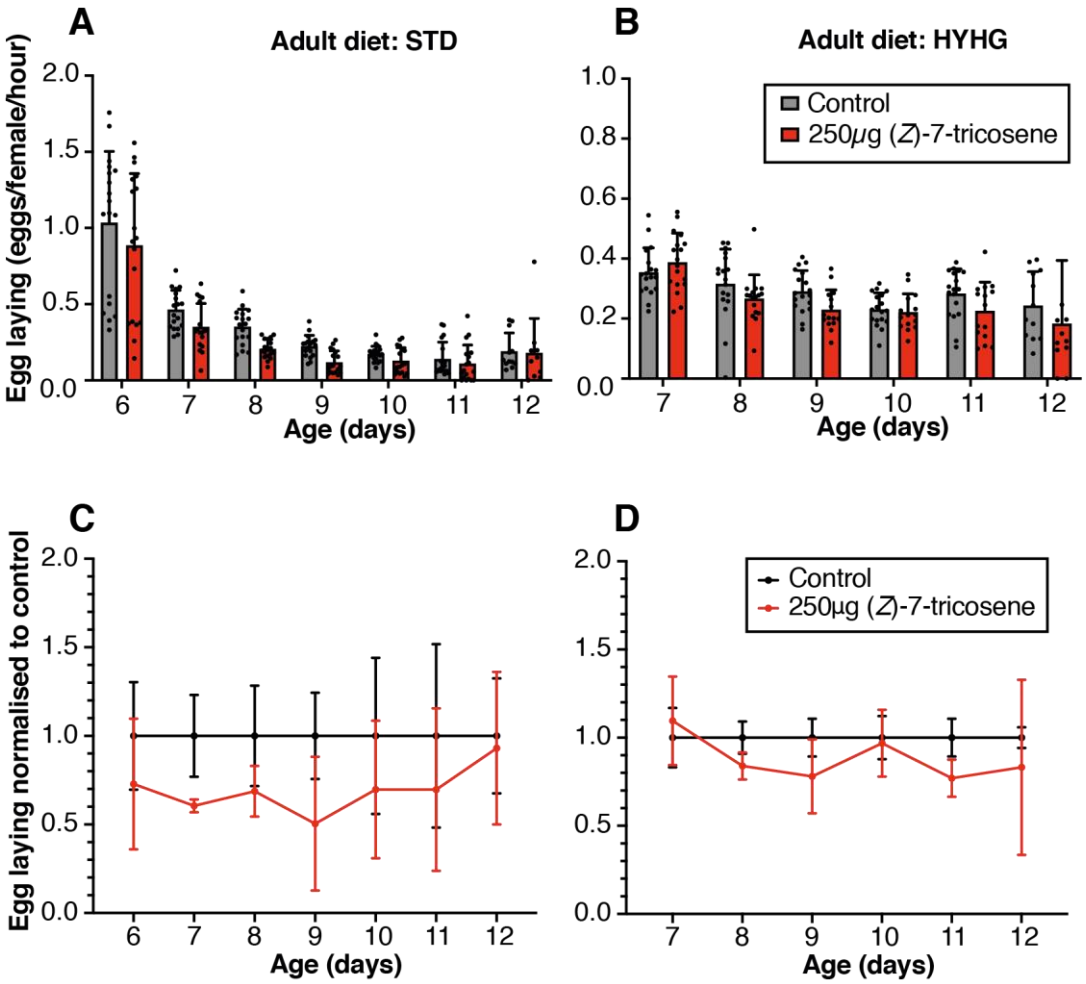

Figure 7.2 Exposure to (*Z*)-7-tricosene does not affect egg laying
Egg laying of $w^{1118\ iso31}$ females in response to direct exposure to 250 µg (*Z*)-7-tricosene shows no significant difference between experimental and control groups. The control group refers to vials treated with hexane alone, the carrier solvent used for (*Z*)-7-triocsene treatment of vials. Results show data combined from three independent experiments with six replicates per experiment. Figure adapted from Stefana et al. (2017) with permission.
A, B: Egg laying calculated for eggs laid per female per hour. Each datapoint represents one vial of 15 flies and the error bars represent standard deviation.
C, D: Egg laying calculated relative to the mean of the control condition at each timepoint, with the error bars representing standard deviation.

Another possible mechanism mediating alkene toxicity could involve microbiota. Previously published data by Obata et al. (2018) showed that an increase in adult lifespan caused by developmental low-dose oxidant exposure was mediated via reprogrammed gut microbiota. These data suggested the hypothesis that alkene exposure may alter the gut microbiota and thus result in a decrease in lifespan. Therefore, the effect of tricosene exposure on lifespan in the presence of two independent antibiotic cocktails was tested. These results indicate that tricosene retained its detrimental effect on survival even in the presence of antibiotics (**Figure 7.3**). The percentage change in median lifespan in the presence of antibiotic does not differ substantially from the percentage change in median lifespan induced by tricosene on a standard diet. Additionally, the antibiotic cocktail alone does not show a detrimental effect on lifespan at this density (15 flies per vial, vial changed every 3 days), in contrast antibiotic exposure at higher densities and less frequent vial changes (see Chapter 6). Together, the eff laying and antibiotic experiments clearly show that alkene autotoxicity is not mediated via increased fecundity or via microbiota.

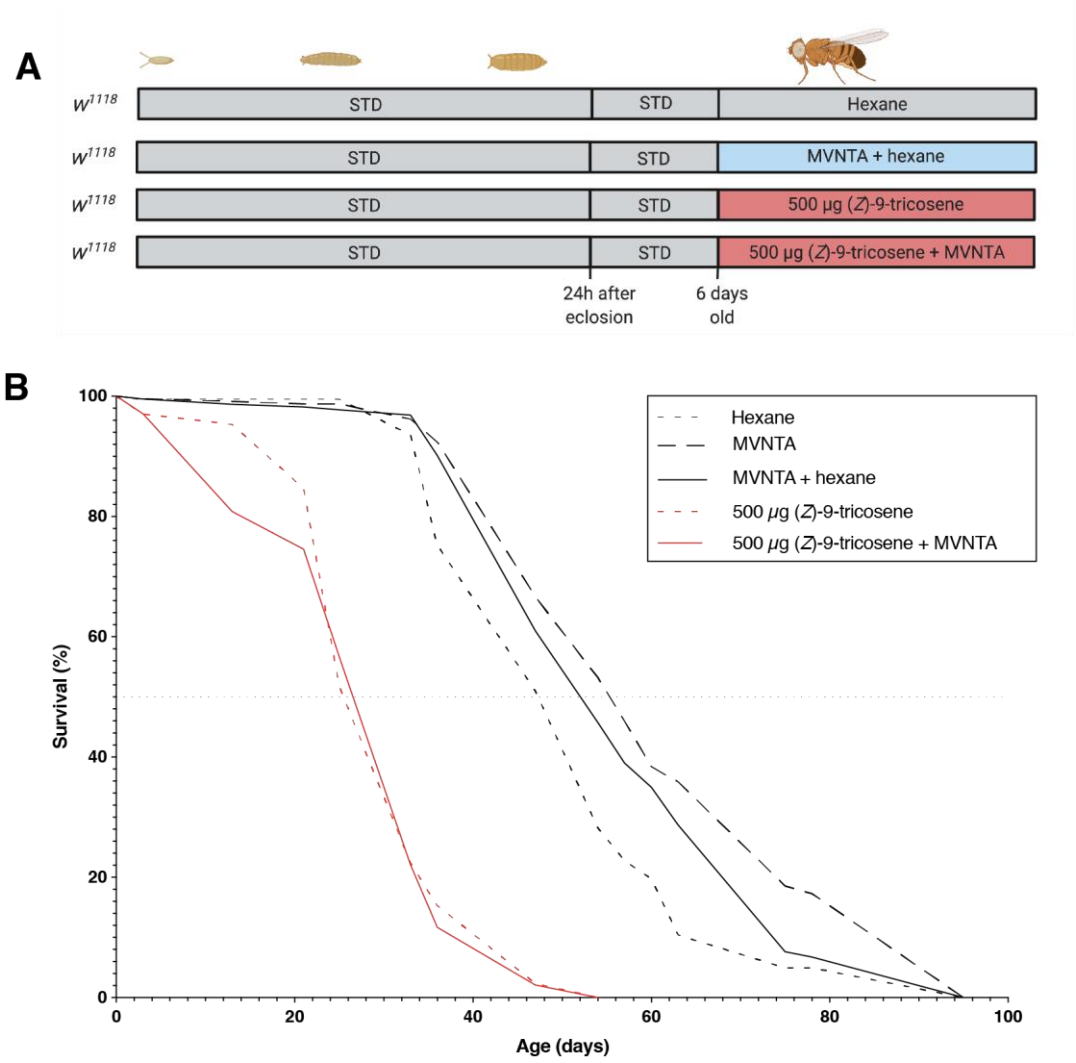

Figure 7.3 Antibiotic-containing food does not rescue tricosene lifespan toxicity
A. Tricosene toxicity is not rescued by constant exposure to a broad-spectrum mixture of antibiotics (MVNTA). Six day old male *Drosophila* housed at a density of 15 flies per vial were fed a diet that contained a mixture of metronidazole, vancomycin, neomycin, tetracycline and ampicillin during constant exposure to 500 µg (*Z*)-9-tricosene.
B. Survival data showing median lifespans of 56 days (MVNTA), 52 days (MVNTA+hexane), 47 days (hexane), 28 days (500 µg (*Z*)-9-tricosene) and 27 days (500 µg (*Z*)-9-tricosene). This graph shows one replicate from a set of two independent replicates (other replicate shown in **Supplementary Figure 9.28** located in the Supplementary Material). For the experiment shown, the number of flies monitored per condition is as follows: Hexane (192), MVNTA (199), MVNTA+hexane (209), 500 µg (*Z*)-9-tricosene (170), 500 µg (*Z*)-9-tricosene + MVNTA (240). On a standard diet, exposure to tricosene results in a ~40% reduction in lifespan compared with a ~48% reduction in lifespan when on a diet containing MVNTA.

7.3 Transcriptomic analysis of exposure to the autotoxin (*Z*)-9-tricosene

To take an unbiased approach towards understanding the mysterious autotoxicity of alkenes, RNASeq analysis was performed on flies exposed to exogenous (*Z*)-9-tricosene. As hydrocarbons are known to act as pheromones (Antony and Jallon, 1982), the non-toxic alkane tricosane was used as a control in addition to the hexane solvent only control. Two different timepoints were analysed to measure the acute and chronic effects of autotoxin exposure on the whole fly transcriptome (**Figure 7.4**). For chronic exposure, tricosene-exposed flies were compared with control flies at the same chronologically aged timepoint or at median survival. This was to control for general transcriptional features changing during ageing. For acute exposure, tricosene-exposed flies were compared with control flies are 24hr of treatment. Given that the data show a marked transcriptional response after only 24 hours exposure to (*Z*)-9-tricosene (but zero genes significantly changed with tricosane), I focused the majority of bioinformatic analysis on this acute timepoint.

The genes differentially up- and down-regulated after 24 hours (*Z*)-9-tricosene exposure were analysed using Gene Ontology (GO) terms (**Figure 7.5**). This revealed an enrichment of genes encoding proteins localised in the extracellular space (secreted proteins), and a slight enrichment of genes encoding proteins localised to lipid particles. There was also a strong enrichment of genes encoding proteins involved in lipid metabolism, in particular fatty acid metabolism. This analysis suggests that tricosene exposure alters lipid metabolism in some way. I also observed an enrichment of genes encoding proteins with potential roles in nutrient uptake and digestion, such as carbohydrate and galactose metabolism, endopeptidases, and carbohydrate binding proteins. This suggests that (*Z*)-9-tricosene exposure may alter nutrient absorption and gut metabolism.

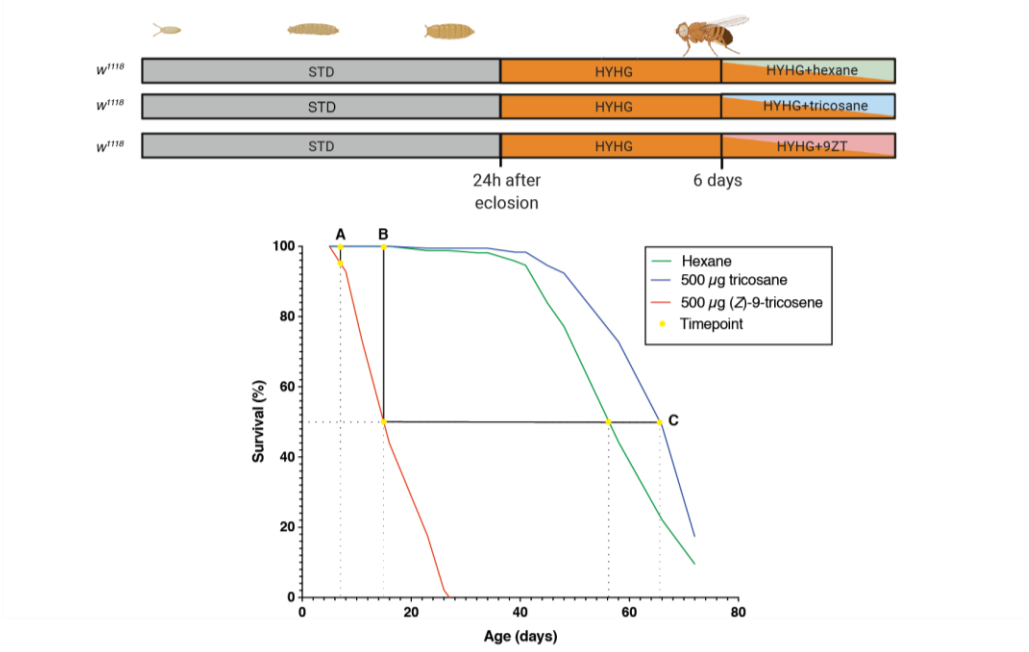
w1118
STD
HYHG
HYHG+hexane
w1118
STD
HYHG
HYHG+tricosane
w1118
STD
HYHG
HYHG+9ZT
24h after eclosion
6 days
A
B
C
Hexane
500 µg tricosane
500 µg (Z)-9-tricosene
Timepoint
Survival (%)
Age (days)

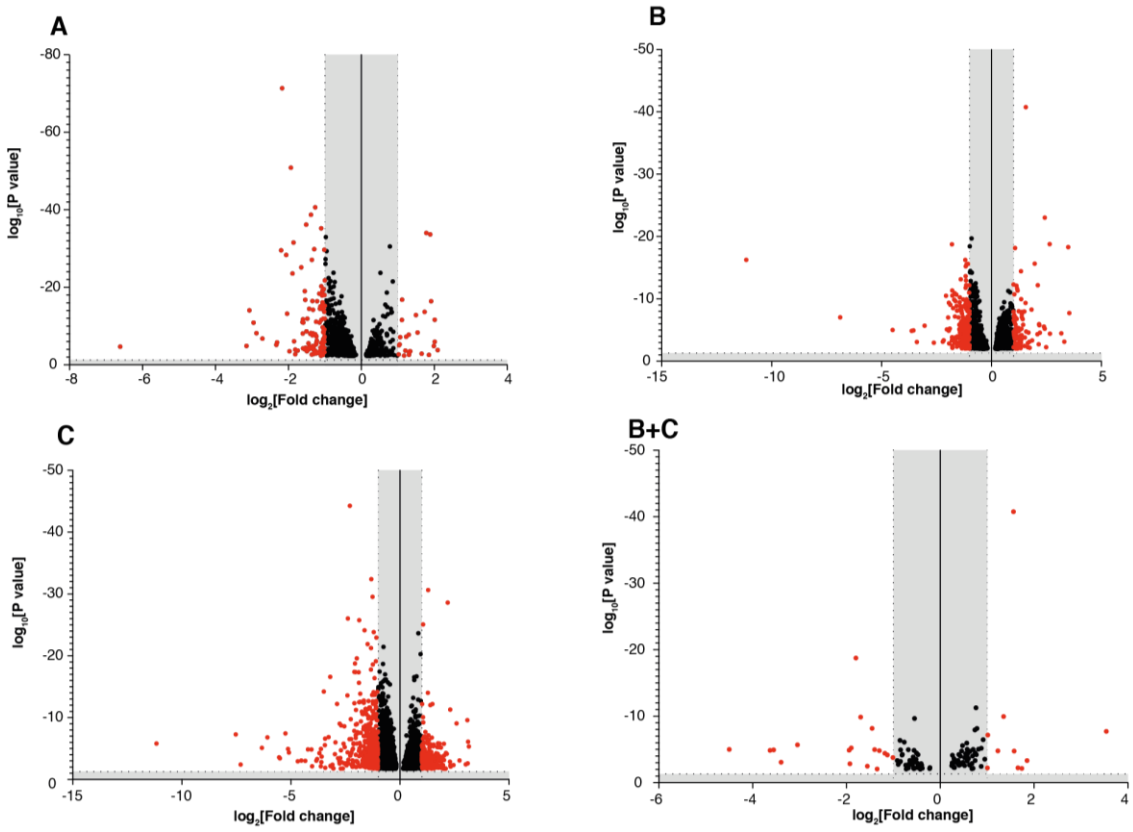
A
B
C
B+C
log10[P value]
log2[Fold change]

Figure 7.4 Transcriptomic response to autotoxin exposure by RNASeq
Transcriptomic analysis of flies exposed to the autotoxin (*Z*)-9-tricosene compared with hexane and tricosane as controls on an adult metabolically stressful high yeast high glucose (HYHG) diet.

The survival graph shows one representative experiment from three independent experiments taken from the same population as the RNASeq samples. In the lifespan graph shown, hexane n=167, median survival ~56 days; 500 µg tricosane n=184, median survival ~66 days; 500 µg (*Z*)-9-tricosene n=133, median survival ~15 days. In this experiment, 500 µg (*Z*)-9-tricosene shows a ~3.5-4.5 fold decrease in lifespan. From the three independent replicates (additional replicates shown in **Supplementary Figure 9.29** located in the Supplementary Material), on an adult HYHG diet 500 µg (*Z*)-9-tricosene shows a 3-4.5 fold decrease in median survival.

Volcano plots showing transcriptional response to 500 µg (*Z*)-9-tricosene exposure. Values shown are those deemed to show a statistically significant change in expression. The grey shaded areas indicate a two-fold increase or decrease in expression ($-1 \geq x \geq 1$) and statistical significance determined ($y \leq 0.05$). Only genes showing a greater than two-fold change in expression were investigated in further detail (labelled in red).
(**A**) Acute response to autotoxin exposure. Comparison between 24h exposure to (*Z*)-9-tricosene and control conditions (hexane and tricosane).
(**B**) Chronic response. Comparison between median survival exposure to (*Z*)-9-tricosene and the equivalent timepoints (16 days of age) for the control conditions (hexane and tricosane).
(**C**) Chronic response. Comparison between median survival exposure to (*Z*)-9-tricosene and the equivalent median survival for control conditions (hexane, 56 days; tricosane, 65 days).
(**B+C**) Chronic response. Data points shown are those that are present in both B and C and are differentially expressed in the same direction. The fold change and p values displayed are those from **B**.

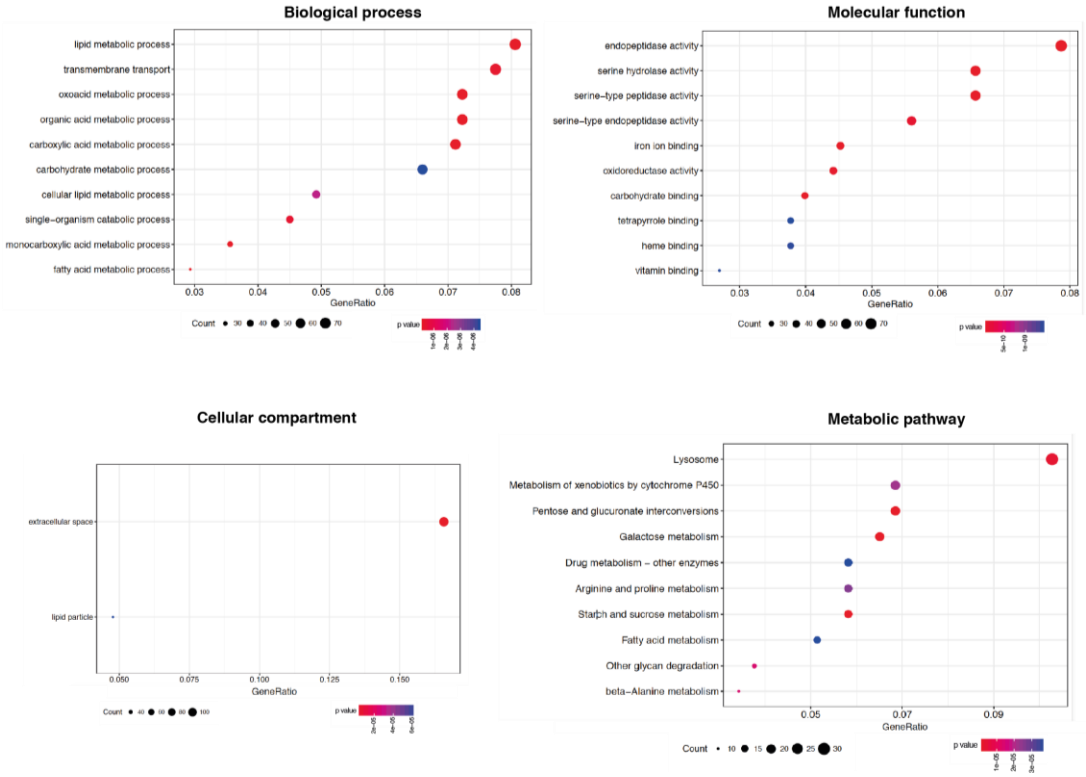

Figure 7.5 GO term enrichment analysis

Enrichment of genes differentially expressed in response to (*Z*)-9-tricosene exposure for 24 hours, compared with both hexane and tricosane treated flies.

To determine which organs were most strongly affected by tricosene exposure, the significantly up- and down-regulated genes at both the acute and chronic timepoints were analysed for their tissue-specific expression using the FlyAtlas database which scores mRNA expression level in different tissues and organs (**Figure 7.6**) (Chintapalli et al., 2007). This revealed an enrichment of upregulated genes in the digestive tract, head and carcass in a broadly similar pattern in both acute and chronic exposure. Acutely downregulated genes were also enriched in the digestive tract, and additionally in the malpighian tubules. Chronically downregulated genes were instead mostly expressed in the head, heard, carcass and fat body. As many of the genes responding to tricosene exposure are expressed in the gut and encode enzymes involved in the digestive process, my dataset was compared with a published RNASeq dataset looking at the transcriptional effects of starvation stress. This comparison revealed many strikingly similar features between tricosene exposure and starvation (**Figure 7.7**). This demonstrates that tricosene exposure leads to a starvation-like transcriptional signature, that could correspond to decreased feeding or malabsorption of nutrients from the gut.

Several of the genes differentially expressed by tricosene exposure in the RNASeq dataset were followed up using RT-qPCR for validation and identification of the tissue in which the differential expression was occurring (**Figure 7.8**). For this analysis RT-qPCR analysis, two tissues were chosen – the digestive tract (includes the malpighian tubules) and the carcass (includes oenocytes). One group of gene encoding three cytochrome P450s (CYP450s), were identified to be downregulated in the fly carcass upon acute exposure to tricosene. No function has yet been assigned to these three CYP450s genes, although a different CYP450 (Cyp4g1) is expressed in oenocytes and known to catalyse the final step in hydrocarbon biosynthesis (Qiu et al., 2012). One enzyme involved in the oxidative stress pathway, *GstD8*, is downregulated in the carcass which suggests that the flies are not undergoing widespread oxidative stress in response to tricosene exposure. It is surprising that this is downregulated, and it would therefore be interesting to test whether exogenous tricosene, like squalene in humans, is oxidised to decrease the oxidative burden

on the fly itself. A carbon-nitrogen hydrolase, *CG32750*, was also found to be downregulated in the fly carcass after acute exposure. Although the function of this protein is unknown, it is predicted to be a biotinidase. As biotin is a cofactor required for many enzymes, including those involved in lipid biosynthesis (Hymes and Wolf, 1999), it is possible that this reflects altered lipid biosynthesis, which is also predicted by gene-set enrichment analysis. Another class of genes downregulated in response to acute tricosene exposure are solute binding proteins which are predicted to be expressed in the malpighian tubules. These proteins are important for maintaining osmotic equilibrium in the organism (Ceder et al., 2020). One of the genes encoding a solute carrier protein, *CG15553*, was analysed by RT-qPCR revealing a strong downregulation in the carcass but not in the digestive tract (which includes malpighian tubules). This is surprising, and suggests that *CG15553* downregulation may be in the epidermis or oenocytes. To follow up this interesting result, it would be useful to test for an RNAi phenotype and to generate solute binding protein antibodies or tagged transgenic lines.

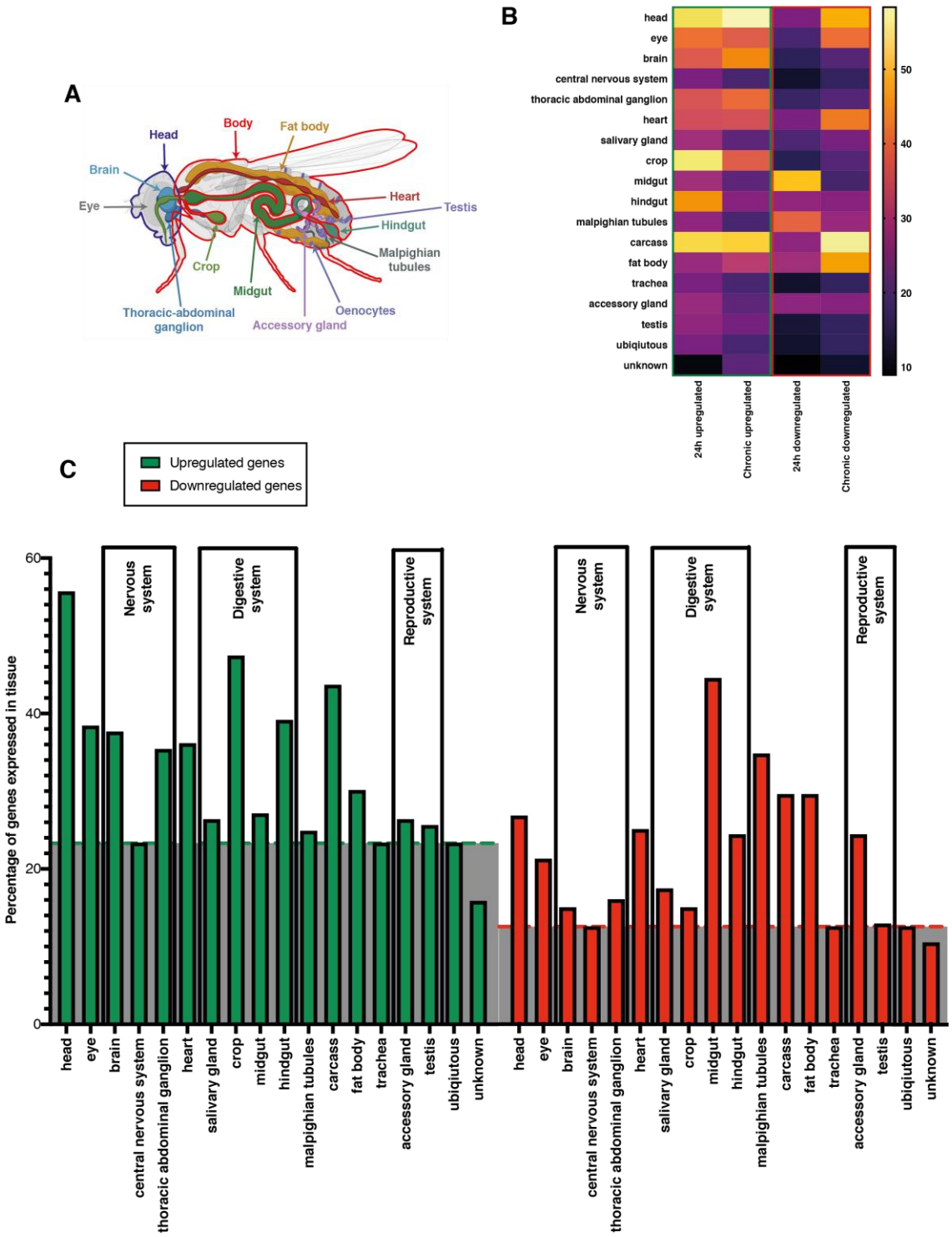
A
Head
Body
Fat body
Brain
Eye
Heart
Testis
Hindgut
Malpighian tubules
Crop
Midgut
Thoracic-abdominal ganglion
Oenocytes
Accessory gland
B
head
eye
brain
central nervous system
thoracic abdominal ganglion
heart
salivary gland
crop
midgut
hindgut
malpighian tubules
carcass
fat body
trachea
accessory gland
testis
ubiqiutous
unknown
50
40
30
20
10
24h upregulated
Chronic upregulated
24h downregulated
Chronic downregulated
C
Upregulated genes
Downregulated genes
Percentage of genes expressed in tissue
60
40
20
0
Nervous system
Digestive system
Reproductive system
Nervous system
Digestive system
Reproductive system
head
eye
brain
central nervous system
thoracic abdominal ganglion
heart
salivary gland
crop
midgut
hindgut
malpighian tubules
carcass
fat body
trachea
accessory gland
testis
ubiqiutous
unknown

Figure 7.6 Tissue-specific expression of genes differentially regulated by alkene exposure
(**A**) Diagram illustrating male *Drosophila* anatomy.
(**B**) Heat map showing percentage of differentially expressed genes enriched in different tissues. Data on tissue-specific expression of RNA is collated from the FlyAtlas tool (Chintapalli et al., 2007) via the FlyBase tool (Thurmond et al., 2018).
(**C**) Tissue-specific expression of RNA differentially regulated by 24 hour exposure to (*Z*)-9-tricosene. Data combines chronic and acute responses. The dotted lines indicate the number of genes with ubiquitous expression. Data for expression in other tissues includes ubiquitously expressed genes. A bar above the grey zone indicates tissue-specific expression above the level represented by ubiquitously expressed genes.

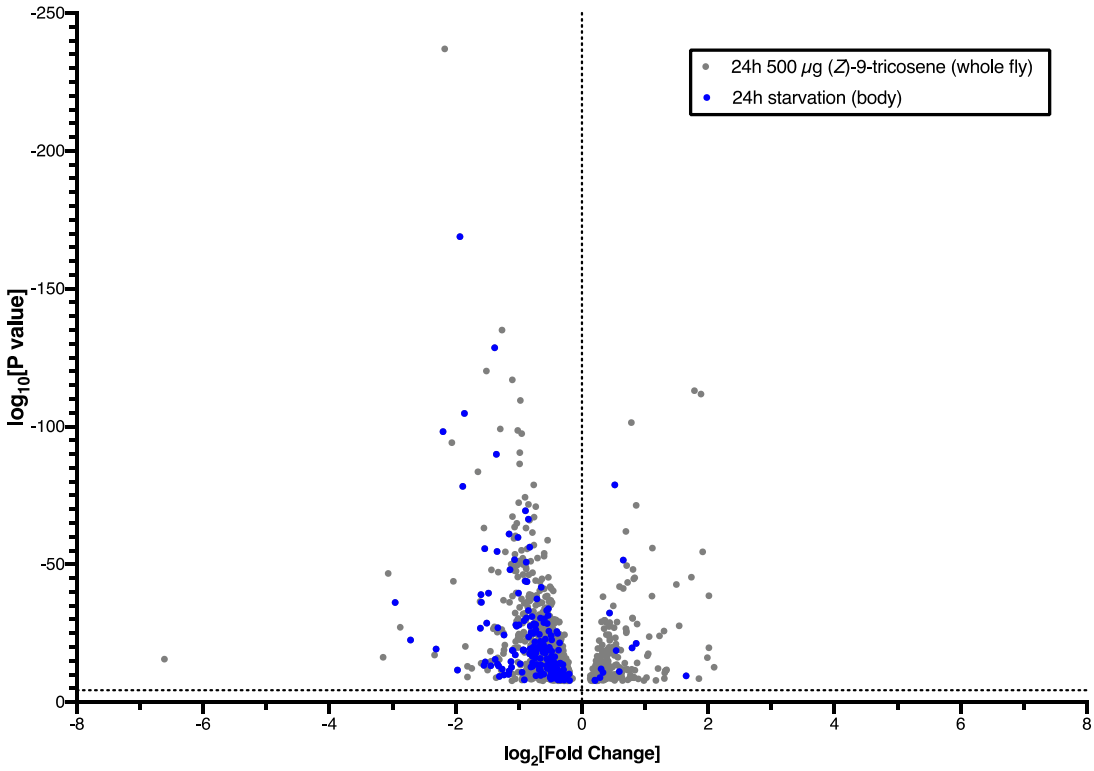

Figure 7.7 Comparison of transcriptional responses to autotoxins exposure and starvation

Volcano plot showing the transcriptional response to 24h exposure to (*Z*)-9-tricosene as determined by RNASeq. Points that are coloured in blue are genes that are also differentially expressed in response to 24h starvation in the same direction as reported by Farhadian et al. (2012) using microarray analysis of the fly body.

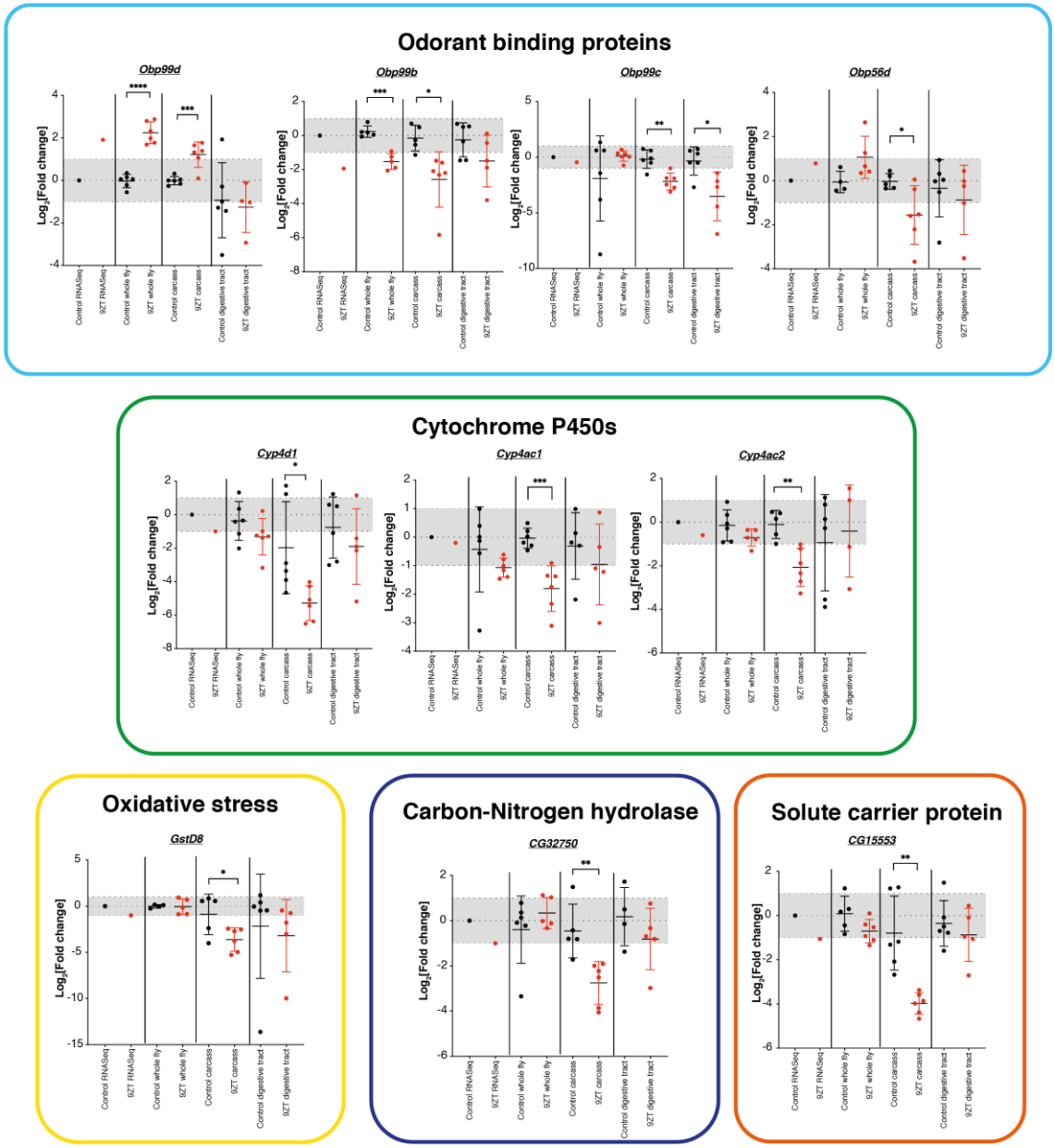

Figure 7.8 Tissue-specific differential expression of selected RNASeq hits

qPCR determination of mRNA levels in acute (24h) (*Z*)-9-tricosene exposure shown relative to the untreated control for each condition. Shown in the graphs are the fold change determined using RNASeq, the fold change detected in whole flies using qPCR, carcasses and digestive tracts. The carcass is mainly composed of the chitinous cuticle, fat body, muscle, epidermal cells, oenocytes and trachea. The digestive tract includes the gut, crop, and Malpighian tubules. Each datapoint represents one sample composed of seven flies (whole flies) or 15 flies (carcass or digestive tract). mRNA levels are calculated relative to *RP49* used as a housekeeping gene.

One class of proteins in the RNASeq data set that were strongly differentially expressed in response to tricosene were odorant binding proteins (Obps). Obps are known to be transcribed in the glia/support cells and secreted into the lymph of the chemosensillar of the antenna (and other organs) (**Figure 1.14**). Here, the Obps in the aqueous lymph bind hydrophobic odorant molecules from the environment and chaperone them to olfactory receptors in the plasma membrane of olfactory neurons (Pelosi et al., 2018). Surprisingly, however, my tissue-specific analysis of odorant binding protein genes identified a significant upregulation of *Obp99d* and downregulation of *Obp99b* and *Obp99c* in the abdominal carcass – which lacks any known odorant responsive chemosensilla (**Figure 7.8**). Very little is known about non-sensilla functions of Obps and my results support the novel concept that Obp gene expression in the abdominal carcass may be regulated by hydrocarbons. In this regard, it is interesting that my datamining of a recently published RNASeq data set for adult oenocytes identified several Obp genes (Huang et al., 2019). Comparing the oenocyte data set with my own tricosene RNASeq results indicates that at least five oenocyte-enriched Obp genes respond to tricosene exposure (**Figure 7.9**). Together with my RT-qPCR results, this indicates that tricosene up- and down-regulation of several Obp genes in the carcass may be occurring in oenocytes, the same cells that synthesise hydrocarbons. This also suggest the hypothesis, explored later in this chapter, that Obp genes may not only respond to hydrocarbons but they could also encode long-sought after transport/binding proteins for cuticular hydrocarbons.

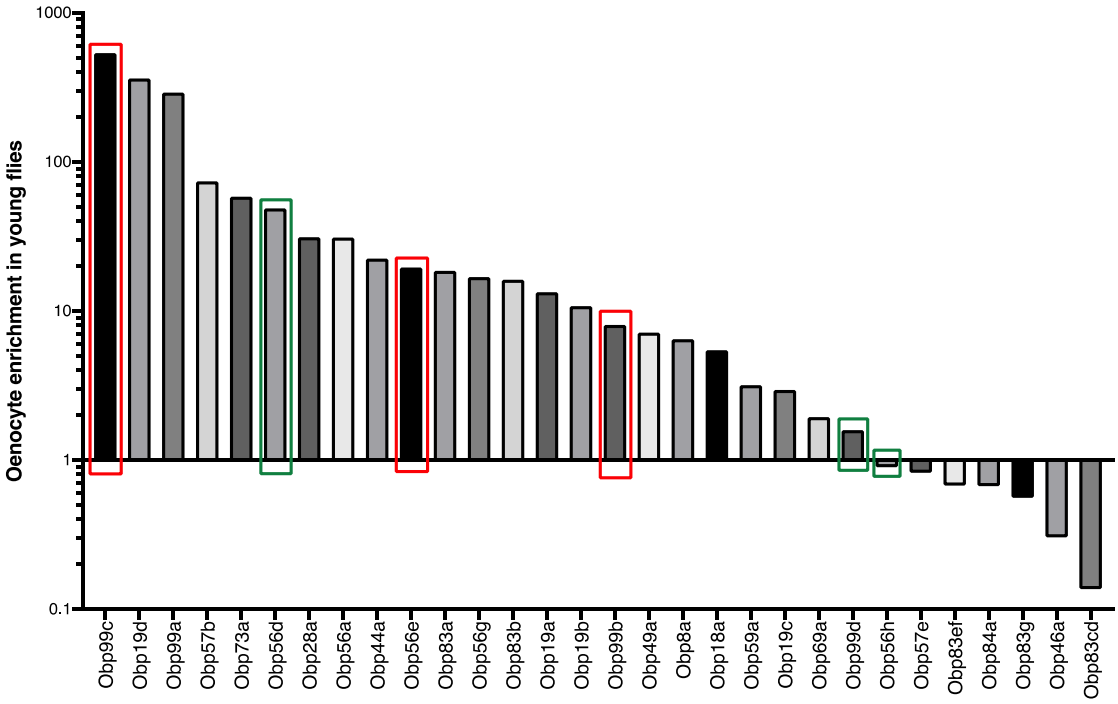

Figure 7.9 Relative enrichment of odorant binding proteins in oenocytes compared with fat body

Data from Huang et al. (2019) showing enrichment of odorant binding proteins in oenocytes relative to the fat body as detected using RiboTag RNASeq. Indicated are odorant binding proteins that were significantly downregulated (red) or upregulated (green) after 24 hours exposure to (*Z*)-9-tricosene in my own RNASeq data from whole flies.

7.4 Phenotypic consequences of autotoxin exposure

I have shown that tricosene exposure leads to a starvation-like transcriptional signature involving downregulation of gut expressed genes with predicted roles in carbohydrate and protein metabolism. I reasoned that if tricosene induces a starvation response, then flies would survive subsequent exposure to actual dietary starvation either for a longer duration (as they are already adapted to starvation), or for a shorter duration (if they have already depleted their nutrient reserves). However, I observed that flies pre-exposed to (*Z*)-9-tricosene exhibited only a minor decrease in survival when exposed to starvation medium (PBS/agar) (**Figure 7.10**). To determine if nutrient reserves had been depleted (and thus weight lost), flies were weighed over a time course of 5 days exposure to (*Z*)-9-tricosene. This showed no significant change in dry weight over the course of 5 days, a time course that would be sufficient to show a phenotype in a true starvation context (**Figure 7.11**). To pinpoint why the alkene and starvation transcriptomic signatures are so similar will require more investigation.

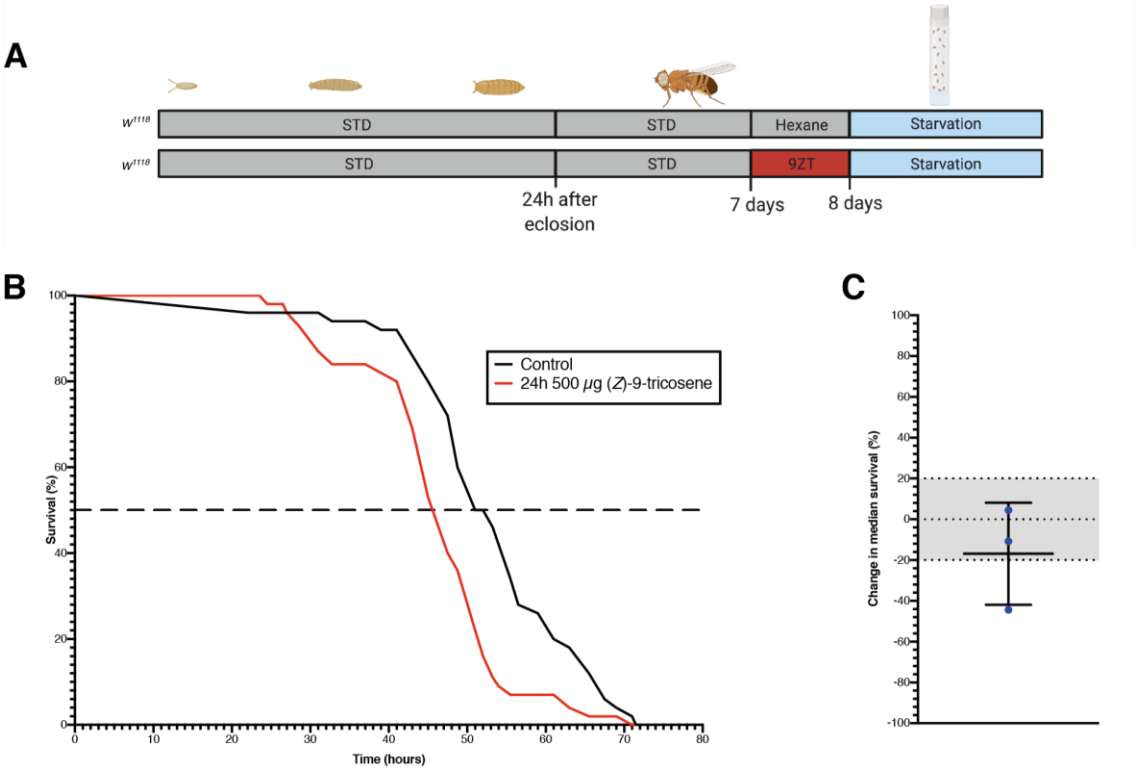

Figure 7.10 Exposure to (*Z*)-9-tricosene does not substantially affect starvation survival
A. Experimental schematic. Flies were raised on a standard diet until seven days of age, then in the experimental condition were treated with 500 µg (*Z*)-9-tricosene (9ZT) for 24 hours or a control of vials treated with the carrier solvent hexane alone. The tricosene was then removed and flies subjected to starvation on PBS/Agar medium until death.
B. One of three replicates showing survival over time on a starvation medium. The dotted line represents 50% survival. In this replicate, the numbers of flies per condition were as follows: Control n=50; 500 µg (*Z*)-9-tricosene n=45. Median survivals were as follows: Control 51 hours; 500 µg (*Z*)-9-tricosene 45.5 hours (decrease of 10.8%). Additional replicates are shown in **Supplementary Figure 9.30** located in the Supplementary Material.
C. Summary of change in median survival for 500 µg (*Z*)-9-tricosene for all three experiments – each dot represents one independent experiment. The grey zone indicates +/- 20% change in median survival.

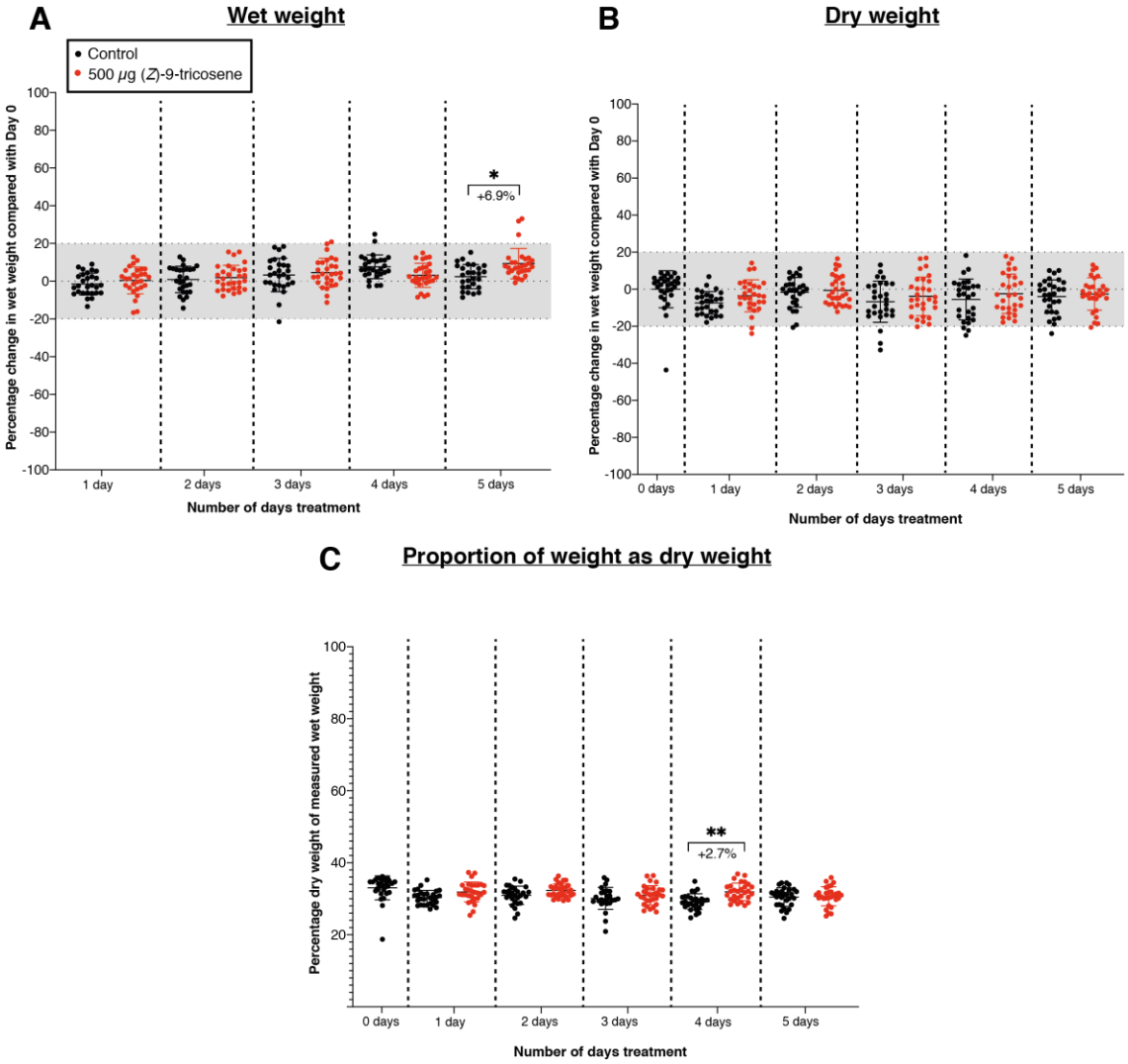

Figure 7.11 Exposure to (*Z*)-9-tricosene does not significantly alter fly weight

Fly wet (**A**) and dry weight (**B**) measured over varying lengths of exposure to 500 µg (*Z*)-9-tricosene. Data is represented relative to the weight of the same flies at Day 0 (wet weight), or a control group of flies at Day 0 (dry weight). The region highlighted in grey represents a +/- 20% change in weight compared with Day 0. Data shown is from two independent experiments.
C. Proportion of total weight as dry weight calculated using the same group of flies for respective wet and dry weight measurements at each timepoint.

Several genes downregulated upon exposure to alkene toxin are indicated on FlyBase to have high expression in the malpighian tubules (**Figure 7.6C**). Many of these genes are predicted ion transporters, and therefore likely regulate osmotic balance (**Table 7.1**). Given that tricosene exposure does not change dry weight, it is therefore possible that it could disrupt water homeostasis and make flies more sensitive to osmotic stress (**Figure 7.11**). To assess this, flies were exposed to a high salt diet with and without a 24h pre-exposure to alkene toxin, and their survival was measured. Intriguingly, I observed that tricosene autotoxin exposure strongly decreases survival on a high salt diet in males but not in females (**Figure 7.12**). The male salt stress phenotype is compatible with tricosene exposure inducing a disruption of osmotic balance via decreased expression of malpighian tubule ion transporters. The lack of this phenotype in female flies indicates that tricosene acts on osmotic balance in a sex-specific manner that could therefore involve sensing via pheromone receptor circuitry, which is known to be highly sexually dimorphic. Future experiments measuring the effects of tricosene on the salt stress response in flies that cannot sense volatile pheromones (Orco mutants) would address this possibility.

Table 7.1 Transporter genes downregulated upon exposure to (*Z*)-9-tricosene

Gene	EXP 24h vs CTRL 24h		EXP 16d vs CTRL 16d		EXP 16d vs CTRL 65d		Description	Tissue Expression
	Log_2[Fold change]	P value	Log_2[Fold change]	P value	Log_2[Fold change]	P value		
CG9981	*-1.089*	*2.1731e-06*					phospholipid transporter	midgut, malpighian tubules, hindgut
CG15553	*-1.065*	*7.36e-20*					folate transporter	carcass
Mdr50	*-0.956*	*5.1958e-12*					ATP-coupled transporter	midgut, hindgut
CG31792	*-0.91*	*3.6766e-06*					ATP-coupled transporter	malpighian tubules
CG8083	*-0.683*	*1.1101e-05*					nucleoside:sodium symporter	midgut
CG32669	*-0.62*	*1.4044e-10*					sodium:glucose symporter	malpighian tubules, midgut, hindgut
CG15408	*-0.612*	*5.7167e-06*					carbohydrate:proton symporter	malpighian tubules
CG15406	*-0.604*	*2.613e-05*					carbohydrate:proton symporter	malpighian tubules
CG1213	*-0.598*	*2.6189e-08*					carbohydrate:proton symporter	ubiquitous
Nha1	*-0.597*	*4.0983e-13*					sodium:proton antiporter	hindgut, salivary gland
CG3285	*-0.569*	*0.00022446*					carbohydrate:proton symporter	
NaPi-T	*-0.521*	*9.7345e-12*					sodium:phosphate cotransporter	malpighian tubules
CG1208	*-0.507*	*5.0702e-09*					carbohydrate:proton symporter	midgut, crop
Dat	*-0.455*	*6.9388e-13*					dopamine transporter	brain, throacic abdominal ganglion
Bmcp	*-0.442*	*4.1854e-05*					transmembrane transporter	
CG8051	*-0.428*	*1.4579e-06*					monocarboxylate transporter	salivary gland, midgut, hindgut
CG10960	*-0.421*	*1.9283e-05*					carbohydrate:proton symporter	ubiquitous
ZnT77C	*-0.417*	*3.1556e-05*					zinc transporter	accessory gland, malpighian tubules
l(2)08717	*-0.357*	*4.1958e-06*					transmembrane transporter	salivary gland, malpighian tubules
ZnT41F	*-0.315*	*0.0012346*					zinc transporter	midgut, malpighian tubules, hindgut, fat body
CG15096			*-0.639*	*0.0005784*	*-0.5*	*9.8936e-05*	transmembrane transporter	ubiquitous
CG2003			*-0.482*	*0.0012373*	*-0.803*	*8.3699e-08*	transmembrane transporter	accessory gland

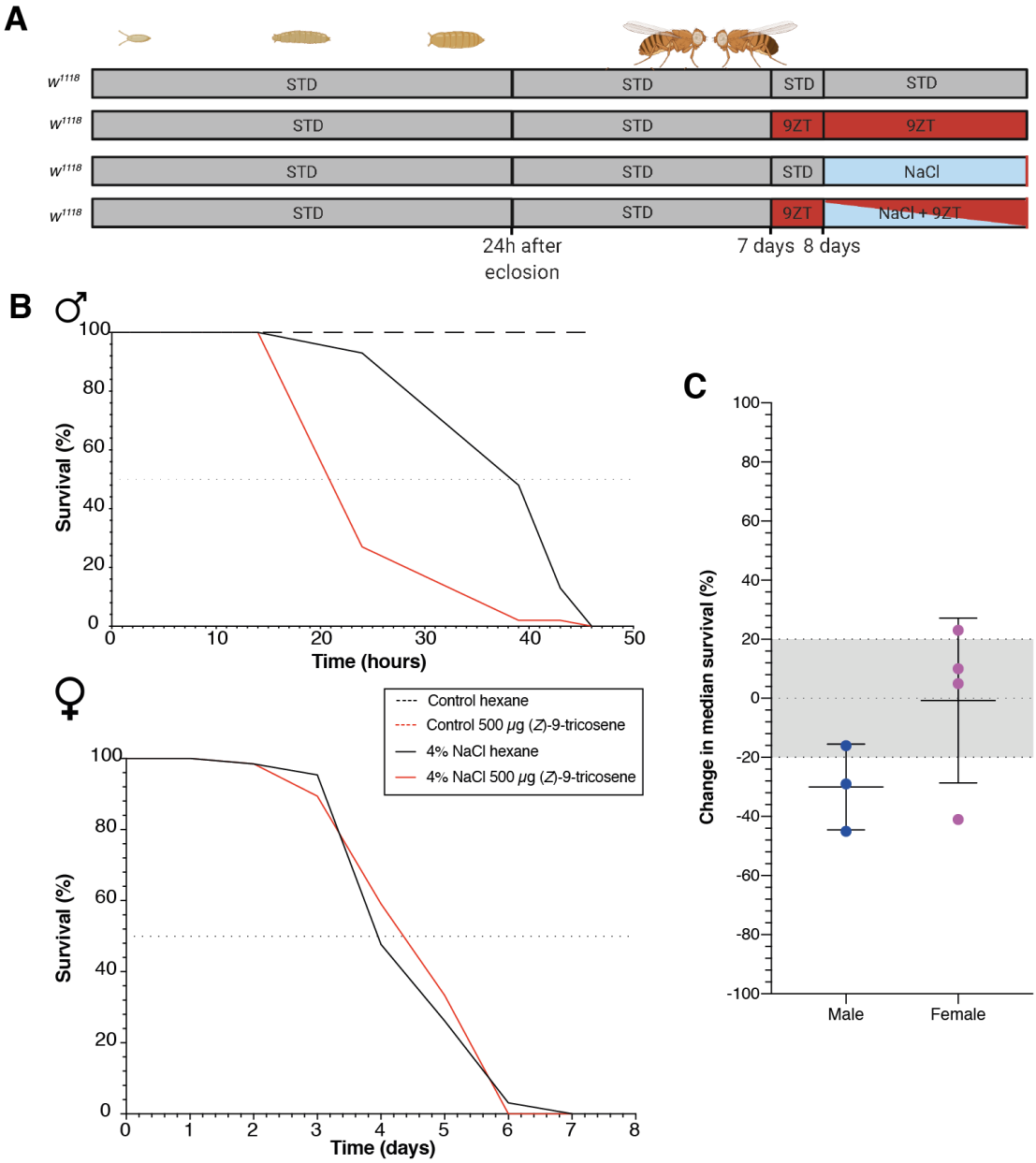

Figure 7.12 Tricosene exposed male but not female flies are more sensitive to salt stress
A. Flies were exposed to a pre-treatment of 500 µg (*Z*)-9-tricosene or a control of hexane carrier solvent alone for 24 hours before the start of the assay. Flies were exposed to vials containing +/- 500 µg (*Z*)-9-tricosene and +/- 4% NaCl until 100% mortality was reached.
B. Survival assay showing the relative survival of flies exposed to 500 µg (*Z*)-9-tricosene under salt stress (4% NaCl). Control conditions show no mortality in groups not exposed to salt stress. Results show one representative experiment from three independent replicates (male, four replicates for female). For all experiments, the number of flies per condition >50. 9ZT = 500 µg (*Z*)-9-tricosene. Control male n=40, median survival ~48h; 9ZT male n=49, median survival ~22h (-54% change in median survival); Control female n=65, median survival ~4 days, 9ZT female n=66, median survival ~4.4 days (+10% change in median survival). Additional replicates are shown in **Supplementary Figure 9.31** located in the Supplementary Material.
C. Change in median survival for (*Z*)-9-tricosene treated flies compared with the NaCl treated control. Each datapoint represents the mean survival of one independent experiment.

The cuticular lipid blend is thought to be important for maintaining the barrier function of the cuticle. Therefore exposure to excess exogenous alkenes will likely change the cuticular lipid blend and thus may alter barrier function. To begin to test this, GC-MS was used to show that flies exposed for 24 hours to 500 µg (*Z*)-9-tricosene have a substantially increased amount of (*Z*)-9-tricosene on their body surface, even after a six hour "chase" period (~60 times, **Figure 7.13**). This does not correlate with an increase in oenocyte lipid droplets, as may be predicted if exogenous tricosene was internalised and stored in oenocytes (**Figure 7.14**). To determine if an increase in the cuticular alkene/alkane ratio (saturation index) has an effect on barrier function, desiccation resistance was assayed after 24 hours exposure to exogenous tricosene. This revealed that both male and female flies exposed to exogenous alkene showed a substantial decrease in median survival under desiccating conditions (**Figure 7.15**). The lack of death after 24 hours within the control group, which were not exposed to the desiccating environment, highlights that the decrease in survival is not due solely to the autotoxic effect of tricosene. Decreases in desiccation and salt resistance could both reflect increased water loss following tricosene exposure but, it so, this link must be male-specific. A more likely hypothesis to explain decreased desiccation resistance in both sexes is that the imbalance in the saturation index of the alkene/alkane ratio of the hydrocarbon blend directly compromises cuticular barrier function. In line with the importance of a tightly regulated alkene/alkane ratio, specifically knocking down oenocyte production of all alkene hydrocarbons, using Desat1 RNAi (Stefana et al., 2017), also results in a decrease in desiccation resistance (**Figure 7.16**).

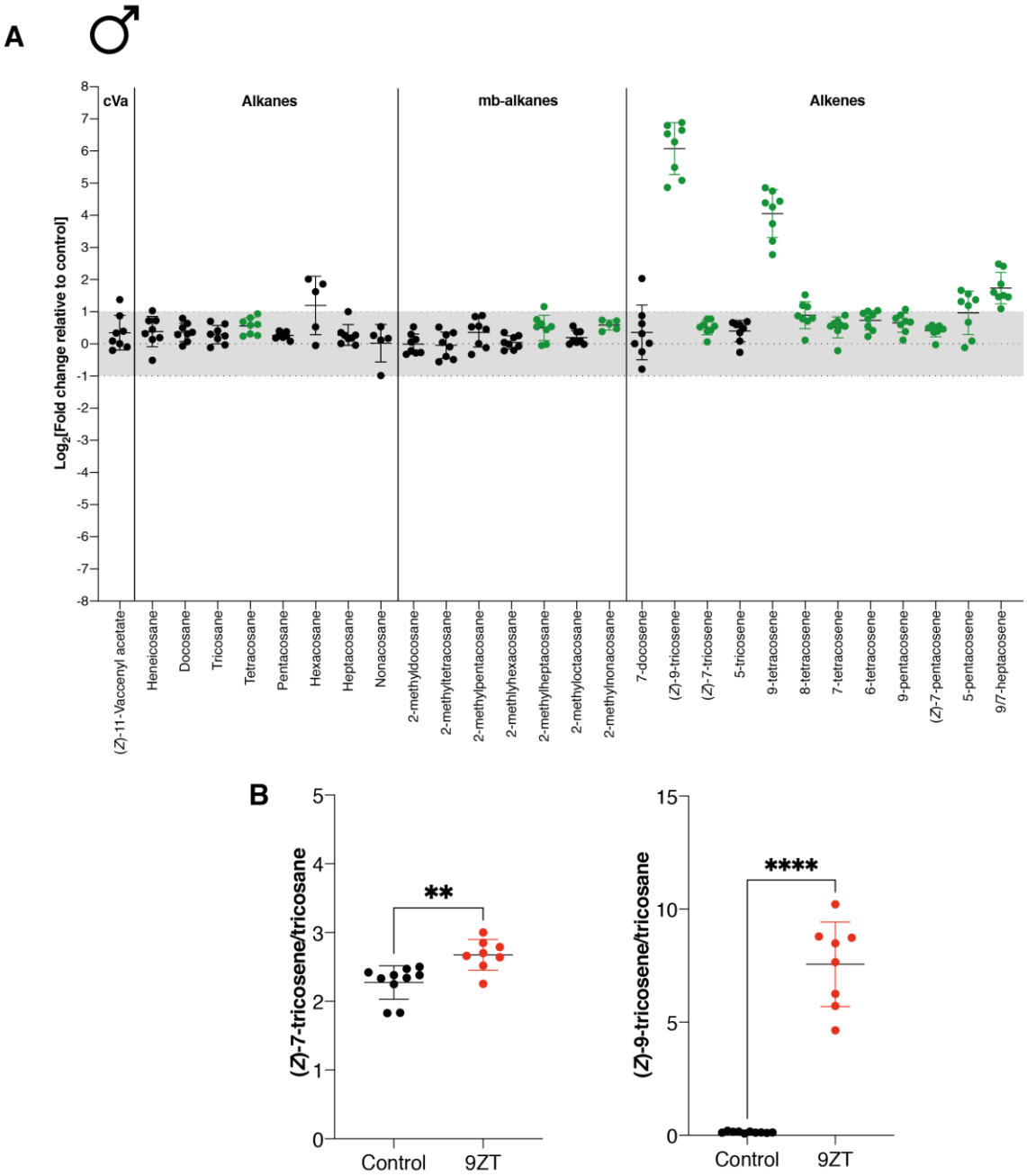

Figure 7.13 Exposure to (*Z*)-9-tricosene in vials leads to accumulation on the cuticle

A. Log_2 fold change in cuticular hydrocarbon abundance after 24 hour exposure to 500 µg (*Z*)-9-tricosene (9ZT) at a density of 10 flies per vial. Hydrocarbons labelled in green show statistically significant changes compared with control (unexposed) flies. Statistical significance: tetracosane (***), 2-methylheptacosane (*), 2-methylnonacosane (****), (*Z*)-9-tricosene (****), (*Z*)-7-tricosene (***), 9-tetracosene (****), 8-tetracosene (****), 7-tetracosene (*), 6-tetracosene (**), 9-pentacosene (*), (*Z*)-7-pentacosene (*), 5-pentacosene (*), 9/7-heptacosene (****).
B. Saturation index as measured as the ratio of (*Z*)-7-tricosene or (*Z*)-9-tricosene divided by tricosane.

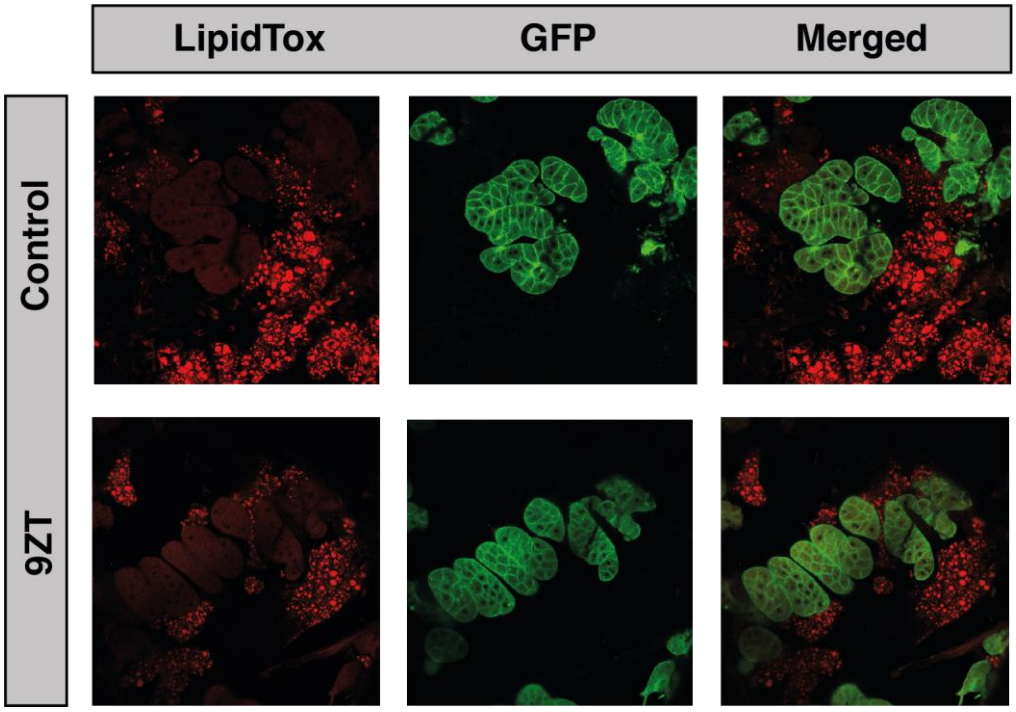

Figure 7.14 Alkene exposure does not induce lipid droplets in oenocytes

Male oenocytes after a 24 hour exposure to 500 µg (*Z*)-9-tricosene (9ZT) in *PromE>GAL4*, *tub>GAL80^{ts}*, *UAS-CD8::*GFP flies at 25°C. Neutral lipids are stained with LipidTox and membrane-targeted GFP marking the oenocytes driven by the *PromE>GAL4* oenocyte-specific driver. This image is representative of a set of three replicates for each condition.

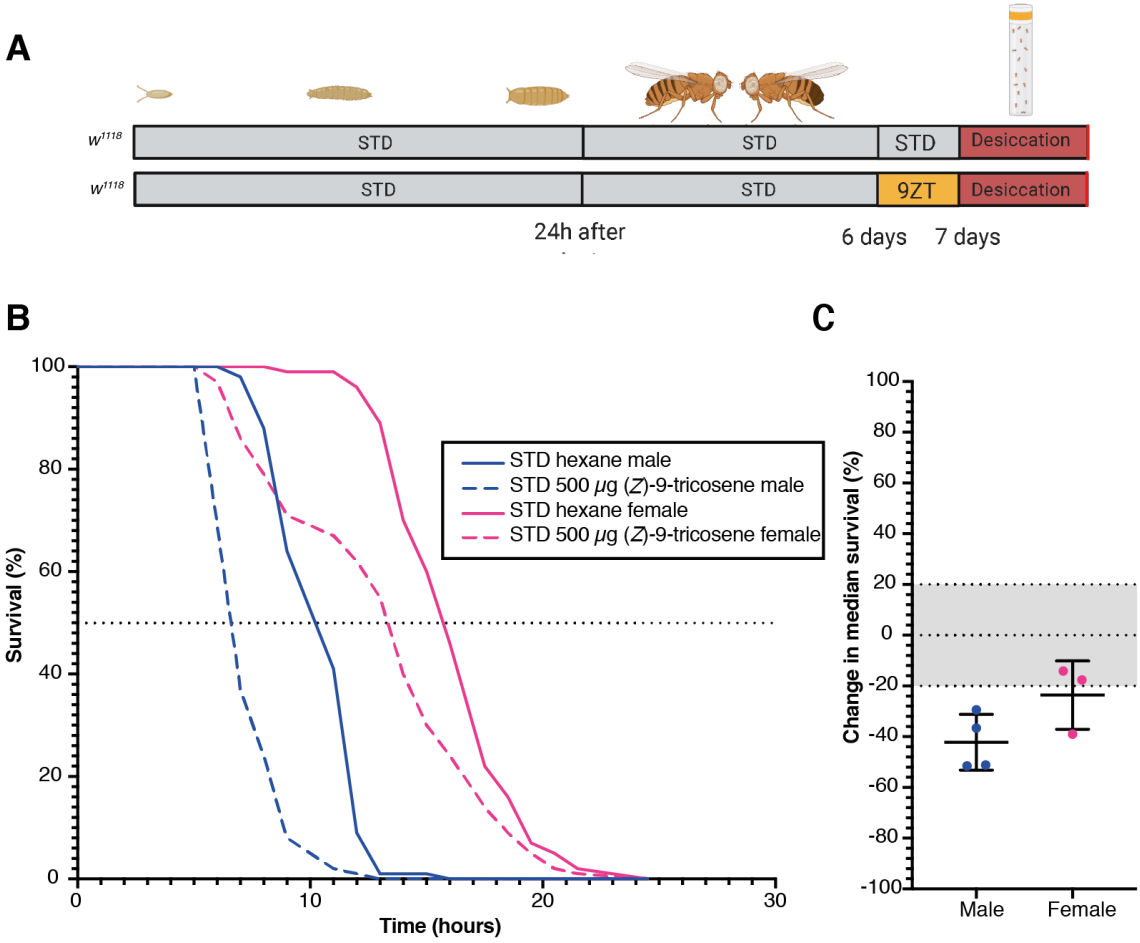

Figure 7.15 Prior exposure to tricosene increases sensitivity to desiccation stress
A 24h pre-exposure to 500 µg (*Z*)-9-tricosene (9ZT) decreases survival under desiccating conditions in both male and female flies.
A. Schematic of experimental conditions. Flies were raised throughout development and adulthood on a standard diet.
B. One experiment from three independent replicates (four replicates for male). The additional two replicates are shown in **Supplementary Figure 9.32** located in the Supplementary Material. STD hexane male n = 88, median survival ~10h; STD 500 µg (*Z*)-9-tricosene male n=86, median survival ~6.5h; STD hexane female n=82, median survival ~16h; STD 500 µg (*Z*)-9-tricosene female n=103, median survival ~13.5h. 24h exposure to 500 µg (*Z*)-9-tricosene in males shows a ~1.5 fold decrease in survival and in females shows a ~1.2 fold decrease in survival.
C. Change in median survival for (*Z*)-9-tricosene treated flies compared with the hexane control (calculated relative to the control for each independent experiment). Each point represents an independent experiment and error bars indicate standard deviation.

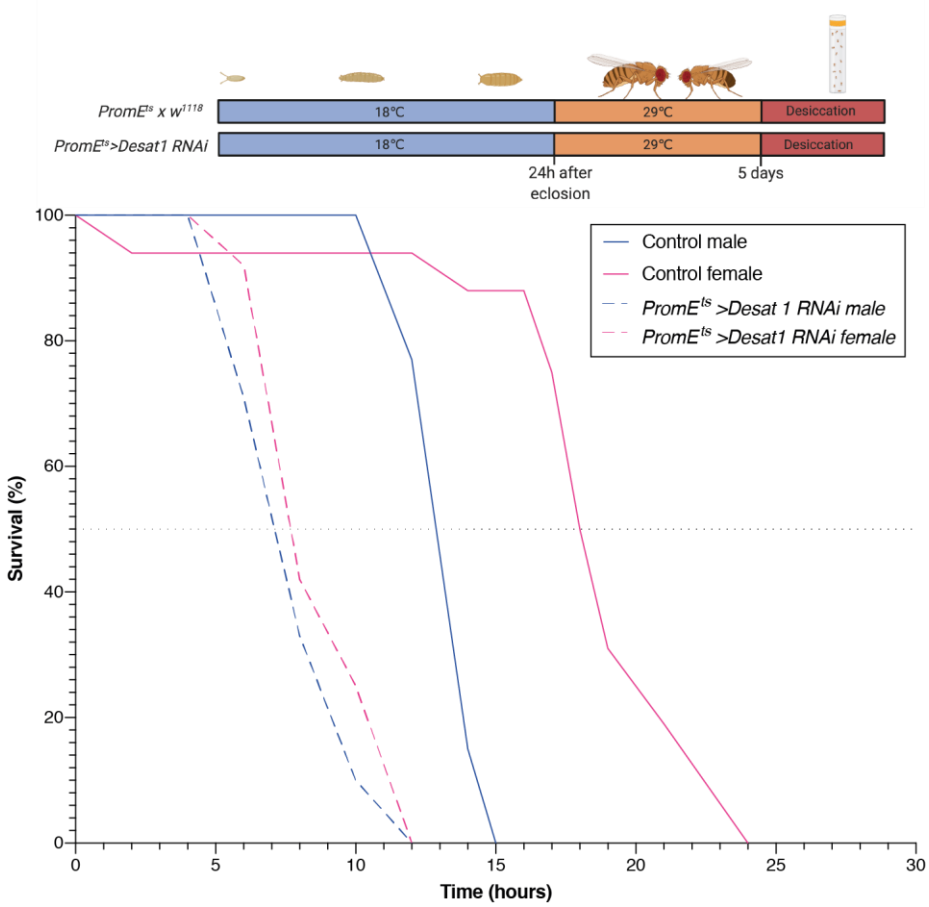

Figure 7.16 *Desat1* knockdown in oenocytes decreases desiccation resistance

Desiccation resistance measured in male and female *Drosophila* after five days of *Desat1 RNAi* induction at 29℃. Median survivals: Control male 13h n=13, control female 18h n=16, *PromE^{TS}>Desat1 RNAi* male 7h n=21 (46% decrease in median survival*), PromE^{ts}>Desat1 RNAi* female 7.75h n=12 (57% decrease in median survival). An additional replicate is shown in **Supplementary Figure 9.33** located in the Supplementary Material.

7.5 Oenocyte Obps regulate cuticular hydrocarbons in response to environmental factors

I showed in Section 7.2 that acute exposure to the autotoxin tricosene results in differential expression in the abdominal carcass of several genes encoding odorant binding proteins and that a published RNASeq data set shows that transcripts from these Obp genes are enriched in oenocytes. Therefore it was reasonable to hypothesis that the observed carcass expression of several odorant binding proteins originates from oenocytes.

To test this hypothesis, I focused on *Obp99b* and *Obp99d* – two genes that are genomic neighbours and that respond significantly to tricosene exposure. Both are expressed in oenocytes (and carcass) but, according to FlyBase, *Obp99b* is also expressed very strongly in the fat body. *Obp99b* and *Obp99d* are expressed in both adult sexes but levels in the whole fly are sexually dimorphic (**Figure 7.17**). To determine if adult oenocyte-specific knockdown of these odorant binding proteins induced a detectable phenotype in males or females, temperature-dependent Gal80^{TS} knockdowns were performed using RNAi. These knockdowns revealed very striking decreases in male and female cuticular alkenes but not alkanes for both *Obp99b* and *Obp99d* (**Figure 7.18, Figure 7.19, Figure 7.20, Figure 7.21**). These alkane decreases also resulted in strong decreases in the saturation index of cuticular hydrocarbons levels. These results demonstrate that *Obp99b* and *Obp99d* are both required in adult oenocytes for normal levels of cuticular alkenes. Interestingly, however, neutral lipids do not “back up” inside *Obp99d RNAi* oenocytes, suggesting that they may still be secreted from these cells (**Figure 7.22**).

To examine the consequences of Obp knockdown on barrier function, I measured the desiccation resistance of oenocyte-specific knockdown *Obp99b* and *Obp99d RNAi* flies. This showed a marked decrease in desiccation resistance in both males and females indicating an important role for *Obp99b* and *Obp99d* in barrier function (**Figure 7.23**). In future, it will be important to replicate these RNAi results using CRISPR/Cas to engineer targeted mutations at the *Obp99b* and *Obp99d*

gene loci. Importantly, the Obp99b and Obp99d RNAi findings are also consistent with my previous results shown that altering the alkene/alkane ratio in two other ways (tricosene exposure or *Desat1 RNAi*) impairs barrier function.

Obp99b and Obp99d knockdowns not only decreased cuticular alkenes, but also slightly increased shorter chain linear and methyl-branched alkanes at the expense of longer chain linear and methyl-branched alkanes (**Figure 7.18B, Figure 7.20B**). It is possible that this is actually representing a failure to alter cuticular hydrocarbon composition in response to the temperature shift required for induction of the RNAi, as the opposite effect is seen in control flies exposed to a two-week temperature shift (**Figure 6.8**). This may be exciting to follow up in the future as oenocytes have not yet been implicated in any temperature sensing/response mechanisms, It has been reported that ligand-binding increases the thermal stability of odorant binding proteins (Pelosi et al., 2018). Therefore, it is possible that the temperature-linked change in cuticular hydrocarbons is mediated via changes in the stability of at least some odorant binding proteins.

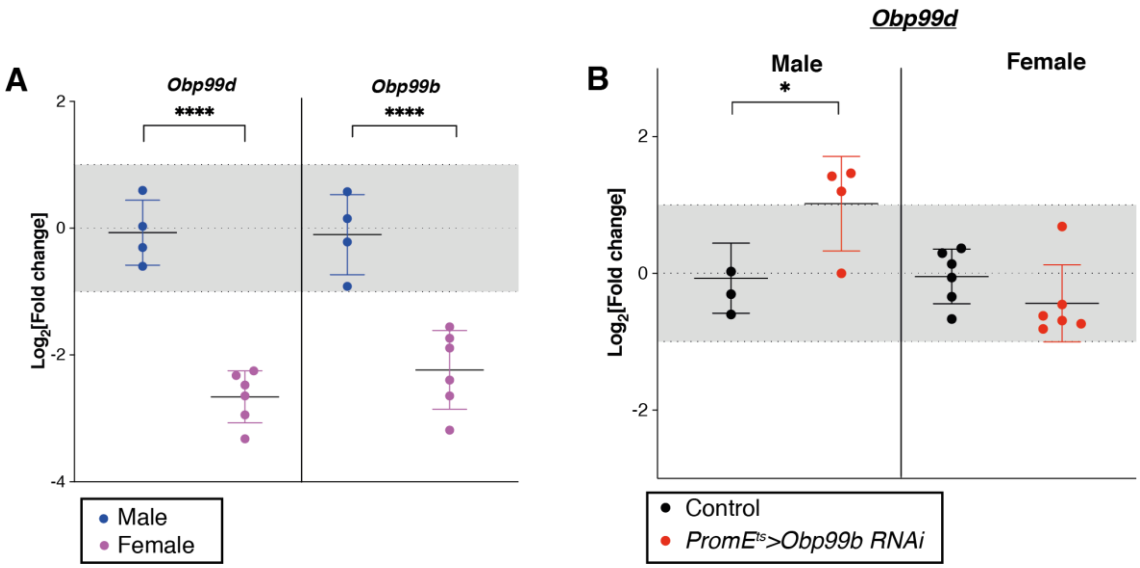

Figure 7.17 Expression of *Obp99b* and *Obp99d* is sexually dimorphic

A. Expression levels of *Obp99d* and *Obp99b* in males and females show sexually dimorphic expression of both genes. Expression shown relative to the expression in males
B. Relative expression of *Obp99d* in control and *PromE^{ts}>Obp99b* RNAi flies show no off-target knockdown of *Obp99d* by *Obp99b RNAi*.
Expression shown relative to the mean of the control condition, calculated in relation to *RP49* which was used as a housekeeping gene. Each datapoint represents one sample which was composed of seven flies.

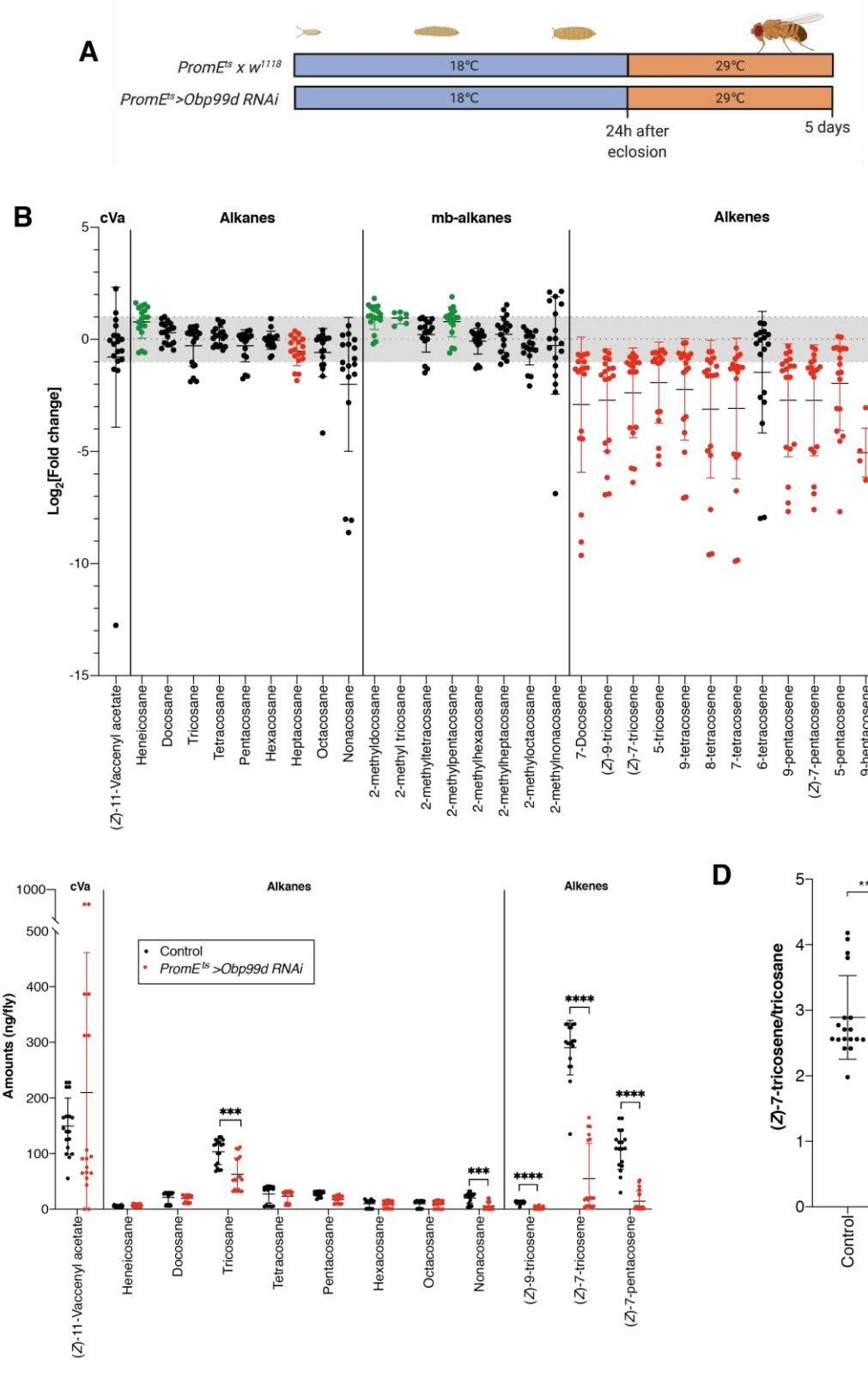
A
PromE^ts x w^1118
PromE^ts>Obp99d RNAi
18°C
29°C
18°C
29°C
24h after eclosion
5 days
B
cVa
Alkanes
mb-alkanes
Alkenes
Log2[Fold change]
(Z)-11-Vaccenyl acetate
Heneicosane
Docosane
Tricosane
Tetracosane
Pentacosane
Hexacosane
Heptacosane
Octacosane
Nonacosane
2-methyldocosane
2-methyl tricosane
2-methyltetracosane
2-methylpentacosane
2-methylhexacosane
2-methylheptacosane
2-methyloctacosane
2-methylnonacosane
7-Docosene
(Z)-9-tricosene
(Z)-7-tricosene
5-tricosene
9-tetracosene
8-tetracosene
7-tetracosene
6-tetracosene
9-pentacosene
(Z)-7-pentacosene
5-pentacosene
9-heptacosene
7-heptacosene
C
cVa
Alkanes
Alkenes
Amounts (ng/fly)
Control
PromE^ts >Obp99d RNAi
***
***
****
****
****
(Z)-11-Vaccenyl acetate
Heneicosane
Docosane
Tricosane
Tetracosane
Pentacosane
Hexacosane
Octacosane
Nonacosane
(Z)-9-tricosene
(Z)-7-tricosene
(Z)-7-pentacosene
D
****
(Z)-7-tricosene/tricosane
Control
PromE^ts >Obp99d RNAi

Figure 7.18 Oenocyte Obp99d is required for male cuticular alkenes

A. Experimental schematic. Flies are housed at 18℃ during development and transferred to 29℃ within 24 hours of eclosion. Flies are housed at a density of 10 flies per vial separated by sex for a period of five days before hydrocarbons are extracted for GC-MS.
B. Fly cuticular hydrocarbon levels as determined by GC-MS shown relative to the mean of the control line. Compounds highlighted in green are significantly increased and in red are significantly decreased. Statistical significance is as follows: heneicosane (**), heptacosane (*), 2-methyldocosane (****), 2-methyltricosane (***), 2-methylpentacosane (**), 7-docosene (**), (*Z*)-9-tricosene (***), (*Z*)-7-tricosene (***), 5-tricosene (**), 9-tetracosene (**), 8-tetracosene (**), 7-tetracosene (**), 9-pentacosene (**), (*Z*)-7-pentacosene (**), 5-pentacosene (*), 9-heptacosene (****), 7-heptacosene (**).
C. Absolute amounts of cuticular hydrocarbons shown in ng per fly.
D. Hydrocarbon saturation index as illustrated using the ratio of (*Z*)-7-tricosene/tricosane.
Results shown are from three independent experiments containing six replicates each. Each datapoint represents one sample composed of hydrocarbons extracted from five flies.

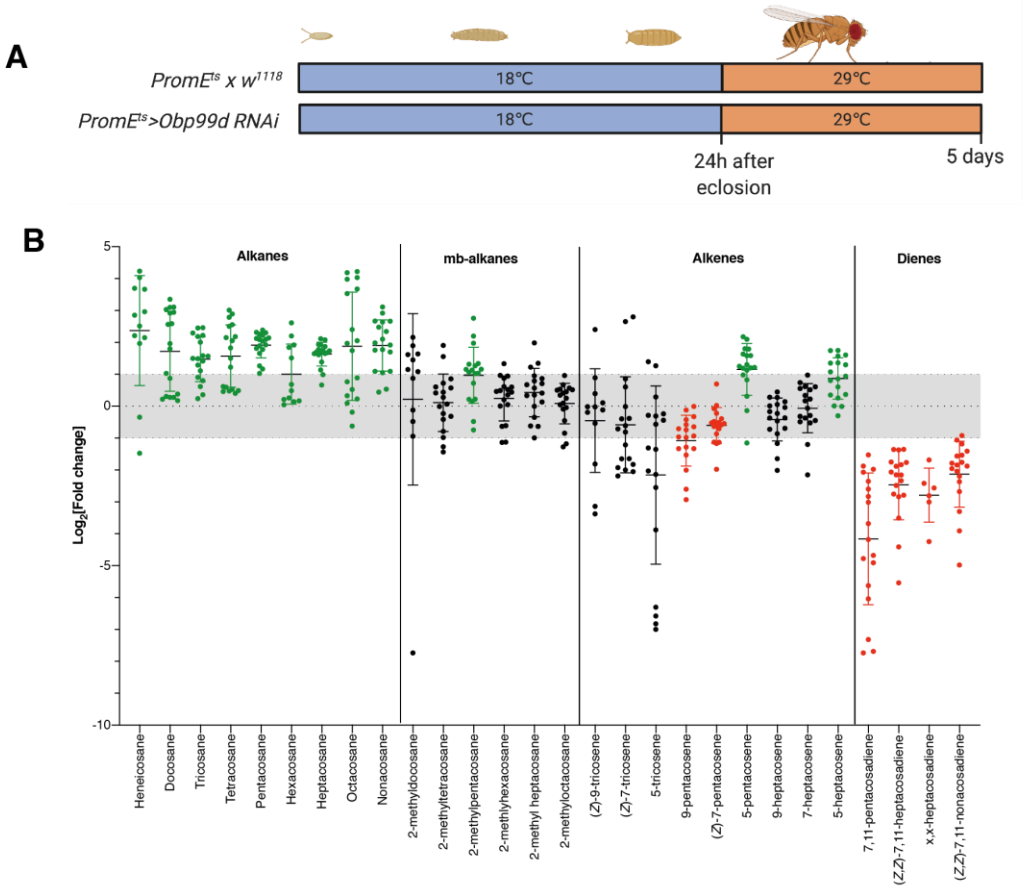
A
PromE^ts x w^1118
PromE^ts>Obp99d RNAi
18°C
29°C
18°C
29°C
24h after eclosion
5 days
B
Alkanes
mb-alkanes
Alkenes
Dienes
Log2[Fold change]
Heneicosane
Docosane
Tricosane
Tetracosane
Pentacosane
Hexacosane
Heptacosane
Octacosane
Nonacosane
2-methyldocosane
2-methyltetracosane
2-methylpentacosane
2-methylhexacosane
2-methyl heptacosane
2-methyloctacosane
(Z)-9-tricosene
(Z)-7-tricosene
5-tricosene
9-pentacosene
(Z)-7-pentacosene
5-pentacosene
9-heptacosene
7-heptacosene
5-heptacosene
7,11-pentacosadiene
(Z,Z)-7,11-heptacosadiene
x,x-heptacosadiene
(Z,Z)-7,11-nonacosadiene

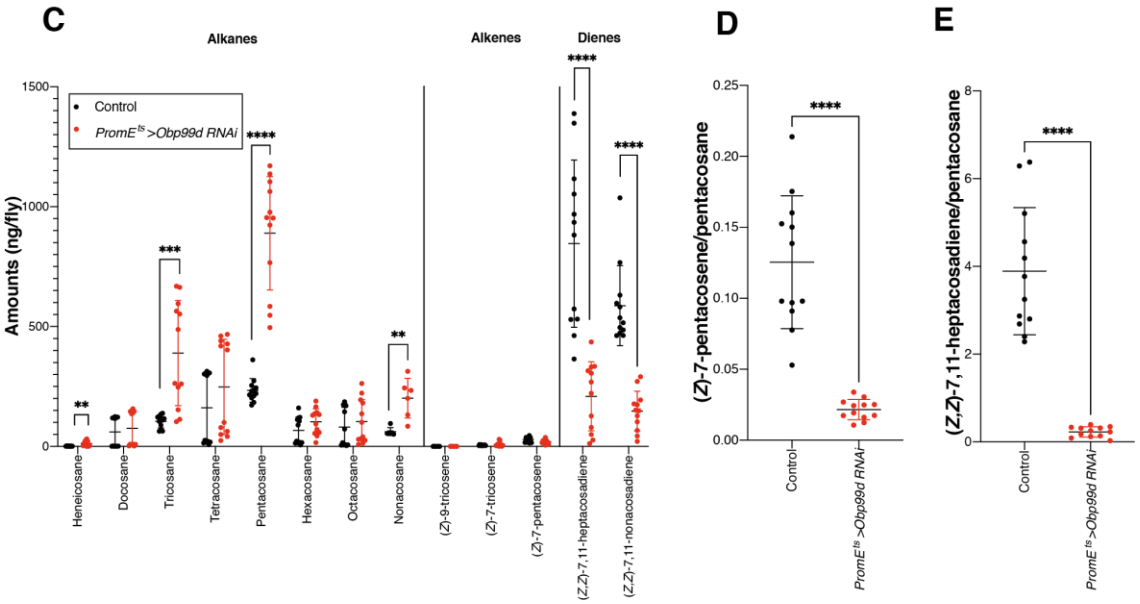
C
Alkanes
Alkenes
Dienes
Control
PromE^ts>Obp99d RNAi
Amounts (ng/fly)
D
(Z)-7-pentacosene/pentacosane
Control
PromE^ts>Obp99d RNAi
E
(Z,Z)-7,11-heptacosadiene/pentacosane
Control
PromE^ts>Obp99d RNAi

Figure 7.19 Oenocyte Obp99d is required for female cuticular dienes

A. Experimental schematic. Flies are housed at 18℃ during development and transferred to 29℃ within 24 hours of eclosion. Flies are housed at a density of 10 flies per vial separated by sex for a period of five days before hydrocarbons are extracted for GC-MS.
B. Fly cuticular hydrocarbon levels as determined by GC-MS shown relative to the mean of the control line. Compounds highlighted in green are significantly increased and in red are significantly decreased. Statistical significance is as follows: heneicosane (***), docosane (****), tricosane (****), tetracosane (****), pentacosane (****), hexacosane (**), heptacosane (****), octacosane (****), nonacosane (****), 2-methylpentacosane (***), 9-pentacosene (****), (*Z*)-7-pentacosene (***), 5-pentacosene (*****), 5-heptacosene (****), 7,11-pentacosadiene (****), (*Z*)-7, (*Z*)-11-heptacosadiene (****), (*Z*)-7, (*Z*)-11-nonacosadiene (****)
C. Absolute amounts of cuticular hydrocarbons shown in ng per fly.
D. Hydrocarbon saturation index as illustrated using the ratio of (*Z*)-7-pentacosene/pentacosane.
E. Hydrocarbon saturation index as illustrated using the ratio of (*Z*)-7, (*Z*)-11-heptacosadiene/pentacosane.
Results shown are from three independent experiments containing six replicates each. Each datapoint represents one sample composed of hydrocarbons extracted from five flies.

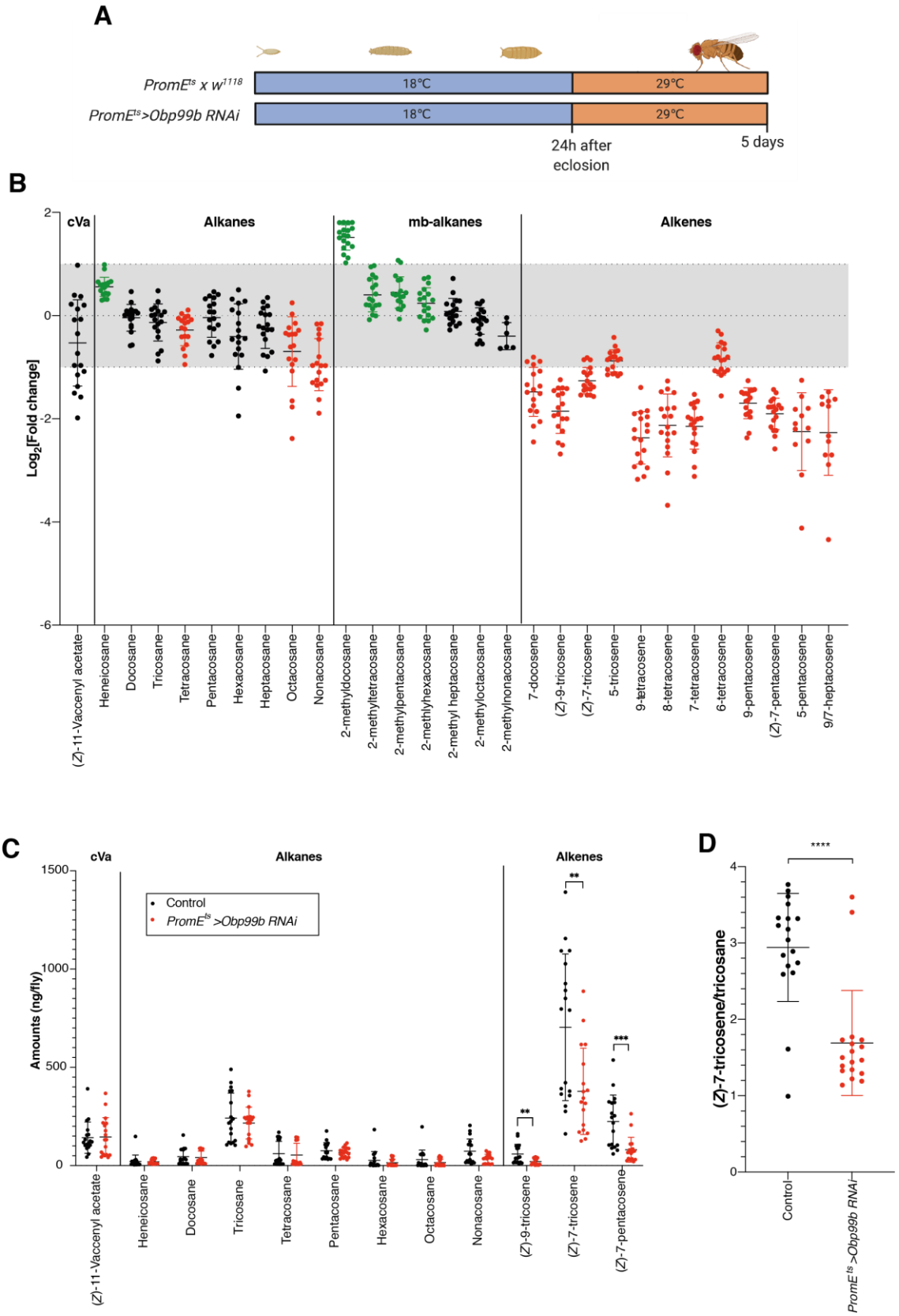
A
PromE^ts x w^1118
PromE^ts>Obp99b RNAi
18°C
29°C
18°C
29°C
24h after eclosion
5 days
B
cVa
Alkanes
mb-alkanes
Alkenes
Log2[Fold change]
(Z)-11-Vaccenyl acetate
Heneicosane
Docosane
Tricosane
Tetracosane
Pentacosane
Hexacosane
Heptacosane
Octacosane
Nonacosane
2-methyldocosane
2-methyltetracosane
2-methylpentacosane
2-methylhexacosane
2-methyl heptacosane
2-methyloctacosane
2-methylnonacosane
7-docosene
(Z)-9-tricosene
(Z)-7-tricosene
5-tricosene
9-tetracosene
8-tetracosene
7-tetracosene
6-tetracosene
9-pentacosene
(Z)-7-pentacosene
5-pentacosene
9/7-heptacosene
C
cVa
Alkanes
Alkenes
Control
PromE^ts >Obp99b RNAi
Amounts (ng/fly)
(Z)-11-Vaccenyl acetate
Heneicosane
Docosane
Tricosane
Tetracosane
Pentacosane
Hexacosane
Octacosane
Nonacosane
(Z)-9-tricosene
(Z)-7-tricosene
(Z)-7-pentacosene
D
(Z)-7-tricosene/tricosane
Control
PromE^ts >Obp99b RNAi

Figure 7.20 Oenocyte Obp99b is required for male cuticular alkenes

A. Experimental schematic. Flies are housed at 18℃ during development and transferred to 29℃ within 24 hours of eclosion. Flies are housed at a density of 15 flies per vial separated by sex for a period of five days before hydrocarbons are extracted for GC-MS.
B. Fly cuticular hydrocarbon levels as determined by GC-MS shown relative to the mean of the control line. Compounds highlighted in green are significantly increased and in red are significantly decreased. Statistical significance is as follows: Docosane (****), tricosane (****), tetracosane (****), pentacosane (****), hexacosane (****), heptacosane (****), octacosane (****), nonacosane (****), (*Z*)-9-tricosene (**), 5-pentacosene (****), 9-heptacosene (***), x,x-pentacosadiene (****), (*Z*)-7,(*Z*)-11-heptacosadiene (***), (*Z*)-7,(*Z*)-11-nonacosadiene (****)
C. Absolute amounts of cuticular hydrocarbons shown in ng per fly.
D. Hydrocarbon saturation index as illustrated using the ratio of (*Z*)-7-tricosene/tricosane.
Results shown are from three independent experiments containing six replicates each. Each datapoint represents one sample composed of hydrocarbons extracted from five flies.

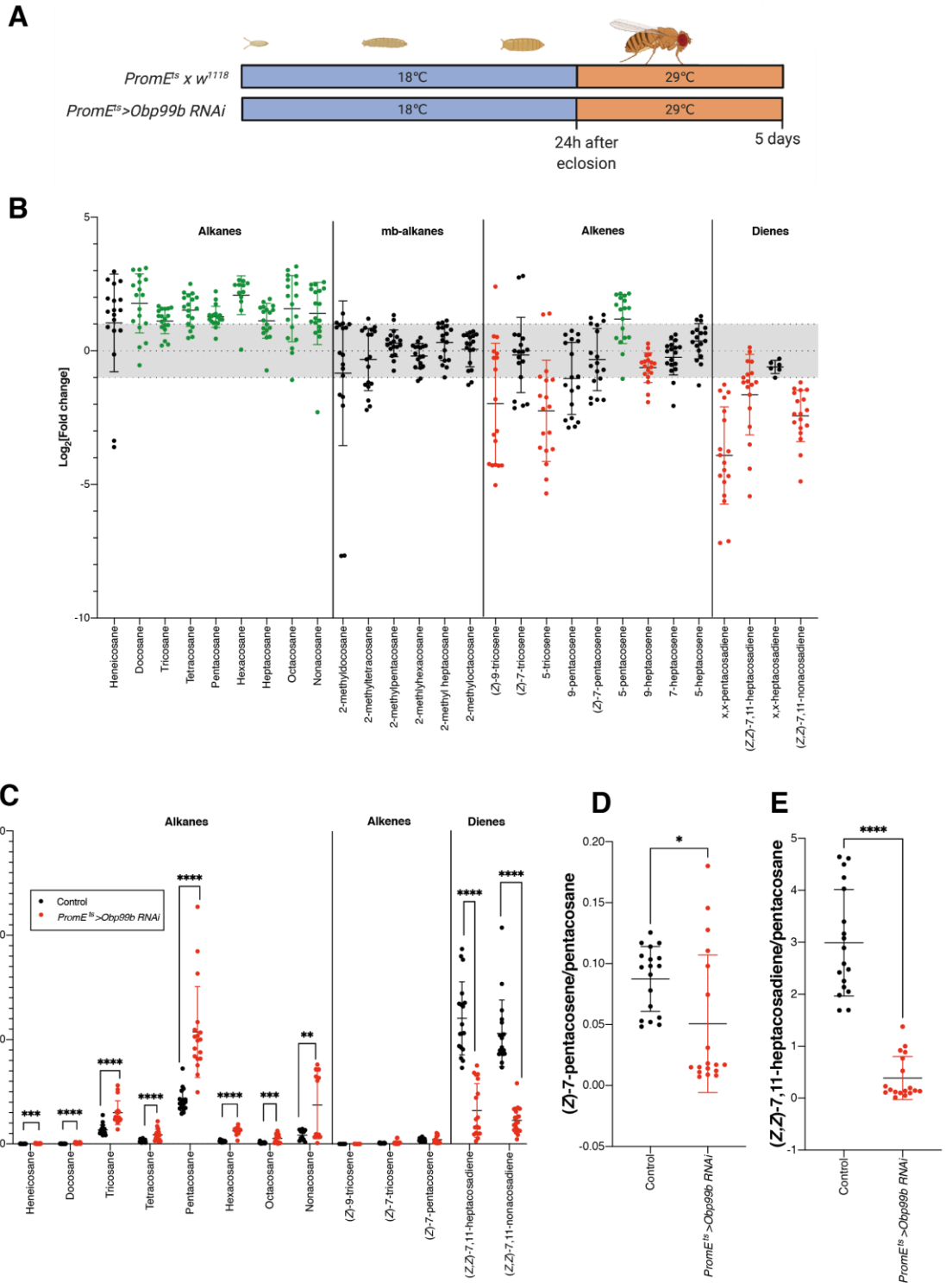
A
PromE^ts x w^1118
PromE^ts>Obp99b RNAi
18°C
29°C
18°C
29°C
24h after eclosion
5 days
B
Alkanes
mb-alkanes
Alkenes
Dienes
Log2[Fold change]
Heneicosane
Docosane
Tricosane
Tetracosane
Pentacosane
Hexacosane
Heptacosane
Octacosane
Nonacosane
2-methyldocosane
2-methyltetracosane
2-methylpentacosane
2-methylhexacosane
2-methyl heptacosane
2-methyloctacosane
(Z)-9-tricosene
(Z)-7-tricosene
5-tricosene
9-pentacosene
(Z)-7-pentacosene
5-pentacosene
9-heptacosene
7-heptacosene
5-heptacosene
x,x-pentacosadiene
(Z,Z)-7,11-heptacosadiene
x,x-heptacosadiene
(Z,Z)-7,11-nonacosadiene
C
Alkanes
Alkenes
Dienes
Control
PromE^ts>Obp99b RNAi
Amounts (ng/fly)
D
(Z)-7-pentacosene/pentacosane
Control
PromE^ts>Obp99b RNAi
E
(Z,Z)-7,11-heptacosadiene/pentacosane
Control
PromE^ts>Obp99b RNAi

Figure 7.21 Oenocyte Obp99b is required for female cuticular dienes

A. Experimental schematic. Flies are housed at 18℃ during development and transferred to 29℃ within 24 hours of eclosion. Flies are housed at a density of 15 flies per vial separated by sex for a period of five days before hydrocarbons are extracted for GC-MS.
B. Fly cuticular hydrocarbon levels as determined by GC-MS shown relative to the mean of the control line. Compounds highlighted in green are significantly increased and in red are significantly decreased. Statistical significance is as follows: heneicosane (****), tetracosane (**), octacosane (*), nonacosane (****), 2-methyldocosane (****), 2-methyltetracosane (****), 2-methylpentacosane (****), 2-methylhexacosane (**), 7-docosene (****), (*Z*)-9-tricosene (****), (*Z*)-7-tricosene (****), 5-tricosene (****), 9-tetracosene (****), 8-tetracosene (****), 7-tetracosene (****), 6-tetracosene (****), 9-pentacosene (****), (*Z*)-7-pentacosene (****), 5-pentacosene (****), 9/7-heptacosene (****).
C. Absolute amounts of cuticular hydrocarbons shown in ng per fly.
D. Hydrocarbon saturation index as illustrated using the ratio of (*Z*)-7-tricosene/tricosane.
Results shown are from three independent experiments containing six replicates each. Each datapoint represents one sample composed of hydrocarbons extracted from five flies.

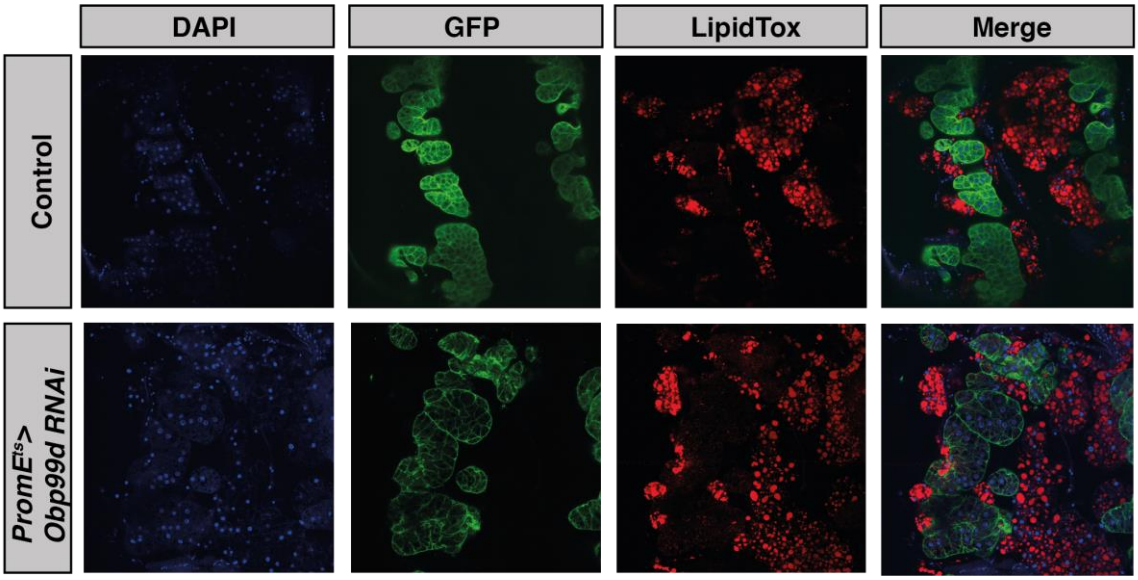

Figure 7.22 Oenocyte knockdown of Obp99d does not induce oenocyte lipid droplets

LipidTox staining of neutral lipids in male fly oenocytes after five days of RNAi induction at 29℃. GFP marks oenocyte cell membranes, as genetically expressed by *PromE>GAL4* driven *UAS-CD8::GFP*. These images are representative of two independent experiments with n=4 replicates and n=3 replicates respectively.

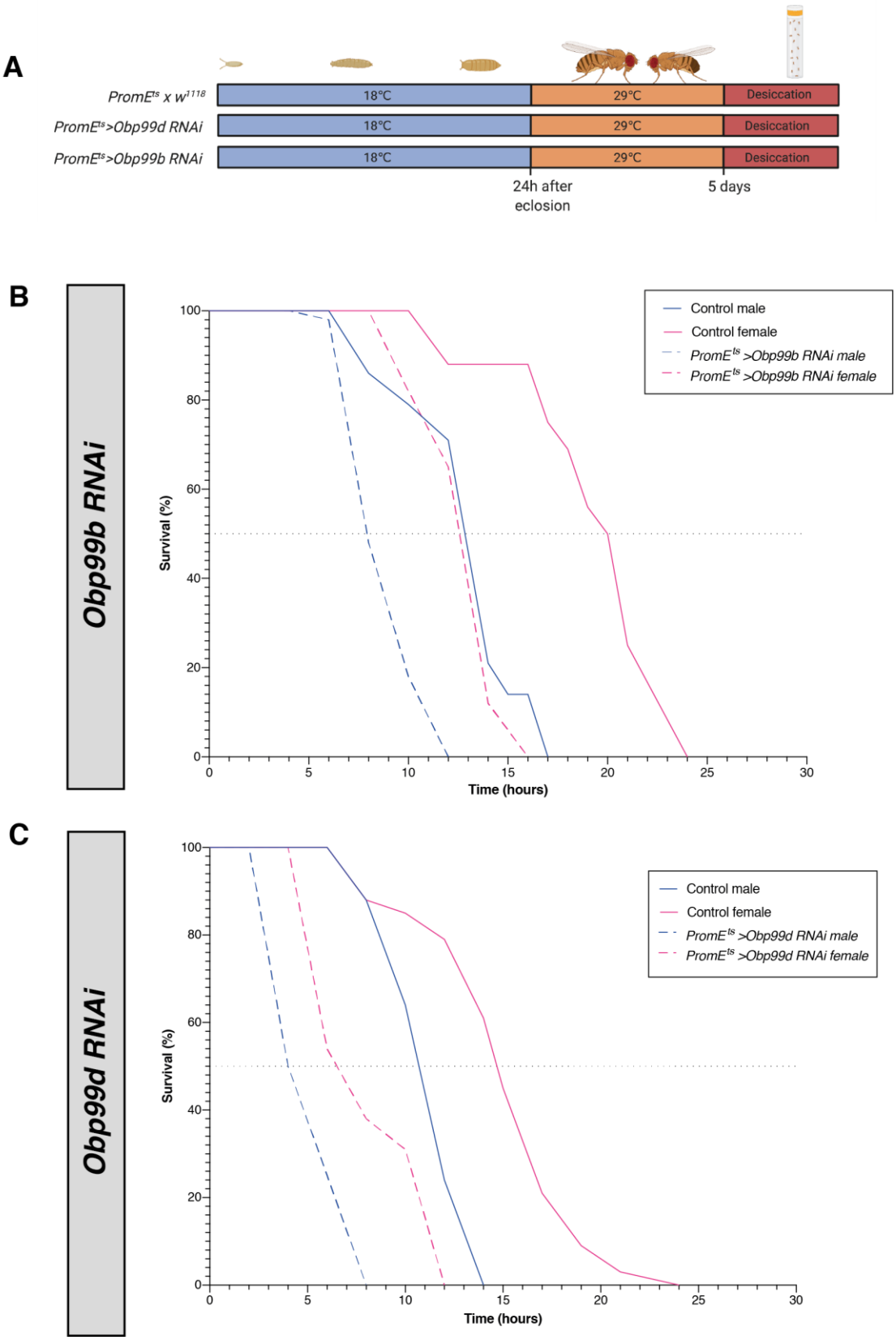
A
PromE^ts x w^1118
PromE^ts>Obp99d RNAi
PromE^ts>Obp99b RNAi
18°C
29°C
Desiccation
24h after eclosion
5 days
B
Obp99b RNAi
Control male
Control female
PromE^ts >Obp99b RNAi male
PromE^ts >Obp99b RNAi female
Survival (%)
Time (hours)
C
Obp99d RNAi
Control male
Control female
PromE^ts >Obp99d RNAi male
PromE^ts >Obp99d RNAi female
Survival (%)
Time (hours)

Figure 7.23 Oenocyte knockdown of Obp99b or Obp99d decreases desiccation resistance

A. Experimental schematic. Crosses are performed at 18℃ and upon eclosion flies are separated by sex and housed at a density of 15 flies per vial at 29℃. The desiccation assay was performed at 25℃.
B. Survival under desiccation of Obp99b RNAi flies and a control line. Median survivals are as follows: Control male 13h n=15, Control female 20h n=16, *Obp99b RNAi* male 8h n=40 (38% decrease in median survival), Obp99b RNAi female 12.5h n=17 (37.5% decrease in median survival). A second replicate of the female desiccation survival is shown in **Supplementary Figure 9.34** located in the Supplementary Material.
C. Survival under desiccation of Obp99d RNAi flies and a control line. Median survivals are as follows: Control male 10.75h n=31, Control female 14.75h n=33, Obp99d RNAi male 4h n=8(63% decrease in median survival), Obp99d RNAi female 6.5h n= 13(56% decrease in median survival).

I next wanted to explore whether regulation of *Obp99b* and *Obp99d* levels could contribute to changes in cuticular alkenes arising from environmental stresses/factors such as diet and housing density (**Chapter 6.3**). For example, could decreased *Obp99b/d* expression account for the observed relative decrease in adult cuticular alkenes resulting from a low yeast (LY) developmental diet (Stefana et al., 2017). Indeed, the change in alkene:alkane ratio seen in *Obp99b* and *Obp99d RNAi* flies is of a similar magnitude to that seen in the LY model. However, I found that *Obp99b* and *Obp99d mRNA* levels do not change significantly in response to a developmental LY diet (**Figure 7.24**). This finding rules out adult downregulation of these two Obp genes, at least at the transcriptional level, as a key mediator of the alkene decrease in the developmental LY model. Hence, the decreased cuticular hydrocarbon saturation index in LY flies may be due to changes in other odorant binding proteins or in hydrocarbon biosynthesis itself.

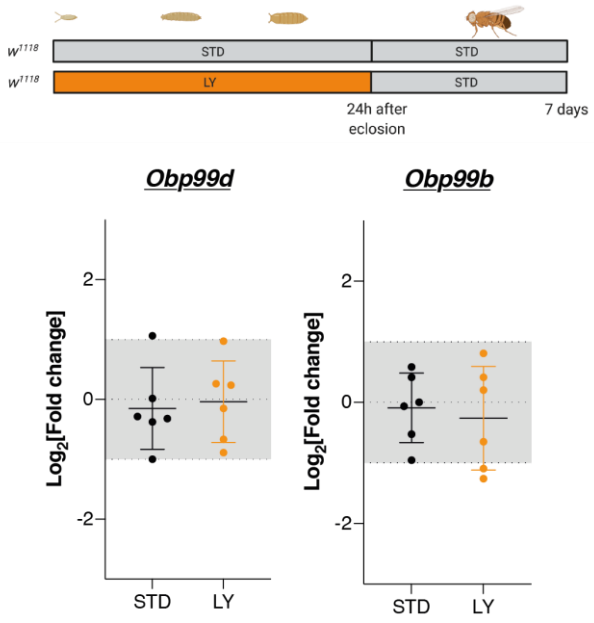

Figure 7.24 Low yeast developmental diet does not alter adult *Obp99b* and *Obp99d* expression

Obp99d and Obp99b mRNA levels in STD and LY flies. Low yeast (LY) flies were fed a diet with 0.1% yeast content during development then transferred to a standard diet within 24 hours of eclosion. mRNA levels are shown relative to the mean of the control, calculated relative to the reference gene *RP49*. Each datapoint represents one sample which is composed of: STD flies seven flies per sample, and LY flies ten flies per sample to account for decreased size.

I next investigated whether a second environmental factor, housing density (**Chapter 6.3**), might regulate *Obp99b/d* expression. I previously showed that housing density is associated with an increase in fly cuticular alkenes (**Figure 6.11**). It was therefore hypothesised that this may be mediated via differential expression of *Obp99b* and/or *Obp99d*. RT-qPCR on whole flies was used to quantify the expression of a panel of hydrocarbon biosynthesis and Obp genes at housing densities of 1-80 flies per vial (**Figure 7.25**) *Cyp4g1* encodes the oenocyte P450 decarbonylase involved in the last step of alkane and alkene synthesis and its expression did not change at different housing densities. *Desat1* encodes the oenocyte desaturase required for alkene synthesis and its expression showed a tendency to increase with higher densities but this was not statistically significant. *Obp56d* is known to be expressed in the adult carcass and gut, and its mRNA levels did not change with increasing housing density in a consistent manner. However, *Obp99b*, *Obp99c* and *Obp99d* all showed a tendency to increase expression with increasing housing density. In the case of *Obp99b* and *Obp99d*, the expression increase was significant, despite small sample sizes. Future experiments will be needed to be sure that these expression changes map to the oenocytes. Nevertheless, this exciting result strongly suggests that housing density regulates Obp expression and that this could contribute to the density-dependent changes in hydrocarbons observed in Chapter 6.

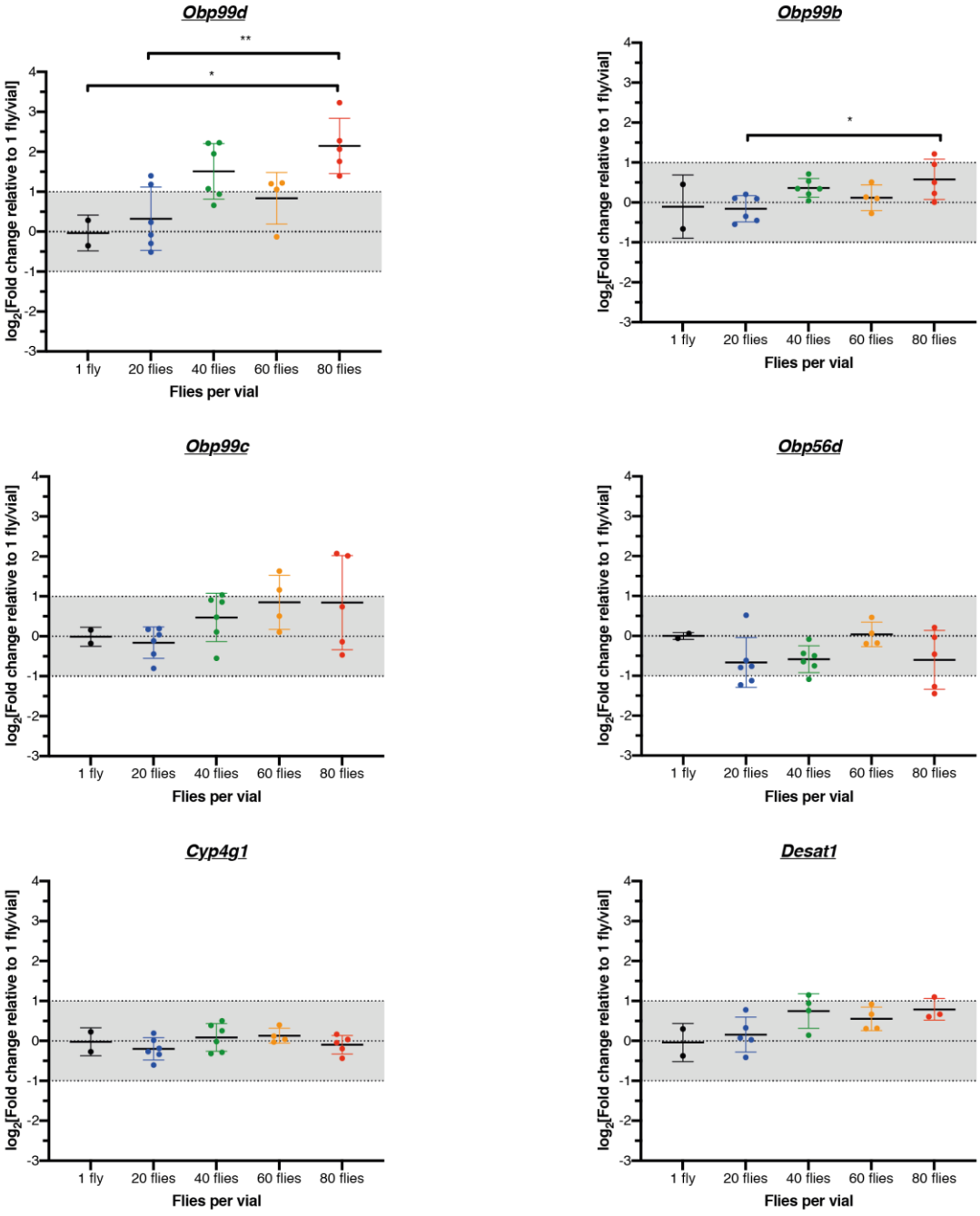

Figure 7.25 Housing density regulates *Obp99b/d* but not *Cyp4g1* expression

Expression of *Obp99d*, *Obp99b*, *Obp99c*, *Obp56d*, *Cyp4g1* and *Desat1* RNA in male whole flies as determined using qPCR. Data shown represents the mean of the gene of interest relative to the three reference genes *RP49*, *RNA Pol II* and *Act*. Each datapoint represents one sample generated from seven flies.

7.6 Discussion

In this chapter, I investigated how flies respond to altered levels of hydrocarbon autotoxins such as tricosene. An important and robust finding here is that either exogenous tricosene supplementation or loss of multiple endogenous alkenes via *Desat1* or *Obp99b/d* knockdowns gave a similar outcome, namely decreased desiccation stress resistance. It was previously suggested that the cuticular barrier to water loss was largely dependent upon alkenes (Ferveur et al., 2018), but my results are more consistent with a model whereby the precise blend of alkenes-to-alkanes is optimal – such that too few or too many alkenes are detrimental. My results do not, however, rule out the possibility that altering cuticular alkene levels affects not only the desiccation barrier but also many other stress responses, perhaps via a general increase in “frailty” (Stefana et al., 2017).

Tricosene autotoxicity is not mediated via increased fecundity or via microbiota, but insights were gained by examining the transcriptome of tricosene-treated flies. The transcriptional signature of tricosene includes many genes that are differentially regulated in a pattern that resembles a starvation response. However, I showed that tricosene-exposed flies are not sensitised to additional starvation and do not lose weight during autotoxin exposure. It would be interesting to examine triglyceride stores and feeding behaviour but the existing data do suggest that tricosene may not substantially impair nutrient uptake. This is because flies with depleted energy stores would be expected to perform worse under starvation stress.

I found that tricosene exposure affected many categories of genes but perhaps the most interesting are those encoding predicted odorant binding proteins (Obps). Many Obps are expressed in tissues that have no known chemosensillar and the vast majority of Obps have not yet been ascribed a specific function. This suggests that some Obps may perform roles that are distinct from their known functions as chaperones for odours or pheromones detected by odorant receptors (ORs). In line with this idea, I found that tricosene exposure altered the expression of at least for Obps in the abdominal carcass. As data mining from a

published study revealed that these Obps are known to be expressed in oenocytes (Huang et al., 2019), it was plausible to suggest that tricosene regulation is occurring in these cells. Furthermore, my results clearly show that *Obp99b* and *Obp99d* are required in oenocytes for normal levels of cuticular alkenes and also for desiccation resistance. It will also be interesting in future to test the consequences of *Obp99b* and *Obp99d* knockdowns on other alkene-dependent functions such as mating and fecundity. For example, male fecundity could be assayed using a mixed population of white-eyed wildtype and red-eyed RNAi males housed with white-eyed wildtype females and measuring the proportion of F1 progeny inheriting red versus white eyes.

As oenocyte-specific knockdowns of Obp99b and Obp99d dramatically decrease cuticular alkenes, it is possible that Obps are involved with hydrocarbon transport. Obp99b and Obp99d could act as binding proteins to chaperone hydrophobic hydrocarbons from oenocytes to the aqueous hemolymph and perhaps also from the hemolymph to the epidermis. Interestingly, however, neutral lipids do not accumulate inside oenocytes in *Obp99d RNAi*, so perhaps it is important for hydrocarbons to interact with Obp99d in the hemolymph rather than as part of the oenocyte hydrocarbon secretion pathway. To provide direct evidence of hydrocarbon binding by Obp99b and Obp99d will require *in vitro* binding assays using recombinant proteins challenged with a variety of hydrophobic ligands. It also remains possible that Obps do not bind hydrocarbons directly but are instead required for other steps of cuticular alkene production such as binding the fatty acid precursors of alkenes.

The increase in expression of *Obp99b* and *Obp99d* in response to elevated housing density is interesting. Taken together with their knockdown phenotypes, this suggests that Obps could contribute to the housing density increase in cuticular autotoxic alkenes and thus provide part of the physiological mechanism underlying the link between increased density and decreased lifespan. One intriguing puzzle that Obps may or may not explain is the observation from the previous chapter that elevated housing density decreases the alkene/alkane ratio in the vial, an opposite effect to that seen for the cuticle. The findings in this

chapter also raise the exciting hypothesis that flies are able to sense environmental stresses such as increased housing density and modulate their cuticular hydrocarbon blend through a regulatory circuit that involves Obps.

Chapter 8. Discussion

In this thesis I have investigated the composition, regulation and function of barrier lipids using a combination of advanced mass spectrometry techniques with genetic analysis. I first increased the capability of OrbiSIMS with a new cryogenic workflow that expands the range of barrier lipids and other molecules that can be analysed on the surface of plants, animals and humans with a single methodology. I then used OrbiSIMS and other mass spectrometry techniques to reveal the presence of hundreds of different lipids on the cuticle of *Drosophila* and on the skin of mice. This provided new insights into the composition of the integument barrier, identifying many lipid species not previously reported in the literature in this biological context. OrbiSIMS imaging in *Drosophila* revealed that once class of lipids, wax esters, are localised in spatially restricted patterns on the cuticle surface. I then used OrbiSIMS and other mass spectrometry methods to show that several environmental factors regulate the composition of the lipid barrier. In particular, I demonstrated that the yeast/protein content of the diet during development can have a long-lasting (programming) effect on the skin/cuticle lipids of both *Drosophila* and mice. This establishes, in two model organisms, new DOHaD paradigms for future mechanistic studies of nutritional programming of the integument.

In *Drosophila*, I extended previous findings, showing that low dietary yeast during development not only decreases cuticular alkene hydrocarbons (Stefana et al., 2017), but also increases a non-hydrocarbon cuticular component, wax esters. Using a genetic approach, I provided evidence that wax esters and other non-hydrocarbons are likely synthesised by the same cell type as hydrocarbons – the oenocyte. Isotopomer analysis was then used to show that developmental energy stores contribute proportionally less carbon resources to cuticular hydrocarbons than to non-hydrocarbons. I therefore investigated adult-specific environmental factors that regulate cuticular hydrocarbons, finding clear effects for temperature but, surprisingly, not for desiccation. Nevertheless, I found that the cuticular barrier to desiccation does depend upon an optimal ratio of alkene-to-alkane hydrocarbons. Population density is an adult environmental factor known to

influence lifespan via alkene hydrocarbons (Stefana et al., 2017). Building on this, I demonstrated that population density also regulates cuticular alkenes. In particular, when population density increases there is a concomitant increase in the proportion of alkenes in the cuticular hydrocarbon blend. Multiple genes that respond to alkene exposure were identified via transcriptome profiling, including several encoding secreted odorant binding proteins (Obps). I then demonstrated that two of these genes, *Obp99b* and *Obp99d*, are both required in oenocytes for normal cuticular alkene levels and also for barrier function. Together, these findings suggest that flies are able to sense population density and then respond by regulating alkene hydrocarbon levels via a regulatory circuit involving Obps.

8.1 Imaging barrier lipids with unprecedented spatial and chemical resolution

To address the challenges surrounding the accurate measurements a wide range of skin/cuticular lipids, I developed a cryogenic workflow for OrbiSIMS (cryo-OrbiSIMS). I have applied this new approach to acquire both spectral and imaging data, supported with GC-MS and LC-MS where appropriate. I have demonstrated the effectiveness of OrbiSIMS and cryo-OrbiSIMS, not only for measuring barrier lipid composition in a range of organisms, but also for preserving the spatial localisation of lipid species. Due to the semi-quantitative nature of mass spectrometry imaging, significant support is still required from more quantitative techniques such as GC-MS and LC-MS. Both of these techniques come with their own advantages and disadvantages: GC-MS is useful for targeted analysis but requires complex separation and derivatisation procedures to increase selectivity. LC-MS is beneficial for more untargeted analyses and it does not usually require derivatisation but it is not suitable for highly apolar compounds such as hydrocarbons. Both techniques come with the loss of spatial selectivity inherent in the requirement for solvent extraction of the sample. Therefore, for this study, where it is essential to differentiate surface lipids from internal lipids, it has been highly beneficial to utilise mass spectrometry imaging. To enable OrbiSIMS to function as a stand-alone technique, significant progress must be made towards making it more quantitative. This is a particularly

challenging task as the chemistry underlying the matrix effects observed under different analysis conditions is still not well understood. The influence of matrix effects on the ionisation efficiency of different lipid species is shown Chapter 3. Using a mixture of lipid standards, OrbiSIMS shows an apparent lower ionisation/detection efficiency of glycerolipids such as TG and DG when compared with LC-MS, where these compounds are separated by the chromatography step and so do not influence the ionisation of each other. By further characterising the molar relative response factors for different lipid species in different environments, it may eventually become possible to derive correction factors which could be used in an effort to make this technique more quantitative. Despite the above limitations, I have demonstrated one experimental context where accurate relative quantitation using OrbiSIMS is possible – Isotopomer analysis (Chapter 5). Here, stable isotope labelled tracers such as glucose or acetate can be combined with OrbiSIMS to calculate accurately the fractional enrichments and patterns of incorporation into almost any molecule that can be detected. Since this is a relative method that involves measuring the ratios of heavy to light atoms within the same molecular species, rather than absolute amounts, calculations are subject to minimal interference from matrix effects.

I showed that the cryogenic analysis system for the OrbiSIMS resulted in a variety of improvements that widen its biological applications (Chapter 3 and Chapter 4). One key challenge in the field of mass spectrometry imaging has been to maintain molecular structure whilst reducing the lateral resolution towards cellular and subcellular scales. Ion beams with the ability to achieve focus on the nanometre scale are typically polyatomic (e.g. Bi_3^+) or monoatomic (e.g. Cs^+) and they usually fragment molecules extensively. In contrast, the “softer” ion beams that are able to image intact molecules are typically cluster ion beams (e.g. Ar_{3500}^+), which are currently only able to achieve focus on the micrometre scale. This resolution is biologically useful in many cases, such as the barrier lipid studies in this thesis, but a drive towards sub-micron resolution would greatly widen the applicability of this technique in cell biology and beyond. I illustrated the substantial advantages of cryogenic analysis in detecting intact lipids which greatly improves the utility of argon gas cluster ion beams for OrbiSIMS (Chapter

3). Combining cryogenic analysis with new developments in ion beam technology may overcome the current barriers associated with the increased fragmentation caused by higher energy transfer per atom. This may enable equally good detection of intact biomolecules at even smaller scales than those currently achievable with cryo-OrbiSIMS. The eventual aim is to progress this technology to detect intact lipids and metabolites on a subcellular scale so that, for example, mitochondria can be distinguished from cytoplasm.

A second key challenge in the field of SIMS imaging has been to detect molecules that would otherwise become volatile in the ultra-high vacuum conditions of the analysis chamber. These include naturally semi-volatile molecules such as polycyclic aromatic hydrocarbons and some alkenes. However, most other hydrocarbons and even free fatty acids and triglycerides are volatilised in the analysis chamber, precluding their accurate analysis using standard temperature SIMS methods. The successful detection of hydrocarbons on plant and fruit fly samples with cryo-OrbiSIMS shows clear promise for applications in the biology, pharmaceutical, environmental and physical disciplines. A proof-of-principle for geology and engineering applications was shown in Chapter 3, with cryo-OrbiSIMS analysis showing near-comparable detection benefits to GC-MS.

8.2 Composition of barrier lipids

The cross-platform analysis utilising cryo-OrbiSIMS and GC-MS enabled direct comparisons of cuticular lipid composition between several different plant and animal species. It was interesting to observe how similar many of the lipid classes are between species, including several which have not yet been ascribed barrier functions such as glycerolipids. These inter-species similarities could reflect either a common evolutionary origin or convergence. It could perhaps be argued that it is convergence, as hierarchical clustering of lipid profiles more closely clusters with sample type than in a pattern that matches evolutionary distances. Either way, molecules shared from plants to insects and even humans are likely to play important barrier functions. In the case of glycerolipids it is possible that, like hydrocarbons, they could act as pheromones, as has already been

suggested in *Drosophila* (Chin et al., 2014). As they are shared between plants and insects, it is also possible that glycerolipids mediate communication between species. OrbiSIMS analysis of *Drosophila* revealed ceramide phosphoethanolamines (PE-Cer) as a new, previously undescribed, component of the cuticle lipid blend. This is interesting from an evolutionary perspective as acyl-ceramides are known to be key components of the mammalian skin barrier to water loss (Coderch et al., 2003). Ceramides are synthesised by keratinocytes and are thought to form crystalline sheets in the stratum corneum of mammalian skin that contribute to effective barrier formation (Coderch et al., 2003). In *Drosophila*, PE-Cer is the only lipid class that is not significantly affected by oenocyte knockdown of fatty acid biosynthesis by SREBP inhibition (Chapter 6). It is possible this lipid class could instead be produced by the sub-cuticular epidermal cells. In this case, the sub-cuticular epidermal cells would be broadly analogous to the mammalian keratinocytes which also produce ceramides. The *Drosophila* oenocytes are strongly analogous to the mammalian sebocytes, and appear to produce the majority of lipids coating the fly cuticle. Asebic mice, which completely lack sebaceous glands, are deficient in a large number of skin lipid classes including waxes, phospholipids, glycerolipids and sterol esters (Wilkinson and Karasek, 1966). SREBP inhibition *in Drosophila* oenocytes also has knock-on effects on waxes, phospholipids and glycerolipids adding further evidence for the functional analogy between *Drosophila* oenocytes and mammalian sebocytes. In mammals, linoleic acid is an essential diet-derived fatty acid that is incorporated into acyl-ceramides and is essential for barrier function (Rabionet et al., 2014). Mice raised on a diet deficient in linoleate have impaired skin barrier function. In flies, I looked at excess rather than deficiency of linoleate but found that it can alter cuticular hydrocarbons and wax esters. A key effect here is that excess dietary linoleate stimulates the biosynthesis of a new diene hydrocarbon (6,9-heptacosadiene) with double bond positions corresponding to that of linoleate. As double bond position is important for determining the behavioural effects of different diene sex pheromones, it is possible that this change impacts upon mating behaviour.

8.3 Developmental diet programmes barrier lipids in *Drosophila* and mice

The concept of DOHaD has been widely studies in a variety of organisms and yet it is surprising that nearly all of these studies have neglected the largest organ of the body, the skin. My experiments show clearly that developmental diet has a substantial influence on the composition of integument lipids in flies and mice. In *Drosophila*, I showed that the consequences of a low yeast (LY) developmental diet extended beyond the alterations of cuticular hydrocarbons observed by Stefana et al. (2017) to several classes of non-hydrocarbon cuticular lipids. It is particularly interesting that the classes of non-hydrocarbon lipids affected in both *Drosophila* and mice appear to share commonalities – both species show an upregulation of cuticular wax esters as a result of a low yeast/protein developmental diet. In *Drosophila*, I showed that developmental diet directly feeds (contributes carbons) to adult cuticular lipid synthesis, particularly non-hydrocarbons, which provides one clear mechanistic link between developmental nutrition and barrier lipid composition. Similar isotopologue studies could be carried out in mice but, in both species, making the mechanistic link between developmental diet and skin lipids requires detailed knowledge of the cell types and enzymes involved in biosynthesising these lipids. With this information, it is then possible to directly manipulate the skin expression of these enzymes to alter the cuticular lipid composition and then test for functional consequences, such as changes in water loss. I have begun to follow this approach in *Drosophila*, finding that a LY diet results in the upregulation of a fatty-acyl reductase, *Far,* which is a good candidate for a wax esterase. Subsequent experiments will knock down this enzyme in oenocytes and measure the effect on cuticular blend and desiccation barrier function. A similar approach in the LP mouse paradigm should also be possible. For example, a published SCD3-Cre sebocyte-specific mouse line has been successfully used to specifically deplete sebaceous lipids resulting in defective water repulsion, thermoregulation and UV protection (Dahlhoff et al., 2016). In mice, it will be essential to genetically manipulate barrier lipid enzymes in keratinocytes as well as in sebocytes. In this regard, a candidate sebocyte

enzyme for the biosynthesis of wax esters is DGAT2. DGAT enzymes have been demonstrated to also have the capacity to act on wax ester biosynthesis (Tomiyama et al., 2017), and whole-body DGAT2 deficient mice have previously been reported to show skin phenotypes including an impaired waterproofing barrier (Stone et al., 2004). Therefore it is possible that an SCD3-Cre mediated knockout of this gene may reveal a sebocyte-specific function for this enzyme. A strong candidate keratinocyte enzyme for the synthesis of skin ceramides is ceramide synthase 3 (CerS3). This enzyme has conclusively been demonstrated to act as a ceramide synthase, and whole body depletion of this gene in mice results in a depletion of skin ceramides and defective protection against trans-epithelial water loss and skin infection (Jennemann et al., 2011). Keratinocyte-specific depletion of this gene could be achieved using the involucrin promoter which has demonstrated specificity for keratinocytes (Carroll et al., 1993).

I have presented evidence in Chapter 5 suggesting that non-hydrocarbon cuticular lipids in *Drosophila* are primarily synthesised during development and they persist over (relatively) long time scales throughout adult life. Isotopologue analysis also suggested that hydrocarbons and non-hydrocarbons may even be synthesised from different fatty acid pools – perhaps in the cytoplasm versus mitochondria. These findings open a new avenue of investigation into how developmental diet influences cuticular lipid composition. Indeed, the fact that I showed that developmental programming of barrier lipid composition through restricted diet is a conserved principle in mice begs the question as to whether this also occurs in humans. In this regard, it would be interesting to investigate whether human intrauterine growth restriction (IUGR) is associated with subsequent skin conditions in adult life. In the current literature, there is little reported on this subject, but a recent study does show that prenatal LP induced IUGR in rats leads to impaired transepithelial water loss and skin inflammation (Polányi et al., 2020).

8.4 Responses to *Drosophila* cuticular lipids and their functions

A central finding in this thesis is that male flies can mount a transcriptional response to the alkene (*Z*)-9-tricosene. This raises the question of how flies sense this compound. One possibility would be that they employ the same signalling pathway that is used to sense alkenes as pheromones. The detection of alkene pheromones is not yet well understood, but it seems clear that both volatile and non-volatile routes are used. These involve antennal odorant receptors as well as leg contact dependent chemoreceptors of the pickpocket family (Sánchez-Gracia et al., 2009, Thistle et al., 2012). For (*Z*)-9-tricosene, the only known mechanism invoked thus far requires the olfactory receptor Or7a to mediate the male aggression response (Lin et al., 2015). It is possible that Or7a could also be the odorant receptor that mediates the tricosene transcriptional response and perhaps autotoxic effects upon lifespan. However, my transcriptomics also showed that *Or59c* is downregulated and *Or94a* is upregulated by tricosene so these are also good candidate receptors. If odorant receptors are indeed involved, it may have to be independent of their common coreceptor Orco, as my preliminary data indicate that Orco mutant flies can still respond to tricosene at the level of decreased lifespan. Additional experiments will be needed to test whether Orco mutants still retain the transcriptional response to tricosene.

An alternative mechanism for detecting tricosene could involve ingestion and subsequent signalling via the gut. This is suggested from my transcriptomics by the dramatic effects of tricosene on gene expression in the gut, which were reminiscent but not identical to a starvation signature. It is possible that this “pseudo-starvation” signature could be connected with inflammation. It has been reported in a different context that a pseudo-starvation state can be indicative of an inflammatory response (O'Neill and Hardie, 2013). Therefore, one hypothesis would be that (*Z*)-9-tricosene exposure is inducing an inflammatory state which is reflected in the transcriptomics data. However, this cannot completely explain the signature observed, as markers of innate immune activation such as antimicrobial peptides are downregulated rather than upregulated in response to

tricosene. One candidate hydrocarbon receptor for detection in the gut would be the lipophorin receptor LpR1, which is expressed in both the adult carcass and gut. I found that *LpR1* is moderately upregulated after acute (*Z*)-9-tricosene exposure. LpR1 has been previously shown to be involved in the uptake of neutral lipids (Parra-Peralbo and Culi, 2011), and whole body mutants for LpR1 show dramatically decreased hydrocarbon levels on the fly cuticle (Wicker-Thomas et al., 2015). To determine if this receptor is indeed involved in the gut, sections of the fly gut could be imaged with cryo-OrbiSIMS to identify uptake of ^{13}C tricosene in control and LpR1 mutant flies. LpR1 could also be involved in hydrocarbon detection by the oenocytes themselves.

It is challenging to determine the individual contributions of specific lipids to barrier functions such as waterproofing, pheromone signalling and antimicrobial protection. Nevertheless, this thesis has shed light on the role of cuticular hydrocarbons in the *Drosophila* barrier to water loss. Earlier experiments indicated that hydrocarbons are required for adult survival, as evidenced in Cyp4g1 null mutants which die upon eclosion with an almost completely deleted hydrocarbon barrier (Gutierrez et al., 2007, Qiu et al., 2012). Previous studies have indicated that specifically alkenes are key for maintaining an effective waterproofing barrier (Ferveur et al., 2018). My findings add to this, strongly suggesting that it is not the absolute amounts of alkenes that is critical but rather the alkene-to-alkane desaturation ratio of the cuticular blend. More specifically, the desiccation barrier is compromised either by a desaturation ratio that is too low (*PromE^{ts}>Desat1 RNAi*, *PromE^{ts}>Obp99b RNAi* or *PromE^{ts}>Obp99d RNAi*) or too high (exogenous tricosene supplementation). Future experiments with more subtle manipulations of the alkene-to-alkane blend with examine whether the physiological changes of cuticular ratios observed in response to environmental factors such as housing density have an impact on barrier functions in desiccation. Alkenes also likely affect other aspects of adult physiology. For example, I showed that an excess of tricosene decreases the capacity to cope with salt stress. This could result either from osmotic problems that map to the cuticle itself or to other organs important for water homeostasis such as the malpighian tubules. It will also be interesting in future to see how

different alkene-alkane blends affect pheromonal functions in mating and other behaviours.

The finding in this thesis that the hydrocarbon desaturation ratio is critical for the desiccation barrier raises questions about the underlying mechanism. One possibility is that the balance of alkenes-to-alkanes plays a physicochemical role in limiting water loss via the cuticle. In this regard, it is interesting that a room temperature, *Drosophila* alkanes are solids whereas alkenes are liquids. It is therefore possible that one important role of alkenes is to act as a solvent for other “solid” cuticular lipids such as alkanes and perhaps also wax esters. In this way, alkenes would facilitate the spreading of other molecules on the cuticle, a process that is presumably aided by behaviours such as grooming. Intriguingly, however, I observed that wax esters are localised in restricted patterns on the body surface, correlating, in part, with different anatomical subtypes of cuticle (e.g. flexible pleura versus stiff sternites). The reasons for this type of spatial localisation are not yet known but could reflect differential affinity/adsorption for specific lipids to specific cuticular subtypes.

A more indirect alternative to explain how the hydrocarbon desaturation ratio is critical for the desiccation barrier could involve signalling mechanisms. Certain alkenes are well known as sex pheromones but perhaps they also correspond to signals that modulate water loss via the cuticle, or via excretory or water resorption organs like the malpighian tubules or the hindgut. It is therefore interesting that my transcriptomics analysis of the tricosene response identified changes in the expression of 14 genes, which have been putatively annotated as “solute-binding proteins”. At least one of these genes, *CG15553*, is differentially expressed in the carcass but it is not part of the published oenocyte transcriptome (Huang et al., 2019). It is therefore possible that CG15553 is expressed in the adult epidermis, which may also respond to alkene exposure, either directly or via the oenocytes.

8.5 Regulation of the cuticular hydrocarbon blend

In this thesis, I identified two binding proteins which are critical for maintaining the barrier lipid composition and therefore effective barrier properties. Without these lipid binding proteins, the composition of the cuticular lipid blend is significantly perturbed and barrier function severely compromised. These lipid binding proteins appear to be closely related to the lipocalin class of proteins in mammals, and future research could potentially identify these as functional homologues (albeit for different classes of barrier lipid) of the odorant binding proteins identified in *Drosophila*.

I tested several environmental factors for potential roles as regulators of the cuticular hydrocarbon blend. Although hydrocarbons are essential for the barrier to water loss, I did not find clear evidence that desiccation actually regulates cuticular hydrocarbon levels. Consistent with previous reports (Rajpurohit et al., 2021, Gibbs et al., 1998, Rajpurohit et al., 2017), I did find that high temperature tends to increase cuticular hydrocarbon chain length. Perhaps the most striking finding in my thesis is that population density is a novel environmental regulator of cuticular hydrocarbons. Density effects on the alkene-to-alkane ratio and/or on the proportion of hydrocarbons retained on the fly cuticle were observed in two different genetic strains (*w^{1118} iso31* and *Oregon R*) in the range of 1 to 20 flies per vial as well as for more crowded conditions. Stefana et al. (2017) previously showed using *PromE^{ts}>Desat1 RNAi* flies that alkenes are required for the density-dependent decrease in lifespan. My findings add substantially to this by showing that, when population density increases, there is a concomitant increase in the proportion of alkenes in the cuticular hydrocarbon blend. Surprisingly, however, this relative alkene increase on the body is mirrored by a relative alkene decrease in the pool of shed hydrocarbons. The underlying explanation for this intriguing observation is not clear but my experiments suggest that it might not be explained by a decrease in grooming behaviour alone. One hypothesis that may explain this would be enrichment of alkenes on different body parts. My preliminary findings support the enrichment of alkenes on the fly wings, which may be more easily groomed away from their initial site of secretion on the

abdomen due to their liquid state at room temperature, as opposed to alkanes which are solid at room temperature. Therefore, at higher housing densities it is possible that the nature of the grooming behaviour changes, resulting in decreased grooming of the wings and subsequent retention of alkenes. This could be tested by recording and analysing grooming behaviours at different housing densities, and analysing cuticular hydrocarbon amounts on different body parts using either cryo-OrbiSIMS or GC-MS. The evolutionary advantage of this altered cuticular lipid blend is not yet clear but it could be a pheromonal response which regulates behaviour in response to altered housing density. Increased abundance of alkenes on the fly cuticle could act either to disperse other flies away from an environment with limited resources, or it could act to increase the “attractiveness” for females within an environment with higher male-male competition for mating. The latter hypothesis could be tested by assaying mating success of males housed for extended periods of time at high density versus low density.

Multiple genes that respond to alkene exposure were identified in *Drosophila* via transcriptomic profiling, including several encoding secreted odorant binding proteins (Obps). Two of these genes, *Obp99b* and *Obp99d*, are significantly upregulated at high population density. I also found that *Obp99b* and *Obp99d* are important and selective genetic regulators of the cuticular hydrocarbon blend. Thus, oenocyte knockdown of either O*bp99b* or *Obp99d* dramatically decreases cuticular alkenes but not alkanes. In turn, both genetic manipulations correlate with an impaired barrier to desiccation. Obp99b and Obp99d have no previously ascribed function, although other secreted odorant binding proteins in the chemosensillar lymph have been demonstrated to be involved in transporting apolar odorants to olfactory receptors in the antenna (Xu et al., 2005). However, I have shown that *Obp99b* and *Obp99d* are required in oenocytes rather than antennal chemosensillar for the correct alkene-to-alkane ratio of the cuticular lipid blend. This suggests the hypothesis that Obp99b and Obp99d may be responsible for binding and transporting hydrocarbons in the oenocyte secretory pathway and/or within the hemolymph *en route* to the epidermis and cuticle. In order to examine the cellular, subcellular and hemolymph localisations of Obp99b

and Obp99d, I have (via commercial partners) raised antibodies and used CRISPR/Cas technology to generate flies with endogenously tagged Obp99b and Obp99d genes. I have also collaborated with the Structural Biology STP at the Crick to produce purified Obp99b and Obp99d proteins from *Drosophila* cell lines. These can now be used to design competition assays in order to determine the ligand binding specificity of these proteins. I hope that these approaches will uncover novel non-canonical functions for odorant binding proteins in regulating the composition of the fly cuticular lipid blend.

Together, the findings in this thesis indicate that flies are able to sense population density and then respond by regulating alkene hydrocarbon levels, perhaps via a regulatory circuit involving Obps. In future, it will be interesting to determine whether mice and other mammals can regulate their skin lipids in response to population density and other environmental factors such as temperature. Currently, almost nothing is known about this. Increased knowledge in this area may therefore shed light on the aetiology of human skin conditions where lipid levels are known to be altered. These include acne, seborrheic dermatitis, sebaceous hyperplasia, and sebaceous gland carcinoma.

References

ABDEL-SHAFY, H. I. & MANSOUR, M. S. M. 2016. A review on polycyclic aromatic hydrocarbons: Source, environmental impact, effect on human health and remediation. *Egyptian Journal of Petroleum,* 25**,** 107-123.

ABRAHAM, J. & MATHEW, S. 2019. Merkel Cells: A Collective Review of Current Concepts. *International journal of applied & basic medical research,* 9**,** 9-13.

ADAMS, M. D., CELNIKER, S. E., HOLT, R. A., EVANS, C. A., GOCAYNE, J. D., AMANATIDES, P. G., SCHERER, S. E., LI, P. W., HOSKINS, R. A., GALLE, R. F., GEORGE, R. A., LEWIS, S. E., RICHARDS, S., ASHBURNER, M., HENDERSON, S. N., SUTTON, G. G., WORTMAN, J. R., YANDELL, M. D., ZHANG, Q., CHEN, L. X., BRANDON, R. C., ROGERS, Y.-H. C., BLAZEJ, R. G., CHAMPE, M., PFEIFFER, B. D., WAN, K. H., DOYLE, C., BAXTER, E. G., HELT, G., NELSON, C. R., GABOR, G. L., MIKLOS, ABRIL, J. F., AGBAYANI, A., AN, H.-J., ANDREWS-PFANNKOCH, C., BALDWIN, D., BALLEW, R. M., BASU, A., BAXENDALE, J., BAYRAKTAROGLU, L., BEASLEY, E. M., BEESON, K. Y., BENOS, P. V., BERMAN, B. P., BHANDARI, D., BOLSHAKOV, S., BORKOVA, D., BOTCHAN, M. R., BOUCK, J., BROKSTEIN, P., BROTTIER, P., BURTIS, K. C., BUSAM, D. A., BUTLER, H., CADIEU, E., CENTER, A., CHANDRA, I., CHERRY, J. M., CAWLEY, S., DAHLKE, C., DAVENPORT, L. B., DAVIES, P., PABLOS, B. D., DELCHER, A., DENG, Z., MAYS, A. D., DEW, I., DIETZ, S. M., DODSON, K., DOUP, L. E., DOWNES, M., DUGAN-ROCHA, S., DUNKOV, B. C., DUNN, P., DURBIN, K. J., EVANGELISTA, C. C., FERRAZ, C., FERRIERA, S., FLEISCHMANN, W., FOSLER, C., GABRIELIAN, A. E., GARG, N. S., GELBART, W. M., GLASSER, K., GLODEK, A., GONG, F., GORRELL, J. H., GU, Z., GUAN, P., HARRIS, M., HARRIS, N. L., HARVEY, D., HEIMAN, T. J., HERNANDEZ, J. R., HOUCK, J., HOSTIN, D., HOUSTON, K. A., HOWLAND, T. J., WEI, M.-H., et al. 2000. The Genome Sequence of *Drosophila melanogaster*. *Science,* 287**,** 2185-2195.

AGUILA, J. R., SUSZKO, J., GIBBS, A. G. & HOSHIZAKI, D. K. 2007. The role of larval fat cells in adult *Drosophila melanogaster*. *Journal of Experimental Biology,* 210**,** 956-963.

ALIBAKHSHI, A. 2017. Enthalpy of vaporization, its temperature dependence and correlation with surface tension: A theoretical approach. *Fluid Phase Equilibria,* 432**,** 62-69.

ALLEN, D. R. & MCWHINNEY, B. C. 2019. Quadrupole Time-of-Flight Mass Spectrometry: A Paradigm Shift in Toxicology Screening Applications. *The Clinical biochemist. Reviews,* 40**,** 135-146.

AMIAR, S., MACRAE, J. I., CALLAHAN, D. L., DUBOIS, D., VAN DOOREN, G. G., SHEARS, M. J., CESBRON-DELAUW, M.-F., MARÉCHAL, E., MCCONVILLE, M. J., MCFADDEN, G. I., YAMARYO-BOTTÉ, Y. & BOTTÉ, C. Y. 2016. Apicoplast-Localized Lysophosphatidic Acid Precursor Assembly Is Required for Bulk Phospholipid Synthesis in Toxoplasma gondii and Relies on an

Algal/Plant-Like Glycerol 3-Phosphate Acyltransferase. *PLOS Pathogens,* 12**,** e1005765.

AMREIN, H. 2016. Mechanism of Taste Perception in *Drosophila*. *In:* ZUFALL, F. & MUNGER, S. D. (eds.) *Chemosensory Transduction.* Academic Press.

ANTONY, C. & JALLON, J.-M. 1982. The chemical basis for sex recognition in *Drosophila melanogaster*. *Journal of Insect Physiology,* 28**,** 873-880.

ARRESE, E. L. & SOULAGES, J. L. 2010. Insect fat body: energy, metabolism, and regulation. *Annu Rev Entomol,* 55**,** 207-25.

AYERS, M. 2012. ChemSpider: The Free Chemical Database. *Reference Reviews,* 26**,** 45-46.

BAILEY, M. J., BRADSHAW, R., FRANCESE, S., SALTER, T. L., COSTA, C., ISMAIL, M., R, P. W., BOSMAN, I., WOLFF, K. & DE PUIT, M. 2015. Rapid detection of cocaine, benzoylecgonine and methylecgonine in fingerprints using surface mass spectrometry. *Analyst,* 140**,** 6254-9.

BAO, M., JOZA, P. J., MASTERS, A. & RICKERT, W. S. 2014. Analysis of Selected Carbonyl Compounds in Tobacco Samples by Using Pentafluorobenzylhydroxylamine Derivatization and Gas Chromatography-Mass Spectrometry. 26**,** 86.

BARKER, D. J. & OSMOND, C. 1986. Infant mortality, childhood nutrition, and ischaemic heart disease in England and Wales. *Lancet,* 1**,** 1077-81.

BARKER, D. J. P. 1998. *Mothers, babies and health in later life,* Edinburgh, Edinburgh : Churchill Livingstone.

BASRA, M. K. & SHAHRUKH, M. 2009. Burden of skin diseases. *Expert Rev Pharmacoecon Outcomes Res,* 9**,** 271-83.

BATESON, P., GLUCKMAN, P. & HANSON, M. 2014. The biology of developmental plasticity and the Predictive Adaptive Response hypothesis. *The Journal of Physiology,* 592**,** 2357-2368.

BENOIT, F. M. & HARRISON, A. G. 1977. Predictive value of proton affinity. Ionization energy correlations involving oxygenated molecules. *Journal of the American Chemical Society,* 99**,** 3980-3984.

BERDYSHEV, E., GOLEVA, E., BRONOVA, I., DYJACK, N., RIOS, C., JUNG, J., TAYLOR, P., JEONG, M., HALL, C. F., RICHERS, B. N., NORQUEST, K. A., ZHENG, T., SEIBOLD, M. A. & LEUNG, D. Y. 2018. Lipid abnormalities in atopic skin are driven by type 2 cytokines. *JCI Insight,* 3.

BIANCO-MIOTTO, T., CRAIG, J. M., GASSER, Y. P., VAN DIJK, S. J. & OZANNE, S. E. 2017. Epigenetics and DOHaD: from basics to birth and beyond. *J Dev Orig Health Dis,* 8**,** 513-519.

BILLETER, J.-C., ATALLAH, J., KRUPP, J. J., MILLAR, J. G. & LEVINE, J. D. 2009. Specialized cells tag sexual and species identity in *Drosophila melanogaster*. *Nature,* 461**,** 987-991.

BLOMQUIST, G. J. 2010. *Insect Hydrocarbons: Biology, Biochemistry, and Chemical Ecology,* Cambridge, Cambridge University Press.

BLOMQUIST, G. J. & GINZEL, M. D. 2021. Chemical Ecology, Biochemistry, and Molecular Biology of Insect Hydrocarbons. *Annu Rev Entomol,* 66**,** 45-60.

BLOMQUIST, G. J. & JACKSON, L. L. 1979. Chemistry and Biochemistry of Insect Waxes. *Prog. Lipid Res. ,* 17**,** 319-345.

BOUSCHEN, W. & SPENGLER, B. 2007. Artifacts of MALDI sample preparation investigated by high-resolution scanning microprobe matrix-assisted laser desorption/ionization (SMALDI) imaging mass spectrometry. *International Journal of Mass Spectrometry,* 266**,** 129-137.

BOUSLIMANI, A., PORTO, C., RATH, C. M., WANG, M., GUO, Y., GONZALEZ, A., BERG-LYON, D., ACKERMANN, G., MOELLER CHRISTENSEN, G. J., NAKATSUJI, T., ZHANG, L., BORKOWSKI, A. W., MEEHAN, M. J., DORRESTEIN, K., GALLO, R. L., BANDEIRA, N., KNIGHT, R., ALEXANDROV, T. & DORRESTEIN, P. C. 2015. Molecular cartography of the human skin surface in 3D. *Proceedings of the National Academy of Sciences,* 112**,** E2120-E2129.

BOUSQUET, F., NOJIMA, T., HOUOT, B., CHAUVEL, I., CHAUDY, S., DUPAS, S., YAMAMOTO, D. & FERVEUR, J.-F. 2012. Expression of a desaturase gene, *desat1*, in neural and nonneural tissues separately affects perception and emission of sex pheromones in *Drosophila*. *Proceedings of the National Academy of Sciences,* 109**,** 249-254.

BRAND, A. H. & PERRIMON, N. 1993. Targeted gene expression as a means of altering cell fates and generating dominant phenotypes. *Development,* 118**,** 401-415.

BRAVO-SANTANO, N., ELLIS, J. K., CALLE, Y., KEUN, H. C., BEHRENDS, V. & LETEK, M. 2019. Intracellular Staphylococcus aureus Elicits the Production of Host Very Long-Chain Saturated Fatty Acids with Antimicrobial Activity. *Metabolites,* 9**,** 148.

BROWN, A., KROON, J., SWARBRECK, D., FEBRER, M., LARSON, T., GRAHAM, I., CACCAMO, M. & SLABAS, A. 2012. Tissue-Specific Whole Transcriptome Sequencing in Castor, Directed at Understanding Triacylglycerol Lipid Biosynthetic Pathways. *PloSONE,* 7**,** 1-13.

BRUCE, K. D., HOXHA, S., CARVALHO, G. B., YAMADA, R., WANG, H.-D., KARAYAN, P., HE, S., BRUMMEL, T., KAPAHI, P. & JA, W. W. 2013. High carbohydrate-low protein consumption maximizes *Drosophila* lifespan. *Experimental gerontology,* 48**,** 1129-1135.

BRUINS, A. P. 1991. Mass spectrometry with ion sources operating at atmospheric pressure. *Mass Spectrometry Reviews,* 10**,** 53-77.

BUCHON, N., SILVERMAN, N. & CHERRY, S. 2014. Immunity in *Drosophila melanogaster* — from microbial recognition to whole-organism physiology. *Nature Reviews Immunology,* 14**,** 796-810.

BUENO, A., ALFARHAN, A., ARAND, K., BURGHARDT, M., DEININGER, A.-C., HEDRICH, R., LEIDE, J., SEUFERT, P., STAIGER, S. & RIEDERER, M. 2019. Effects of temperature on the cuticular transpiration barrier of two desert plants with water-spender and water-saver strategies. *Journal of Experimental Botany,* 70**,** 1613-1625.

BURTON, J. L., CUNLIFFE, W. J., MILLAR, D. G. & SHUSTER, S. 1970. Effect of pregnancy on sebum excretion. *Br Med J,* 2**,** 769-71.

BUSER, H. R., ARN, H., GUERIN, P. & RAUSCHER, S. 1983. Determination of double bond position in mono-unsaturated acetates by mass spectrometry of dimethyl disulfide adducts. *Analytical Chemistry,* 55**,** 818-822.

CAMPANA, J. E. 1980. Elementary theory of the quadrupole mass filter. *International Journal of Mass Spectrometry and Ion Physics,* 33**,** 101-117.

CANDI, E., KNIGHT, R. A., PANATTA, E., SMIRNOV, A. & MELINO, G. 2016. Cornification of the Skin: A Non-apoptotic Cell Death Mechanism. *eLS.*

CARLSON, M. 2019. org.Dm.eg.db: Genome wide annotation for Fly. R package version 3.4.1.

CARROLL, J. M., ALBERS, K. M., GARLICK, J. A., HARRINGTON, R. & TAICHMAN, L. B. 1993. Tissue- and stratum-specific expression of the human involucrin promoter in transgenic mice. *Proc Natl Acad Sci U S A,* 90**,** 10270-4.

CEDER, M. M., AGGARWAL, T., HOSSEINI, K., MATURI, V., PATIL, S., PERLAND, E., WILLIAMS, M. J. & FREDRIKSSON, R. 2020. CG4928 Is Vital for Renal Function in Fruit Flies and Membrane Potential in Cells: A First In-Depth Characterization of the Putative Solute Carrier UNC93A. *Frontiers in Cell and Developmental Biology,* 8.

CHERTEMPS, T., DUPORTETS, L., LABEUR, C., UEYAMA, M. & WICKER-THOMAS, C. 2006. A female-specific desaturase gene responsible for diene hydrocarbon biosynthesis and courtship behaviour in *Drosophila melanogaster*. *Insect Mol Biol,* 15**,** 465-73.

CHIANG, Y. N., TAN, K. J., CHUNG, H., LAVRYNENKO, O., SHEVCHENKO, A. & YEW, J. Y. 2016. Steroid Hormone Signaling Is Essential for Pheromone Production and Oenocyte Survival. *PLOS Genetics,* 12**,** e1006126.

CHIN, J. S., ELLIS, S. R., PHAM, H. T., BLANKSBY, S. J., MORI, K., KOH, Q. L., ETGES, W. J. & YEW, J. Y. 2014. Sex-specific triacylglycerides are widely conserved in *Drosophila* and mediate mating behavior. *Elife,* 3**,** e01751.

CHINTAPALLI, V. R., WANG, J. & DOW, J. A. T. 2007. Using FlyAtlas to identify better Drosophila melanogaster models of human disease. *Nature Genetics,* 39**,** 715-720.

CHONG, J., WISHART, D. S. & XIA, J. 2019. Using MetaboAnalyst 4.0 for Comprehensive and Integrative Metabolomics Data Analysis. *Current Protocols in Bioinformatics,* 68**,** e86.

CLAYTON, K., VALLEJO, A. F., DAVIES, J., SIRVENT, S. & POLAK, M. E. 2017. Langerhans Cells—Programmed by the Epidermis. *Frontiers in Immunology,* 8.

CLAYTON, R. W., LANGAN, E. A., ANSELL, D. M., DE VOS, I. J. H. M., GÖBEL, K., SCHNEIDER, M. R., PICARDO, M., LIM, X., VAN STEENSEL, M. A. M. & PAUS, R. 2020. Neuroendocrinology and neurobiology of sebaceous glands. *Biological Reviews,* 95**,** 592-624.

CODERCH, L., LÓPEZ, O., DE LA MAZA, A. & PARRA, J. L. 2003. Ceramides and skin function. *Am J Clin Dermatol,* 4**,** 107-29.

COOPER, C., KUH, D., EGGER, P., WADSWORTH, M. & BARKER, D. 1996. Childhood growth and age at menarche. *BJOG: An International Journal of Obstetrics & Gynaecology,* 103**,** 814-817.

COULOMBE, P. A. & LEE, C.-H. 2012. Defining Keratin Protein Function in Skin Epithelia: Epidermolysis Bullosa Simplex and Its Aftermath. *Journal of Investigative Dermatology,* 132**,** 763-775.

CVACKA, J. & SVATOS, A. 2003. Matrix-assisted laser desorption/ionization analysis of lipids and high molecular weight hydrocarbons with lithium 2,5-dihydroxybenzoate matrix. *Rapid Commun Mass Spectrom,* 17**,** 2203-7.

DAHLHOFF, M., CAMERA, E., SCHÄFER, M., EMRICH, D., RIETHMACHER, D., FOSTER, A., PAUS, R. & SCHNEIDER, M. R. 2016. Sebaceous lipids are essential for water repulsion, protection against UVB-induced apoptosis and ocular integrity in mice. *Development,* 143**,** 1823-1831.

DALLERAC, R., LABEUR, C., JALLON, J.-M., KNIPPLE, D. C., ROELOFS, W. L. & WICKER-THOMAS, C. 2000. A Δ9 desaturase gene with a different substrate specificity is responsible for the cuticular diene hydrocarbon polymorphism in *Drosophila melanogaster*. *Proceedings of the National Academy of Sciences,* 97**,** 9449-9454.

DARRAGH, K., ORTEU, A., BLACK, D., BYERS, K. J. R. P., SZCZERBOWSKI, D., WARREN, I. A., RASTAS, P., PINHARANDA, A., DAVEY, J. W., FERNANDA GARZA, S., ABONDANO ALMEIDA, D., MERRILL, R. M., MCMILLAN, W. O., SCHULZ, S. & JIGGINS, C. D. 2021. A novel terpene synthase controls differences in anti-aphrodisiac pheromone production between closely related Heliconius butterflies. *PLOS Biology,* 19**,** e3001022.

DE HOFFMANN, E. & STROOBANT, V. 2007. *Mass Spectrometry Principles and Applications*, Wiley.

DE MARTE, M. L. & ENESCO, H. E. 1986. Influence of low tryptophan diet on survival and organ growth in mice. *Mechanisms of Ageing and Development,* 36**,** 161-171.

DELUCA, H. F. 1997. Chapter 29 - The Genetics and Biology of Vitamin D. *In:* BITTAR, E. E. & BITTAR, N. (eds.) *Principles of Medical Biology.* Elsevier.

DEMBECK, L. M., BÖRÖCZKY, K., HUANG, W., SCHAL, C., ANHOLT, R. R. & MACKAY, T. F. 2015. Genetic architecture of natural variation in cuticular hydrocarbon composition in Drosophila melanogaster. *Elife,* 4.

DENISOV, E., DAMOC, E., LANGE, O. & MAKAROV, A. 2012. Orbitrap mass spectrometry with resolving powers above 1,000,000. *International Journal of Mass Spectrometry,* 325-327**,** 80-85.

DETTMER, K., ARONOV, P. A. & HAMMOCK, B. D. 2007. Mass spectrometry-based metabolomics. *Mass Spectrometry Reviews,* 26**,** 51-78.

DHOUAILLY, D. & OFTEDAL, O. T. 2016. 12 - Integument and Associated Integumentary Appendages. *In:* BALDOCK, R., BARD, J., DAVIDSON, D. R. & MORRISS-KAY, G. (eds.) *Kaufman's Atlas of Mouse Development Supplement.* Boston: Academic Press.

DIETSCHY, J. M. & BROWN, M. S. 1974. Effect of alterations of the specific activity of the intracellular acetyl CoA pool on apparent rates of hepatic cholesterogenesis. *J Lipid Res,* 15**,** 508-16.

DJAWDAN, M., SUGIYAMA, T. T., SCHLAEGER, L. K., BRADLEY, T. J. & ROSE, M. R. 1996. Metabolic Aspects of the Trade-Off between Fecundity and Longevity in *Drosophila melanogaster*. *Physiological Zoology,* 69**,** 1176-1195.

DOŁOWY, M. & PYKA, A. 2015. Chromatographic Methods in the Separation of Long-Chain Mono- and Polyunsaturated Fatty Acids. *Journal of Chemistry,* 2015**,** 120830.

DORMAN, F. L., WHITING, J. J., COCHRAN, J. W. & GARDEA-TORRESDEY, J. 2010. Gas Chromatography. *Analytical Chemistry,* 82**,** 4775-4785.

DÖRNER, G. 1973. Die mögliche Bedeutung der prä- und/oder perinatalen Ernährung für die Pathogenese der Obesitas. *Acta biologica medica Ger,* 30**,** 19-22.

DÖRNER, G., HALLER, K. & LEONHARDT, M. 1973. Zur möglichen Bedeutung der prä- und/oder früh postnatalen Ernährung für die Pathogenese der Arteriosklerose. *Acta Biol Med Ger,* 31**,** 31-35.

DÖRNER, G. & MOHNIKE, A. 1973. Zur möglichen Bedeutung der prä- und/oder frühpostnatalen Ernährung für die Pathogenese der Diabetes Mellitus. *Acta Biol Med Ger,* 31**,** 7-10.

DORSEY, J. G., COOPER, W. T., SILES, B. A., FOLEY, J. P. & BARTH, H. G. 1996. Liquid Chromatography: Theory and Methodology. *Analytical Chemistry,* 68**,** 515-568.

DRAKE, D. R., BROGDEN, K. A., DAWSON, D. V. & WERTZ, P. W. 2008. Thematic review series: skin lipids. Antimicrobial lipids at the skin surface. *J Lipid Res,* 49**,** 4-11.

DUNKELBLUM, E., TAN, S. H. & SILK, P. J. 1985. Double-bond location in monounsaturated fatty acids by dimethyl disulfide derivatization and mass spectrometry: Application to analysis of fatty acids in pheromone glands of four lepidoptera. *Journal of Chemical Ecology,* 11**,** 265-277.

EGLINTON, G., GONZALEZ, A. G., HAMILTON, R. J. & RAPHAEL, R. A. 1962. Hydrocarbon constituents of the wax coatings of plant leaves: A taxonomic survey. *Phytochemistry,* 1**,** 89-102.

EJIMA, A. 2015. Pleiotropic actions of the male pheromone cis-vaccenyl acetate in Drosophila melanogaster. *Journal of comparative physiology. A, Neuroethology, sensory, neural, and behavioral physiology,* 201**,** 927-932.

EJIMA, A., SMITH, B. P., LUCAS, C., VAN DER GOES VAN NATERS, W., MILLER, C. J., CARLSON, J. R., LEVINE, J. D. & GRIFFITH, L. C. 2007. Generalization of courtship learning in *Drosophila* is mediated by cis-vaccenyl acetate. *Curr Biol,* 17**,** 599-605.

ERHUMA, A., SALTER, A. M., SCULLEY, D. V., LANGLEY-EVANS, S. C. & BENNETT, A. J. 2007. Prenatal exposure to a low-protein diet programs disordered regulation of lipid metabolism in the aging rat. *Am J Physiol Endocrinol Metab,* 292**,** E1702-14.

ESLER, W. P., TESZ, G. J., HELLERSTEIN, M. K., BEYSEN, C., SIVAMANI, R., TURNER, S. M., WATKINS, S. M., AMOR, P. A., CARVAJAL-GONZALEZ, S., GEOLY, F. J., BIDDLE, K. E., PURKAL, J. J., FITCH, M., BUCKERIDGE, C., SILVIA, A. M., GRIFFITH, D. A., GORGOGLIONE, M., HASSOUN, L., BOSANAC, S. S., VERA, N. B., ROLPH, T. P., PFEFFERKORN, J. A. & SONNENBERG, G. E. 2019. Human sebum requires de novo lipogenesis, which is increased in acne vulgaris and suppressed by acetyl-CoA carboxylase inhibition. *Science Translational Medicine,* 11**,** eaau8465.

EZKURDIA, I., JUAN, D., RODRIGUEZ, J. M., FRANKISH, A., DIEKHANS, M., HARROW, J., VAZQUEZ, J., VALENCIA, A. & TRESS, M. L. 2014. Multiple evidence strands suggest that there may be as few as 19,000 human protein-coding genes. *Human molecular genetics,* 23**,** 5866-5878.

FAHY, E., SUD, M., COTTER, D. & SUBRAMANIAM, S. 2007. LIPID MAPS online tools for lipid research. *Nucleic acids research,* 35**,** W606-W612.

FARHADIAN, S. F., SUÁREZ-FARIÑAS, M., CHO, C. E., PELLEGRINO, M. & VOSSHALL, L. B. 2012. Post-fasting olfactory, transcriptional, and feeding responses in Drosophila. *Physiology & Behavior,* 105**,** 544-553.

FEINGOLD, K. R. 2009. The outer frontier: the importance of lipid metabolism in the skin. *Journal of Lipid Research,* 50**,** S417-S422.

FENN, J. B., MANN, M., MENG, C. K., WONG, S. F. & WHITEHOUSE, C. M. 1989. Electrospray ionization for mass spectrometry of large biomolecules. *Science,* 246**,** 64-71.

FERVEUR, J. F., CORTOT, J., RIHANI, K., COBB, M. & EVERAERTS, C. 2018. Desiccation resistance: effect of cuticular hydrocarbons and water content in *Drosophila melanogaster* adults. *PeerJ,* 6**,** e4318.

FERVEUR, J. F., SAVARIT, F., O'KANE, C. J., SUREAU, G., GREENSPAN, R. J. & JALLON, J. M. 1997. Genetic feminization of pheromones and its behavioral consequences in Drosophila males. *Science,* 276**,** 1555-8.

FERVEUR, J. F., STÖRTKUHL, K. F., STOCKER, R. F. & GREENSPAN, R. J. 1995. Genetic feminization of brain structures and changed sexual orientation in male Drosophila. *Science,* 267**,** 902-5.

FINET, C., SLAVIK, K., PU, J., CARROLL, S. B. & CHUNG, H. 2019. Birth-and-Death Evolution of the Fatty Acyl-CoA Reductase (FAR) Gene Family and Diversification of Cuticular Hydrocarbon Synthesis in Drosophila. *Genome Biology and Evolution,* 11**,** 1541-1551.

FURSE, S., EGMOND, M. R. & KILLIAN, J. A. 2015. Isolation of lipids from biological samples. *Molecular Membrane Biology,* 32**,** 55-64.

GALPERIN, M. Y. & KOONIN, E. V. 2012. Divergence and Convergence in Enzyme Evolution. *Journal of Biological Chemistry,* 287**,** 21-28.

GAO, J., LIU, C., ZHANG, S., TECHER, M. P., BOUABBACHE, S., POURADIER, F. & PANHARD, S. 2019. Revisiting, in vivo, the hair regreasing process by the Sebuprint method. *Skin Research and Technology,* 25**,** 79-87.

GEMS, D. & PARTRIDGE, L. 2013. Genetics of longevity in model organisms: debates and paradigm shifts. *Annu Rev Physiol,* 75**,** 621-44.

GENNSER, G., RYMARK, P. & ISBERG, P. E. 1988. Low birth weight and risk of high blood pressure in adulthood. *British medical journal (Clinical research ed.),* 296**,** 1498-1500.

GIBBS, A. G. 2002. Lipid melting and cuticular permeability: new insights into an old problem. *J Insect Physiol,* 48**,** 391-400.

GIBBS, A. G., FUKUZATO, F. & MATZKIN, L. M. 2003. Evolution of water conservation mechanisms in Drosophila. *Journal of Experimental Biology,* 206**,** 1183-1192.

GIBBS, A. G., LOUIE, A. K. & AYALA, J. A. 1998. Effects of temperature on cuticular lipids and water balance in a desert Drosophila: is thermal acclimation beneficial? *J Exp Biol,* 201**,** 71-80.

GIL-DE-LA-FUENTE, A., GODZIEN, J., SAUGAR, S., GARCIA-CARMONA, R., BADRAN, H., WISHART, D. S., BARBAS, C. & OTERO, A. 2019. CEU Mass Mediator 3.0: A Metabolite Annotation Tool. *Journal of Proteome Research,* 18**,** 797-802.

GILES, K., WILDGOOSE, J. L., LANGRIDGE, D. J. & CAMPUZANO, I. 2010. A method for direct measurement of ion mobilities using a travelling wave ion guide. *International Journal of Mass Spectrometry,* 298**,** 10-16.

GLUCKMAN, P. D., BUKLIJAS, T. & HANSON, M. A. 2016. Chapter 1 - The Developmental Origins of Health and Disease (DOHaD) Concept: Past, Present, and Future. *In:* ROSENFELD, C. S. (ed.) *The Epigenome and Developmental Origins of Health and Disease.* Boston: Academic Press.

GODFREY, K. M., SHEPPARD, A., GLUCKMAN, P. D., LILLYCROP, K. A., BURDGE, G. C., MCLEAN, C., RODFORD, J., SLATER-JEFFERIES, J. L., GARRATT, E., CROZIER, S. R., EMERALD, B. S., GALE, C. R., INSKIP, H. M., COOPER, C. & HANSON, M. A. 2011. Epigenetic gene promoter methylation at birth is associated with child's later adiposity. *Diabetes,* 60**,** 1528-34.

GOHLKE, R. S. 1959. Time-of-Flight Mass Spectrometry and Gas-Liquid Partition Chromatography. *Analytical Chemistry,* 31**,** 535-541.

GOHLKE, R. S. & MCLAFFERTY, F. W. 1993. Early gas chromatography/mass spectrometry. *Journal of the American Society for Mass Spectrometry,* 4**,** 367-371.

GRATZ, S. J., CUMMINGS, A. M., NGUYEN, J. N., HAMM, D. C., DONOHUE, L. K., HARRISON, M. M., WILDONGER, J. & O'CONNOR-GILES, K. M. 2013. Genome Engineering of *Drosophila*with the CRISPR RNA-Guided Cas9 Nuclease. *Genetics,* 194**,** 1029-1035.

GREEN, F. M., SALTER, T. L., GILMORE, I. S., STOKES, P. & O'CONNOR, G. 2010. The effect of electrospray solvent composition on desorption electrospray ionisation (DESI) efficiency and spatial resolution. *Analyst,* 135**,** 731-737.

GRONNIER, J., GERMAIN, V., GOUGUET, P., CACAS, J. L. & MONGRAND, S. 2016. GIPC: Glycosyl Inositol Phospho Ceramides, the major sphingolipids on earth. *Plant Signal Behav,* 11**,** e1152438.

GUERRERO-BOSAGNA, C., SETTLES, M., LUCKER, B. & SKINNER, M. K. 2010. Epigenetic Transgenerational Actions of Vinclozolin on Promoter Regions of the Sperm Epigenome. *PLOS ONE,* 5**,** e13100.

GUIOCHON, G. & GUILLEMIN, C. L. 1990. Gas chromatography. *Review of Scientific Instruments,* 61**,** 3317-3339.

GUIRAUDIE-CAPRAZ, G., PHO, D. B. & JALLON, J.-M. 2007. Role of the ejaculatory bulb in biosynthesis of the male pheromone cis-vaccenyl acetate in Drosophila melanogaster. *Integrative Zoology,* 2**,** 89-99.

GUTIERREZ, E., WIGGINS, D., FIELDING, B. & GOULD, A. P. 2007. Specialized hepatocyte-like cells regulate Drosophila lipid metabolism. *Nature,* 445**,** 275-280.

GUZMÁN-QUEVEDO, O., DA SILVA ARAGÃO, R., PÉREZ GARCÍA, G., MATOS, R. J. B., DE SA BRAGA OLIVEIRA, A., DE CASTRO, R. M. & BOLAÑOS-JIMÉNEZ, F. 2013. Impaired Hypothalamic mTOR Activation in the Adult Rat Offspring Born to Mothers Fed a Low-Protein Diet. *PLOS ONE,* 8**,** e74990.

HA, T. S. & SMITH, D. P. 2006. A pheromone receptor mediates 11-cis-vaccenyl acetate-induced responses in Drosophila. *J Neurosci,* 26**,** 8727-33.

HADLEY, N. F. 1989. Lipid water barriers in biological systems. *Progress in Lipid Research,* 28**,** 1-33.

HAHN, O., DREWS, L. F., NGUYEN, A., TATSUTA, T., GKIONI, L., HENDRICH, O., ZHANG, Q., LANGER, T., PLETCHER, S., WAKELAM, M. J. O., BEYER, A., GRÖNKE, S. & PARTRIDGE, L. 2019. A nutritional memory effect counteracts the benefits of dietary restriction in old mice. *Nature Metabolism,* 1**,** 1059-1073.

HALES, C. N. & BARKER, D. J. P. 1992. Type 2 (non-insulin-dependent) diabetes mellitus: the thrifty phenotype hypothesis. *Diabetologia,* 35**,** 595-601.

HAMID, A. M., IBRAHIM, Y. M., GARIMELLA, S. V. B., WEBB, I. K., DENG, L., CHEN, T.-C., ANDERSON, G. A., PROST, S. A., NORHEIM, R. V., TOLMACHEV, A. V. & SMITH, R. D. 2015. Characterization of Traveling Wave Ion Mobility Separations in Structures for Lossless Ion Manipulations. *Analytical chemistry,* 87**,** 11301-11308.

HENG, A. H. S. & CHEW, F. T. 2020. Systematic review of the epidemiology of acne vulgaris. *Scientific Reports,* 10**,** 5754.

HITES, R. A. 2016. Development of Gas Chromatographic Mass Spectrometry. *Analytical Chemistry,* 88**,** 6955-6961.

HO, C. S., LAM, C. W. K., CHAN, M. H. M., CHEUNG, R. C. K., LAW, L. K., LIT, L. C. W., NG, K. F., SUEN, M. W. M. & TAI, H. L. 2003. Electrospray ionisation mass spectrometry: principles and clinical applications. *The Clinical biochemist. Reviews,* 24**,** 3-12.

HOLZE, H., SCHRADER, L. & BUELLESBACH, J. 2021. Advances in deciphering the genetic basis of insect cuticular hydrocarbon biosynthesis and variation. *Heredity,* 126**,** 219-234.

HU, Q., NOLL, R. J., LI, H., MAKAROV, A., HARDMAN, M. & GRAHAM COOKS, R. 2005. The Orbitrap: a new mass spectrometer. *J Mass Spectrom,* 40**,** 430-43.

HUANG, E. C., WACHS, T., CONBOY, J. J. & HENION, J. D. 1990. Atmospheric pressure ionization mass spectrometry. *Analytical Chemistry,* 62**,** 713A-725A.

HUANG, K., CHEN, W., ZHU, F., LI, P. W.-L., KAPAHI, P. & BAI, H. 2019. RiboTag translatomic profiling of Drosophila oenocytes under aging and induced oxidative stress. *BMC Genomics,* 20**,** 50.

HYMES, J. & WOLF, B. 1999. Human Biotinidase Isn't Just for Recycling Biotin. *The Journal of Nutrition,* 129**,** 485S-489S.

IBÁÑEZ, L. & DE ZEGHER, F. 2006. Puberty and prenatal growth. *Molecular and Cellular Endocrinology,* 254-255**,** 22-25.

JAJOO, A., MEKALA, N. R., TOMAR, R. S., GRIECO, M., TIKKANEN, M. & ARO, E.-M. 2014. Inhibitory effects of polycyclic aromatic hydrocarbons (PAHs) on photosynthetic performance are not related to their aromaticity. *Journal of Photochemistry and Photobiology B: Biology,* 137**,** 151-155.

JAMES, A. T. & MARTIN, A. J. P. 1954. Gas-Liquid Chromatography: A Technique for the Analysis and Identification of Volatile Materials. *Brit. med. Bull.,* 10**,** 170-176.

JASKOLLA, T. W., KARAS, M., ROTH, U., STEINERT, K., MENZEL, C. & REIHS, K. 2009. Comparison between vacuum sublimed matrices and conventional dried droplet preparation in MALDI-TOF mass spectrometry. *Journal of the American Society for Mass Spectrometry,* 20**,** 1104-1114.

JASKOLLA, T. W., LEHMANN, W.-D. & KARAS, M. 2008. 4-Chloro-α-cyanocinnamic acid is an advanced, rationally designed MALDI matrix. *Proceedings of the National Academy of Sciences,* 105**,** 12200-12205.

JASTI, J., FURUKAWA, H., GONZALES, E. B. & GOUAUX, E. 2007. Structure of acid-sensing ion channel 1 at 1.9 A resolution and low pH. *Nature,* 449**,** 316-23.

JASZCZAK, J. S. & HALME, A. 2016. Arrested development: coordinating regeneration with development and growth in Drosophila melanogaster. *Current Opinion in Genetics & Development,* 40**,** 87-94.

JENNEMANN, R., RABIONET, M., GORGAS, K., EPSTEIN, S., DALPKE, A., ROTHERMEL, U., BAYERLE, A., VAN DER HOEVEN, F., IMGRUND, S., KIRSCH, J., NICKEL, W., WILLECKE, K., RIEZMAN, H., GRÖNE, H.-J. & SANDHOFF, R. 2011. Loss of ceramide synthase 3 causes lethal skin barrier disruption. *Human Molecular Genetics,* 21**,** 586-608.

JOHNSON, M. B. & BUTTERWORTH, F. M. 1985. Maturation and aging of adult fat body and oenocytes in Drosophila as revealed by light microscopic morphometry. *J Morphol,* 184**,** 51-9.

JUMP, D. B. 2009. Mammalian fatty acid elongases. *Methods in molecular biology (Clifton, N.J.),* 579**,** 375-389.

KAFKAFI, U. & GANMORE - NEUMANN, R. 1997. Ammonium in plant tissue: Real or artifact? *Journal of Plant Nutrition,* 20**,** 107-118.

KAFTAN, F., VRKOSLAV, V., KYNAST, P., KULKARNI, P., BÖCKER, S., CVAČKA, J., KNADEN, M. & SVATOŠ, A. 2014. Mass spectrometry imaging of surface lipids on intact Drosophila melanogaster flies. *Journal of Mass Spectrometry,* 49**,** 223-232.

KAPAHI, P., CHEN, D., ROGERS, A. N., KATEWA, S. D., LI, P. W.-L., THOMAS, E. L. & KOCKEL, L. 2010. With TOR, Less Is More: A Key Role for the Conserved Nutrient-Sensing TOR Pathway in Aging. *Cell Metabolism,* 11**,** 453-465.

KEENAN, M. R. & KOTULA, P. G. 2004. Accounting for Poisson noise in the multivariate analysis of ToF-SIMS spectrum images. *Surface and Interface Analysis,* 36**,** 203-212.

KENNERDELL, J. R. & CARTHEW, R. W. 2000. Heritable gene silencing in Drosophila using double-stranded RNA. *Nature Biotechnology,* 18**,** 896-898.

KERMACK, W., MCKENDRICK, A. & MCKINLAY, P. 2001. Death-rates in Great Britain and Sweden. Some general regularities and their significance*. *International Journal of Epidemiology,* 30**,** 678-683.

KIM, S. K. & KARADENIZ, F. 2012. Biological importance and applications of squalene and squalane. *Adv Food Nutr Res,* 65**,** 223-33.

KIND, T. & FIEHN, O. 2006. Metabolomic database annotations via query of elemental compositions: mass accuracy is insufficient even at less than 1 ppm. *BMC bioinformatics,* 7**,** 234-234.

KOHL, J., HUOVIALA, P. & JEFFERIS, G. S. 2015. Pheromone processing in Drosophila. *Current opinion in neurobiology,* 34**,** 149-157.

KOMPAUER, M., HEILES, S. & SPENGLER, B. 2017. Atmospheric pressure MALDI mass spectrometry imaging of tissues and cells at 1.4-μm lateral resolution. *Nature Methods,* 14**,** 90-96.

KOTOWSKA, A. M., TRINDADE, G. F., MENDES, P. M., WILLIAMS, P. M., AYLOTT, J. W., SHARD, A. G., ALEXANDER, M. R. & SCURR, D. J. 2020. Protein identification by 3D OrbiSIMS to facilitate in situ imaging and depth profiling. *Nature Communications,* 11**,** 5832.

KÜHNLEIN, R. P. 2012. Thematic review series: Lipid droplet synthesis and metabolism: from yeast to man. Lipid droplet-based storage fat metabolism in Drosophila. *Journal of lipid research,* 53**,** 1430-1436.

KURSU, V. A., PIETIKÄINEN, L. P., FONTANESI, F., AALTONEN, M. J., SUOMI, F., RAGHAVAN NAIR, R., SCHONAUER, M. S., DIECKMANN, C. L., BARRIENTOS, A., HILTUNEN, J. K. & KASTANIOTIS, A. J. 2013. Defects in mitochondrial fatty acid synthesis result in failure of multiple aspects of mitochondrial biogenesis in Saccharomyces cerevisiae. *Mol Microbiol,* 90**,** 824-40.

LAGARDE, M., GÉLOËN, A., RECORD, M., VANCE, D. & SPENER, F. 2003. Lipidomics is emerging. *Biochimica et Biophysica Acta (BBA) - Molecular and Cell Biology of Lipids,* 1634**,** 61.

LAKOWSKI, B. & HEKIMI, S. 1998. The genetics of caloric restriction in *Caenorhabditis elegans*. *Proceedings of the National Academy of Sciences,* 95**,** 13091-13096.

LANGAN, S. M., IRVINE, A. D. & WEIDINGER, S. 2020. Atopic dermatitis. *The Lancet,* 396**,** 345-360.

LANGLEY, S. C. & JACKSON, A. A. 1994. Increased systolic blood pressure in adult rats induced by fetal exposure to maternal low protein diets. *Clin Sci (Lond),* 86**,** 217-22; discussion 121.

LAPLANTE, M. & SABATINI, D. M. 2013. Regulation of mTORC1 and its impact on gene expression at a glance. *J Cell Sci,* 126**,** 1713-9.

LARSSON, M. C., DOMINGOS, A. I., JONES, W. D., CHIAPPE, M. E., AMREIN, H. & VOSSHALL, L. B. 2004. Or83b encodes a broadly expressed odorant receptor essential for Drosophila olfaction. *Neuron,* 43**,** 703-14.

LAZZARO, B. P., FLORES, H. A., LORIGAN, J. G. & YOURTH, C. P. 2008. Genotype-by-Environment Interactions and Adaptation to Local Temperature Affect Immunity and Fecundity in Drosophila melanogaster. *PLOS Pathogens,* 4**,** e1000025.

LEE, B. Y., HOGAN, D. J., URSINE, S., YANAMANDRA, K. & BOCCHINI, J. A. 2006. Personal observation of skin disorders in malnutrition. *Clinics in Dermatology,* 24**,** 222-227.

LEE, J. L., GILMORE, I. S., SEAH, M. P. & FLETCHER, I. W. 2011. Topography and field effects in secondary ion mass spectrometry--part I: conducting samples. *J Am Soc Mass Spectrom,* 22**,** 1718-28.

LEE, J. L. S., GILMORE, I. S., SEAH, M. P., LEVICK, A. P. & SHARD, A. G. 2012. Topography and field effects in secondary ion mass spectrometry Part II: insulating samples. *Surface and Interface Analysis,* 44**,** 238-245.

LETUNIC, I. & BORK, P. 2007. Interactive Tree Of Life (iTOL): an online tool for phylogenetic tree display and annotation. *Bioinformatics,* 23**,** 127-8.

LI, B. & DEWEY, C. N. 2011. RSEM: accurate transcript quantification from RNA-Seq data with or without a reference genome. *BMC Bioinformatics,* 12**,** 323.

LI, W., SANDHOFF, R., KONO, M., ZERFAS, P., HOFFMANN, V., DING, B. C., PROIA, R. L. & DENG, C. X. 2007. Depletion of ceramides with very long chain fatty acids causes defective skin permeability barrier function, and neonatal lethality in ELOVL4 deficient mice. *Int J Biol Sci,* 3**,** 120-8.

LILLYCROP, K. A., PHILLIPS, E. S., JACKSON, A. A., HANSON, M. A. & BURDGE, G. C. 2005. Dietary protein restriction of pregnant rats induces and folic acid supplementation prevents epigenetic modification of hepatic gene expression in the offspring. *J Nutr,* 135**,** 1382-6.

LIN, C. C., PROKOP-PRIGGE, K. A., PRETI, G. & POTTER, C. J. 2015. Food odors trigger Drosophila males to deposit a pheromone that guides aggregation and female oviposition decisions. *Elife,* 4.

LIN, S.-J., DEFOSSEZ, P.-A. & GUARENTE, L. 2000. Requirement of NAD and *SIR2* for Life-Span Extension by Calorie Restriction in *Saccharomyces cerevisiae*. *Science,* 289**,** 2126-2128.

LIU, T., WANG, Y., TIAN, Y., ZHANG, J., ZHAO, J. & GUO, A. 2020. The receptor channel formed by ppk25, ppk29 and ppk23 can sense the Drosophila female pheromone 7,11-heptacosadiene. *Genes Brain Behav,* 19**,** e12529.

LOVE, M. I., HUBER, W. & ANDERS, S. 2014. Moderated estimation of fold change and dispersion for RNA-seq data with DESeq2. *Genome Biology,* 15**,** 550.

LUEBKE, R. W., CHEN, D. H., DIETERT, R., YANG, Y., KING, M. & LUSTER, M. I. 2006. The Comparative Immunotoxicity of Five Selected Compounds Following Developmental or Adult Exposure. *Journal of Toxicology and Environmental Health, Part B,* 9**,** 1-26.

LUNDE, E. R., WASHBURN, S. E., GOLDING, M. C., BAKE, S., MIRANDA, R. C. & RAMADOSS, J. 2016. Alcohol-Induced Developmental Origins of Adult-Onset Diseases. *Alcohol Clin Exp Res,* 40**,** 1403-14.

LUNG, S.-C. C. & LIU, C.-H. 2015. Fast analysis of 29 polycyclic aromatic hydrocarbons (PAHs) and nitro-PAHs with ultra-high performance liquid chromatography-atmospheric pressure photoionization-tandem mass spectrometry. *Scientific reports,* 5**,** 12992-12992.

LUQUE, P., BRUQUE, S. & HEREDIA, A. 1995. Water permeability of isolated cuticular membranes: a structural analysis. *Arch Biochem Biophys,* 317**,** 417-22.

MACHA, S. F., LIMBACH, P. A. & SAVICKAS, P. J. 2000. Application of nonpolar matrices for the analysis of low molecular weight nonpolar synthetic polymers by matrix-assisted laser desorption/ionization time-of-flight mass spectrometry. *Journal of the American Society for Mass Spectrometry,* 11**,** 731-737.

MACHIN, J. 1980. Cuticle water relations: Towards a new cuticle waterproofing model. *In:* LOCKE, M. & SMITH, D. S. (eds.) *Insect Biology in the Future.* Academic Press.

MADHAVAN, M. M. & MADHAVAN, K. 1980. Morphogenesis of the epidermis of adult abdomen of Drosophila. *J Embryol Exp Morphol,* 60**,** 1-31.

MAIR, W., GOYMER, P., PLETCHER, S. D. & PARTRIDGE, L. 2003. Demography of dietary restriction and death in Drosophila. *Science,* 301**,** 1731-3.

MAKAROV, A. 2000. Electrostatic Axially Harmonic Orbital Trapping: A High-Performance Technique of Mass Analysis. *Analytical Chemistry,* 72**,** 1156-1162.

MAKKI, R., CINNAMON, E. & GOULD, A. P. 2014. The Development and Functions of Oenocytes. *Annual Review of Entomology,* 59**,** 405-425.

MARTIN, M. 2011. Cutadapt removes adapter sequences from high-throughput sequencing reads. *2011,* 17**,** 3.

MAURES, T. J., BOOTH, L. N., BENAYOUN, B. A., IZRAYELIT, Y., SCHROEDER, F. C. & BRUNET, A. 2014. Males shorten the life span of C. elegans hermaphrodites via secreted compounds. *Science,* 343**,** 541-4.

MCCANCE, R. A. & WIDDOWSON, E. M. 1974. The determinants of growth and form. *Proceedings of the Royal Society of London. Series B. Biological Sciences,* 185**,** 1-17.

MCGUIRE, S. E., MAO, Z. & DAVIS, R. L. 2004. Spatiotemporal gene expression targeting with the TARGET and gene-switch systems in Drosophila. *Sci STKE,* 2004**,** pl6.

MILLER, R. A., BUEHNER, G., CHANG, Y., HARPER, J. M., SIGLER, R. & SMITH-WHEELOCK, M. 2005. Methionine-deficient diet extends mouse lifespan, slows immune and lens aging, alters glucose, T4, IGF-I and insulin levels, and increases hepatocyte MIF levels and stress resistance. *Aging Cell,* 4**,** 119-125.

MIYAZAKI, M., DOBRZYN, A., ELIAS, P. M. & NTAMBI, J. M. 2005. Stearoyl-CoA desaturase-2 gene expression is required for lipid synthesis during early skin and liver development. *Proc Natl Acad Sci U S A,* 102**,** 12501-6.

MOORE, S. E. 2017. Early-Life Nutritional Programming of Health and Disease in The Gambia. *Annals of Nutrition and Metabolism,* 70**,** 179-183.

MUELLER, J. M., ZHANG, N., CARLSON, J. M. & SIMPSON, J. H. 2020. Variation and variability in *Drosophila* grooming behavior. *bioRxiv***,** 2020.08.15.252627.

MUKHERJEE, S., STAMATIS, D., BERTSCH, J., OVCHINNIKOVA, G., SUNDARAMURTHI, JAGADISH C., LEE, J., KANDIMALLA, M., CHEN, I.-M. A., KYRPIDES, N. C. & REDDY, T. B. K. 2020. Genomes OnLine Database (GOLD) v.8: overview and updates. *Nucleic Acids Research,* 49**,** D723-D733.

NASR, A. N. 1967. Histochemically demonstrable lipids in human eccrine and apocrine sweat glands. *Journal of the Royal Microscopical Society,* 86**,** 427-432.

NELLIOT, A., BOND, N. & HOSHIZAKI, D. K. 2006. Fat-body remodeling in Drosophila melanogaster. *Genesis,* 44**,** 396-400.

NEWELL, C. L., VORNG, J.-L., MACRAE, J. I., GILMORE, I. S. & GOULD, A. P. 2020. Cryogenic OrbiSIMS Localizes Semi-Volatile Molecules in Biological Tissues. *Angewandte Chemie International Edition,* 59**,** 18194-18200.

NG, S. F., LIN, R. C., LAYBUTT, D. R., BARRES, R., OWENS, J. A. & MORRIS, M. J. 2010. Chronic high-fat diet in fathers programs β-cell dysfunction in female rat offspring. *Nature,* 467**,** 963-6.

NICHOLAS, L. M. & OZANNE, S. E. 2019. Early life programming in mice by maternal overnutrition: mechanistic insights and interventional approaches. *Philosophical Transactions of the Royal Society B: Biological Sciences,* 374**,** 20180116.

NORDBY, H. E. & NAGY, S. 1977. Hydrocarbons from epicuticular waxes of Citrus peels. *Phytochemistry,* 16**,** 1393-1397.

NOWELL, C. & RADTKE, F. 2013. Cutaneous Notch signaling in health and disease. *Cold Spring Harb Perspect Med,* 3**,** a017772.

O'NEILL, L. A. J. & HARDIE, D. G. 2013. Metabolism of inflammation limited by AMPK and pseudo-starvation. *Nature,* 493**,** 346-355.

OBATA, F., FONS, C. O. & GOULD, A. P. 2018. Early-life exposure to low-dose oxidants can increase longevity via microbiome remodelling in Drosophila. *Nature Communications,* 9**,** 975.

ONG, C., YUNG, L.-Y. L., CAI, Y., BAY, B.-H. & BAEG, G.-H. 2015. Drosophila melanogaster as a model organism to study nanotoxicity. *Nanotoxicology,* 9**,** 396-403.

OZANNE, S. E. & HALES, C. N. 2004. Catch-up growth and obesity in male mice. *Nature,* 427**,** 411-412.

PALANKER, L., TENNESSEN, J. M., LAM, G. & THUMMEL, C. S. 2009. Drosophila HNF4 regulates lipid mobilization and beta-oxidation. *Cell Metab,* 9**,** 228-39.

PANEVSKA, A., SKOČAJ, M., KRIŽAJ, I., MAČEK, P. & SEPČIĆ, K. 2019. Ceramide phosphoethanolamine, an enigmatic cellular membrane sphingolipid. *Biochimica et Biophysica Acta (BBA) - Biomembranes,* 1861**,** 1284-1292.

PAPPAS, A. 2009. Epidermal surface lipids. *Dermato-endocrinology,* 1**,** 72-76.

PARRA-PERALBO, E. & CULI, J. 2011. Drosophila Lipophorin Receptors Mediate the Uptake of Neutral Lipids in Oocytes and Imaginal Disc Cells by an Endocytosis-Independent Mechanism. *PLOS Genetics,* 7**,** e1001297.

PARTRIDGE, L., DEELEN, J. & SLAGBOOM, P. E. 2018. Facing up to the global challenges of ageing. *Nature,* 561**,** 45-56.

PARTRIDGE, L., PIPER, M. D. & MAIR, W. 2005. Dietary restriction in Drosophila. *Mech Ageing Dev,* 126**,** 938-50.

PARVY, J. P., NAPAL, L., RUBIN, T., POIDEVIN, M., PERRIN, L., WICKER-THOMAS, C. & MONTAGNE, J. 2012. Drosophila melanogaster Acetyl-CoA-carboxylase sustains a fatty acid-dependent remote signal to waterproof the respiratory system. *PLoS Genet,* 8**,** e1002925.

PASSARELLI, M. K., PIRKL, A., MOELLERS, R., GRINFELD, D., KOLLMER, F., HAVELUND, R., NEWMAN, C. F., MARSHALL, P. S., ARLINGHAUS, H., ALEXANDER, M. R., WEST, A., HORNING, S., NIEHUIS, E., MAKAROV, A., DOLLERY, C. T. & GILMORE, I. S. 2017. The 3D OrbiSIMS-label-free metabolic imaging with subcellular lateral resolution and high mass-resolving power. *Nat Methods,* 14**,** 1175-1183.

PATEL, D. & WITT, S. N. 2017. Ethanolamine and Phosphatidylethanolamine: Partners in Health and Disease. *Oxidative Medicine and Cellular Longevity,* 2017**,** 4829180.

PELOSI, P., ZHU, J. & KNOLL, W. 2018. Odorant-Binding Proteins as Sensing Elements for Odour Monitoring. *Sensors (Basel, Switzerland),* 18**,** 3248.

PENKOV, S., OGAWA, A., SCHMIDT, U., TATE, D., ZAGORIY, V., BOLAND, S., GRUNER, M., VORKEL, D., VERBAVATZ, J.-M., SOMMER, R. J., KNÖLKER, H.-J. & KURZCHALIA, T. V. 2014. A wax ester promotes collective host finding in the nematode Pristionchus pacificus. *Nature Chemical Biology,* 10**,** 281-285.

PERRY, W. J., PATTERSON, N. H., PRENTICE, B. M., NEUMANN, E. K., CAPRIOLI, R. M. & SPRAGGINS, J. M. 2020. Uncovering matrix effects on lipid analyses in MALDI imaging mass spectrometry experiments. *Journal of Mass Spectrometry,* 55**,** e4491.

PHAN, N. T. N., MUNEM, M., EWING, A. G. & FLETCHER, J. S. 2017. MS/MS analysis and imaging of lipids across Drosophila brain using secondary ion mass spectrometry. *Analytical and Bioanalytical Chemistry,* 409**,** 3923-3932.

PIETROCOLA, F., GALLUZZI, L., BRAVO-SAN PEDRO, J. M., MADEO, F. & KROEMER, G. 2015. Acetyl coenzyme A: a central metabolite and second messenger. *Cell Metab,* 21**,** 805-21.

PLEIK, S., SPENGLER, B., SCHAFER, T., URBACH, D., LUHN, S. & KIRSCH, D. 2016. Fatty Acid Structure and Degradation Analysis in Fingerprint Residues. *J Am Soc Mass Spectrom,* 27**,** 1565-74.

PLETCHER, S. D., MACDONALD, S. J., MARGUERIE, R., CERTA, U., STEARNS, S. C., GOLDSTEIN, D. B. & PARTRIDGE, L. 2002. Genome-Wide Transcript Profiles in Aging and Calorically Restricted Drosophila melanogaster. *Current Biology,* 12**,** 712-723.

PLIKUS, M. V., BAKER, R. E., CHEN, C. C., FARE, C., DE LA CRUZ, D., ANDL, T., MAINI, P. K., MILLAR, S. E., WIDELITZ, R. & CHUONG, C. M. 2011. Self-organizing and stochastic behaviors during the regeneration of hair stem cells. *Science,* 332**,** 586-9.

PLIKUS, M. V., MAYER, J. A., DE LA CRUZ, D., BAKER, R. E., MAINI, P. K., MAXSON, R. & CHUONG, C.-M. 2008. Cyclic dermal BMP signalling regulates stem cell activation during hair regeneration. *Nature,* 451**,** 340-344.

POLÁNYI, L., NIESSEN, C. M., VOHLEN, C., STINN, J., KRETSCHMER, T., JENTGEN, V., HIRANI, D., KONINGSBRUGGEN-RIETSCHEL, S. V., DÖTSCH, J. & ALEJANDRE ALCAZAR, M. A. 2020. Intrauterine growth restriction induces skin inflammation, increases TSLP and impairs epidermal barrier function. *J Mol Med (Berl),* 98**,** 279-289.

PONGRAC, P., BALTRENAITE, E., VAVPETIČ, P., KELEMEN, M., KLADNIK, A., BUDIČ, B., VOGEL-MIKUŠ, K., REGVAR, M., BALTRENAS, P. & PELICON, P. 2019. Tissue-specific element profiles in Scots pine (Pinus sylvestris L.) needles. *Trees,* 33**,** 91-101.

PORTRAIT, F., TEEUWISZEN, E. & DEEG, D. 2011. Early life undernutrition and chronic diseases at older ages: the effects of the Dutch famine on cardiovascular diseases and diabetes. *Soc Sci Med,* 73**,** 711-8.

QIU, Y., TITTIGER, C., WICKER-THOMAS, C., LE GOFF, G., YOUNG, S., WAJNBERG, E., FRICAUX, T., TAQUET, N., BLOMQUIST, G. J. & FEYEREISEN, R. 2012. An insect-specific P450 oxidative decarbonylase for cuticular hydrocarbon biosynthesis. *Proceedings of the National Academy of Sciences,* 109**,** 14858-14863.

QUEHENBERGER, O., ARMANDO, A. M. & DENNIS, E. A. 2011. High sensitivity quantitative lipidomics analysis of fatty acids in biological samples by gas chromatography-mass spectrometry. *Biochimica et biophysica acta,* 1811**,** 648-656.

R CORE TEAM 2018. R: A language and environment for statistical computing.

RABIONET, M., GORGAS, K. & SANDHOFF, R. 2014. Ceramide synthesis in the epidermis. *Biochim Biophys Acta,* 1841**,** 422-34.

RAJPUROHIT, S., HANUS, R., VRKOSLAV, V., BEHRMAN, E. L., BERGLAND, A. O., PETROV, D., CVAČKA, J. & SCHMIDT, P. S. 2017. Adaptive dynamics of cuticular hydrocarbons in Drosophila. *J Evol Biol,* 30**,** 66-80.

RAJPUROHIT, S., VRKOSLAV, V., HANUS, R., GIBBS, A. G., CVAČKA, J. & SCHMIDT, P. S. 2021. Post-eclosion temperature effects on insect cuticular hydrocarbon profiles. *Ecol Evol,* 11**,** 352-364.

RAO, X., HUANG, X., ZHOU, Z. & LIN, X. 2013. An improvement of the 2ˆ(-delta delta CT) method for quantitative real-time polymerase chain reaction data analysis. *Biostatistics, bioinformatics and biomathematics,* 3**,** 71-85.

RAVELLI, G. P., STEIN, Z. A. & SUSSER, M. W. 1976. Obesity in young men after famine exposure in utero and early infancy. *N Engl J Med,* 295**,** 349-53.

REA, J., NEWHOUSE, M. L. & HALIL, T. 1976. Skin disease in Lambeth. A community study of prevalence and use of medical care. *Journal of Epidemiology & Community Health,* 30**,** 107-114.

REITER, L. T., POTOCKI, L., CHIEN, S., GRIBSKOV, M. & BIER, E. 2001. A systematic analysis of human disease-associated gene sequences in Drosophila melanogaster. *Genome research,* 11**,** 1114-1125.

RIEDL, C. A., OSTER, S., BUSTO, M., MACKAY, T. F. & SOKOLOWSKI, M. B. 2016. Natural variability in Drosophila larval and pupal NaCl tolerance. *J Insect Physiol,* 88**,** 15-23.

ROGERS, J., HARDING, C., MAYO, A., BANKS, J. & RAWLINGS, A. 1996. Stratum corneum lipids: the effect of ageing and the seasons. *Arch Dermatol Res,* 288**,** 765-70.

ROMANOVSKY, A. A. 2014. Skin temperature: its role in thermoregulation. *Acta physiologica (Oxford, England),* 210**,** 498-507.

RUSSO, M. F., WOJCIECHOWSKI, I. A. & GARRISON, B. J. 2006. Sputtering of amorphous ice induced by C60 and Au3 clusters. *Applied Surface Science,* 252**,** 6423-6425.

SABERI, M. & SEYED-ALLAEI, H. 2016. Odorant receptors of Drosophila are sensitive to the molecular volume of odorants. *Scientific Reports,* 6**,** 25103.

SAHAY, M. & SAHAY, R. 2012. Rickets-vitamin D deficiency and dependency. *Indian journal of endocrinology and metabolism,* 16**,** 164-176.

SAMPATH, H. & NTAMBI, J. M. 2014. Role of stearoyl-CoA desaturase-1 in skin integrity and whole body energy balance. *J Biol Chem,* 289**,** 2482-8.

SÁNCHEZ-GRACIA, A., VIEIRA, F. G. & ROZAS, J. 2009. Molecular evolution of the major chemosensory gene families in insects. *Heredity,* 103**,** 208-216.

SATO, K. & YAMAMOTO, D. 2020. Contact-Chemosensory Evolution Underlying Reproductive Isolation in Drosophila Species. *Frontiers in Behavioral Neuroscience,* 14.

SAVARIT, F. & FERVEUR, J. F. 2002. Genetic study of the production of sexually dimorphic cuticular hydrocarbons in relation with the sex-determination gene transformer in Drosophila melanogaster. *Genet Res,* 79**,** 23-40.

SCHNEIDER, M. R., SCHMIDT-ULLRICH, R. & PAUS, R. 2009. The Hair Follicle as a Dynamic Miniorgan. *Current Biology,* 19**,** R132-R142.

SCHURIG, V. 2002. Chiral separations using gas chromatography. *TrAC Trends in Analytical Chemistry,* 21**,** 647-661.

SCOTT, D. 1994. Genetic Variation for Female Mate Discrimination in Drosophila melanogaster. *Evolution,* 48**,** 112-121.

SEEGMILLER, A. C., DOBROSOTSKAYA, I., GOLDSTEIN, J. L., HO, Y. K., BROWN, M. S. & RAWSON, R. B. 2002. The SREBP pathway in Drosophila: regulation by palmitate, not sterols. *Dev Cell,* 2**,** 229-38.

SENONER, M. & UNGER, W. E. S. 2007. Lateral resolution of secondary ion mass spectrometry–results of an inter-laboratory comparison. *Surface and Interface Analysis,* 39**,** 16-25.

SHI, C., RUNNELS, A. M. & MURPHY, C. T. 2017. Mating and male pheromone kill Caenorhabditis males through distinct mechanisms. *Elife,* 6.

SIEK, K., PATRICK, J. S. & BINKLEY, J. 2013. High-Resolution Time-of-Flight Mass Spectrometry for Rapid Petroleum Characterization. *LCGC,* 11**,** 30-37.

SIMÕES-COSTA, M. & BRONNER, M. E. 2013. Insights into neural crest development and evolution from genomic analysis. *Genome Res,* 23**,** 1069-80.

SMITH, C. A. 1947. Effects of maternal undernutrition upon thenewborn infant in Holland (1944–1945). *The Journal of Pediatrics,* 30**,** 229-243.

SMITH, K. R. & THIBOUTOT, D. M. 2008. Thematic review series: Skin Lipids. Sebaceous gland lipids: friend or foe? *Journal of Lipid Research,* 49**,** 271-281.

STAROSTINA, E., LIU, T., VIJAYAN, V., ZHENG, Z., SIWICKI, K. K. & PIKIELNY, C. W. 2012. A *Drosophila* DEG/ENaC Subunit Functions Specifically in Gustatory Neurons Required for Male Courtship Behavior. *The Journal of Neuroscience,* 32**,** 4665-4674.

STEFANA, M. I., DRISCOLL, P. C., OBATA, F., PENGELLY, A. R., NEWELL, C. L., MACRAE, J. I. & GOULD, A. P. 2017. Developmental diet regulates Drosophila lifespan via lipid autotoxins. *Nature Communications,* 8**,** 1384.

STINZIANO, J. R., SOVÉ, R. J., RUNDLE, H. D. & SINCLAIR, B. J. 2015. Rapid desiccation hardening changes the cuticular hydrocarbon profile of Drosophila melanogaster. *Comparative Biochemistry and Physiology Part A: Molecular & Integrative Physiology,* 180**,** 38-42.

STONE, S. J., MYERS, H. M., WATKINS, S. M., BROWN, B. E., FEINGOLD, K. R., ELIAS, P. M. & FARESE, R. V., JR. 2004. Lipopenia and Skin Barrier Abnormalities in DGAT2-deficient Mice *. *Journal of Biological Chemistry,* 279**,** 11767-11776.

STOPKA, S. A., SAMARAH, L. Z., SHAW, J. B., LIYU, A. V., VELIČKOVIĆ, D., AGTUCA, B. J., KUKOLJ, C., KOPPENAAL, D. W., STACEY, G., PAŠA-TOLIĆ, L., ANDERTON, C. R. & VERTES, A. 2019. Ambient Metabolic Profiling and Imaging of Biological Samples with Ultrahigh Molecular Resolution Using Laser Ablation Electrospray Ionization 21 Tesla FTICR Mass Spectrometry. *Anal Chem,* 91**,** 5028-5035.

STORELLI, G., NAM, H. J., SIMCOX, J., VILLANUEVA, C. J. & THUMMEL, C. S. 2019. Drosophila HNF4 Directs a Switch in Lipid Metabolism that Supports the Transition to Adulthood. *Dev Cell,* 48**,** 200-214.e6.

STRAUSS, J. S., KLIGMAN, A. M. & POCHI, P. E. 1962. The Effect of Androgens and Estrogens on Human Sebaceous Glands. *Journal of Investigative Dermatology,* 39**,** 139-155.

SWANSON, L. W. 1983. Liquid metal ion sources: Mechanism and applications. *Nuclear Instruments and Methods in Physics Research,* 218**,** 347-353.

TADA, A., JIN, Z.-L., SUGIMOTO, N., SATO, K., YAMAZAKI, T. & TANAMOTO, K. 2005. Analysis of the Constituents in Jojoba Wax Used as a Food Additive by LC/MS/MS. *Food Hygiene and Safety Science (Shokuhin Eiseigaku Zasshi),* 46**,** 198-204.

TAKEMURA, T., WERTZ, P. W. & SATO, K. 1989. Free fatty acids and sterols in human eccrine sweat. *British Journal of Dermatology,* 120**,** 43-47.

TARRY-ADKINS, J. L. & OZANNE, S. E. 2017. Nutrition in early life and age-associated diseases. *Ageing Res Rev,* 39**,** 96-105.

THISTLE, R., CAMERON, P., GHORAYSHI, A., DENNISON, L. & SCOTT, K. 2012. Contact chemoreceptors mediate male-male repulsion and male-female attraction during Drosophila courtship. *Cell,* 149**,** 1140-1151.

THURMOND, J., GOODMAN, J. L., STRELETS, V. B., ATTRILL, H., GRAMATES, L S., MARYGOLD, S. J., MATTHEWS, B. B., MILLBURN, G., ANTONAZZO, G., TROVISCO, V., KAUFMAN, T. C., CALVI, B. R. & CONSORTIUM, T. F. 2018. FlyBase 2.0: the next generation. *Nucleic Acids Research,* 47**,** D759-D765.

TIAN, H., SPARVERO, L. J., AMOSCATO, A. A., BLOOM, A., BAYIR, H., KAGAN, V. E. & WINOGRAD, N. 2017. Gas Cluster Ion Beam Time-of-Flight Secondary Ion Mass Spectrometry High-Resolution Imaging of Cardiolipin Speciation in the Brain: Identification of Molecular Losses after Traumatic Injury. *Anal Chem,* 89**,** 4611-4619.

TILLNER, J., WU, V., JONES, E. A., PRINGLE, S. D., KARANCSI, T., DANNHORN, A., VESELKOV, K., MCKENZIE, J. S. & TAKATS, Z. 2017. Faster, More Reproducible DESI-MS for Biological Tissue Imaging. *Journal of The American Society for Mass Spectrometry,* 28**,** 2090-2098.

TODD, S. E., OLIVER, M. H., JAQUIERY, A. L., BLOOMFIELD, F. H. & HARDING, J. E. 2009. Periconceptional Undernutrition of Ewes Impairs Glucose Tolerance in Their Adult Offspring. *Pediatric Research,* 65**,** 409-413.

TOMIYAMA, T., KURIHARA, K., OGAWA, T., MARUTA, T., OGAWA, T., OHTA, D., SAWA, Y. & ISHIKAWA, T. 2017. Wax Ester Synthase/Diacylglycerol Acyltransferase Isoenzymes Play a Pivotal Role in Wax Ester Biosynthesis in Euglena gracilis. *Scientific Reports,* 7**,** 13504.

TOYODA, N. & YAMADA, I. 2008. Gas Cluster Ion Beam Equipment and Applications for Surface Processing. *IEEE Transactions on Plasma Science,* 36**,** 1471-1488.

TRIVEDI, D. K., SINCLAIR, E., XU, Y., SARKAR, D., WALTON-DOYLE, C., LISCIO, C., BANKS, P., MILNE, J., SILVERDALE, M., KUNATH, T., GOODACRE, R. & BARRAN, P. 2019. Discovery of Volatile Biomarkers of Parkinson's Disease from Sebum. *ACS Cent Sci,* 5**,** 599-606.

TSWETT, M. S. 1905. О новой категории адсорбционных явлений и о применении их к биохимическому анализу (On a new catagory of adsorption phenomena and on its application to biochemical analysis). *Proceedings of the Warsaw Society of Naturalists,* 14**,** 20-39.

TSYBIN, Y. O., NAGORNOV, K. O. & KOZHINOV, A. N. 2019. Chapter 5 - Advanced fundamentals in Fourier transform mass spectrometry. *In:* KANAWATI, B. & SCHMITT-KOPPLIN, P. (eds.) *Fundamentals and Applications of Fourier Transform Mass Spectrometry.* Elsevier.

VICKERMAN, J. C. 2009. Molecular Surface Mass Spectrometry by SIMS. *Surface Analysis – The Principal Techniques.*

VICKERMAN, J. C. 2011. Molecular imaging and depth profiling by mass spectrometry—SIMS, MALDI or DESI? *Analyst,* 136**,** 2199-2217.

VICKERMAN, J. C. & BRIGGS, D. 2013. *ToF-SIMS: Surface Analysis by Mass Spectrometry*.

VICKERS, M. H., BREIER, B. H., CUTFIELD, W. S., HOFMAN, P. L. & GLUCKMAN, P. D. 2000. Fetal origins of hyperphagia, obesity, and hypertension and postnatal amplification by hypercaloric nutrition. *Am J Physiol Endocrinol Metab,* 279**,** E83-7.

VICKERS, M. H., GLUCKMAN, P. D., COVENY, A. H., HOFMAN, P. L., CUTFIELD, W. S., GERTLER, A., BREIER, B. H. & HARRIS, M. 2005. Neonatal leptin treatment reverses developmental programming. *Endocrinology,* 146**,** 4211-6.

VIEIRA, F. G., SÁNCHEZ-GRACIA, A. & ROZAS, J. 2007. Comparative genomic analysis of the odorant-binding protein family in 12 Drosophila genomes: purifying selection and birth-and-death evolution. *Genome Biology,* 8**,** R235.

WALSH, K., MCCORMACK, C. A., WEBSTER, R., PINTO, A., LEE, S., FENG, T., KRAKOVSKY, H. S., O'GRADY, S. M., TYCKO, B., CHAMPAGNE, F. A., WERNER, E. A., LIU, G. & MONK, C. 2019. Maternal prenatal stress phenotypes associate with fetal neurodevelopment and birth outcomes. *Proceedings of the National Academy of Sciences,* 116**,** 23996-24005.

WANG, L., HAN, X., MEHREN, J., HIROI, M., BILLETER, J.-C., MIYAMOTO, T., AMREIN, H., LEVINE, J. D. & ANDERSON, D. J. 2011. Hierarchical chemosensory regulation of male-male social interactions in Drosophila. *Nature neuroscience,* 14**,** 757-762.

WANG, Z., CAI, Y., WANG, Y., ZHOU, X., ZHANG, Y. & LU, H. 2017. Improved MALDI imaging MS analysis of phospholipids using graphene oxide as new matrix. *Scientific Reports,* 7**,** 44466.

WATKINS, A. J., WILKINS, A., CUNNINGHAM, C., PERRY, V. H., SEET, M. J., OSMOND, C., ECKERT, J. J., TORRENS, C., CAGAMPANG, F. R., CLEAL, J., GRAY, W. P., HANSON, M. A. & FLEMING, T. P. 2008. Low protein diet fed exclusively during mouse oocyte maturation leads to behavioural and cardiovascular abnormalities in offspring. *J Physiol,* 586**,** 2231-44.

WENK, M. R. 2005. The emerging field of lipidomics. *Nature Reviews Drug Discovery,* 4**,** 594-610.

WERHMEISTER, F. C., NUNES, B. P., LORET DE MOLA, C., GÓMEZ-COFRÉ, N., DE OLIVEIRA, P. D., MARCO, P. L., ASSUNÇÃO, M. C. F., GONÇALVES, H., HORTA, B. L. & MENEZES, A. M. B. 2015. Intrauterine exposure to smoking and wheezing in adolescence: the 1993 Pelotas Birth Cohort. *Journal of Developmental Origins of Health and Disease,* 6**,** 217-224.

WICKER-THOMAS, C. & CHERTEMPS, T. 2010. *Molecular biology and genetics of hydrocarbon production,* Cambridge, Cambridge University Press.

WICKER-THOMAS, C., GARRIDO, D., BONTONOU, G., NAPAL, L., MAZURAS, N., DENIS, B., RUBIN, T., PARVY, J.-P. & MONTAGNE, J. 2015. Flexible origin of hydrocarbon/pheromone precursors in Drosophila melanogaster. *Journal of lipid research,* 56**,** 2094-2101.

WICKS, NADINE L., CHAN, JASON W., NAJERA, JULIA A., CIRIELLO, JONATHAN M. & OANCEA, E. 2011. UVA Phototransduction Drives Early Melanin Synthesis in Human Melanocytes. *Current Biology,* 21**,** 1906-1911.

WILKINSON, D. I. & KARASEK, M. A. 1966. Skin Lipids of a Normal and a Mutant (Asebic) Mouse Strain*. *Journal of Investigative Dermatology,* 47**,** 449-455.

WIMMER, E. A. 2003. Applications of insect transgenesis. *Nature Reviews Genetics,* 4**,** 225-232.

WOODALL, S. M., JOHNSTON, B. M., BREIER, B. H. & GLUCKMAN, P. D. 1996. Chronic maternal undernutrition in the rat leads to delayed postnatal growth and elevated blood pressure of offspring. *Pediatr Res,* 40**,** 438-43.

XU, P., ATKINSON, R., JONES, D. N. & SMITH, D. P. 2005. Drosophila OBP LUSH is required for activity of pheromone-sensitive neurons. *Neuron,* 45**,** 193-200.

YAMADA, I., MATSUO, J., TOYODA, N. & KIRKPATRICK, A. 2001. Materials processing by gas cluster ion beams. *Materials Science and Engineering: R: Reports,* 34**,** 231-295.

YEATS, T. H. & ROSE, J. K. C. 2013. The Formation and Function of Plant Cuticles. *Plant Physiology,* 163**,** 5-20.

YODER, J. H. 2012. Abdominal segment reduction: development and evolution of a deeply fixed trait. *Fly (Austin),* 6**,** 240-5.

YU, G., WANG, L.-G., HAN, Y. & HE, Q.-Y. 2012. clusterProfiler: an R package for comparing biological themes among gene clusters. *Omics : a journal of integrative biology,* 16**,** 284-287.

ZEISLER-DIEHL, V., MÜLLER, Y. & SCHREIBER, L. 2018. Epicuticular wax on leaf cuticles does not establish the transpiration barrier, which is essentially formed by intracuticular wax. *Journal of Plant Physiology,* 227**,** 66-74.

ZHANG, J., DONG, X., CHENG, J., LI, J. & WANG, Y. 2011. Efficient Analysis of Non-Polar Environmental Contaminants by MALDI-TOF MS with Graphene as Matrix. *Journal of the American Society for Mass Spectrometry,* 22**,** 1294-1298.

ZHANG, N., GUO, L. & SIMPSON, J. H. 2020. Spatial Comparisons of Mechanosensory Information Govern the Grooming Sequence in Drosophila. *Curr Biol,* 30**,** 988-1001.e4.

ZIEGLER, A. B., MÉNAGÉ, C., GRÉGOIRE, S., GARCIA, T., FERVEUR, J. F., BRETILLON, L. & GROSJEAN, Y. 2015. Lack of Dietary Polyunsaturated Fatty Acids Causes Synapse Dysfunction in the Drosophila Visual System. *PLoS One,* 10**,** e0135353.

ZONG, L., RAMANATHAN, S. & CHEN, C.-C. 2010. Fragment-Based Approach for Estimating Thermophysical Properties of Fats and Vegetable Oils for Modeling Biodiesel Production Processes. *Industrial & Engineering Chemistry Research,* 49**,** 3022-3023.

ZOUBOULIS, C. C. 2017. Further Evidence of Sebaceous Differentiation Uniqueness: Holocrine Secretion of Sebocytes Is a Multistep, Cell-Specific Lysosomal DNase2-Mediated Mode of Programmed Cell Death. *Journal of Investigative Dermatology,* 137**,** 537-539.

ZOUBOULIS, C. C. & BOSCHNAKOW, A. 2001. Chronological ageing and photoageing of the human sebaceous gland. *Clin Exp Dermatol,* 26**,** 600-7.

ZUBAREV, R. A. & MAKAROV, A. 2013. Orbitrap Mass Spectrometry. *Analytical Chemistry,* 85**,** 5288-5296.

Supplementary material for:

Mass Spectrometry and Genetic Analysis of Biological Barrier Lipids

Clare Laura Louise Newell

University College London

and

The Francis Crick Institute

and

The National Physical Laboratory

Primary Supervisor: Dr Alex P. Gould (Crick)

Subsidiary Supervisors: Prof. Ian S. Gilmore (NPL), Prof. Franck Pichaud (UCL)

A thesis submitted for the degree of

Doctor of Philosophy

University College London

March 2021

Table of Contents

List of Figures

List of Tables

Chapter 9. Appendices

9.1 Material and Methods Supplementary Information

Table 9.1 Details of commercial standards used in this study

Standard	Reference	Composition	Application
Arachidyl dodecanoate	Sigma-Aldrich #L0506	Arachidyl dodecanoate ≥99%	GC-MS
ASTM reference gas oil	Sigma-Aldrich #506419 D2887 Lot 2	Mixture of n-alkanes	Cryo-OrbiSIMS GC-MS
Differential Ion Mobility System Suitability Lipidomix Kit	Avanti #330708X	1mg/ml cholesterol 1mg/ml 18:1 TG 1mg/ml 18:1 SM 1mg/ml 18:1 Ceramide 1mg/mg 18:1 Lyso-PC 1mg/ml 19:0 Chol Ester 1mg/ml 14:1 DG 1mg/ml 14:1 CL 1mg/ml 14:1 PC 1mg/ml 14:1 PS 1mg/ml 14:1 PG 1mg/ml 14:1 PE 0.25mg/ml 14:1 PI 1mg/ml 14:1 PA Prepared in 1:1 chloroform:methanol	LC-MS OrbiSIMS
Docosane	Sigma-Aldrich #134457	Docosane 99%	GC-MS
Glyceryl trioleate (Triolein)	Sigma-Aldrich #T7140	Glyceryl trioleate ≥99%	Cryo-SIMS ToF-SIMS
Heneicosane	Sigma-Aldrich #286052	Heneicosane 98%	GC-MS
Hexacosane	Sigma-Aldrich #241687	Hexacosane 99%	GC-MS
Lauric aldehyde	Sigma-Aldrich #W261513	Lauric aldehyde ≥95%	GC-MS
Linoleic acid	Sigma-Aldrich #L1376	Linoleic acid ≥99%	GC-MS
Methyl tetracosanoate	Sigma-Aldrich #87115	Methyl tetracosanoate ≥99%	GC-MS
N,N-didodecylmethlamine	Tokyo Chemical Industry #D3338	N,N-didodecylmethlamine >85%	GC-MS
Nonacosane	Sigma-Aldrich #284246	Nonacosane 99%	GC-MS
Octacosane	Sigma-Aldrich #O504	Octacosane 99%	GC-MS
Octadecane	Sigma-Aldrich #O652	Octadecane 99%	GC-MS

Supelco 37 Component FAME Mix	Sigma-Aldrich #CRM47885	Methyl butyrate 400 µg/mL Methyl hexanoate 400 µg/mL Methyl octanoate 400 µg/mL Methyl decanoate 400 µg/mL Methyl undecanoate 200 µg/mL Methyl dodecanoate400 µg/mL Methyl tridecanoate 200 µg/mL Methyl (Z)-myristoleate tetradec-9-enoate 200 µg/mL Methyl tetradecanoate 400 µg/mL Methyl (Z)-pentadec-10-enoate 200 µg/mL Methyl pentadecanoate 200 µg/mL Methyl (Z)-hexadec-9-enoate 200 µg/mL Methyl hexadecanoate 600 µg/mL Methyl (Z)-heptadec-10-enoate 200 µg/mL Methyl heptadecanoate 200 µg/mL Methyl (Z,Z,Z)-octadeca-6,9,12-trienoate 200 µg/mL Methyl (Z,Z,Z)-octadeca-9,12,15-trienoate 200 µg/mL Methyl (Z,Z)-octadeca-9,12-dienoate 200 µg/mL Methyl (E,E)-octadeca-9,12-dienoate 200 µg/mL Methyl (E)-octadece-9-enoate 200 µg/mL Methyl (Z)-octadec-9-enoate 400 µg/mL Methyl octadecanoate 400 µg/mL Methyl (Z,Z,Z,Z,Z)-icosa-5,8,11,14,17-pentaenoate 200 µg/mL Methyl (Z,Z,Z,Z)-icosa-5,8,11,14-tetraenate 200 µg/mL Methyl (Z,Z,Z)-icosa-8,11,14-trienoate 200 µg/mL Methyl (Z,Z,Z)-icosa-11,14,17-trienoate 200 µg/mL Methyl (Z,Z)-icosa-1,14-dienoate 200 µg/mL Methyl (Z)-icos-11-enoate $\leq$ 200 μ g/mL Methyl icosanoate 400 µg/mL Methyl heneicosanoate 200 µg/mL Methyl (Z,Z,Z,Z,Z,Z)-docosa-4,7,10,13,16,19-hexaenoate 200 µg/mL	GC-MS

		Methyl (Z,Z)-docosa-13,16-dienoate 200 µg/mL Methyl (Z)-docos-13-enoate 200 µg/mL Methyl docosanoate 400 µg/mL Methyl tricosanoate 200 µg/mL Methyl (Z)-tetracos-15-enoate 200 µg/mL Methyl tetracosanoate 400 µg/mL	
Tetracosane	Sigma-Aldrich #T8752	Tetracosane 99%	GC-MS
Tricosane	Sigma-Aldrich #263850	Tricosane 99%	Cryo-OrbiSIMS Cryo-SIMS GC-MS Orbitrap direct infusion
(*Z*)-7-tricosene	Cayman chemical #9000313	20mg/ml (*Z*)-7-tricosene in hexane	Cryo-OrbiSIMS Cryo-SIMS GC-MS
(*Z*)-7-pentacosene	Cayman chemical #9000530	(*Z*)-9-pentacosene >98%	GC-MS
(*Z,Z*)-7,11-heptacosadiene	Cayman chemical #100462-58-6	(*Z,Z*)-7,11-heptacosadiene >98%	GC-MS
(*Z*)-7,(*Z*)-11-nonacosadiene	Cayman chemical #104410-91-5	(*Z,Z*)-7,11-nonacosadiene >98%	GC-MS
(*Z*)-9-tricosene	Sigma-Aldrich #859885	(*Z*)-9-tricosene ≥97%	GC-MS Cryo-SIMS Cryo-OrbiSIMS Orbitrap direct infusion
(*Z*)-11-Vaccenyl acetate	Cayman chemical #10010101	(*Z*)-11-Vaccenyl acetate >98%	GC-MS

Table 9.2 Plant samples used in this study

Plant sample	Scientific name
Gooseberry	*Ribes uva-crispa* cv. Hinamaki red
Apple tree	*Malus domestica* cv. Bountiful
Tomato	*Solanum lycopersicum* cv. Sweet Millions
Asparagus	*Asparagus officinalis* cv. Gijnlim
Kiwi berry	*Actinidia arguta* cv. Issai
Victoria plum	*Prunus domestica* cv. Victoria
Golden gage plum	*Prunus domestica* cv. Oullins Golden Gage
Pine needle	*Pinus nigra*

Table 9.3 qPCR primer sequences

Gene	Forward primer sequence (5'-3')	Reverse primer sequence (5'-3')	Reference
RP49	cggatcgatatgctaagctgt	cgacgcactctgttgtcg	Roche UPL #117
tub	tgtcgcgtgtgaaacacttc	agcaggcgtttccaatctg	Ponton et al. (2011)
act	gcgtcggtcaattcaatctt	aagctgcaacctcttcgtca	Ponton et al. (2011)
RNA Pol II	ccttcaggagtacggctatcatct	ccaggaagacctgagcattaatct	(Chiang and Kurnit, 2003)
Cyp4g1	tcaggagcaaagaagcaaca	gttgcagcgtctcctgaact	Roche UPL #86
FarO	caaggatggcgagaatcc	ccagtaatagtgtatcgtccttcca	Roche UPL #140
Far	ccaccccagagtccattg	tgcaggatatgatggagcag	Roche UPL #137
Desat2	gtggtgcttccagctaaacat	tctgggtaggattcatggtctt	Roche UPL #20
Desat1	tgggcgttccctcttttt	gctgcgatcagtgagtctga	Roche UPL #104
GstD5	ccacctcacagtggctgata	tcaaagatttcgaaagtggaaac	Roche UPL #55
Obp99c	tctggccctctgtgctgt	cattggggaagatcaggttc	Roche UPL #14
Obp56d	tctaccgaaaatgaagttcctgat	catcggatagttgcagctcag	Roche UPL #55
Obp99b	tattgggtctggcctttgtc	gcgtcttcaccacatagtcg	Roche UPL #9
Cyp4ac2	tcaggttattcctcagtttacgc	cctccgacaagtcatcaagtt	Roche UPL #118
Cyp4ac1	gtggtttacgaactgattagaccat	cgtctggaatgccatttgt	Roche UPL #14
CG15553	ccctctgacactggtaagctg	ctggccagggattccttatag	Roche UPL #149
GstD8	acaccttcctggaggacca	caatgtcggcaatggtga	Roche UPL #5
CG32750	tggcaactatttcgatgagtatg	aacagcagggttcccaatct	Roche UPL #22
Cyp4d1	tcgaggactgcgagatcaat	aagatattgggctcgctaaaga	Roche UPL #113
Obp99d	cagatggaggagctgatgct	gctcgtgtcctgctccat	Roche UPL #22

VBA code for OrbiSIMS data collation

```
Sub Main()
AddWorksheet
Columnizer
QuickCull
End Sub


Sub AddWorksheet()

Worksheets.Add().Name = "DATA"

End Sub

Sub Columnizer()
   Dim sh As Worksheet, d As Worksheet
   Dim N As Long, M As Long
   Dim rn1 As Range, rng2 As Range
   Set d = Sheets("DATA")

   For Each sh In Sheets
      If sh.Name <> d.Name Then
         N = sh.Cells(Rows.Count, "A").End(xlUp).Row
            Set rRng = d.Range("A1")
               If IsEmpty(rRng.Value) Then
               Set rng1 = sh.Range("A1:S" & N)
               Else: Set rng1 = sh.Range("A2:S" & N)
               End If

               If IsEmpty(rRng.Value) Then
         M = d.Cells(Rows.Count, "A").End(xlUp).Row
         Else
         M = d.Cells(Rows.Count, "A").End(xlUp).Row + 1
         End If
         Set rng2 = d.Range("A" & M)
         rng1.Copy rng2
         rng2.Offset(0, 19).Resize(N, 1).Value = sh.Name
      End If
   Next sh
End Sub
Sub QuickCull()
   On Error Resume Next
   Columns("B").SpecialCells(xlBlanks).EntireRow.Delete
End Sub
```

Macronutrients (%)	STD	LP (4%)
Crude protein	18.6	4
Fat	6.2	4.3
Carbohydrate	44.2	74.3
Crude fibre	3.5	n/a
Neutral Detergent Fibre	14.7	5
Ash	5.3	0

Minerals	STD	LP (4%)
Calcium (%)	1	3.7
Phosphorous (%)	0.7	2.4
Non-phytate phosphorous (%)	0.4	2.4
Sodium (%)	0.2	0.7
Potassium (%)	0.6	3
Chloride (%)	0.4	0.4
Magnesium (%)	0.2	0.7
Zing (mg/kg)	70	82.5
Manganese (mg/kg)	100	31.5
Copper (mg/kg)	15	15.5
Iodine (mg/kg)	6	0.5
Iron (mg/kg)	200	303
Selenium (mg/kg)	0.23	0.52
Molybdenum (mg/kg)	n/a	0.4
Silicon (mg/kg)	n/a	72.5
Chromium (mg/kg)	n/a	13.75
Lithium (mg/kg)	n/a	1.4
Fluorine (mg/kg)	n/a	3.2
Nickel (mg/kg)	n/a	1.6
Vanadium (mg/kg)	n/a	0.3
Boron (mg//kg)	n/a	4.1

Vitamins	STD	LP (4%)
Vitamin A (retinol) (IU/g)	15	6
Vitamin D_3 (cholecalciferol) (IU/g)	1.5	1.5
Vitamin E (IU/kg)	110	0.1
Vitamin K_3 (menadione) (mg/kg)	50	0
Vitamin B_1 (thiamin) (mg/kg)	17	0.007
Vitamin B_2 (riboflavin) (mg/kg)	15	0.003
Niacin (nicotinic acid) (mg/kg)	70	0.045
Vitamin B_6 (pyridoxine) (mg/kg)	18	0.01
Pantothenic acid (mg/kg)	0.33	0.024
Vitamin B_{12} (cyanocobalamin) (mg/kg)	0.08	0.0375
Biotin (mg/kg)	0.4	0.0003
Folate (mg/kg)	4	0.003
Choline (mg/kg)	1200	3000
Vitamin B_3 (niacin) (mg/kg)	n/a	0.045

Additional components	STD	LP (4%)
TBHQ (antioxidant) (g/kg)	0	0.008
Orange food colour (g/kg)	0	0.1

Amino Acids (%)	STD
Aspartic acid	1.4
Glutamic acid	3.4
Alanine	1.1
Glycine	0.8
Threonine	0.7
Proline	1.6
Serine	1.1
Leucine	1.8
Isoleucine	0.8
Valine	0.9
Phenylalanine	1.0
Tryosine	0.6
Methionine	0.4
Cystine	0.3
Lysine	0.9
Histidine	0.4
Arginine	1.0
Tryptophan	0.2

Fatty acids (%)	STD
C16:0 Palmitic	0.7
C18:0 Stearic	0.2
C18:1ω9 Oleic	1.2
C18:2ω6 Linoleic	3.1
C18:3ω3 Linolenic	0.3
Total Saturated	0.9
Total Monounsaturated	1.3
Total Polyunsaturated	3.4

Table 9.4 Detailed composition of mouse diets

Detailed information provided by Envigo on the composition of the different diets. Information on the STD diet is provided from analytical testing by Envigo, information on the 4% diet is provided based on addition of isolated ingredients and does not take into account contribution from natural ingredients. The 4% protein diet contains protein from casein with the addition of methionine, whereas the STD diet contains protein from yeast with the addition of lysine and methionine. Neutral detergent fibre is an estimate of insoluble fibre including cellulose, hemicellulose and lignin. A value of n/a indicates no information is available about the abundance of this component.

9.2 Chapter 3 Supplementary Information

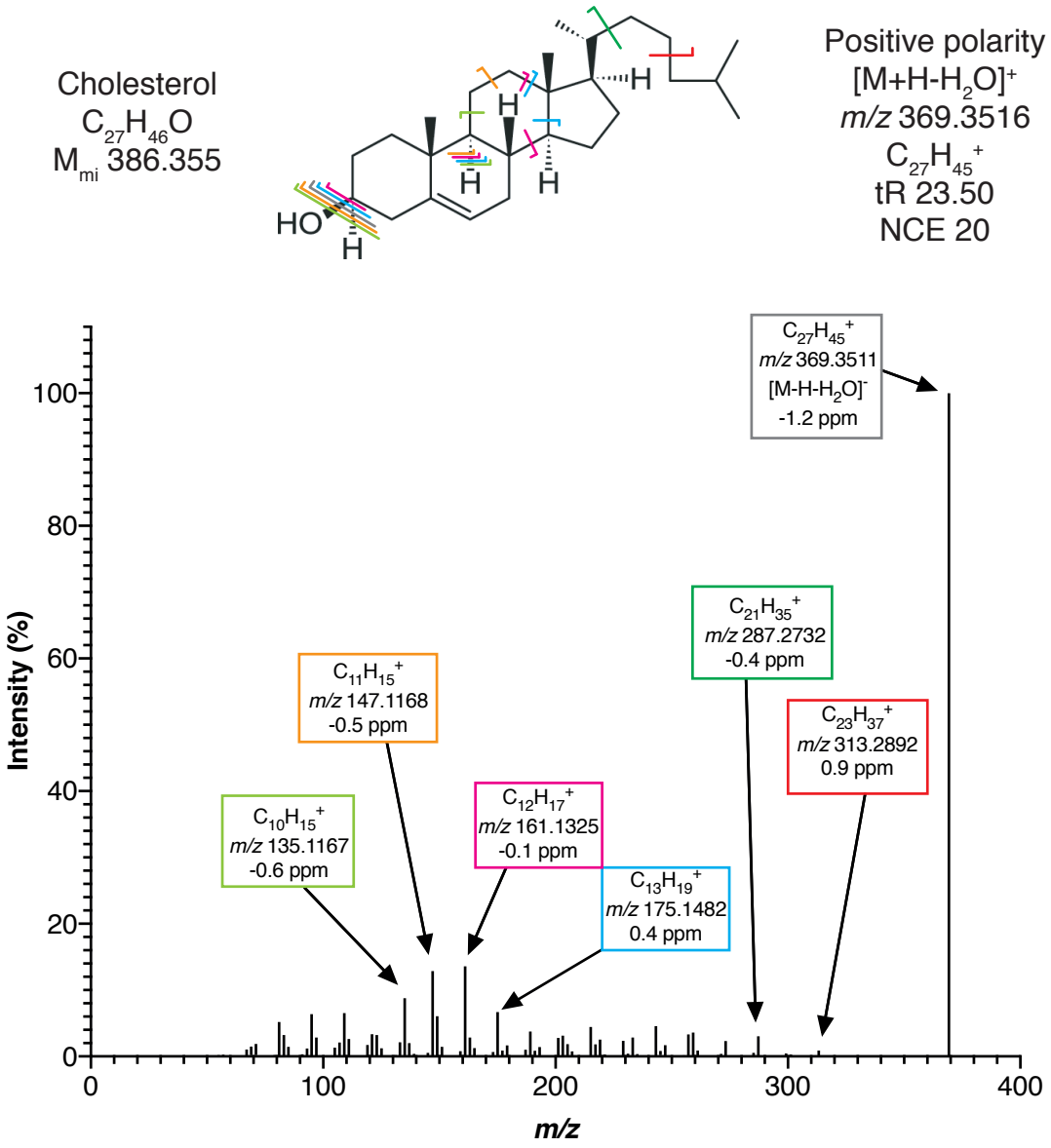

Figure 9.1 LC-MS/MS of a Cholesterol standard
Fragmentation patterns of a cholesterol standard from an LC-MS run with Orbitrap-based HCD in positive polarity. The fragmented adducts are labelled with their formula and mass.

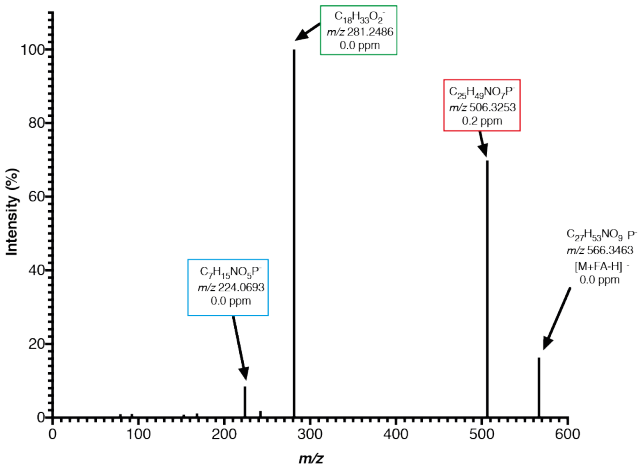

Lyso-PC(18:1/0:0)
$C_{26}H_{52}NO_7P$
M_{mi} 521.3481

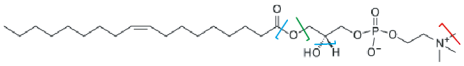

Negative polarity
$[M+HCOOH-H]^-$
m/z 566.3463
$C_{27}H_{53}NO_9P^-$
t_R 5.86
NCE 20

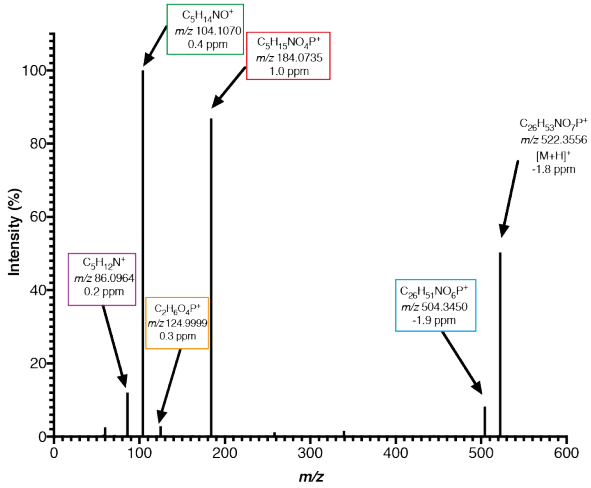

Lyso-PC(18:1/0:0)
$C_{26}H_{52}NO_7P$
M_{mi} 521.3481

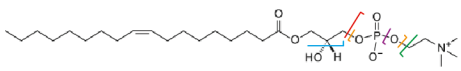

Positive polarity
$[M+H]^+$
m/z 522.3554
$C_{26}H_{53}NO_7P^+$
t_R 5.93
NCE 20

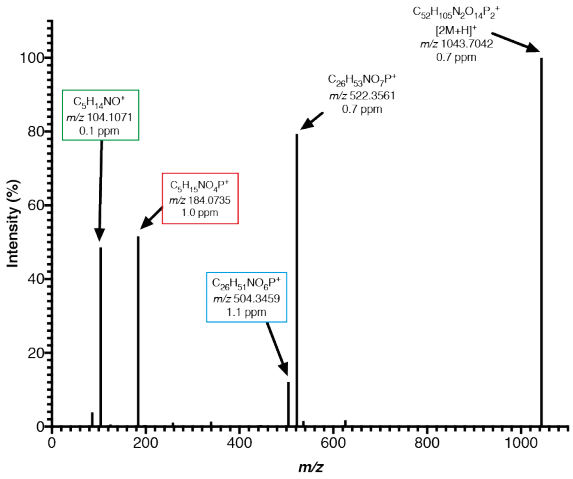

Lyso-PC(18:1/0:0)
$C_{26}H_{52}NO_7P$
M_{mi} 521.3481

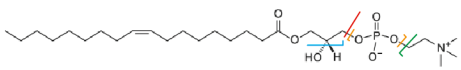

Positive polarity
$[2M+H]^+$
m/z 2014.7036
$C_{52}H_{105}N_2O_{14}P_2^+$
t_R 5.97
NCE 20

Figure 9.2 LC-MS/MS of a Lyso-Phosphatidylcholine standard
Fragmentation patterns of a Lyso-PC(18:1/0:0) standard from an LC-MS run with Orbitrap-based HCD in positive and negative polarities. The fragmented adducts are labelled with their formula and mass..

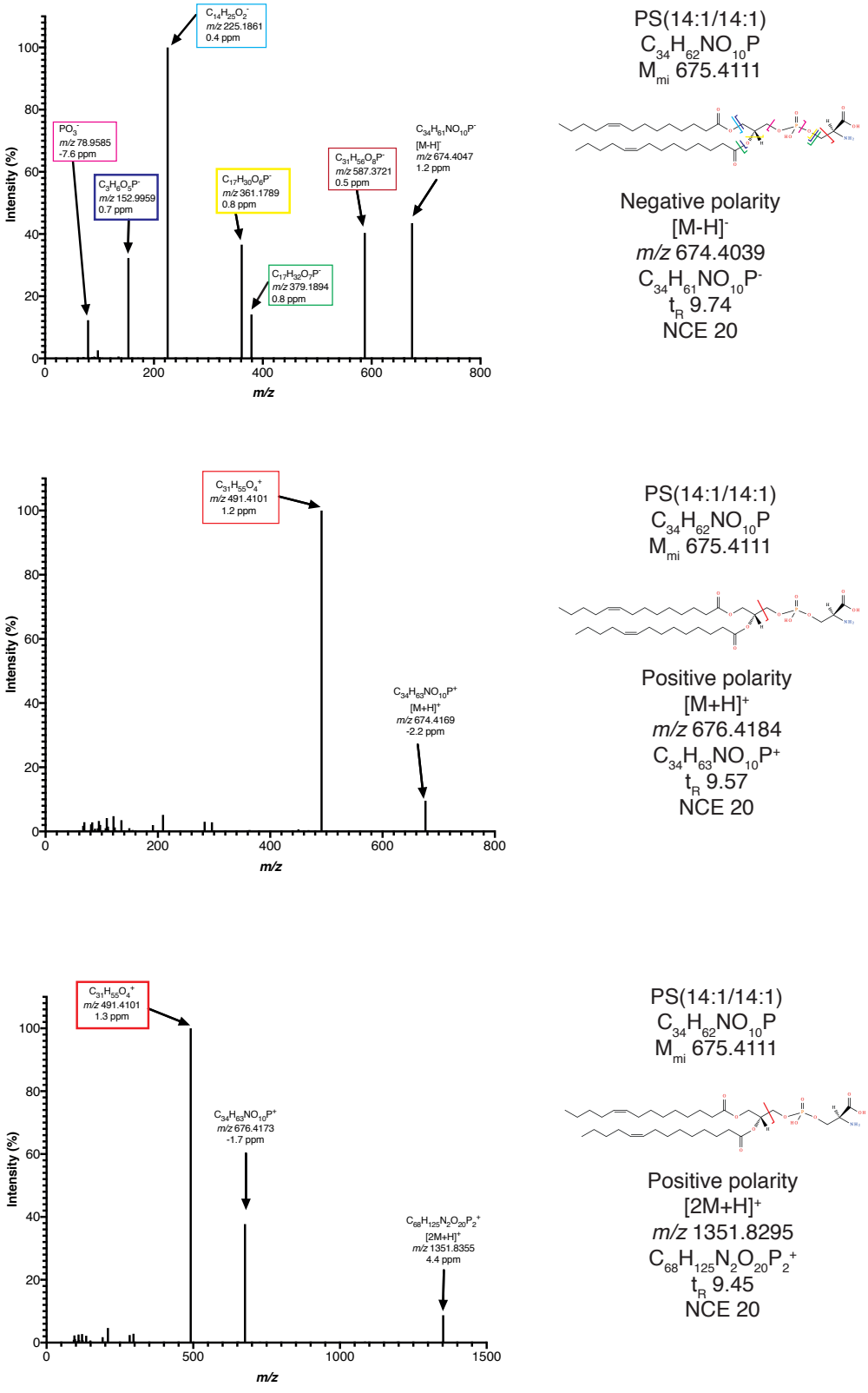

Figure 9.3 LC-MS/MS of a Phosphatidylserine Standard
Fragmentation patterns of a PS(14:1/14:1) standard from an LC-MS run with Orbitrap-based HCD in positive and negative polarities. The fragmented adducts are labelled with their formula and mass

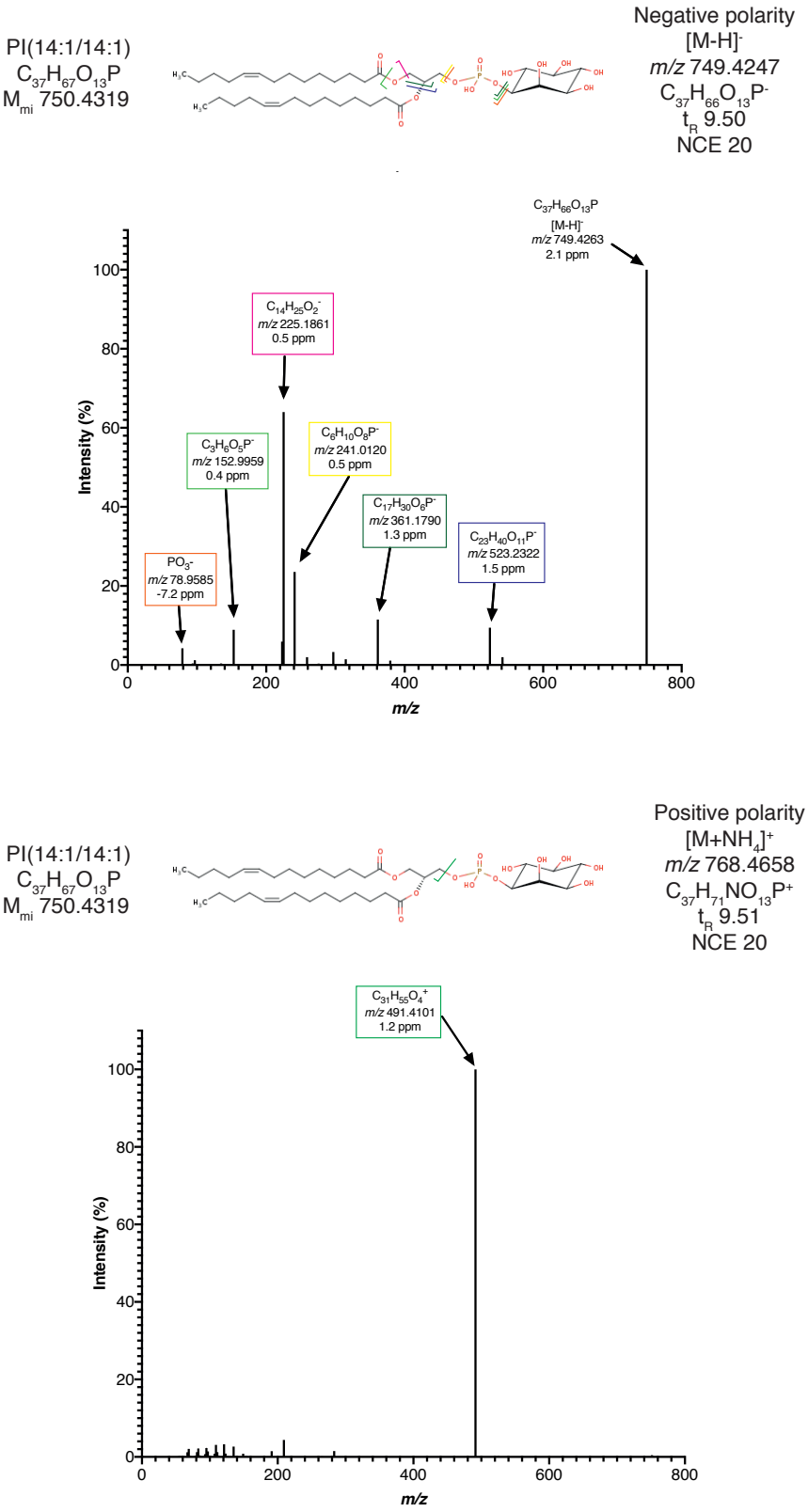

Figure 9.4 LC-MS/MS of a Phosphatidylinositol standard
Fragmentation patterns of a PI(14:1/14:1) standard from an LC-MS run with Orbitrap-based HCD in positive and negative polarities. The fragmented adducts are labelled with their formula and mass.

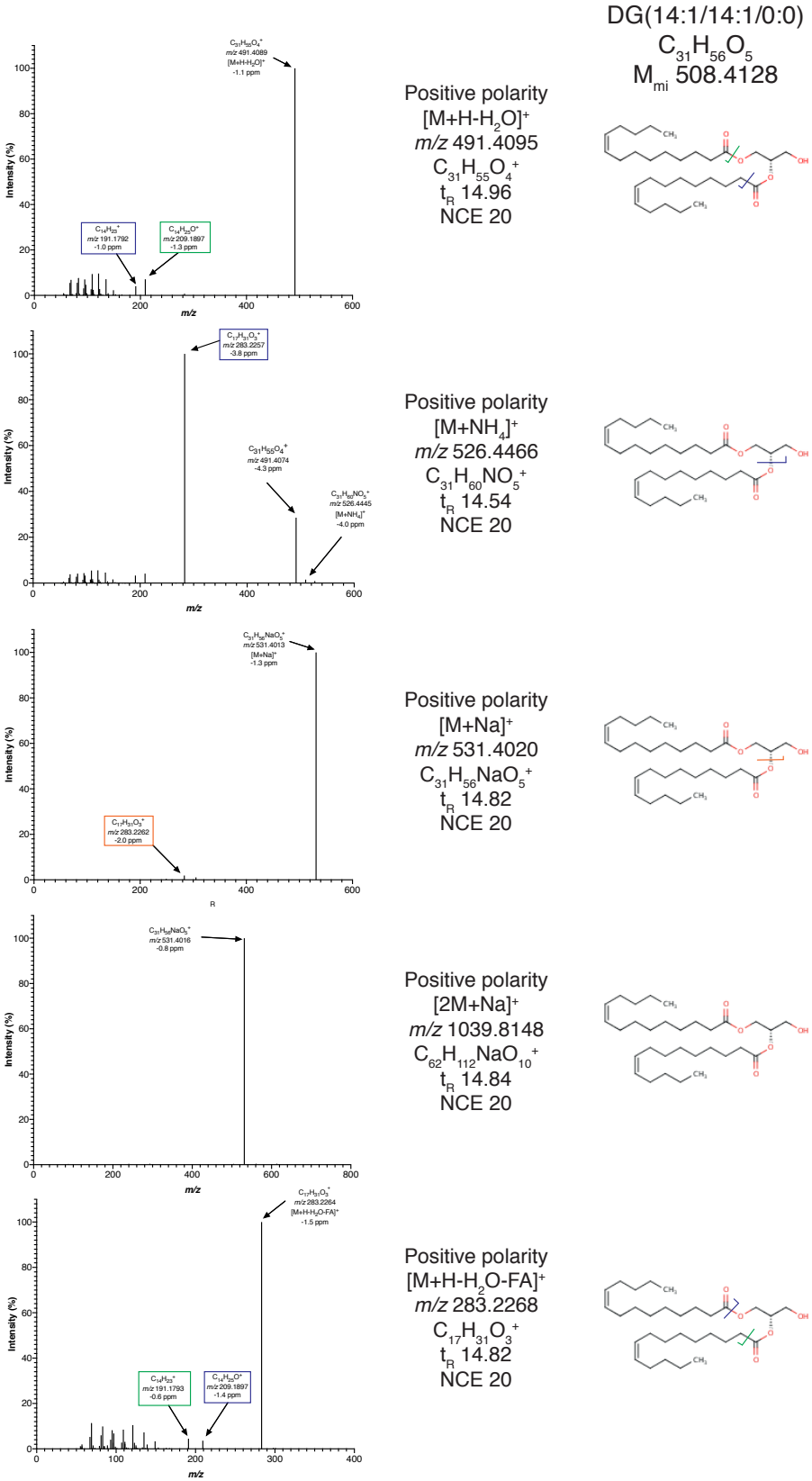

Figure 9.5 LC-MS/MS of a Diglyceride standard
Fragmentation patterns of a DG(14:1/14:1/0:0) standard from an LC-MS run with Orbitrap-based HCD in positive and negative polarities. The fragmented adducts are labelled with their formula and mass.

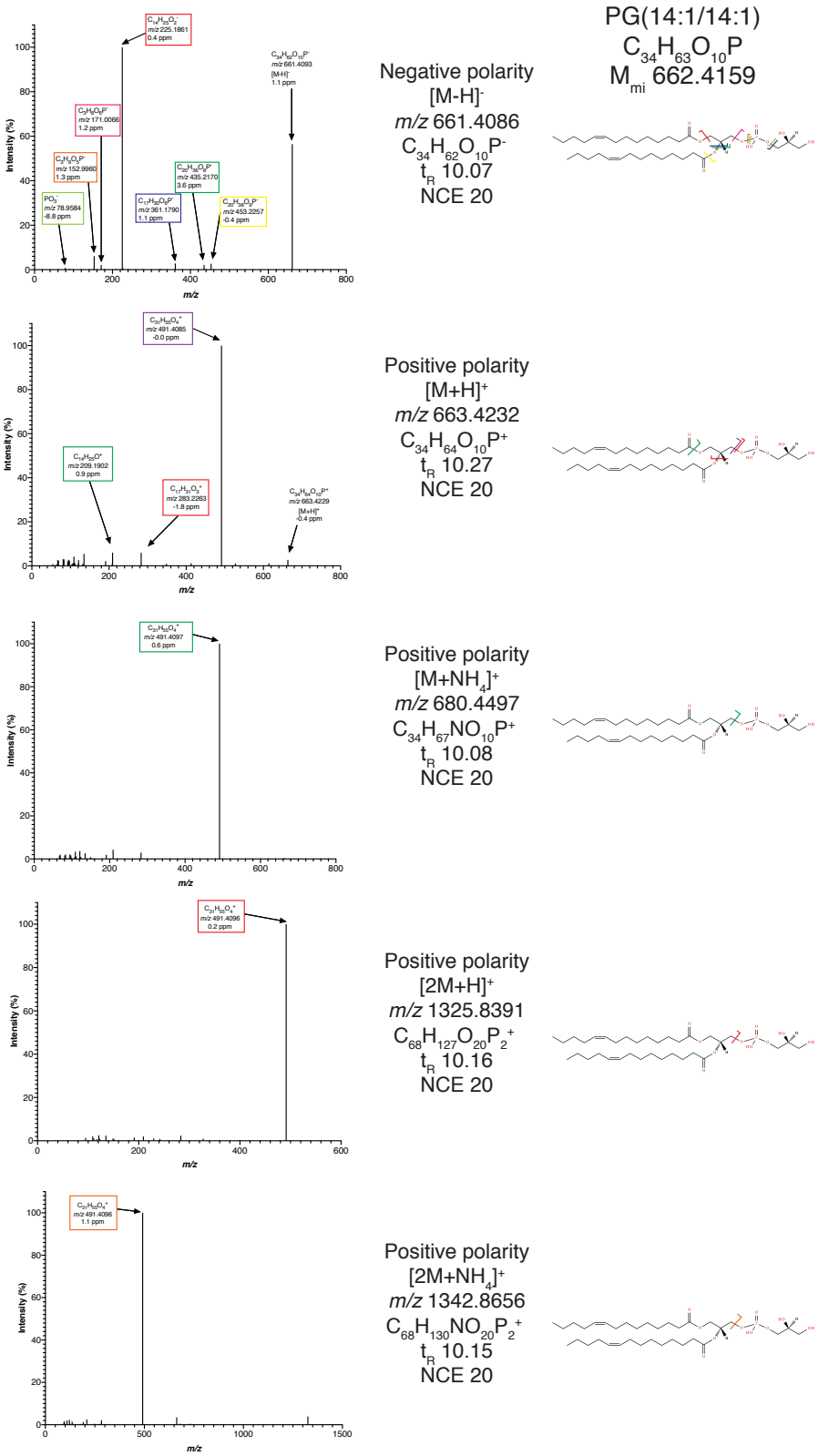

Figure 9.6 LC-MS/MS of a Phosphatidylglycerol standard
Fragmentation patterns of a PG(14:1/14:1) standard from an LC-MS run with Orbitrap-based HCD in positive and negative polarities. The fragmented adducts are labelled with their formula and mass.

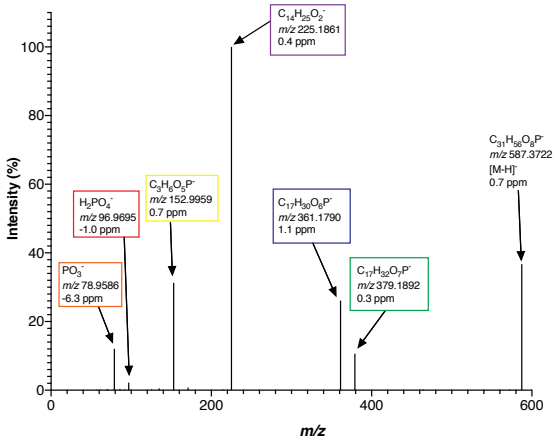

PA(14:1/14:1)
$C_{31}H_{57}O_8P$
M_{mi} 588.3791

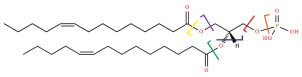

Negative polarity
$[M-H]^-$
m/z 587.3718
$C_{31}H_{56}O_8P^-$
t_R 10.65
NCE 20

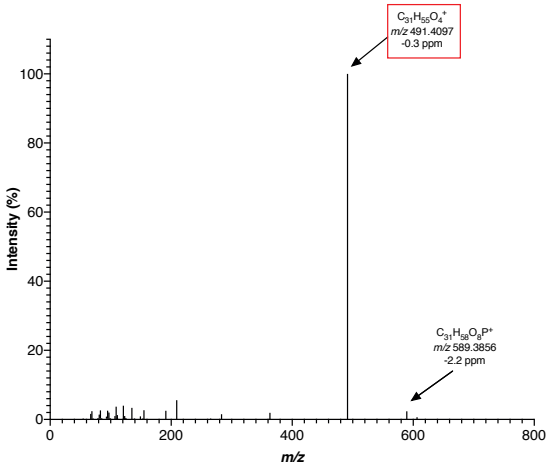

PA(14:1/14:1)
$C_{31}H_{57}O_8P$
M_{mi} 588.3791

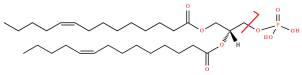

Positive polarity
$[M+NH_4]^-$
m/z 606.4129
$C_{31}H_{61}NO_8P^+$
t_R 10.55
NCE 20

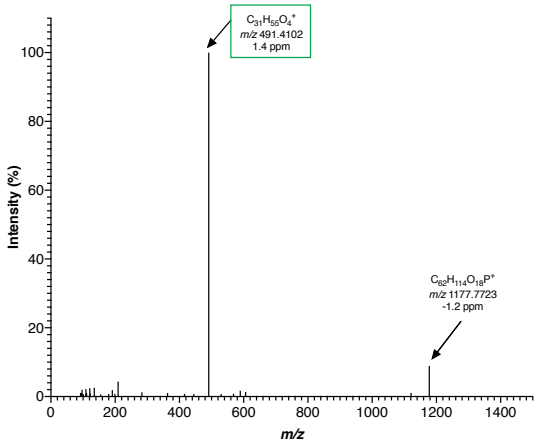

PA(14:1/14:1)
$C_{31}H_{57}O_8P$
M_{mi} 588.3791

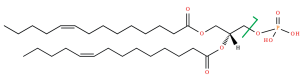

Positive polarity
$[2M+NH_4]^-$
m/z 1194.7920
$C_{62}H_{118}NO_{16}P_2^+$
t_R 10.65
NCE 20

Figure 9.7 LC-MS/MS of a Phosphatidic Acid standard
Fragmentation patterns of a PA(14:1/14:1) standard from an LC-MS run with Orbitrap-based HCD in positive and negative polarities. The fragmented adducts are labelled with their formula and mass.

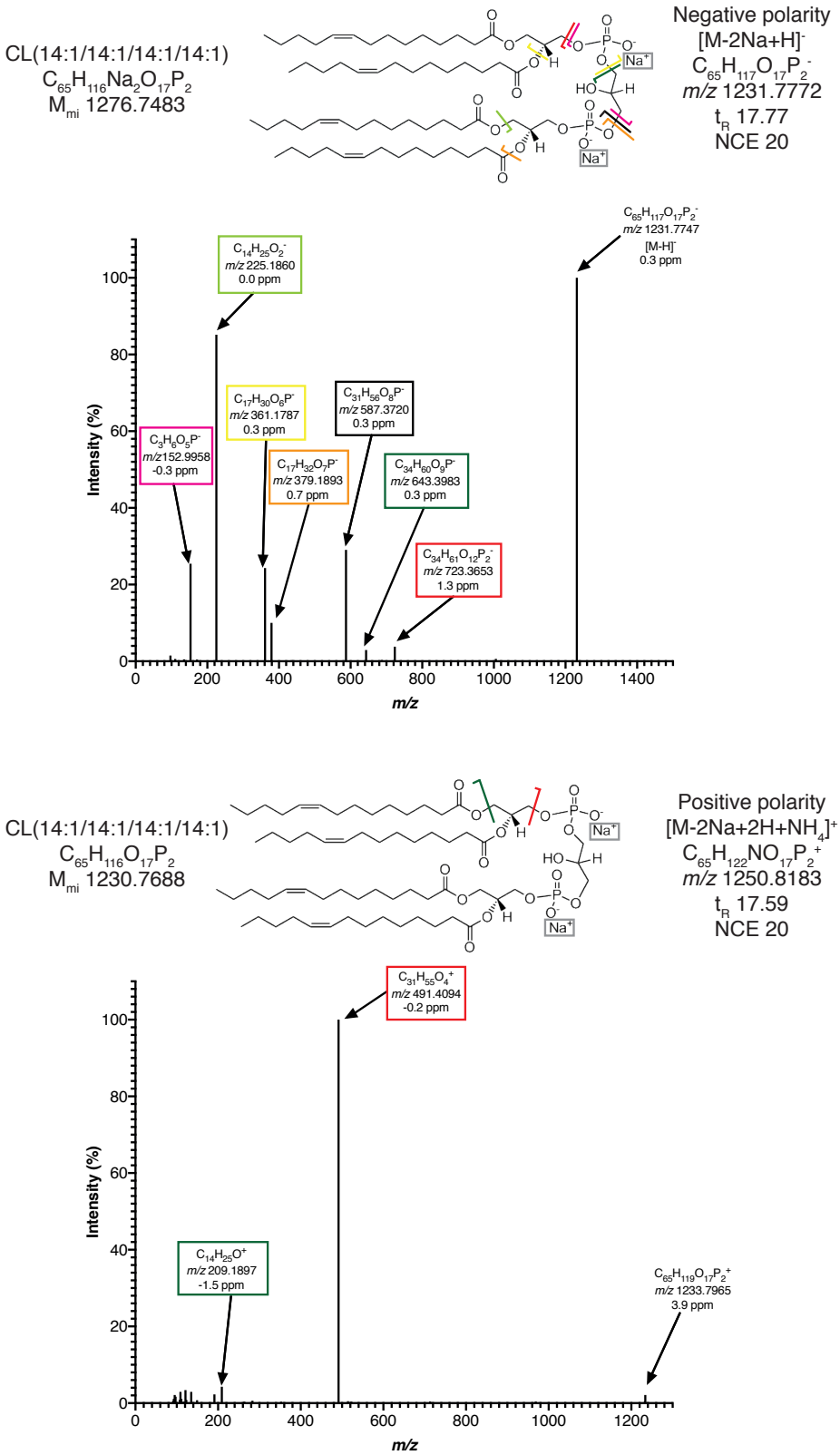

Figure 9.8 LC-MS/MS of a Cardiolipin standard
Fragmentation patterns of a CL(14:1/14:1/14:1/14:1) standard from an LC-MS run with Orbitrap-based HCD in positive and negative polarities. The fragmented adducts are labelled with their formula and mass.

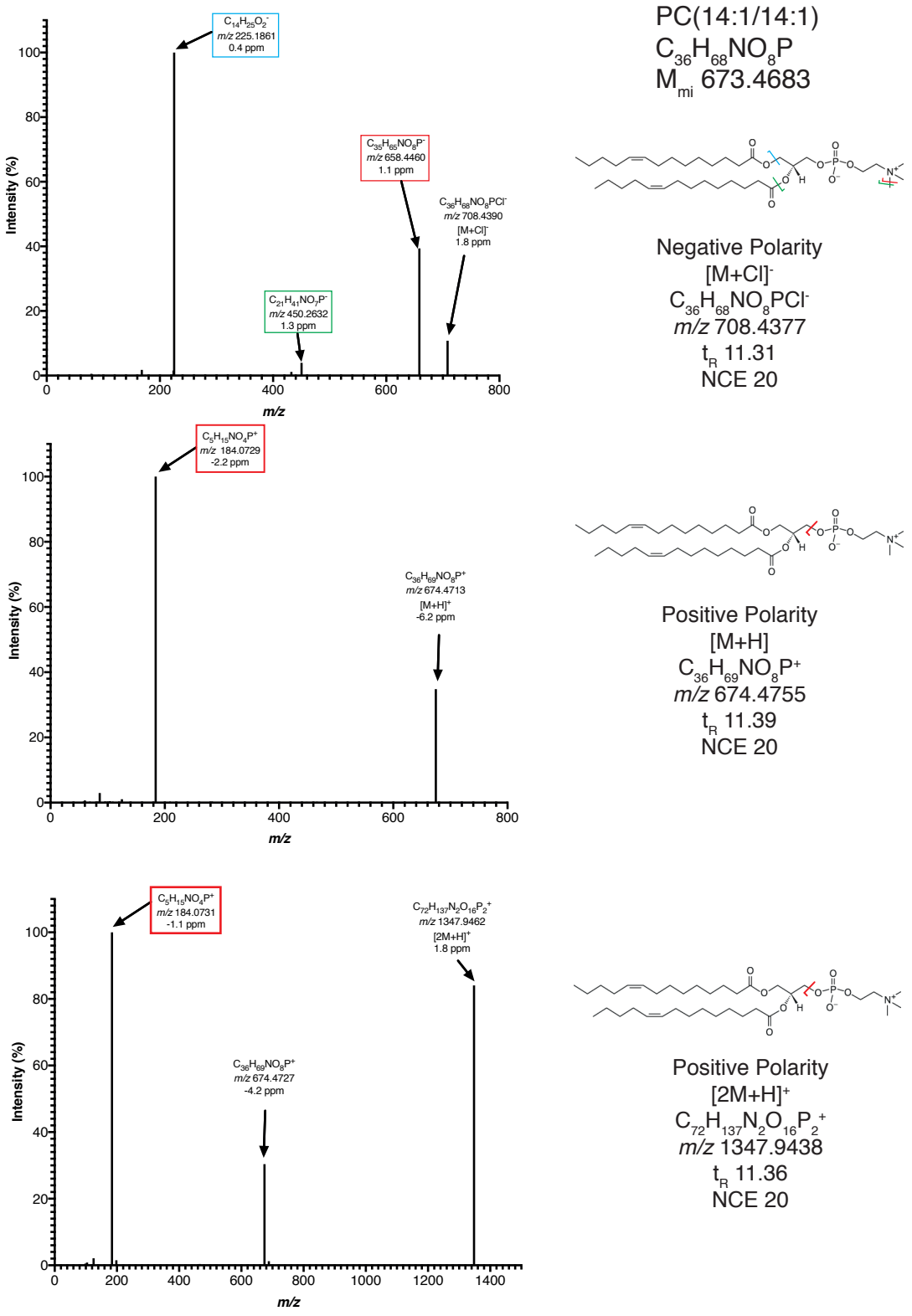

Figure 9.9 LC-MS/MS of a Phosphatidylcholine standard
Fragmentation patterns of a PC(14:1/14:1) standard from an LC-MS run with Orbitrap-based HCD in positive and negative polarities. The fragmented adducts are labelled with their formula and mass

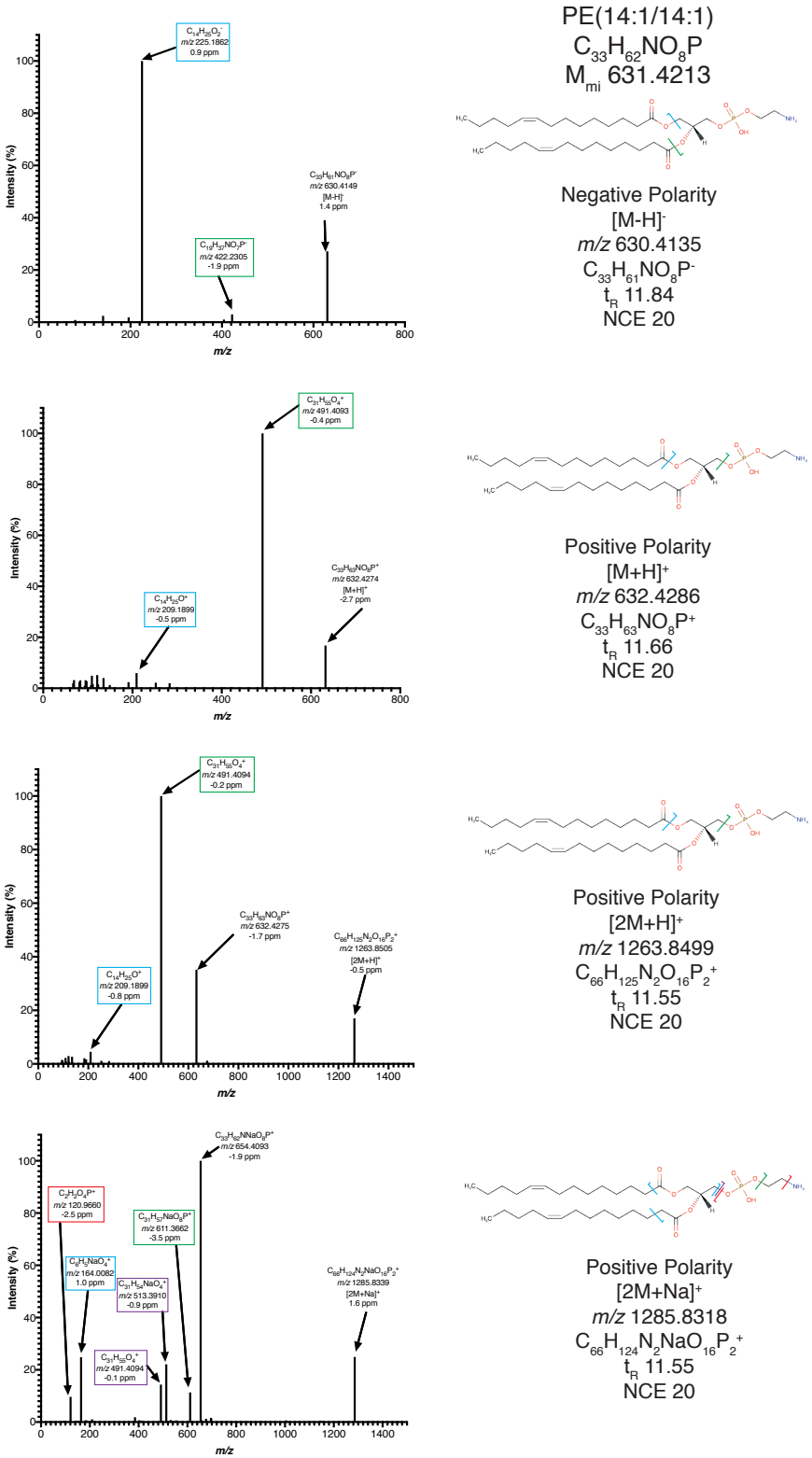

Figure 9.10 LC-MS/MS of a Phosphatidylethanolamine standard
Fragmentation patterns of a PE(14:1/14:1) standard from an LC-MS run with Orbitrap-based HCD in positive and negative polarities. The fragmented adducts are labelled with their formula and mass

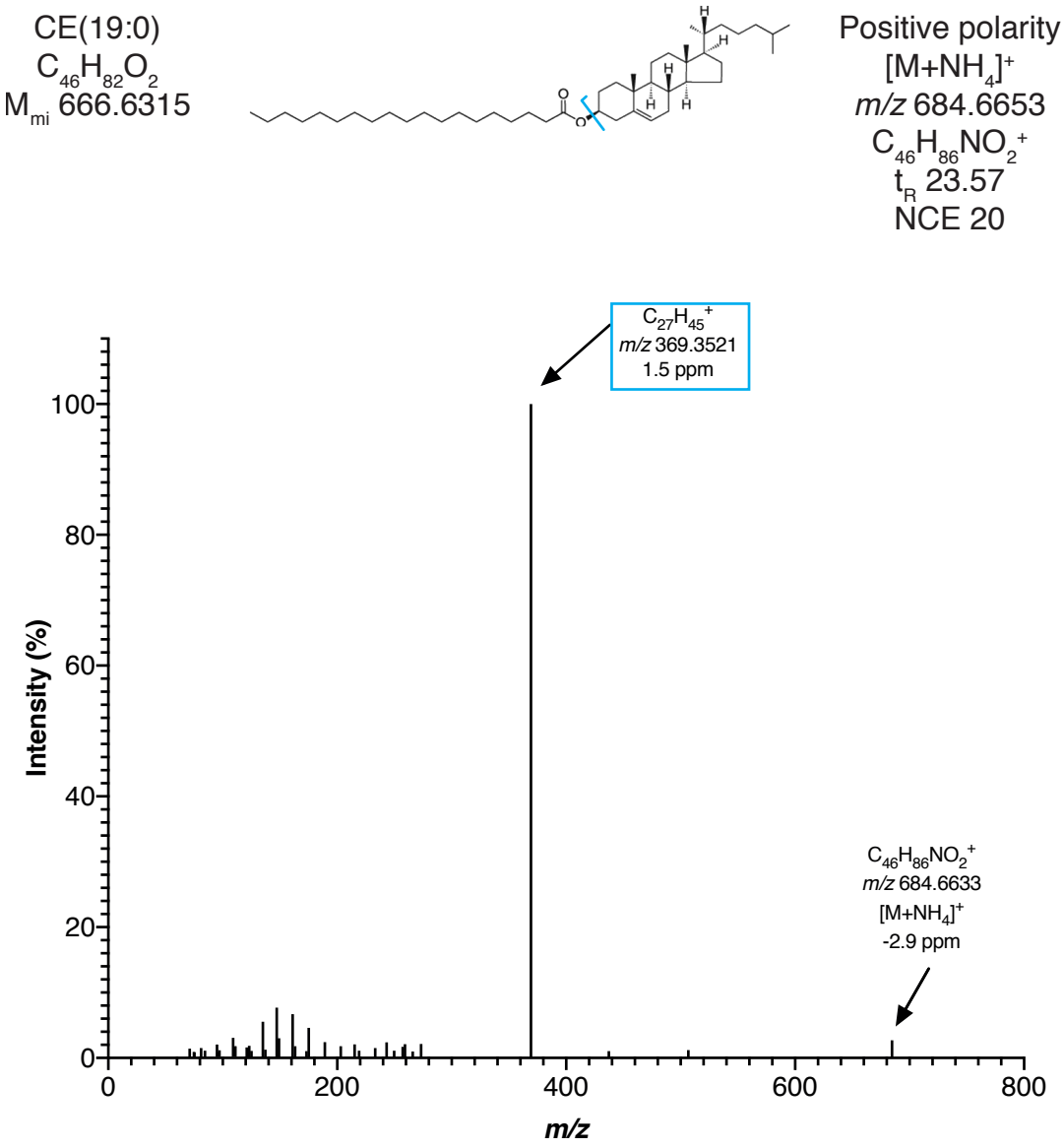

Figure 9.11 LC-MS/MS of a Cholesterol ester standard
Fragmentation patterns of a CE(19:0) standard from an LC-MS run with Orbitrap-based HCD in positive polarity. The fragmented adduct is labelled with its formula and mass.

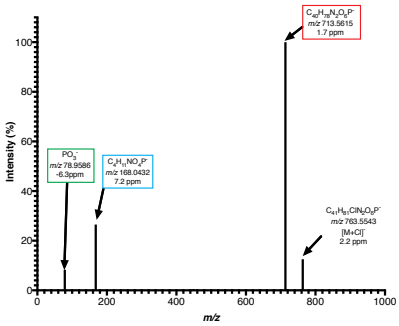

SM(18:1/18:1)
$C_{41}H_{81}N_2O_6P$
M_{mi} 728.5832

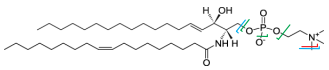

Negative polarity
$[M+Cl]^-$
m/z 763.5521
$C_{41}H_{81}ClN_2O_6P^-$
t_R 14.83
NCE 20

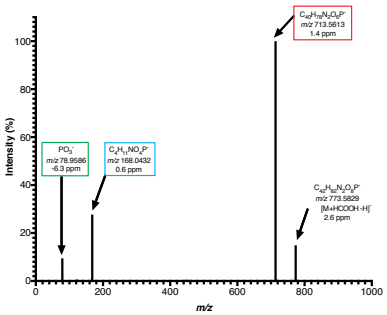

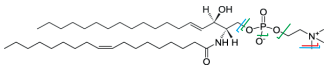

Negative polarity
$[M+HCOOH-H]^-$
m/z 773.5814
$C_{42}H_{82}N_2O_8P^-$
t_R 14.82
NCE 20

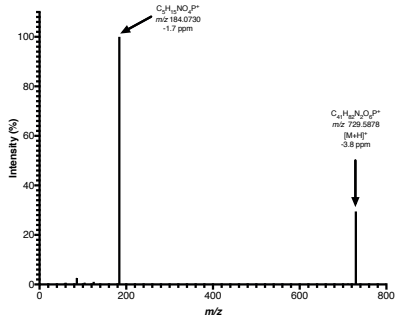

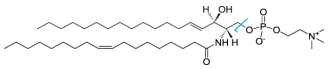

Positive polarity
$[M+H]^+$
m/z 761.5803
$C_{41}H_{82}N_2O_8P^+$
t_R 14.97
NCE 20

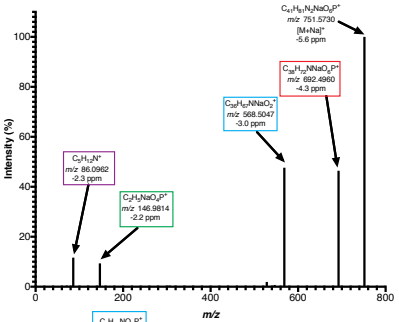

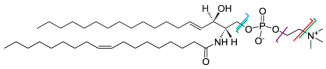

Positive polarity
$[M+Na]^+$
m/z 783.5623
$C_{41}H_{81}N_2NaO_8P^+$
t_R 14.83
NCE 20

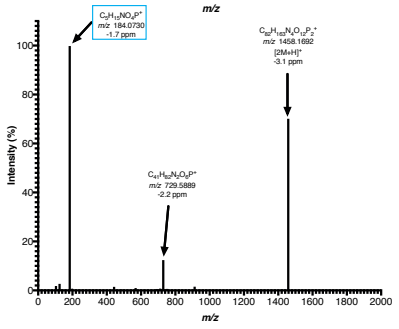

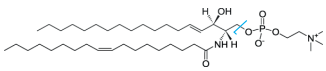

Positive polarity
$[2M+H]^+$
m/z 1458.1737
$C_{82}H_{163}N_4O_{12}P_2^+$
t_R 14.88
NCE 20

Figure 9.12 LC-MS/MS of a Sphingomyelin standard
Fragmentation patterns of a SM(18:1/18:1) standard from an LC-MS run with Orbitrap-based HCD in positive and negative polarities. The fragmented adducts are labelled with their formula and mass.

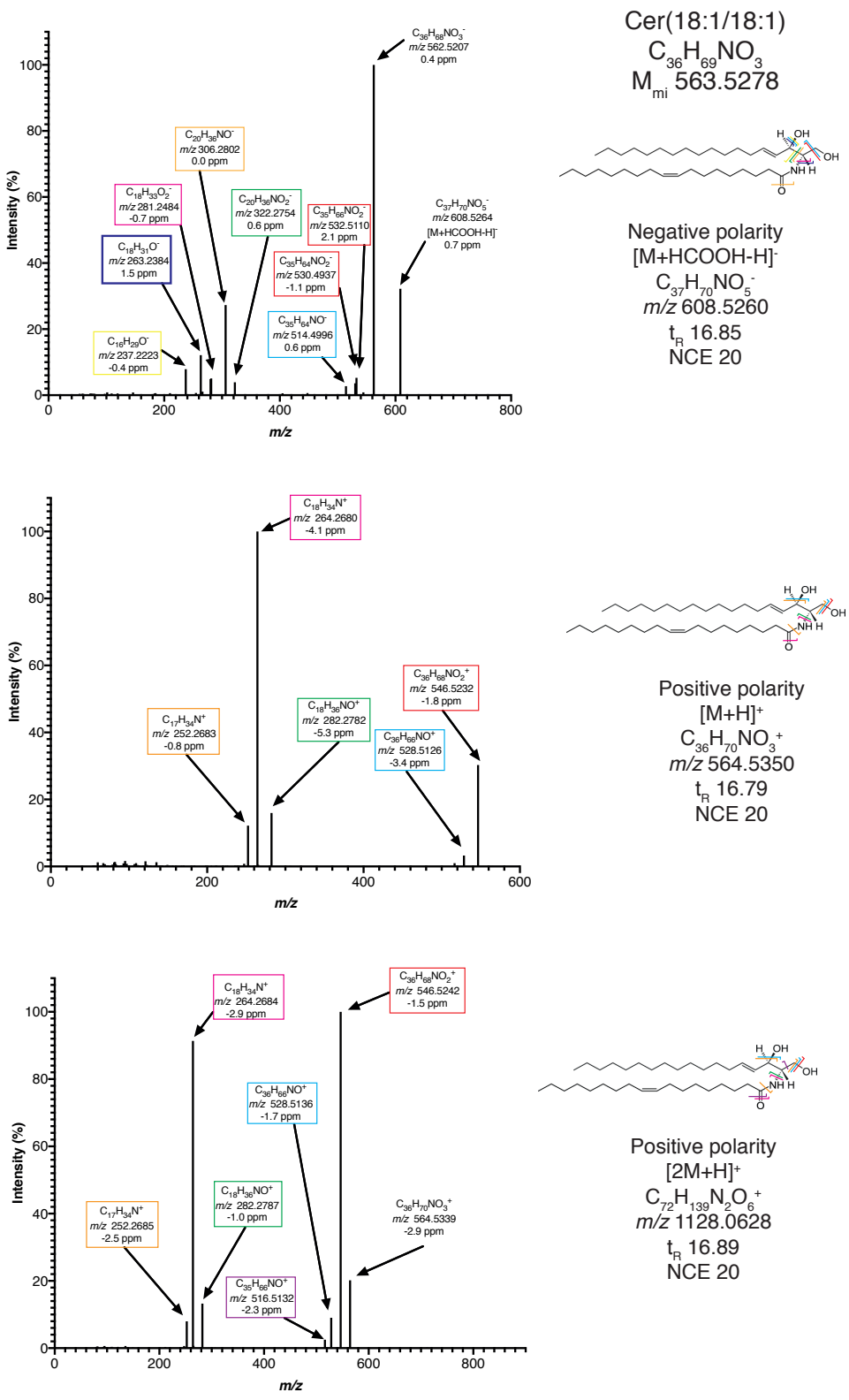

Figure 9.13 LC-MS/MS of a Ceramide standard
Fragmentation patterns of a Cer(18:1/18:1) standard from an LC-MS run with Orbitrap-based HCD in positive and negative polarities. The fragmented adducts are labelled with their formula and mass

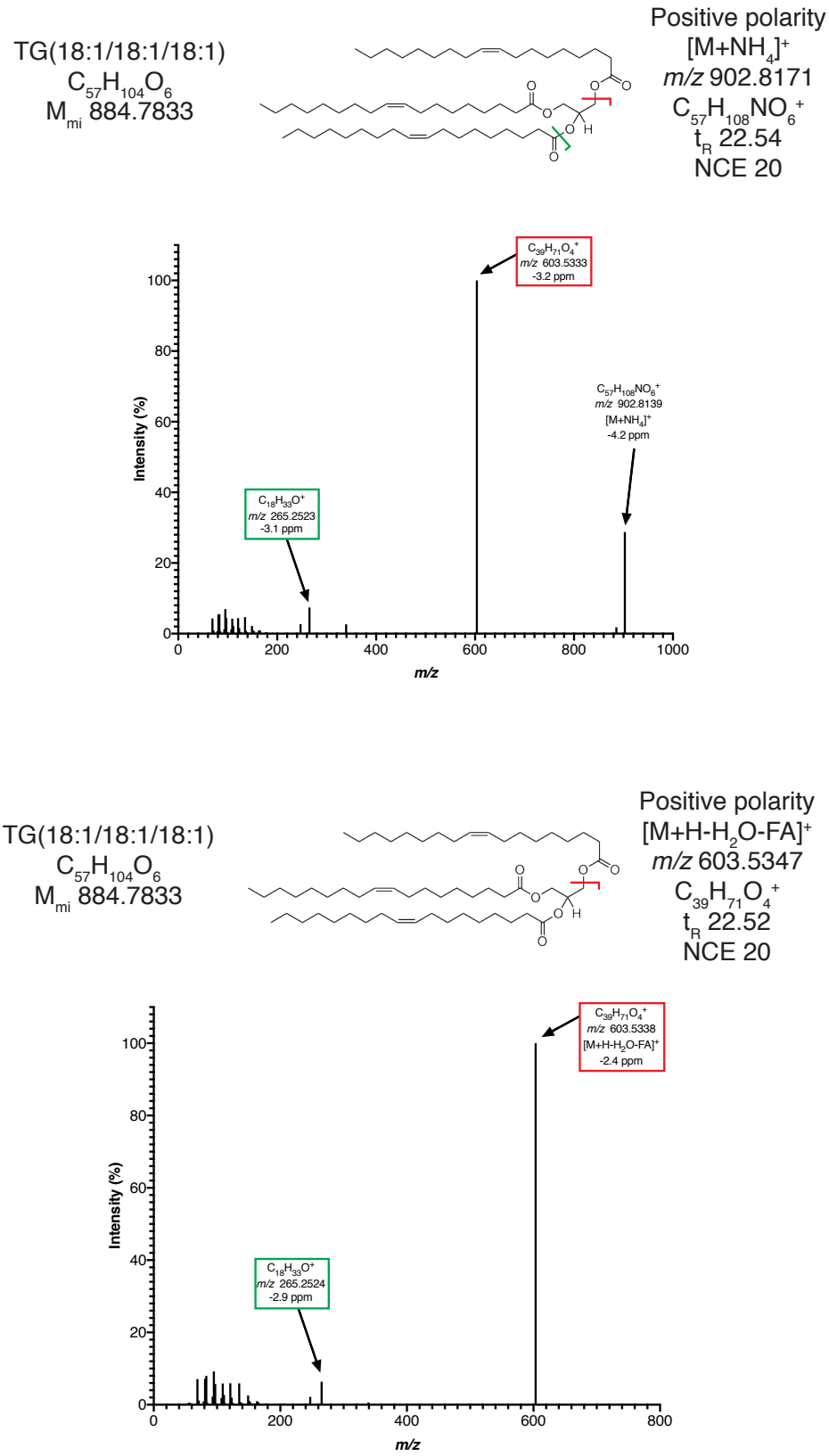

Figure 9.14 LC-MS/MS of a Triglyceride standard
Fragmentation patterns of a TG(18:1/18:1/18:1) standard from an LC-MS run with Orbitrap-based HCD in positive polarity. The fragmented adducts are labelled with their formula and mass.

m/z	ID	Compound Formula	Adduct	Adduct Formula	Adduct exact mass	Mass deviation (ppm)	Average spectral representation
665.6241	CE(19:0)	$C_{46}H_{82}O_2$	$[M-H]^-$	$C_{46}H_{81}O_2^-$	665.62421	-0.17	0.0413%
451.3795	FA C14:1	$C_{14}H_{26}O_2$	$[2M-H]^-$	$C_{28}H_{51}O_4^-$	451.37928	0.49	0.0173%
562.5210	Cer(18:1/18:1)	$C_{36}H_{69}NO_3$	$[M-H]^-$	$C_{36}H_{68}NO_3^-$	562.52047	0.94	0.3487%
385.348	Cholesterol	$C_{27}H_{46}O$	$[M-H]^-$	$C_{27}H_{45}O^-$	385.34759	0.03	0.0013%
1,231.7752	CL(14:1/14:1/14:1/14:1)	$C_{65}H_{118}O_{17}P_2$	$[M-H]^-$	$C_{65}H_{117}O_{17}P_2^-$	1231.77715	-1.58	0.3857%
1,253.7560	CL(14:1/14:1/14:1/14:1)	$C_{65}H_{118}O_{17}P_2$	$[M+Na-2H]^-$	$C_{65}H_{116}NaO_{17}P_2^-$	1253.75909	-2.46	1.0621%
507.4056	DG(14:1/14:1/0:0)	$C_{31}H_{56}O_5$	$[M-H]^-$	$C_{31}H_{55}O_5^-$	507.40550	0.20	0.0034%
543.3817	DG(14:1/14:1/0:0)	$C_{31}H_{56}O_5$	$[M+Cl]^-$	$C_{31}H_{56}ClO_5^-$	543.38218	-0.88	0.0272%
361.1786	PA(14:1/14:1)	$C_{31}H_{57}O_8P$	$[M-H-H_2O-FA]^-$	$C_{17}H_{30}O_6P^-$	361.17855	0.14	0.0001%
379.1894	PA(14:1/14:1)	$C_{31}H_{57}O_8P$	$[M-H-FA]^-$	$C_{17}H_{32}O_7P^-$	379.18911	0.76	2.6744%
401.1714	PA(14:1/14:1)	$C_{31}H_{57}O_8P$	$[M+Na-2H-FA]^-$	$C_{17}H_{31}NaO_7P^-$	401.17106	0.85	0.9796%
587.3719	PA(14:1/14:1)	$C_{31}H_{57}O_8P$	$[M-H]^-$	$C_{31}H_{56}O_8P^-$	587.37183	0.12	0.0255%
609.3543	PA(14:1/14:1)	$C_{31}H_{57}O_8P$	$[M+Na-2H]^-$	$C_{31}H_{55}NaO_8P^-$	609.35377	0.87	2.8547%
404.2212	PE(14:1/14:1)	$C_{33}H_{62}NO_8P$	$[M-H-H_2O-FA]^-$	$C_{19}H_{35}NO_6P^-$	404.22075	1.11	0.0591%
422.2317	PE(14:1/14:1)	$C_{33}H_{62}NO_8P$	$[M-H-FA]^-$	$C_{19}H_{37}NO_7P^-$	422.23131	0.92	0.0122%
630.4145	PE(14:1/14:1)	$C_{33}H_{62}NO_8P$	$[M-H]^-$	$C_{33}H_{61}NO_8P^-$	630.41403	0.75	0.0942%
435.2157	PG(14:1/14:1)	$C_{34}H_{63}O_{10}P$	$[M-H-H_2O-FA]^-$	$C_{20}H_{36}O_8P^-$	435.21533	0.85	0.6263%
453.2262	PG(14:1/14:1)	$C_{34}H_{63}O_{10}P$	$[M-H-FA]^-$	$C_{20}H_{38}O_9P^-$	453.22589	0.68	0.2000%
643.3984	PG(14:1/14:1)	$C_{34}H_{63}O_{10}P$	$[M-H-H_2O]^-$	$C_{34}H_{60}O_9P^-$	643.39804	0.56	0.2465%
661.4086	PG(14:1/14:1)	$C_{34}H_{63}O_{10}P$	$[M-H]^-$	$C_{34}H_{62}O_{10}P^-$	661.40861	-0.02	0.0883%
523.2315	PI(14:1/14:1)	$C_{37}H_{67}O_{13}P$	$[M-H-H_2O-FA]^-$	$C_{23}H_{40}O_{11}P^-$	523.23137	0.25	0.0538%
541.2420	PI(14:1/14:1)	$C_{37}H_{67}O_{13}P$	$[M-H-FA]^-$	$C_{23}H_{42}O_{12}P^-$	541.24194	0.07	0.2415%
749.4247	PI(14:1/14:1)	$C_{37}H_{67}O_{13}P$	$[M-H]^-$	$C_{37}H_{66}O_{13}P^-$	749.42465	0.07	0.0901%
488.2034	PS(14:1/14:1)	$C_{34}H_{62}NO_{10}P$	$[M+Na-2H-FA]^-$	$C_{20}H_{36}NNaO_9P^-$	488.20309	0.63	1.6729%
674.4044	PS(14:1/14:1)	$C_{34}H_{62}NO_{10}P$	$[M-H]^-$	$C_{34}H_{61}NO_{10}P^-$	674.40386	0.80	0.0766%
696.3861	PS(14:1/14:1)	$C_{34}H_{62}NO_{10}P$	$[M+Na-2H]^-$	$C_{34}H_{60}NNaO_{10}P^-$	696.38580	0.43	0.5200%
727.5754	SM(18:1/18:1)	$C_{41}H_{81}N_2O_6P$	$[M-H]^-$	$C_{41}H_{80}N_2O_6P^-$	727.57595	-0.76	0.1479%
883.7755	TG(18:1/18:1/018:1)	$C_{57}H_{104}O_6$	$[M-H]^-$	$C_{57}H_{103}O_6^-$	883.77601	-0.58	0.0003%

Table 9.5 Lipidomix compound identities negative polarity OrbiSIMS

m/z	ID	Compound Formula	Adduct	Adduct Formula	Adduct exact mass	Mass deviation (ppm)	Average spectral representation
586.5177	Cer(18:1/18:1)	$C_{36}H_{69}NO_3$	$[M+Na]^+$	$C_{36}H_{69}NNaO_3^+$	586.51697	1.24	1.63922%
531.4025	DG(14:1/14:1/0:0)	$C_{31}H_{56}O_5$	$[M+Na]^+$	$C_{31}H_{56}NaO_5^+$	531.40200	0.94	0.18310%
491.4099	DG(14:1/14:1/0:0)	$C_{31}H_{56}O_5$	$[M+H-H_2O]^+$	$C_{31}H_{55}O_4^+$	491.40949	0.83	0.21518%
1065.6851	Lyso-PC(18:1/0:0)	$C_{26}H_{52}NO_7P$	$[2M+Na]^+$	$C_{52}H_{104}N_2NaO_{14}P_2^+$	1065.68550	-0.38	0.16903%
544.3379	Lyso-PC(18:1/0:0)	$C_{26}H_{52}NO_7P$	$[M+Na]^+$	$C_{26}H_{52}NNaO_7P^+$	544.33736	0.99	2.01476%
522.3559	Lyso-PC(18:1/0:0)	$C_{26}H_{52}NO_7P$	$[M+H]^+$	$C_{26}H_{53}NO_7P^+$	522.35542	0.92	0.22909%
504.3453	Lyso-PC(18:1/0:0)	$C_{26}H_{52}NO_7P$	$[M+H-H_2O]^+$	$C_{26}H_{51}NO_6P^+$	504.34485	0.89	0.42689%
633.3512	PA(14:1/14:1)	$C_{31}H_{57}O_8P$	$[M+2Na-H]^+$	$C_{31}H_{56}Na_2O_8P^+$	633.35027	1.47	0.32096%
1369.9272	PC(14:1/14:1)	$C_{36}H_{68}NO_8P$	$[2M+Na]^+$	$C_{72}H_{136}N_2NaO_{16}P_2^+$	1369.92573	1.07	0.09817%
696.4586	PC(14:1/14:1)	$C_{36}H_{68}NO_8P$	$[M+Na]^+$	$C_{36}H_{68}NNaO_8P^+$	696.45748	1.61	2.03151%
674.4766	PC(14:1/14:1)	$C_{36}H_{68}NO_8P$	$[M+H]^+$	$C_{36}H_{69}NO_8P^+$	674.47553	1.59	0.48057%
676.3935	PE(14:1/14:1)	$C_{33}H_{62}NO_8P$	$[M+2Na-H]^+$	$C_{33}H_{61}NNa_2O_8P+$	676.39247	1.52	0.24335%
654.4115	PE(14:1/14:1)	$C_{33}H_{62}NO_8P$	$[M+Na]^+$	$C_{33}H_{62}NNaO_8P^+$	654.41053	1.48	0.10024%
751.5739	SM(18:1/18:1)	$C_{41}H_{81}N_2O_6P$	$[M+Na]^+$	$C_{41}H_{81}N_2NaO_6P^+$	751.57245	1.93	1.39366%
729.5919	SM(18:1/18:1)	$C_{41}H_{81}N_2O_6P$	$[M+H]^+$	$C_{41}H_{82}N_2O_6P^+$	729.59050	1.92	0.14878%
907.7741	TG(18:1/18:1/18:1)	$C_{57}H_{104}O_6$	$[M+Na]^+$	$C_{57}H_{104}NaO_6^+$	907.77251	1.75	0.15069%

Table 9.6 Lipidomix compound identities positive polarity OrbiSIMS

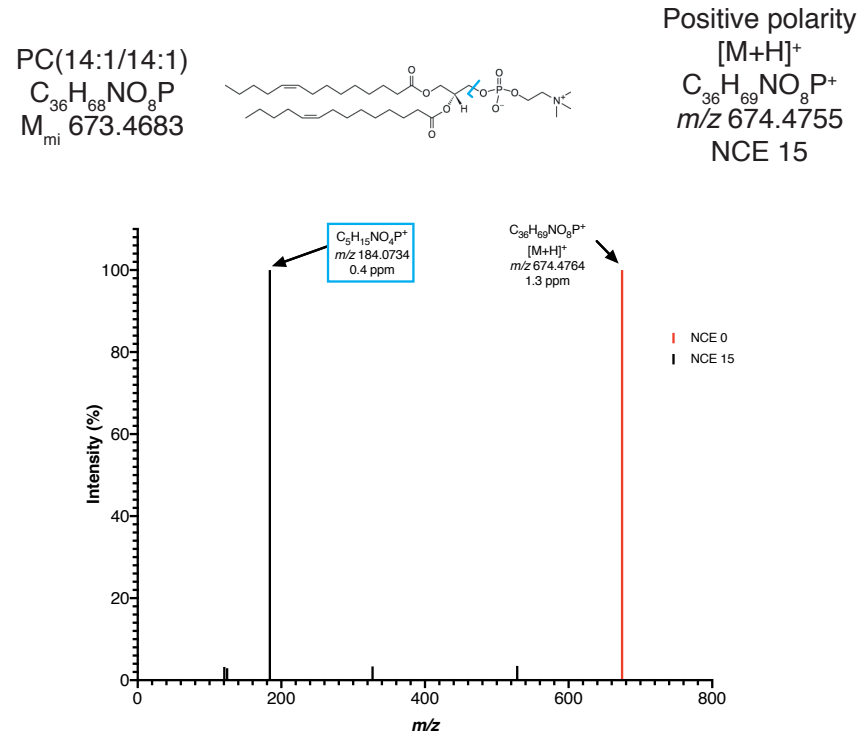

Figure 9.15 OrbiSIMS MS/MS of a Phosphatidylcholine standard
Fragmentation patterns of a PC(14:1/14:1) standard from OrbiSIMS analysis run with Orbitrap-based HCD in positive polarity. The fragmented adducts are labelled with their formula and mass.

SM(18:1/18:1)
$C_{41}H_{81}N_2O_6P$
M_{mi} 728.5832

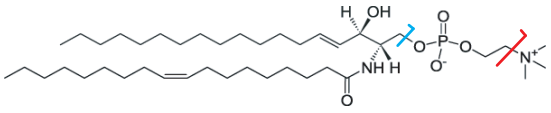

Positive polarity
$[M+Na]^+$
m/z 763.5521
$C_{41}H_{81}N_2NaO_6P^-$
NCE 20

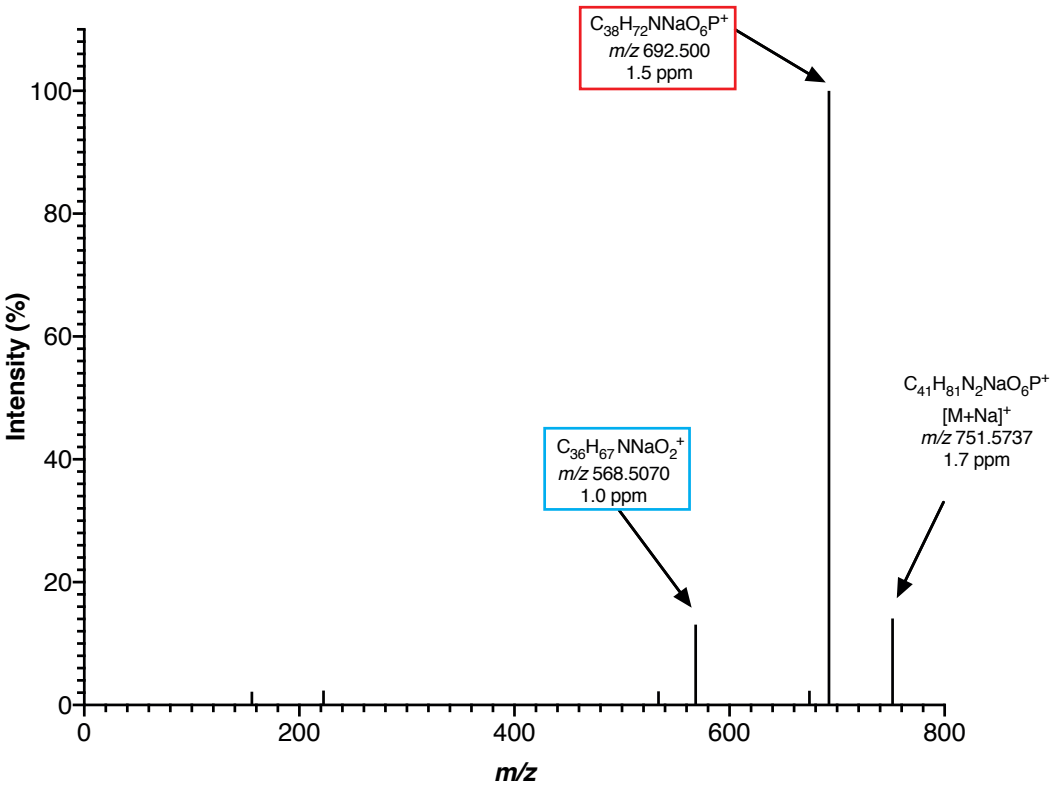

Figure 9.16 OrbiSIMS MS/MS of a Sphingomyelin standard
Fragmentation patterns of a SM(18:1/18:1) standard from OrbiSIMS analysis run with Orbitrap-based HCD in positive polarity. The fragmented adduct is labelled with its formula and mass.

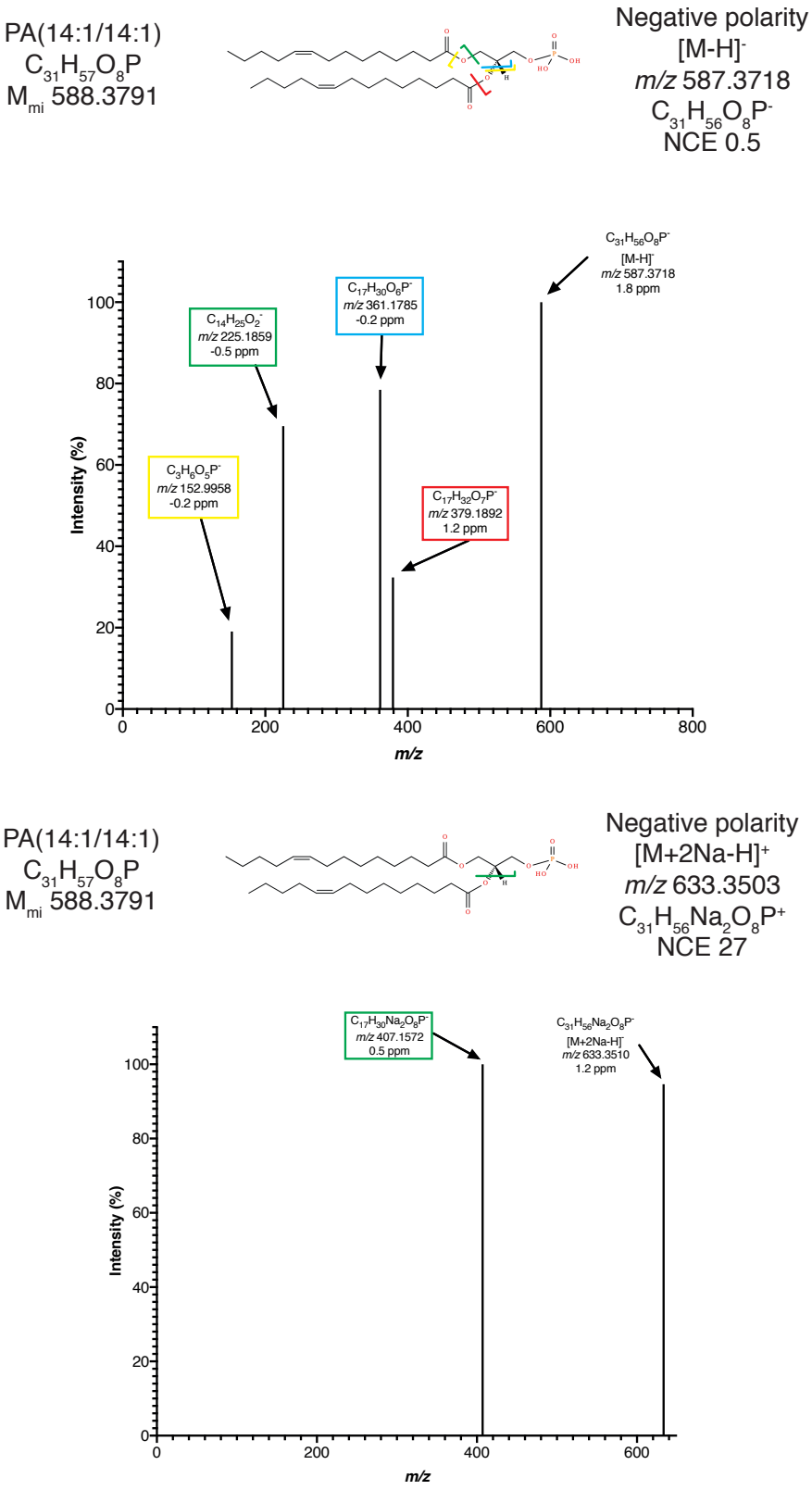

Figure 9.17 OrbiSIMS MS/MS of a Phosphatidic Acid standard
Fragmentation patterns of a PA(14:1/14:1) standard from OrbiSIMS analysis run with Orbitrap-based HCD in positive and negative polarities. The fragmented adducts are labelled with their formula and mass.

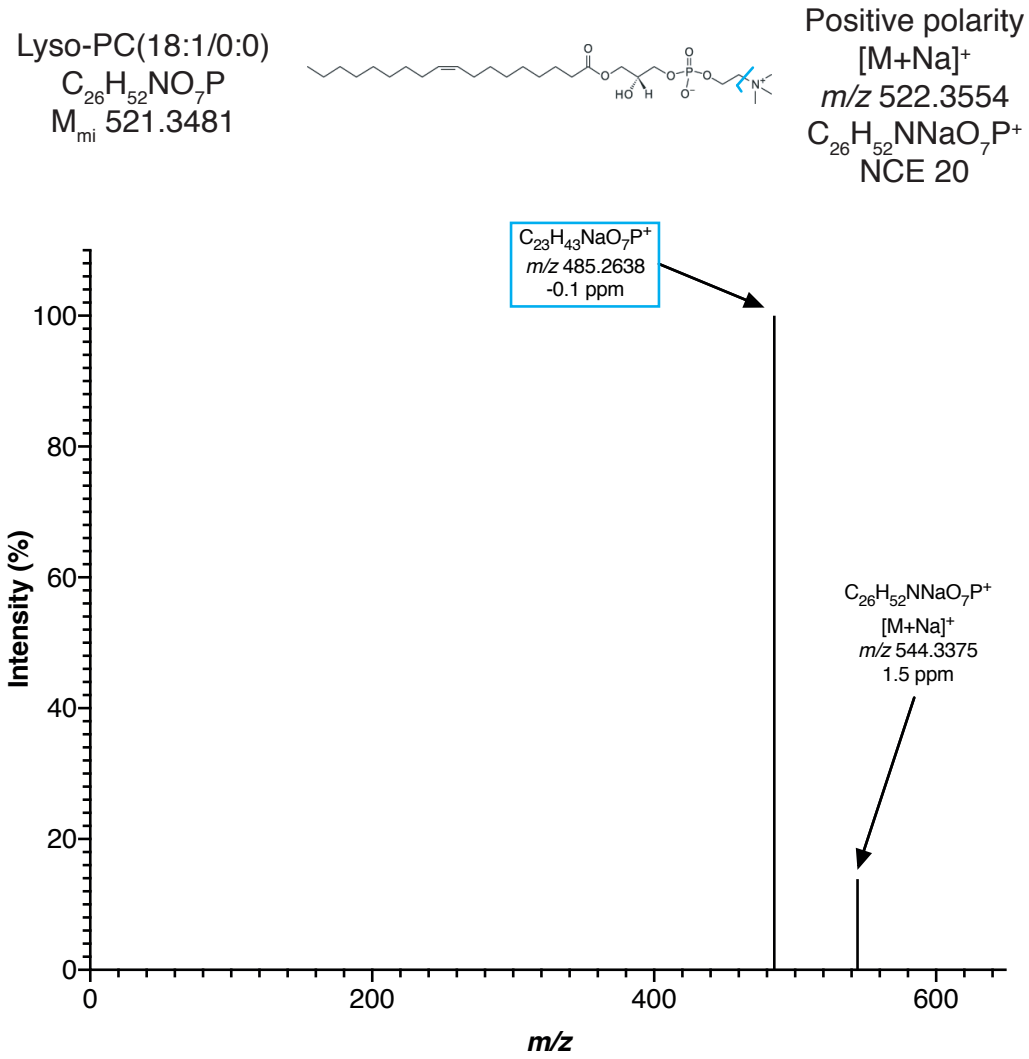

Figure 9.18 OrbiSIMS MS/MS of a Lyso-Phosphatidylcholine standard
Fragmentation patterns of a lyso-PC(18:1/0:0) standard from OrbiSIMS analysis run with Orbitrap-based HCD in positive polarity. The fragmented adduct is labelled with its formula and mass

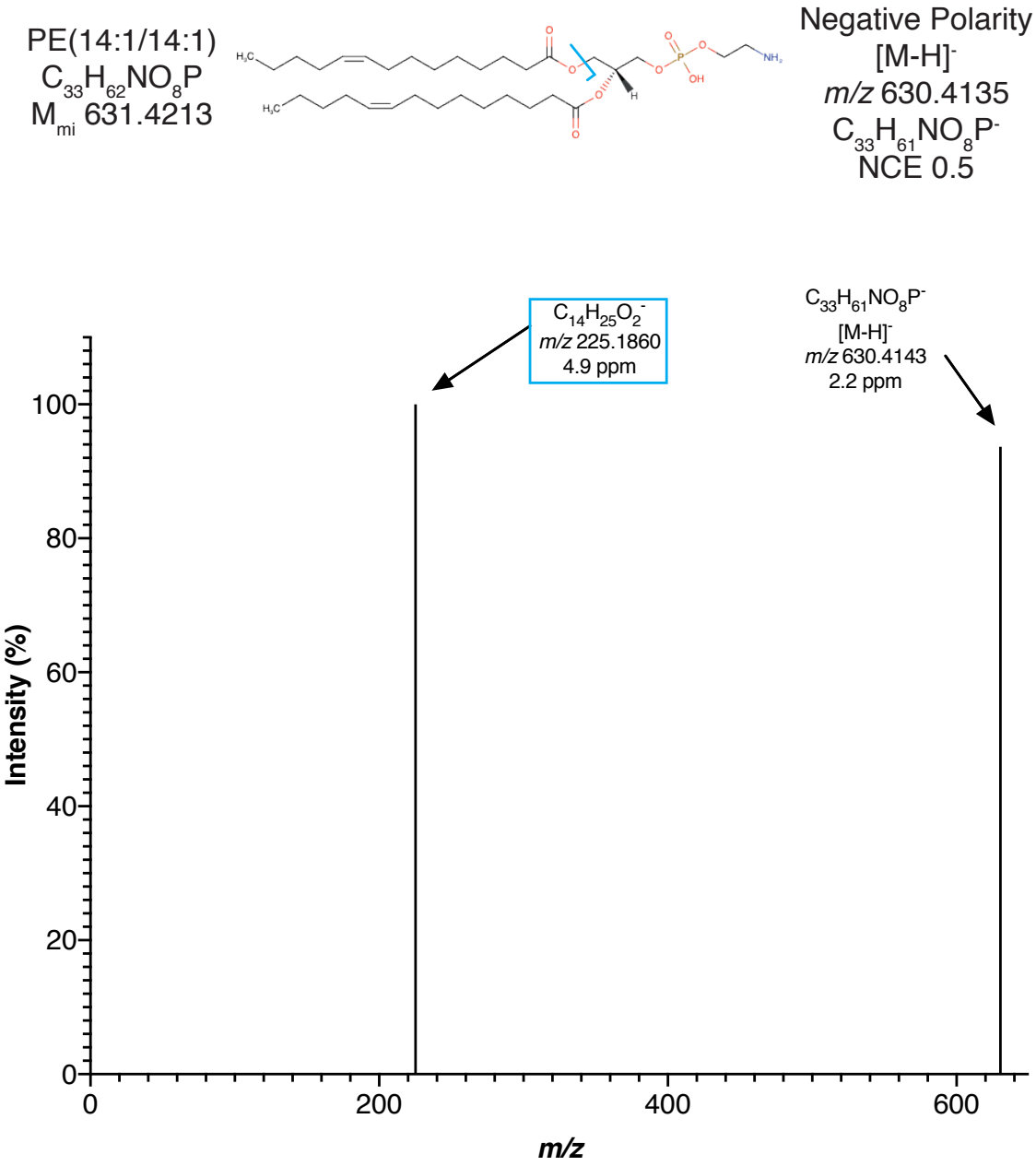

Figure 9.19 OrbiSIMS MS/MS of a Phosphatidylethanolamine standard
Fragmentation patterns of a PE(14:1/14:1) standard from OrbiSIMS analysis run with Orbitrap-based HCD in negative polarity. The fragmented adduct is labelled with its formula and mass.

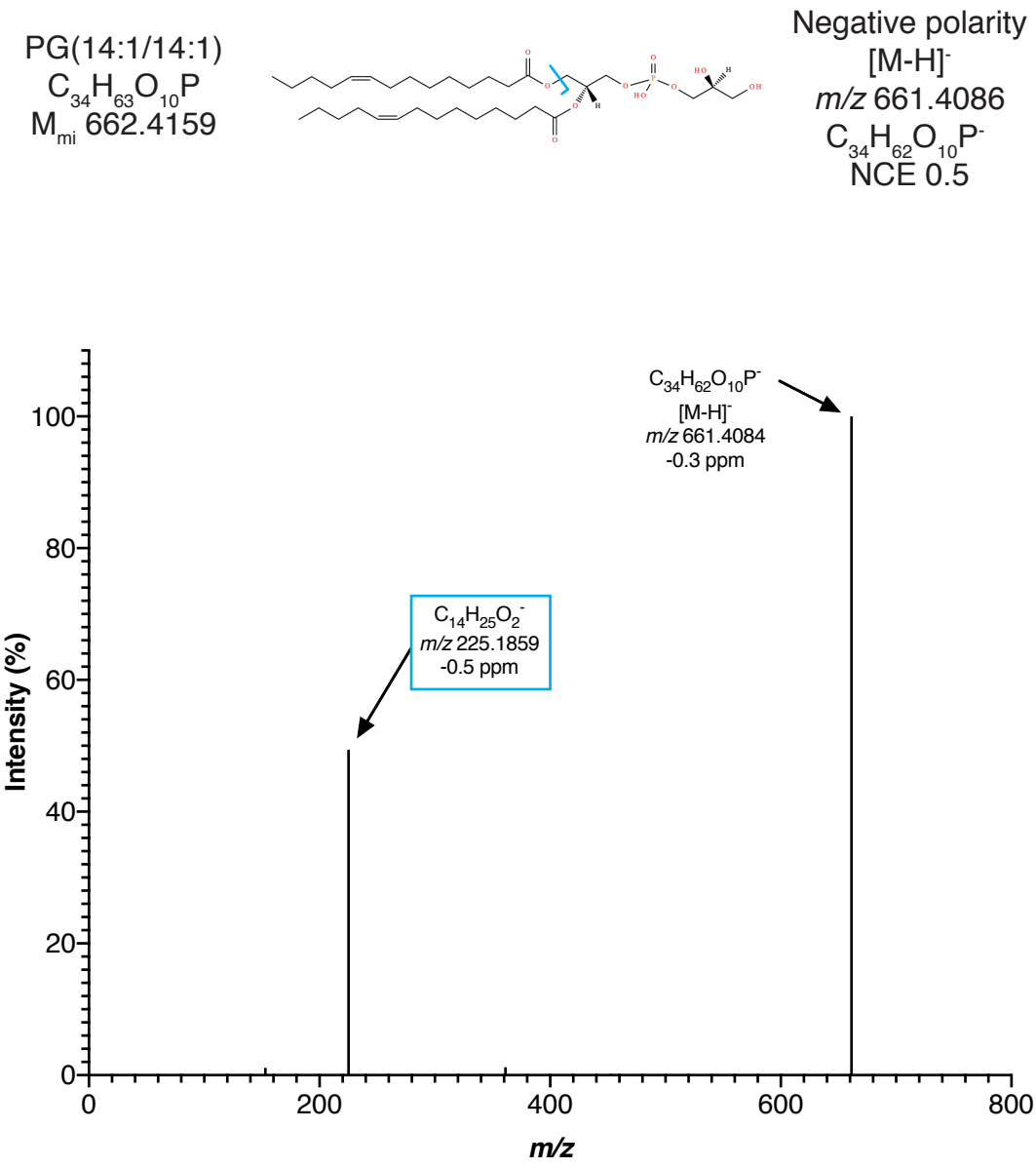

Figure 9.20 OrbiSIMS MS/MS of a Phosphatidylglycerol standard
Fragmentation patterns of a PG(14:1/14:1) standard from OrbiSIMS analysis run with Orbitrap-based HCD in negative polarity. The fragmented adduct is labelled with its formula and mass.

PI(14:1/14:1)
$C_{37}H_{67}O_{13}P$
M_{mi} 750.4319

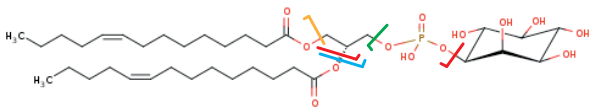

Negative polarity
$[M-H]^-$
m/z 749.4247
$C_{37}H_{66}O_{13}P^-$
NCE 15

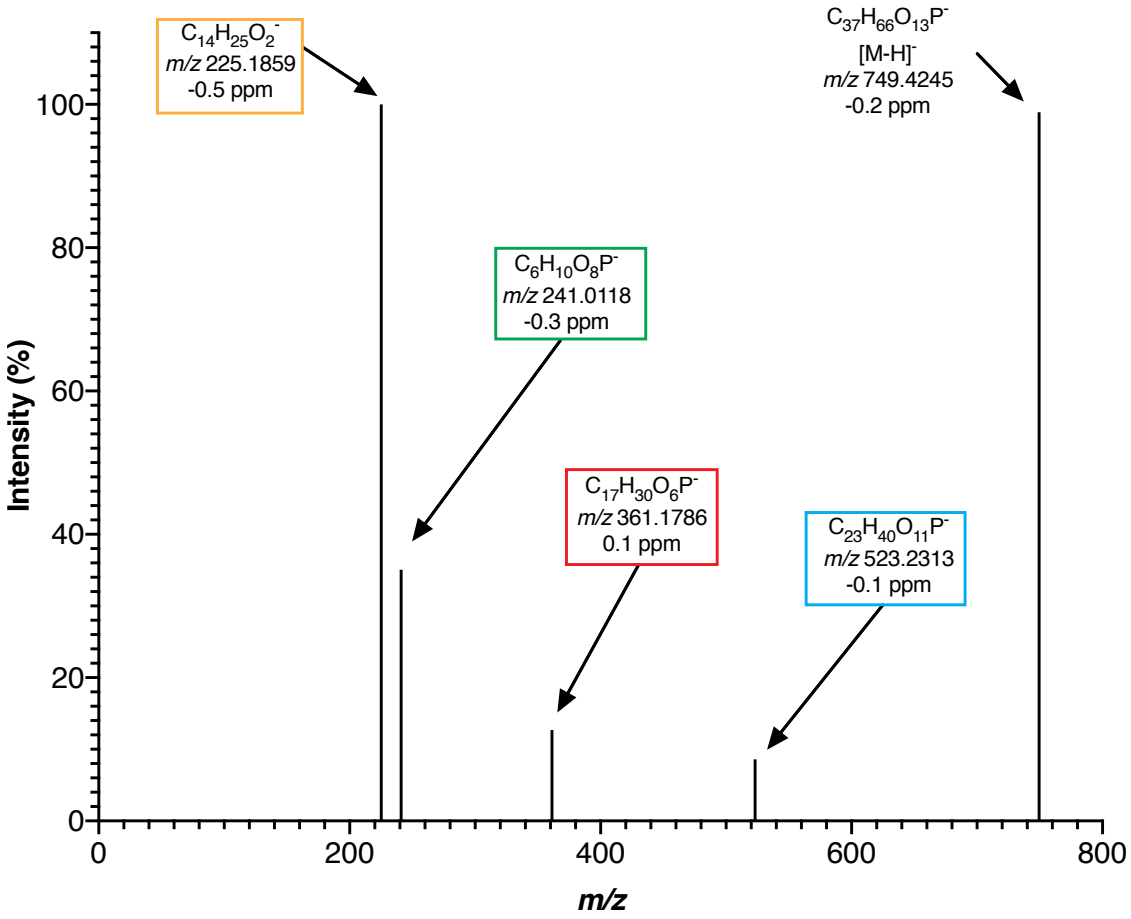

Figure 9.21 OrbiSIMS MS/MS of a Phosphatidylinositol standard
Fragmentation patterns of a PG(14:1/14:1) standard from OrbiSIMS analysis run with Orbitrap-based HCD in negative polarity. The fragmented adduct is labelled with its formula and mass.

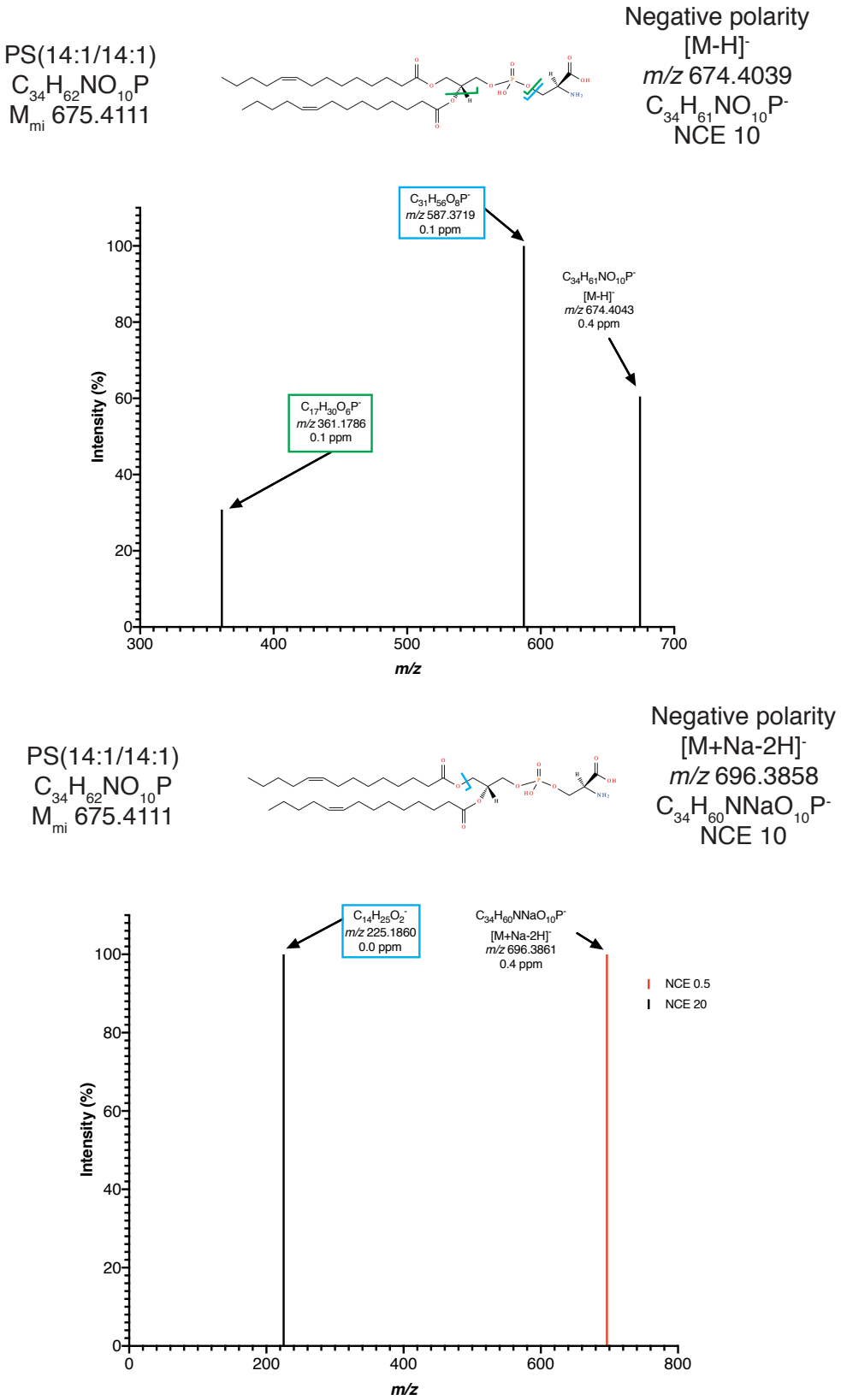

Figure 9.22 OrbiSIMS MS/MS of a Phosphatidylserine standard
Fragmentation patterns of a PS(14:1/14:1) standard from OrbiSIMS analysis run with Orbitrap-based HCD in negative polarity. The fragmented adducts are labelled with their formula and mass.

Table 9.7 Cryo-OrbiSIMS analysis of ASTM reference gas oil

m/z	Putative I.D.	Experimental formula	Adduct	Mass Deviation (ppm)
156.1746	C10:0	$C_{10}H_{22}N^+$	$[M+N]^+$	-0.93
170.1902	C11:0	$C_{11}H_{24}N^+$	$[M+N]^+$	-1.53
184.2059	C12:0	$C_{12}H_{26}N^+$	$[M+N]^+$	-1.04
198.2215	C13:0	$C_{13}H_{28}N^+$	$[M+N]^+$	-1.11
212.2372	C14:0	$C_{14}H_{30}N^+$	$[M+N]^+$	-1.08
226.2528	C15:0	$C_{15}H_{32}N^+$	$[M+N]^+$	-1.06
240.2685	C16:0	$C_{16}H_{34}N^+$	$[M+N]^+$	-1.14
254.2841	C17:0	$C_{17}H_{36}N^+$	$[M+N]^+$	-1.15
268.2997	C18:0	$C_{18}H_{38}N^+$	$[M+N]^+$	-1.17
282.3154	C19:0	$C_{19}H_{40}N^+$	$[M+N]^+$	-1.04
296.3311	C20:0	$C_{20}H_{42}N^+$	$[M+N]^+$	-1.03
310.3467	C21:0	$C_{21}H_{44}N^+$	$[M+N]^+$	-1.13
324.3624	C22:0	$C_{22}H_{46}N^+$	$[M+N]^+$	-0.95
338.3780	C23:0	$C_{23}H_{48}N^+$	$[M+N]^+$	-1.15
352.3936	C24:0	$C_{24}H_{50}N^+$	$[M+N]^+$	-1.17
366.4093	C25:0	$C_{25}H_{52}N^+$	$[M+N]^+$	-1.17
380.4249	C26:0	$C_{26}H_{54}N^+$	$[M+N]^+$	-1.11
394.4406	C27:0	$C_{27}H_{56}N^+$	$[M+N]^+$	-1.03
408.4562	C28:0	$C_{28}H_{58}N^+$	$[M+N]^+$	-1.15
422.4719	C29:0	$C_{29}H_{60}N^+$	$[M+N]^+$	-1.09
436.4876	C30:0	$C_{30}H_{62}N^+$	$[M+N]^+$	-0.99
450.5032	C31:0	$C_{31}H_{64}N^+$	$[M+N]^+$	-0.87
464.5189	C32:0	$C_{32}H_{66}N^+$	$[M+N]^+$	-0.93
478.5345	C33:0	$C_{33}H_{68}N^+$	$[M+N]^+$	-0.87
492.5503	C34:0	$C_{34}H_{70}N^+$	$[M+N]^+$	-0.74
506.5659	C35:0	$C_{35}H_{72}N^+$	$[M+N]^+$	-0.80
520.5816	C36:0	$C_{36}H_{74}N^+$	$[M+N]^+$	-0.75
534.5971	C37:0	$C_{37}H_{76}N^+$	$[M+N]^+$	-0.92
548.6128	C38:0	$C_{38}H_{78}N^+$	$[M+N]^+$	-0.76
562.6284	C39:0	$C_{39}H_{80}N^+$	$[M+N]^+$	-0.95
576.6442	C40:0	$C_{40}H_{82}N^+$	$[M+N]^+$	-0.63
590.6597	C41:0	$C_{41}H_{84}N^+$	$[M+N]^+$	-0.96
604.6755	C42:0	$C_{42}H_{86}N^+$	$[M+N]^+$	-0.71
618.6911	C43:0	$C_{43}H_{88}N^+$	$[M+N]^+$	-0.71
632.7067	C44:0	$C_{44}H_{90}N^+$	$[M+N]^+$	-0.90
646.7224	C45:0	$C_{45}H_{92}N^+$	$[M+N]^+$	-0.72
660.7382	C46:0	$C_{46}H_{94}N^+$	$[M+N]^+$	-0.59
674.7537	C47:0	$C_{47}H_{96}N^+$	$[M+N]^+$	-0.75
688.7692	C48:0	$C_{48}H_{98}N^+$	$[M+N]^+$	-0.96
702.7850	C49:0	$C_{49}H_{100}N^+$	$[M+N]^+$	-0.77
716.8005	C50:0	$C_{50}H_{102}N^+$	$[M+N]^+$	-0.93
730.8162	C51:0	$C_{51}H_{104}N^+$	$[M+N]^+$	-0.86
744.8319	C52:0	$C_{52}H_{106}N^+$	$[M+N]^+$	-0.87

9.3 Chapter 4 Supplementary Information

Aldehydes/Ketones

Observed *m/z*	Putative I.D.	Formula (observed)	Polarity	OrbiSIMS Adduct	Mass deviation (δppm)	Gooseberry	Apple blossom	Asparagus	Kiwi leaf	Tomato leaf	Pine needle	Victoria plum	Golden Gage plum	Gooseberry leaf	Validation?
256.263	C16:1	$C_{16}H_{34}NO^+$	Positive	$[M+NH_4]^+$	-0.9	-	-	-	-	✓	-	-	-	-	-
284.295	C18:1	$C_{18}H_{38}NO^+$	Positive	$[M+NH_4]^+$	-0.8	-	-	-	-	✓	-	-	-	-	-
296.295	C19:2	$C_{19}H_{38}NO^+$	Positive	$[M+NH_4]^+$	-0.6	-	-	-	-	✓	-	-	-	-	-
312.326	C20:1	$C_{20}H_{42}NO^+$	Positive	$[M+NH_4]^+$	-0.8	-	-	-	-	✓	-	-	-	-	-
340.357	C22:1	$C_{22}H_{46}NO^+$	Positive	$[M+NH_4]^+$	-0.8	-	-	-	-	✓	-	-	-	-	-
354.373	C23:1	$C_{23}H_{48}NO^+$	Positive	$[M+NH_4]^+$	-0.7	-	-	-	-	✓	-	-	-	-	-
366.373	C24:2	$C_{24}H_{48}NO^+$	Positive	$[M+NH_4]^+$	-0.7	-	-	-	-	✓	-	-	-	-	-
368.389	C24:1	$C_{24}H_{50}NO^+$	Positive	$[M+NH_4]^+$	-0.8	-	-	-	-	✓	-	-	-	-	-
370.404	C24:0	$C_{24}H_{52}NO^+$	Positive	$[M+NH_4]^+$	-0.9	-	-	-	-	✓	-	-	-	-	-
380.389	C25:2	$C_{25}H_{50}NO^+$	Positive	$[M+NH_4]^+$	-0.8	-	-	-	-	✓	-	-	-	-	-
382.404	C25:1	$C_{25}H_{52}NO^+$	Positive	$[M+NH_4]^+$	-0.7	-	-	-	-	✓	-	-	-	-	-
384.420	C25:0	$C_{25}H_{54}NO^+$	Positive	$[M+NH_4]^+$	-0.7	-	-	-	-	✓	-	-	-	-	-
392.389	C26:3	$C_{26}H_{50}NO^+$	Positive	$[M+NH_4]^+$	-0.6	-	-	-	-	✓	-	-	-	-	-
394.404	C26:2	$C_{26}H_{52}NO^+$	Positive	$[M+NH_4]^+$	-0.7	-	-	✓	-	✓	-	-	-	-	-
396.420	C26:1	$C_{26}H_{54}NO^+$	Positive	$[M+NH_4]^+$	-0.7	✓	-	✓	-	✓	-	-	-	-	-
398.436	C26:0	$C_{26}H_{56}NO^+$	Positive	$[M+NH_4]^+$	-0.8	-	-	✓	-	✓	-	-	-	-	-
408.420	C27:2	$C_{27}H_{54}NO^+$	Positive	$[M+NH_4]^+$	-0.5	✓	-	-	-	✓	-	-	-	-	-
410.436	C27:1	$C_{27}H_{56}NO^+$	Positive	$[M+NH_4]^+$	-0.6	-	-	-	-	✓	-	-	-	-	-
412.451	C27:0	$C_{27}H_{58}NO^+$	Positive	$[M+NH_4]^+$	-0.8	-	-	-	-	✓	-	-	-	-	-
420.420	C28:3	$C_{28}H_{54}NO^+$	Positive	$[M+NH_4]^+$	-0.5	✓	-	-	-	-	-	-	-	-	-
422.436	C28:2	$C_{28}H_{56}NO^+$	Positive	$[M+NH_4]^+$	-0.6	✓	-	✓	-	✓	-	-	-	-	-
424.451	C28:1	$C_{28}H_{58}NO^+$	Positive	$[M+NH_4]^+$	-0.7	✓	-	✓	-	✓	-	-	-	✓	-
426.467	C28:0	$C_{28}H_{60}NO^+$	Positive	$[M+NH_4]^+$	-0.7	-	-	-	-	✓	-	-	-	-	-
434.436	C29:3	$C_{29}H_{56}NO^+$	Positive	$[M+NH_4]^+$	-0.4	✓	-	-	-	-	-	-	-	-	-
436.451	C29:2	$C_{29}H_{58}NO^+$	Positive	$[M+NH_4]^+$	-0.4	✓	-	-	-	-	✓	-	-	-	-
438.467	C29:1	$C_{29}H_{60}NO^+$	Positive	$[M+NH_4]^+$	-0.6	✓	-	✓	-	✓	✓	-	-	-	-
440.483	C29:0	$C_{29}H_{62}NO^+$	Positive	$[M+NH_4]^+$	-0.6	-	-	-	-	✓	✓	✓	✓	-	-
452.483	C30:1	$C_{30}H_{62}NO^+$	Positive	$[M+NH_4]^+$	-0.6	✓	-	✓	-	✓	-	-	-	-	-
454.498	C30:0	$C_{30}H_{64}NO^+$	Positive	$[M+NH_4]^+$	-0.6	-	-	-	-	✓	-	-	-	-	-
466.498	C31:1	$C_{31}H_{64}NO^+$	Positive	$[M+NH_4]^+$	-0.6	-	-	✓	-	-	-	-	-	-	-
480.514	C32:1	$C_{32}H_{66}NO^+$	Positive	$[M+NH_4]^+$	-0.5	-	-	-	-	✓	-	-	-	-	-
508.545	C34:1	$C_{34}H_{70}NO^+$	Positive	$[M+NH_4]^+$	-0.4	-	-	-	-	✓	-	-	-	-	-

Observed *m/z*	Putative I.D.	Formula (observed)	Polarity	OrbiSIMS Adduct	Mass deviation (δppm)	Gooseberry	Apple blossom	Asparagus	Kiwi leaf	Tomato leaf	Pine needle	Victoria plum	Golden Gage plum	Gooseberry leaf	Validation?
197.191	C13:0	$C_{13}H_{25}O$	Negative	$[M-H]^-$	-0.5	-	-	-	-	-	✓	-	-	-	-
209.191	C14:1	$C_{14}H_{25}O$	Negative	$[M-H]^-$	-0.4	-	-	-	-	-	✓	-	-	-	-
223.207	C15:1	$C_{15}H_{27}O$	Negative	$[M-H]^-$	1.2	-	-	-	-	-	✓	-	-	-	-
265.254	C18:1	$C_{18}H_{33}O$	Negative	$[M-H]^-$	1.2	-	-	-	-	-	✓	-	-	-	-
281.285	C19:1	$C_{19}H_{33}O$	Negative	$[M-H]^-$	0.0	-	-	-	-	-	✓	-	-	-	-
293.285	C20:1	$C_{20}H_{37}O$	Negative	$[M-H]^-$	0.0	-	-	-	-	-	✓	-	-	-	-
307.301	C21:1	$C_{21}H_{39}O$	Negative	$[M-H]^-$	1.2	-	-	-	-	-	✓	-	-	-	-
309.316	C21:0	$C_{21}H_{41}O$	Negative	$[M-H]^-$	-0.9	-	-	-	-	-	✓	-	-	-	-
335.332	C23:1	$C_{23}H_{43}O$	Negative	$[M-H]^-$	0.2	-	-	-	-	-	✓	-	-	-	-
351.363	C24:0	$C_{24}H_{47}O$	Negative	$[M-H]^-$	-0.7	-	-	✓	-	✓	✓	-	-	-	-
365.379	C25:1	$C_{25}H_{49}O$	Negative	$[M-H]^-$	0.3	-	-	-	-	-	✓	-	-	-	-
379.395	C26:0	$C_{26}H_{51}O$	Negative	$[M-H]^-$	-0.7	✓	-	✓	-	✓	✓	-	-	-	-
391.395	C27:1	$C_{27}H_{51}O$	Negative	$[M-H]^-$	1.2	-	-	-	-	-	✓	-	-	-	-
393.410	C27:0	$C_{27}H_{53}O$	Negative	$[M-H]^-$	-0.4	✓	-	-	-	-	✓	-	-	-	-
407.426	C28:0	$C_{28}H_{55}O$	Negative	$[M-H]^-$	-0.7	✓	-	✓	-	-	✓	-	-	-	-
419.426	C29:1	$C_{29}H_{55}O$	Negative	$[M-H]^-$	0.6	-	-	-	-	-	✓	-	-	-	-
421.442	C29:0	$C_{29}H_{57}O$	Negative	$[M-H]^-$	1.2	-	-	-	-	-	✓	-	-	-	-
435.457	C30:0	$C_{30}H_{59}O$	Negative	$[M-H]^-$	-0.8	✓	-	-	-	-	✓	-	-	-	-
449.473	C31:0	$C_{31}H_{61}O$	Negative	$[M-H]^-$	0.5	-	-	-	-	-	✓	-	-	-	-
463.488	C32:0	$C_{32}H_{63}O$	Negative	$[M-H]^-$	-1.0	-	-	-	-	-	✓	-	-	-	-
477.504	C33:0	$C_{33}H_{65}O$	Negative	$[M-H]^-$	-0.2	-	-	-	-	-	✓	-	-	-	-

Table 9.8 Cryo-OrbiSIMS Plant Aldehydes/Ketones

Polycyclic aromatic hydrocarbons (PAHs)

Observed *m/z*	Putative I.D.	Formula (observed)	Polarity	OrbiSIMS Adduct	Mass deviation (δppm)	Gooseberry	Apple blossom	Asparagus	Kiwi leaf	Tomato leaf	Pine needle	Victoria plum	Golden Gage plum	Gooseberry leaf	Validation?
130.065		$C_9H_8N^+$	Positive	$[M+N]^+$	-0.7	-	-	-	-	✓	-	✓	✓	-	-
142.065		$C_{10}H_8N^+$	Positive	$[M+N]^+$	-0.7	-	-	-	-	✓	-	-	-	-	-
154.065		$C_{11}H_8N^+$	Positive	$[M+N]^+$	-1.0	-	-	-	-	✓	-	✓	-	✓	-
156.081		$C_{11}H_{10}N^+$	Positive	$[M+N]^+$	-0.7	-	-	-	-	✓	-	-	-	-	-
168.081		$C_{12}H_{10}N^+$	Positive	$[M+N]^+$	-0.8	-	-	-	-	✓	-	-	-	-	-
180.081		$C_{13}H_{10}N^+$	Positive	$[M+N]^+$	-0.9	-	-	-	-	✓	-	-	-	✓	-
190.065		$C_{14}H_8N^+$	Positive	$[M+N]^+$	-0.7	-	-	-	-	-	-	-	-	✓	-
194.096		$C_{14}H_{12}N^+$	Positive	$[M+N]^+$	-0.5	-	-	-	-	✓	-	-	-	-	-
204.081		$C_{15}H_{10}N^+$	Positive	$[M+N]^+$	1.1	-	-	-	-	-	-	-	-	✓	-
216.081		$C_{16}H_{10}N^+$	Positive	$[M+N]^+$	1.0	-	-	-	-	-	-	-	-	✓	-
254.096		$C_{19}H_{12}N^+$	Positive	$[M+N]^+$	-0.9	-	-	-	-	-	-	-	-	✓	-

Linear/branched chain hydrocarons

Observed *m/z*	Putative I.D.	Formula (observed)	Polarity	OrbiSIMS adduct	Mass deviation (δppm)	Gooseberry		Apple blossom		Asparagus		Kiwi leaf		Tomato leaf		Pine needle		Victoria plum		Golden Gage plum		Gooseberry leaf	
						cryo-OrbiSIMS	GC-MS	cryo-OrbiSIMS	GC-MS	cryo-OrbiSIMS	GC-MS	cryo-OrbiSIMS	GC-MS	cryo-OrbiSIMS	GC-MS	cryo-OrbiSIMS	GC-MS	cryo-OrbiSIMS	GC-MS	cryo-OrbiSIMS	GC-MS	cryo-OrbiSIMS	GC-MS
254.284	C17:0	$C_{17}H_{36}N^+$	Positive	$[M+N]^+$	-0.9	✓	-	-	-	-	-	-	-	-	-	-	-	-	-	-	-	-	-
266.284	C18:1	$C_{18}H_{36}N^+$	Positive	$[M+N]^+$	-0.7	✓	-	-	-	-	-	-	-	-	-	-	-	-	-	-	-	-	-
268.300	C18:0	$C_{18}H_{38}N^+$	Positive	$[M+N]^+$	-0.8	✓	-	-	-	-	-	-	-	✓	-	-	-	✓	-	-	-	-	-
280.300	C19:1	$C_{19}H_{38}N^+$	Positive	$[M+N]^+$	-0.8	✓	-	-	-	-	-	-	-	-	-	-	-	✓	-	-	-	-	-
282.316	C19:0	$C_{19}H_{40}N^+$	Positive	$[M+N]^+$	-0.7	-	-	-	-	-	-	-	-	✓	-	-	-	-	✓	-	-	-	-
294.316	C20:1	$C_{20}H_{40}N^+$	Positive	$[M+N]^+$	-0.7	✓	-	-	-	-	-	-	-	-	-	-	-	-	-	-	-	-	-
296.331	C20:0	$C_{20}H_{42}N^+$	Positive	$[M+N]^+$	-0.8	✓	-	-	-	-	-	-	-	✓	-	-	-	-	-	-	-	-	-
308.331	C21:1	$C_{21}H_{42}N^+$	Positive	$[M+N]^+$	-0.8	✓	-	-	-	-	-	-	-	-	-	-	-	-	-	-	-	-	-
310.347	C21:0	$C_{21}H_{44}N^+$	Positive	$[M+N]^+$	-0.8	✓	-	-	-	-	-	-	-	✓	-	-	-	-	✓	-	✓	-	✓
322.347	C22:1	$C_{22}H_{44}N^+$	Positive	$[M+N]^+$	-0.9	✓	-	-	-	-	-	-	-	-	-	-	-	-	-	-	-	-	-
324.362	C22:0	$C_{22}H_{46}N^+$	Positive	$[M+N]^+$	-0.8	✓	-	✓	-	-	-	-	-	✓	-	-	✓	-	-	-	-	-	-
336.362	C23:1	$C_{23}H_{46}N^+$	Positive	$[M+N]^+$	-0.9	✓	-	✓	-	-	-	-	-	-	-	-	-	-	-	-	-	-	-
338.378	C23:0	$C_{23}H_{48}N^+$	Positive	$[M+N]^+$	-1.0	✓	✓	✓	-	-	-	-	-	✓	-	-	✓	-	✓	-	✓	-	✓
350.378	C24:1	$C_{24}H_{46}N^+$	Positive	$[M+N]^+$	-0.8	✓	-	-	-	-	-	-	-	✓	✓	-	-	-	-	-	-	-	-
352.394	C24:0	$C_{24}H_{48}N^+$	Positive	$[M+N]^+$	-0.9	✓	-	✓	-	✓	-	-	-	✓	-	-	-	✓	-	-	-	-	-
364.394	C25:1	$C_{25}H_{46}N^+$	Positive	$[M+N]^+$	-0.8	✓	-	-	-	-	-	-	-	✓	-	-	-	-	-	-	-	-	-
366.409	C25:0	$C_{25}H_{48}N^+$	Positive	$[M+N]^+$	-0.9	✓	✓	✓	-	✓	-	-	-	✓	✓	-	✓	-	✓	-	✓	✓	✓
378.409	C26:1	$C_{26}H_{48}N^+$	Positive	$[M+N]^+$	-0.8	✓	-	-	-	✓	-	-	-	✓	-	-	-	-	-	-	-	-	-
380.425	C26:0	$C_{26}H_{50}N^+$	Positive	$[M+N]^+$	-0.9	✓	-	-	-	✓	-	-	-	✓	-	-	-	✓	-	-	-	✓	-
392.425	C27:1	$C_{27}H_{50}N^+$	Positive	$[M+N]^+$	-0.6	✓	-	-	-	-	-	-	-	-	-	-	-	-	-	-	-	✓	-
394.441	C27:0	$C_{27}H_{52}N^+$	Positive	$[M+N]^+$	-0.8	✓	✓	✓	-	✓	-	✓	-	✓	✓	-	✓	-	✓	-	✓	✓	✓
404.425	C28:2	$C_{28}H_{52}N^+$	Positive	$[M+N]^+$	-0.6	✓	-	-	-	-	-	-	-	-	-	-	-	-	-	-	-	-	-
406.441	C28:1	$C_{28}H_{54}N^+$	Positive	$[M+N]^+$	-0.7	✓	-	-	-	✓	-	-	-	-	-	-	-	✓	-	✓	-	✓	-
408.456	C28:0	$C_{28}H_{56}N^+$	Positive	$[M+N]^+$	-0.7	✓	-	✓	-	✓	-	-	-	✓	-	-	-	-	-	-	-	✓	-
418.441	C29:2	$C_{29}H_{56}N^+$	Positive	$[M+N]^+$	-0.6	✓	-	-	-	-	-	-	-	-	-	-	-	✓	-	-	-	-	-
420.456	C29:1	$C_{29}H_{58}N^+$	Positive	$[M+N]^+$	-0.8	✓	-	✓	-	-	-	-	-	-	-	✓	-	✓	-	✓	-	✓	-
422.472	C29:0	$C_{29}H_{60}N^+$	Positive	$[M+N]^+$	-0.7	✓	✓	✓	-	-	-	✓	-	✓	✓	✓	✓	✓	✓	✓	✓	✓	✓
434.472	C30:1	$C_{30}H_{60}N^+$	Positive	$[M+N]^+$	-0.5	✓	-	-	-	-	-	-	-	-	-	-	-	✓	-	-	-	✓	-
436.488	C30:0	$C_{30}H_{62}N^+$	Positive	$[M+N]^+$	-0.6	✓	✓	-	-	✓	-	✓	-	✓	✓	-	-	✓	✓	✓	✓	✓	✓
448.488	C31:1	$C_{31}H_{62}N^+$	Positive	$[M+N]^+$	-0.6	✓	-	-	-	-	-	✓	-	-	-	-	-	-	-	-	-	✓	-
450.503	C31:0	$C_{31}H_{64}N^+$	Positive	$[M+N]^+$	-0.6	✓	✓	-	-	-	-	✓	-	-	✓	-	-	-	✓	-	-	✓	✓
462.503	C32:1	$C_{32}H_{64}N^+$	Positive	$[M+N]^+$	-0.5	✓	-	-	-	-	-	✓	-	-	-	-	-	-	-	-	-	✓	-
464.519	C32:0	$C_{32}H_{66}N^+$	Positive	$[M+N]^+$	-0.6	✓	✓	-	-	-	-	✓	-	-	✓	-	-	-	-	-	✓	✓	-
476.519	C33:1	$C_{33}H_{66}N^+$	Positive	$[M+N]^+$	-0.4	-	-	-	-	-	-	✓	-	-	-	-	-	-	-	-	-	✓	-
478.535	C33:0	$C_{33}H_{68}N^+$	Positive	$[M+N]^+$	-0.6	-	✓	-	-	-	-	✓	-	-	✓	-	-	-	-	-	-	✓	-

Table 9.9 Cryo-OrbiSIMS plant linear/branched chain and polycyclic aromatic hydrocarbons

Table 9.10 Cryo-OrbiSIMS plant linear/branched chain fatty acids/wax esters

Linear/branched chain Fatty acids/Wax esters

Observed *m/z*	Putative I.D.	Formula (observed)	Polarity	OrbiSIMS adduct	Mass deviation (δppm)	Gooseberry	Apple blossom	Asparagus	Kiwi leaf	Tomato leaf	Pine needle	Victoria plum	Golden Gage plum	Gooseberry leaf	Validation?
255.232	C16:1	$C_{16}H_{31}O_2^+$	Positive	$[M+H]^+$	0.6	-	-	-	-	-	✓	-	-	-	-
297.279	C19:1	$C_{19}H_{37}O_2^+$	Positive	$[M+H]^+$	0.6	-	-	-	-	-	-	-	-	✓	-
325.310	C21:1	$C_{21}H_{41}O_2^+$	Positive	$[M+H]^+$	-0.3	-	-	-	-	-	-	-	-	✓	-
337.346	C23:0	$C_{23}H_{45}O^+$	Positive	$[M+H-H_2O]^+$	-1.5	-	-	-	-	-	✓	-	-	-	-
397.404	C26:0	$C_{26}H_{53}O_2^+$	Positive	$[M+H]^+$	0.0	-	-	-	-	-	-	-	-	✓	-
419.386	C26:0	$C_{26}H_{52}NaO_2^+$	Positive	$[M+Na]^+$	0.1	-	-	-	-	✓	-	-	-	-	-
425.435	C28:0	$C_{28}H_{57}O_2^+$	Positive	$[M+H]^+$	-0.7	-	-	-	-	-	-	-	-	✓	-
437.435	C29:1	$C_{29}H_{57}O_2^+$	Positive	$[M+H]^+$	-0.7	-	-	-	-	-	-	✓	✓	-	-
439.451	C29:0	$C_{29}H_{59}O_2^+$	Positive	$[M+H]^+$	0.1	-	-	-	-	-	✓	✓	-	-	-
447.417	C28:0	$C_{28}H_{52}NaO_2^+$	Positive	$[M+Na]^+$	-0.6	-	-	-	-	✓	-	-	-	-	-
453.467	C30:0	$C_{30}H_{61}O_2^+$	Positive	$[M+H]^+$	0.9	-	-	-	-	-	-	-	-	✓	-
473.435	C32:4	$C_{32}H_{57}O_2^+$	Positive	$[M+Na]^+$	-0.7	-	-	-	-	-	✓	-	-	-	-
481.498	C32:0	$C_{32}H_{65}O_2^+$	Positive	$[M+H]^+$	0.2	-	-	-	-	-	-	-	-	✓	-

Observed *m/z*	Putative I.D.	Formula (observed)	Polarity	OrbiSIMS Adduct	Mass deviation (δppm)	Gooseberry	Apple blossom	Asparagus	Kiwi leaf	Tomato leaf	Pine needle	Victoria plum	Golden Gage plum	Gooseberry leaf	Validation?
169.123	C10:1	$C_{10}H_{17}O_2^-$	Negative	$[M-H]^-$	-1.3	-	✓	✓	-	-	-	-	-	-	-
171.139	C10:0	$C_{10}H_{19}O_2^-$	Negative	$[M-H]^-$	-0.3	-	-	-	-	-	✓	-	-	-	-
183.139	C11:1	$C_{11}H_{19}O_2^-$	Negative	$[M-H]^-$	-1.6	✓	✓	✓	-	-	✓	-	-	-	-
185.155	C11:0	$C_{11}H_{21}O_2^-$	Negative	$[M-H]^-$	1.6	-	-	-	-	-	✓	-	-	-	-
195.139	C12:2	$C_{12}H_{19}O_2^-$	Negative	$[M-H]^-$	-0.3	-	-	-	-	-	✓	-	-	-	-
197.155	C12:1	$C_{12}H_{21}O_2^-$	Negative	$[M-H]^-$	-1.4	✓	✓	✓	-	-	✓	-	-	-	-
199.170	C12:0	$C_{12}H_{23}O_2^-$	Negative	$[M-H]^-$	-1.8	-	-	-	-	-	✓	-	-	-	-
211.170	C13:1	$C_{13}H_{23}O_2^-$	Negative	$[M-H]^-$	-1.2	✓	✓	✓	-	-	✓	-	-	-	-
213.186	C13:0	$C_{13}H_{25}O_2^-$	Negative	$[M-H]^-$	0.0	-	-	-	-	-	✓	-	-	-	-
223.170	C14:2	$C_{14}H_{23}O_2^-$	Negative	$[M-H]^-$	-1.6	-	-	-	-	-	✓	-	-	-	-
225.186	C14:1	$C_{14}H_{25}O_2^-$	Negative	$[M-H]^-$	-1.2	✓	✓	✓	-	-	✓	-	-	-	-
227.202	C14:0	$C_{14}H_{27}O_2^-$	Negative	$[M-H]^-$	-1.2	-	-	✓	-	-	✓	-	-	-	-
239.202	C15:1	$C_{15}H_{27}O_2^-$	Negative	$[M-H]^-$	-1.1	✓	✓	✓	-	-	✓	-	-	-	-
241.217	C15:0	$C_{15}H_{29}O_2^-$	Negative	$[M-H]^-$	-1.1	✓	✓	✓	-	-	✓	-	-	-	-
251.202	C16:2	$C_{16}H_{27}O_2^-$	Negative	$[M-H]^-$	1.4	-	-	-	-	-	✓	-	-	-	-
251.238	C17:0	$C_{17}H_{31}O^-$	Negative	$[M-H-H_2O]^-$	-0.2	-	-	-	-	-	✓	-	-	-	-
253.217	C16:1	$C_{16}H_{29}O_2^-$	Negative	$[M-H]^-$	-1.0	✓	✓	✓	-	-	✓	-	-	-	-
255.233	C16:0	$C_{16}H_{31}O_2^-$	Negative	$[M-H]^-$	-1.0	✓	✓	✓	-	-	✓	-	-	-	-
267.233	C17:1	$C_{17}H_{31}O_2^-$	Negative	$[M-H]^-$	-1.0	✓	-	-	-	-	✓	-	-	-	-
269.249	C17:0	$C_{17}H_{33}O_2^-$	Negative	$[M-H]^-$	1.5	-	-	-	-	-	✓	-	-	-	-
277.217	C18:3	$C_{18}H_{29}O_2^-$	Negative	$[M-H]^-$	-1.1	-	✓	-	-	-	-	-	-	-	-
279.233	C18:2	$C_{18}H_{31}O_2^-$	Negative	$[M-H]^-$	-1.1	-	✓	✓	-	-	✓	-	-	-	-
281.248	C18:1	$C_{18}H_{33}O_2^-$	Negative	$[M-H]^-$	-1.1	✓	✓	-	-	-	✓	-	-	-	-
283.264	C18:0	$C_{18}H_{35}O_2^-$	Negative	$[M-H]^-$	-1.0	✓	✓	✓	-	-	✓	-	-	-	-
291.269	C20:1	$C_{20}H_{35}O^-$	Negative	$[M-H-H_2O]^-$	-1.2	-	-	-	-	-	✓	-	-	-	-
295.264	C19:1	$C_{19}H_{35}O_2^-$	Negative	$[M-H]^-$	-1.1	✓	-	-	-	-	✓	-	-	-	-
297.280	C19:0	$C_{19}H_{37}O_2^-$	Negative	$[M-H]^-$	0.3	-	-	-	-	-	✓	-	-	-	-
307.264	C20:2	$C_{20}H_{35}O_2^-$	Negative	$[M-H]^-$	-0.8	-	-	-	-	-	✓	-	-	-	-
309.280	C20:1	$C_{20}H_{37}O_2^-$	Negative	$[M-H]^-$	-0.8	✓	-	✓	-	-	✓	-	-	-	-
311.296	C20:0	$C_{20}H_{39}O_2^-$	Negative	$[M-H]^-$	-0.7	✓	-	✓	-	-	✓	-	-	-	-
319.300	C22:1	$C_{22}H_{39}O^-$	Negative	$[M-H-H_2O]^-$	-2.0	-	-	-	-	-	✓	-	-	-	-
321.316	C22:0	$C_{22}H_{41}O^-$	Negative	$[M-H]^-$	-0.9	-	-	-	-	-	✓	-	-	-	-
323.295	C21:1	$C_{21}H_{39}O_2^-$	Negative	$[M-H]^-$	-1.7	-	-	-	-	-	✓	-	-	-	-
325.311	C21:0	$C_{21}H_{41}O_2^-$	Negative	$[M-H]^-$	-0.6	-	-	-	-	-	✓	-	-	-	-
335.295	C22:2	$C_{22}H_{39}O_2^-$	Negative	$[M-H]^-$	-1.6	-	-	-	-	-	✓	-	-	-	-
337.311	C22:1	$C_{22}H_{41}O_2^-$	Negative	$[M-H]^-$	-0.5	✓	-	✓	-	-	✓	-	-	-	-
339.327	C22:0	$C_{22}H_{43}O_2^-$	Negative	$[M-H]^-$	-1.0	✓	✓	✓	-	✓	✓	-	-	-	-
347.332	C24:1	$C_{24}H_{43}O^-$	Negative	$[M-H-H_2O]^-$	0.2	-	-	-	-	-	✓	-	-	-	-
349.348	C24:0	$C_{24}H_{45}O^-$	Negative	$[M-H-H_2O]^-$	1.2	-	-	-	-	-	✓	-	-	-	-
351.327	C23:1	$C_{23}H_{43}O_2^-$	Negative	$[M-H]^-$	0.4	-	-	-	-	-	✓	-	-	-	-
353.342	C23:0	$C_{23}H_{45}O_2^-$	Negative	$[M-H]^-$	-0.7	-	✓	-	-	-	✓	-	-	-	-
363.327	C24:2	$C_{24}H_{43}O_2^-$	Negative	$[M-H]^-$	-0.4	-	-	✓	-	-	✓	-	-	-	-
365.342	C24:1	$C_{24}H_{45}O_2^-$	Negative	$[M-H]^-$	-0.9	✓	✓	✓	-	✓	✓	-	-	-	-
367.358	C24:0	$C_{24}H_{47}O_2^-$	Negative	$[M-H]^-$	-0.9	✓	✓	✓	✓	✓	✓	-	-	-	-
377.379	C26:0	$C_{26}H_{49}O^-$	Negative	$[M-H-H_2O]^-$	0.3	-	-	-	-	-	✓	-	-	-	-
379.358	C25:1	$C_{25}H_{47}O_2^-$	Negative	$[M-H]^-$	-0.6	✓	-	✓	-	-	✓	-	-	-	-
381.374	C25:0	$C_{25}H_{49}O_2^-$	Negative	$[M-H]^-$	-0.6	✓	✓	✓	-	✓	✓	-	-	-	-
391.358	C26:2	$C_{26}H_{47}O_2^-$	Negative	$[M-H]^-$	-0.4	-	-	-	-	-	✓	-	-	-	-
393.374	C26:1	$C_{26}H_{49}O_2^-$	Negative	$[M-H]^-$	-0.4	✓	-	✓	-	✓	✓	-	-	-	-
395.389	C26:0	$C_{26}H_{51}O_2^-$	Negative	$[M-H]^-$	-0.9	✓	✓	✓	✓	✓	✓	-	-	-	-
405.410	C28:0	$C_{28}H_{53}O^-$	Negative	$[M-H-H_2O]^-$	-0.5	-	-	-	-	-	✓	-	-	-	-
407.389	C27:1	$C_{27}H_{51}O_2^-$	Negative	$[M-H]^-$	-0.7	✓	-	✓	-	-	✓	-	-	-	-
409.405	C27:0	$C_{27}H_{53}O_2^-$	Negative	$[M-H]^-$	-0.7	✓	-	✓	-	✓	✓	-	-	-	-
421.405	C28:1	$C_{28}H_{53}O_2^-$	Negative	$[M-H]^-$	-0.4	✓	-	✓	-	✓	✓	-	-	-	-
423.421	C28:0	$C_{28}H_{55}O_2^-$	Negative	$[M-H]^-$	-0.5	✓	✓	✓	✓	✓	✓	-	-	-	-
433.405	C29:2	$C_{29}H_{53}O_2^-$	Negative	$[M-H]^-$	-0.2	-	-	-	-	-	✓	-	-	-	-
433.442	C30:0	$C_{30}H_{57}O^-$	Negative	$[M-H-H_2O]^-$	1.2	-	-	-	-	-	✓	-	-	-	-
435.421	C29:1	$C_{29}H_{55}O_2^-$	Negative	$[M-H]^-$	-0.8	✓	-	-	-	-	✓	-	-	-	-
437.436	C29:0	$C_{29}H_{57}O_2^-$	Negative	$[M-H]^-$	-0.7	✓	-	-	-	✓	✓	-	-	-	-
447.421	C30:2	$C_{30}H_{55}O_2^-$	Negative	$[M-H]^-$	0.6	-	-	-	-	-	✓	-	-	-	-
447.457	C31:0	$C_{31}H_{59}O^-$	Negative	$[M-H-H_2O]^-$	-0.3	-	-	-	-	-	✓	-	-	-	-
449.436	C30:1	$C_{30}H_{57}O_2^-$	Negative	$[M-H]^-$	-0.6	✓	-	-	-	-	✓	-	-	-	-
451.452	C30:0	$C_{30}H_{59}O_2^-$	Negative	$[M-H]^-$	-0.7	✓	✓	✓	✓	✓	✓	-	-	-	-
461.437	C31:2	$C_{31}H_{57}O_2^-$	Negative	$[M-H]^-$	1.3	-	-	-	-	-	✓	-	-	-	-
461.473	C32:0	$C_{32}H_{61}O^-$	Negative	$[M-H-H_2O]^-$	0.5	-	-	-	-	-	✓	-	-	-	-
463.452	C31:1	$C_{31}H_{59}O_2^-$	Negative	$[M-H]^-$	-0.1	-	-	-	-	-	✓	-	-	-	-
465.468	C31:0	$C_{31}H_{61}O_2^-$	Negative	$[M-H]^-$	0.7	-	-	-	-	-	✓	-	-	-	-
475.452	C32:2	$C_{32}H_{59}O_2^-$	Negative	$[M-H]^-$	-1.0	-	✓	-	-	-	✓	-	-	-	-
475.489	C33:0	$C_{33}H_{63}O^-$	Negative	[M-H-H2O]-	1.2	-	-	-	-	-	✓	-	-	-	-
477.468	C32:1	$C_{32}H_{61}O_2^-$	Negative	$[M-H]^-$	-1.0	-	-	-	-	✓	✓	-	-	-	-
479.483	C32:0	$C_{32}H_{63}O_2^-$	Negative	$[M-H]^-$	-1.1	-	-	-	✓	-	✓	-	-	-	-
489.504	C34:0	$C_{34}H_{65}O^-$	Negative	$[M-H-H_2O]^-$	-0.2	-	-	-	-	-	✓	-	-	-	-
491.483	C33:1	$C_{33}H_{63}O_2^-$	Negative	$[M-H]^-$	-0.7	-	-	-	-	-	✓	-	-	-	-
493.499	C33:0	$C_{33}H_{65}O2^-$	Negative	$[M-H]^-$	0.0	-	-	-	-	-	✓	-	-	-	-
503.423	C31:0	$C_{31}H_{59}KO_2^-$	Negative	$[M+K-2H]^-$	-1.2	-	-	-	-	-	✓	-	-	-	-
503.483	C34:2	$C_{34}H_{63}O_2^-$	Negative	$[M-H]^-$	-0.7	-	-	-	-	-	✓	-	-	-	-
505.499	C34:1	$C_{34}H_{65}O_2^-$	Negative	$[M-H]^-$	-0.8	-	-	-	-	✓	✓	-	-	-	-
507.515	C34:0	$C_{34}H_{67}O_2^-$	Negative	$[M-H]^-$	0.7	-	-	-	-	-	✓	-	-	-	-
515.483	C35:3	$C_{35}H_{63}O_2^-$	Negative	$[M-H]^-$	-1.2	-	✓	-	-	-	-	-	-	-	-
517.499	C35:2	$C_{35}H_{65}O_2^-$	Negative	$[M-H]^-$	-1.3	-	✓	-	-	-	-	-	-	-	-
517.535	C36:0	$C_{36}H_{69}O^-$	Negative	$[M-H-H_2O]^-$	-0.8	-	-	-	-	-	✓	-	-	-	-
519.514	C35:1	$C_{35}H_{67}O_2^-$	Negative	$[M-H]^-$	-1.3	-	-	-	✓	-	✓	-	-	-	-
521.530	C35:0	$C_{35}H_{69}O2^-$	Negative	$[M-H]^-$	-0.6	-	-	-	-	-	✓	-	-	-	-
531.515	C36:2	$C_{36}H_{67}O_2^-$	Negative	$[M-H]^-$	-0.6	-	-	-	-	-	✓	-	-	-	-
533.530	C36:1	$C_{36}H_{69}O_2^-$	Negative	$[M-H]^-$	-1.2	-	-	-	-	✓	✓	-	-	-	-
535.546	C36:0	$C_{36}H_{71}O_2^-$	Negative	$[M-H]^-$	0.1	-	-	-	-	-	✓	-	-	-	-
547.546	C37:1	$C_{37}H_{71}O_2^-$	Negative	$[M-H]^-$	-1.2	-	-	-	✓	-	✓	-	-	-	-
561.561	C38:1	$C_{38}H_{73}O_2^-$	Negative	$[M-H]^-$	-0.9	-	-	-	-	✓	-	-	-	-	-
563.577	C38:0	$C_{38}H_{75}O_2^-$	Negative	$[M-H]^-$	-0.5	-	-	-	-	-	✓	-	-	-	-

Table 9.11 Cryo-OrbiSIMS plant modified linear/branched chain fatty acids/wax esters and peptide fragments

Modified linear/branched chain Fatty acids/Wax esters

Observed *m/z*	Putative I.D.	Formula (observed)	Polarity	OrbiSIMS adduct	Mass deviation (δppm)	Gooseberry	Apple blossom	Asparagus	Kiwi leaf	Tomato leaf	Pine needle	Victoria plum	Golden Gage plum	Gooseberry leaf	Validation?
313.274	x-oxo C19:0	$C_{19}H_{37}O_3^+$	Positive	$[M+H]^+$	0.9							✓			-

Observed *m/z*	Putative I.D.	Formula (observed)	Polarity	OrbiSIMS adduct	Mass deviation (δppm)	Gooseberry	Apple blossom	Asparagus	Kiwi leaf	Tomato leaf	Pine needle	Victoria plum	Golden Gage plum	Gooseberry leaf	Validation?
109.029	x-oxo-C6:1	$C_6H_5O_2^-$	Negative	$[M-H-H_2O]^-$	-1.5	-	✓	-	-	-	-	-	-	-	-
171.103	x-oxo-C9:0	$C_9H_{15}O_3^-$	Negative	$[M-H]^-$	-1.2	-	✓	-	-	-	-	-	-	-	-
173.118	x-hydroxy C9:0	$C_9H_{17}O_3^-$	Negative	$[M-H]^-$	-1.9	-	-	-	-	-	✓	-	-	-	-
185.118	x-oxo C10:0	$C_{10}H_{17}O_3^-$	Negative	$[M-H]^-$	-1.4	-	✓	-	-	-	-	-	-	-	-
199.134	x-hydroxy C11:1	$C_{11}H_{19}O_3^-$	Negative	$[M-H]^-$	0.2	-	-	-	-	-	✓	-	-	-	-
213.15	x-oxo C12:0	$C_{12}H_{21}O_3^-$	Negative	$[M-H]^-$	1.8	-	-	-	-	-	✓	-	-	-	-
215.165	x-hydroxy C12:0	$C_{12}H_{23}O_3^-$	Negative	$[M-H]^-$	-1.3	-	-	-	-	-	✓	-	-	-	-
227.165	x-oxo C13:0	$C_{13}H_{23}O_3^-$	Negative	$[M-H]^-$	-1.2	-	-	-	-	-	✓	-	-	-	-
239.165	x-oxo C14:1	$C_{14}H_{23}O_3^-$	Negative	$[M-H]^-$	-1.1	-	-	-	-	-	✓	-	-	-	-
241.181	x-oxo C14:1	$C_{14}H_{25}O_3^-$	Negative	$[M-H]^-$	0.3	-	-	-	-	-	✓	-	-	-	-
255.197	x-oxo C15:0	$C_{15}H_{27}O_3^-$	Negative	$[M-H]^-$	1.7	-	-	-	-	-	✓	-	-	-	-
257.212	x-hydroxy C15:0	$C_{15}H_{29}O_3^-$	Negative	$[M-H]^-$	-0.9	-	-	-	-	-	✓	-	-	-	-
263.163	x-oxo C14:0	$C_{14}H_{25}NaO_3^-$	Negative	$[M+Na-2H]^-$	0.5	-	-	-	-	-	✓	-	-	-	-
267.196	x-hydroxy, x-oxo C16:1	$C_{16}H_{27}O_3^-$	Negative	$[M-H-H_2O]^-$	-1.0	-	✓	-	-	-	-	-	-	-	-
269.212	x-oxo C16:0	$C_{16}H_{29}O_3^-$	Negative	$[M-H]^-$	-1.0	-	✓	-	-	-	✓	-	-	-	-
271.228	x-hydroxy C16:0	$C_{16}H_{31}O_3^-$	Negative	$[M-H]^-$	-0.9	-	✓	-	-	-	✓	-	-	-	-
285.207	x-hydroxy-x-oxo C16:0	$C_{16}H_{29}O_4^-$	Negative	$[M-H]^-$	-0.9	-	✓	-	-	-	-	-	-	-	-
291.194	x-oxo C16:0	$C_{16}H_{28}NaO_3^-$	Negative	$[M+Na-2H]^-$	-0.6	-	-	-	-	-	✓	-	-	-	-
293.21	x-hydroxy C16:0	$C_{16}H_{30}NaO_3^-$	Negative	$[M+Na-2H]^-$	0.7	-	-	-	-	-	✓	-	-	-	-
297.243	x-hydroxy C18:0	$C_{18}H_{33}O_3^-$	Negative	$[M-H]^-$	-1.8	-	-	-	-	-	✓	-	-	-	-
299.259	x-hydroxy C18:0	$C_{18}H_{35}O_3^-$	Negative	$[M-H]^-$	-0.6	-	-	-	-	-	✓	-	-	-	-
307.168	x-oxo C16:0	$C_{16}H_{28}KO_3^-$	Negative	$[M+Na-2H]^-$	-0.3	-	-	-	-	-	✓	-	-	-	-
313.275	x-hydroxy C19:0	$C_{19}H_{37}O_3^-$	Negative	$[M-H]^-$	0.6	-	-	-	-	-	✓	-	-	-	-
325.275	x-oxo C20:0	$C_{20}H_{37}O_3^-$	Negative	$[M-H]^-$	0.6	-	-	-	-	-	✓	-	-	-	-
327.29	x-hydroxy C20:0	$C_{20}H_{39}O_3^-$	Negative	$[M-H]^-$	-1.4	-	-	-	-	-	✓	-	-	-	-
341.306	x-hydroxy C21:0	$C_{21}H_{41}O_3^-$	Negative	$[M-H]^-$	-0.4	-	-	-	-	-	✓	-	-	-	-
353.306	x-oxo C22:0	$C_{22}H_{41}O_3^-$	Negative	$[M-H]^-$	-0.3	-	-	-	-	-	✓	-	-	-	-
355.322	x-hydroxy C22:0	$C_{22}H_{43}O_3^-$	Negative	$[M-H]^-$	0.7	-	-	-	-	-	✓	-	-	-	-
367.322	x-oxo C23:0	$C_{23}H_{43}O_3^-$	Negative	$[M-H]^-$	0.6	-	-	-	-	-	✓	-	-	-	-
369.337	x-hydroxy C23:0	$C_{23}H_{45}O_3^-$	Negative	$[M-H]^-$	-1.1	-	-	-	-	-	✓	-	-	-	-
379.322	x-oxo C24:1	$C_{24}H_{43}O_3^-$	Negative	$[M-H]^-$	-0.5	-	-	✓	-	-	✓	-	-	-	-
381.337	x-oxo C24:0	$C_{24}H_{45}O_3^-$	Negative	$[M-H]^-$	-0.5	-	-	✓	-	-	-	-	-	-	-
383.353	x-hydroxy C24:0	$C_{24}H_{47}O_3^-$	Negative	$[M-H]^-$	-0.5	-	-	✓	-	-	✓	-	-	-	-
397.369	x-hydroxy C25:0	$C_{25}H_{49}O_3^-$	Negative	$[M-H]^-$	0.7	-	-	-	-	-	✓	-	-	-	-
409.369	x-oxo C26:0	$C_{26}H_{49}O_3^-$	Negative	$[M-H]^-$	-0.5	✓	-	✓	-	-	✓	-	-	-	-
411.384	x-hydroxy C26:0	$C_{26}H_{51}O_3^-$	Negative	$[M-H]^-$	-0.6	✓	-	✓	-	-	✓	-	-	-	-
425.400	x-hydroxy C27:0	$C_{27}H_{53}O_3^-$	Negative	$[M-H]^-$	-0.3	✓	-	-	-	-	-	-	-	-	-
435.384	x-oxo C28:1	$C_{28}H_{51}O_3^-$	Negative	$[M-H]^-$	-0.9	-	-	-	-	-	✓	-	-	-	-
437.400	x-oxo C28:0	$C_{28}H_{53}O_3^-$	Negative	$[M-H]^-$	-0.7	✓	-	-	-	-	✓	-	-	-	-
439.416	x-hydroxy C28:0	$C_{28}H_{55}O_3^-$	Negative	$[M-H]^-$	-0.7	✓	-	✓	-	-	✓	-	-	-	-
467.447	x-hydroxy C30:0	$C_{30}H_{59}O_3^-$	Negative	$[M-H]^-$	0.1	-	-	-	-	-	✓	-	-	-	-
483.442	x,x-dihydroxy C30:0	$C_{30}H_{59}O_4^-$	Negative	$[M-H]^-$	0.3	-	-	-	-	-	✓	-	-	-	-
537.525	x-hydroxy C35:0	$C_{35}H_{69}O_3^-$	Negative	$[M-H]^-$	-0.4	-	-	-	-	-	✓	-	-	-	-

Peptide fragments

Observed *m/z*	Putative I.D.	Formula (observed)	Polarity	OrbiSIMS adduct	Mass deviation (δppm)	Gooseberry	Apple blossom	Asparagus	Kiwi leaf	Tomato leaf	Pine needle	Victoria plum	Golden Gage plum	Gooseberry leaf	Validation?
253.097		$C_7H_{17}N_4O_4S^+$	Positive	$[M+NH_4]^+$	0.0	-	-	-	-	-	-	-	-	✓	-
275.081		$C_7H_{16}N_4O_4S$	Positive	$[M+H-H_2O]^+$	-0.2	-	-	-	-	-	-	-	-	✓	-

Observed *m/z*	Putative I.D.	Formula (observed)	Polarity	OrbiSIMS adduct	Mass deviation (δppm)	Gooseberry	Apple blossom	Asparagus	Kiwi leaf	Tomato leaf	Pine needle	Victoria plum	Golden Gage plum	Gooseberry leaf	Validation?
219.081		$C_8H_{15}N_2O_3S^-$	Negative	$[M-H]^-$	0.5	-	-	-	-	-	✓	-	-	-	-
235.076		$C_8H_{15}N_2O_4S^-$	Negative	$[M-H]^-$	0.9	-	-	-	-	-	✓	-	-	-	-
294.182		$C_{13}H_{24}N_3O_3^-$	Negative	$[M-H-H_2O]^-$	-1.1	-	-	-	-	-	✓	-	-	-	-
295.175		$C_{12}H_{24}N_4NaO_3^-$	Negative	$[M+Na-2H]^-$	-0.5	-	-	-	-	-	✓	-	-	-	-
298.156		$C_{17}H_{22}NO_2^-$	Negative	$[M-H-H_2O]^-$	-0.3	-	-	-	-	-	✓	-	-	-	-
354.204		$C_{17}H_{28}NO_3^-$	Negative	$[M-H-H_2O]^-$	1.6	-	-	-	-	-	✓	-	-	-	-
356.14		$C_{14}H_{26}N_3O_5S^-$	Negative	$[M-H]^-$	0.6	-	-	-	-	-	✓	-	-	-	-
361.124		$C_{16}H_{24}N_6NaO_3^-$	Negative	$[M+Na-2H]^-$	-0.5	-	-	-	-	-	✓	-	-	-	-
369.118		$C_{16}H_{24}N_6NaO_5^-$	Negative	$[M+Na-2H]^-$	-0.1	-	-	-	-	-	✓	-	-	-	-
370.155		$C_{16}H_{26}N_5O_5S^-$	Negative	$[M-H]^-$	-1.2	-	-	-	-	-	✓	-	-	-	-
371.115		$C_{15}H_{23}N_6O_5S^-$	Negative	$[M-H]^-$	1.9	-	-	-	-	-	✓	-	-	-	-
386.15		$C_{16}H_{24}N_6O_5S$	Negative	$[M-H-H_2O]^-$	-0.9	-	-	-	-	-	✓	-	-	-	-
450.212		$C_{22}H_{29}N_5NaO_4^-$	Negative	$[M+Na-2H]^-$	-0.6	-	-	-	-	-	✓	-	-	-	-

Table 9.12 Cryo-OrbiSIMS plant glycerolipids

Glycerolipids (MAG/DAG/TAG)

Observed *m/z*	Putative LD.	Formula (observed)	Polarity	OrbiSIMS adduct	Mass deviation (5ppm)	Gooseberry	Apple blossom	Asparagus	Kiwi leaf	Tomato leaf	Pine needle	Victoria plum	Golden Gage plum	Gooseberry leaf	Validation?
425.36	DAG(23:0)	$C_{26}H_{49}O_4^+$	Positive	$[M+H-H_2O]^+$	-1.3	-	-	-	-	-	✓	-	-	-	-
453.39	DAG(25:0)	$C_{28}H_{53}O_4^+$	Positive	$[M+H-H_2O]^+$	0.4	-	-	-	-	-	✓	-	-	-	-
481.43	DAG(27:0)	$C_{30}H_{57}O_4^+$	Positive	$[M+H-H_2O]^+$	-0.3	-	-	-	-	-	✓	-	-	-	-
509.45	DAG(29:0)	$C_{32}H_{61}O_4^+$	Positive	$[M+H-H_2O]^+$	-0.9	-	-	-	-	-	✓	-	-	-	-
549.45	DAG(29:0)	$C_{32}H_{62}NaO_5^+$	Positive	$[M+Na]^+$	0.1	-	-	-	-	-	✓	-	-	-	-
551.50	DAG(32:0)	$C_{35}H_{67}O_4^+$	Positive	$[M+H-H_2O]^+$	-0.7	-	-	-	-	-	-	✓	-	-	-
563.43	TAG(29:0)	$C_{32}H_{60}NaO_6^+$	Positive	$[M+Na]^+$	-0.4	-	-	-	-	-	✓	-	-	-	-
579.54	DAG(34:0)	$C_{37}H_{71}O_4^+$	Positive	$[M+H-H_2O]^+$	0.5	-	-	-	-	-	-	✓	-	-	-
607.57	DAG(36:0)	$C_{39}H_{75}O_4^+$	Positive	$[M+H-H_2O]^+$	0.0	-	-	-	-	-	-	✓	-	-	-
679.59	TAG(39:1)	$C_{42}H_{79}O_6^+$	Positive	$[M+H]^+$	-0.2	-	-	-	-	-	✓	-	-	-	-
689.61	DAG(41:3)	$C_{44}H_{81}O_5^+$	Positive	$[M+H]^+$	-1.2	-	-	-	-	-	✓	-	-	-	-
707.62	TAG(41:1)	$C_{44}H_{83}O_6^+$	Positive	$[M+H]^+$	-0.6	-	-	-	-	-	✓	-	-	-	-
735.65	TAG(43:1)	$C_{46}H_{87}O_6^+$	Positive	$[M+H]^+$	-1.0	-	-	-	-	-	✓	-	-	-	-
745.67	TAG(45:1)	$C_{48}H_{89}O_5^+$	Positive	$[M+H-H_2O]^+$	-0.6	-	-	-	-	-	✓	-	-	-	-
763.68	TAG(45:1)	$C_{48}H_{91}O_6^+$	Positive	$[M+H]^+$	-1.3	-	-	-	-	-	✓	-	-	-	-

Observed *m/z*	Putative LD.	Formula (observed)	Polarity	OrbiSIMS adduct	Mass deviation (5ppm)	Gooseberry	Apple blossom	Asparagus	Kiwi leaf	Tomato leaf	Pine needle	Victoria plum	Golden Gage plum	Gooseberry leaf	Validation?
281.212	MAG(14:0)	$C_{17}H_{33}O_3^-$	Negative	$[M-H-H_2O]^-$	-0.8	-	-	-	-	-	✓	-	-	-	-
287.223	MAG(13:0)	$C_{16}H_{31}O_4^-$	Negative	$[M-H]^-$	-0.8	-	✓	-	-	-	✓	-	-	-	-
309.243	MAG(16:1)	$C_{19}H_{33}O_3^-$	Negative	$[M-H-H_2O]^-$	-1.7	-	-	-	-	-	✓	-	-	-	-
325.238	DAG(16:0)	$C_{19}H_{33}O_4^-$	Negative	$[M-H-H_2O]^-$	-1.3	-	-	-	-	-	✓	-	-	-	-
339.290	MAG(18:0)	$C_{21}H_{39}O_3^-$	Negative	$[M-H-H_2O]^-$	-1.4	-	-	-	-	-	✓	-	-	-	-
343.285	MAG(17:0)	$C_{20}H_{39}O_4^-$	Negative	$[M-H]^-$	-1.1	-	-	-	-	-	✓	-	-	-	-
365.306	MAG(20:1)	$C_{23}H_{41}O_3^-$	Negative	$[M-H-H_2O]^-$	-0.3	-	-	-	-	-	✓	-	-	-	-
381.337	MAG(21:0)	$C_{24}H_{45}O_3^-$	Negative	$[M-H-H_2O]^-$	-1.1	-	-	-	-	-	✓	-	-	-	-
383.317	MAG(20:1)	$C_{24}H_{45}O_4^-$	Negative	$[M-H]^-$	0.8	-	-	-	-	-	✓	-	-	-	-
393.337	MAG(22:1)	$C_{25}H_{45}O_3^-$	Negative	$[M-H-H_2O]^-$	-1.1	-	-	-	-	-	✓	-	-	-	-
395.317	DAG(21:0)	$C_{24}H_{43}O_4^-$	Negative	$[M-H-H_2O]^-$	-0.6	-	-	✓	-	-	✓	-	-	-	-
395.353	MAG(22:0)	$C_{25}H_{47}O_3^-$	Negative	$[M-H-H_2O]^-$	-0.2	-	-	-	-	-	✓	-	-	-	-
399.348	MAG(21:0)	$C_{24}H_{47}O_4^-$	Negative	$[M-H]^-$	-0.6	-	-	✓	-	-	-	-	-	-	-
409.332	MAG(22:0)	$C_{25}H_{45}O_4^-$	Negative	$[M-H]^-$	-0.5	-	-	✓	-	-	✓	-	-	-	-
411.348	MAG(22:1)	$C_{25}H_{47}O_4^-$	Negative	$[M-H]^-$	0.1	-	-	-	-	-	✓	-	-	-	-
413.327	DAG(21:0)	$C_{24}H_{45}O_5^-$	Negative	$[M-H]^-$	-0.6	-	-	-	-	-	✓	-	-	-	-
421.369	MAG(24:1)	$C_{27}H_{49}O_3^-$	Negative	$[M-H-H_2O]^-$	0.7	-	-	-	-	-	✓	-	-	-	-
423.348	DAG(23:0)	$C_{26}H_{47}O_4^-$	Negative	$[M-H-H_2O]^-$	0.1	-	-	-	-	-	✓	-	-	-	-
423.385	MAG(24:0)	$C_{27}H_{51}O_3^-$	Negative	$[M-H-H_2O]^-$	1.5	-	-	-	-	-	✓	-	-	-	-
427.343	DAG(22:0)	$C_{26}H_{51}O_5^-$	Negative	$[M-H]^-$	0.2	-	-	-	-	-	✓	-	-	-	-
437.364	DAG(24:0)	$C_{27}H_{49}O_4^-$	Negative	$[M-H-H_2O]^-$	0.9	-	-	-	-	-	✓	-	-	-	-
439.379	MAG(24:1)	$C_{27}H_{51}O_4^-$	Negative	$[M-H]^-$	-0.6	-	-	-	-	-	✓	-	-	-	-
441.359	DAG(23:0)	$C_{26}H_{49}O_5^-$	Negative	$[M-H]^-$	1.0	-	-	-	-	-	✓	-	-	-	-
451.379	DAG(25:0)	$C_{28}H_{51}O_4^-$	Negative	$[M-H-H_2O]^-$	-0.6	-	-	-	-	-	✓	-	-	-	-
465.395	DAG(26:0)	$C_{29}H_{53}O_4^-$	Negative	$[M-H-H_2O]^-$	0.2	-	-	-	-	-	✓	-	-	-	-
469.353	TAG(24:0)	$C_{27}H_{49}O_6^-$	Negative	$[M-H]^-$	-1.0	-	-	-	-	-	✓	-	-	-	-
469.39	DAG(25:0)	$C_{28}H_{53}O_5^-$	Negative	$[M-H]^-$	0.3	-	-	-	-	-	✓	-	-	-	-
479.411	DAG(27:0)	$C_{29}H_{51}O_4^-$	Negative	$[M-H-H_2O]^-$	0.9	-	-	-	-	-	✓	-	-	-	-
483.405	DAG(26:0)	$C_{28}H_{53}O_5^-$	Negative	$[M-H]^-$	-1.0	-	-	-	-	-	✓	-	-	-	-
493.426	DAG(28:0)	$C_{31}H_{53}O_4^-$	Negative	$[M-H-H_2O]^-$	-0.5	-	-	-	-	-	✓	-	-	-	-
497.384	TAG(26:0)	$C_{29}H_{53}O_6^-$	Negative	$[M-H]^-$	-1.5	-	-	-	-	-	✓	-	-	-	-
497.421	DAG(27:0)	$C_{29}H_{53}O_5^-$	Negative	$[M-H]^-$	-0.3	-	-	-	-	-	✓	-	-	-	-
507.442	DAG(29:0)	$C_{31}H_{55}O_4^-$	Negative	$[M-H-H_2O]^-$	0.2	-	-	-	-	-	✓	-	-	-	-
509.421	DAG(28:1)	$C_{31}H_{57}O_5^-$	Negative	$[M-H]^-$	-0.3	-	-	-	-	-	✓	-	-	-	-
511.437	DAG(28:0)	$C_{31}H_{59}O_5^-$	Negative	$[M-H]^-$	0.4	-	-	-	-	-	✓	-	-	-	-
515.411	DAG(30:3)	$C_{33}H_{55}O_4^-$	Negative	$[M-H-H_2O]^-$	0.8	-	-	-	-	-	✓	-	-	-	-
521.421	TAG(29:0)	$C_{32}H_{57}O_6^-$	Negative	$[M-H-H_2O]^-$	-0.3	-	-	-	-	-	✓	-	-	-	-
521.458	DAG(30:0)	$C_{33}H_{61}O_4^-$	Negative	$[M-H-H_2O]^-$	0.9	-	-	-	-	-	✓	-	-	-	-
525.416	TAG(28:0)	$C_{31}H_{57}O_6^-$	Negative	$[M-H]^-$	-0.1	-	-	-	-	-	✓	-	-	-	-
525.452	DAG(29:0)	$C_{32}H_{61}O_5^-$	Negative	$[M-H]^-$	-0.9	-	-	-	-	-	✓	-	-	-	-
529.426	DAG(31:3)	$C_{34}H_{57}O_5^-$	Negative	$[M-H-H_2O]^-$	-0.4	-	-	-	-	-	✓	-	-	-	-
531.442	DAG(31:2)	$C_{34}H_{59}O_5^-$	Negative	$[M-H-H_2O]^-$	-1.0	-	✓	-	-	✓	-	-	-	-	-
533.457	DAG(31:1)	$C_{34}H_{61}O_5^-$	Negative	$[M-H-H_2O]^-$	-1.1	-	✓	-	-	-	-	-	-	-	-
535.473	DAG(31:0)	$C_{34}H_{63}O_5^-$	Negative	$[M-H-H_2O]^-$	-0.3	-	-	-	-	-	✓	-	-	-	-
537.452	DAG(30:1)	$C_{33}H_{61}O_6^-$	Negative	$[M-H]^-$	-0.8	-	-	-	-	-	✓	-	-	-	-
539.432	TAG(29:0)	$C_{32}H_{59}O_7^-$	Negative	$[M-H]^-$	0.5	-	-	-	-	-	✓	-	-	-	-
539.468	DAG(30:0)	$C_{33}H_{63}O_6^-$	Negative	$[M-H]^-$	-0.2	-	-	-	-	-	✓	-	-	-	-
551.468	DAG(31:1)	$C_{34}H_{63}O_6^-$	Negative	$[M-H]^-$	-0.2	-	-	-	-	-	✓	-	-	-	-
553.447	TAG(30:0)	$C_{33}H_{61}O_7^-$	Negative	$[M-H]^-$	-0.7	-	-	-	-	-	✓	-	-	-	-
553.484	DAG(31:0)	$C_{34}H_{65}O_6^-$	Negative	$[M-H]^-$	0.5	-	-	-	-	-	✓	-	-	-	-
559.473	DAG(33:2)	$C_{36}H_{63}O_5^-$	Negative	$[M-H-H_2O]^-$	-0.9	-	✓	-	-	✓	-	-	-	-	-
561.414	TAG(29:0)	$C_{32}H_{58}NaO_8^-$	Negative	$[M+Na-2H]^-$	0.6	-	-	-	-	-	✓	-	-	-	-
561.489	DAG(33:1)	$C_{36}H_{65}O_5^-$	Negative	$[M-H-H_2O]^-$	-0.9	-	✓	-	-	✓	-	-	-	-	-
563.505	DAG(33:0)	$C_{36}H_{67}O_5^-$	Negative	$[M-H-H_2O]^-$	0.9	-	-	-	-	-	✓	-	-	-	-
567.463	TAG(31:0)	$C_{34}H_{63}O_8^-$	Negative	$[M-H]^-$	0.0	-	-	-	-	-	✓	-	-	-	-
579.499	DAG(33:1)	$C_{36}H_{67}O_6^-$	Negative	$[M-H]^-$	-0.7	-	-	-	-	-	✓	-	-	-	-
581.478	TAG(32:0)	$C_{35}H_{65}O_8^-$	Negative	$[M-H]^-$	-1.1	-	-	-	-	-	✓	-	-	-	-
581.515	DAG(33:0)	$C_{36}H_{69}O_6^-$	Negative	$[M-H]^-$	-0.1	-	-	-	-	-	✓	-	-	-	-
585.489	DAG(35:3)	$C_{38}H_{65}O_5^-$	Negative	$[M-H-H_2O]^-$	-0.9	-	-	-	-	✓	-	-	-	-	-
587.504	DAG(35:2)	$C_{38}H_{67}O_5^-$	Negative	$[M-H-H_2O]^-$	-1.0	-	✓	-	-	✓	-	-	-	-	-
589.520	DAG(35:1)	$C_{38}H_{69}O_5^-$	Negative	$[M-H-H_2O]^-$	-0.9	-	✓	-	-	✓	-	-	-	-	-
591.536	DAG(35:0)	$C_{38}H_{71}O_5^-$	Negative	$[M-H-H_2O]^-$	0.4	-	-	-	-	-	✓	-	-	-	-
593.515	DAG(34:1)	$C_{37}H_{69}O_6^-$	Negative	$[M-H]^-$	-0.1	-	-	-	-	-	✓	-	-	-	-
595.494	TAG(33:0)	$C_{36}H_{67}O_8^-$	Negative	$[M-H]^-$	-0.5	-	-	-	-	-	✓	-	-	-	-
595.531	DAG(34:0)	$C_{37}H_{71}O_6^-$	Negative	$[M-H]^-$	0.5	-	-	-	-	-	✓	-	-	-	-
607.531	DAG(35:1)	$C_{38}H_{71}O_6^-$	Negative	$[M-H]^-$	0.5	-	-	-	-	-	✓	-	-	-	-
609.547	DAG(35:0)	$C_{38}H_{73}O_6^-$	Negative	$[M-H]^-$	1.1	-	-	-	-	-	✓	-	-	-	-
613.520	DAG(37:3)	$C_{40}H_{69}O_5^-$	Negative	$[M-H-H_2O]^-$	-0.7	-	-	-	-	✓	-	-	-	-	-
621.546	DAG(36:1)	$C_{39}H_{73}O_6^-$	Negative	$[M-H]^-$	-0.6	-	-	-	-	-	✓	-	-	-	-
623.525	TAG(35:0)	$C_{38}H_{71}O_8^-$	Negative	$[M-H]^-$	-1.0	-	-	-	-	-	✓	-	-	-	-
635.562	DAG(37:1)	$C_{40}H_{75}O_6^-$	Negative	$[M-H]^-$	0.0	-	-	-	-	-	✓	-	-	-	-
637.541	TAG(36:0)	$C_{39}H_{73}O_8^-$	Negative	$[M-H]^-$	-0.4	-	-	-	-	-	✓	-	-	-	-
641.551	DAG(39:3)	$C_{42}H_{73}O_5^-$	Negative	$[M-H-H_2O]^-$	-1.0	-	-	-	-	✓	-	-	-	-	-
651.557	TAG(37:0)	$C_{40}H_{75}O_8^-$	Negative	$[M-H]^-$	0.1	-	-	-	-	-	✓	-	-	-	-
665.572	TAG(38:0)	$C_{41}H_{77}O_8^-$	Negative	$[M-H]^-$	-0.8	-	-	-	-	-	✓	-	-	-	-
707.619	TAG(41:0)	$C_{44}H_{83}O_8^-$	Negative	$[M-H]^-$	-0.7	-	-	-	-	-	✓	-	-	-	-
721.672	DAG(43:0)	$C_{46}H_{89}O_5^-$	Negative	$[M-H]^-$	0.6	-	-	-	-	-	✓	-	-	-	-
763.681	TAG(45:0)	$C_{48}H_{91}O_8^-$	Negative	$[M-H]^-$	-1.5	-	-	-	-	-	✓	-	-	-	-
767.631	DAG(44:2)	$C_{47}H_{84}ClO_5^-$	Negative	$[M+Cl]^-$	-2.1	-	-	-	-	-	✓	-	-	-	-
795.662	TAG(46:2)	$C_{49}H_{88}ClO_6^-$	Negative	$[M+Cl]^-$	-2.4	-	-	-	-	-	✓	-	-	-	-

Phospholipids

Observed *m/z*	Putative I.D.	Formula (observed)	Polarity	OrbiSIMS adduct	Mass deviation (δppm)	Gooseberry	Apple blossom	Asparagus	Kiwi leaf	Tomato leaf	Pine needle	Victoria plum	Golden Gage plum	Gooseberry leaf	Validation?
599.444	PA(31:1)	$C_{34}H_{64}O_8P^+$	Positive	$[M+H-H_2O]^+$	0.8	-	✓	-	-	-	-	-	-	-	-
670.517	PE(33:1)/PC(30:1)	$C_{38}H_{73}NO_8P^+$	Positive	$[M+H-H_2O]^+$	0.0	-	-	-	-	✓	-	-	-	-	-
763.575	PC(36:5)	$C_{44}H_{80}N_2O_6P^+$	Positive	$[M+NH_4-H_2O]^+$	0.2	-	-	-	-	-	✓	-	-	-	-
791.607	PC(38:5)	$C_{46}H_{84}N_2O_6P^+$	Positive	$[M+NH_4-H_2O]^+$	1.1	-	-	-	-	-	✓	-	-	-	-
805.680	PE(40:1)/PC(37:0)	$C_{45}H_{94}N_2O_7P^+$	Positive	$[M+NH_4]^+$	0.8	-	-	-	-	-	✓	-	-	-	-
819.638	PC(40:5)	$C_{48}H_{88}N_2O_6P^+$	Positive	$[M+NH_4-H_2O]^+$	0.7	-	-	-	-	-	✓	-	-	-	-
820.641	PS(39:0)	$C_{45}H_{91}NO_9P^+$	Positive	$[M+H]^+$	-2.0	-	-	-	-	-	✓	-	-	-	-
833.617	PC(40:7)	$C_{48}H_{86}N_2O_7P^+$	Positive	$[M+NH_4]^+$	0.3	-	-	-	-	-	✓	-	-	-	-
834.621	PS(39:0)	$C_{45}H_{88}NO_{10}P^+$	Positive	$[M+H]^+$	-1.0	-	-	-	-	-	✓	-	-	-	-

Observed *m/z*	Putative I.D.	Formula (observed)	Polarity	OrbiSIMS adduct	Mass deviation (δppm)	Gooseberry	Apple blossom	Asparagus	Kiwi leaf	Tomato leaf	Pine needle	Victoria plum	Golden Gage plum	Gooseberry leaf	Validation?
577.388	PA(27:0)	$C_{30}H_{58}O_8P^-$	Negative	$[M-H]^-$	0.9	-	-	-	-	-	✓	-	-	-	-
739.6	PA(41:1)	$C_{44}H_{84}O_8P^-$	Negative	$[M-H-H_2O]^-$	-1.5	-	-	-	-	-	✓	-	-	-	-
578.382	PC(21:0)/PE(24:0)	$C_{29}H_{57}NO_8P^-$	Negative	$[M-H]^-$	-1.3	-	-	-	-	-	✓	-	-	-	-
640.375	PE(26:1)	$C_{31}H_{60}ClNO_8P^-$	Negative	$[M+Cl]^-$	-0.1	-	-	-	-	-	✓	-	-	-	-
831.611	PG(40:1)	$C_{46}H_{88}O_{10}P^-$	Negative	$[M-H]^-$	-1.3	-	-	-	-	-	✓	-	-	-	-

Alcohols

Observed *m/z*	Putative I.D.	Formula (observed)	Polarity	OrbiSIMS Adduct	Mass deviation (δppm)	Gooseberry	Apple blossom	Asparagus	Kiwi leaf	Tomato leaf	Pine needle	Victoria plum	Golden Gage plum	Gooseberry leaf	Validation?
253.254	C17:1	$C_{17}H_{33}O^-$	Negative	$[M-H]^-$	1.2	-	-	-	-	-	✓	-	-	-	-
267.269	C18:1	$C_{18}H_{35}O^-$	Negative	$[M-H]^-$	-1.3	-	-	-	-	-	✓	-	-	-	-
295.300	C20:1	$C_{20}H_{39}O^-$	Negative	$[M-H]^-$	-1.2	-	-	✓	-	-	✓	-	-	-	-
297.316	C20:0	$C_{20}H_{41}O^-$	Negative	$[M-H]^-$	-1.0	-	-	-	-	-	✓	-	-	-	-
309.316	C21:1	$C_{21}H_{41}O^-$	Negative	$[M-H]^-$	-0.8	-	-	✓	-	-	-	-	-	-	-
423.457	C29:0	$C_{29}H_{59}O^-$	Negative	$[M-H]^-$	-0.3	-	-	-	-	-	✓	-	-	-	-

Ceramides and Sphingomyelins

Observed *m/z*	Putative I.D.	Formula (observed)	Polarity	OrbiSIMS Adduct	Mass deviation (δppm)	Gooseberry	Apple blossom	Asparagus	Kiwi leaf	Tomato leaf	Pine needle	Victoria plum	Golden Gage plum	Gooseberry leaf	Validation?
514.403	Cer(30:2)	$C_{30}H_{57}ClNO_3^-$	Negative	$[M+Cl]^-$	-0.5	-	-	-	-	-	✓	-	-	-	-
865.713	SM(44:0)	$C_{49}H_{98}N_2NaO_6P^-$	Negative	$[M+Na-2H]^-$	-1.6	-	-	-	-	-	✓	-	-	-	-

Table 9.13 Cryo-OrbiSIMS plant phospholipids, alcohols, ceramides and sphingomyelins

Table 9.14 Mouse skin lipids – sterols and FAs/WEs

Sterols

m/z	Putative I.D.	Experimental formula	Exact mass	Adduct	Mass deviation
255.211	alpha-androst-x-en-x-one	$C_{19}H_{27}^+$	255.21073	$[M+H-H_2O]^+$	1.06
257.226	alpha-androstenol	$C_{19}H_{29}^+$	257.22638	$[M+H-H_2O]^+$	-1.48
259.242	a-Androstan-x-ol	$C_{19}H_{31}^+$	259.24203	$[M+H-H_2O]^+$	-0.12
353.320	x-norcholestenone	$C_{26}H_{41}^+$	353.32028	$[M+H-H_2O]^+$	-0.79
367.336	Cholestenone	$C_{27}H_{43}^+$	367.33593	$[M+H-H_2O]^+$	0.19
369.352	Cholesterol	$C_{27}H_{45}^+$	369.35158	$[M+H-H_2O]^+$	1.14
392.389	x-norcholestanol	$C_{26}H_{50}NO^+$	392.38869	$[M+NH_4]^+$	0.79
420.420	Campestanol	$C_{28}H_{54}NO^+$	420.41999	$[M+NH_4]^+$	0.02
543.231	cholesterol sulfate	$C_{27}H_{45}K_2O_4S^+$	543.23072	$[M+2K-H]^+$	0.52
617.567	Campesteryl ester(16:2)	$C_{44}H_{73}O^+$	617.56559	$[M+H-H_2O]^+$	2.28
633.562	Campesteryl ester(16:3)	$C_{44}H_{73}O_2^+$	633.56051	$[M+H]^+$	2.35
659.614	Cholesteryl ester(20:2)	$C_{47}H_{79}O^+$	659.61254	$[M+H-H_2O]^+$	2.21
671.614	Campesteryl ester(20:3)	$C_{48}H_{79}O^+$	671.61254	$[M+H-H_2O]^+$	2.17
675.609	Cholesteryl ester(20:3)	$C_{47}H_{79}O_2^+$	675.60746	$[M+H]^+$	2.28
687.609	Dimethyl cholesteryl ester	$C_{48}H_{79}O_2^+$	687.60746	$[M+H-H_2O]^+$	2.24
691.604	Methyl cholesteryl ester	$C_{47}H_{79}O_3^+$	691.60237	$[M+H]^+$	2.36
701.661	Campesteryl ester(22:2)	$C_{50}H_{85}O^+$	701.65949	$[M+H-H_2O]^+$	2.15
717.656	Campesteryl ester(22:3)	$C_{50}H_{85}O_2^+$	717.65441	$[M+H]^+$	2.22
733.651	Dimethyl cholesteryl ester	$C_{50}H_{85}O_3^+$	733.64932	$[M+H]^+$	2.29
1053.995	Palmitoleoyloxy-triacontenoic acid cholesterol ester	$C_{73}H_{129}O_3^+$	1053.99362	$[M+H-H_2O]^+$	1.31

Fatty acids/wax esters

Experimental mass	Putative I.D.	Experimental formula	Exact mass	Adduct	Mass deviation
119.049	C8:4	$C_8H_7O^+$	119.04914	$[M+H-H_2O]^+$	-1.18
125.000	C4:1	$C_4H_6KO_2^+$	124.99994	$[M+K]^+$	0.48
145.065	C10:5	$C_{10}H_9O^+$	145.06479	$[M+H-H_2O]^+$	1.45
162.956	C4:1	$C_4H_5K_2O_2^+$	162.95582	$[M+2K-H]^+$	1.10
239.237	C16:0	$C_{16}H_{31}O^+$	239.23694	$[M+H-H_2O]^+$	0.25
252.232	C16:2	$C_{16}H_{30}NO^+$	252.23219	$[M+NH_4-H_2O]^+$	-0.75
263.237	C18:2	$C_{18}H_{31}O^+$	263.23694	$[M+H-H_2O]^+$	0.23
265.253	C18:1	$C_{18}H_{33}O^+$	265.25259	$[M+H-H_2O]^+$	1.55
283.263	C18:1	$C_{18}H_{35}O_2^+$	283.26316	$[M+H]^+$	-0.56
309.279	C20:2	$C_{20}H_{37}O_2^+$	309.27881	$[M+H]^+$	0.61
319.263	C21:4	$C_{21}H_{35}O_2^+$	319.26316	$[M+H]^+$	-0.50
325.211	C18:2	$C_{18}H_{31}Na_2O_2^+$	325.21140	$[M+2Na-H]^+$	-1.23
327.227	C18:1	$C_{18}H_{33}Na_2O_2^+$	327.22705	$[M+2Na-H]^+$	-0.15
351.305	C26:5	$C_{26}H_{39}^+$	351.30463	$[M+H-2H_2O]^+$	1.05
357.159	C18:2	$C_{18}H_{31}K_2O_2^+$	357.15927	$[M+2K-H]^+$	-0.76
359.175	C18:1	$C_{18}H_{33}K_2O_2^+$	359.17492	$[M+2K-H]^+$	0.22
364.357	C24:2	$C_{24}H_{46}NO^+$	364.35739	$[M+NH_4-H_2O]^+$	-1.07
401.300	x-hydroxy C22:0	$C_{22}H_{43}Na_2O_3^+$	401.30021	$[M+2Na-H]^+$	-0.52
413.337	C24:0	$C_{24}H_{47}Na_2O_2^+$	413.33660	$[M+2Na-H]^+$	0.97
429.332	x-methyl C24:0	$C_{24}H_{47}Na_2O_3^+$	429.33151	$[M+2Na-H]^+$	1.14
445.285	C24:0	$C_{24}H_{47}K_2O_2^+$	445.28447	$[M+2K-H]^+$	1.19
455.347	x-oxo C26:0	$C_{26}H_{49}Na_2O_3^+$	455.34716	$[M+2Na-H]^+$	-0.35
457.363	x-hydroxy C26:0	$C_{26}H_{51}Na_2O_3^+$	457.36281	$[M+2Na-H]^+$	0.42
549.561	C37:1	$C_{37}H_{73}O_2^+$	549.56051	$[M+H]^+$	0.89
561.561	C38:2	$C_{38}H_{73}O_2^+$	561.56051	$[M+H]^+$	0.87
563.576	C38:1	$C_{38}H_{75}O_2^+$	563.57616	$[M+H]^+$	-0.28
577.592	C39:0	$C_{39}H_{77}O_2^+$	577.59181	$[M+H]^+$	0.33
589.592	C40:2	$C_{40}H_{77}O_2^+$	589.59181	$[M+H]^+$	0.32
591.608	C40:1	$C_{40}H_{79}O_2^+$	591.60746	$[M+H]^+$	0.91
604.603	C40:2	$C_{40}H_{78}NO_2^+$	604.60271	$[M+NH_4]^+$	0.48

Table 9.15 Mouse skin lipids - aldehydes/alcohols, ceramides and phospholipids

Aldehydes/Alcohols

Experimental mass	Putative I.D.	Experimental formula	Exact mass	Adduct	Mass deviation
104.107	Pentanal	$C_5H_{14}NO^+$	104.10699	$[M+NH_4]^+$	0.10
105.07	Octatrienal	$C_8H_9^+$	105.06988	$[M+H-H_2O]^+$	1.14
109.101	Octenal	$C_8H_{13}^+$	109.10118	$[M+H-H_2O]^+$	-1.65
111.117	Octenol	$C_8H_{15}^+$	111.11683	$[M+H-H_2O]^+$	1.53
121.101	Nonadienal	$C_9H_{13}^+$	121.10118	$[M+H-H_2O]^+$	-1.49
123.117	Nonenal	$C_9H_{15}^+$	123.11683	$[M+H-H_2O]^+$	1.38

Ceramides

Experimental mass	Putative I.D.	Experimental formula	Exact mass	Adduct	Mass deviation
268.263	C17 Sphingosine	$C_{17}H_{34}NO^+$	268.26349	$[M+H-H_2O]^+$	-1.83
544.470	Cer(d33:2)	$C_{33}H_{63}NNaO_3^+$	544.47002	$[M+Na]^+$	-0.04
558.486	Cer(34:2)	$C_{34}H_{65}NNaO_3^+$	558.48567	$[M+Na]^+$	0.59
560.501	Cer(34:0)	$C_{34}H_{67}NNaO_3^+$	560.50132	$[M+Na]^+$	-0.57
574.481	Cer(34:2(2OH))	$C_{34}H_{65}NNaO_4^+$	574.48058	$[M+Na]^+$	0.73
576.496	Cer(34:1(2OH))	$C_{34}H_{67}NNaO_4^+$	576.49623	$[M+Na]^+$	-0.40
576.497	Cer(34:1(2OH))	$C_{34}H_{67}NNaO_4^+$	576.49623	$[M+Na]^+$	1.34
586.517	Cer(36:2)	$C_{36}H_{69}NNaO_3^+$	586.51697	$[M+Na]^+$	0.05
588.533	Cer(36:1)	$C_{36}H_{71}NNaO_3^+$	588.53262	$[M+Na]^+$	0.65
600.533	Cer(d37:2)	$C_{37}H_{71}NNaO_3^+$	600.53262	$[M+Na]^+$	0.63
602.512	Cer(36:2(2OH))	$C_{36}H_{69}NNaO_4^+$	602.51188	$[M+Na]^+$	0.20
602.549	Cer(37:1)	$C_{37}H_{73}NNaO_3^+$	602.54827	$[M+Na]^+$	1.21
604.528	Cer(36:1(2OH))	$C_{36}H_{71}NNaO_4^+$	604.52753	$[M+Na]^+$	0.78
614.548	Cer(38:2)	$C_{38}H_{73}NNaO_3^+$	614.54827	$[M+Na]^+$	-0.44
616.528	Cer(37:2(2OH))	$C_{37}H_{71}NNaO_4^+$	616.52753	$[M+Na]^+$	0.76
616.564	Cer(38:1)	$C_{38}H_{75}NNaO_3^+$	616.56392	$[M+Na]^+$	0.13
618.619	Cer(41:1)	$C_{41}H_{80}NO_2^+$	618.61836	M+H-H2O	1.03
620.523	Cer(36:1(2OH))	$C_{36}H_{71}NNaO_5^+$	620.52245	$[M+Na]^+$	0.89
620.634	Cer(41:0)	$C_{41}H_{82}NO_2^+$	620.63401	$[M+H-H_2O]^+$	-0.02
628.564	Cer(39:2)	$C_{39}H_{75}NNaO_3^+$	628.56392	$[M+Na]^+$	0.13
630.543	Cer(38:2(2OH))	$C_{38}H_{73}NNaO_4^+$	630.54318	$[M+Na]^+$	-0.29
630.580	Cer(39:1)	$C_{39}H_{77}NNaO_3^+$	630.57957	$[M+Na]^+$	0.68
632.559	Cer(38:1(2OH))	$C_{38}H_{75}NNaO_4^+$	632.55883	$[M+Na]^+$	0.27
632.634	Cer(42:2)	$C_{42}H_{82}NO_2^+$	632.63401	$[M+H]^+$	-0.02
634.650	Cer(42:1)	$C_{42}H_{84}NO_2^+$	634.64966	$[M+H]^+$	0.54
644.595	Cer(40:1)	$C_{40}H_{79}NNaO_3^+$	644.59522	$[M+Na]^+$	-0.34
648.554	Cer(38:1(2OH))	$C_{38}H_{75}NNaO_5^+$	648.55375	$[M+Na]^+$	0.39
654.616	Cer(42:2)	$C_{42}H_{81}NNaO_2^+$	654.61595	$[M+Na]^+$	0.08
656.595	Cer(41:2)	$C_{41}H_{79}NNaO_3^+$	656.59522	$[M+Na]^+$	-0.34
658.575	Cer(40:2(2OH))	$C_{40}H_{77}NNaO_4^+$	658.57448	$[M+Na]^+$	0.79
658.611	Cer(41:1)	$C_{41}H_{81}NNaO_3^+$	658.61087	$[M+Na]^+$	0.20
660.590	Cer(40:1(2OH))	$C_{40}H_{79}NNaO_4^+$	660.59013	$[M+Na]^+$	-0.20
670.611	Cer(42:2)	$C_{42}H_{81}NNaO_3^+$	670.61087	$[M+Na]^+$	0.19
686.606	GlcCer(42:2(2OH))	$C_{42}H_{81}NNaO_4^+$	686.60578	$[M+Na]^+$	0.32
686.642	Cer(43:1)	$C_{43}H_{85}NNaO_3^+$	686.64217	$[M+Na]^+$	-0.25
698.642	Cer(44:2)	$C_{44}H_{85}NNaO_3^+$	698.64217	$[M+Na]^+$	-0.24
700.658	Cer(44:1)	$C_{44}H_{87}NNaO_3^+$	700.65782	$[M+Na]^+$	0.26
704.616	Cer(42:1(2OH))	$C_{42}H_{83}NNaO_5^+$	704.61635	$[M+Na]^+$	-0.50
722.618	SM(34:0)	$C_{39}H_{85}N_2O_6P^+$	722.61705	$[M+NH_4]^+$	1.31
732.648	Cer(44:1(2OH))	$C_{44}H_{87}NNaO_5^+$	732.64765	$[M+Na]^+$	0.48
736.634	SM(35:0)	$C_{40}H_{87}N_2O_6P^+$	736.63270	$[M+NH_4]^+$	1.76
748.643	Cer(44:1(5OH))	$C_{44}H_{87}NNaO_6^+$	748.64256	$[M+Na]^+$	0.59

Phospholipids

Experimental mass	Putative I.D.	Experimental formula	Exact mass	Adduct	Mass deviation
437.204	CPA(16:0)	$C_{19}H_{36}Na_2O_6P^+$	437.20394	$[M+2Na-H]^+$	0.14
441.238	CPA(18:1)	$C_{21}H_{39}NaO_6P^+$	441.23765	$[M+Na]^+$	0.79
443.253	CPA(18:0)	$C_{21}H_{41}NaO_6P^+$	443.25330	$[M+Na]^+$	-0.68
459.248	PA(18:1)	$C_{21}H_{41}NaO_7P^+$	459.24821	$[M+Na]^+$	-0.46
461.204	CPA(18:2)	$C_{21}H_{38}Na_2O_6P^+$	461.20394	$[M+2Na-H]^+$	0.13
463.22	CPA(18:1)	$C_{21}H_{38}Na_2O_6P^+$	463.21959	$[M+2Na-H]^+$	0.89
465.235	CPA(18:0)	$C_{21}H_{40}Na_2O_6P^+$	465.23524	$[M+2Na-H]^+$	-0.52
487.28	PA(20:1)	$C_{23}H_{45}NaO_7P^+$	487.27951	$[M+Na]^+$	1.01
497.183	CPA(18:0)	$C_{21}H_{40}K_2O_6P^+$	497.18312	$[M+2K-H]^+$	-0.24
558.236	PE(18:0)	$C_{23}H47K_2NO_7P^+$	558.23588	$[M+2K-H]^+$	0.21
562.327	PE(21:0)	$C_{26}H_{54}KNO_7P^+$	562.32695	$[M+K]^+$	0.09
697.478	PA(34:1)	$C_{37}H_{71}NaO_8P^+$	697.47788	$[M+Na]^+$	0.17
713.452	PA(34:1)	$C_{37}H_{71}KO_8P^+$	713.45181	$[M+K]^+$	0.27
720.591	PE(35:0)	$C_{40}H_{83}NO_7P^+$	720.59017	$[M+H]^+$	1.15
734.606	PE(36:0)	$C_{41}H_{85}NO_7P^+$	734.60582	$[M+H]^+$	0.25
736.585	PA(37:0)	$C_{40}H_{83}NO_8P^+$	736.58508	M+NH4	-0.11
737.452	PA(36:3)	$C_{39}H_{71}KO_8P^+$	737.45181	$[M+K]^+$	0.26
739.468	PA(36:2)	$C_{39}H_{73}KO_8P^+$	739.46746	$[M+K]^+$	0.73
748.622	PE(37:0	$C_{42}H_{87}NO_7P^+$	748.62147	$[M+H]^+$	0.71
750.601	PA(38:0)	$C_{41}H_{85}NO_8P^+$	750.60073	$[M+NH_4]^+$	0.36
767.499	PA(38:2)	$C_{41}H_{77}KO_8P^+$	767.49876	$[M+K]^+$	0.31
798.541	PE(40:6)	$C_{45}H_{78}NNaO_7P^+$	798.54081	$[M+Na]^+$	0.24
804.492	PE(38:5)	$C_{43}H_{76}KNO_8P^+$	804.49401	$[M+K]^+$	-2.50
808.583	PE(39:2)	$C_{44}H_{84}NNaO_8P^+$	808.58268	$[M+Na]^+$	0.40
810.599	PE(39:1)	$C_{44}H_{86}NNaO_8P^+$	810.59833	$[M+Na]^+$	0.83
820.466	PE(36:2)	$C_{41}H_{77}K_2NO_8P^+$	820.46554	$[M+2K-H]^+$	0.56
824.557	PE(39:2)	$C_{44}H_{84}KNO_8P^+$	824.55661	$[M+K]^+$	0.47
826.573	PE(39:1)	$C_{44}H_{86}KNO_8P^+$	826.57226	$[M+K]^+$	0.90
845.676	PE(42:2)	$C_{47}H_{94}N_2O_8P^+$	845.67423	$[M+NH_4]^+$	2.09

Table 9.16 Mouse skin lipids – glycerolipids and other lipids

Glycerolipids

Experimental mass	Putative I.D.	Experimental formula	Exact mass	Adduct	Mass deviation
313.274	MG(16:0)	$C_{19}H_{37}O_3^+$	313.27372	$[M+H-H_2O]^+$	0.893787069
337.274	MG(18:2)	$C_{21}H_{37}O_3^+$	337.27372	$[M+H-H_2O]^+$	0.830186236
339.289	MG(18:1)	$C_{21}H_{39}O_3^+$	339.28937	$[M+H-H_2O]^+$	-1.090514566
341.305	MG(18:0)	$C_{21}H_{41}O_3^+$	341.30502	$[M+H-H_2O]^+$	-0.058598611
547.472	DG(32:2)	$C_{35}H_{63}O_4^+$	547.47209	$[M+H-H_2O]^+$	-0.164391942
549.488	DG(32:1)	$C_{35}H_{65}O_4^+$	549.48774	$[M+H-H_2O]^+$	0.473167973
551.504	DG(32:0)	$C_{35}H_{67}O_4^+$	551.50339	$[M+H-H_2O]^+$	1.106067544
573.488	DG(34:3)	$C_{37}H_{65}O_4^+$	573.48774	$[M+H-H_2O]^+$	0.453366274
575.504	DG(34:2)	$C_{37}H_{67}O_4^+$	575.50339	$[M+H-H_2O]^+$	1.059941628
577.519	DG(34:1)	$C_{37}H_{69}O_4^+$	577.51904	$[M+H-H_2O]^+$	-0.069261786
579.535	DG(34:0)	$C_{37}H_{71}O_4^+$	579.53469	$[M+H-H_2O]^+$	0.534911896
599.503	DG(36:4)	$C_{39}H_{67}O_4^+$	599.50339	$[M+H-H_2O]^+$	-0.65053844
601.519	DG(36:3)	$C_{39}H_{69}O_4^+$	601.51904	$[M+H-H_2O]^+$	-0.066498311
603.535	DG(36:2)	$C_{39}H_{71}O_4^+$	603.53469	$[M+H-H_2O]^+$	0.513640732
605.551	DG(36:1)	$C_{39}H_{73}O_4^+$	605.55034	$[M+H-H_2O]^+$	1.089917644
613.481	DG(34:3)	$C_{37}H_{66}NaO_5^+$	613.48025	$[M+Na]^+$	1.222533244
615.496	DG(34:2)	$C_{37}H_{68}NaO_5^+$	615.4959	$[M+Na]^+$	0.162470619
617.512	DG(34:1)	$C_{37}H_{70}NaO_5^+$	617.51155	$[M+Na]^+$	0.728731309
639.496	DG(36:4)	$C_{39}H_{68}NaO_5^+$	639.4959	$[M+Na]^+$	0.156373168
641.512	DG(36:3)	$C_{39}H_{70}NaO_5^+$	641.51155	$[M+Na]^+$	0.701468274
649.557	DG(41:5)	$C_{44}H_{73}O_3^+$	649.55542	$[M+H-2H_2O]^+$	2.43243294
677.588	DG(43:5)	$C_{46}H_{77}O_3^+$	677.58672	$[M+H-2H_2O]^+$	1.889057094
707.599	DG(44:5)	$C_{47}H_{79}O_4^+$	707.59729	$[M+H-H_2O]^+$	2.416628814
719.635	DG(46:5)	$C_{49}H_{83}O_3^+$	719.63367	$[M+H-2H_2O]^+$	1.848162552
723.494	DG(40:8)	$C_{44}H_{68}Na_2O_5^+$	723.49349	$[M+2Na-H]^+$	0.704913046
730.669	DG(44:3)	$C_{47}H_{88}NO_4^+$	730.67079	M+NH4-H2O	-2.449803693
732.612	TG(142:4)	$C_{45}H_{82}NO_6^+$	732.61367	$[M+NH_4]^+$	-2.279509745
735.63	DG(46:6)	$C_{49}H_{83}O_4^+$	735.62859	$[M+H-H_2O]^+$	1.916728114
746.664	DG(44:4)	$C_{47}H_{88}NO_5^+$	746.6657	$[M+NH_4]^+$	-2.276788662
749.646	TG(47:4)	$C_{50}H_{85}O_4^+$	749.64424	$[M+H-2H_2O]^+$	2.347780328
751.625	DG(46:7)	$C_{49}H_{83}O_5^+$	751.6235	$[M+H]^+$	1.995680018
823.679	TG(48:3)	$C_{51}H_{92}NaO_6^+$	823.67861	$[M+Na]^+$	0.473485647
825.695	TG(48:2)	$C_{51}H_{94}NaO_6^+$	825.69426	$[M+Na]^+$	0.896215507
825.806	TG(53:1)	$C_{56}H_{105}O_3^+$	825.80582	$[M+H-2H_2O]^+$	0.217968917
828.742	TG(50:5)	$C_{53}H_{98}NO_5^+$	828.74395	$[M+NH_4]^+$	-2.352958354
851.783	TG(54:4)	$C_{57}H_{103}O_4^+$	851.78509	$[M+H-H_2O]^+$	-2.453670561
853.726	TG(50:2)	$C_{53}H_{98}NaO_6^+$	853.72556	$[M+Na]^+$	0.515388107
867.684	TG(50:3)	$C_{53}H_{96}KO_6^+$	867.68385	$[M+K]^+$	0.172874025
869.7	TG(50:2)	$C_{53}H_{96}KO6^+$	869.6995	$[M+K]^+$	0.574911219
870.789	TG(53:5)	$C_{56}H_{104}NO_5^+$	870.7909	$[M+NH_4]^+$	-2.181924501
875.71	TG(52:5)	$C_{55}H_{96}NaO_6^+$	875.70991	$[M+Na]^+$	0.10277376
877.726	TG(52:4)	$C_{55}H_{98}NaO_6^+$	877.72556	$[M+Na]^+$	0.501295644
879.742	TG(52:3)	$C_{55}H_{100}NaO_6^+$	879.74121	$[M+Na]^+$	0.897991354
881.758	TG(54:5)	$C_{57}H_{101}O_5^+$	881.75927	$[M+H]^+$	-1.440302408
881.83	TG(56:3)	$C_{59}H_{109}O_4^+$	881.83204	$[M+H-H_2O]^+$	-2.313365706
891.684	TG(52:5)	$C_{55}H_{96}KO_6^+$	891.68385	$[M+K]^+$	0.168221057
893.7	TG(52:4)	$C_{55}H_{98}KO_6^+$	893.6995	$[M+K]^+$	0.559472172
895.716	TG(52:3)	$C_{55}H_{100}KO_6^+$	895.71515	$[M+K]^+$	0.948962402
897.731	TG(52:2)	$C_{55}H_{102}KO_6^+$	897.7308	$[M+K]^+$	0.222783935
898.82	TG(55:5)	$C_{58}H_{106}NO_5^+$	898.8222	$[M+NH_4]^+$	-2.447647599
901.726	TG(56:9)	$C_{59}H_{97}O_6^+$	901.72797	$[M+H]^+$	-2.184694349
907.773	TG(56:6)	$C_{59}H_{103}O_6^+$	907.77492	$[M+H]^+$	-2.115061738
911.877	TG(58:2)	$C_{61}H_{115}O_4^+$	911.87899	$[M+H-H_2O]^+$	-2.182307106
912.836	TG(56:5)	$C_{59}H_{110}NO_5^+$	912.83785	$[M+NH_4]^+$	-2.026646901
913.839	TG(60:6)	$C_{63}H_{109}O_3^+$	913.83712	$[M+H-2H_2O]^+$	2.057259394
914.815	TG(55:4)	$C_{58}H_{108}NO_6^+$	914.81712	$[M+NH_4]^+$	-2.317403067
917.7	TG(54:6)	$C_{57}H_{98}KO_6^+$	917.6995	$[M+K]^+$	0.544840659
919.715	TG(54:5)	$C_{57}H_{100}KO_6^+$	919.71515	$[M+K]^+$	-0.163093975
921.731	TG(54:4)	$C_{57}H_{102}KO_6^+$	921.7308	$[M+K]^+$	0.216983093
923.747	TG(54:3)	$C_{57}H_{104}KO_6^+$	923.74645	$[M+K]^+$	0.595401476
926.851	TG(57:3)	$C_{60}H_{112}NO_5^+$	926.8535	$[M+NH_4-H_2O]^+$	-2.697297901
928.831	TG(56:4)	$C_{59}H_{110}NO_6^+$	928.83277	$[M+NH_4]^+$	-1.90561752
941.87	TG(62:6)	$C_{65}H_{113}O_3^+$	941.86842	$[M+H-2H_2O]^+$	1.677516696
942.825	TG(60:9)	$C_{63}H_{108}NO_4^+$	942.82729	$[M+NH_4-H_2O]^+$	-2.428864782
956.862	TG(58:4)	$C_{61}H_{114}NO_6^+$	956.86407	$[M+NH_4]^+$	-2.163316677
957.865	TG(62:7)	$C_{65}H_{113}O_4^+$	957.86334	$[M+H-H_2O]^+$	1.733023836
968.898	TG(60:5)	$C_{63}H_{118}NO_5^+$	968.90045	$[M+NH_4]^+$	-2.528639552
969.901	TG(64:6)	$C_{67}H_{117}O_3^+$	969.89972	$[M+H-2H_2O]^+$	1.319724064
984.893	TG(60:4)	$C_{63}H_{118}NO_6^+$	984.89537	$[M+NH_4]^+$	-2.406346981
997.912	TG(60:0)	$C_{63}H_{122}NaO_6^+$	997.91336	$[M+Na]^+$	-1.362843764
998.909	TG(61:4)	$C_{64}H_{120}NO_6^+$	998.91102	$[M+NH_4]^+$	-2.022202138
1010.945	TG(63:3)	$C_{66}H_{124}NO_5^+$	1010.9474	M+NH4-H2O	-2.374010755
1024.961	TG(64:5)	$C_{67}H_{126}NO_5^+$	1024.96305	$[M+NH_4]^+$	-2.0000721
1026.94	TG(62:4)	$C_{66}H_{124}NO_6^+$	1026.94232	$[M+NH_4]^+$	-2.259133697
1052.992	TG(66:3)	$C_{69}H_{130}NO_5^+$	1052.99435	$[M+NH_4-H_2O]^+$	-2.231730873
1054.971	TG(65:4)	$C_{68}H_{128}NO_6^+$	1054.97362	$[M+NH_4]^+$	-2.483474421
1065.958	TG(70:7)	$C_{73}H_{125}O_4^+$	1065.95724	$[M+H-2H_2O]^+$	0.71297419
1081.953	TG(70:8)	$C_{73}H_{125}O_5^+$	1081.95215	$[M+H-H_2O]^+$	0.785616998
1090.971	TG(68:7)	$C_{71}H_{128}NO_6^+$	1090.97362	$[M+NH_4]^+$	-2.401524612

Other lipids

Experimental mass	Putative I.D.	Experimental formula	Exact mass	Adduct	Mass deviation
236.237	Palmitoleamide	$C_{16}H_{30}N^+$	236.23728	$[M+H-H_2O]^+$	-1.19
238.253	Palmitamide	$C_{16}H_{32}N^+$	238.25293	$[M+H-H_2O]^+$	0.29
262.253	Linoleamide	$C_{18}H_{32}N^+$	262.25293	$[M+H-H_2O]^+$	0.27
264.268	Oleamide	$C_{18}H_{34}N^+$	264.26858	$[M+H-H_2O]^+$	-2.19
282.279	Oleamide	$C_{18}H_{36}NO^+$	282.27914	$[M+H]^+$	-0.50
562.481	Hexacosanoyl carnitine	$C_{33}H_{65}NNaO_4^+$	562.48058	$[M+Na]^+$	0.75

Table 9.17 *Drosophila* cuticular lipids – aldehydes/ketones, linear/branched chain FAs

Aldehydes/Ketones

Observed *m/z*	Putative I.D.	Formula (observed)	Polarity	OrbiSIMS Adduct	Mass deviation (δppm)	Validation?	Standard?
256.263	C16:1	$C_{16}H_{34}NO^+$	Positive	$[M+NH_4]^+$	-0.7	-	-
324.326	C21:2	$C_{21}H_{42}NO^+$	Positive	$[M+NH_4]^+$	1.5	-	-

Linear/branched chain hydrocarbons

Observed *m/z*	Putative I.D.	Formula (observed)	Polarity	OrbiSIMS Adduct	Mass deviation (δppm)	Validation?	Standard?
308.331	C21:0	$C_{21}H_{42}N^+$	Positive	$[M+N]^+$	1.4	GC-MS	✓
320.331	C22:1	$C_{22}H_{42}N^+$	Positive	$[M+N]^+$	1.3	GC-MS	x
322.347	C22:0	$C_{22}H_{44}N^+$	Positive	$[M+N]^+$	1.0	GC-MS	✓
336.362	C23:1	$C_{23}H_{46}N^+$	Positive	$[M+N]^+$	1.4	GC-MS	✓
338.378	C23:0	$C_{23}H_{48}N^+$	Positive	$[M+N]^+$	1.4	GC-MS	✓
350.378	C24:1	$C_{24}H_{48}N^+$	Positive	$[M+N]^+$	1.4	GC-MS	x
352.393	C24:0	$C_{24}H_{50}N^+$	Positive	$[M+N]^+$	1.3	GC-MS	✓
364.393	C25:1	$C_{25}H_{50}N^+$	Positive	$[M+N]^+$	1.4	GC-MS	✓
366.409	C25:0	$C_{25}H_{52}N^+$	Positive	$[M+N]^+$	1.3	GC-MS	x
380.425	C26:0	$C_{26}H_{54}N^+$	Positive	$[M+N]^+$	1.1	GC-MS	✓
392.425	C27:1	$C_{27}H_{54}N^+$	Positive	$[M+N]^+$	1.1	GC-MS	x
394.440	C27:0	$C_{27}H_{56}N^+$	Positive	$[M+N]^+$	1.0	GC-MS	x
408.456	C28:0	$C_{28}H_{58}N^+$	Positive	$[M+N]^+$	1.2	GC-MS	✓
422.472	C29:0	$C_{29}H_{60}N^+$	Positive	$[M+N]^+$	1.0	GC-MS	✓

Linear/branched chain Fatty acid/Wax ester

Observed *m/z*	Putative I.D.	Formula (observed)	Polarity	OrbiSIMS Adduct	Mass deviation (δppm)	Validation?	Standard?
197.155	C12:1	$C_{12}H_{21}O_2^-$	Negative	$[M-H]^-$	-0.8	-	-
199.170	C12:0	$C_{12}H_{23}O_2^-$	Negative	$[M-H]^-$	-0.7	-	-
225.186	C14:1	$C_{14}H_{25}O_2^-$	Negative	$[M-H]^-$	-0.6	-	-
227.202	C14:0	$C_{14}H_{27}O_2^-$	Negative	$[M-H]^-$	-0.5	LC-MS/MS	x
239.201	C15:1	$C_{15}H_{27}O_2^-$	Negative	$[M-H]^-$	-0.8	-	-
241.217	C15:0	$C_{15}H_{29}O_2^-$	Negative	$[M-H]^-$	-0.5	-	-
251.202	C16:2	$C_{16}H_{27}O_2^-$	Negative	$[M-H]^-$	-0.6	-	-
253.217	C16:1	$C_{16}H_{29}O_2^-$	Negative	$[M-H]^-$	0.4	-	-
255.233	C16:0	$C_{16}H_{31}O_2^-$	Negative	$[M-H]^-$	0.6	LC-MS/MS	x
267.233	C17:1	$C_{17}H_{31}O_2^-$	Negative	$[M-H]^-$	-0.6	-	-
277.217	C18:3	$C_{18}H_{29}O_2^-$	Negative	$[M-H]^-$	0.4	-	-
279.233	C18:2	$C_{18}H_{31}O_2^-$	Negative	$[M-H]^-$	0.2	-	-
281.249	C18:1	$C_{18}H_{33}O_2^-$	Negative	$[M-H]^-$	0.0	-	-
283.264	C18:0	$C_{18}H_{35}O_2^-$	Negative	$[M-H]^-$	0.2	-	-
295.264	C19:1	$C_{19}H_{35}O_2^-$	Negative	$[M-H]^-$	-2.5	-	-
309.280	C20:1	$C_{20}H_{37}O_2^-$	Negative	$[M-H]^-$	-0.7	-	-
311.296	C20:0	$C_{20}H_{39}O_2^-$	Negative	$[M-H]^-$	2.7	-	-
323.296	C21:1	$C_{21}H_{39}O_2^-$	Negative	$[M-H]^-$	2.6	LC-MS/MS	x
337.311	C22:1	$C_{22}H_{41}O_2^-$	Negative	$[M-H]^-$	-0.6	LC-MS/MS	x
339.327	C22:0	$C_{22}H_{43}O_2^-$	Negative	$[M-H]^-$	0.1	LC-MS	x
351.327	C23:1	$C_{23}H_{43}O_2^-$	Negative	$[M-H]^-$	-0.5	LC-MS/MS	x
353.342	C23:0	$C_{23}H_{45}O_2^-$	Negative	$[M-H]^-$	-0.5	-	-
365.342	C24:1	$C_{24}H_{45}O_2^-$	Negative	$[M-H]^-$	-0.7	LC-MS/MS	x
367.358	C24:0	$C_{24}H_{47}O_2^-$	Negative	$[M-H]^-$	-0.1	-	-
379.359	C25:1	$C_{25}H_{47}O_2^-$	Negative	$[M-H]^-$	2.8	LC-MS/MS	x
381.374	C25:0	$C_{25}H_{49}O_2^-$	Negative	$[M-H]^-$	-0.5	-	-
393.374	C26:1	$C_{26}H_{49}O_2^-$	Negative	$[M-H]^-$	-0.2	LC-MS/MS	x
395.390	C26:0	$C_{26}H_{51}O_2^-$	Negative	$[M-H]^-$	0.1	LC-MS	x
407.389	C27:1	$C_{27}H_{51}O_2^-$	Negative	$[M-H]^-$	-0.4	LC-MS	x
409.405	C27:0	$C_{27}H_{53}O_2^-$	Negative	$[M-H]^-$	-0.4	-	-
421.405	C28:1	$C_{28}H_{53}O_2^-$	Negative	$[M-H]^-$	-0.1	LC-MS/MS	x
423.421	C28:0	$C_{28}H_{55}O_2^-$	Negative	$[M-H]^-$	0.8	-	-
435.421	C29:1	$C_{29}H_{55}O_2^-$	Negative	$[M-H]^-$	-0.4	-	-
437.437	C29:0	$C_{29}H_{57}O_2^-$	Negative	$[M-H]^-$	1.6	-	-
449.361	C25:0	$C_{26}H_{50}NaO_4^-$	Negative	$[M-H+HCOONa]^-$	-0.3	-	-
449.436	C30:1	$C_{30}H_{57}O_2^-$	Negative	$[M-H]^-$	-0.2	-	-
451.452	C30:0	$C_{30}H_{59}O_2^-$	Negative	$[M-H]^-$	0.8	-	-
463.452	C31:1	$C_{31}H_{59}O_2^-$	Negative	$[M-H]^-$	-0.1	-	-
465.467	C31:0	$C_{31}H_{61}O_2^-$	Negative	$[M-H]^-$	-0.5	-	-
475.377	C27:1	$C_{28}H_{50}NaO_4^-$	Negative	$[M-H+HCOONa]^-$	-0.5	-	-
475.488	C33:0	$C_{33}H_{65}O^-$	Negative	$[M-H-H_2O]^-$	-0.5	-	-
477.469	C32:1	$C_{32}H_{61}O_2^-$	Negative	$[M-H]^-$	2.1	-	-
479.483	C32:0	$C_{32}H_{63}O_2^-$	Negative	$[M-H]^-$	-0.3	-	-
491.483	C33:1	$C_{33}H_{63}O_2^-$	Negative	$[M-H]^-$	-1.5	-	-
501.392	C29:2	$C_{30}H_{50}NaO_4^-$	Negative	$[M-H+HCOONa]^-$	-0.5	-	-
503.408	C29:1	$C_{30}H_{52}NaO_4^-$	Negative	$[M-H+HCOONa]^-$	-0.3	-	-
503.483	C34:2	$C_{34}H_{63}O_2^-$	Negative	$[M-H]^-$	-0.2	-	-
503.520	C35:0	$C_{35}H_{67}O^-$	Negative	$[M-H-H_2O]^-$	-0.4	-	-
505.499	C34:1	$C_{34}H_{65}O_2^-$	Negative	$[M-H]^-$	0.2	-	-
507.514	C34:0	$C_{34}H_{67}O_2^-$	Negative	$[M-H]^-$	-1.1	-	-
519.514	C35:1	$C_{35}H_{67}O_2^-$	Negative	$[M-H]^-$	-0.7	-	-
527.408	C31:3	$C_{32}H_{50}NaO_4^-$	Negative	$[M-H+HCOONa]^-$	-0.7	LC-MS	x
529.424	C31:2	$C_{32}H_{52}NaO_4^-$	Negative	$[M-H+HCOONa]^-$	-0.6	LC-MS	x
529.499	C36:3	$C_{36}H_{65}O_2^-$	Negative	$[M-H]^-$	-0.6	LC-MS/MS	x
531.439	C31:1	$C_{32}H_{54}NaO_4^-$	Negative	$[M-H+HCOONa]^-$	-0.5	-	-
531.516	C36:2	$C_{36}H_{67}O_2^-$	Negative	$[M-H]^-$	2.9	-	-
531.551	C37:0	$C_{37}H_{71}O^-$	Negative	$[M-H-H_2O]^-$	-0.6	-	-
533.455	C31:0	$C_{32}H_{56}NaO_4^-$	Negative	$[M-H+HCOONa]^-$	-0.5	-	-
533.530	C36:1	$C_{36}H_{69}O_2^-$	Negative	$[M-H]^-$	-0.4	-	-
535.546	C36:0	$C_{36}H_{71}O_2^-$	Negative	$[M-H]^-$	0.3	-	-
547.546	C37:1	$C_{37}H_{71}O_2^-$	Negative	$[M-H]^-$	-0.6	-	-
555.439	C33:3	$C_{34}H_{52}NaO_4^-$	Negative	$[M-H+HCOONa]^-$	-0.4	-	-
557.455	C33:2	$C_{34}H_{54}NaO_4^-$	Negative	$[M-H+HCOONa]^-$	-0.4	-	-
559.471	C33:1	$C_{34}H_{56}NaO_4^-$	Negative	$[M-H+HCOONa]^-$	-0.5	-	-
559.547	C38:2	$C_{38}H_{71}O_2^-$	Negative	$[M-H]^-$	2.6	-	-
561.562	C38:1	$C_{38}H_{73}O_2^-$	Negative	$[M-H]^-$	1.4	-	-
563.588	C38:0	$C38H_{75}O_2^-$	Negative	$[M-H]^-$	19.2	-	-
575.577	C39:1	$C_{39}H_{75}O_2^-$	Negative	$[M-H]^-$	-0.4	-	-
585.486	C35:2	$C_{36}H_{58}NaO_4^-$	Negative	$[M-H+HCOONa]^-$	-0.3	-	-
587.577	C40:2	$C_{40}H_{75}O_2^-$	Negative	$[M-H]^-$	-0.4	-	-
589.593	C40:1	$C_{40}H_{77}O_2^-$	Negative	$[M-H]^-$	-0.5	-	-
603.608	C41:1	$C_{41}H_{79}O_2^-$	Negative	$[M-H]^-$	-0.4	-	-
617.624	C42:1	$C_{42}H_{81}O_2^-$	Negative	$[M-H]^-$	-0.3	-	-
675.702	C46:0	$C_{46}H_{91}O_2^-$	Negative	$[M-H]^-$	-0.5	-	
703.734	C48:1	$C_{48}H_{95}O_2^-$	Negative	$[M-H]^-$	0.5	-	-
717.750	C49:0	$C_{49}H_{97}O_2^-$	Negative	$[M-H]^-$	0.1	-	-
731.766	C50:0	$C_{50}H_{99}O_2^-$	Negative	$[M-H]^-$	0.7	-	-
745.781	C51:0	$C_{51}H_{101}O_2^-$	Negative	$[M-H]^-$	0.3	-	-
759.796	C52:0	$C_{52}H_{103}O_2^-$	Negative	$[M-H]^-$	-0.3	-	-
773.812	C53:0	$C_{53}H_{105}O_2^-$	Negative	$[M-H]^-$	0.5	-	-
787.827	C54:0	$C_{54}H_{107}O_2^-$	Negative	$[M-H]^-$	-0.7	-	-
815.858	C56:0	$C_{56}H_{111}O_2^-$	Negative	$[M-H]^-$	-1.7	-	-
841.875	C58:1	$C_{58}H_{113}O_2^-$	Negative	$[M-H]^-$	-0.1	-	-
843.890	C58:0	$C_{58}H_{115}O_2^-$	Negative	$[M-H]^-$	-0.5	LC-MS	x
867.926	C61:0	$C_{61}H_{119}O^-$	Negative	$[M-H-H_2O]^-$	-0.9	-	-

Observed *m/z*	Putative I.D.	Formula (observed)	Polarity	OrbiSIMS Adduct	Mass deviation (δppm)	Validation?	Standard?
273.180	C14:0	$C_{14}H_{27}NaO_2^+$	Positive	$[M+2Na-H]^+$	-0.9	LC-MS/MS	x
283.263	C18:1	$C_{18}H_{35}O_2^+$	Positive	$[M+H]^+$	-0.6	-	-
299.196	C16:1	$C_{16}H_{28}NaO_2^+$	Positive	$[M+2Na-H]^+$	-0.6	-	-
301.211	C16:0	$C_{16}H_{30}NaO_2^+$	Positive	$[M+2Na-H]^+$	-0.6	LC-MS/MS	x
309.279	C20:2	$C_{20}H_{37}O_2^+$	Positive	$[M+H]^+$	-0.7	-	-
311.294	C20:1	$C_{20}H_{39}O_2^+$	Positive	$[M+H]^+$	-0.6	-	-
324.326	C21:1	$C_{21}H_{42}NO^+$	Positive	$[M+NH_4-H_2O]^+$	-0.4	LC-MS/MS	x
327.227	C18:1	$C_{18}H_{32}NaO_2^+$	Positive	$[M+2Na-H]^+$	-0.6	-	-
354.373	C23:0	$C_{23}H_{48}NO^+$	Positive	$[M+NH_4-H_2O]^+$	-0.5	-	-
382.404	C25:0	$C_{25}H_{52}NO^+$	Positive	$[M+NH_4-H_2O]^+$	-0.7	-	-
410.436	C27:0	$C_{27}H_{56}NO^+$	Positive	$[M+NH_4-H_2O]^+$	0.0	-	-

Table 9.18 *Drosophila* cuticular lipids – modified FAs, glycerolipids, phospholipids, ceramides

Modified linear/branched chain Fatty acids/Wax esters

Observed *m/z*	Putative I.D.	Formula (observed)	Polarity	OrbiSIMS Adduct	Mass deviation (δppm)	Validation?	Standard?
243.196	x-hydroxy C14:0	$C_{14}H_{27}O_3^-$	Negative	$[M-H]^-$	-1.1	-	
269.212	x-hydroxy C16:1	$C_{16}H_{29}O_3^-$	Negative	$[M-H]^-$	-0.7	-	
271.228	x-hydroxy C16:0	$C_{16}H_{31}O_3^-$	Negative	$[M-H]^-$	-0.7	-	
291.194	x-hydroxy C16:1	$C_{16}H_{28}NaO_3^-$	Negative	$[M+Na-2H]^-$	-0.7	-	
631.640	x-hydroxy C43:0	$C_{43}H_{85}O_2^-$	Negative	$[M-H-H_2O]^-$	-0.4	-	
659.671	x-hydroxy C45:0	$C_{45}H_{89}O_2^-$	Negative	$[M-H-H_2O]^-$	-0.2	-	
673.687	x-hydroxy C46:0	$C_{46}H_{91}O_2^-$	Negative	$[M-H-H_2O]^-$	-0.4	-	
701.718	x-hydroxy C48:0	$C_{48}H_{95}O_2^-$	Negative	$[M-H-H_2O]^-$	-0.5	-	
965.965	x-hydroxy C66:2	$C_{66}H_{125}O_3^-$	Negative	$[M-H]^-$	1.5	-	

Glycerolipids (MG/DG/TG)

Observed *m/z*	Putative I.D.	Formula (observed)	Polarity	OrbiSIMS Adduct	Mass deviation (δppm)	Validation?	Standard?
891.724	TG(52:3)	$C_{55}H_{103}ClO_6^-$	Negative	$[M+Cl]^-$	2.8	-	
933.757	TG(56:8)	$C_{60}H_{101}O_7^-$	Negative	$[M+HCOOH-H]^-$	2.1	-	
931.742	TG(56:9)	$C_{60}H_{99}O_7^-$	Negative	$[M+HCOOH-H]^-$	2.1	-	
931.778	TG(58:7)	$C_{61}H_{103}O_6^-$	Negative	$[M-H]^-$	2.2	-	
951.721	TG(57:8)	$C_{60}H_{100}ClO_6^-$	Negative	$[M+Cl]^-$	-0.3	-	
961.789	TG(58:8)	$C_{62}H_{105}O_7^-$	Negative	$[M+HCOOH-H]^-$	2.6	-	
989.820	TG(60:8)	$C_{64}H_{109}O_7^-$	Negative	$[M+HCOOH-H]^-$	2.1	-	

Observed *m/z*	Putative I.D.	Formula (observed)	Polarity	OrbiSIMS Adduct	Mass deviation (δppm)	Validation?	Standard?
430.389	MG(22:1)	$C_{25}H_{52}NO_4^+$	Positive	$[M+NH_4]^+$	-1.1	LC-MS/MS	x
467.409	DG(26:0)	$C_{29}H_{55}O_4^+$	Positive	$[M+H-H_2O]^+$	-0.6	LC-MS/MS	x
493.425	DG(28:1)	$C_{31}H_{57}O_4^+$	Positive	$[M+H-H_2O]^+$	-0.6	LC-MS/MS	x
495.440	DG(28:0)	$C_{31}H_{59}O_4^+$	Positive	$[M+H-H_2O]^+$	-0.7	LC-MS/MS	x
521.456	DG(30:1)	$C_{33}H_{61}O_4^+$	Positive	$[M+H-H_2O]^+$	-0.5	LC-MS/MS	x
523.472	DG(30:0)	$C_{33}H_{63}O_4^+$	Positive	$[M+H-H_2O]^+$	-0.8	LC-MS/MS	x
547.472	DG(32:2)	$C_{35}H_{63}O_4^+$	Positive	$[M+H-H_2O]^+$	-0.5	LC-MS/MS	x
549.488	DG(32:1)	$C_{35}H_{65}O_4^+$	Positive	$[M+H-H_2O]^+$	-0.3	LC-MS/MS	x
640.587	DG(36:1)	$C_{39}H_{78}NO_5^+$	Positive	$[M+NH_4]^+$	-0.7	-	
668.618	DG(38:1)	$C_{41}H_{82}NO_5^+$	Positive	$[M+NH_4]^+$	-0.7	-	
696.650	DG(40:1)	$C_{43}H_{86}NO_5^+$	Positive	$[M+NH_4]^+$	-0.5	-	
717.600	TG(40:0)	$C_{43}H_{82}NaO_6^+$	Positive	$[M+Na]^+$	-0.5	-	
743.615	TG(42:1)	$C_{45}H_{84}NaO_6^+$	Positive	$[M+Na]^+$	-0.7	LC-MS/MS	x
745.631	TG(42:0)	$C_{45}H_{86}NaO_6^+$	Positive	$[M+Na]^+$	-0.5	LC-MS/MS	x
769.631	TG(44:2)	$C_{47}H_{86}NaO_6^+$	Positive	$[M+Na]^+$	-0.5	-	
771.647	TG(44:1)	$C_{47}H_{88}NaO_6^+$	Positive	$[M+Na]^+$	-0.6	-	
797.663	TG(46:2)	$C_{49}H_{90}NaO_6^+$	Positive	$[M+Na]^+$	-0.5	LC-MS/MS	x
799.678	TG(46:1)	$C_{49}H_{92}NaO_6^+$	Positive	$[M+Na]^+$	-0.4	LC-MS/MS	x
823.678	TG(48:3)	$C_{51}H_{92}NaO_6^+$	Positive	$[M+Na]^+$	-1.1	LC-MS/MS	x
825.694	TG(48:2)	$C_{51}H_{94}NaO_6^+$	Positive	$[M+Na]^+$	-0.5	LC-MS/MS	x
827.710	TG(48:1)	$C_{51}H_{96}NaO_6^+$	Positive	$[M+Na]^+$	-0.4	LC-MS/MS	x

Phospholipids

Observed *m/z*	Putative I.D.	Formula (observed)	Polarity	OrbiSIMS Adduct	Mass deviation (δppm)	Validation?	Standard?
569.273	PI(16:1)	$C_{25}H_{46}O_{12}P^-$	Negative	$[M-H]^-$	-0.3	-	
584.371	PC(21:1)/PE(24:1)	$C_{29}H_{56}NaNO_7P^-$	Negative	$[M+Na-2H]^-$	1.4	-	
612.402	PC(25:2)/PE(28:2)	$C_{33}H_{59}NO_7P^-$	Negative	$[M-H-H_2O]^-$	-2.6	-	
640.433	PC(27:2)/PE(30:2)	$C_{35}H_{63}NO_7P^-$	Negative	$[M-H-H_2O]^-$	-2.5	-	
646.481	PC(27:0)/PE(30:0)	$C_{35}H_{69}NO_7P^-$	Negative	$[M-H]^-$	-1.1	-	
668.464	PC(29:2)/PE(30:0)	$C_{35}H_{65}NaNO_7P^-$	Negative	$[M+Na-2H]^-$	1.0	-	
674.512	PC(29:0)/PE(32:0)	$C_{37}H_{73}NO_7P^-$	Negative	$[M-H]^-$	-1.8	-	
702.543	PC(31:0)/PE(34:0)	$C_{39}H_{77}NO_7P^-$	Negative	$[M-H]^-$	-2.5	-	
722.569	PC(30:0)/PE(33:0)	$C_{39}H_{81}NO_8P^-$	Negative	$[M+HCOOH-H]^-$	-1.9	-	
746.569	PC(33:0)/PE(36:0)	$C_{41}H_{81}NO_8P^-$	Negative	$[M-H]^-$	-2.0	-	
750.600	PC(32:0)/PE(35:0)	$C_{41}H_{85}NO_8P^-$	Negative	$[M+HCOOH-H]^-$	-1.8	-	
774.600	PC(35:0)/PE(38:0)	$C_{43}H_{85}NO_8P^-$	Negative	$[M-H]^-$	-1.9	-	
776.616	PC(34:1)/PE(37:1)	$C_{43}H_{87}NO_8P^-$	Negative	$[M+HCOOH-H]^-$	-2.0	-	
778.631	PC(34:0)/PE(37:0)	$C_{43}H_{89}NO_8P^-$	Negative	$[M+HCOOH-H]^-$	-2.3	-	
800.616	PC(37:1)/PE(40:1)	$C_{45}H_{87}NO_8P^-$	Negative	$[M-H]^-$	-2.4	-	
802.632	PC(37:0)/PE(40:0)	$C_{45}H_{89}NO_8P^-$	Negative	$[M-H]^-$	-1.8	-	
828.647	PC(39:1)/PE(42:1)	$C_{47}H_{91}NO_8P^-$	Negative	$[M-H]^-$	-2.4	-	
934.762	PC(48:2)/PE(51:2)	$C_{56}H_{105}NO_7P^-$	Negative	$[M-H-H_2O]^-$	-1.4	-	
946.761	PC(46:1)/PE(49:1)	$C_{54}H_{103}FNO_8P^-$	Negative	$[M+F]^-$	-3.4	-	
990.825	PC(49:0)/PE(52:0)	$C_{57}H_{113}FNO_8P^-$	Negative	$[M+F]^-$	-2.3	-	

Ceramides and Sphingolipids

Observed *m/z*	Putative I.D.	Formula (observed)	Polarity	OrbiSIMS Adduct	Mass deviation (δppm)	Validation?	Standard?
657.497	PE-Cer(32:2)	$C_{36}H_{74}N_2O_6P^-$	Negative	$[M-H]^-$	-0.3	-	
659.513	PE-Cer(34:1)	$C_{36}H_{76}N_2O_6P^-$	Negative	$[M-H]^-$	-0.3	LC-MS/MS	x
685.529	PE-Cer(36:2)	$C_{38}H_{78}N_2O_6P^-$	Negative	$[M-H]^-$	-0.4	LC-MS/MS	x
687.545	PE-Cer(36:1)	$C_{38}H_{80}N_2O_6P^-$	Negative	$[M-H]^-$	-0.1	LC-MS/MS	x
693.535	PE-Cer(38:3)	$C_{40}H_{74}N_2O_5P^-$	Negative	$[M-H-H_2O]^-$	1.2	-	
701.560	PE-Cer(37:1)	$C_{39}H_{78}N_2O_6P^-$	Negative	$[M-H]^-$	-0.5	-	
713.560	PE-Cer(38:2)	$C_{40}H_{78}N_2O_6P^-$	Negative	$[M-H]^-$	-0.6	LC-MS	x
715.576	PE-Cer(38:1)	$C_{40}H_{80}N_2O_6P^-$	Negative	$[M-H]^-$	-0.6	LC-MS/MS	x
719.550	PE-Cer(37:2)	$C_{39}H_{77}FN_2O_6P^-$	Negative	$[M+F]^-$	-0.6	-	
721.566	PE-Cer(40:3)	$C_{42}H_{78}N_2O_5P^-$	Negative	$[M-H-H_2O]^-$	0.8	-	
723.521	PE-Cer(36:1)	$C_{38}H_{77}ClN_2O_6P^-$	Negative	$[M+Cl]^-$	0.1	LC-MS/MS	x
745.566	SM(36:3)	$C_{41}H_{79}FN_2O_6P^-$	Negative	$[M+F]^-$	-0.9	-	
747.581	PE-Cer(39:2)	$C_{41}H_{81}FN_2O_6P^-$	Negative	$[M+F]^-$	-0.9	LC-MS	x
749.597	PE-Cer(39:1)	$C_{41}H_{83}FN_2O_6P^-$	Negative	$[M+F]^-$	-0.8	-	
751.553	PE-Cer(38:1)	$C_{40}H_{81}ClN_2O_6P^-$	Negative	$[M+Cl]^-$	0.2	LC-MS/MS	x
773.597	SM(38:3)	$C_{43}H_{83}FN_2O_6P^-$	Negative	$[M+F]^-$	-1.1	-	
775.613	SM(38:2)	$C_{43}H_{85}FN_2O_6P^-$	Negative	$[M+F]^-$	-0.9	-	
777.570	PE-Cer(40:2)	$C_{42}H_{83}ClN_2O_6P^-$	Negative	$[M+Cl]^-$	2.7	-	
777.628	SM(38:1)	$C_{43}H_{87}FN_2O_6P^-$	Negative	$[M+F]^-$	-1.1	-	
799.612	SM(40:4)	$C_{45}H_{85}FN_2O_6P^-$	Negative	$[M+F]^-$	-1.3	-	
801.628	SM(40:3)	$C_{45}H_{87}FN_2O_6P^-$	Negative	$[M+F]^-$	-1.3	-	
803.644	SM(40:2)	$C_{45}H_{89}FN_2O_6P^-$	Negative	$[M+F]^-$	-1.3	-	
829.659	SM(42:3)	$C_{47}H_{91}FN_2O_6P^-$	Negative	$[M+F]^-$	-1.4	-	

Observed *m/z*	Putative I.D.	Formula (observed)	Polarity	OrbiSIMS Adduct	Mass deviation (δppm)	Validation?	Standard?
705.491	PE-Cer(34:1)	$C_{36}H_{72}N_2Na_2O_6P^+$	Positive	$[M+2Na-H]^+$	-0.9	LC-MS/MS	x
731.507	PE-Cer(36:2)	$C_{38}H_{74}N_2Na_2O_6P^+$	Positive	$[M+2Na-H]^+$	-0.4	LC-MS/MS	x
733.523	PE-Cer(36:1)	$C_{38}H_{76}N_2Na_2O_6P^+$	Positive	$[M+2Na-H]^+$	-0.6	LC-MS/MS	x
762.531	PI-Cer(34:0)	$C_{40}H_{77}NO_{10}P^+$	Positive	$[M+H-2H_2O]^+$	3.6	-	
790.562	PI-Cer(36:0)	$C_{42}H_{81}NO_{10}P^+$	Positive	$[M+H-2H_2O]^+$	3.8	-	
813.559	PI-Cer(34:0(2OH))	$C_{40}H_{82}N_2O_{12}P^+$	Positive	$[M+NH_4-H_2O]^+$	-1.3	-	
815.574	PI-Cer(34:0)	$C_{40}H_{84}N_2O_{12}P^+$	Positive	$[M+NH_4]^+$	-1.7	-	
843.605	PI-Cer(36:0)	$C_{42}H_{88}N_2O_{12}P^+$	Positive	$[M+NH_4]^+$	-1.9	-	

Cardiolipins

Observed *m/z*	Putative I.D.	Formula (observed)	Polarity	OrbiSIMS Adduct	Mass deviation (δppm)	Validation?	Standard?
1,223.689	CL(54:6)	$C_{63}H_{114}KO_{16}P_2^-$	Negative	$[M+K-2H]^-$	-2.1	-	

Observed mass		Actual mass	Formula	Compound	Deviation (ppm)		Observed ion
Wing	Cuticle				Wing	Cuticle	
253.2174	253.2174	253.2173	$C_{16}H_{30}O_2$	FA C16:1	0.5	0.4	$[M-H]^-$
255.2331	255.2331	255.233	$C_{16}H_{32}O_2$	FA C16:0	0.7	0.7	$[M-H]^-$
267.2331	267.2328	267.2334	$C_{17}H_{34}O_2$	FA C17:1	0.4	-0.6	$[M-H]^-$
269.2487	-	269.2486	$C_{17}H_{34}O_2$	FA C17:0	0.3	-	$[M-H]^-$
-	277.2174	277.2173	$C_{18}H_{30}O_2$	FA C18:3	-	0.4	$[M-H]^-$
-	279.233	279.233	$C_{18}H_{32}O_2$	FA C18:2	-	0.1	$[M-H]^-$
281.2486	281.2486	281.2486	$C_{18}H_{34}O_2$	FA C18:1	0.1	0.1	$[M-H]^-$
283.2644	283.2643	283.2643	$C_{18}H_{36}O_2$	FA C18:0	0.4	0	$[M-H]^-$
295.2643	295.2635	295.2643	$C_{19}H_{36}O_2$	FA C19:1	0.2	-2.5	$[M-H]^-$
297.28	-	297.2799	$C_{19}H_{38}O_2$	FA C19:0	0.2	-	$[M-H]^-$
309.28	309.2816	309.2799	$C_{20}H_{38}O_2$	FA C20:1	0.2	5.4	$[M-H]^-$
311.2957	311.2964	311.2956	$C_{20}H_{40}O_2$	FA C20:0	0.5	2.7	$[M-H]^-$
323.2955	323.2964	323.2956	$C_{21}H_{40}O_2$	FA C21:1	0	2.6	$[M-H]^-$
325.3113	-	325.3112	$C_{21}H_{42}O_2$	FA C21:0	0.1	-	$[M-H]^-$
337.3113	-	337.112	$C_{22}H_{42}O_2$	FA C22:1	0.2	-	$[M-H]^-$
339.3268	339.3269	339.3269	$C_{22}H_{44}O_2$	FA C22:0	-0.3	0.1	$[M-H]^-$
351.327	351.3249	351.3269	$C_{23}H_{44}O_2$	FA C23:1	0.4	-5.5	$[M-H]^-$
353.3425	-	353.3425	$C_{23}H_{46}O_2$	FA C23:0	-0.2	-	$[M-H]^-$
365.3425	365.3439	365.3425	$C_{24}H_{46}O_2$	FA C24:1	0	3.7	$[M-H]^-$
367.3581	367.3581	367.3582	$C_{24}H_{48}O_2$	FA C24:0	-0.2	-0.2	$[M-H]^-$
379.3584	379.3592	379.3582	$C_{25}H_{48}O_2$	FA C25:1	0.5	2.6	$[M-H]^-$
381.3739	-	381.3738	$C_{25}H_{50}O_2$	FA C25:0	0.1	-	$[M-H]^-$
393.3741	-	393.3738	$C_{26}H_{50}O_2$	FA C26:1	0.8	-	$[M-H]^-$
395.3895	395.3895	395.3895	$C_{26}H_{52}O_2$	FA C26:0	0	0.1	$[M-H]^-$
407.39	407.3923	407.3895	$C_{27}H_{52}O_2$	FA C27:1	1.4	7	$[M-H]^-$
409.4051	409.4067	409.4051	$C_{27}H_{54}O_2$	FA C27:0	0	3.9	$[M-H]^-$
421.4055	421.4084	421.4051	$C_{28}H_{54}O_2$	FA C28:1	1	7.8	$[M-H]^-$
423.421	423.4211	423.4208	$C_{28}H_{56}O_2$	FA C28:0	0.6	0.7	$[M-H]^-$
435.4212	-	435.4208	$C_{28}H_{56}O_2$	FA C29:1	1.1	-	$[M-H]^-$
437.4367	437.4371	437.4364	$C_{29}H_{58}O_2$	FA C29:0	0.6	1.6	$[M-H]^-$
449.4367	449.4379	449.4364	$C_{30}H_{58}O_2$	FA C30:1	0.8	3.3	$[M-H]^-$
451.4524	451.4524	451.4521	$C_{30}H_{60}O_2$	FA C30:0	0.7	0.7	$[M-H]^-$
463.4525	-	463.4521	$C_{31}H_{60}O_2$	FA C31:1	0.9	-	$[M-H]^-$
465.4675	-	465.4677	$C_{31}H_{62}O_2$	FA C31:0	-0.4	-	$[M-H]^-$
477.4678	477.4687	477.4677	$C_{32}H_{62}O_2$	FA C32:1	0.3	0.2	$[M-H]^-$
479.4835	479.4832	479.4834	$C_{32}H_{64}O_2$	FA C32:0	0.3	-0.2	$[M-H]^-$
491.484	491.4826	491.4834	$C_{33}H_{64}O_2$	FA C33:1	1.3	-1.6	$[M-H]^-$
493.4998	-	493.499	$C_{33}H_{66}O_2$	FA C33:0	1.7	-	$[M-H]^-$
505.4994	505.4991	505.499	$C_{34}H_{66}O_2$	WE C34:1	0.8	0.2	$[M-H]^-$
507.5146	507.5141	507.5147	$C_{34}H_{68}O_2$	WE C34:0	-0.1	-1	$[M-H]^-$
-	519.511	519.5147	$C_{35}H_{68}O_2$	WE C35:0	-	-7	$[M-H]^-$
-	531.5162	531.5147	$C_{36}H_{68}O_2$	WE C36:2	-	3	$[M-H]^-$
533.5307	533.5301	533.5303	$C_{36}H_{70}O_2$	WE C36:1	0.8	-0.4	$[M-H]^-$
535.5456	535.5461	535.546	$C_{36}H_{72}O_2$	WE C36:0	-0.6	0.3	$[M-H]^-$
-	559.5474	559.546	$C_{38}H_{72}O_2$	WE C38:2	-	2.6	$[M-H]^-$
561.5622	561.5624	561.5616	$C_{38}H_{74}O_2$	WE C38:1	1	1.4	$[M-H]^-$
563.5772	563.5881	563.5885	$C_{28}H_{76}O_2$	WE C38:0	-0.1	-0.7	$[M-H]^-$
589.593	-	589.5929	$C_{40}H_{78}O_2$	WE C40:1	0.2	-	$[M-H]^-$
591.6083	591.6123	591.6086	$C_{40}H_{80}O_2$	WE C40:0	-0.4	6.3	$[M-H]^-$
633.6554	-	633.6555	$C_{43}H_{86}O_2$	WE C43:0	-0.2	-	$[M-H]^-$

Observed mass		Actual mass	Formula	Compound	Deviation (ppm)		Observed ion
Wing	Cuticle				Wing	Cuticle	
-	646.481	646.4817	$C_{35}H_{70}NO_7P$	PE O-30:1	-	-1	$[M-H]^-$
665.4462	-	665.4431	$C_{34}H_{67}N_2O_6P$	PE-Cer C32:2	4.7	-	$[M+Cl]^-$
667.4617	-	667.4587	$C_{34}H_{69}N_2O_6P$	PE-Cer C32:1	4.5	-	$[M+Cl]^-$
674.512	674.5118	674.513	$C_{37}H_{74}NO_7P$	PE P-32:0	-1.6	-1.7	$[M-H]^-$
-	687.5446	687.5446	$C_{38}H_{77}N_2O_6P$	SM d33:1	-	0.1	$[M-H]^-$
693.4769	-	693.4744	$C_{36}H_{71}N_2O_6P$	PE-Cer C34:2	3.6	-	$[M+Cl]^-$
695.4926	-	695.49	$C_{36}H_{73}N_2O_6P$	PE-Cer C34:1	3.7	-	$[M+Cl]^-$
-	702.5445	702.5443	$C_{37}H_{74}NO_7P$	PC P-31:0	-	0.2	$[M-H]^-$
703.7341	703.7341	703.7338	$C_{49}H_{98}O_2$	WE C48:1	0.5	0.5	$[M-H]^-$
707.4924	-	707.49	$C_{37}H_{73}N_2O_6P$	PE-Cer C35:2	3.4	-	$[M+Cl]^-$
709.5072	-	709.5057	$C_{37}H_{75}N_2O_6P$	PE-Cer C35:1	2.1	-	$[M+Cl]^-$
717.7496	717.7495	717.7494	$C_{49}H_{98}O_2$	WE C49:0	0.2	0.1	$[M-H]^-$
721.5079	-	721.5057	$C_{38}H_{75}N_2O_6P$	PE-Cer C36:2	3.1	-	$[M+Cl]^-$
723.5238	723.5214	723.5213	$C_{38}H_{77}N_2O_6P$	PE-Cer C36:1	3.5	0.2	$[M+Cl]^-$
731.7656	731.7656	731.7651	$C_{50}H_{100}O_2$	WE C50:0	0.7	0.8	$[M-H]^-$
735.5207	-	735.5213	$C_{39}H_{77}N_2O_6P$	PE-Cer C37:2	-0.9	-	$[M+Cl]^-$
737.5386	-	737.537	$C_{39}H_{79}N_2O_6P$	PE-Cer C37:1	2.2	-	$[M+Cl]^-$
745.7806	745.7809	745.7807	$C_{53}H_{102}O_2$	WE C51:0	-0.1	0.3	$[M-H]^-$
749.5396	-	749.537	$C_{40}H_{79}N_2O_6P$	PE-Cer C38:2	3.5	-	$[M+Cl]^-$
751.5546	751.5528	751.5526	$C_{40}H_{81}N_2O_6P$	PE-Cer C38:1	2.6	0.2	$[M+Cl]^-$
759.7961	759.7961	759.7964	$C_{52}H_{104}O_2$	WE C52:0	-0.3	-0.3	$[M-H]^-$
773.8117	773.8124	773.812	$C_{53}H_{106}O_2$	WE C53:0	-0.4	0.5	$[M-H]^-$
777.5709	-	777.568	$C_{42}H_{83}N_2O_6P$	PE-Cer C40:2	3.3	-	$[M+Cl]^-$
779.5857	-	779.5839	$C_{42}H_{85}N_2O_6P$	PE-Cer C40:1	2.3	-	$[M+Cl]^-$
787.8276	787.8271	787.8277	$C_{54}H_{108}O_2$	WE C54:0	0	-0.7	$[M-H]^-$
805.6008	-	805.5996	$C_{44}H_{87}N_2O_6P$	SM d39:2	1.6	-	$[M+Cl]^-$
807.6174	-	807.6152	$C_{44}H_{89}N_2O_6P$	SM d39:1	2.6	-	$[M+Cl]^-$
-	815.8576	815.859	$C_{56}H_{112}O_2$	WE C56:0	-	-1.6	$[M-H]^-$
833.632	-	833.6309	$C_{44}H_{87}N_2O_6P$	SM d41:2	1.4	-	$[M+Cl]^-$
835.6475	835.6816	835.6821	$C_{46}H_{93}N_2O_6P$	SM d41:1	1.1	-0.6	$[M+Cl]^-$
-	841.8745	841.8746	$C_{58}H_{114}O_2$	WE C58:0	-	-0.1	$[M-H]^-$
863.6798	-	863.6778	$C_{48}H_{97}N_2O_6P$	SM d43:1	1.9	-	$[M+Cl]^-$
-	891.7239	891.7214	$C_{55}H_{100}O_6$	TG C52:3	-	2.8	$[M+Cl]^-$
903.7246	-	903.7214	$C_{56}H_{100}O_6$	TG C53:4	3.6	-	$[M+Cl]^-$
-	904.7343	904.7376	$C_{51}H_{104}NO_8P$	PC-O41:0	-	-3.7	$[M-H]^-$
931.7502	-	931.7527	$C_{58}H_{104}O_6$	TG C55:4	-2.7	-	$[M+Cl]^-$
934.7617	934.7621	934.7634	$C_{56}H_{108}NO_8P$	PC C48:2	-1.9	-1.4	$[M-H2O-H]^-$
946.7619	946.7616	946.7646	$C_{54}H_{106}NO_8P$	PC C46:1	-2.9	-3.1	$[M+F]^-$
948.7777	948.7776	948.7802	$C_{54}H_{108}NO_8$	PE C49:0	-2.9	-2.7	$[M+F]^-$
-	951.7211	951.7214	$C_{60}H_{100}O_6$	TG C57:8	-	-0.3	$[M+Cl]^-$
962.7926	962.7926	962.7959	$C_{55}H_{110}NO_8P$	PE C50:0	-3.4	-3.4	$[M+F]^-$
-	965.9649	965.9634	$C_{66}H_{126}O_3$	WE hydroxy-C66:2	-	1.5	$[M-H]^-$
976.8085	976.8085	976.8115	$C_{56}H_{112}NO_8P$	PC C48:0	-3.1	-3	$[M+F]^-$
990.824	990.8249	990.826	$C_{64}H_{113}O_8$	PC 49:0	-2	-1.1	$[M+F]^-$
1004.8404	1,004.8387	1004.8428	$C_{58}H_{116}NO_8P$	PC C50:0	-2.4	-4.1	$[M+F]^-$
-	1,032.8794	1032.8741	$C_{60}H_{120}NO_8P$	PC C52:0	-	5.1	$[M+F]^-$
-	1,062.6679	1062.663	$C_{57}H_{102}NO_{16}P$	MIPC d40:0	-	4.5	$[M+Cl]^-$
-	1,085.9203	1085.9248	$C_{69}H_{126}O_6$	TG C66:4	-	-4.2	$[M+Cl]^-$
-	1,223.6886	1223.6912	$C_{83}H_{112}O_{16}P_2$	CL C54:6	-	-2.1	$[M+K-2H]^-$

FA
WE
PE
PE-Cer
SM
PC
TG
Other

Table 9.19 *Drosophila* abdominal and wing lipids

9.4 Chapter 5 Supplementary Information

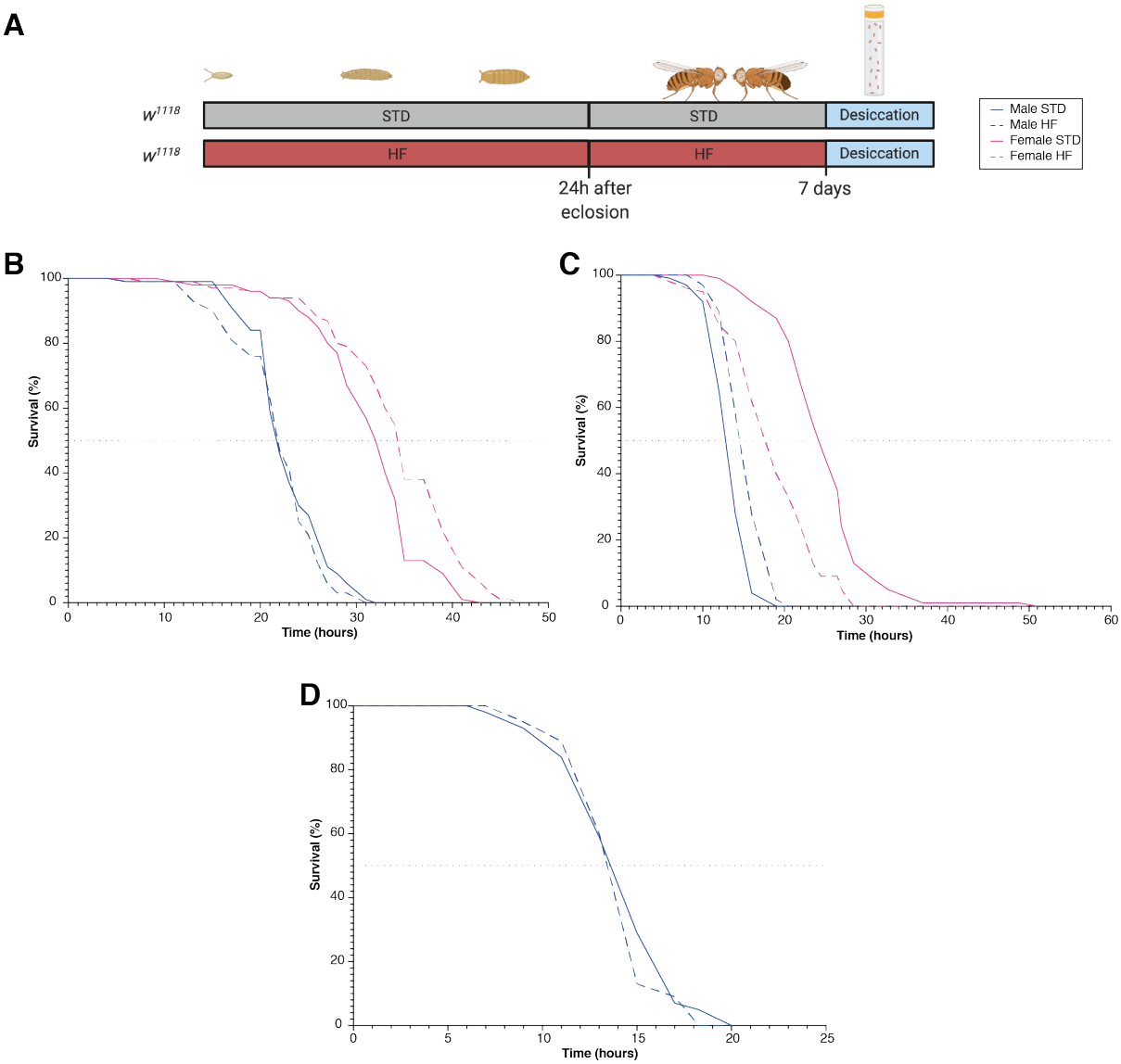

Figure 9.23 Additional replicates of desiccation resistance under HF diet for Figure 5.5
A. Experimental paradigm for high fat diet throughout development and adulthood, followed by desiccation assay.
B. In this experiment, Male STD n=70, Male HF=68, Female STD =82 and Female HF=89. Median survivals are as follows: Male STD=22 hours, Male HF=22 hours (0% change compared with STD), Female STD=32 hours, Female HF=34 hours (+6.3% change compared with STD).
C. In this experiment, Male STD=58, Male HF=55, Female STD=51, Female HF=15. Median survivals are as follows: Male STD=13 hours, Male HF=14.5 hours (+11.5% change compared with STD), Female STD=24 hours, Female HF=17.5 hours (-27.1% change compared with STD).
D. In this experiment, Male STD=58, Male HF=55. Median survivals are as follows: Male STD=14 hours, Male HF=13.5 hours (-3.6% change compared with STD).

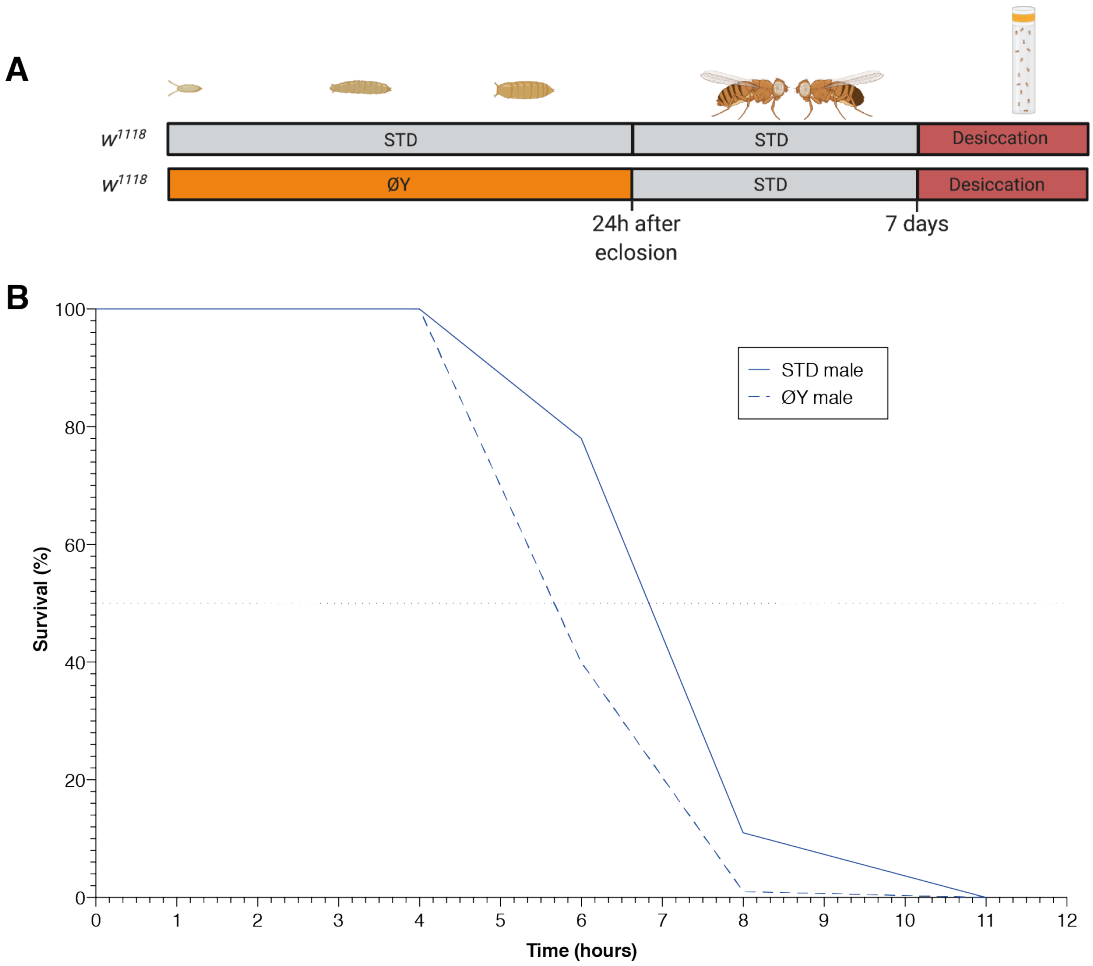

Figure 9.24 Desiccation resistance of ØY flies: Additional replicate for Figure 5.7

A. Flies were raised on a diet containing no yeast (ØY), or standard (STD) during development, then transferred to an adult STD diet for 7 days before desiccation survival was assayed.
B. Desiccation survival for male ØY and STD flies. In this experiment, STD male n=90, median survival ~6.8 hours; ØY male n=70, median survival ~5.6 hours (~17.6% decrease in median survival compared with STD control).

9.5 Chapter 6 Supplementary Information

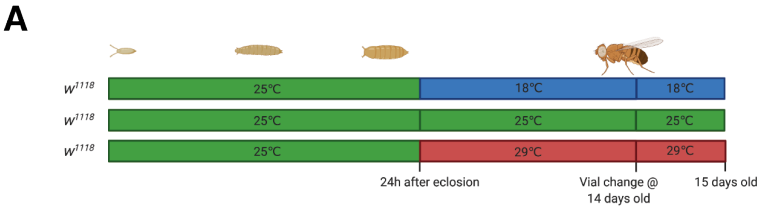

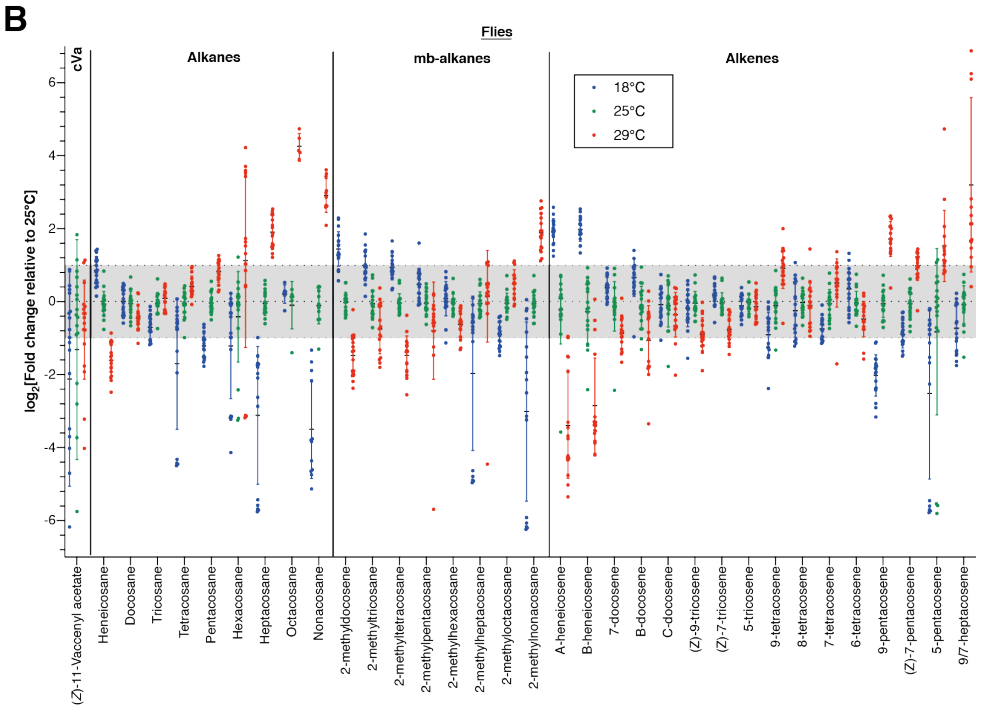

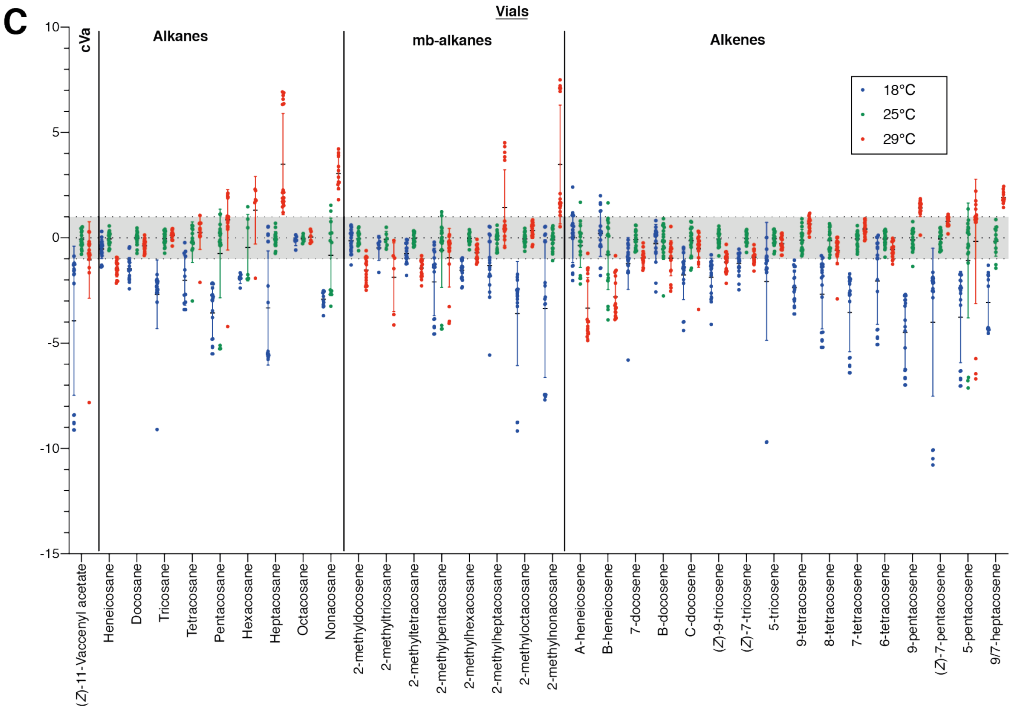

Figure 9.25 Relative abundance of fly cuticule and vial hydrocarbons at different housing temperatures

Additional information from the experiment shown in **Figure 6.8** and **Figure 6.9**.
A. Experimental schematic for temperature shift. All flies were housed at 25°C during development and transferred to the indicated temperatures within 24 hours of eclosion.
B. Relative abundance of cuticular hydrocarbons shown relative to housing at 25°C. Statistical significance for comparisons in this graph are shown in **Table 9.20**.
C. Relative abundance of vial hydrocarbons shown relative to housing at 25°C. Statistical significance for comparisons in this graph are shown in **Table 9.21**.

Table 9.20 Statistical significance for Figure 9.25B

Significance	Hexacosane	Significance	2-methyltetracosane	Significance	A-heneicosene	Significance	(*Z*)-7-tricosene	Significance	9-pentacosene	Significance
*	18°C vs. 25°C	*	18°C vs. 25°C	**	18°C vs. 25°C	****	18°C vs. 25°C	ns	18°C vs. 25°C	****
****	18°C vs. 29°C	****	18°C vs. 29°C	****	18°C vs. 29°C	****	18°C vs. 29°C	*	18°C vs. 29°C	****
ns	25°C vs. 29°C	****	25°C vs. 29°C	****	25°C vs. 29°C	****	25°C vs. 29°C	ns	25°C vs. 29°C	****
Significance	**Heptacosane**	**Significance**	**2-methylpentacosane**	**Significance**	**B-heneicosene**	**Significance**	**5-tricosene**	**Significance**	**(*Z*)-7-pentacosene**	**Significance**
**	18°C vs. 25°C	****	18°C vs. 25°C	ns	18°C vs. 25°C	****	18°C vs. 25°C	ns	18°C vs. 25°C	*
****	18°C vs. 29°C	****	18°C vs. 29°C	***	18°C vs. 29°C	****	18°C vs. 29°C	ns	18°C vs. 29°C	****
****	25°C vs. 29°C	****	25°C vs. 29°C	*	25°C vs. 29°C	****	25°C vs. 29°C	ns	25°C vs. 29°C	**
Significance	**Octacosane**	**Significance**	**2-methylhexacosane**	**Significance**	**7-docosene**	**Significance**	**9-tetracosene**	**Significance**	**5-pentacosene**	**Significance**
ns	18°C vs. 25°C	ns	18°C vs. 25°C	ns	18°C vs. 25°C	ns	18°C vs. 25°C	*	18°C vs. 25°C	****
ns	18°C vs. 29°C	****	18°C vs. 29°C	ns	18°C vs. 29°C	***	18°C vs. 29°C	****	18°C vs. 29°C	****
ns	25°C vs. 29°C	****	25°C vs. 29°C	ns	25°C vs. 29°C	ns	25°C vs. 29°C	**	25°C vs. 29°C	****
Significance	**Nonacosane**	**Significance**	**2-methylheptacosane**	**Significance**	**B-docosene**	**Significance**	**8-tetracosene**	**Significance**	**9/7-heptacosene**	**Significance**
ns	18°C vs. 25°C	****	18°C vs. 25°C	****	18°C vs. 25°C	*	18°C vs. 25°C	ns	18°C vs. 25°C	ns
*	18°C vs. 29°C	****	18°C vs. 29°C	****	18°C vs. 29°C	****	18°C vs. 29°C	ns	18°C vs. 29°C	****
ns	25°C vs. 29°C	****	25°C vs. 29°C	ns	25°C vs. 29°C	*	25°C vs. 29°C	ns	25°C vs. 29°C	****
Significance	**2-methyldocosene**	**Significance**	**2-methyloctacosane**	**Significance**	**C-docosene**	**Significance**	**7-tetracosene**	**Significance**		
****	18°C vs. 25°C	****	18°C vs. 25°C	*	18°C vs. 25°C	ns	18°C vs. 25°C	ns		
****	18°C vs. 29°C	****	18°C vs. 29°C	****	18°C vs. 29°C	ns	18°C vs. 29°C	***		
ns	25°C vs. 29°C	****	25°C vs. 29°C	ns	25°C vs. 29°C	ns	25°C vs. 29°C	ns		
Significance	**2-methyltricosane**	**Significance**	**2-methylnonacosane**	**Significance**	**(*Z*)-9-tricosene**	**Significance**	**6-tetracosene**	**Significance**		
***	18°C vs. 25°C	**	18°C vs. 25°C	****	18°C vs. 25°C	ns	18°C vs. 25°C	ns		
****	18°C vs. 29°C	****	18°C vs. 29°C	****	18°C vs. 29°C	ns	18°C vs. 29°C	*		
*	25°C vs. 29°C	ns	25°C vs. 29°C	****	25°C vs. 29°C	*	25°C vs. 29°C	ns		

Table 9.21 Statistical significance for Figure 9.25C

(*Z*)-11-Vaccenyl acetate	Significance	Hexacosane	Significance	2-methyltetracosane	Significance	A-heneicosene	Significance	(*Z*)-7-tricosene	Significance	9-pentacosene	Significance
18°C vs. 25°C	****	18°C vs. 25°C	ns	18°C vs. 25°C	ns	18°C vs. 25°C	ns	18°C vs. 25°C	*	18°C vs. 25°C	****
18°C vs. 29°C	****	18°C vs. 29°C	****	18°C vs. 29°C	ns	18°C vs. 29°C	****	18°C vs. 29°C	ns	18°C vs. 29°C	****
25°C vs. 29°C	ns	25°C vs. 29°C	ns	25°C vs. 29°C	**	25°C vs. 29°C	****	25°C vs. 29°C	ns	25°C vs. 29°C	**
Heneicosane	**Significance**	**Heptacosane**	**Significance**	**2-methylpentacosane**	**Significance**	**B-heneicosene**	**Significance**	**5-tricosene**	**Significance**	**(Z)-7-pentacosene**	**Significance**
18°C vs. 25°C	ns	18°C vs. 25°C	****	18°C vs. 25°C	**	18°C vs. 25°C	ns	18°C vs. 25°C	****	18°C vs. 25°C	****
18°C vs. 29°C	ns	18°C vs. 29°C	****	18°C vs. 29°C	*	18°C vs. 29°C	****	18°C vs. 29°C	***	18°C vs. 29°C	****
25°C vs. 29°C	**	25°C vs. 29°C	****	25°C vs. 29°C	ns	25°C vs. 29°C	****	25°C vs. 29°C	ns	25°C vs. 29°C	ns
Docosane	**Significance**	**Octacosane**	**Significance**	**2-methylhexacosane**	**Significance**	**7-docosene**	**Significance**	**9-tetracosene**	**Significance**	**5-pentacosene**	**Significance**
18°C vs. 25°C	**	18°C vs. 25°C	ns	18°C vs. 25°C	**	18°C vs. 25°C	*	18°C vs. 25°C	****	18°C vs. 25°C	****
18°C vs. 29°C	*	18°C vs. 29°C	ns	18°C vs. 29°C	ns	18°C vs. 29°C	ns	18°C vs. 29°C	****	18°C vs. 29°C	****
25°C vs. 29°C	ns	25°C vs. 29°C	ns	25°C vs. 29°C	ns	25°C vs. 29°C	ns	25°C vs. 29°C	ns	25°C vs. 29°C	ns
Tricosane	**Significance**	**Nonacosane**	**Significance**	**2-methylheptacosane**	**Significance**	**B-docosene**	**Significance**	**8-tetracosene**	**Significance**	**9/7-heptacosene**	**Significance**
18°C vs. 25°C	****	18°C vs. 25°C	***	18°C vs. 25°C	*	18°C vs. 25°C	ns	18°C vs. 25°C	****	18°C vs. 25°C	****
18°C vs. 29°C	****	18°C vs. 29°C	****	18°C vs. 29°C	****	18°C vs. 29°C	ns	18°C vs. 29°C	****	18°C vs. 29°C	****
25°C vs. 29°C	ns	25°C vs. 29°C	****	25°C vs. 29°C	**	25°C vs. 29°C	ns	25°C vs. 29°C	ns	25°C vs. 29°C	***
Tetracosane	**Significance**	**2-methyldocosene**	**Significance**	**2-methyloctacosane**	**Significance**	**C-docosene**	**Significance**	**7-tetracosene**	**Significance**		
18°C vs. 25°C	**	18°C vs. 25°C	ns	18°C vs. 25°C	****	18°C vs. 25°C	***	18°C vs. 25°C	****		
18°C vs. 29°C	***	18°C vs. 29°C	**	18°C vs. 29°C	****	18°C vs. 29°C	*	18°C vs. 29°C	****		
25°C vs. 29°C	ns	25°C vs. 29°C	**	25°C vs. 29°C	ns	25°C vs. 29°C	ns	25°C vs. 29°C	ns		
Pentacosane	**Significance**	**2-methyltricosane**	**Significance**	**2-methylnonacosane**	**Significance**	**(Z)-9-tricosene**	**Significance**	**6-tetracosene**	**Significance**		
18°C vs. 25°C	****	18°C vs. 25°C	ns	18°C vs. 25°C	****	18°C vs. 25°C	***	18°C vs. 25°C	****		
18°C vs. 29°C	****	18°C vs. 29°C	ns	18°C vs. 29°C	****	18°C vs. 29°C	ns	18°C vs. 29°C	**		
25°C vs. 29°C	**	25°C vs. 29°C	ns	25°C vs. 29°C	****	25°C vs. 29°C	*	25°C vs. 29°C	ns		

Table 9.22 Statistical significance for comparisons shown in Figure 6.9

(*Z*)-11-Vaccenyl acetate	Significance	Heptacosane	Significance
18°C vs. 25°C	*	18°C vs. 25°C	ns
18°C vs. 29°C	ns	18°C vs. 29°C	**
25°C vs. 29°C	*	25°C vs. 29°C	*
Heneicosane	**Significance**	**Octacosane**	**Significance**
18°C vs. 25°C	****	18°C vs. 25°C	ns
18°C vs. 29°C	****	18°C vs. 29°C	ns
25°C vs. 29°C	ns	25°C vs. 29°C	ns
Docosane	**Significance**	**Nonacosane**	**Significance**
18°C vs. 25°C	****	18°C vs. 25°C	*
18°C vs. 29°C	****	18°C vs. 29°C	ns
25°C vs. 29°C	ns	25°C vs. 29°C	ns
Tricosane	**Significance**	**(*Z*)-9-tricosene**	**Significance**
18°C vs. 25°C	****	18°C vs. 25°C	****
18°C vs. 29°C	****	18°C vs. 29°C	***
25°C vs. 29°C	ns	25°C vs. 29°C	ns
Tetracosane	**Significance**	**(*Z*)-7-tricosene**	**Significance**
18°C vs. 25°C	ns	18°C vs. 25°C	***
18°C vs. 29°C	ns	18°C vs. 29°C	***
25°C vs. 29°C	ns	25°C vs. 29°C	ns
Pentacosane	**Significance**	**(*Z*)-7-pentacosene**	**Significance**
18°C vs. 25°C	****	18°C vs. 25°C	****
18°C vs. 29°C	****	18°C vs. 29°C	****
25°C vs. 29°C	ns	25°C vs. 29°C	ns
Hexacosane	**Significance**		
18°C vs. 25°C	ns		
18°C vs. 29°C	ns		
25°C vs. 29°C	ns		

Table 9.23 Statistical significance values for comparisons Figure 6.11B

(*Z*)-11-Vaccenyl acetate	Significance	Hexacosane	Significance	2-methylpentacosane	Significance	(*Z*)-9-tricosene	Significance	6-tetracosene	Significance
1 fly vs. 20 flies	****	1 fly vs. 20 flies	ns	1 fly vs. 20 flies	ns	1 fly vs. 20 flies	*	1 fly vs. 20 flies	ns
1 fly vs. 40 flies	****	1 fly vs. 40 flies	ns	1 fly vs. 40 flies	ns	1 fly vs. 40 flies	****	1 fly vs. 40 flies	****
1 fly vs. 60 flies	****	1 fly vs. 60 flies	*	1 fly vs. 60 flies	ns	1 fly vs. 60 flies	****	1 fly vs. 60 flies	****
1 fly vs. 80 flies	****	1 fly vs. 80 flies	***	1 fly vs. 80 flies	***	1 fly vs. 80 flies	****	1 fly vs. 80 flies	****
20 flies vs. 40 flies	ns	20 flies vs. 40 flies	ns	20 flies vs. 40 flies	**	20 flies vs. 40 flies	****	20 flies vs. 40 flies	****
20 flies vs. 60 flies	ns	20 flies vs. 60 flies	**	20 flies vs. 60 flies	**	20 flies vs. 60 flies	****	20 flies vs. 60 flies	****
20 flies vs. 80 flies	ns	20 flies vs. 80 flies	****	20 flies vs. 80 flies	****	20 flies vs. 80 flies	****	20 flies vs. 80 flies	****
40 flies vs. 60 flies	ns	40 flies vs. 60 flies	ns	40 flies vs. 60 flies	ns	40 flies vs. 60 flies	ns	40 flies vs. 60 flies	ns
40 flies vs. 80 flies	ns	40 flies vs. 80 flies	**	40 flies vs. 80 flies	ns	40 flies vs. 80 flies	ns	40 flies vs. 80 flies	**
60 flies vs. 80 flies	ns	60 flies vs. 80 flies	ns	60 flies vs. 80 flies	ns	60 flies vs. 80 flies	ns	60 flies vs. 80 flies	ns
Heneicosane	**Significance**	**Heptacosane**	**Significance**	**2-methylhexacosane**	**Significance**	**(*Z*)-7-tricosene**	**Significance**	**9-pentacosene**	**Significance**
1 fly vs. 20 flies	*	1 fly vs. 20 flies	ns	1 fly vs. 20 flies	ns	1 fly vs. 20 flies	ns	1 fly vs. 20 flies	ns
1 fly vs. 40 flies	****	1 fly vs. 40 flies	***	1 fly vs. 40 flies	ns	1 fly vs. 40 flies	****	1 fly vs. 40 flies	****
1 fly vs. 60 flies	****	1 fly vs. 60 flies	***	1 fly vs. 60 flies	ns	1 fly vs. 60 flies	****	1 fly vs. 60 flies	****
1 fly vs. 80 flies	****	1 fly vs. 80 flies	****	1 fly vs. 80 flies	***	1 fly vs. 80 flies	****	1 fly vs. 80 flies	****
20 flies vs. 40 flies	****	20 flies vs. 40 flies	ns	20 flies vs. 40 flies	ns	20 flies vs. 40 flies	****	20 flies vs. 40 flies	****
20 flies vs. 60 flies	****	20 flies vs. 60 flies	ns	20 flies vs. 60 flies	ns	20 flies vs. 60 flies	****	20 flies vs. 60 flies	****
20 flies vs. 80 flies	****	20 flies vs. 80 flies	**	20 flies vs. 80 flies	***	20 flies vs. 80 flies	****	20 flies vs. 80 flies	****
40 flies vs. 60 flies	ns	40 flies vs. 60 flies	ns	40 flies vs. 60 flies	ns	40 flies vs. 60 flies	ns	40 flies vs. 60 flies	ns
40 flies vs. 80 flies	ns	40 flies vs. 80 flies	ns	40 flies vs. 80 flies	ns	40 flies vs. 80 flies	ns	40 flies vs. 80 flies	**
60 flies vs. 80 flies	ns	60 flies vs. 80 flies	ns	60 flies vs. 80 flies	ns	60 flies vs. 80 flies	ns	60 flies vs. 80 flies	*
Docosane	**Significance**	**Nonacosane**	**Significance**	**2-methylheptacosane**	**Significance**	**5-tricosene**	**Significance**	**(*Z*)-7-pentacosene**	**Significance**
1 fly vs. 20 flies	ns	1 fly vs. 20 flies	*	1 fly vs. 20 flies	ns	1 fly vs. 20 flies	ns	1 fly vs. 20 flies	ns
1 fly vs. 40 flies	****	1 fly vs. 40 flies	***	1 fly vs. 40 flies	ns	1 fly vs. 40 flies	****	1 fly vs. 40 flies	****
1 fly vs. 60 flies	****	1 fly vs. 60 flies	****	1 fly vs. 60 flies	ns	1 fly vs. 60 flies	****	1 fly vs. 60 flies	****
1 fly vs. 80 flies	****	1 fly vs. 80 flies	****	1 fly vs. 80 flies	ns	1 fly vs. 80 flies	****	1 fly vs. 80 flies	****
20 flies vs. 40 flies	**	20 flies vs. 40 flies	ns	20 flies vs. 40 flies	ns	20 flies vs. 40 flies	****	20 flies vs. 40 flies	****
20 flies vs. 60 flies	****	20 flies vs. 60 flies	ns	20 flies vs. 60 flies	ns	20 flies vs. 60 flies	****	20 flies vs. 60 flies	****
20 flies vs. 80 flies	****	20 flies vs. 80 flies	***	20 flies vs. 80 flies	ns	20 flies vs. 80 flies	****	20 flies vs. 80 flies	****
40 flies vs. 60 flies	ns	40 flies vs. 60 flies	ns	40 flies vs. 60 flies	ns	40 flies vs. 60 flies	ns	40 flies vs. 60 flies	ns
40 flies vs. 80 flies	*	40 flies vs. 80 flies	*	40 flies vs. 80 flies	ns	40 flies vs. 80 flies	ns	40 flies vs. 80 flies	*
60 flies vs. 80 flies	ns	60 flies vs. 80 flies	ns	60 flies vs. 80 flies	ns	60 flies vs. 80 flies	ns	60 flies vs. 80 flies	ns
Tricosane	**Significance**	**2-methyldocosene**	**Significance**	**2-methyloctacosane**	**Significance**	**9-tetracosene**	**Significance**	**5-pentacosene**	**Significance**
1 fly vs. 20 flies	ns	1 fly vs. 20 flies	ns	1 fly vs. 20 flies	ns	1 fly vs. 20 flies	ns	1 fly vs. 20 flies	ns
1 fly vs. 40 flies	****	1 fly vs. 40 flies	****	1 fly vs. 40 flies	*	1 fly vs. 40 flies	****	1 fly vs. 40 flies	****
1 fly vs. 60 flies	****	1 fly vs. 60 flies	****	1 fly vs. 60 flies	*	1 fly vs. 60 flies	****	1 fly vs. 60 flies	****
1 fly vs. 80 flies	****	1 fly vs. 80 flies	****	1 fly vs. 80 flies	****	1 fly vs. 80 flies	****	1 fly vs. 80 flies	****
20 flies vs. 40 flies	**	20 flies vs. 40 flies	****	20 flies vs. 40 flies	ns	20 flies vs. 40 flies	****	20 flies vs. 40 flies	****
20 flies vs. 60 flies	**	20 flies vs. 60 flies	****	20 flies vs. 60 flies	ns	20 flies vs. 60 flies	****	20 flies vs. 60 flies	****
20 flies vs. 80 flies	****	20 flies vs. 80 flies	****	20 flies vs. 80 flies	***	20 flies vs. 80 flies	****	20 flies vs. 80 flies	****
40 flies vs. 60 flies	ns	40 flies vs. 60 flies	ns	40 flies vs. 60 flies	ns	40 flies vs. 60 flies	ns	40 flies vs. 60 flies	ns
40 flies vs. 80 flies	ns	40 flies vs. 80 flies	ns	40 flies vs. 80 flies	ns	40 flies vs. 80 flies	**	40 flies vs. 80 flies	**
60 flies vs. 80 flies	ns	60 flies vs. 80 flies	ns	60 flies vs. 80 flies	ns	60 flies vs. 80 flies	*	60 flies vs. 80 flies	ns
Tetracosane	**Significance**	**2-methyltricosane**	**Significance**	**2-methylnonacosane**	**Significance**	**8-tetracosene**	**Significance**	**9/7-heptacosene**	**Significance**
1 fly vs. 20 flies	ns	1 fly vs. 20 flies	ns	1 fly vs. 20 flies	ns	1 fly vs. 20 flies	ns	1 fly vs. 20 flies	ns
1 fly vs. 40 flies	*	1 fly vs. 40 flies	*	1 fly vs. 40 flies	***	1 fly vs. 40 flies	****	1 fly vs. 40 flies	****
1 fly vs. 60 flies	**	1 fly vs. 60 flies	**	1 fly vs. 60 flies	****	1 fly vs. 60 flies	****	1 fly vs. 60 flies	****
1 fly vs. 80 flies	****	1 fly vs. 80 flies	****	1 fly vs. 80 flies	****	1 fly vs. 80 flies	****	1 fly vs. 80 flies	****
20 flies vs. 40 flies	*	20 flies vs. 40 flies	**	20 flies vs. 40 flies	ns	20 flies vs. 40 flies	****	20 flies vs. 40 flies	****
20 flies vs. 60 flies	**	20 flies vs. 60 flies	**	20 flies vs. 60 flies	ns	20 flies vs. 60 flies	****	20 flies vs. 60 flies	****
20 flies vs. 80 flies	****	20 flies vs. 80 flies	****	20 flies vs. 80 flies	****	20 flies vs. 80 flies	****	20 flies vs. 80 flies	****
40 flies vs. 60 flies	ns	40 flies vs. 60 flies	ns	40 flies vs. 60 flies	ns	40 flies vs. 60 flies	ns	40 flies vs. 60 flies	ns
40 flies vs. 80 flies	*	40 flies vs. 80 flies	ns	40 flies vs. 80 flies	ns	40 flies vs. 80 flies	***	40 flies vs. 80 flies	****
60 flies vs. 80 flies	ns	60 flies vs. 80 flies	ns	60 flies vs. 80 flies	ns	60 flies vs. 80 flies	*	60 flies vs. 80 flies	**
Pentacosane	**Significance**	**2-methyltetracosane**	**Significance**	**7-docosene**	**Significance**	**7-tetracosene**	**Significance**		
1 fly vs. 20 flies	ns	1 fly vs. 20 flies	ns	1 fly vs. 20 flies	ns	1 fly vs. 20 flies	ns		
1 fly vs. 40 flies	**	1 fly vs. 40 flies	***	1 fly vs. 40 flies	****	1 fly vs. 40 flies	****		
1 fly vs. 60 flies	**	1 fly vs. 60 flies	**	1 fly vs. 60 flies	****	1 fly vs. 60 flies	****		
1 fly vs. 80 flies	****	1 fly vs. 80 flies	****	1 fly vs. 80 flies	****	1 fly vs. 80 flies	****		
20 flies vs. 40 flies	ns	20 flies vs. 40 flies	**	20 flies vs. 40 flies	****	20 flies vs. 40 flies	****		
20 flies vs. 60 flies	ns	20 flies vs. 60 flies	**	20 flies vs. 60 flies	****	20 flies vs. 60 flies	****		
20 flies vs. 80 flies	***	20 flies vs. 80 flies	****	20 flies vs. 80 flies	****	20 flies vs. 80 flies	****		
40 flies vs. 60 flies	ns	40 flies vs. 60 flies	ns	40 flies vs. 60 flies	ns	40 flies vs. 60 flies	ns		
40 flies vs. 80 flies	ns	40 flies vs. 80 flies	ns	40 flies vs. 80 flies	ns	40 flies vs. 80 flies	*		
60 flies vs. 80 flies	ns	60 flies vs. 80 flies	ns	60 flies vs. 80 flies	ns	60 flies vs. 80 flies	ns		

Table 9.24 Statistical information for comparisons made in Figure 6.11C

(*Z*)-11-Vaccenyl acetate	Significance	Hexacosane	Significance	2-methylpentacosane	Significance	(*Z*)-9-tricosene	Significance	6-tetracosene	Significance
1 fly vs. 20 flies	****	1 fly vs. 20 flies	****	1 fly vs. 20 flies	****	1 fly vs. 20 flies	**	1 fly vs. 20 flies	***
1 fly vs. 40 flies	****	1 fly vs. 40 flies	****	1 fly vs. 40 flies	****	1 fly vs. 40 flies	ns	1 fly vs. 40 flies	*
1 fly vs. 60 flies	****	1 fly vs. 60 flies	****	1 fly vs. 60 flies	****	1 fly vs. 60 flies	****	1 fly vs. 60 flies	***
1 fly vs. 80 flies	****	1 fly vs. 80 flies	****	1 fly vs. 80 flies	****	1 fly vs. 80 flies	****	1 fly vs. 80 flies	****
20 flies vs. 40 flies	ns	20 flies vs. 40 flies	ns	20 flies vs. 40 flies	ns	20 flies vs. 40 flies	ns	20 flies vs. 40 flies	ns
20 flies vs. 60 flies	****	20 flies vs. 60 flies	ns	20 flies vs. 60 flies	ns	20 flies vs. 60 flies	ns	20 flies vs. 60 flies	ns
20 flies vs. 80 flies	****	20 flies vs. 80 flies	ns	20 flies vs. 80 flies	ns	20 flies vs. 80 flies	*	20 flies vs. 80 flies	ns
40 flies vs. 60 flies	**	40 flies vs. 60 flies	ns	40 flies vs. 60 flies	ns	40 flies vs. 60 flies	ns	40 flies vs. 60 flies	ns
40 flies vs. 80 flies	****	40 flies vs. 80 flies	ns	40 flies vs. 80 flies	*	40 flies vs. 80 flies	***	40 flies vs. 80 flies	*
60 flies vs. 80 flies	**	60 flies vs. 80 flies	ns	60 flies vs. 80 flies	ns	60 flies vs. 80 flies	ns	60 flies vs. 80 flies	ns
Heneicosane	**Significance**	**Heptacosane**	**Significance**	**2-methylhexacosane**	**Significance**	**(*Z*)-7-tricosene**	**Significance**	**9-pentacosene**	**Significance**
1 fly vs. 20 flies	**	1 fly vs. 20 flies	*	1 fly vs. 20 flies	****	1 fly vs. 20 flies	****	1 fly vs. 20 flies	**
1 fly vs. 40 flies	ns	1 fly vs. 40 flies	ns	1 fly vs. 40 flies	****	1 fly vs. 40 flies	****	1 fly vs. 40 flies	ns
1 fly vs. 60 flies	***	1 fly vs. 60 flies	ns	1 fly vs. 60 flies	****	1 fly vs. 60 flies	****	1 fly vs. 60 flies	ns
1 fly vs. 80 flies	****	1 fly vs. 80 flies	**	1 fly vs. 80 flies	****	1 fly vs. 80 flies	****	1 fly vs. 80 flies	****
20 flies vs. 40 flies	ns	20 flies vs. 40 flies	ns	20 flies vs. 40 flies	ns	20 flies vs. 40 flies	ns	20 flies vs. 40 flies	ns
20 flies vs. 60 flies	ns	20 flies vs. 60 flies	ns	20 flies vs. 60 flies	ns	20 flies vs. 60 flies	ns	20 flies vs. 60 flies	ns
20 flies vs. 80 flies	ns	20 flies vs. 80 flies	ns	20 flies vs. 80 flies	*	20 flies vs. 80 flies	**	20 flies vs. 80 flies	ns
40 flies vs. 60 flies	ns	40 flies vs. 60 flies	ns	40 flies vs. 60 flies	ns	40 flies vs. 60 flies	ns	40 flies vs. 60 flies	ns
40 flies vs. 80 flies	**	40 flies vs. 80 flies	ns	40 flies vs. 80 flies	*	40 flies vs. 80 flies	***	40 flies vs. 80 flies	*
60 flies vs. 80 flies	ns	60 flies vs. 80 flies	ns	60 flies vs. 80 flies	ns	60 flies vs. 80 flies	ns	60 flies vs. 80 flies	ns
Docosane	**Significance**	**Nonacosane**	**Significance**	**2-methylheptacosane**	**Significance**	**5-tricosene**	**Significance**	**(*Z*)-7-pentacosene**	**Significance**
1 fly vs. 20 flies	****	1 fly vs. 20 flies	**	1 fly vs. 20 flies	ns	1 fly vs. 20 flies	**	1 fly vs. 20 flies	***
1 fly vs. 40 flies	**	1 fly vs. 40 flies	ns	1 fly vs. 40 flies	ns	1 fly vs. 40 flies	*	1 fly vs. 40 flies	*
1 fly vs. 60 flies	****	1 fly vs. 60 flies	ns	1 fly vs. 60 flies	ns	1 fly vs. 60 flies	****	1 fly vs. 60 flies	****
1 fly vs. 80 flies	****	1 fly vs. 80 flies	**	1 fly vs. 80 flies	*	1 fly vs. 80 flies	****	1 fly vs. 80 flies	****
20 flies vs. 40 flies	ns	20 flies vs. 40 flies	ns	20 flies vs. 40 flies	ns	20 flies vs. 40 flies	ns	20 flies vs. 40 flies	ns
20 flies vs. 60 flies	ns	20 flies vs. 60 flies	ns	20 flies vs. 60 flies	ns	20 flies vs. 60 flies	ns	20 flies vs. 60 flies	ns
20 flies vs. 80 flies	ns	20 flies vs. 80 flies	ns	20 flies vs. 80 flies	ns	20 flies vs. 80 flies	ns	20 flies vs. 80 flies	ns
40 flies vs. 60 flies	ns	40 flies vs. 60 flies	ns	40 flies vs. 60 flies	ns	40 flies vs. 60 flies	ns	40 flies vs. 60 flies	ns
40 flies vs. 80 flies	ns	40 flies vs. 80 flies	ns	40 flies vs. 80 flies	ns	40 flies vs. 80 flies	**	40 flies vs. 80 flies	*
60 flies vs. 80 flies	ns	60 flies vs. 80 flies	ns	60 flies vs. 80 flies	ns	60 flies vs. 80 flies	ns	60 flies vs. 80 flies	ns
Tricosane	**Significance**	**2-methyldocosene**	**Significance**	**2-methyloctacosane**	**Significance**	**9-tetracosene**	**Significance**	**5-pentacosene**	**Significance**
1 fly vs. 20 flies	****	1 fly vs. 20 flies	****	1 fly vs. 20 flies	**	1 fly vs. 20 flies	***	1 fly vs. 20 flies	**
1 fly vs. 40 flies	***	1 fly vs. 40 flies	**	1 fly vs. 40 flies	*	1 fly vs. 40 flies	ns	1 fly vs. 40 flies	ns
1 fly vs. 60 flies	****	1 fly vs. 60 flies	****	1 fly vs. 60 flies	***	1 fly vs. 60 flies	**	1 fly vs. 60 flies	ns
1 fly vs. 80 flies	****	1 fly vs. 80 flies	****	1 fly vs. 80 flies	****	1 fly vs. 80 flies	****	1 fly vs. 80 flies	**
20 flies vs. 40 flies	ns	20 flies vs. 40 flies	ns	20 flies vs. 40 flies	ns	20 flies vs. 40 flies	ns	20 flies vs. 40 flies	ns
20 flies vs. 60 flies	ns	20 flies vs. 60 flies	ns	20 flies vs. 60 flies	ns	20 flies vs. 60 flies	ns	20 flies vs. 60 flies	ns
20 flies vs. 80 flies	ns	20 flies vs. 80 flies	*	20 flies vs. 80 flies	ns	20 flies vs. 80 flies	ns	20 flies vs. 80 flies	ns
40 flies vs. 60 flies	ns	40 flies vs. 60 flies	ns	40 flies vs. 60 flies	ns	40 flies vs. 60 flies	ns	40 flies vs. 60 flies	ns
40 flies vs. 80 flies	*	40 flies vs. 80 flies	***	40 flies vs. 80 flies	ns	40 flies vs. 80 flies	**	40 flies vs. 80 flies	ns
60 flies vs. 80 flies	ns	60 flies vs. 80 flies	ns	60 flies vs. 80 flies	ns	60 flies vs. 80 flies	ns	60 flies vs. 80 flies	ns
Tetracosane	**Significance**	**2-methyltricosane**	**Significance**	**2-methylnonacosane**	**Significance**	**8-tetracosene**	**Significance**	**9/7-heptacosene**	**Significance**
1 fly vs. 20 flies	****	1 fly vs. 20 flies	****	1 fly vs. 20 flies	ns	1 fly vs. 20 flies	**	1 fly vs. 20 flies	ns
1 fly vs. 40 flies	****	1 fly vs. 40 flies	****	1 fly vs. 40 flies	ns	1 fly vs. 40 flies	ns	1 fly vs. 40 flies	ns
1 fly vs. 60 flies	****	1 fly vs. 60 flies	****	1 fly vs. 60 flies	ns	1 fly vs. 60 flies	ns	1 fly vs. 60 flies	ns
1 fly vs. 80 flies	****	1 fly vs. 80 flies	****	1 fly vs. 80 flies	**	1 fly vs. 80 flies	****	1 fly vs. 80 flies	ns
20 flies vs. 40 flies	ns	20 flies vs. 40 flies	ns	20 flies vs. 40 flies	ns	20 flies vs. 40 flies	ns	20 flies vs. 40 flies	***
20 flies vs. 60 flies	ns	20 flies vs. 60 flies	ns	20 flies vs. 60 flies	ns	20 flies vs. 60 flies	ns	20 flies vs. 60 flies	**
20 flies vs. 80 flies	ns	20 flies vs. 80 flies	**	20 flies vs. 80 flies	ns	20 flies vs. 80 flies	ns	20 flies vs. 80 flies	*
40 flies vs. 60 flies	ns	40 flies vs. 60 flies	ns	40 flies vs. 60 flies	ns	40 flies vs. 60 flies	ns	40 flies vs. 60 flies	ns
40 flies vs. 80 flies	ns	40 flies vs. 80 flies	***	40 flies vs. 80 flies	ns	40 flies vs. 80 flies	*	40 flies vs. 80 flies	ns
60 flies vs. 80 flies	ns	60 flies vs. 80 flies	ns	60 flies vs. 80 flies	ns	60 flies vs. 80 flies	ns	60 flies vs. 80 flies	ns
Pentacosane	**Significance**	**2-methyltetracosane**	**Significance**	**7-docosene**	**Significance**	**7-tetracosene**	**Significance**		
1 fly vs. 20 flies	***	1 fly vs. 20 flies	****	1 fly vs. 20 flies	*	1 fly vs. 20 flies	**		
1 fly vs. 40 flies	***	1 fly vs. 40 flies	****	1 fly vs. 40 flies	ns	1 fly vs. 40 flies	ns		
1 fly vs. 60 flies	***	1 fly vs. 60 flies	****	1 fly vs. 60 flies	*	1 fly vs. 60 flies	*		
1 fly vs. 80 flies	****	1 fly vs. 80 flies	****	1 fly vs. 80 flies	****	1 fly vs. 80 flies	****		
20 flies vs. 40 flies	ns	20 flies vs. 40 flies	ns	20 flies vs. 40 flies	ns	20 flies vs. 40 flies	ns		
20 flies vs. 60 flies	ns	20 flies vs. 60 flies	ns	20 flies vs. 60 flies	ns	20 flies vs. 60 flies	ns		
20 flies vs. 80 flies	ns	20 flies vs. 80 flies	**	20 flies vs. 80 flies	ns	20 flies vs. 80 flies	ns		
40 flies vs. 60 flies	ns	40 flies vs. 60 flies	ns	40 flies vs. 60 flies	ns	40 flies vs. 60 flies	ns		
40 flies vs. 80 flies	ns	40 flies vs. 80 flies	**	40 flies vs. 80 flies	***	40 flies vs. 80 flies	**		
60 flies vs. 80 flies	ns	60 flies vs. 80 flies	ns	60 flies vs. 80 flies	ns	60 flies vs. 80 flies	ns		

Table 9.25 Significance values for comparisons in Figure 6.12D

(*Z*)-11-Vaccenyl acetate	Significance	Hexacosane	Significance
1 fly vs. 20 flies	****	1 fly vs. 20 flies	*
1 fly vs. 40 flies	****	1 fly vs. 40 flies	*
1 fly vs. 60 flies	****	1 fly vs. 60 flies	****
1 fly vs. 80 flies	****	1 fly vs. 80 flies	****
20 flies vs. 40 flies	ns	20 flies vs. 40 flies	ns
20 flies vs. 60 flies	**	20 flies vs. 60 flies	ns
20 flies vs. 80 flies	****	20 flies vs. 80 flies	**
40 flies vs. 60 flies	ns	40 flies vs. 60 flies	ns
40 flies vs. 80 flies	**	40 flies vs. 80 flies	**
60 flies vs. 80 flies	ns	60 flies vs. 80 flies	ns
Heneicosane	**Significance**	**Heptacosane**	**Significance**
1 fly vs. 20 flies	*	1 fly vs. 20 flies	**
1 fly vs. 40 flies	****	1 fly vs. 40 flies	**
1 fly vs. 60 flies	****	1 fly vs. 60 flies	***
1 fly vs. 80 flies	****	1 fly vs. 80 flies	****
20 flies vs. 40 flies	ns	20 flies vs. 40 flies	ns
20 flies vs. 60 flies	**	20 flies vs. 60 flies	ns
20 flies vs. 80 flies	****	20 flies vs. 80 flies	*
40 flies vs. 60 flies	ns	40 flies vs. 60 flies	ns
40 flies vs. 80 flies	****	40 flies vs. 80 flies	*
60 flies vs. 80 flies	**	60 flies vs. 80 flies	ns
Docosane	**Significance**	**Nonacosane**	**Significance**
1 fly vs. 20 flies	**	1 fly vs. 20 flies	*
1 fly vs. 40 flies	****	1 fly vs. 40 flies	*
1 fly vs. 60 flies	****	1 fly vs. 60 flies	**
1 fly vs. 80 flies	****	1 fly vs. 80 flies	****
20 flies vs. 40 flies	ns	20 flies vs. 40 flies	ns
20 flies vs. 60 flies	*	20 flies vs. 60 flies	ns
20 flies vs. 80 flies	****	20 flies vs. 80 flies	*
40 flies vs. 60 flies	ns	40 flies vs. 60 flies	ns
40 flies vs. 80 flies	****	40 flies vs. 80 flies	**
60 flies vs. 80 flies	*	60 flies vs. 80 flies	ns
Tricosane	**Significance**	**(*Z*)-9-tricosene**	**Significance**
1 fly vs. 20 flies	***	1 fly vs. 20 flies	*
1 fly vs. 40 flies	****	1 fly vs. 40 flies	****
1 fly vs. 60 flies	****	1 fly vs. 60 flies	****
1 fly vs. 80 flies	****	1 fly vs. 80 flies	****
20 flies vs. 40 flies	ns	20 flies vs. 40 flies	**
20 flies vs. 60 flies	**	20 flies vs. 60 flies	****
20 flies vs. 80 flies	****	20 flies vs. 80 flies	****
40 flies vs. 60 flies	ns	40 flies vs. 60 flies	ns
40 flies vs. 80 flies	****	40 flies vs. 80 flies	****
60 flies vs. 80 flies	*	60 flies vs. 80 flies	*
Tetracosane	**Significance**	**(*Z*)-7-tricosene**	**Significance**
1 fly vs. 20 flies	**	1 fly vs. 20 flies	***
1 fly vs. 40 flies	****	1 fly vs. 40 flies	****
1 fly vs. 60 flies	****	1 fly vs. 60 flies	****
1 fly vs. 80 flies	****	1 fly vs. 80 flies	****
20 flies vs. 40 flies	ns	20 flies vs. 40 flies	**
20 flies vs. 60 flies	ns	20 flies vs. 60 flies	****
20 flies vs. 80 flies	****	20 flies vs. 80 flies	****
40 flies vs. 60 flies	ns	40 flies vs. 60 flies	ns
40 flies vs. 80 flies	***	40 flies vs. 80 flies	****
60 flies vs. 80 flies	*	60 flies vs. 80 flies	*
Pentacosane	**Significance**	**(*Z*)-7-pentacosene**	**Significance**
1 fly vs. 20 flies	**	1 fly vs. 20 flies	**
1 fly vs. 40 flies	****	1 fly vs. 40 flies	****
1 fly vs. 60 flies	****	1 fly vs. 60 flies	****
1 fly vs. 80 flies	****	1 fly vs. 80 flies	****
20 flies vs. 40 flies	ns	20 flies vs. 40 flies	**
20 flies vs. 60 flies	ns	20 flies vs. 60 flies	****
20 flies vs. 80 flies	***	20 flies vs. 80 flies	****
40 flies vs. 60 flies	ns	40 flies vs. 60 flies	ns
40 flies vs. 80 flies	**	40 flies vs. 80 flies	****
60 flies vs. 80 flies	ns	60 flies vs. 80 flies	**

Table 9.26 Statistical significance for comparisons shown in Figure 6.13B

(*Z*)-11-Vaccenyl acetate	Significance	Hexacosane	Significance	2-methylhexacosane	Significance	(*Z*)-7-tricosene	Significance	9-pentacosene	Significance
1 fly vs. 20 flies	*	1 fly vs. 20 flies	ns	1 fly vs. 20 flies	ns	1 fly vs. 20 flies	ns	1 fly vs. 20 flies	ns
1 fly vs. 80 flies	***	1 fly vs. 80 flies	ns	1 fly vs. 80 flies	**	1 fly vs. 80 flies	ns	1 fly vs. 80 flies	ns
20 flies vs. 80 flies	ns	20 flies vs. 80 flies	ns	20 flies vs. 80 flies	ns	20 flies vs. 80 flies	ns	20 flies vs. 80 flies	**
Heneicosane	**Significance**	**Heptacosane**	**Significance**	**2-methylheptacosane**	**Significance**	**5-tricosene**	**Significance**	**(*Z*)-7-pentacosene**	**Significance**
1 fly vs. 20 flies	ns	1 fly vs. 20 flies	ns	1 fly vs. 20 flies	*	1 fly vs. 20 flies	ns	1 fly vs. 20 flies	*
1 fly vs. 80 flies	ns	1 fly vs. 80 flies	ns	1 fly vs. 80 flies	**	1 fly vs. 80 flies	ns	1 fly vs. 80 flies	ns
20 flies vs. 80 flies	ns	20 flies vs. 80 flies	ns	20 flies vs. 80 flies	ns	20 flies vs. 80 flies	ns	20 flies vs. 80 flies	***
Docosane	**Significance**	**2-methyldocosene**	**Significance**	**2-methyloctacosane**	**Significance**	**9-tetracosene**	**Significance**	**5-pentacosene**	**Significance**
1 fly vs. 20 flies	ns	1 fly vs. 20 flies	ns	1 fly vs. 20 flies	ns	1 fly vs. 20 flies	ns	1 fly vs. 20 flies	****
1 fly vs. 80 flies	ns	1 fly vs. 80 flies	ns	1 fly vs. 80 flies	ns	1 fly vs. 80 flies	ns	1 fly vs. 80 flies	ns
20 flies vs. 80 flies	ns	20 flies vs. 80 flies	ns	20 flies vs. 80 flies	ns	20 flies vs. 80 flies	ns	20 flies vs. 80 flies	***
Tricosane	**Significance**	**2-methyltricosane**	**Significance**	**2-methylnonacosane**	**Significance**	**8-tetracosene**	**Significance**	**9/7-heptacosene**	**Significance**
1 fly vs. 20 flies	ns	1 fly vs. 20 flies	ns	1 fly vs. 20 flies	ns	1 fly vs. 20 flies	**	1 fly vs. 20 flies	**
1 fly vs. 80 flies	ns	1 fly vs. 80 flies	ns	1 fly vs. 80 flies	ns	1 fly vs. 80 flies	ns	1 fly vs. 80 flies	ns
20 flies vs. 80 flies	ns	20 flies vs. 80 flies	ns	20 flies vs. 80 flies	ns	20 flies vs. 80 flies	**	20 flies vs. 80 flies	****
Tetracosane	**Significance**	**2-methyltetracosane**	**Significance**	**7-docosene**	**Significance**	**7-tetracosene**	**Significance**		
1 fly vs. 20 flies	ns	1 fly vs. 20 flies	ns	1 fly vs. 20 flies	ns	1 fly vs. 20 flies	ns		
1 fly vs. 80 flies	ns	1 fly vs. 80 flies	*	1 fly vs. 80 flies	ns	1 fly vs. 80 flies	ns		
20 flies vs. 80 flies	ns	20 flies vs. 80 flies	ns	20 flies vs. 80 flies	ns	20 flies vs. 80 flies	ns		
Pentacosane	**Significance**	**2-methylpentacosane**	**Significance**	**(*Z*)-9-tricosene**	**Significance**	**6-tetracosene**	**Significance**		
1 fly vs. 20 flies	ns	1 fly vs. 20 flies	*	1 fly vs. 20 flies	ns	1 fly vs. 20 flies	****		
1 fly vs. 80 flies	ns	1 fly vs. 80 flies	**	1 fly vs. 80 flies	ns	1 fly vs. 80 flies	ns		
20 flies vs. 80 flies	ns	20 flies vs. 80 flies	ns	20 flies vs. 80 flies	ns	20 flies vs. 80 flies	*		

Table 9.27 Statistical information for comparisons shown in Figure 6.13C

(*Z*)-11-Vaccenyl acetate	Significance	Hexacosane	Significance	2-methylhexacosane	Significance	(*Z*)-7-tricosene	Significance	9-pentacosene	Significance
1 fly vs. 20 flies	****	1 fly vs. 20 flies	****	1 fly vs. 20 flies	****	1 fly vs. 20 flies	****	1 fly vs. 20 flies	****
1 fly vs. 80 flies	****	1 fly vs. 80 flies	****	1 fly vs. 80 flies	****	1 fly vs. 80 flies	****	1 fly vs. 80 flies	****
20 flies vs. 80 flies	****	20 flies vs. 80 flies	ns	20 flies vs. 80 flies	ns	20 flies vs. 80 flies	ns	20 flies vs. 80 flies	ns
Heneicosane	**Significance**	**Heptacosane**	**Significance**	**2-methylheptacosane**	**Significance**	**5-tricosene**	**Significance**	**(*Z*)-7-pentacosene**	**Significance**
1 fly vs. 20 flies	****	1 fly vs. 20 flies	****	1 fly vs. 20 flies	****	1 fly vs. 20 flies	****	1 fly vs. 20 flies	****
1 fly vs. 80 flies	****	1 fly vs. 80 flies	****	1 fly vs. 80 flies	****	1 fly vs. 80 flies	****	1 fly vs. 80 flies	****
20 flies vs. 80 flies	ns	20 flies vs. 80 flies	ns	20 flies vs. 80 flies	ns	20 flies vs. 80 flies	ns	20 flies vs. 80 flies	ns
Docosane	**Significance**	**2-methyldocosene**	**Significance**	**2-methyloctacosane**	**Significance**	**9-tetracosene**	**Significance**	**5-pentacosene**	**Significance**
1 fly vs. 20 flies	****	1 fly vs. 20 flies	****	1 fly vs. 20 flies	****	1 fly vs. 20 flies	****	1 fly vs. 20 flies	****
1 fly vs. 80 flies	****	1 fly vs. 80 flies	****	1 fly vs. 80 flies	****	1 fly vs. 80 flies	****	1 fly vs. 80 flies	****
20 flies vs. 80 flies	ns	20 flies vs. 80 flies	*	20 flies vs. 80 flies	ns	20 flies vs. 80 flies	ns	20 flies vs. 80 flies	ns
Tricosane	**Significance**	**2-methyltricosane**	**Significance**	**2-methylnonacosane**	**Significance**	**8-tetracosene**	**Significance**	**9/7-heptacosene**	**Significance**
1 fly vs. 20 flies	****	1 fly vs. 20 flies	****	1 fly vs. 20 flies	****	1 fly vs. 20 flies	****	1 fly vs. 20 flies	****
1 fly vs. 80 flies	****	1 fly vs. 80 flies	****	1 fly vs. 80 flies	****	1 fly vs. 80 flies	****	1 fly vs. 80 flies	****
20 flies vs. 80 flies	ns	20 flies vs. 80 flies	**	20 flies vs. 80 flies	ns	20 flies vs. 80 flies	ns	20 flies vs. 80 flies	**
Tetracosane	**Significance**	**2-methyltetracosane**	**Significance**	**7-docosene**	**Significance**	**7-tetracosene**	**Significance**		
1 fly vs. 20 flies	****	1 fly vs. 20 flies	****	1 fly vs. 20 flies	****	1 fly vs. 20 flies	****		
1 fly vs. 80 flies	****	1 fly vs. 80 flies	****	1 fly vs. 80 flies	****	1 fly vs. 80 flies	****		
20 flies vs. 80 flies	ns	20 flies vs. 80 flies	*	20 flies vs. 80 flies	ns	20 flies vs. 80 flies	ns		
Pentacosane	**Significance**	**2-methylpentacosane**	**Significance**	**(*Z*)-9-tricosene**	**Significance**	**6-tetracosene**	**Significance**		
1 fly vs. 20 flies	****	1 fly vs. 20 flies	****	1 fly vs. 20 flies	****	1 fly vs. 20 flies	****		
1 fly vs. 80 flies	****	1 fly vs. 80 flies	****	1 fly vs. 80 flies	****	1 fly vs. 80 flies	****		
20 flies vs. 80 flies	ns	20 flies vs. 80 flies	ns	20 flies vs. 80 flies	ns	20 flies vs. 80 flies	ns		

Table 9.28 Statistical significance for comparisons shown in Figure 6.14D

(*Z*)-11-Vaccenyl acetate	Significance	Hexacosane	Significance
1 fly vs. 20 flies	****	1 fly vs. 20 flies	****
1 fly vs. 80 flies	****	1 fly vs. 80 flies	****
20 flies vs. 80 flies	****	20 flies vs. 80 flies	ns
Heneicosane	**Significance**	**Heptacosane**	**Significance**
1 fly vs. 20 flies	****	1 fly vs. 20 flies	****
1 fly vs. 80 flies	****	1 fly vs. 80 flies	****
20 flies vs. 80 flies	ns	20 flies vs. 80 flies	ns
Docosane	**Significance**	**(*Z*)-9-tricosene**	**Significance**
1 fly vs. 20 flies	****	1 fly vs. 20 flies	****
1 fly vs. 80 flies	****	1 fly vs. 80 flies	****
20 flies vs. 80 flies	ns	20 flies vs. 80 flies	**
Tricosane	**Significance**	**(*Z*)-7-tricosene**	**Significance**
1 fly vs. 20 flies	****	1 fly vs. 20 flies	****
1 fly vs. 80 flies	****	1 fly vs. 80 flies	****
20 flies vs. 80 flies	ns	20 flies vs. 80 flies	**
Tetracosane	**Significance**	**(*Z*)-7-pentacosene**	**Significance**
1 fly vs. 20 flies	****	1 fly vs. 20 flies	****
1 fly vs. 80 flies	****	1 fly vs. 80 flies	****
20 flies vs. 80 flies	ns	20 flies vs. 80 flies	*
Pentacosane	**Significance**		
1 fly vs. 20 flies	****		
1 fly vs. 80 flies	****		
20 flies vs. 80 flies	ns		

Table 9.29 Statistical significance for data shown in Figure 6.15D

(*Z*)-11-Vaccenyl acetate	Significance	Hexacosane	Significance	2-methyltetracosane	Significance	7-docosene	Significance	7-tetracosene	Significance
1 fly vs. 20 flies	**	1 fly vs. 20 flies	ns	1 fly vs. 20 flies	****	1 fly vs. 20 flies	****	1 fly vs. 20 flies	****
1 fly vs. 80 flies	ns	1 fly vs. 80 flies	****	1 fly vs. 80 flies	ns	1 fly vs. 80 flies	**	1 fly vs. 80 flies	****
20 flies vs. 80 flies	****	20 flies vs. 80 flies	ns	20 flies vs. 80 flies	*	20 flies vs. 80 flies	****	20 flies vs. 80 flies	**
Heneicosane	**Significance**	**Heptacosane**	**Significance**	**2-methylpentacosane**	**Significance**	**(*Z*)-9-tricosene**	**Significance**	**6-tetracosene**	**Significance**
1 fly vs. 20 flies	****	1 fly vs. 20 flies	*	1 fly vs. 20 flies	**	1 fly vs. 20 flies	****	1 fly vs. 20 flies	****
1 fly vs. 80 flies	ns	1 fly vs. 80 flies	****	1 fly vs. 80 flies	ns	1 fly vs. 80 flies	****	1 fly vs. 80 flies	****
20 flies vs. 80 flies	****	20 flies vs. 80 flies	ns	20 flies vs. 80 flies	ns	20 flies vs. 80 flies	**	20 flies vs. 80 flies	**
Docosane	**Significance**	**Octacosane**	**Significance**	**2-methylhexacosane**	**Significance**	**(*Z*)-7-tricosene**	**Significance**	**9-pentacosene**	**Significance**
1 fly vs. 20 flies	****	1 fly vs. 20 flies	****	1 fly vs. 20 flies	ns	1 fly vs. 20 flies	****	1 fly vs. 20 flies	****
1 fly vs. 80 flies	**	1 fly vs. 80 flies	***	1 fly vs. 80 flies	ns	1 fly vs. 80 flies	**	1 fly vs. 80 flies	****
20 flies vs. 80 flies	*	20 flies vs. 80 flies	ns	20 flies vs. 80 flies	ns	20 flies vs. 80 flies	***	20 flies vs. 80 flies	ns
Tricosane	**Significance**	**Nonacosane**	**Significance**	**2-methylheptacosane**	**Significance**	**5-tricosene**	**Significance**	**(*Z*)-7-pentacosene**	**Significance**
1 fly vs. 20 flies	****	1 fly vs. 20 flies	***	1 fly vs. 20 flies	**	1 fly vs. 20 flies	****	1 fly vs. 20 flies	****
1 fly vs. 80 flies	**	1 fly vs. 80 flies	****	1 fly vs. 80 flies	*	1 fly vs. 80 flies	***	1 fly vs. 80 flies	****
20 flies vs. 80 flies	ns	20 flies vs. 80 flies	ns	20 flies vs. 80 flies	ns	20 flies vs. 80 flies	***	20 flies vs. 80 flies	ns
Tetracosane	**Significance**	**2-methyldocosene**	**Significance**	**2-methyloctacosane**	**Significance**	**9-tetracosene**	**Significance**	**5-pentacosene**	**Significance**
1 fly vs. 20 flies	**	1 fly vs. 20 flies	****	1 fly vs. 20 flies	*	1 fly vs. 20 flies	****	1 fly vs. 20 flies	****
1 fly vs. 80 flies	***	1 fly vs. 80 flies	ns	1 fly vs. 80 flies	***	1 fly vs. 80 flies	****	1 fly vs. 80 flies	****
20 flies vs. 80 flies	ns	20 flies vs. 80 flies	****	20 flies vs. 80 flies	ns	20 flies vs. 80 flies	*	20 flies vs. 80 flies	ns
Pentacosane	**Significance**	**2-methyltricosane**	**Significance**	**2-methylnonacosane**	**Significance**	**8-tetracosene**	**Significance**	**9/7-heptacosene**	**Significance**
1 fly vs. 20 flies	*	1 fly vs. 20 flies	****	1 fly vs. 20 flies	****	1 fly vs. 20 flies	****	1 fly vs. 20 flies	****
1 fly vs. 80 flies	***	1 fly vs. 80 flies	ns	1 fly vs. 80 flies	****	1 fly vs. 80 flies	****	1 fly vs. 80 flies	****
20 flies vs. 80 flies	ns	20 flies vs. 80 flies	**	20 flies vs. 80 flies	ns	20 flies vs. 80 flies	**	20 flies vs. 80 flies	ns

Table 9.30 Statistical significance for data shown in Figure 6.15E

(*Z*)-11-Vaccenyl acetate	Significance	Hexacosane	Significance	2-methyltetracosane	Significance	7-docosene	Significance	7-tetracosene	Significance
1 fly vs. 20 flies	****	1 fly vs. 20 flies	ns	1 fly vs. 20 flies	ns	1 fly vs. 20 flies	ns	1 fly vs. 20 flies	ns
1 fly vs. 80 flies	****	1 fly vs. 80 flies	ns	1 fly vs. 80 flies	****	1 fly vs. 80 flies	****	1 fly vs. 80 flies	**
20 flies vs. 80 flies	****	20 flies vs. 80 flies	ns	20 flies vs. 80 flies	*	20 flies vs. 80 flies	****	20 flies vs. 80 flies	***
Heneicosane	**Significance**	**Heptacosane**	**Significance**	**2-methylpentacosane**	**Significance**	**(*Z*)-9-tricosene**	**Significance**	**6-tetracosene**	**Significance**
1 fly vs. 20 flies	ns	1 fly vs. 20 flies	***	1 fly vs. 20 flies	ns	1 fly vs. 20 flies	****	1 fly vs. 20 flies	ns
1 fly vs. 80 flies	****	1 fly vs. 80 flies	ns	1 fly vs. 80 flies	***	1 fly vs. 80 flies	****	1 fly vs. 80 flies	****
20 flies vs. 80 flies	****	20 flies vs. 80 flies	ns	20 flies vs. 80 flies	ns	20 flies vs. 80 flies	**	20 flies vs. 80 flies	****
Docosane	**Significance**	**Octacosane**	**Significance**	**2-methylhexacosane**	**Significance**	**(*Z*)-7-tricosene**	**Significance**	**9-pentacosene**	**Significance**
1 fly vs. 20 flies	ns	1 fly vs. 20 flies	****	1 fly vs. 20 flies	ns	1 fly vs. 20 flies	**	1 fly vs. 20 flies	ns
1 fly vs. 80 flies	***	1 fly vs. 80 flies	****	1 fly vs. 80 flies	*	1 fly vs. 80 flies	****	1 fly vs. 80 flies	ns
20 flies vs. 80 flies	****	20 flies vs. 80 flies	ns	20 flies vs. 80 flies	ns	20 flies vs. 80 flies	**	20 flies vs. 80 flies	ns
Tricosane	**Significance**	**Nonacosane**	**Significance**	**2-methylheptacosane**	**Significance**	**5-tricosene**	**Significance**	**(Z)-7-pentacosene**	**Significance**
1 fly vs. 20 flies	ns	1 fly vs. 20 flies	****	1 fly vs. 20 flies	ns	1 fly vs. 20 flies	ns	1 fly vs. 20 flies	****
1 fly vs. 80 flies	**	1 fly vs. 80 flies	**	1 fly vs. 80 flies	ns	1 fly vs. 80 flies	****	1 fly vs. 80 flies	**
20 flies vs. 80 flies	ns	20 flies vs. 80 flies	ns	20 flies vs. 80 flies	ns	20 flies vs. 80 flies	****	20 flies vs. 80 flies	ns
Tetracosane	**Significance**	**2-methyldocosene**	**Significance**	**2-methyloctacosane**	**Significance**	**9-tetracosene**	**Significance**	**5-pentacosene**	**Significance**
1 fly vs. 20 flies	ns	1 fly vs. 20 flies	ns	1 fly vs. 20 flies	ns	1 fly vs. 20 flies	ns	1 fly vs. 20 flies	ns
1 fly vs. 80 flies	ns	1 fly vs. 80 flies	****	1 fly vs. 80 flies	ns	1 fly vs. 80 flies	*	1 fly vs. 80 flies	ns
20 flies vs. 80 flies	ns	20 flies vs. 80 flies	****	20 flies vs. 80 flies	ns	20 flies vs. 80 flies	**	20 flies vs. 80 flies	ns
Pentacosane	**Significance**	**2-methyltricosane**	**Significance**	**2-methylnonacosane**	**Significance**	**8-tetracosene**	**Significance**	**9/7-heptacosene**	**Significance**
1 fly vs. 20 flies	ns	1 fly vs. 20 flies	****	1 fly vs. 20 flies	****	1 fly vs. 20 flies	ns	1 fly vs. 20 flies	****
1 fly vs. 80 flies	ns	1 fly vs. 80 flies	****	1 fly vs. 80 flies	***	1 fly vs. 80 flies	***	1 fly vs. 80 flies	***
20 flies vs. 80 flies	ns	20 flies vs. 80 flies	*	20 flies vs. 80 flies	ns	20 flies vs. 80 flies	****	20 flies vs. 80 flies	ns

Table 9.31 Statistical information for data in Figure 6.16D

(*Z*)-11-Vaccenyl acetate	Significance	Hexacosane	Significance	(*Z*)-7-pentacosene	Significance
1 fly vs. 20 flies	****	1 fly vs. 20 flies	ns	1 fly vs. 20 flies	****
1 fly vs. 80 flies	****	1 fly vs. 80 flies	*	1 fly vs. 80 flies	****
20 flies vs. 80 flies	**	20 flies vs. 80 flies	ns	20 flies vs. 80 flies	*
Heneicosane	**Significance**	**Heptacosane**	**Significance**		
1 fly vs. 20 flies	***	1 fly vs. 20 flies	ns		
1 fly vs. 80 flies	***	1 fly vs. 80 flies	ns		
20 flies vs. 80 flies	ns	20 flies vs. 80 flies	ns		
Docosane	**Significance**	**Octacosane**	**Significance**		
1 fly vs. 20 flies	*	1 fly vs. 20 flies	****		
1 fly vs. 80 flies	**	1 fly vs. 80 flies	****		
20 flies vs. 80 flies	ns	20 flies vs. 80 flies	ns		
Tricosane	**Significance**	**Nonacosane**	**Significance**		
1 fly vs. 20 flies	**	1 fly vs. 20 flies	ns		
1 fly vs. 80 flies	**	1 fly vs. 80 flies	ns		
20 flies vs. 80 flies	ns	20 flies vs. 80 flies	ns		
Tetracosane	**Significance**	**(*Z*)-9-tricosene**	**Significance**		
1 fly vs. 20 flies	ns	1 fly vs. 20 flies	****		
1 fly vs. 80 flies	ns	1 fly vs. 80 flies	****		
20 flies vs. 80 flies	ns	20 flies vs. 80 flies	****		
Pentacosane	**Significance**	**(*Z*)-7-tricosene**	**Significance**		
1 fly vs. 20 flies	ns	1 fly vs. 20 flies	****		
1 fly vs. 80 flies	ns	1 fly vs. 80 flies	****		
20 flies vs. 80 flies	ns	20 flies vs. 80 flies	ns		

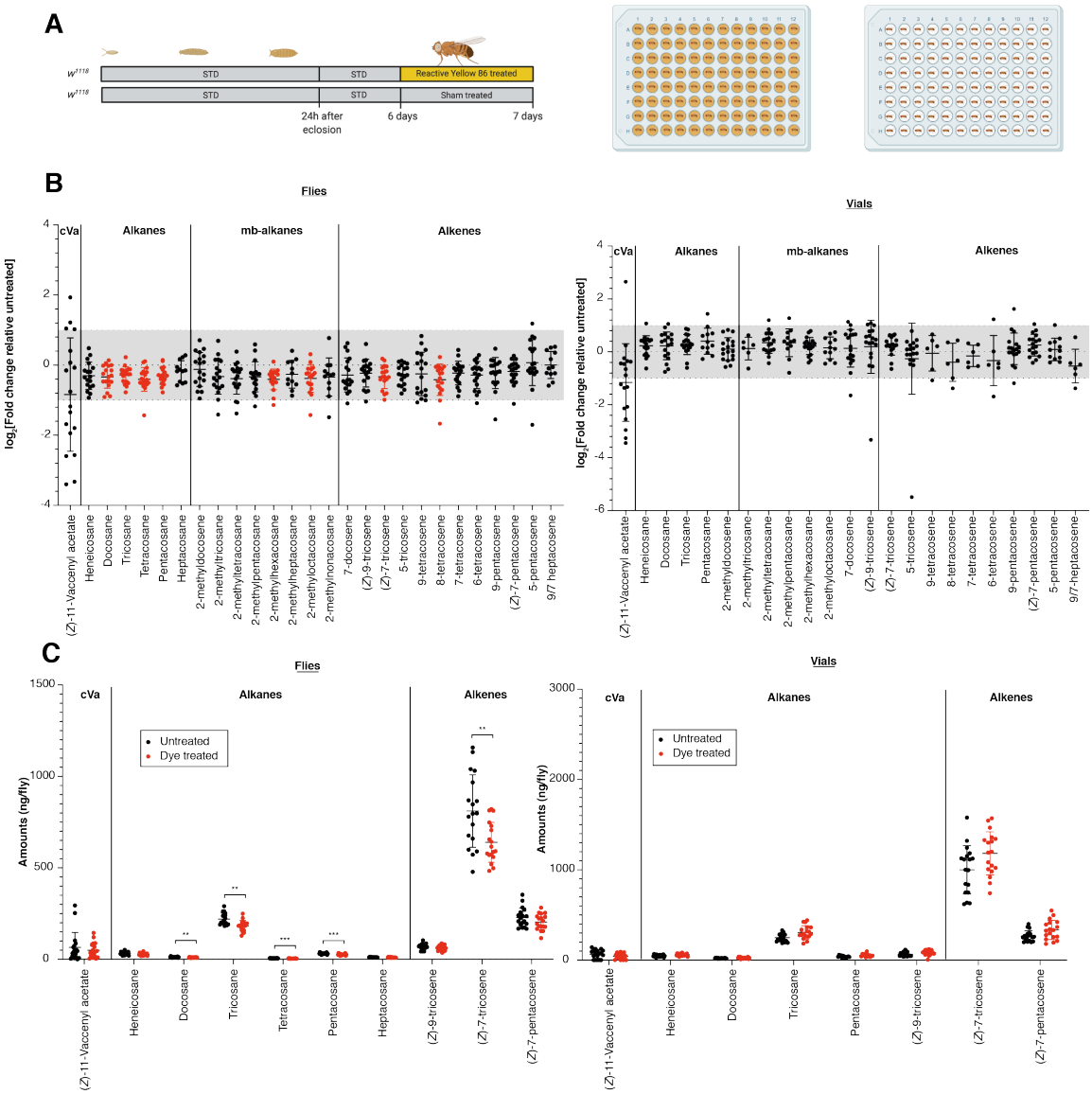

Figure 9.26 Relative and absolute hydrocarbon levels with induced grooming for Figure 6.17

A. Experimental schematic for dye treatment. Flies were coated with Reactive Yellow 86 dye or exposed to a similar “sham” treatment, then housed in fresh vials at a density of 1 fly per vial for 24 hours.
B. Relative abundance of hydrocarbons on the fly surface and fly vial in the dye treated experimental group plotted relative to the control “sham” group.
C. Absolute abundance of hydrocarbons on the fly surface and vial calculated with GC-MS relative to commercial standards of a known concentration.

9.6 Chapter 7 Supplementary Information

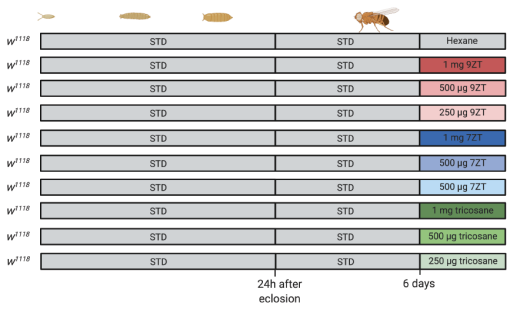

A

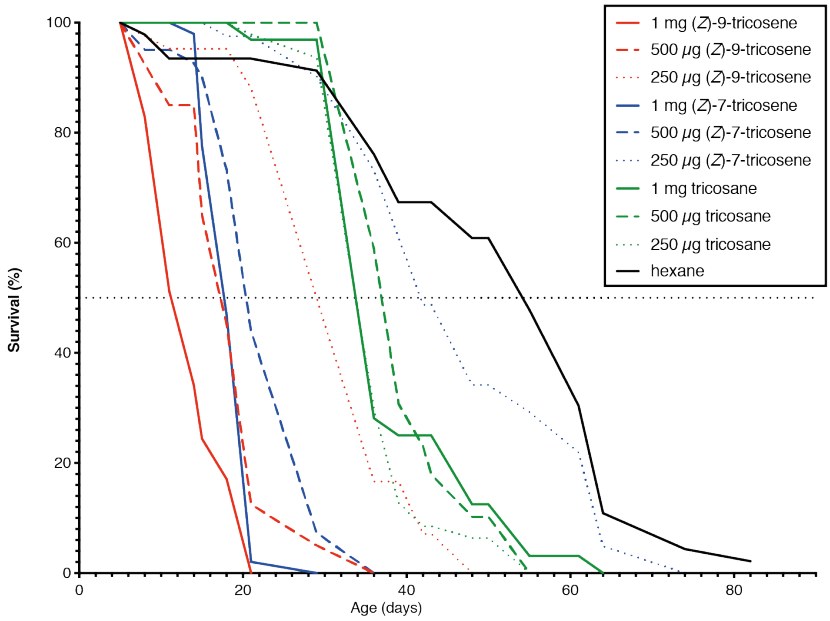

B

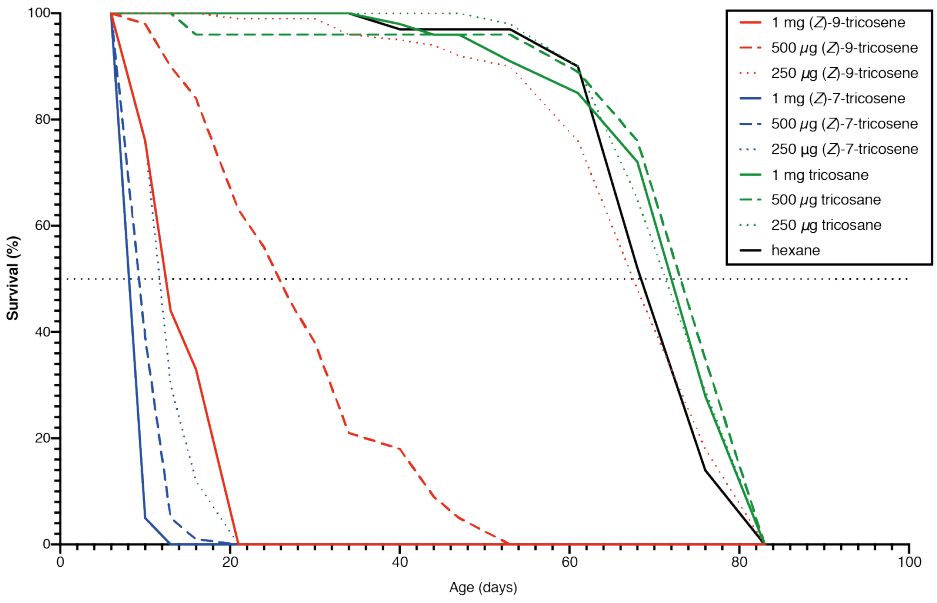

Figure 9.27 Dose-dependency of alkene toxicity: Additional replicates for Figure 7.1
Lifespan of male flies on a standard (STD) diet, exposed to varying concentrations of toxic alkenes (*Z*)-9-tricosene and (*Z*)-7-tricosene with varying concentrations of non-toxic alkane tricosane and hexane solvent as controls.
(**A**) 1 mg (*Z*)-9-tricosene n=41, median survival ~11 days; 500 μg (*Z*)-9-tricosene n=40, median survival ~17 days, 250 μg (*Z*)-9-tricosene n=42, median survival ~29 days; 1 mg (*Z*)-7-tricosene n=49, median survival ~18 days; 500 μg (*Z*)-7-tricosene n=41, median survival ~20 days, n=41, median survival ~42 days; 1 mg tricosane n=32, median survival ~34 days; 500 μg tricosane n=39, median survival ~37 days; 250 μg tricosane n=47, median survival ~34 days; hexane n=46, median survival ~54 days. Median survival of control conditions ~40 days. 1 mg (*Z*)-9-tricosene shows a ~3.5 fold decrease in survival, 500 μg (*Z*)-9-tricosene shows a ~2 fold decrease in survival and 250 μg (*Z*)-9-tricosene shows a ~1.4 fold decrease in survival. 1 mg (*Z*)-7-tricosene shows a ~2.2 fold decrease in survival, 500 μg (*Z*)-7-tricosene shows a ~2 fold decrease in survival and 250 μg (*Z*)-7-tricosene shows a ~1.2 fold decrease in survival.
(**B**) 1 mg (*Z*)-9-tricosene n=84, median survival ~12 days; 500 μg (*Z*)-9-tricosene n=80, median survival ~26 days, 250 μg (*Z*)-9-tricosene n=79, median survival ~67 days; 1 mg (*Z*)-7-tricosene n=83, median survival ~8 days; 500 μg (*Z*)-7-tricosene n=75, median survival ~9 days, 250 μg (*Z*)-7-tricosene n=83, median survival ~12 days; 1 mg tricosane n=47, median survival ~72 days; 500 μg tricosane n=54, median survival ~74 days; 250 μg tricosane n=49, median survival ~71 days; hexane n=63, median survival ~68 days. Median survival of control conditions ~71 days. 1 mg (*Z*)-9-tricosene shows a ~6 fold decrease in survival, 500 μg (*Z*)-9-tricosene shows a ~3 fold decrease in survival and 250 μg (*Z*)-9-tricosene shows a ~1.1 fold decrease in survival. 1 mg (*Z*)-7-tricosene shows a ~9 fold decrease in survival, 500 μg (*Z*)-7-tricosene shows a ~8.5 fold decrease in survival and 250 μg (*Z*)-7-tricosene shows a ~8 fold decrease in survival.

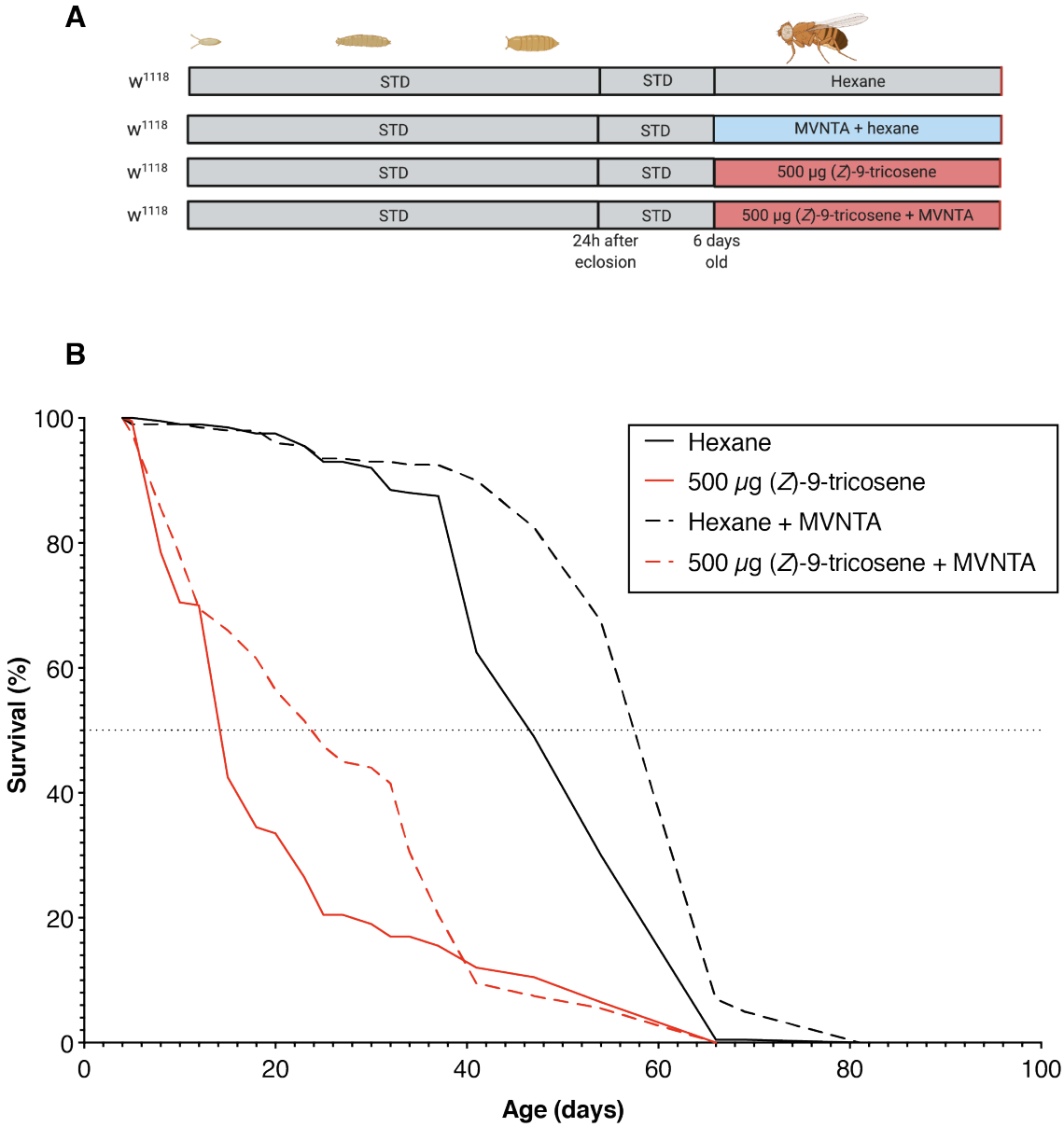

Figure 9.28 Survival with tricosene exposure combined with antibiotics: Additional replicate of lifespan in Figure 7.3

A. Lifespan of male flies with and without constant exposure to 500 µg (*Z*)-9-tricosene, with and without antibiotic exposure (MVNTA). Hexane is used as a solvent-only control for (*Z*)-9-tricosene treatment.
B. Hexane n=200, median survival ~46 days; 500µg (Z)-9-tricosene n=200, median survival ~14 days (~69.5% decrease in median survival compared with Hexane control); Hexane + MVNTA n=200, median survival ~58 days; 500µg (Z)-9-tricosene + MVNTA n=200, median survival ~24 days (~59% decrease in median survival compared with Hexane + MVNTA control)

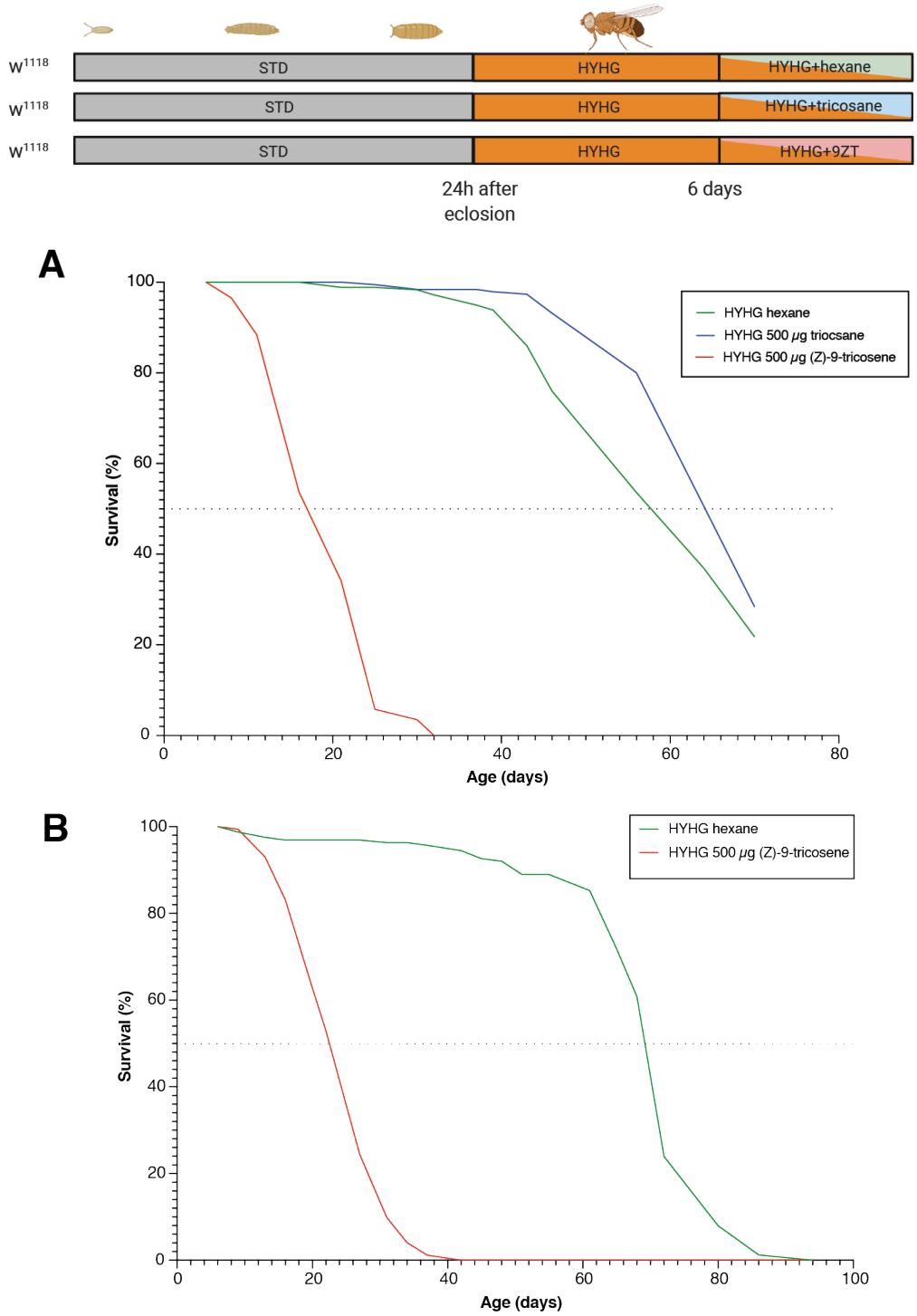

Figure 9.29 Survival with (*Z*)-9-tricosene exposure on HYHG diet: Additional replicates of lifespan in Figure 7.4

Lifespan of male flies on an adult high yeast high glucose (HYHG) diet exposed to the 500 µg (*Z*)-9-tricosene, with hexane solvent and 500 µg tricosane (non-toxic alkane) as control conditions.

A. HYHG hexane n=179, median survival ~58 days; HYHG 500 µg tricosane n=190, median survival ~64 days; HYHG 500 µg (*Z*)-9-tricosene n=173, median survival ~17 days. (*Z*)-9-tricosene shows a ~3-4 fold decrease in lifespan.

B. HYHG hexane n=163, median survival ~69 days; HYHG 500 µg (*Z*)-9-tricosene n=172, median survival ~22 days. (*Z*)-9-tricosene shows ~3 fold decrease in lifespan.

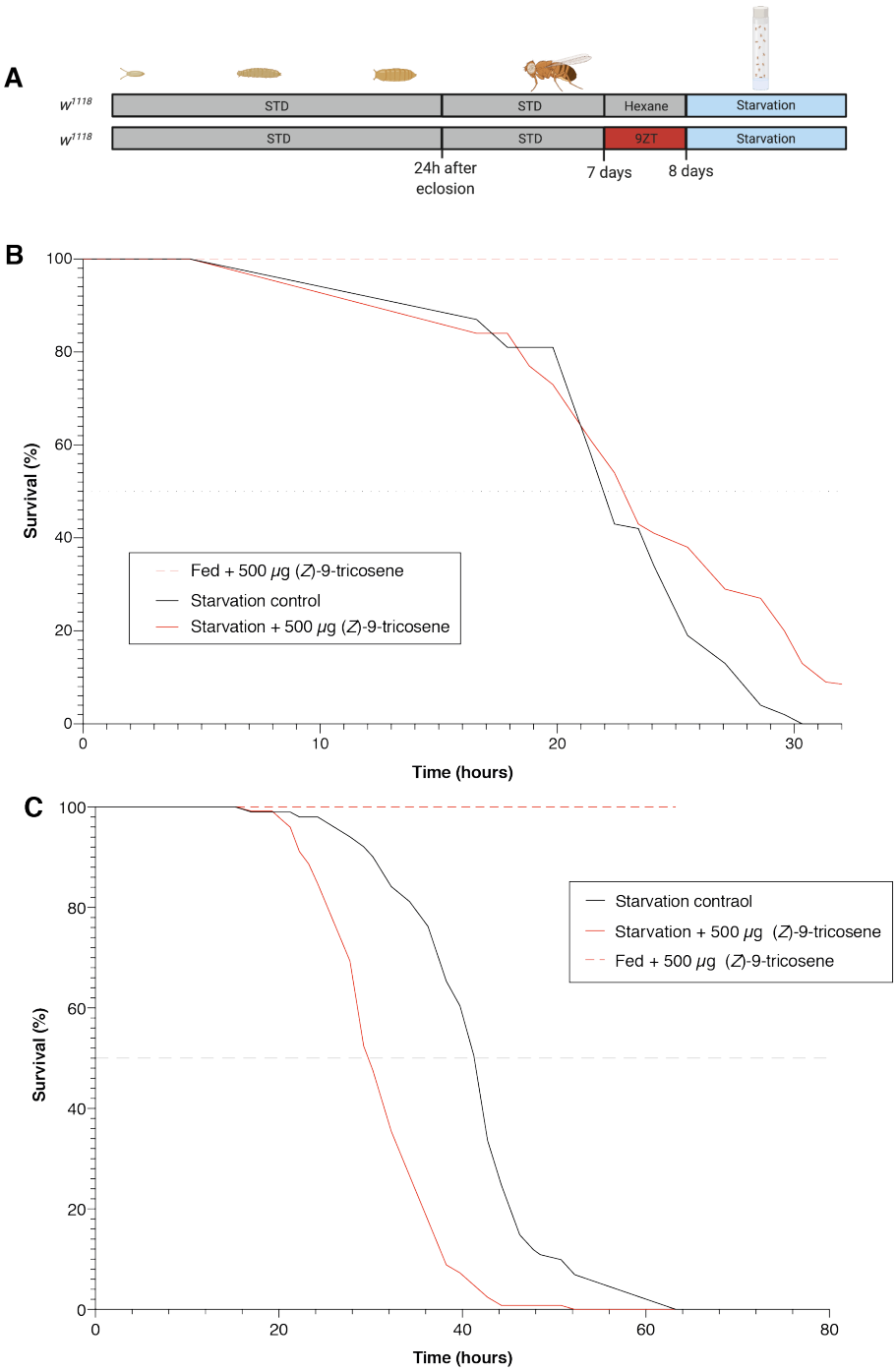

Figure 9.30 Exposure to (*Z*)-9-tricosene does not substantially affect starvation resistance: Additional replicates for Figure 7.10

A. Experimental schematic. Flies were raised on a standard diet until seven days of age, then in the experimental condition were treated with 500 μg (*Z*)-9-tricosene (9ZT) for 24 hours or a control of vials treated with the carrier solvent hexane alone. The tricosene was then removed and flies subjected to starvation on PBS/Agar medium until death.
B. Control n=53, median survival ~22h; 500 μg (*Z*)-9-tricosene n=56, median survival ~23h (+4.5% change in median survival).
C. Control n=101, median survival ~42h; 500 μg (*Z*)-9-tricosene n=124, median survival ~30h (-28.5% change in median survival).

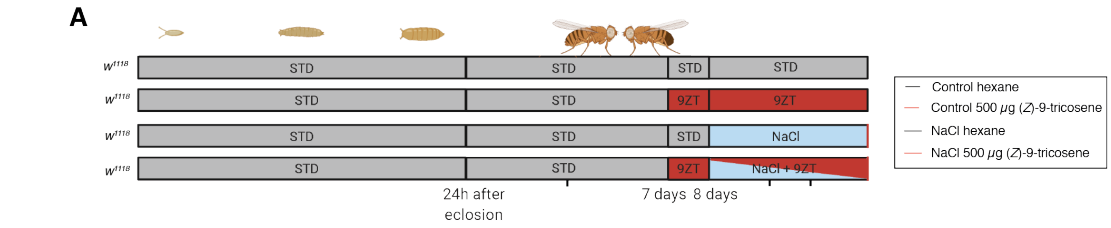
A
w1118
STD
STD
STD
STD
w1118
STD
STD
9ZT
9ZT
w1118
STD
STD
STD
NaCl
w1118
STD
STD
9ZT
NaCl + 9ZT
24h after eclosion
7 days 8 days
Control hexane
Control 500 µg (Z)-9-tricosene
NaCl hexane
NaCl 500 µg (Z)-9-tricosene

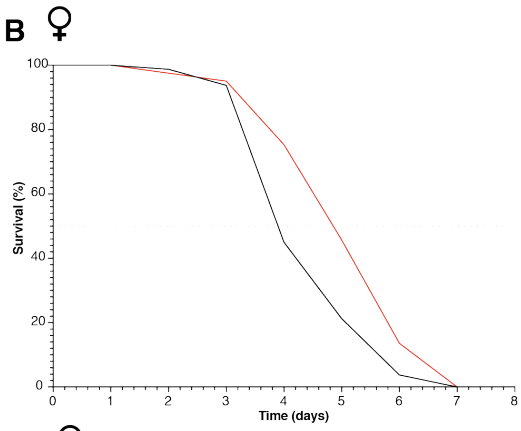
B ♀
Survival (%)
Time (days)

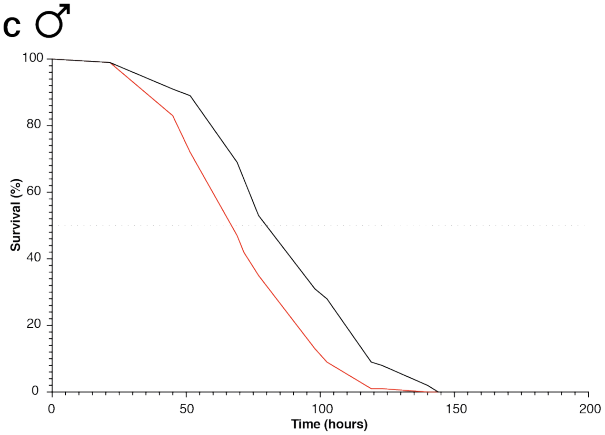
C ♂
Survival (%)
Time (hours)

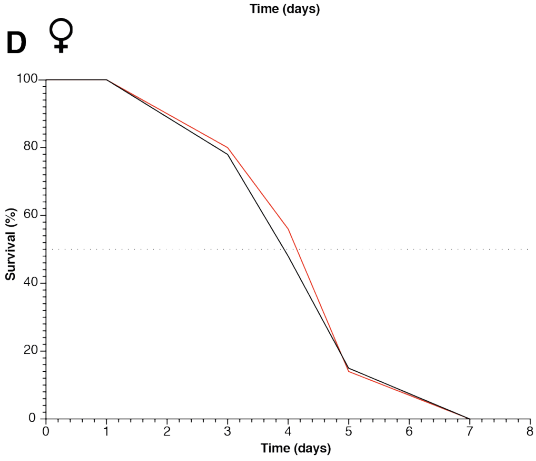
D ♀
Survival (%)
Time (days)

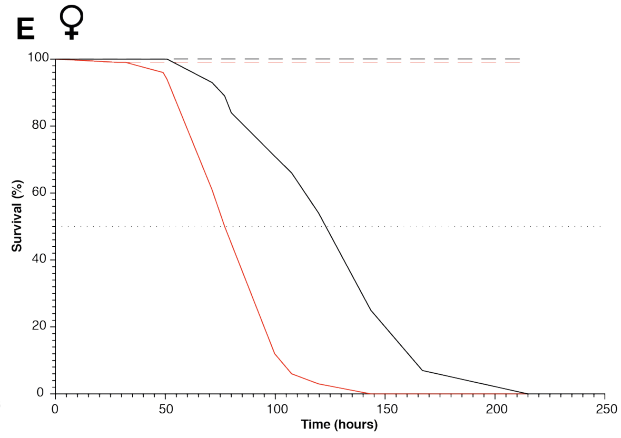
E ♀
Survival (%)
Time (hours)

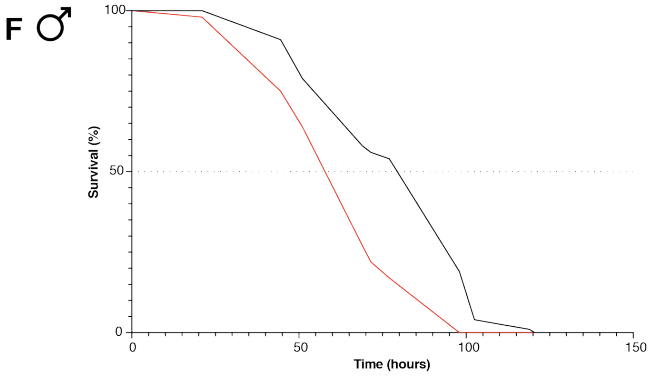
F ♂
Survival (%)
Time (hours)

Figure 9.31 Tricosene exposed male but not female flies are more sensitive to salt stress:

Additional replicates for Figure 7.12

A. Flies were exposed to a pre-treatment of 500 μg (*Z*)-9-tricosene or a control of hexane carrier solvent alone for 24 hours before the start of the assay. Flies were exposed to vials containing +/- 500 μg (*Z*)-9-tricosene and +/- 4% NaCl until 100% mortality was reached.
B. Control n=80, median survival ~3.8 days; 9ZT n=81, median survival ~4.8 days (+26% change in median survival).
C. Control n=138, median survival ~80h; 9ZT n=141, median survival ~65h (-18.75% change in median survival).
D. Control n=67, median survival ~4 days; 9ZT n=66, median survival ~4.2 days (+5% change in median survival).
E. Control n=95, median survival ~122h; 9ZT n=101, median survival ~75h (-38.5% change in median survival).
F. Control n=85, median survival ~80h; 9ZT n=83, median survival ~57h (-28.75% change in median survival).

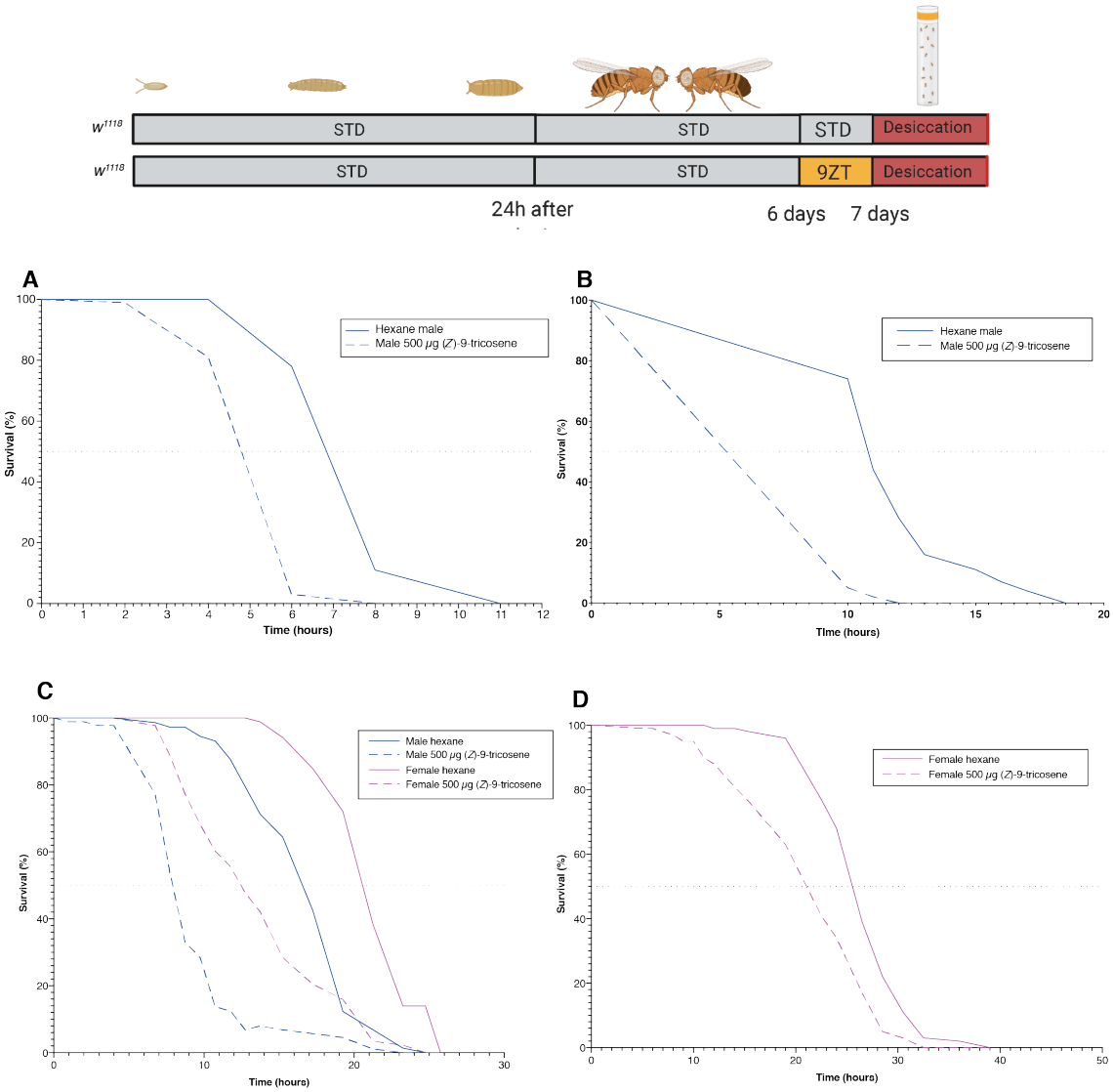

Figure 9.32 Desiccation resistance with (Z)-9-tricosene treatment: Additional replicates for Figure 7.15

Desiccation resistance measured for male and female w1118 iso31 flies in response to 24h exposure to 500 µg (*Z*)-9-tricosene.
A. Male hexane n=90, median survival ~6.8 hours; Male 500 µg (*Z*)-9-tricosene n=88, median survival ~4.8 hours (~29% decrease in median survival compared with male control).
B. Male hexane n=57, median survival ~10.75 hours; Male 500 µg (*Z*)-9-tricosene n=57, median survival ~5.5 hours (~49% decrease in median survival compared with male control).
C. Male hexane n=73, median survival ~16.5 hours; Male 500 µg (*Z*)-9-tricosene n=88, median survival ~8 hours (~51.5% decrease in median survival compared with male control); Female hexane n=86, median survival ~20.5 hours; Female 500 µg (*Z*)-9-tricosene n=88, median survival ~12.5 hours (~39% decrease in median survival compared with female control).
D. Female hexane n=228, median survival ~25.5 hours; Female 500 µg (*Z*)-9-tricosene n=226, median survival ~21 hours (~17.6% decrease in median survival compared with female control)

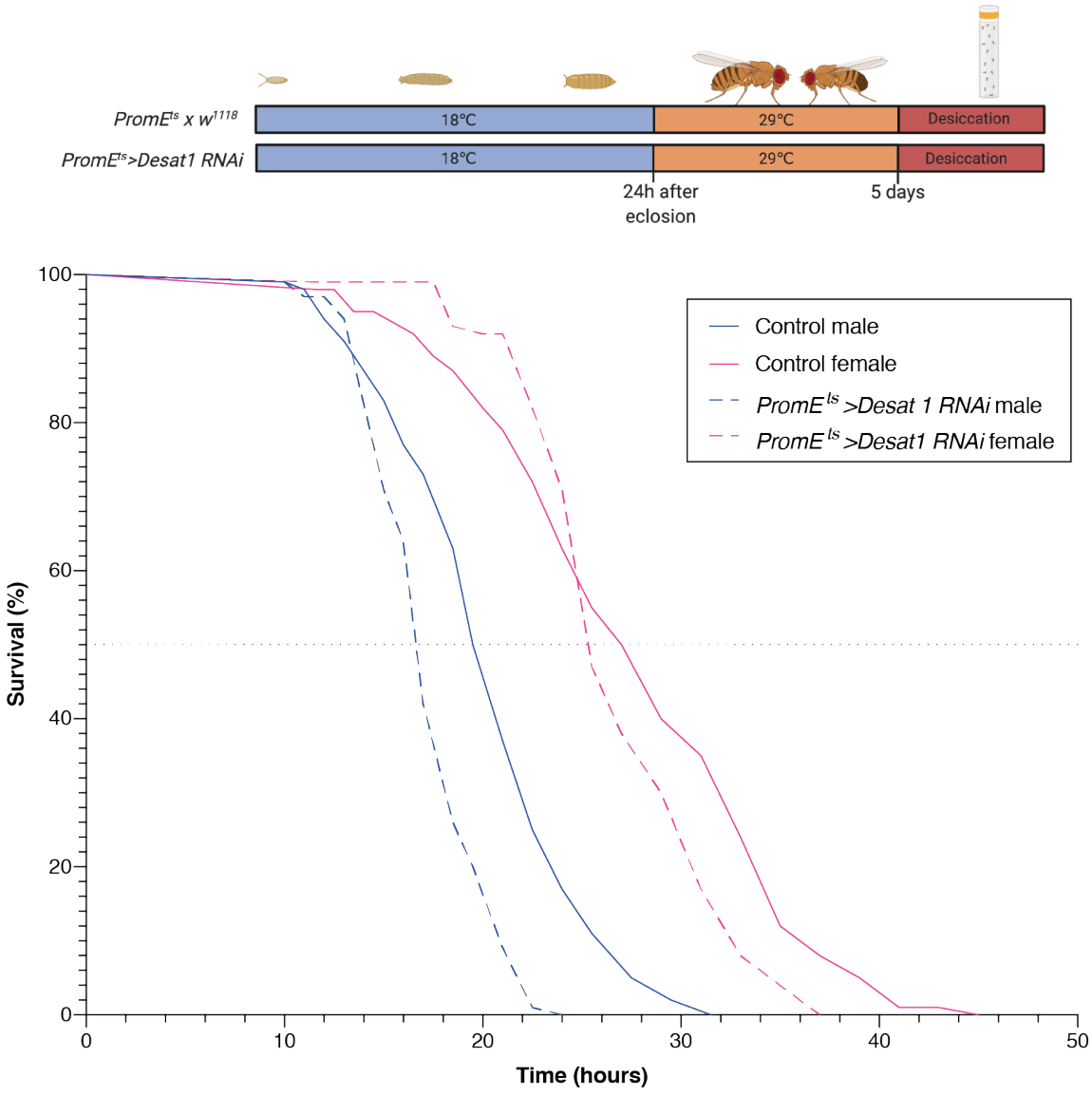

Figure 9.33 Desiccation resistance of oenocyte Desat1 knockdown: Additional replicate for Figure 7.16

Desiccation resistance measured in male and female *Drosophila* after five days RNAi induction at 29°C. Median survivals: Control male 19.75h n=76, control female 27h n=131, *PromE^{ts}>Desat1 RNAi* male 16h n=69 (19% decrease in median survival), *PromE^{ts}>Desat1 RNAi* female 25.5h n=76 (5.5% decrease in median survival).

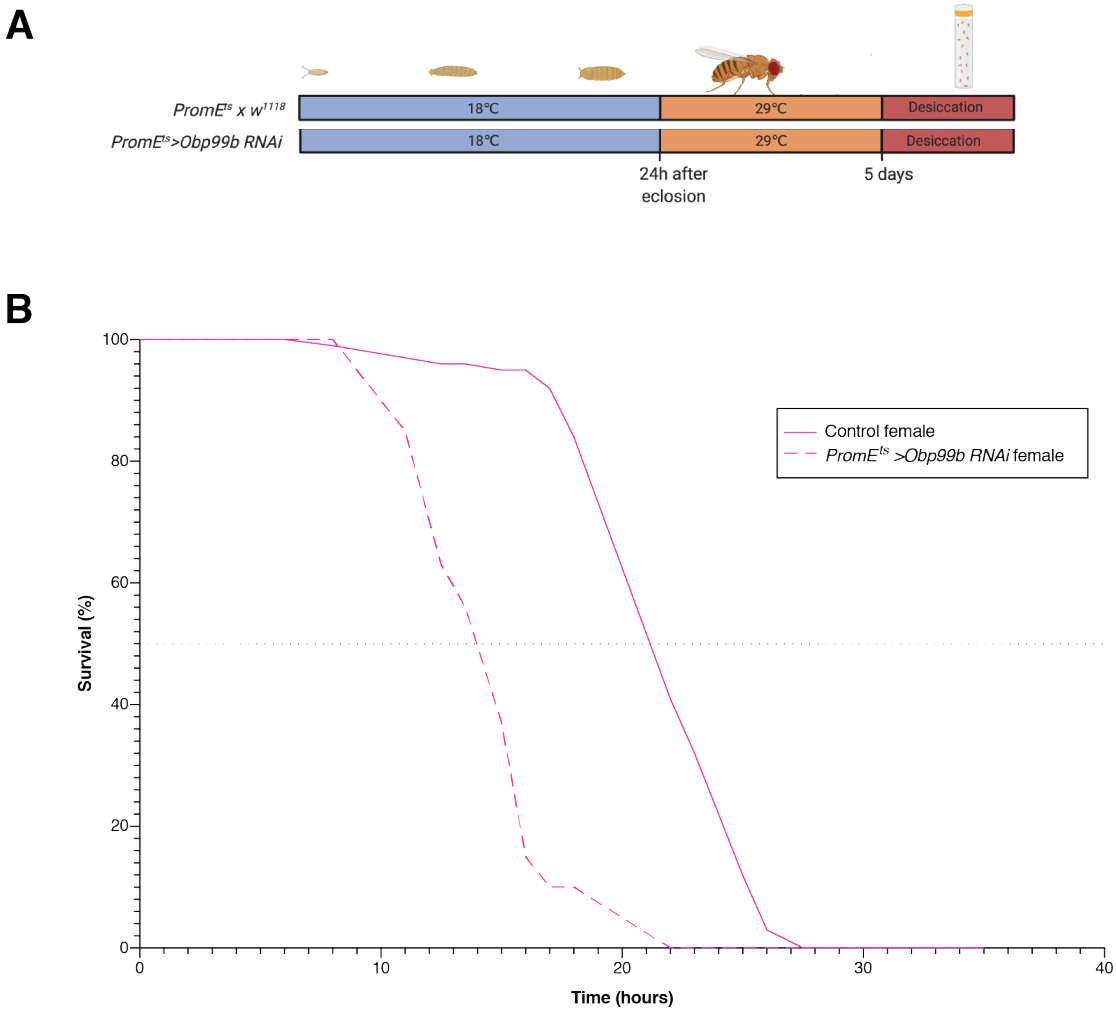

Figure 9.34 *Obp99b RNAi* decreases desiccation resistance: Additional replicate for Figure 7.23B

A. Experimental schematic. Flies were housed at 18°C during development before transfer to 29°C within 24 hours of eclosure. The desiccation survival was measured at 25°C five days after the temperature shift induced RNAi induction.
B. Desiccation survival of control *and PromE^{ts}>Obp99b RNAi* flies at 25°C. Median survivals are as follows: Control female 21h n=13, *Obp99b RNAi* female 14h n=7 (33% decrease in median survival).